SANDIA REPORT

SAND93–1986 • UC–721
Unlimited Release
Printed October 1995

Coupled Multiphase Flow and Closure Analysis of Repository Response to Waste-Generated Gas at the Waste Isolation Pilot Plant (WIPP)

G. A. Freeze, K. W. Larson, P. B. Davies

Prepared by
Sandia National Laboratories
Albuquerque, New Mexico 87185 and Livermore, California 94550
for the United States Department of Energy
under Contract DE-AC04-94AL85000

SF2900Q(8-81)

Issued by Sandia National Laboratories, operated for the United States Department of Energy by Sandia Corporation.

Available to DOE and DOE contractors from
Office of Scientific and Technical Information
PO Box 62
Oak Ridge, TN 37831

Prices available from (615) 576-8401, FTS 626-8401

Available to the public from
National Technical Information Service
US Department of Commerce
5285 Port Royal Rd
Springfield, VA 22161

NTIS price codes
Printed copy: A22
Microfiche copy: A01

SAND93-1986
Unlimited Release
Printed October 1995

Distribution
Category UC-721

Coupled Multiphase Flow and Closure Analysis of Repository Response to Waste-Generated Gas at the Waste Isolation Pilot Plant (WIPP)

G.A. Freeze and K.W. Larson
INTERA Inc.
Austin, Texas

P.B. Davies
Geohydrology Department
Sandia National Laboratories
Albuquerque, New Mexico 87185

ABSTRACT

A long-term assessment of the Waste Isolation Pilot Plant (WIPP) repository performance must consider the impact of gas generation resulting from the corrosion and microbial degradation of the emplaced waste. A multiphase fluid flow code, TOUGH2/EOS8, was adapted to model the processes of gas generation, disposal room creep closure, and multiphase (brine and gas) fluid flow, as well as the coupling between the three processes. System response to gas generation was simulated with a single, isolated disposal room surrounded by homogeneous halite containing two anhydrite interbeds, one above and one below the room. The interbeds were assumed to have flow connections to the room through high-permeability, excavation-induced fractures.

System behavior was evaluated by tracking four performance measures: (1) peak room pressure; (2) maximum brine volume in the room; (3) total mass of gas expelled from the room; and (4) the maximum gas migration distance in an interbed. A deterministic approach, including baseline and sensitivity simulations, was used. Baseline simulations used current best estimates of system parameters, selected through an evaluation of available data, to predict system response to gas generation under best-estimate conditions. Sensitivity simulations quantified the effects of parameter uncertainty by evaluating the change in the performance measures in

response to parameter variations. In the sensitivity simulations, a single parameter value was varied to its minimum and maximum values, representative of the extreme expected values, with all other parameters held at best- estimate values.

Simulation results indicated that (1) in the absence of interbed fracturing, disposal room pressures will exceed lithostatic, even at gas-generation rates representative of vapor-limited conditions, (2) under best-estimate conditions, brine availability was insufficient to fully exhaust the brine-dependent gas-generation potential, (3) the mass of gas expelled from the room and the gas migration distance are much more sensitive to the total mass of gas generated than to the gas-generation rate, and (4) the halite properties are important to gas migration because gas movement in the interbeds is limited by the displacement of interbed brine into the surrounding halite.

Sensitivity simulations identified the following parameters as important to gas expulsion and migration away from a disposal room: interbed porosity; interbed permeability; gas-generation potential; halite permeability; and interbed threshold pressure. The uncertainty in multiphase flow parameters was not adequately characterized because of the lack of WIPP-specific data. Simulations also showed that the inclusion of interbed fracturing and a disturbed rock zone had a significant impact on system performance.

The TOUGH2/EOS8 deterministic simulation and sensitivity results were similar to stochastic results obtained by WIPP Performance Assessment from a repository-scale model. Because the deterministic approach allows conceptual models to be quantitatively evaluated at a sub-system level using specific mechanistically-based performance measures, rather than at the level of overall repository performance, it can be used to support WIPP Performance Assessment in sensitivity and uncertainty simulations and in choices between alternative conceptual models. However, it can not be used to address regulatory compliance.

ACKNOWLEDGEMENTS

The authors thank Steve Webb, Karsten Pruess, and George Moridis for their support of the TOUGH2/EOS8 code. Helpful review comments were provided by Palmer Vaughn, Steve Webb, Karsten Pruess, Al Lappin, and Mike Stone.

The authors also recognize the contributions of Mark Reeves and Toya Jones for early scoping simulations with the ECLIPSE code, Toya Jones for compiling parts of Appendix A, and Tina Johnson, Tricia Johnson, Steve Womack, and Lydia Biggs for figure preparation.

CONTENTS

CONTENTS (Continued)

CONTENTS (Continued)

Figures

Figures (Continued)

Figures (Continued)

Figures (Continued)

Figures (Continued)

Figures (Continued)

Figures (Continued)

Figures (Continued)

Tables

1.0 INTRODUCTION

The Waste Isolation Pilot Plant (WIPP) is a U.S. Department of Energy (DOE) research and development facility designed to demonstrate the safe underground disposal of transuranic (TRU) waste from U.S. defense-related activities. For regulatory compliance, the DOE must reasonably demonstrate that there will be no release of radioactive or hazardous constituents from the repository in violation of regulatory standards. If it can be demonstrated to the U.S. Environmental Protection Agency (EPA) that the WIPP is in compliance with relevant regulatory standards, then disposal of TRU wastes being generated by and stored at various DOE facilities will occur.

The WIPP repository is located 655 m underground, within the Salado Formation. The Salado Formation is comprised of beds of pure and impure halite with thin interbeds of anhydrite and associated clay seams. Elevated repository pressures in response to gas generation from post-operational corrosion and degradation by microbial activity of the emplaced waste could increase gas expulsion from the repository and produce fracturing in near-repository anhydrite interbeds, enhancing contaminant movement towards regulatory boundaries. An assessment of the long-term performance of the WIPP repository must therefore consider the impact of waste-generated gas.

Experimental and analytic studies are currently being performed to evaluate the physical and chemical processes that control gas generation and repository response to gas pressurization. Preliminary results from these studies suggest that gas generation and the corresponding repository response are characterized by a strong coupling between chemical, hydrologic, and geomechanical processes (Davies et al., 1992; Webb, 1992a). For example, gas generation may be controlled to a large degree by the availability of brine. Brine availability, in turn, is controlled by the rate at which brine is consumed by the corrosion reactions, by the hydrologic characteristics governing the rate of brine inflow from the surrounding rock, and by the rate at which gas pressure builds in the repository thereby opposing brine inflow. Gas pressure in the repository is strongly influenced not only by the gas-generation rate, but also by gas release from the repository into the surrounding rock and by changes in gas-storage volume caused by creep closure and/or expansion of the repository. Repository assessment must consider the chemical processes (gas generation), hydrologic processes (multiphase brine and gas flow), and

geomechanical processes (interbed fracture, room closure and expansion due to salt creep) as well as the complex coupling between the processes.

The WIPP Performance Assessment (PA) Department (1992b) developed a computer model to evaluate total repository performance which incorporates conceptual models to represent a large number of physical processes. Due to the large number of physical processes included in the WIPP PA model, simplified conceptualizations were used to represent some of the processes. A stochastic (Monte Carlo) approach was used to predict repository behavior and to perform sensitivity analyses. Overall repository performance is evaluated by comparing complementary cumulative distribution functions for several performance measures with regulatory containment requirements.

This study uses a deterministic framework to focus on room-scale conceptual models of the processes of gas generation, disposal room closure and expansion, and multiphase fluid flow and on the coupling between them. Freeze et al. (1995) evaluated several alternative methods for approximating room closure and expansion in a numerical model of multiphase flow, TOUGH2/EOS8. Two methods, boundary backstress and pressure-time-porosity line interpolation (pressure lines), were found to most accurately simulate the coupled processes of gas generation, room closure and expansion, and multiphase flow. In this study, these two coupling methods are used:

- To simulate repository behavior and brine and gas movement through the Salado Formation using the current "best estimates" of system parameters;
- To examine the sensitivity of system behavior to variations in system parameters over their expected ranges;
- To identify uncertain aspects of the modeling approach and develop alternative conceptual models where justified by the present lack of data and/or differing ideas regarding the important physical processes;
- To identify the limitations of our knowledge of system behavior and the corresponding limitations of the process couplings; and
- To quantify parameter sensitivity and importance to provide feedback to experimental programs.

This deterministic approach uses best estimates of system parameters. A single best-estimate value was selected for each parameter through an evaluation of available data. The best-estimate value represents a most likely value, but has no statistical significance (i.e., it is not a calculated mean, median, average, or expected value). The deterministic approach, focusing on only a few interdependent processes, was used to evaluate and, if possible, provide justification for the simplified implementations used in the WIPP PA model. This approach also demonstrates a methodology by which multiple conceptual models can be quantitatively evaluated at a sub-system level using specific mechanistically-based performance measures, rather than at the level of overall repository performance.

This report provides an introductory discussion of issues related to waste-generated gas and its impact on repository performance (Section 1), describes the model conceptualization for coupling multiphase flow with repository creep closure (Section 2), summarizes the system parameters required by the numerical model and discusses the selection of best- estimate parameters (Section 3), and presents an analysis of the results of deterministic simulations in which the model was applied to predict the response of the WIPP repository and surrounding Salado Formation to waste-generated gas. Two sets of simulations were performed: baseline simulations (Section 4), which predicted system behavior under best- estimate conditions; and sensitivity simulations (Section 5), which examined system response to variations in system parameters. Conclusions about system behavior and process coupling derived from the model study are presented in Section 6.

Because of the large number of system parameters, only a parameter summary was presented in Section 3. A detailed discussion of the rationales for the selection of the parameter best estimates and sensitivity ranges used in the model was reserved for Appendix A. Parameter selection was based on data collected through June, 1993. Model development was based on information available up to August, 1993. Due to the large number of simulations that were performed, simulation results are summarized in Sections 4 and 5, with detailed results from all simulations presented in Appendix B. The model development and simulations discussed in this report were performed by INTERA Inc., Albuquerque, New Mexico and Austin, Texas, under the technical direction of Sandia National Laboratories, Albuquerque, New Mexico.

1.1 Background

The WIPP is located approximately 30 miles (50 km) east of Carlsbad in southeastern New Mexico (Figure 1-1). The WIPP is situated in the northern part of the Delaware Basin, which contains several Permian-age sedimentary deposits (Figure 1-2). Site characterization activities at the WIPP began in the mid 1970's and excavations at the repository horizon began in the early 1980's. Site characterization investigations have focused on the Salado Formation, which contains the repository, on the water-bearing units of the Rustler Formation (primarily the Culebra Dolomite), which overlay the Salado Formation, and on the occurrence of pressurized brine in the Castile Formation, which underlies the Salado Formation. This investigation considers only the Salado Formation.

1.1.1 Repository Configuration

The WIPP repository lies in the lower portion of the Salado Formation at a depth of approximately 655 m below land surface. The underground facility consists of an experimental area at the north end and a waste storage area at the south end. Waste will be emplaced in rooms within the waste storage area. The waste storage area is designed to have eight waste disposal panels, each of which will contain seven rooms (Figure 1-3). Currently, only Waste Panel 1 has been excavated. Future waste panels are designed to be similar to Panel 1. Each disposal room is approximately 4 m high, 10 m wide, and 91 m long. Waste disposal rooms within a panel will be separated by salt pillars approximately 30 m in width. Access between disposal rooms, panels, and within the experimental area are through a network of tunnel-like drifts. Four shafts provide access to the surface. Repository excavation is designed to follow a single stratigraphic horizon. Because the Salado Formation is dips gently (less than 1° slope) to the southeast, the north end of the repository will be approximately 10 m higher than the south end (WIPP PA Division, 1991).

Under current operational plans, each disposal room is to be filled with 6,804 55-gallon drums and/or steel boxes (Beraun and Davies, 1992) containing contact-handled (CH) transuranic (TRU) waste, primarily metals, glass, combustibles, and process sludges (Butcher, 1989). A small volume of remote-handled (RH) waste will be inserted into individually drilled and sealed horizontal boreholes in the room walls. Following waste emplacement, each room will be backfilled above and between the waste drums with crushed salt or a crushed salt and

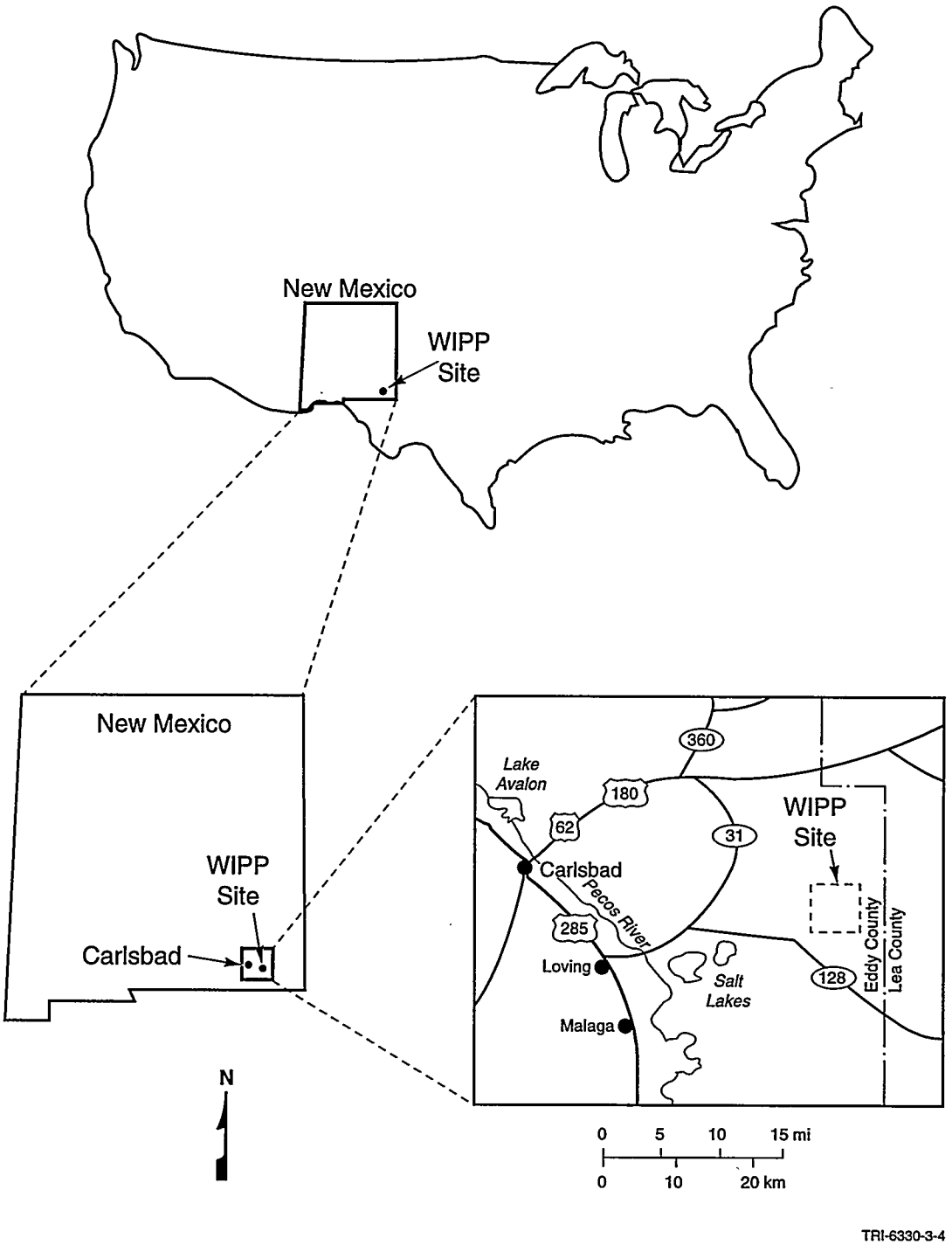

Figure 1-1. Location of the Waste Isolation Pilot Plant (after Beauheim et al., 1991).

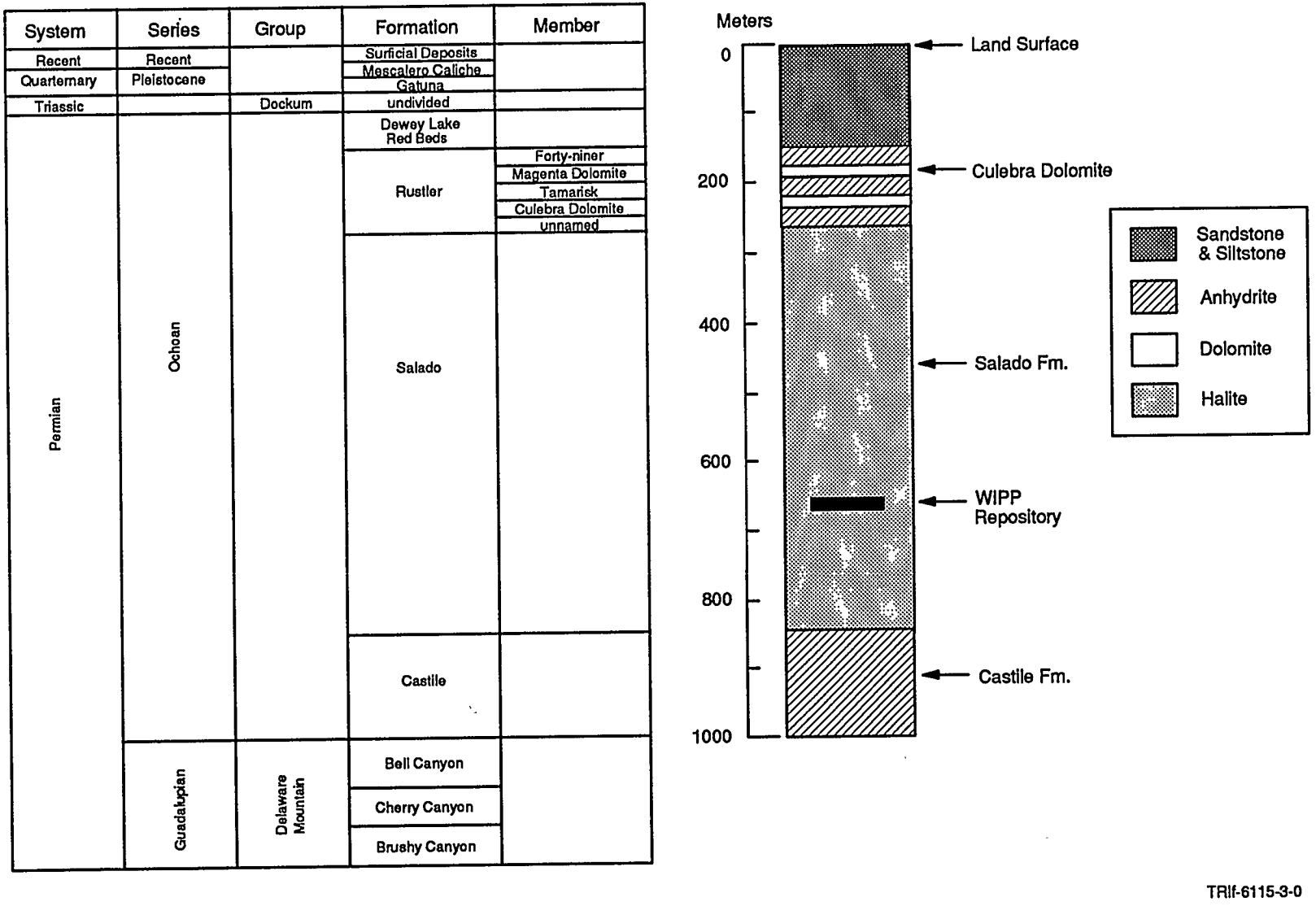

Figure 1-2. Stratigraphic section in the vicinity of the Waste Isolation Pilot Plant (after Davies et al., 1992).

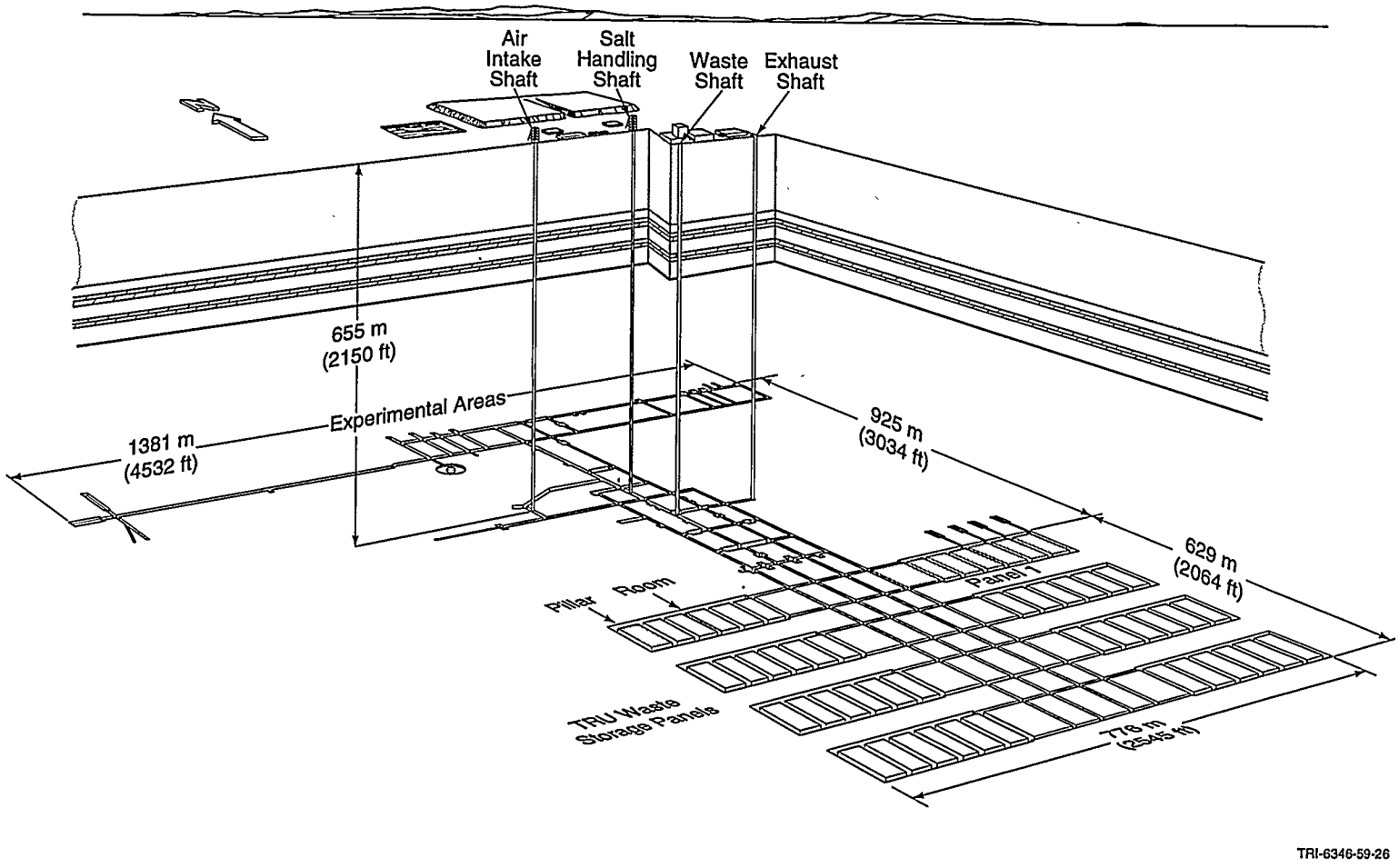

Figure 1-3. Underground configuration of the WIPP repository (after WIPP PA Department, 1992a).

bentonite mixture. Disposal room volumes will change due to salt creep. Room closure is discussed in Section 1.1.5.

Simulations presented in this report consider only two-dimensional flow in a vertical plane around a single, isolated disposal room. Simulation results do not consider the possible effects of adjoining rooms in the same waste panel, or the effects of repository dip, and they are not directly comparable to simulations of the repository using radial or three-dimensional flow geometry.

1.1.2 Salado Formation Hydrogeology

The Salado Formation is approximately 600 m thick, extending from the bottom of the Rustler/Salado Contact at about 260 m below land surface to the top of the Castile Formation at about 860 m below land surface. The Salado Formation consists of a large number of beds of relatively pure halite and impure halite containing interspersed clay and polyhalite. Thin interbeds of anhydrite, with associated underlying clay seams, are present in laterally continuous layers. The thicker, laterally extensive anhydrite interbeds have been designated as Marker Beds, numbered from 100 to 144 with increasing depth (Jones et al., 1960). The repository horizon is separated by a few meters of halite from the overlying Marker Bed 138 and the underlying Marker Bed 139. A stratigraphic section of the Salado Formation in the vicinity of the repository is shown in Figure 1-4.

Factors controlling gas and brine flow within the Salado Formation include, but are not limited to, the physical properties (intrinsic permeability, porosity, and rock compressibility), the fluid properties (phase pressures, saturations, and compressibilities), and the two-phase flow relationships (relative permeability and capillary pressure). In-situ testing has been performed to determine the hydrologic properties for the halite and the anhydrite interbeds under both undisturbed and excavation-disturbed conditions. The Salado Formation hydrologic parameters are summarized in Section 3, and a complete discussion of parameter selection is contained in Appendix A.

In-situ permeability testing indicates a large variability in intrinsic permeability, ranging from less than 10^{-23} m^2 for pure halite to as high as 10^{-18} m^2 for anhydrite interbeds (Beauheim et al., 1991; Howarth et al., 1991; Beauheim et al., 1993a). The porosity of the Salado

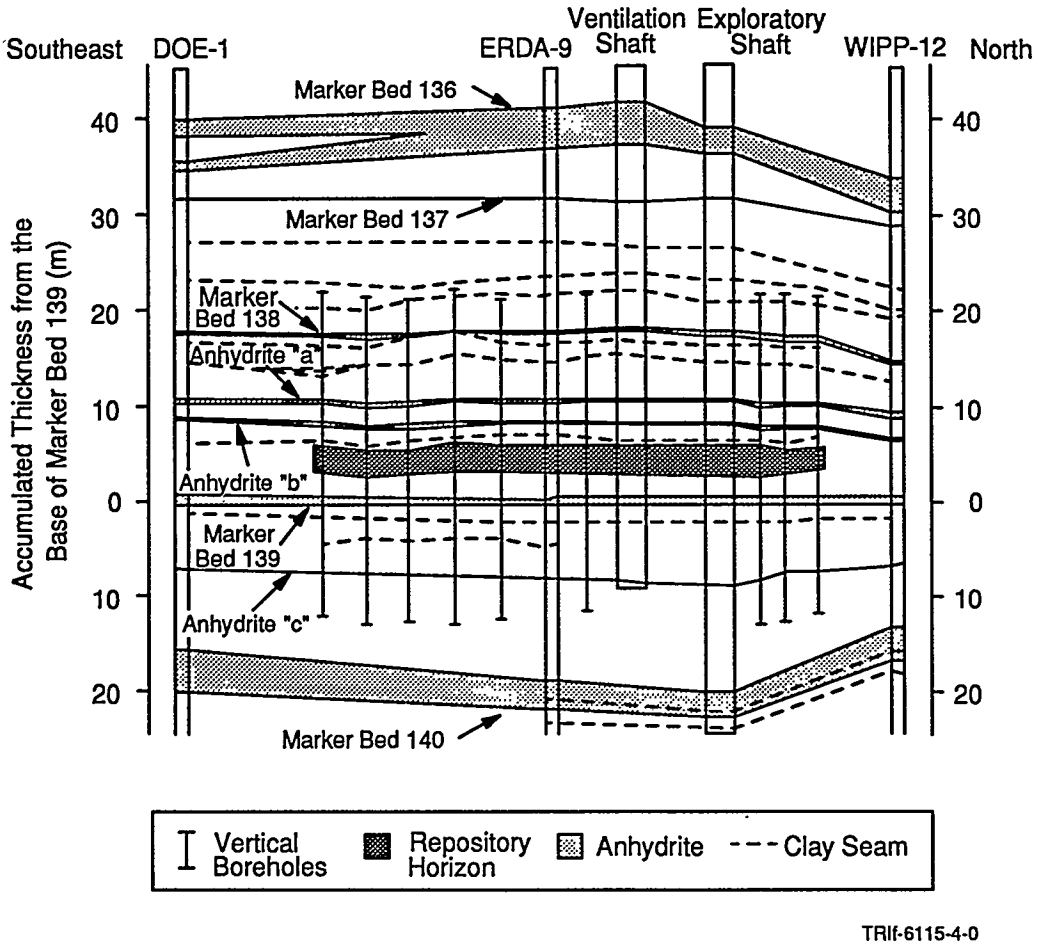

Figure 1-4. Stratigraphic section in the Salado Formation directly above and below the repository horizon (after Davies et al., 1992).

Formation (for both the halite beds and the anhydrite interbeds) is estimated to be 0.01 (Skokan et al., 1989). A maximum porosity for Salado Formation halite and anhydrite is 0.03 (Skokan et al., 1989). Minimum porosities of 0.0006 for the anhydrite (see discussion in Appendix A) and 0.001 for the halite (Powers et al., 1978) have been proposed. These permeability and porosity measurements are considered representative of undisturbed (i.e., far-field) values, although the maximum values may be somewhat influenced by excavation.

Based on in-situ testing results, the undisturbed brine pore pressure in both halite and anhydrite units at the elevation of the repository is estimated to be approximately 12 MPa, which is between hydrostatic (6 MPa) and lithostatic (15 MPa) (Peterson et al., 1987; Nowak et al., 1988; Lappin et al., 1989, Beauheim et al., 1991). Pore pressures are much lower within the first few meters of the excavation due to depressurization resulting from brine flow toward the excavation and/or to dilatation of pores caused by high deviatoric stresses near the excavation (Beauheim et al., 1991). Immediately after excavation, there is a significant inward pressure gradient from the Salado Formation to the repository, which is initially at atmospheric pressure (0.1 MPa).

Repository excavation has created a zone surrounding the repository having disturbed hydrologic and geomechanical properties. The disturbed rock zone (DRZ) is present within the first few meters of the WIPP excavations, at a minimum (Nowak and McTigue, 1987; Stormont et al., 1987; Borns and Stormont, 1988; 1989; Beauheim et al., 1993a). Within the DRZ, intrinsic permeability and porosity are increased due to local fracturing and possible dilatation. Also, elastic and inelastic changes in pore volume, driven by excavation-related stress redistribution, may cause variations in the near-field fluid pressure distribution that are superimposed on fluid-pressure gradients associated with brine flow toward the excavation. Dilatation, drying, and exsolution of dissolved gas that occurs naturally in Salado brines may lead to reduced brine saturations within the DRZ. Increased permeability, decreased pore-fluid pressure, and partially saturated conditions within the DRZ all contribute to enhancing potential gas flow pathways between the waste disposal rooms and nearby higher permeability interbed units. The DRZ is expected to undergo time-dependent changes in properties, with disturbed halite eventually healing to a final state equivalent to undisturbed halite (Lappin et al., 1989).

The Salado Formation contains approximately 0.1 wt% to 1 wt% brine (Nowak et al., 1988). Brine accumulation in the disposal rooms, shafts, and drifts in response to excavation has been observed. Two mechanisms for brine movement through the Salado Formation have

been proposed. Brine may flow in response to pressure gradients and gravitational forces, with the halite acting as an equivalent porous medium in both the near- and far-field. Brine flow in the anhydrite interbeds is likely fracture-dominated. Alternatively, McTigue et al. (1989) proposed that the Salado Formation may contain isolated pores of near-lithostatic brine that become interconnected in response to shear deformation and dilatation around an opening. Connected porosity would be present only in the near-field. Deal and Roggenthen (1991) suggests that under the latter scenario, brine is available only from compaction of undercompacted clay seams that are directly connected to the disposal rooms in response to excavation, and that brine does not flow into the repository from the adjacent halite or anhydrite interbeds.

In the event of repository pressurization in response to waste-generated gas, there will likely be a reversal of the pressure gradient, resulting in brine and gas flow out of the repository. Flow of brine and gas away from the repository will be strongly controlled by the two-phase flow relationships, which are discussed further in Section 1.1.3.

For this study, both the halite and the anhydrite interbeds were modeled as equivalent porous media, with homogeneous properties within each modeled stratigraphic unit. The interbed properties were averaged over the interbed thickness to represent an equivalent porous media. This conceptualization is supported by test results from Beauheim et al. (1993a). A fractured interbed conceptualization was also examined (Section 2.5.1). The baseline and sensitivity simulations did not include an explicit DRZ, although enhanced flow pathways between the rooms and the interbeds, characteristic of the early-time DRZ, were incorporated. An alternative conceptual model was developed to explicitly simulate a simple DRZ (Section 2.5.2).

1.1.3 Multiphase Flow Overview

Multiphase flow occurs due to the interaction of multiple fluid phases (in this case aqueous and gaseous) and multiple components (in this case brine and several waste-generated gases). The aqueous phase may contain both brine and dissolved gases while the gaseous phase may contain both free gases and water vapor. In simulations presented in this report, the quantities of dissolved gases and water vapor were insignificant. The aqueous phase consisted almost

exclusively of brine and the gaseous phase consisted almost exclusively of free gas. As a result, the terms "brine" and "gas" are used to refer to both the components and the phases.

Radionuclides and other hazardous constituents could be released from the repository in either the aqueous or gaseous phases. Simulations tracked the expulsion and migration of waste-generated gas that may contain small concentrations of volatile organic compounds (VOC's), and the expulsion of brine that may contain dissolved radionuclides or hazardous contaminants. This modeling study did not consider retardation of VOC's or dissolved contaminants.

A pressure difference between the brine and gas phases can exist in the pores. This difference is the gas-brine capillary pressure. The capillary pressure is function of the pore size, the relative fluid (gas and brine) properties, and the degree of saturation. Brine will flow out of the repository in response to an outward brine pressure gradient. Similarly, gas will flow out of the repository in response to gas pressure gradients. An outward gas pressure gradient cannot be achieved until the disposal room gas pressure exceeds the capillary resistance (quantified by the sum of the gas-brine capillary pressure and the brine pore pressure) within the surrounding Salado Formation, at which time gas is able to displace brine from the pores.

Gas expulsion from the repository is also controlled by the relative permeability of the phases in a disposal room. The relative permeability of a phase describes the ability of that phase to flow in the presence of another phase. The relative permeability of a phase increases as the saturation of that phase increases. In many rock types, each phase has a residual saturation, below which a continuous phase throughout the pore structure does not exist. Below residual saturation, a phase is not mobile and is considered to have zero relative permeability. Gas and brine within the room could segregate due to density differences and create conditions where the lower part of the room is highly saturated with brine and the upper part is highly saturated with gas. Under these conditions, gas expulsion might occur preferentially from the top of the room because of the high relative permeability to gas and brine expulsion might occur from the lower part of the room.

Gas and brine migration away from the repository are dependent not only on the intrinsic permeability and porosity, but also on the relative permeabilities to brine and gas and the gas-brine capillary pressure of the Salado Formation. Gas saturations in the Salado Formation must exceed the residual gas saturation in order for gas migration to occur. High gas saturations will enhance gas migration but may impede brine flow.

Davies (1991) used an empirical correlation with intrinsic permeability to estimate gas-threshold pressure, a measure of the capillary resistance that must be overcome by gas to displace brine from the rock pores. Gas-threshold pressure was quantified as the gas-brine capillary pressure at residual brine saturation. Estimated threshold pressures ranged from less than 1 MPa for anhydrite interbeds to greater than 50 MPa for pure halite. The combination of relatively high intrinsic permeability and low threshold pressure suggests that the anhydrite interbeds will provide the dominant pathway for waste-generated gas away from the repository.

An initial presence of free gas in the Salado Formation would enhance gas migration if the quantity was sufficient to produce a non-zero relative permeability to gas (i.e., greater than residual saturation). During in-situ testing, Beauheim et al. (1991) observed some gas bubbling into wellbores. However, it could not be determined whether the bubbling resulted from an existing free gas phase or from exsolution of gas dissolved in brine in response to depressurization. The baseline simulations presented in this report assumed two-phase porous media flow with only a brine phase initially present in the Salado Formation. An alternative conceptual model (Section 2.5.4) was implemented to examine the effect of initial gas in the Salado Formation.

1.1.4 Gas Generation Overview

The potential for significant gas generation from transuranic waste at the WIPP was first recognized in the 1970's. The steel waste drums, iron, and other metals in the waste will corrode in the presence of brine. The corrosion process has the potential to produce significant quantities of hydrogen gas (H_2). Microbial degradation of cellulosics (paper, wood, cloth) in the waste has the potential to produce significant quantities of various other gases (CO_2, CH_4, H_2S, N_2) in the presence of sufficient microorganisms and nutrients.

Initial laboratory experiments examined corrosion, microbial activity, radiolysis, and thermal decomposition (Molecke, 1979). Based on early measurements of salt permeability in boreholes drilled from the surface, calculations of gas flow into the surrounding rock suggested that salt permeability was sufficiently high to dissipate waste-generated gas without adverse pressurization of the disposal rooms (Hunter, 1979). However, during the 1980's, the salt became directly accessible from underground excavations and in-situ testing revealed that salt permeability was orders of magnitude lower than indicated by the earlier laboratory and well

testing (Lappin et al., 1989; Beauheim et al., 1991). Under these conditions, much higher gas pressures are possible and there has been significant renewed effort to fully characterize gas-generation processes.

Current laboratory experiments focus on quantifying gas-generation rates for corrosion, microbial activity, and radiolysis (Brush, 1990). These experiments examine gas generation under two scenarios, brine-inundated and vapor-limited (humid) conditions. In the brine-inundated experiments, the test specimen is immersed in brine in a closed brine-water vapor system. This corresponds to in-situ fully-brine-saturated conditions or to partially-brine-saturated conditions where the waste is in direct contact (perhaps thinly coated) with brine. In vapor-limited experiments, the test specimen is suspended in water vapor in equilibrium with brine in a closed brine-water vapor system.

Results from the laboratory experiments (Brush, 1991; Brush, 1995) suggest that gas-generation rates for anoxic corrosion may be significantly higher under brine-inundated conditions than under vapor-limited conditions. The dependence of anoxic corrosion on brine is apparent from examining the most likely anoxic corrosion reactions (Brush, 1995):

$$Fe + 2\,H_2O = Fe(OH)_2 + H_2 \qquad (1\text{-}1a)$$

$$3\,Fe + 4\,H_2O = Fe_3O_4 + 4\,H_2 \qquad (1\text{-}1b)$$

These reactions indicate that H_2O (from brine) is necessary for, and is consumed by, the corrosion process. Reactions 1-1a and 1-1b will occur at low fugacities of CO_2 and H_2S (i.e., the repository is predominantly filled with other gases such as H_2 and N_2). At higher fugacities, CO_2 and/or H_2S will be consumed along with H_2O to produce H_2 and $FeCO_3$, a process that may lead to passivation (Brush, 1995). Because the laboratory experiments test the extremes of brine availability, the brine-inundated corrosion experiments likely produce an upper bound on the in-situ hydrogen (H_2) generation rate while the vapor-limited corrosion experiments likely produce a lower bound.

Interim results (Brush, 1991) from the ongoing laboratory experiments have been incorporated into the simulations presented in this report. Interim anoxic corrosion results indicate a best-estimate gas-generation rate of approximately 1 mole of gas per drum of CH TRU waste per year under brine-inundated conditions. The gas-generation rate under vapor-limited conditions was estimated to be 0.1 moles per drum per year, but may possibly be zero depending

on the local relative humidity. The estimated total gas generation potential for corrosion is 1,050 moles per drum of CH TRU waste (Beraun and Davies, 1992).

The role of brine in microbial activity is less apparent. Microbial degradation of cellulosics in the waste produces various gases. The likely significant microbial processes, shown below, are denitrification (Reaction 1-2a), Fe(III) reduction (Reaction 1-2b), SO_4^{2-} reduction (Reaction 1-2c), and methanogenesis (Reactions 1-2d and 1-2e) (Brush, 1995).

$$CH_2O + 0.8\,H^+ + 0.8\,NO_3^- = 1.4\,H_2O + CO_2 + 0.4\,N_2 \quad (1\text{-}2a)$$

$$CH_2O + H_2O + 4\,FeO(OH) = + CO_2 + 4\,Fe(OH)_2 \quad (1\text{-}2b)$$

$$CH_2O + H^+ + 0.5\,SO_4^{2-} = H_2O + CO_2 + 0.5\,H_2S \quad (1\text{-}2c)$$

$$2\,CH_2O = CO_2 + CH_4 \quad (1\text{-}2d)$$

$$4\,H_2 + CO_2 = 2\,H_2O + CH_4 \quad (1\text{-}2e)$$

Reactions 1-2a through 1-2e indicate that H_2O may be both produced and consumed by microbial activity. CH_2O (glucose) is used to represent the cellulose in the waste. Ongoing laboratory experiments have observed significant microbial gas production by halophilic organisms that exist in brine from the WIPP underground with glucose as the substrate. However, cellulose is the primary potential substrate in the WIPP waste and these experiments did not yield significant gas production with a cellulose substrate. The latter results are contrary to earlier WIPP studies by Molecke (1979), which produced significant microbial gas under apparently realistic repository conditions. New experiments are currently under way to resolve this discrepancy.

A best estimate for microbial gas-generation rate under brine-inundated conditions of 1 mole of gas per drum of CH TRU waste per year was assumed by Brush (1991), based on the earlier studies by Molecke (1979). The dependence of microbial activity on brine remains uncertain pending the completion of laboratory experiments for microbial activity under vapor-limited conditions. However, based on results to date, a gas-generation rate under vapor-limited conditions of 0.1 moles per drum per year was estimated. The estimated total gas-generation potential for microbial activity is 550 moles per drum of CH TRU waste (Beraun and Davies, 1992).

Ongoing laboratory experiments to examine alpha radiolysis of WIPP brines containing various concentrations of dissolved plutonium indicate relatively slow gas generation, but are not

yet far enough along to quantify gas-generation rates. Radiolysis is expected to make only a minor contribution to the total gas-generation rate.

Baseline simulations examined several gas-generation rate histories (Section 2.4), all of which assumed a total gas-generation potential of 1,600 moles per drum of CH TRU waste per year, representative of waste-generated gas from anoxic corrosion and microbial activity. Baseline simulations did not include gas from radiolysis, plastic degradation, or RH waste. Sensitivity simulations examined different total gas-generation potentials and gas exsolution in the host rock. Reduced pressures in the host rock in the vicinity of the repository as a result of excavation will reduce gas solubility in the brine and may lead to the exsolution of gas. At early time under the inward pressure gradient, exsolved gas may flow into the repository. Following gradient reversal, it may be expelled along with waste-generated gas.

Additional laboratory results recently became available (Brush, 1995). These results indicate that the best-estimate gas-generation rate due to anoxic corrosion may be lower than previously estimated (0.6 moles per drum per year under brine-inundated conditions, 0 moles per drum per year under vapor-limited conditions). Although these results were received too late to be incorporated into the baseline simulations, they were considered in the sensitivity simulations (Section 5.2.1).

For this report, gas-generation rates were calculated from the independent laboratory experiments for corrosion and microbial activity. The production and/or consumption of H_2O was not simulated. However, independent experiments can only provide bounding estimates for the gas-generation rates. The corrosion and microbial activity reactions are coupled by the availability of H_2O and various gases (H_2, CO_2, H_2S, N_2, CH_4), making it difficult to predict in-situ gas-generation rates based on laboratory estimates from the individual processes. In-situ gas-generation rates are also strongly influenced by the chemical and physical properties of the waste, backfill, host rock, and groundwater. A thermodynamic and kinetic reaction-path gas-generation model is currently under development to help quantify the chemical reaction coupling (Brush, 1995).

Given the non-homogeneous nature of the repository contents, better predictions of in-situ gas-generation rates also require a better understanding of H_2O movement through the waste and backfill and of how in-situ saturation conditions relate to laboratory brine-inundated and vapor-limited conditions. Because of density differences it is expected that gas and brine will be

segregated within the room, with brine moving preferentially to the bottom. It is conceivable that brine-inundated corrosion could be occurring in the bottom of the room while vapor-limited conditions exist at the top. Two brine-dependent gas-generation methodologies are presented in Section 2.4.2 that examine this phenomena. Brine-inundated conditions may also be created in disposal rooms that are downdip in the repository.

1.1.5 Geomechanics Overview

Long-term salt creep is driven by deviatoric stresses that develop within the intact salt surrounding an excavation. Prior to repository excavation, an undisturbed stress state existed in the Salado Formation in response to lithostatic loading. The presence of the repository excavations produces high deviatoric stresses in the Salado Formation near the disposal rooms, decreasing towards the undisturbed state with distance away from the repository.

Room closure and consolidation is driven by the inward forces resulting from the excavation-related stress redistribution in the Salado Formation surrounding the room. Resistance to room closure is developed by the outward forces (backstress on the room walls) resulting from the stress distribution in the waste and backfill and from the pressure of the waste-generated gas. As room closure occurs, consolidation and compaction of the waste and backfill is expected to produce an increase in the backstress. Over time, gas generation will increase the number of moles of waste-generated gas and room closure will decrease the void volume available for gas storage. Both factors are likely to contribute to increasing room pressures, which will provide additional resistance to closure. Room pressurization may be mitigated by gas expulsion or by room expansion.

In the WIPP underground, room closure was observed immediately following room excavation with early time closure rates of several centimeters per year (Munson et al., 1989). Salt creep has produced inward bowing of the walls, ceilings, and floors of existing disposal rooms. Spalling of the ceilings and walls of the rooms and excavated drifts has necessitated the installation of rock bolts. Differential displacement was observed in experimental boreholes. These observations all suggest that significant salt creep is occurring.

Consolidation of the waste-filled disposal rooms is expected. Backstress due to consolidation is provided predominantly by the waste. Backfill consolidates more rapidly and

with little resistance. Even with high gas-generation rates as under brine-inundated conditions, room closure and consolidation is expected to cause a significant reduction in the void volume available to store waste-generated gas within a disposal room.

Extensive in-situ and laboratory testing has been performed to determine the constitutive models and parameter values for creep deformation in halite (Krieg, 1984; Munson et al., 1989) and for consolidation of waste and backfill (Sjaardema and Krieg, 1987; Butcher, 1989; Butcher et al., 1991a; Butcher et al., 1991b). These models and parameters were used to perform simulations of room closure using a finite element creep closure code, SANCHO (Stone et al., 1985). With SANCHO, salt creep is simulated by the deformation of the model elements as defined by an elastic-secondary creep constitutive model. The relationships between stress and deformation in the waste and in the backfill are defined by separate constitutive models.

Following repository excavation, the hydrologic and geochemical processes in the disposal rooms and the surrounding Salado Formation work to re-establish an equilibrium. This equilibrium state is achieved through the concurrent processes of salt creep and fluid flow and the complex interactions between the two processes. Two possible mechanisms for fluid movement in conjunction with salt creep in the Salado Formation were discussed in Section 1.1.2. In either case, inflowing brine will occupy void volume in a disposal room that would otherwise be available to gas, which tends to increase gas pressure and retard room closure. The formation of a disturbed rock zone around repository excavations was also discussed in Section 1.1.2.

For this study, both the halite and the anhydrite interbeds were modeled as porous media. Salt creep will produce a deforming halite matrix which will result in some deformation and/or fracturing in the interbeds. A deforming halite matrix will alter intrinsic rock properties, such as permeability and effective porosity, which may have a significant effect on fluid flow. The effects of deforming halite were not included in baseline simulations. However, the effects of altered rock properties, representative of a DRZ, were examined in sensitivity simulations (Section 2.5.2). Fracturing in the interbeds, whether in response to deforming halite or near-lithostatic repository pressures, will alter the flow properties in the interbeds, although double-porosity responses have not been observed during hydraulic testing (Beauheim et al., 1993a). The effects of interbed fracture were not included in baseline simulations, but were examined in sensitivity simulations (Section 2.5.1).

1.2 Summary of Driving Issues

The primary long-term concern related to gas generation at the WIPP is the potential release of contaminated brine and gas to the accessible environment. A secondary concern is the potential for room pressurization above lithostatic pressure and the resulting impact on contaminant migration. These concerns are interrelated in that room pressures near lithostatic could result in fracturing of the nearby anhydrite interbeds, increasing the potential for brine and gas release from the repository. This report addresses the issues of migration and room pressurization with baseline and sensitivity simulations. The effects of interbed fracturing are addressed with sensitivity simulations.

1.2.1 Regulatory Concerns Relative to Waste-Generated Gas

There are two long-term regulatory concerns related to the release of contaminants from the WIPP repository. These regulations govern the release of radionuclides (40 CFR 191, Subpart B) and the migration of hazardous constituents (40 CFR 268.6). The short-term, operational-phase impacts of waste-generated gas are not evaluated in this report.

40 CFR 191, Subpart B is codified from the Environmental Radiation Protection Standards for Management and Disposal of Spent Nuclear Fuel, High-Level and Transuranic Radioactive Wastes (U.S. EPA, 1985). It set limits on the 10,000 year cumulative release of radionuclides to the accessible environment under both undisturbed and human intrusion scenarios. Compliance with 40 CFR 191, Subpart B is addressed biannually (annually prior to 1994) by WIPP PA, most recently in WIPP PA Department (1992a; 1992b; 1992c; and 1993a), which examined release of radionuclides dissolved in brine through the Culebra Dolomite of the Rustler Formation, the anhydrite interbeds of the Salado Formation, the shafts, and a human intrusion borehole.

40 CFR 268.6 is codified from the Land Disposal Restrictions of the Hazardous and Solid Waste Amendments (U.S. EPA, 1986) of the Resource Conservation and Recovery Act (RCRA). The current interpretation of 40 CFR 268.6 is that there must be no migration of RCRA hazardous wastes at concentrations above health- or environmentally-based standards beyond the site boundary for as long as the waste remains hazardous. Human intrusion scenarios need not be considered. Of particular interest at the WIPP is the migration of lead and other heavy

metals dissolved in the brine and of volatile organic compounds (which are RCRA hazardous wastes) as gases. Long-term compliance with 40 CFR 268.6 has been addressed most recently by the WIPP PA Department (1993b and 1992d), which examined contaminant migration through the shafts, seals, and anhydrite interbeds.

In the simulations presented in this report, fluid releases from the repository were predominantly to the anhydrite interbeds. Gas phase migration was easily tracked, but migration of contaminated brine could only be inferred. Because of the simplified model geometry, (single isolated room, two-dimensional flow) a direct comparison to regulatory standards was not possible. However the simulation results did provide some guidance to gas migration, under two-phase conditions, pertinent to 40 CFR 268.6. Additionally, some qualitative information about the effects of two-phase flow on brine migration was gained.

An additional regulatory consideration is the National Environmental Policy Act (described in U.S. EPA, 1978), which requires a statement of the environmental consequences of the WIPP repository. A Final Environmental Impact Statement (U.S. DOE, 1980), a Draft Supplement Environmental Impact Statement (DSEIS) (U.S. DOE, 1989), and a Final Supplement Environmental Impact Statement (FSEIS) (U.S. DOE, 1990) have been prepared. Lappin et al. (1989) and Lappin et al. (1990) were prepared in support of the DSEIS and FSEIS, respectively. They summarized modeling results of radionuclide transport in the Culebra Dolomite under both undisturbed and human intrusion scenarios and examined gas generation and available gas-storage volume within the repository. However, they did not address gas migration away from the repository. The simulations of gas migration in the anhydrite interbeds presented in this report will supplement future environmental impact statements.

1.2.2 Gas-Storage Volume Analysis

Lappin et al. (1989) performed scoping calculations to determine whether a non-ideal mixture of gases (H_2, CO_2, CH_4) having a total gas potential of 1483 moles per drum could be contained within a specified storage volume at less than lithostatic pressure. Within the WIPP repository, gas-storage volume is available in the excavated waste panel area (Area G on Figure 1-5), consisting of eight waste panels, the southern and northern equivalent panels (Areas C and D, respectively), and the adjoining drifts. The waste panel area has a total excavated volume of 433,400 m^3 (Lappin et al., 1989). In the event of seal failure, additional gas-storage

volume is available in the excavated experimental area (Area F), access drifts (Area E), and shafts. With this additional volume included, the entire repository area (Area H on Figure 1-5) has a total excavated volume of 583,370 m^3 (Lappin et al., 1989). To account for waste, backfill, and room closure, gas-storage volumes in the excavated areas were assumed to be 3% of the excavated volumes.

Lappin et al. (1989) also identified the following mechanisms for the creation of additional gas-storage volume at the WIPP: expansion of the disposal rooms in the waste panel area; fracturing of the anhydrite interbeds; and creation or expansion of the DRZ. A 1.5 m thick DRZ around the waste panel area having a porosity of 0.14 was assumed to provide an additional gas-storage volume of 80,000 m^3. The interbeds above and below the waste panel area were assumed to provide an additional gas-storage volume of 12,000 m^3. Results of the scoping calculations indicated that, even with this additional storage from the DRZ and the interbeds included, repository pressures at or above lithostatic would be required to store the waste-generated gas.

An extension of those scoping calculations is presented here, using an estimated total gas potential of 1,600 moles per drum (8.896×10^8 total moles). Two storage volume assumptions were considered: gas storage limited to the waste panel area and interbeds; and gas storage in the entire repository and interbeds. Storage volume within the repository was calculated for each of three repository closure conditions, initial, intermediate, and final (fully consolidated). The fraction of excavated volume available for gas storage was 0.66 for the initial state (which represents the initial porosity in a room), 0.21 for the intermediate state, and 0.09 for the fully consolidated state (which represents backfill and waste consolidated under lithostatic pressure (15 MPa) and having a small, but non-zero, porosity). Storage volume in the interbeds was calculated by assuming gas storage was available in only the closest interbeds: anhydrites "a" and "b" above the repository and Marker Bed 139 below. The closest interbeds were assumed to have a total composite thickness of 1.2 m, a total (fracture plus matrix) porosity of 0.01, and no residual brine. The interbed storage volume was assumed to be a 1.2 m thick disk, extending radially to cover the enclosed area of the waste panels (Area G) for the case of storage limited to the waste panel area, or the entire enclosed repository area (Area H) for the case of storage in the entire repository.

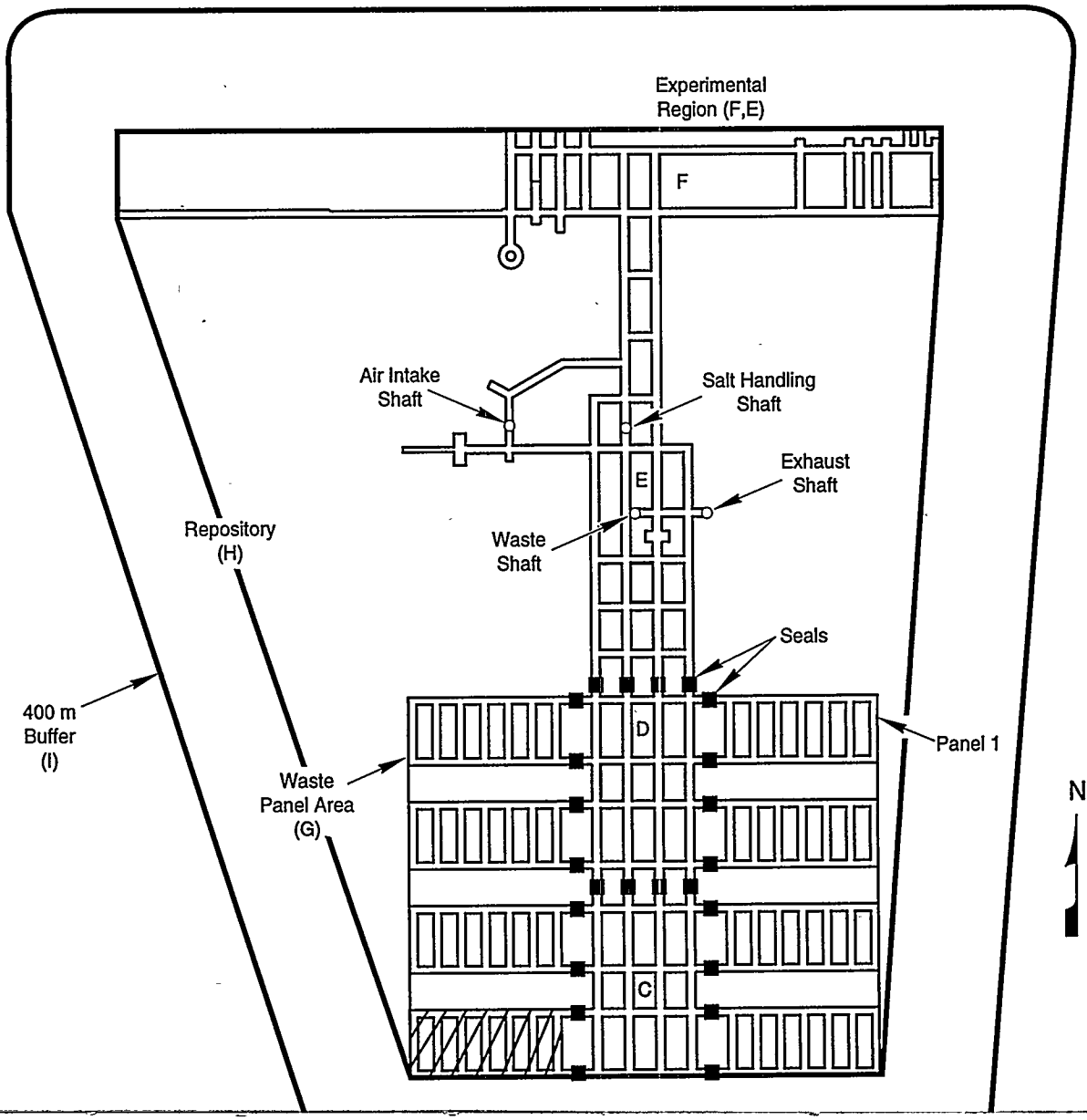
Experimental
Region (F,E)
F
Air Intake
Shaft
Salt Handling
Shaft
Exhaust
Shaft
E
Repository
(H)
Waste
Shaft
Seals
400 m
Buffer
(I)
D
Panel 1
Waste
Panel Area
(G)
N
C

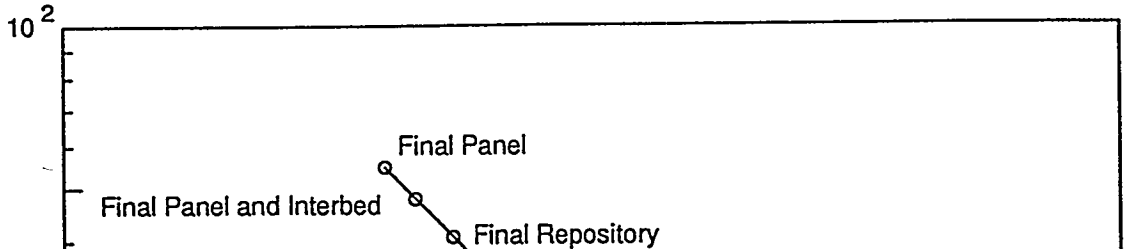
10 2
Final Panel
Final Panel and Interbed
Final Repository

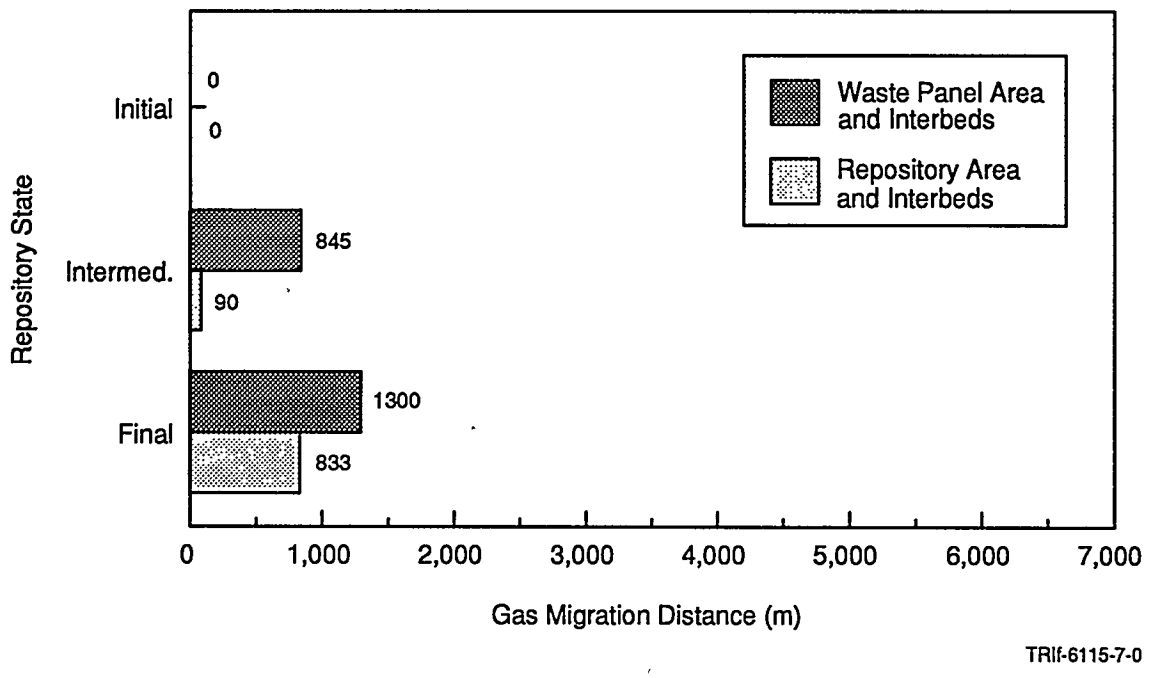

Figure 1-7. Gas migration distance in Marker Bed 139 and anhydrites "a" and "b" under three fixed repository states with an assumed interbed porosity of 0.01.

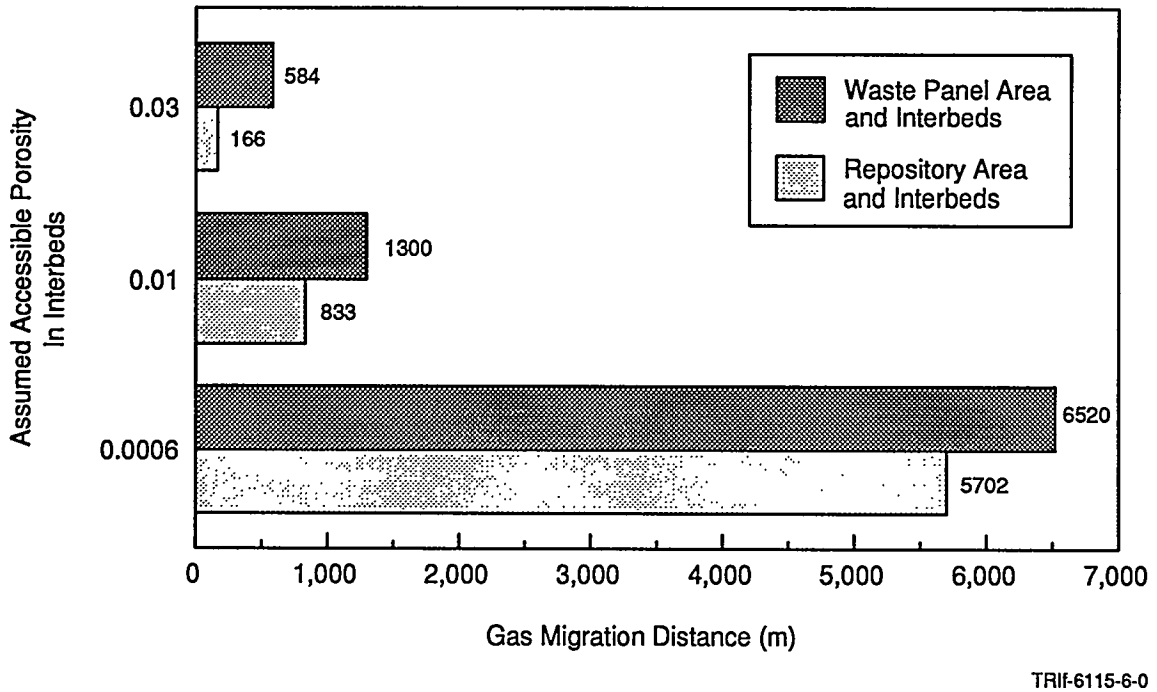

Figure 1-8. Gas migration distance in Marker Bed 139 and anhydrites "a" and "b" under for the final repository state with three assumed interbed porosities.

These scoping calculations indicate that, under certain scenarios, room pressurization to lithostatic pressure and gas release and migration in the anhydrite interbeds are both likely to occur. A detailed model is required to more fully examine the effects of gas-generation rate, multiphase flow, and room closure rate on gas generation, expulsion, and migration from the WIPP repository.

1.2.3 Process Coupling

Developing a rigorous understanding of the impact of waste-generated gas on repository performance requires analysis of complex, interrelated chemical, hydrologic, and geomechanical processes. In order to evaluate potential process relationships, it is useful to evaluate the potential coupling between primary processes. Figure 1-9 is a schematic diagram illustrating these primary relationships. Some discussion of these relationships was presented by Davies et al. (1992). Many of these processes are coupled through room pressure. Gas generation, driven by chemical processes, increases the quantity of gas in a room, thereby increasing room pressure. The geomechanical processes of room closure, room expansion, and interbed fracture cause direct changes in the void volume available to store gas, thereby directly impacting pressure. The hydrologic process of gas flow out of the room reduces the quantity of gas in the room, thereby tending to reduce room pressure. The hydrologic process of brine flow to and from the room changes the quantity of brine that occupies some of the available void volume in the room, thereby impacting room pressure.

All of the process relations described in the previous paragraph are discussed from the perspective of how each process impacts room pressure. One must also consider how changing room pressure impacts each of these processes. Increasing room pressure provides backstress on the room walls which tends to resist room closure and inhibit consolidation of the room contents and may produce room expansion. Increasing room pressure impacts the pressure gradients that affect brine inflow and eventually drive brine and gas from the room into the surrounding rock. Increasing room pressure to near-lithostatic may cause dilatation of pre-existing fractures and/or formation of new fractures in the interbeds. Interbed fracture may limit the room pressure to lithostatic and cause changes in the flow properties, both of which influence gas migration away from the repository. Because gas generation may require brine, slowing and then reversing brine inflow could have major impact on gas-generation rates, which brings the complex coupling relations full circle.

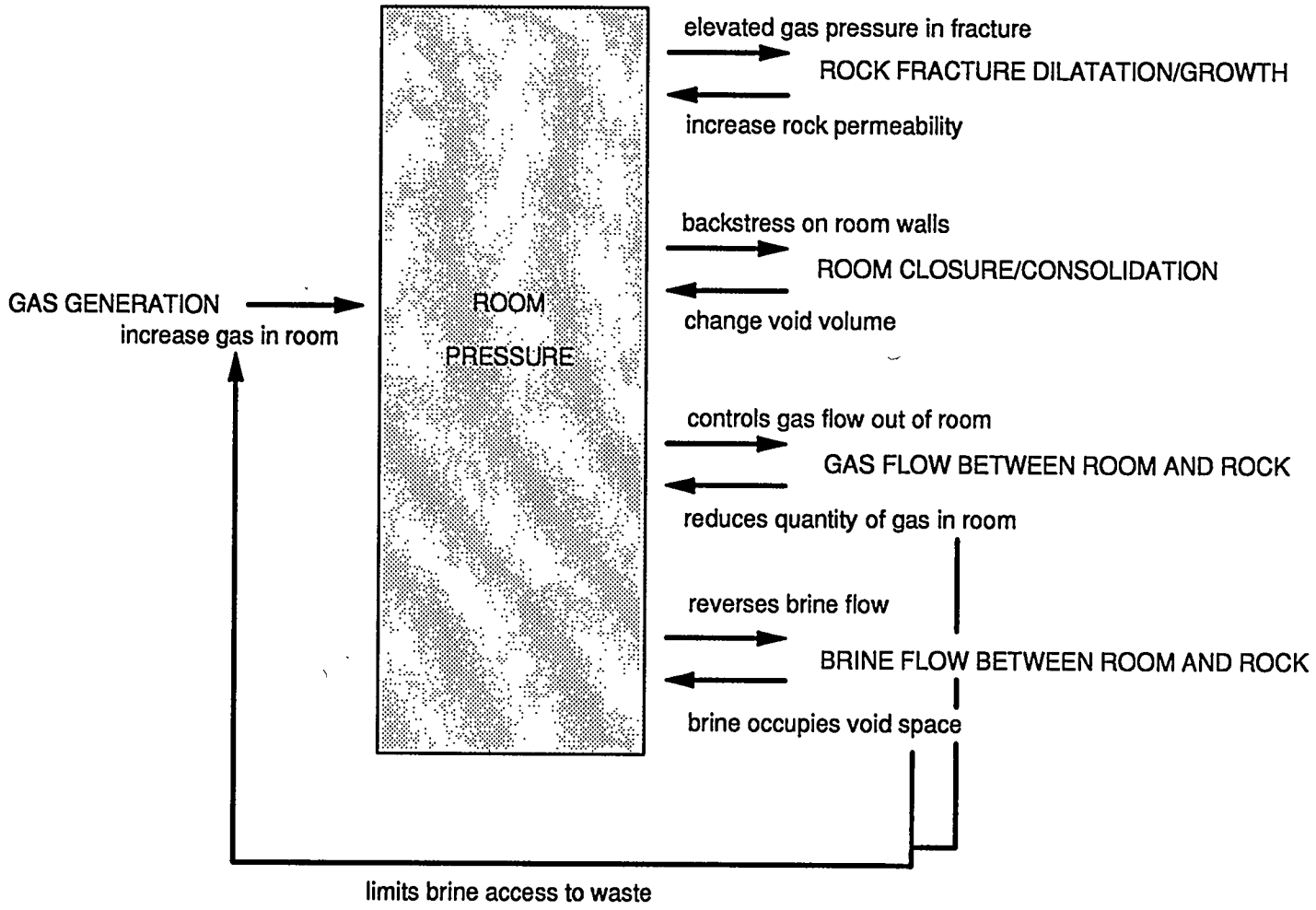

Figure 1-9. Schematic illustration of the chemical, hydrologic, and mechanical coupling that control repository response to waste-generated gas (after Davies et al., 1992).

Stone (1995a) used SANCHO to simulate the closure of a perfectly sealed disposal room under five different gas-generation rate histories ranging from zero to the best-estimate brine-inundated rate. In addition to constitutive models describing salt creep, waste consolidation, and backfill consolidation, the resistance to closure provided by the pressure of waste-generated gas, calculated from the ideal gas law, was simulated. System parameters were selected, a priori, to be consistent with the parameters presented in this report. These SANCHO results provided the basis for the coupling between multiphase flow and room closure used in both the pressure lines method (Section 2.3.1) and the boundary backstress method (Section 2.3.2).

The SANCHO results showed that at higher gas-generation rates, room pressurization occurred quickly, and room closure was moderate. At elevated gas pressures, room closure was actually reversed, producing expansion with a corresponding increase in void volume. This expansion had a moderating effect on room pressurization. At lower gas-generation rates room closure was greater. The resulting compression of the waste was significant and the resistance to room closure was provided by both the gas pressure and the stresses in the waste. At the lower gas-generation rates, the backstress was large enough to stop room closure prior to reaching a fully compacted state, but gas pressures were not high enough to produce room expansion. With no gas generation, the room achieved a fully compacted state. This state, referred to as fully consolidated in this report, represents backfill and waste consolidated under lithostatic pressure (15 MPa) and having a small, but non-zero, porosity.

Assuming 6,804 drums per room, the anoxic corrosion potential (1,050 moles per drum) corresponds to approximately 7.1×10^7 moles of gas per room. The H_2O required to completely exhaust the corrosion potential is between 7.1×10^7 moles (Reaction 1-1b) and 1.4×10^8 moles (Reaction 1-1a). For a 1,200 kg/m^3 density brine, this corresponds to between 107 m^3 and 214 m^3 of brine. The initial brine saturation of the waste and backfill in the disposal rooms is expected to be very low, approximately 0.01 (Section 3.1.1.3). This corresponds to an initial volume of brine of 24 m^3. The availability of H_2O in the room may be further limited by capillary effects in the backfill, the absorption capacity of the backfill, and the groundwater chemistry. Therefore, it is likely that significant brine inflow from the Salado Formation will be required to drive the anoxic corrosion process at brine-inundated rates.

The relationship between brine flow and gas pressure in the room may be particularly important given the strong dependence of anoxic corrosion (and possibly microbial activity) on the availability of brine. The expulsion of brine from the disposal room and the consumption

of brine by corrosion may make gas generation from corrosion a self-limiting process. Brine flows into the repository at early time, driving gas generation. As repository pressurization occurs, pressure gradients reverse and brine flows out of the room. As the available brine in the room decreases due to outflow and H_2O consumption, gas generation decreases and eventually ceases. Repository pressures decrease as gas release continues. This process may be cyclic if the repository pressure decrease re-establishes an inward pressure gradient and brine inflow occurs once more. Gas pressurization could also create unsaturated conditions within the repository that limit brine access to radionuclides and RCRA hazardous substances and thereby limit transport of contaminants dissolved in brine.

1.2.4 Impact of Parameter Uncertainty

At present, a number of the key parameters which are used to describe the processes of gas generation, multiphase flow, and room closure are not very well known. Because of the complex coupling between the three processes it is difficult to predict which are the important parameters in an overall assessment of gas generation and release from the WIPP repository. The development of a model which couples the three processes allows some parameter sensitivity and importance analysis to be performed. These deterministic parameter sensitivity and importance results provide quantitative information about which parameters may be important in controlling gas and brine release to the Salado Formation. They also provide guidance for further work in hydrologic testing (room, halite, interbed, and two-phase properties), gas-generation experiments (rates, potentials, brine-dependency), and geomechanical parameter determination. A detailed discussion of deterministic uncertainty evaluation is presented in Section 2.6.

This page intentionally left blank

2.0 METHODOLOGY

A numerical model to couple fluid flow and salt creep was created to simulate gas generation, room closure, and multiphase brine and gas flow in a single, isolated disposal room and in the surrounding halite and interbeds of the Salado Formation (Freeze et al., 1995). A multiphase flow code, TOUGH2 (Pruess, 1987; Pruess, 1991), provided the basis for implementing the process coupling. Room closure simulations performed by Stone (1995a) using the mechanical creep closure code SANCHO provided guidance for room void volume changes representative of room closure. Gas generation was implemented by situating a number of gas sources within the modeled disposal room.

Two empirically-based approaches for approximating salt creep and room closure were implemented in TOUGH2: a porosity function approach and a fluid phase salt approach. Both approaches utilized links to the SANCHO f-series simulation results of Stone (1995a) to calculate room void volume changes with time during a simulation. Freeze et al. (1995) identified one porosity-function-based method (pressure-time-porosity line interpolation) and one fluid-phase-salt-based method (boundary backstress) which were best able to couple the processes of multiphase flow and room closure.

This section contains descriptions of the enhanced code, TOUGH2/EOS8 (Section 2.1), the baseline model conceptualization (Section 2.2), the two selected flow and closure coupling methods, pressure lines and boundary backstress (Section 2.3), the gas-generation source term implementation (Section 2.4), alternative conceptual models (Section 2.5), and uncertainty evaluation (Section 2.6).

2.1 TOUGH2/EOS8 Code

TOUGH2/EOS8, used to couple multiphase flow, gas generation, and room closure, was adapted from TOUGH2 (Pruess, 1987; Pruess, 1991). TOUGH2 is a numerical simulator for multi-dimensional, coupled fluid and heat flow of multiphase, multicomponent mixtures in porous and fractured (dual porosity/dual permeability) media. The heat flow and dual porosity/permeability capabilities were not used for this application. A detailed description of the capabilities of TOUGH2 can be found in Pruess (1991); a short summary is presented here.

In TOUGH2, fluid flow follows Darcy's Law with relative permeability and capillary pressure relationships used to describe interference between the phases. Spatial discretization follows the integral finite difference method. Time stepping follows a fully-implicit backward finite difference scheme. The resulting set of coupled non-linear equations are solved using a Newton-Raphson iteration technique. The linear equations at each iteration are solved using sparse LU-decomposition and back-substitution.

TOUGH2 is comprised of five modules, with the fluid properties contained primarily within an equation-of-state (EOS) module. A three-phase, three-component equation-of-state module, EOS8 (water, air, "dead" oil) was adapted specifically for this application from the two-phase, two-component EOS3 (water, air) module by Karsten Pruess at Lawrence Berkeley Laboratories. The third "dead" oil phase was used with the boundary backstress method to represent "fluid" salt. A test version of the preconditioned conjugate gradient linear equation solver, developed by Karsten Pruess and George Moridis at Lawrence Berkeley Laboratories, was incorporated into TOUGH2/EOS8.

Enhancements were made to the EOS8 module by Stephen Webb at Sandia National Laboratories and by INTERA. The enhanced EOS8H (brine, hydrogen, salt) module includes: fluid properties representative of WIPP brine rather than water; and hydrogen properties as in EOS5 (water, hydrogen) rather than air properties. Additional enhancements made to the code include: the capability to adjust region (room) porosity based on porosity-time relationships; the capability to adjust gas-generation rate based on region (room) phase saturations; and pressure-dependent flow properties in the interbed regions. The porosity-time relationships were used with the pressure lines method to adjust the room void volume; the saturation-dependent injections rates were used to simulate the brine-dependency of gas generation; and the pressure-dependent interbed properties were used to approximate the effects of interbed fracture.

2.2 Baseline Model Conceptualization

The baseline model used a two-dimensional fluid-flow continuum representative of a disposal room surrounded by halite and anhydrite interbeds of the Salado Formation. The fluid-flow continuum was used to model multiphase brine and gas flowing through a fixed matrix of low-porosity halite with anhydrite interbeds. The Salado Formation was conceptualized as a homogeneous halite containing two anhydrite interbeds, one above and one below the disposal

room (Figure 2-1). A single, isolated, half-width disposal room (with symmetry across the centerline assumed) was simulated. Each of the four regions (disposal room, halite, upper interbed, and lower interbed) in the fluid-flow continuum was defined by a different set of physical properties. A similar conceptualization was used by Davies et al. (1992) and Webb (1992a).

The near-field discretization of the fluid-flow continuum is shown in Figure 2-2. To reduce effects from the model boundaries, a relatively extensive section of the Salado Formation around the disposal room was modeled. The far-field extent of the fluid-flow continuum is shown in Figure 2-3. The total vertical dimension of the model was 262.5 m and the total horizontal model dimension was 2,285.0 m. The third model dimension was assumed to be 1.0 m. As shown in Figure 2-3, the interbeds had a finer horizontal discretization to better capture migration distances. Changes in fluid pressures at the external no-flow boundaries were monitored during simulations. It was found that pressure changes of 1 MPa or less at the model boundaries had little effect on room void volume or room pressures. In certain sensitivity simulations, model boundaries were extended to ensure less than 1 MPa pressure changes. The expanded grid was particularly important in simulations where large gas migration distances were expected. Only extremely minor changes in other physical measures such as saturations were tolerated at the boundaries.

The U.S. DOE (1986) design document specifies excavated room dimensions of 3.96 m high by 10.06 m wide by 91.44 m long. The modeled two-dimensional disposal room had a height of 4.0 m, a half-width of 5.0 m, and a unit length of 1.0 m. The volume of the modeled disposal room, scaled to full width and length, was 3,658 m^3. An initial porosity of 0.66 was assumed based on a room-averaged value of the initial waste and backfill porosities (Beraun and Davies, 1992). The initial room void volume was 2,415 m^2. The disposal room was discretized into 16 equal-sized elements (Figure 2-2) with gas sources located in the 6 elements in the interior of the room.

The fluid-flow continuum includes a 0.3 m thick upper composite interbed, located 2.1 m above the room. The thickness of the upper interbed is equal to the sum of the thicknesses of anhydrite "a" and anhydrite "b". A 0.9 m thick lower interbed, equal to the thickness of Marker Bed 139, was included 1.6 m below the room. Composite interbeds were utilized to simplify the problem for computational efficiency. Interbeds more distant from the room (i.e., Marker Bed 138, anhydrite "c") were not included in the composite interbeds because they are not

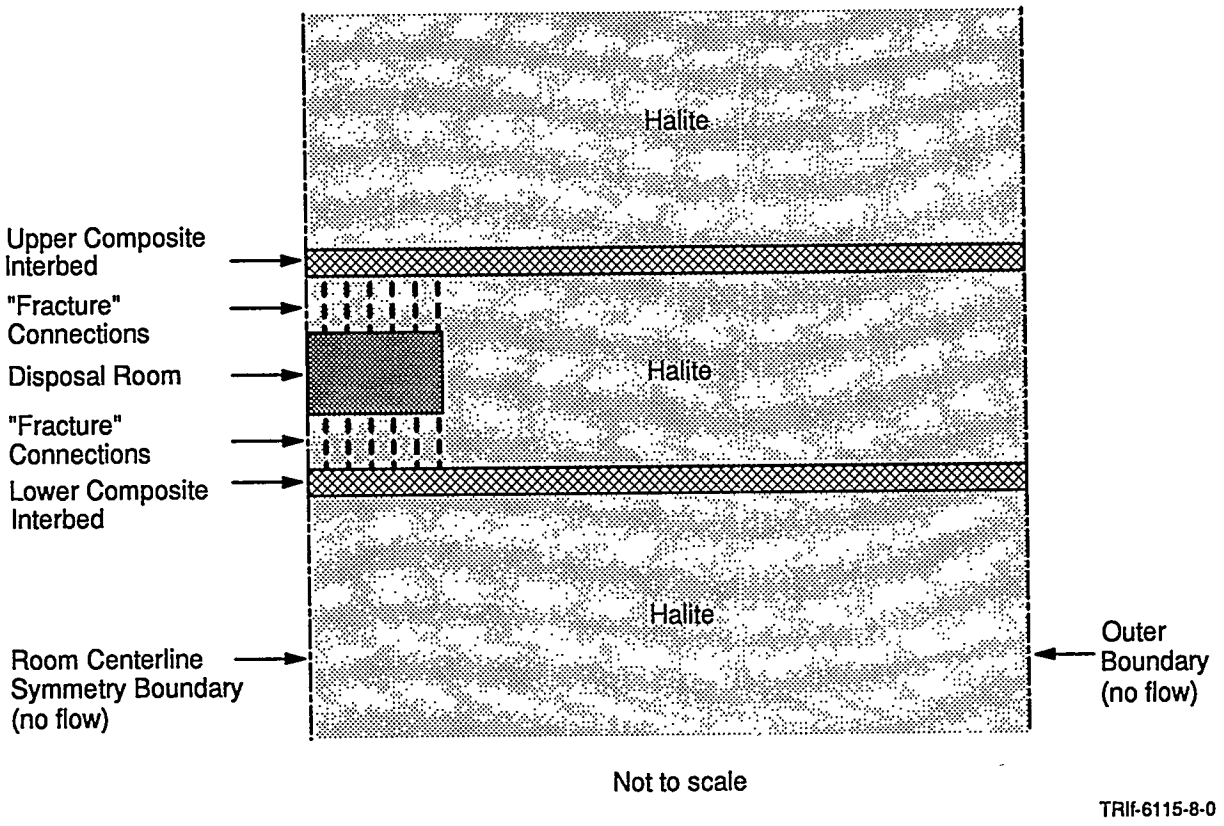

Figure 2-1. Schematic representation of the fluid-flow continuum (after Davies et al., 1992).

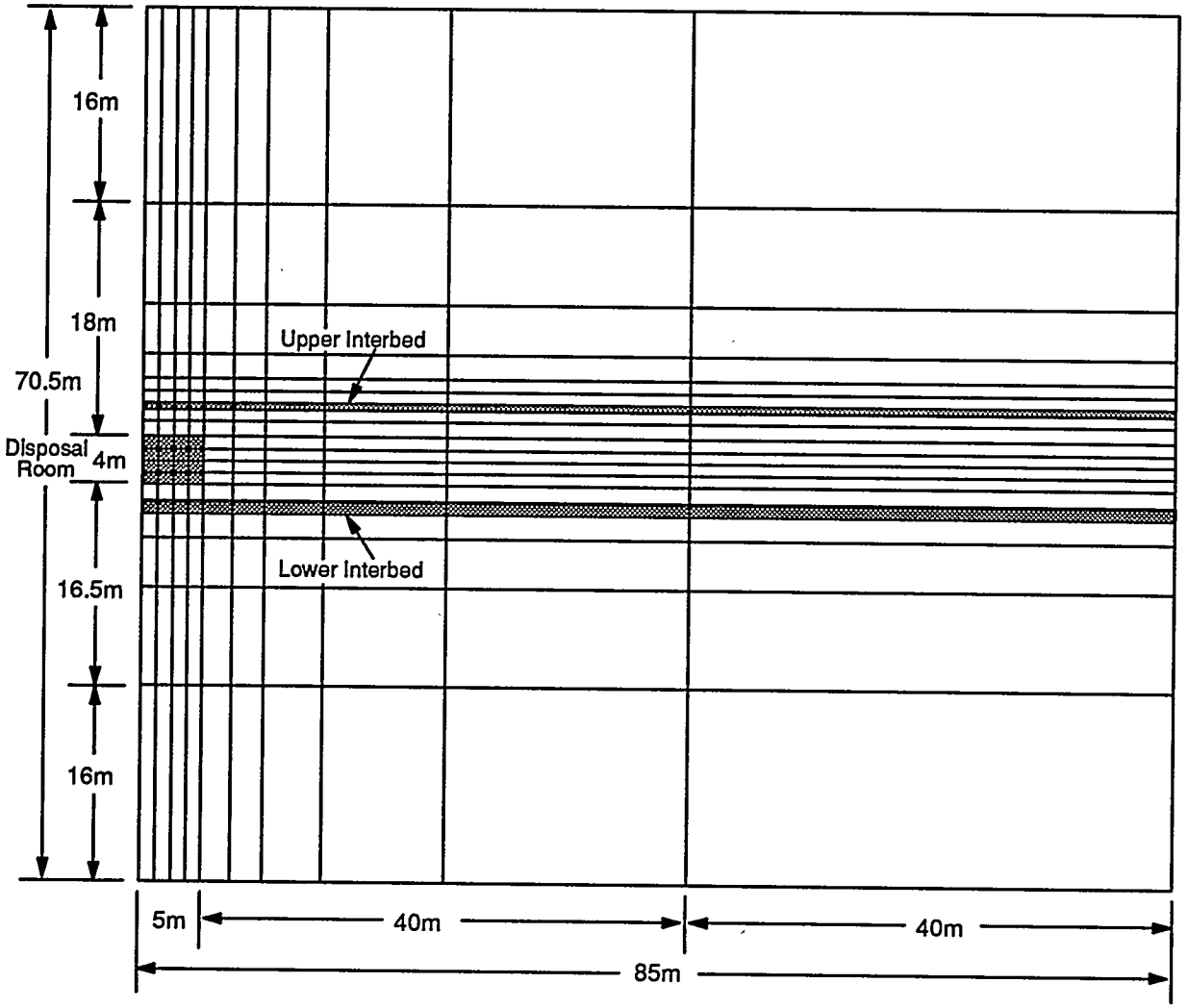

Figure 2-2. TOUGH2/EOS8 discretization of the fluid-flow continuum in the vicinity of the disposal room.

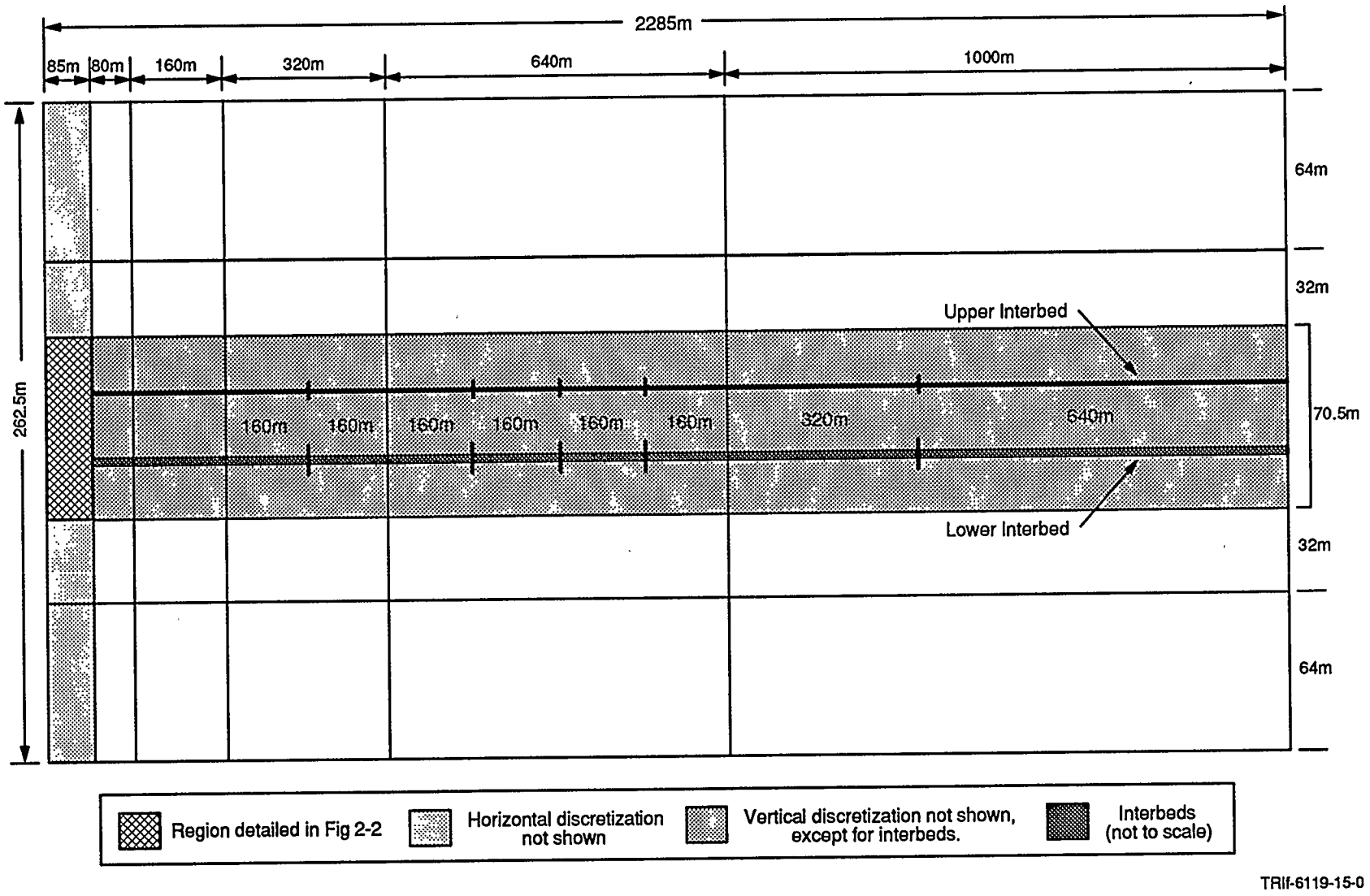

Figure 2-3. Far-field extent of the fluid-flow continuum.

expected to maintain hydrologic connection to the room for an extended period of time. Direct connections between interbed elements and elements on the edge of the disposal room were specified. These connections were specified to have large transmissivities, representative of fracture-like connections. The connection transmissivities were constant throughout each simulation.

2.3 Flow and Closure Coupling Methods

The simulations presented in this report used two different methods for approximating room closure in TOUGH2/EOS8. The two methods, pressure-time-porosity line interpolation and boundary backstress, are described in detail in Freeze et al. (1995). A short summary in presented here.

2.3.1 Pressure-Time-Porosity Line Interpolation

With the pressure lines method, the disposal room porosity (void volume) was recalculated at each time step as a function of the gas pressure in the room and time. By correlating simulated pressure-time conditions in the disposal room with a specified pressure-time-porosity relationship, a corresponding porosity for the simulated room was determined. The original concept for a porosity relationship based on the SANCHO f-series room closure results was developed by Butcher and Mendenhall (1993).

A pressure-time-porosity line was calculated from each of the five SANCHO f-series simulations performed by Stone (1995a) based on the room porosity vs. time and gas pressure in the room vs. time results. To mitigate possible adverse effects of numerical oscillations apparent in the original SANCHO results, sections of the data were smoothed. The result was a smoothed pressure-time-porosity data set internally consistent with respect to time, moles of gas in the room, room porosity, and room pressure.

At each time step, the TOUGH2/EOS8 room porosity was set by interpolation between the pressure-time-porosity lines which bounded the TOUGH2/EOS8 simulated time and gas pressure in the room. A four-point interpolation algorithm was added to TOUGH2/EOS8 for this purpose. With this process, the room porosity-room gas pressure-time relationship, established

by SANCHO simulations of room closure, was transferred to TOUGH2/EOS8 where it was simulated in conjunction with multiphase fluid flow. In cases where the TOUGH2/EOS8 simulated time and pressure conditions were not bounded by four SANCHO data points, extrapolation was used to obtain a room porosity value.

For reasons discussed in Section 4, the coupled flow and closure simulations presented in this report extended to 12,000 years, which exceeds the 2,000-year duration of the SANCHO simulations. Therefore, the pressure-time-porosity lines were extrapolated to 12,000 years. Because conditions changed little in the final years of the SANCHO simulations, the 12,000 year conditions of the pressure-time-porosity lines were set identically to the 2,000 year conditions.

2.3.2 Boundary Backstress Method

The boundary backstress method uses a Darcy flow approximation to represent salt creep. Salt was modeled as a fluid phase having high viscosity, increasing the number of simulated phases from two to three (gas, brine, and salt). Room closure was simulated by the salt phase flowing into the disposal room. A dual continuum conceptualization was used with multiphase brine and gas flow confined to the same fluid-flow continuum (Figures 2-2 and 2-3) that was used with the pressure lines method. The salt phase was confined to a salt-flow continuum, which contained only two regions, disposal room and "fluid" halite. The two continuums were connected via the disposal room. The salt-flow continuum was used to model single-phase flow of "fluid" salt through a fixed matrix with an assumed porosity of 1.0. The flow properties of "fluid" salt were selected such that the flow of salt into the disposal room would simulate room closure. The presence of salt in the disposal room altered both the void volume available to gas and brine and the gas pressure, thereby impacting the multiphase flow of brine and gas in the fluid-flow continuum.

The boundary backstress method provides resistance to closure analogous to waste and backfill consolidation using an artificial boundary within the disposal room. A calibration process was employed to derive empirical relationships between the salt phase flow parameters (i.e., viscosity) and mechanical salt creep parameters that could be used in combination with the properties of the artificial boundary to reproduce the room closures and pressures from the SANCHO f-series simulations. The calibration process is described by Freeze et al. (1995).

A single set of parameters was selected which produced a close match with closure results for the entire range of gas-generation rates simulated by Stone (1995a).

No adjustments were made to the empirically calibrated salt phase properties to extend the method from the 2,000-year duration of the SANCHO simulations to the 12,000-year duration of the coupled flow and closure simulations (see Section 4 for discussion of the 12,000 year duration). This approach assumes that trends extrapolated from the salt creep and room closure response in the first 2,000 years adequately characterize the response beyond 2,000 years.

2.4 Gas-Generation Source-Term Implementation

To examine the dependence of gas generation on brine availability, Brush (1991) performed gas-generation experiments under both brine-inundated and vapor-limited conditions, as described in Section 1.1.4. These experimental conditions likely provide upper (brine-inundated) and lower (vapor-limited) bounds to in-situ gas-generation rates. Correlating these experimental conditions with actual room conditions is a complex process. Typically, a disposal room will have a heterogeneous saturation distribution with conditions somewhere between brine-inundated and vapor-limited. Brine flowing into a disposal room may accumulate at the bottom of the room due to density effects. Under these conditions of gravity-driven phase segregation, the lower portion of the room may exhibit brine-inundated behavior, while the upper portion of the room exhibits vapor-limited behavior. Direct multiphase simulation with a grid fine enough to adequately characterize the heterogeneities and saturation distribution in the room is computationally demanding and was not incorporated into the baseline and sensitivity simulations. The effects of a finely gridded disposal room were examined using an alternative conceptual model (Section 2.5.3).

The baseline and sensitivity simulations used two simple implementations of gas-generation behavior, specified rates (Section 2.4.1) and brine-dependent rates (Section 2.4.2). Gas generation was modeled using gas sources within a room. The specified gas-generation rates were not dependent on brine availability. However, specified rates covering the range of experimentally-determined rates were simulated. Brine-dependent rate simulations correlated gas-generation rates with brine saturation, which changed due to brine flow in and out of the room, but did not account for brine consumption.

All baseline simulations assumed a fixed gas generation potential of 1,600 moles per drum of CH TRU waste (1.09×10^7 moles per room assuming 6,804 drums per room), which is comprised of 1,050 moles per drum from anoxic corrosion and 550 moles per drum from microbial activity. These estimates assume that there is sufficient brine available to fully exhaust the potential.

2.4.1 Specified Rate

In specified rate simulations, gas-generation rate was specified independent of brine availability. Four different specified rate histories were utilized (Table 2-1). The four specified gas-generation rate histories cover the range (maximum, best estimate, and minimum) of experimentally-determined brine-inundated and vapor-limited rates, as estimated by Brush (1991). The rate histories are denoted by the first and second phase rates. In each simulation, gas-generation rates were specified for the duration of the simulation, changing from the first phase rate to the second phase rate when the microbial potential was exhausted, and changing to zero when the corrosion potential was exhausted. Note that the 2/1 rate history is equivalent to the f=1.0 rate history used by Stone (1995a) in SANCHO simulations.

Table 2-1. Specified Gas-Generation Rates (moles per drum per year)

Designation	First Stage[1]	Second Stage[2]	Experimental Rate Description
7 / 2	7	2	maximum brine-inundated
2 / 1 (f=1.0)	2	1	best-estimate brine-inundated, maximum vapor-limited
0.2/0.1	0.2	0.1	best-estimate vapor-limited
0 / 0 (f=0.0)	0	0	minimum brine-inundated, minimum vapor-limited

(1) During the first stage, gas is generated from both corrosion and microbial activity.

(2) During the second stage, gas is generated from corrosion only because microbial potential has been exhausted.

Because the specified rate simulations did not directly correlate gas generation with brine availability, an indication of the influence of brine on system behavior is obtained by comparing results over the range of specified rate histories. The experimentally-based range of rates is assumed to provide bounding estimates of in-situ gas-generation rates.

2.4.2 Brine-Dependent Rate

In brine-dependent rate simulations, the gas-generation rate was directly correlated with brine availability. Brine availability was measured by brine phase saturation (S_b) at various locations within the disposal room. At each time step, a gas-generation rate that was a composite of the experimentally-determined brine-inundated and vapor-limited rates was estimated based on the local brine phase saturation distribution. The calculated brine-dependent rate varied with time, changing as saturation conditions changed and as corrosion and microbial potentials were exhausted.

Three different brine-dependent gas-generation rate assumptions (Table 2-2) were simulated, corresponding to the experimentally-determined range of rates (maximum, best estimate, and minimum) estimated by Brush (1991). For each range of gas-generation rates presented in Table 2-2, the lower bound represents a disposal room entirely under vapor-limited conditions while the upper bound represents an entirely brine-inundated room. Under highly brine-saturated conditions, the composite brine-dependent rate approached the experimental brine-inundated rate. In the case where the brine saturation was insufficient to produce brine-inundated conditions anywhere in the room, the brine-dependent rates decreased to the experimental vapor-limited rates. Note that the minimum brine-dependent rate is identical to the specified 0/0 rate history (no gas generation) regardless of saturation conditions.

As discussed previously, computational demands precluded the direct simulation of gravity-driven phase segregation within the room for large numbers of sensitivity simulations. In order to properly address the effects of phase segregation on brine-dependent gas-generation rates, two methods of correlating gas-generation rates with saturation distribution within the room were utilized, the capillary fringe method (Section 2.4.2.1) and the linear correlation method (Section 2.4.2.2).

Table 2-2. Brine-Dependent Gas-Generation Rates (moles per drum per year)

	First Stage[1]	Second Stage[2]
Maximum	2 - 7	1 - 2
Best Estimate	0.2 - 2	0.1 - 1
Minimum	0	0

(1) During the first stage, gas is generated from both corrosion and microbial activity.

(2) During the second stage, gas is generated from corrosion only because microbial potential has been exhausted.

2.4.2.1 CAPILLARY FRINGE METHOD

The capillary fringe method predicts aqueous and gaseous phase segregation within the room based on the volume of brine present. Brine is expected to accumulate at the bottom of the room and is likely to be drawn upward through the pore spaces in the waste and backfill due to capillary forces to form a capillary fringe. The capillary fringe will be bounded by a pool of brine on the floor of the room having maximum brine saturation (only residual gas remains) and a gas-saturated pocket in the upper portion of the room having minimum (residual) brine saturation (Figure 2-4). For a given set of waste and backfill properties, the position of the capillary fringe relative to the floor of the room is dependent on the volume of brine in the room. Therefore, at each time step, a theoretical disposal room saturation distribution can be calculated from the simulated volume of brine in the room.

Under quasi-static conditions, as would occur if brine inflow was slow relative to the rate of brine movement within the room, a balance between downward gravitational and upward capillary forces exists (de Marsily, 1986):

$$\frac{dp}{dz} = -\rho g \qquad (2\text{-}1)$$

where:

- p = fluid pressure,
- ρ = fluid density, and
- g = gravitational acceleration.

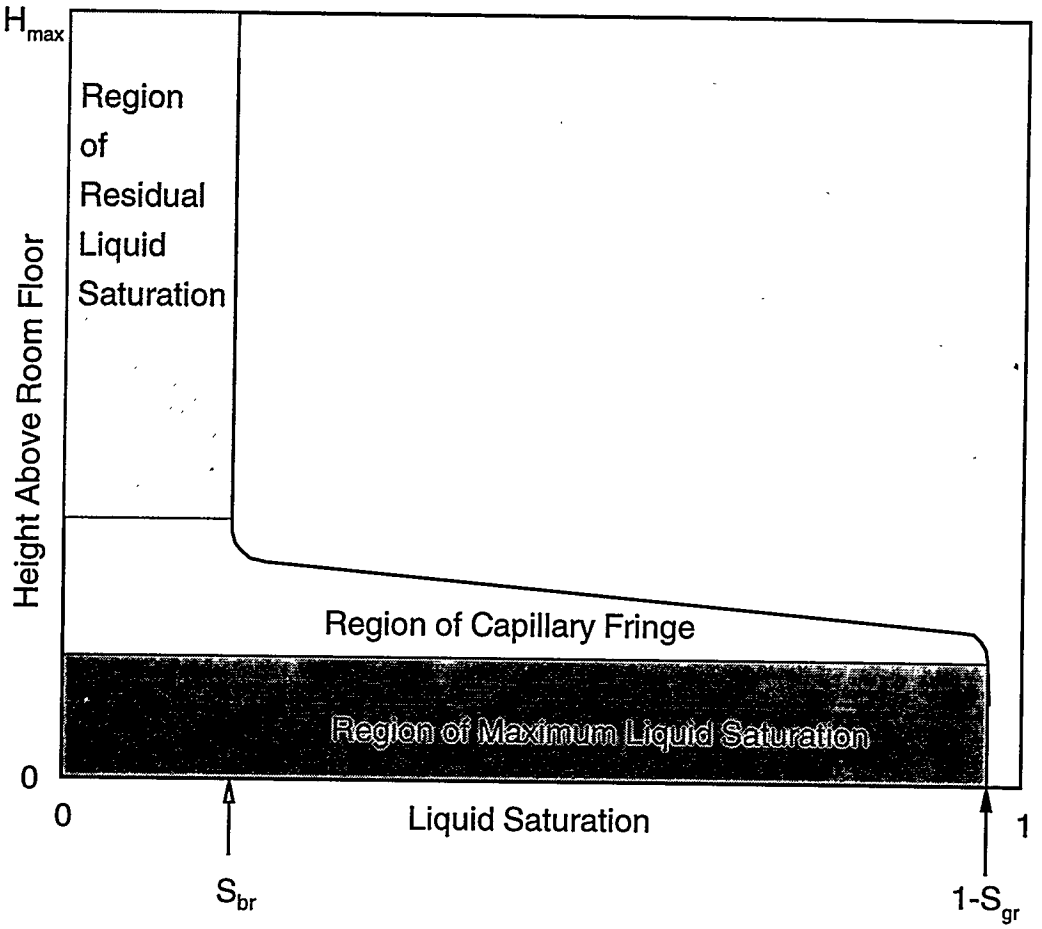

Figure 2-4. Schematic diagram of capillary fringe.

The capillary pressure, p_c, between two immiscible fluids (gas, g, and brine, b) is (de Marsily, 1986):

$$p_c = p_g - p_b \tag{2-2}$$

Combining Equations 2-1 and 2-2 yields:

$$p_c = p_{co} + (\rho_b - \rho_g)gh \tag{2-3}$$

where:

p_c = capillary pressure at height h,
p_{co} = capillary pressure at reference datum, and
h = height above reference datum.

The relationship between capillary pressure and saturation in the disposal room is assumed to follow the modified Brooks and Corey (1964) model (Section 3.1.1.2):

$$p_c = \frac{p_t}{S_e^{1/\lambda}} \tag{2-4}$$

where:

p_t = threshold pressure,
S_e = effective wetting phase (brine) saturation, and
λ = pore-size distribution index.

Brooks and Corey (1964) refer to p_t in Equation 2-4 as bubbling pressure, and define it as the approximate capillary pressure at which gas flow can first be observed. The term threshold pressure is used here to represent the capillary pressure at the point gas forms a continuous phase ($S_b = 1 - S_{gr}$ which corresponds to $S_e = 1$) and is therefore equivalent to the bubbling pressure.

The effective brine saturation, S_e, is modified from Brooks and Corey (1964) to account for a non-zero residual gas saturation, S_{gr}, as presented by Burdine (1953):

$$S_e = \frac{S_b - S_{br}}{1 - S_{gc} - S_{br}} \tag{2-5}$$

where:

S_b = wetting phase (brine) saturation,
S_{br} = residual brine saturation, and
S_{gr} = residual (critical) gas saturation.

Combining Equations 2-3 through 2-5 produces an equation for theoretical brine saturation as a function of height above a datum (i.e., floor of the room):

$$S_b = \left[\frac{p_t}{p_{co} + (\rho_b - \rho_g)gh}\right]^{\lambda} (1 - S_{gr} - S_{br}') + S_{br} \qquad (2\text{-}6)$$

In Equation 2-6, the only unknown is the theoretical capillary pressure at the base of the room, p_{co}. However, p_{co} can be determined for each of the three possible brine saturation conditions at the base of the room. The three possible conditions are: maximum brine ($S_b = 1 - S_{gr}$), resulting in a fully developed capillary fringe; minimum brine ($S_b = S_{br}$), resulting in no capillary fringe; or intermediate brine ($1 - S_{gr} > S_b > S_{br}$), resulting in a partially developed capillary fringe. For any condition, a theoretical p_{co} and S_b can be determined from the simulated volume of brine in the room.

A saturation threshold is defined such that room segments where the theoretical brine saturation is above the threshold are assumed to generate gas at a rate equivalent to brine-inundated conditions and room segments where brine saturation is below the threshold are assumed to generate gas at the slower, vapor-limited rate. The threshold saturation is assumed to be similar to the residual brine saturation, so that vapor-limited conditions correspond to room segments where brine is immobile because relative permeability to brine is at or near zero. This implementation allows gas generation to occur at a brine-inundated rate throughout the capillary fringe where brine is drawn upward into partially saturated regions by capillary forces.

2.4.2.2 LINEAR CORRELATION METHOD

The linear correlation method uses a linear relationship between brine saturation and gas generation to calculate brine-dependent gas-generation rates. Although simulated saturation distributions were used, phase segregation was not directly accounted for because gravitational

effects were not included and the room had a coarse vertical discretization. The brine-dependent gas-generation rate, R, is calculated from the experimental brine-inundated, R_{BI}, and experimental vapor-limited, R_{VL}, rates as follows:

$$R = (S_b)(R_{BI}) + (S_g)(R_{VL}) \quad (2\text{-}7)$$

The linear correlation method was applied to each element of the room and an average gas-generation rate for the entire disposal room calculated. The linear correlation method is analogous to the methodology used in WIPP PA Department (1993a and 1993b) calculations, except that WIPP PA simulations included brine consumption.

In the absence of a capillary fringe, the brine might be expected to form a puddle on the floor of the room. Assuming that the brine puddle produces gas at the brine-inundated rate and the remainder of the room produces gas at the vapor-limited rate, the total gas-generation rate for the disposal room would be equivalent to the rate predicted by the linear correlation method.

2.5 Alternative Conceptual Models

In addition to the baseline and sensitivity simulations, performed with the basic conceptual model, several alternative conceptual models were developed to investigate certain repository scenarios.

2.5.1 Interbed Fracture

The interbed fracture conceptualization assesses the impact on system behavior of fracturing of the interbeds in response to near-lithostatic gas pressures in the room. The model implemented in TOUGH2/EOS8 was based on a preliminary model developed by WIPP PA and used in preliminary PA calculations (Stoelzel et al., 1995). Conceptually, the model simulates the effects of fractures in anhydrite interbeds by increasing the interbed porosity and intrinsic permeability as gas pressure rises.

In TOUGH2/EOS8, the porosity, ϕ, is related to the pore volume compressibility, α_p, and the pressure, p, by:

$$\alpha_p = \frac{1}{\phi}\frac{\partial \phi}{\partial p} \tag{2-8}$$

Integration of Equation 2-8 yields:

$$\phi = \phi_o \exp\left[\int_{p_o}^{p} \alpha_p(s)ds\right] \tag{2-9}$$

where ϕ_o is the porosity at a reference pressure p_o.

Two fracturing pressures were specified: an initial fracturing pressure, p_{if}, at which fractures begin to form or, alternatively, pre-existing fractures begin to open; and a final (maximum) fracturing pressure, p_{ff}, above which fractures no longer open. To represent the effects of interbed fracture, the pore volume compressibility was assumed to increase linearly with gas pressure from α_{po} at p_{if} to $\alpha_{p\,max}$ at p_{ff} (Figure 2-5a). The corresponding increase in porosity with pressure, calculated from Equation 2-9, is shown in Figure 2-5b. Changes in interbed intrinsic permeability, k, were assumed to be proportional to the magnitude of the porosity change raised to a power, n:

$$k = k_o\left[\frac{\phi}{\phi_o}\right]^n \tag{2-10}$$

The interbed permeability is shown as a function of pressure in Figure 2-5c and as a function of porosity in Figure 2-5d.

In the case of $p \leq p_{if}$, there are assumed to be no fracture-initiated changes to the interbed rock properties. The pore volume compressibility is α_{po} and the intrinsic permeability is k_o.

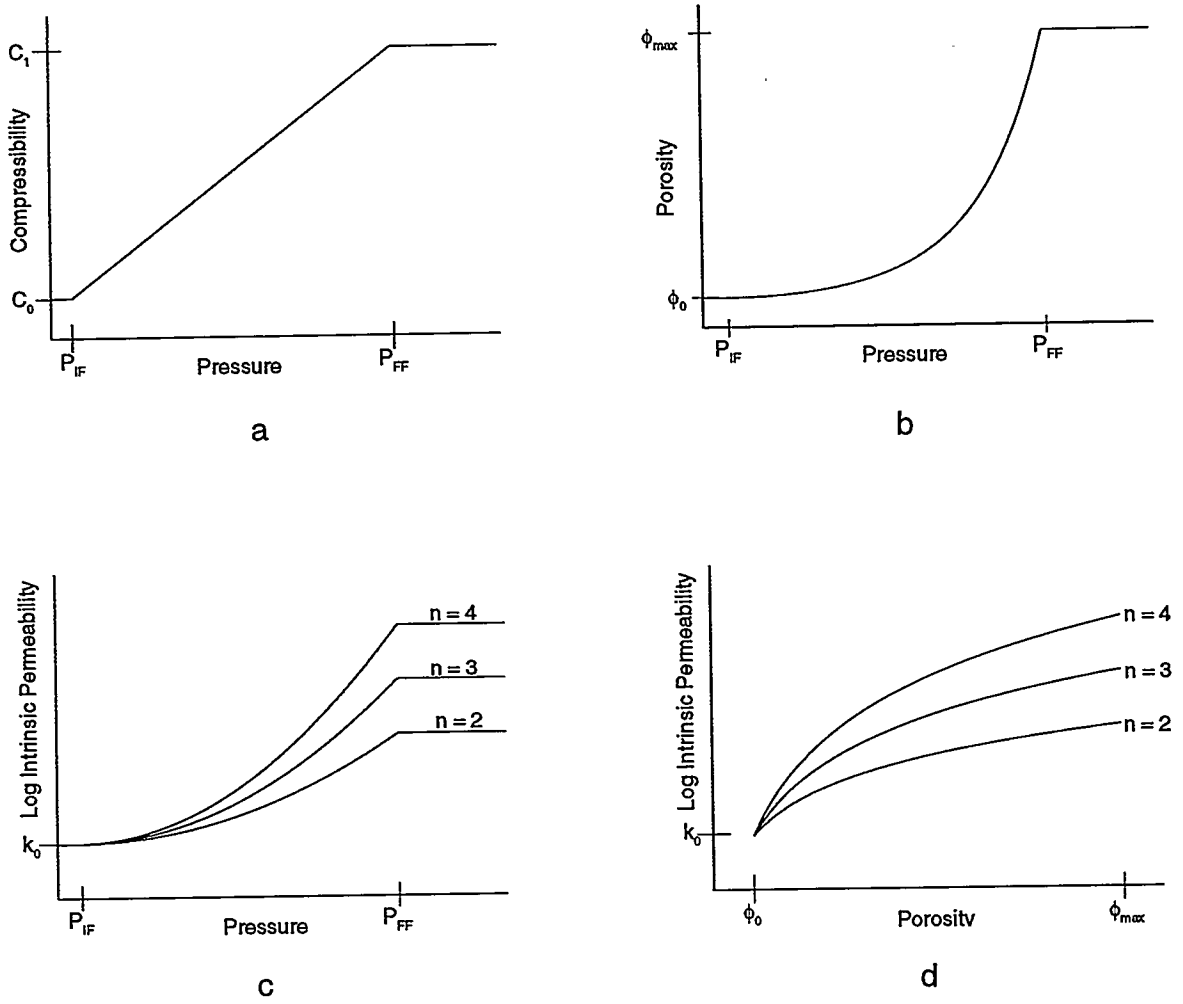

Figure 2-5. Relationships between pore volume compressibility, porosity, permeability, and pressure using the interbed fracture alternative conceptual model.

In the case of $p_{if} < p \leq p_{ff}$, there are assumed to be open fractures:

$$\alpha_p = \alpha_{po} + \frac{\alpha_{pf} - \alpha_{po}}{p_{ff} - p_{if}}(p - p_{if}) \tag{2-11}$$

$$\phi = \phi_o \exp\left[\alpha_{po}(p - p_o) + \frac{(\alpha_{pf} - \alpha_{po})}{(P_{ff} - p_{if})}\frac{(p - p_{if})^2}{2}\right] \tag{2-12}$$

and intrinsic permeability is calculated as a function of porosity using Equation 2-10.

In the case of $p > p_{ff}$, there is a constant fracture porosity, ϕ_{max}, and a constant intrinsic permeability, k_{max}, calculated from Equation 2-10 with $\phi = \phi_{max}$.

The interbed fracture model does not consider the impact that fracture formation and expansion might have on the multiphase flow properties in the interbeds. For simplicity, the gas-brine capillary pressure in the interbeds was set to zero for all of the fracture simulations. Results of the interbed fracture model simulations are discussed in Section 5.3.2.1.

2.5.2 Disturbed Rock Zone

The baseline model assumes that fracture connections, characteristic of a disturbed zone, exist between the disposal room and the interbeds. However, no adjustments are made to the rock properties to reflect the disturbed rock zone (DRZ).

Fracturing and dilation in response to excavation is expected to create a zone of enhanced permeability, porosity, and interconnectivity that decreases with distance from the excavation (Stormont, 1990). However, fractures in the DRZ are expected to close and heal as room closure and consolidation reach their maximum extent, returning the zone to its original, undisturbed state (Butcher and Mendenhall, 1993). The DRZ conceptual model assesses the impact of these changes in the rock properties in the halite near the room.

The conceptual DRZ implemented in TOUGH2/EOS8 was assumed to extend 10 m into the Salado Formation from the room and have an initial brine pressure of 7.5 MPa. The assumed initial pressure of the DRZ is based on a relationship between brine pore pressure and distance

from the excavation presented by Beauheim et al. (1993a). The relationship, shown in Figure 2-6, indicates that pore pressures in the Salado Formation are reduced within about ten meters of the excavation. Determining the extent of rock deformation due to excavation-related stresses is more complex. For simplicity of implementation, an average pressure of 7.5 MPa was used to represent the distribution of pressures over the 10 m depressurized interval and the rock properties were assumed to be disturbed within 10 m of the disposal room.

The initial intrinsic permeability and compressibility were assumed to be higher than undisturbed values in response to fracturing and expansion of the halite in the DRZ. The permeability and compressibility were reduced to undisturbed values at 200 years to simulate the healing of the DRZ. The porosity of the DRZ was not altered from the undisturbed value. The storage effects of the expected enhanced porosity in the DRZ were simulated indirectly with the enhanced compressibility. The effects of altered multiphase flow properties in the DRZ fractures relative to undisturbed conditions were not simulated due to a lack of data. The results of the DRZ simulation are discussed in Section 5.3.2.2.

2.5.3 Effects of Gravity

The baseline conceptual model ignores gravitational forces acting on the fluids. This assumption was made because scoping simulations revealed that incorporating a gravitational vector in the simulations does not significantly affect system behavior and greatly increases execution time. The effects of gravity are manifested primarily in the disposal room, where the brine and gas phases can segregate with brine pooling on the floor and gas occupying the overlying region. Phase segregation of this sort can result in differences in gas-generation rates throughout the room and in the preferential expulsion of gas to the upper interbed and brine to the lower interbed. To explicitly model phase segregation, a finer vertical discretization was used for the disposal room (eight elements) than with the baseline conceptualization (four elements) and gravitational effects were simulated. The results are discussed in Section 5.3.2.3.

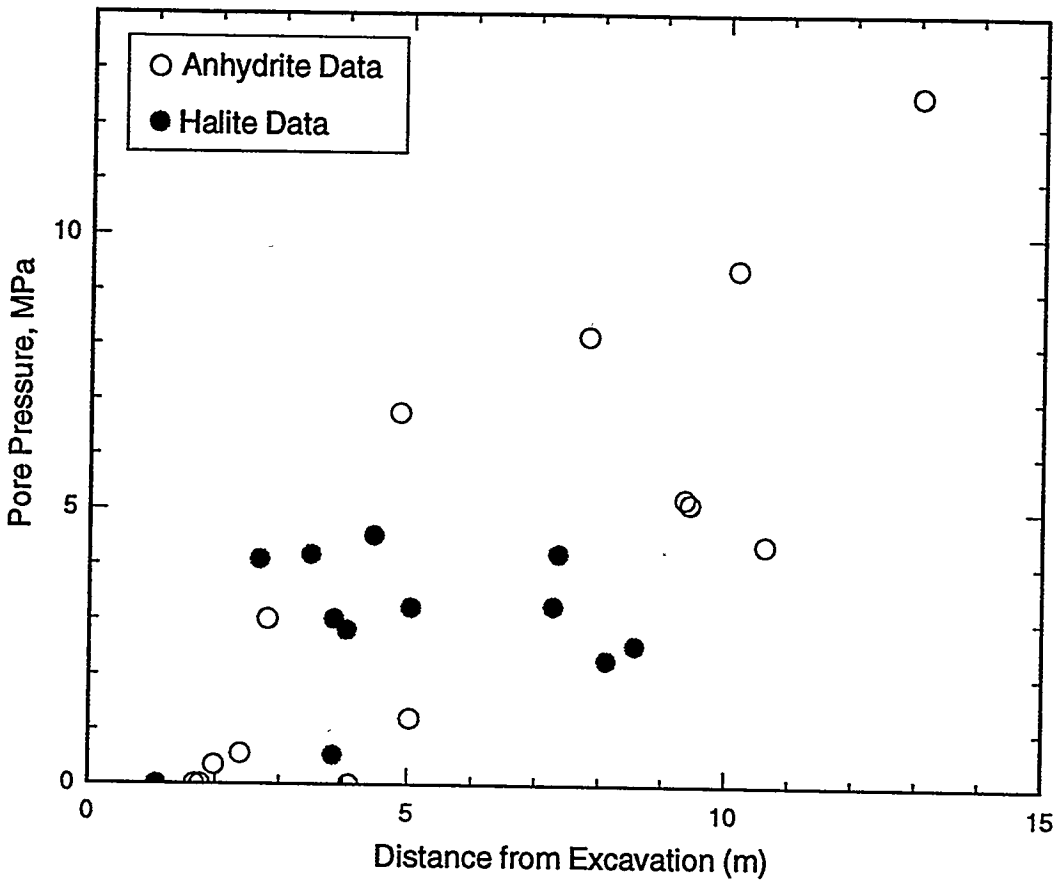

Figure 2-6. Formation pore pressures interpreted from in-situ testing in the vicinity of excavations (after Beauheim et al., 1993a).

2.5.4 Gas Exsolution From the Salado Formation

During the operational phase of the WIPP facility, it is expected that the pore pressure will drop near the excavation (Figure 2-6). The pressure drop should decrease the solubility of gas in brine, potentially causing exsolution of gas from brine in the Salado Formation pore spaces. Thus when the post-operational phase commences, there may be elevated gas saturations near the repository.

To evaluate the effects of increased gas saturation near the repository, TOUGH2/EOS8 simulations with increased initial gas saturation throughout the Salado Formation were performed. By increasing the gas saturations everywhere in the Salado Formation it was assumed that the maximum effects of gas exsolution would be observed. The results of the simulation are discussed in Section 5.3.2.4.

2.5.5 Instantaneous Room Depressurization

The room depressurization conceptual model was implemented to assess the impact on system behavior of an instantaneous gas depressurization in the room. This is similar to a human intrusion scenario, in which there is inadvertent penetration of the repository by a borehole from the surface. The room depressurization simulations were started with baseline conditions, but at 1,000 years the disposal room was depressurized instantaneously to 7.7 MPa, corresponding to a repository breach by a borehole that was sealed immediately after the penetration. Under these circumstances, gas can only leave the depressurized room by flowing into the Salado. TOUGH2/EOS8 room depressurization simulations were performed using both the 2/1 and 0.2/0.1 specified gas-generation rate histories. The results of the simulations are discussed in Section 5.3.2.5.

2.6 Uncertainty Evaluation

Any modeling study must recognize the sources of model and parameter uncertainty and the effects of these uncertainties on simulation results. Potential sources of uncertainty are discussed in Sections 2.6.1 and 2.6.2. A method for quantifying the effects of uncertainty is presented in Section 2.6.3 and 2.6.4.

2.6.1 Model Uncertainty

The development of the coupled flow and closure simulator, TOUGH2/EOS8, incorporates several important assumptions that may lead to uncertainty in its ability to predict actual repository performance. These assumptions can be broadly categorized under either process coupling or system conceptualization.

Coupling between the processes of gas generation, room closure, and multiphase flow was described in detail in Section 1.2.3. In the absence of a reaction-path gas-generation model, the simple gas-generation approximations and couplings with multiphase flow are reasonable. Baseline simulation results (Section 4.2) showed that the brine-dependent rate implementation was bounded by the minimum and maximum specified rates. The two methods for implementing room closure were calibrated to SANCHO simulation results, and, therefore, inherently incorporate the uncertainty in SANCHO. Some additional uncertainties related to the closure coupling methods were discussed by Freeze et al. (1995).

Because TOUGH2/EOS8 is based on a multiphase flow code, its conceptual treatment of multiphase flow is sound, although some multiphase processes are simplified. Conceptual uncertainty is introduced by modeling fluid flow through a non-deforming porous medium, when the Salado Formation halite and interbeds may actually be deforming and fracturing due to near-field excavation-related stresses and/or elevated gas pressures.

The primary process coupling uncertainty is the behavior of the disposal room and the Salado Formation at pressures at and above lithostatic. The TOUGH2/EOS8 simulations did not assign any significance to lithostatic pressure. Room pressures in excess of 15 MPa did not produce any changes to hydrologic properties such as might be associated with deformation or fracturing (except in simulations using the interbed fracture alternative conceptual model). Under certain conditions, simulated room pressures well in excess 15 MPa were achieved, even though actual repository pressures would likely be limited by some near-lithostatic fracturing pressure.

System conceptualization uncertainty results from model geometry, processes not being included, and numerical considerations. The conceptual model simulates a two-dimensional vertical cross-section containing a half-width room surrounded by homogeneous halite and upper and lower composite interbeds. The model interbeds are connected to the room by high

transmissivity connections. The actual repository is of course three-dimensional, containing panels of adjacent disposal rooms and surrounded by heterogeneous pure and impure halite and polyhalite with several anhydrite interbeds above and below the room. The interbeds are connected to the room through boreholes, rock bolts, and excavation-related fracturing. Scaling of simulation results from room-scale to panel- or repository-scale and from two- to three-dimensional is not straightforward given the complexity of the system and process coupling. The model was not intended to provide a direct comparison with regulatory standards. Rather, it is a tool for developing a mechanistic understanding of system behavior, testing alternative conceptual models, and determining parameter sensitivity.

Alternative conceptual models were developed to address the issues of a DRZ, phase segregation in the room, initial gas in Salado Formation, and instantaneous room depressurization. The processes of brine consumption, which impacts gas generation, and fingering and gaseous diffusion, which impact gas flow, were not included in baseline or sensitivity simulations. These two processes are difficult to implement numerically and are difficult to conceptualize due to a lack of data.

Numerical considerations include: grid size; boundary effects; numerical dispersion; and oscillatory convergence of iterative solutions. Grid size and boundary effects were addressed through scoping simulations, and were not found to have a deleterious effect on simulation results.

2.6.2 Parameter Uncertainty

The TOUGH2/EOS8 input parameters are discussed in Section 3. These parameters are used to describe system behavior in response to waste-generated gas. The hydrologic parameters (Section 3.1) control multiphase flow, the gas-generation parameters (Section 3.2) control the gas-generation rate, and the room closure parameters (Section 3.3) control salt creep and room void volume. Uncertainty in parameter values results from a lack of representative experimental or in-situ measurements and/or uncertainty in measured values. Uncertainty in measured values may be due to: measurement or experimental error; interpretive assumptions; or natural variations in measured properties, as in a heterogeneous medium.

The WIPP PA Department (1992a) used a stochastic framework to evaluate repository performance and compliance. For each input parameter, values are assigned a probability of occurrence in accordance with a probability density function (PDF). The range of possible parameter values is defined by non-zero probabilities of occurrence. Stochastic simulation results are in the form of complementary cumulative distribution functions (CCDF) which can be compared to regulatory standards, also in the form of a CCDF.

In contrast, with TOUGH2/EOS8, parameter uncertainty was characterized using a deterministic approach. For each input parameter, a minimum, a maximum, and a best- estimate value were selected. The best estimate represents a most likely value, but has no statistical significance (i.e., it is not a calculated mean, median, average, or expected value). Minimum and maximum values were chosen to represent the extreme expected values for a parameter. Typically, the deterministic parameter value range (minimum to maximum) corresponded to the range of non-zero probabilities for the PDF.

The baseline simulations were performed with all parameters at best-estimate values (Section 4). To evaluate the effects of parameter uncertainty, sensitivity simulations were performed in which a single parameter value was varied to its minimum and maximum values with all other parameters held at best-estimate values (Section 5). The effects of parameter uncertainty on simulation results were quantified by evaluating the change in selected performance measures in response to parameter variations. Parameter sensitivity was performed on most hydrologic and gas-generation parameters. In addition, some sensitivity was performed on model geometry and conceptualization.

2.6.3 Performance Measures

Simulation of multiphase flow using TOUGH2/EOS8 produced time histories of element and region properties (phase pressures, porosity, phase saturations) and of the flow of each phase between elements and regions. Additionally, the spatial distribution of certain properties and phase and component mass balance information were available at user specified times during and at the end of a simulation. Analysis of simulation results was performed by examining the following six parameters over time: room void volume (porosity), a measure of room closure behavior; room gas phase pressure; mass of gas in the room; mass of gas generated in the room; brine phase flow (inflow and expulsion) between the room and the Salado Formation (halite and

interbeds); and gas phase flow out of the room (gas release). Analysis also included an examination of gas saturations and migration distances in the upper and lower interbeds at the end of a simulation. These eight results were evaluated graphically for each simulation.

To evaluate parameter sensitivity and importance, four performance measures were selected to describe system behavior. These were: maximum gas phase pressure in the room; maximum brine volume in the room; total gas release from the room; and maximum gas migration distance in a single interbed.

Total gas release and maximum migration distance are indicators of gas flow away from the repository. Although these performance measures seemingly provide direct comparisons with regulatory standards, simulated gas migration distances are not representative of actual migration away from the repository because of the simplified system geometry (single isolated room, composite interbeds, two-dimensional cartesian flow). Instead they were used in a comparative fashion to provide an indication of which scenarios were likely to enhance or limit gas release and migration relative to baseline results. To avoid possible misuse of migration distances, they are presented as normalized values, equivalent to the simulated migration distance divided by the room width. The other two performance measures are not directly related to regulatory compliance. However, they were considered important because maximum room pressure provides guidance to interbed fracture behavior and maximum brine inflow provides guidance to gas-generation behavior.

2.6.4 Quantification of Sensitivity and Importance

To better evaluate the sensitivity of system behavior to variations in hydrologic and gas-generation parameters, gas-generation source-term implementation, and model conceptualizations, a method to quantify parameter sensitivity and importance was developed based on the methodology presented by Reeves et al. (1991). Parameter sensitivity was quantified using a sensitivity coefficient, S, a dimensionless derivative defined as:

$$S = \frac{P_o}{\Psi_o}\left[\frac{\delta\Psi}{\delta P}\right]_o \qquad (2\text{-}13)$$

where:

P = parameter, and
Ψ = performance measure.

The parameter, P, may be any quantifiable system variable such as a hydrologic parameter or a gas-generation rate. The performance measure, Ψ, may be any of the four previously described performance measures. Equation 2-13 is written in general form where the subscript, o, represents a baseline or best-estimate value. In this context, parameter sensitivity is evaluated about the baseline conditions. A simulation wherein a parameter was changed from P_o to P_1 that produced a result, Ψ_1, would have a sensitivity coefficient where $\delta\Psi = \Psi_1 - \Psi_o$ and $\delta P = P_1 - P_o$. The sensitivity coefficient, S, provides a single value that describes the change in the performance measure in response to a unit change in the parameter within the range P_o to P_1. However, sensitivity is often non-linear over the entire uncertainty range of a parameter. In this study, a typical parameter range included three parameter values, P_o, P_{min}, and P_{max}. Two sensitivity coefficients were calculated for each performance measure, S^- (applicable between P_{min} and P_o) and S^+ (applicable between P_o and P_{max}). Sensitivities were also presented graphically, giving a better indication of the parameter sensitivity over the range of uncertainty.

Parameter importance was quantified using a dimensionless importance coefficient, I, defined as:

$$I = \frac{R_P}{\Psi_o}\left[\frac{\delta\Psi}{\delta P}\right]_o = \frac{R_P}{P_o}(S) \qquad (2\text{-}14)$$

where:

R_P = range of parameter P.

The importance coefficient quantifies the effect on system behavior of variations in a parameter value over its expected range. As indicated by Equation 2-14, the parameter importance is a product of the parameter sensitivity and the normalized parameter range. The parameters that have the greatest effect on system behavior (i.e., greatest importance) are likely to be both sensitive and uncertain (a large uncertainty corresponds to a large range). Sensitive but certain parameters and uncertain but insensitive parameters are not necessarily important. The dependence of the importance coefficient on parameter range cannot be overstated. A change in the expected range of a parameter may produce a significant change in the importance coefficient.

The parameter range, R_P, used in Equation 2-14 should be evaluated over the same range as the sensitivity (in this case R_P^- and R_P^+). As with the sensitivity coefficient, the importance coefficient is a single value that may not be representative over the entire uncertainty range of

a parameter. Two importance coefficients were calculated for each performance measure, I^- corresponding to the range (P_{min} to P_o) for S^- and I^+ corresponding to the range (P_o to P_{max}) for S^+.

In this study, R_P was usually equivalent to δP, in which case Equation 2-14 simplifies to:

$$I = \frac{\delta \Psi}{\Psi_o} \tag{2-15}$$

Equation 2-15 shows the importance coefficient to be simply the normalized change in the performance measure. This form of the importance equation is desirable because it does not require quantitative parameter values and ranges. It will be used to evaluate the relative importance of conceptual uncertainty in such non-quantifiable concepts as gas-generation source-term implementation and model conceptualization.

A comparison of the parameter importance coefficients with the conceptual importance coefficients provides an indication of the direction for future work. High parameter importance suggests that refinement of parameter best estimates and ranges is necessary. High conceptual importance suggests that improvements to the model conceptualization are required.

3.0 PARAMETER SUMMARY

A set of best-estimate parameters were selected for the baseline simulations. Parameter minimum and maximum values were also selected to perform sensitivity simulations. The parameter selection was based on data available as of June, 1993. Rationales and comments concerning the selection of these parameters and their expected ranges are presented in Appendix A. Brief descriptions of the hydrologic parameters (Section 3.1), the gas-generation parameters (Section 3.2), and the room closure parameters (Section 3.3) are given here.

3.1 Hydrologic Parameters

Hydrologic parameters include all physical properties, multiphase flow properties, and initial conditions controlling multiphase brine and gas flow within the disposal room (Section 3.1.1) and the Salado Formation halite and anhydrite interbeds in the fluid-flow continuum (Section 3.1.2). Fluid properties of brine and gas are also presented (Section 3.1.3). Minimums, best estimates, and maximums for the hydrologic parameters are summarized in Table 3-1 for the disposal room, in Table 3-2 for the halite, and in Table 3-3 for the anhydrite interbeds.

Table 3-1. Simulated Hydrologic Parameters for the Disposal Room

Parameter	Units	Minimum	Intermed.	Best Estimate	Intermed.	Maximum
Intrinsic Permeability (k)	m^2	--		$1x10^{-17}$		$1x10^{-14}$
Initial Porosity (ϕ)	*	--		0.66		--
Rock Compressibility (α)	Pa^{-1}	--		0.0		--
Residual Brine Saturation (S_{br})	*	0.01	0.10	0.276		--
Residual Gas Saturation (S_{gr})	*	0.001		0.02		0.10
Pore-Size Lambda (λ)	*	0.2		2.89		10
Threshold Pressure (p_t)	MPa	--		0.0		--
Initial Gas Pressure (p_g)	MPa	--		0.1		--
Initial Brine Saturation (S_{bo})	*	0.0003		0.01		0.066

* dimensionless parameter

Table 3-2. Simulated Hydrologic Parameters for Salado Formation Halite

Parameter	Units	Minimum	Intermed.	Best Estimate	Intermed.	Maximum
Intrinsic Permeability (k)	m^2	$1x10^{-25}$		$1x10^{-21}$	$1x10^{-20}$	$1x10^{-19}$
Porosity (ϕ)	*	0.001		0.01		0.03
Rock Compressibility (α)	Pa^{-1}	$5.6x10^{-12}$	$2.4x10^{-11}$	$2.7x10^{-11}$		$3.9x10^{-11}$
Residual Brine Saturation (S_{br})	*	0.00		0.20		0.40
Residual Gas Saturation (S_{gr})	*	0.00		0.20		0.40
Pore-Size Lambda (λ)	*	0.2		0.7		10.0
Threshold Pressure (p_t)	MPa	2.1	4.7	10.3		22.9
Initial Brine Pressure (p_o)	MPa	11.0		12.0		15.0

* dimensionless parameter

Table 3-3. Simulated Hydrologic Parameters for Salado Formation Interbeds

Parameter	Units	Minimum	Intermed.	Best Estimate	Intermed.	Maximum
Intrinsic Permeability (k)	m^2	$1x10^{-21}$	$1x10^{-20}$	$1x10^{-19}$		$1x10^{-18}$
Porosity (ϕ)	*	0.0006	0.005	0.01		0.03
Rock Compressibility (α)	Pa^{-1}	$5.7x10^{-12}$		$8.3x10^{-12}$		$1.9x10^{-11}$
Residual Brine Saturation (S_{br})	*	0.0		0.2		0.4
Residual Gas Saturation (S_{gr})	*	0.0		0.2		0.4
Pore-Size Lambda (λ)	*	0.2		0.7		10.0
Threshold Pressure (p_t)	MPa	0.2		0.3	2.1	4.7
Initial Brine Pressure (p_o)	MPa	11.0		12.0		15.0
Upper Interbed Thickness	m	--		0.30		--
Lower Interbed Thickness	m	0.40		0.90		1.25

* dimensionless parameter

3.1.1 Disposal Room

3.1.1.1 DISPOSAL ROOM PHYSICAL PROPERTIES

Intrinsic permeability estimates for the disposal room range from 1×10^{-17} m^2 for fully consolidated sludge-filled waste containers (Butcher et al., 1991b) to 1×10^{-11} m^2 for initially emplaced crushed salt backfill (Nowak et al., 1990). Because the simulations were not sensitive to the room permeability over this range, 1×10^{-17} m^2 was used as a baseline value to minimize computer execution time. A maximum permeability of 1×10^{-14} m^2 was used in sensitivity simulations.

The initial room porosity was 0.66, based on a volume average of the porosities of the room contents (Beraun and Davies, 1992). The simulated disposal room had a total volume of 3,658 m^2, with an initial void volume of 2,415 m^3 and an initial solids volume of 1,243 m^3. Each disposal room was assumed to contain 6,804 waste drums (Beraun and Davies, 1992), consisting of 2,722 drums of solid organic waste (cellulosics) having an initial porosity of 0.8, 2,722 drums of solid inorganic waste (metals and glass) having an initial porosity of 0.8, and 1,360 drums of sludges having an initial porosity of 0.5. The average initial porosity of all waste drums is 0.74 . The initial backfill porosity was assumed to be 0.4 (Beraun and Davies, 1992). The room porosity changed with time as salt creep occurred.

The mixture of waste and backfill within the disposal rooms is extremely heterogeneous. Compaction of the waste and backfill occurs during room closure, resulting in a time-varying compressibility. The two coupling methods (pressure lines and boundary backstress) incorporated various room conceptualizations and empirical relationships to simulate the changing backstress. Since the effects of room pore volume compressibility were already incorporated indirectly through the backstress approximations, simulations used a room (waste and backfill) compressibility of zero. As a result, pore volumes in the room were adjusted by the coupling methods rather than through waste and backfill compressibility.

3.1.1.2 DISPOSAL ROOM MULTIPHASE FLOW PROPERTIES

There are no measured relative permeability or gas-brine capillary pressure relationships for the material in the WIPP waste disposal rooms. In the absence of site-specific data, multiphase flow properties were estimated from actual measurements on an approximate

analogue material. The disposal rooms are expected to contain a heterogenous mix of partially crushed drums and backfill. The backfill will consist of crushed salt or a mixture of crushed salt and bentonite. Because of its high degree of heterogeneity, a mixture of unconsolidated fragmented clay, sandstone, and volcanic sand (Brooks and Corey, 1964) was selected as an approximate analogue to provide the relative permeability and capillary pressure characteristics of a disposal room.

The brine phase relative permeability, k_{rb}, and the gas phase relative permeability, k_{rg}, were calculated from the following relationships, based on the Brooks and Corey (1964) model:

$$k_{rb} = S_e^{(2+3\lambda)/\lambda} \tag{3-1}$$

$$k_{rg} = (1 - S_e)^2 \, (1 - S_e^{(2+\lambda)/\lambda}) \tag{3-2}$$

The effective brine saturation, S_e, was modified from Brooks and Corey (1964) to account for a non-zero residual gas saturation, as proposed by Burdine (1953):

$$S_e = \frac{S_b - S_{br}}{1 - S_{gr} - S_{br}} \tag{3-3}$$

where:

λ = pore-size distribution index,
S_b = brine saturation,
S_{br} = residual brine saturation, and
S_{gr} = residual gas saturation.

The gas-brine capillary pressure, p_c, was calculated from the threshold pressure, p_t, based on the relationships of Brooks and Corey (1964):

$$p_c = \frac{p_t}{S_e^{1/\lambda}} \tag{3-4}$$

The threshold pressure, referred to as the bubbling pressure by Brooks and Corey (1964), is representative of the capillary pressure at $S_b = S_{br}$ and corresponds to the point gas becomes mobile as a continuous phase. The impact of modifications to the Brooks and Corey (1964) model on capillary pressure and relative permeability is small, given the small S_{gr} value.

Brooks and Corey (1964) fit the measured data from the analogue fragmented mixture to obtain the following parameter values, $S_{br} = 0.276$ and $\lambda = 2.89$. The measured air relative permeability data were used to extrapolate to $S_{gr} = 0.02$ and the measured capillary pressure data were used to estimate $p_t = 0.0017$ MPa. The data used to determine these parameters are included in Appendix A.

These parameters were assumed to provide the best estimate for the disposal room multiphase flow properties. The TOUGH2/EOS8 simulated disposal room relative permeability and capillary pressure relationships are shown in Figures 3-1 and 3-2, respectively. Equation 3-4 predicts near-zero capillary pressures, except as the brine saturation approaches S_{br} and a theoretically infinite capillary pressure at $S_b = S_{br}$ (see Figure 3-2). However, an infinite capillary pressure is physically unrealistic (Gray and Hassanizadeh, 1991) and the largest capillary pressure measured by Brooks and Corey (1964) on the fragmented mixture was 0.005 MPa. Therefore, for simplicity, a zero gas-brine capillary pressure was simulated (Figure 3-2), so that gas and brine phase pressures were equal within the room.

To examine the sensitivity of system behavior to disposal room multiphase flow properties, the residual brine saturation was varied from 0.276 to 0.01, the residual gas saturation was varied from 0.001 to 0.10, and the pore-size λ was varied from 0.2 to 10.0. The rationale for these ranges is discussed in Appendix A.

The analogue soil mixture had a porosity of 0.44 and an intrinsic permeability of 1.5×10^{-5} m^2. The porosity of the analogue material was within the range expected for the disposal room during closure, but the permeability of the analogue material was higher than the estimated room permeability by at least six orders of magnitude. Demond and Roberts (1987) suggest that, for many materials, relative permeability relationships are insensitive to intrinsic permeability, in which case the difference between the permeabilities of the analogue soil mixture and the disposal room may not be a major issue. However, the degree to which the soil mixture represents the pore-size distribution and pore structure likely to exist in the room is of importance. The large difference in permeabilities between the soil mixture and the room may suggest a different pore structure.

For example, the pore structure in the backfill may be such that the analogue soil mixture underestimates the capacity of the backfill to immobilize water by capillary trapping in small pores. Alternative analogues for the room contents that focus on imbibition behavior are

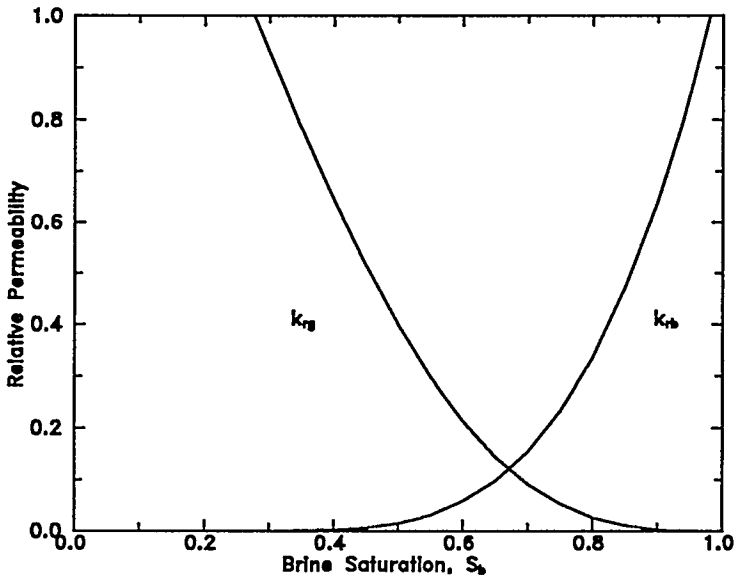

Figure 3-1. Simulated relative permeability relationships for the disposal room.

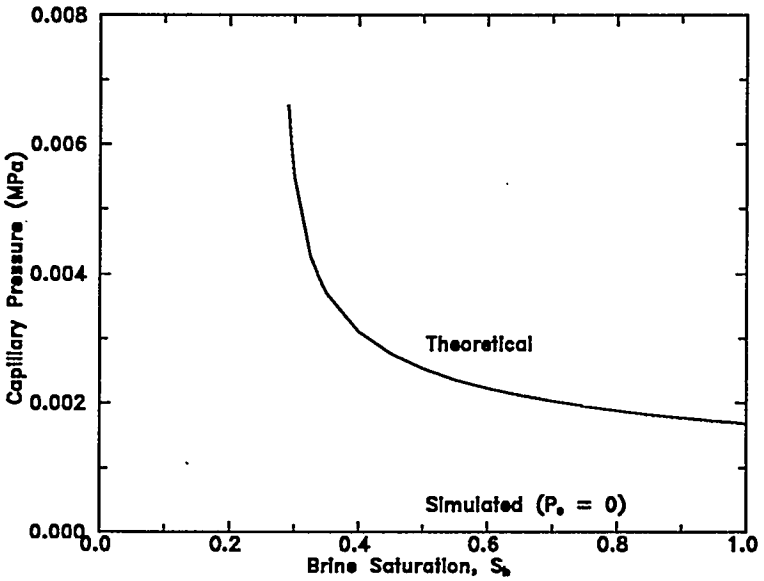

Figure 3-2. Simulated gas-brine capillary pressure relationships for the disposal room.

required to examine this aspect of room behavior. However, in the absence of any WIPP-specific data, the relative permeability and capillary pressure relationships for the analogue soil mixture provided the best available estimates for a disposal room.

3.1.1.3 DISPOSAL ROOM INITIAL CONDITIONS

The initial conditions were selected to be representative of the time immediately after a disposal room had been backfilled and sealed. Therefore, the initial pressure in a room was specified as atmospheric (0.10 MPa). All simulations started with an initial gas pressure of 0.10 MPa in the entire disposal room. Because the simulated gas-brine capillary pressure in the room was zero, initial brine pressures were also 0.10 MPa.

The amount of brine initially present in a disposal room is dependent on the amount of water and brine present in the emplaced waste and the backfill. The emplaced waste was assumed to have a volume of 1,663 m^3 (Beraun and Davies, 1992) and an initial water content of 1% by volume, corresponding to the upper limit specified in the WIPP Waste Acceptance Criteria (U.S. DOE, 1991). The corresponding initial volume of water in the waste within a single disposal room was 16.6 m^3. The emplaced backfill was assumed to be crushed salt although a 70/30 mixture of crushed salt and bentonite is also being considered. The crushed salt backfill was assumed to have a volume of 1,327 m^3, an initial density of 1,300 kg/m^3, and contain 0.5% water by weight (Pfeifle, 1987). The corresponding initial volume of brine in the backfill within a single room was 7.2 m^3.

The resulting initial volume of brine in a room filled with waste and crushed salt backfill was 23.8 m^3. For a disposal room with an initial void volume of 2,415 m^3, the corresponding initial brine saturation was 0.01. All baseline simulations started with an initial brine saturation of 0.01 and an initial gas saturation of 0.99 in the disposal room. This initial brine saturation assumes that none of the brine in the room is bound (immobilized) by the waste or backfill.

There is uncertainty both in the initial volume of brine in the room and in how much of the initial brine is available to drive the gas-generation reactions. There is also uncertainty in the initial water content of the waste. The Waste Acceptance Criteria specifies that the waste will contain less than 1% water by volume. However, some of the waste forms (in particular, sludge material) may contain significant amounts of water that may or may not be bound by uncured cement. There is uncertainty in the initial brine content of the backfill. If a salt/bentonite

mixture with a water content of 3.3% by weight (Pfeifle, 1987) is used, the volume of brine in the backfill would be about three times greater than calculated above. However, some of the brine would be bound by the bentonite. In the absence of WIPP-specific two-phase properties, the impact of the initial brine saturation on the behavior of multiphase flow within the room is also uncertain. The initial brine saturation (0.01) is much less than the residual brine saturation (0.276), suggesting that the initial brine may be immobile or bound. To partially examine these uncertainties, the initial brine saturation in a room was varied from 0.0003 (Butcher and Lincoln, 1995a) to 0.066 (Butcher and Lincoln, 1995b). The residual brine saturation was also varied (Section 3.1.1.2).

3.1.2 Salado Formation Halite and Anhydrite Interbeds

3.1.2.1 SALADO FORMATION PHYSICAL PROPERTIES

Intrinsic permeability in the Salado Formation varies significantly in different lithologic units. The model permeability ranges are based on analyses of in-situ permeability tests (Beauheim et al., 1991; Howarth et al., 1991). The selected ranges are from tests thought to be most representative of undisturbed conditions (i.e., they do not reflect excavation effects). For halite, intrinsic permeability ranges from 1×10^{-25} m^2 to 1×10^{-19} m^2 with a best estimate of 1×10^{-21} m^2. For the interbeds, intrinsic permeability ranges from 1×10^{-20} m^2 to 1×10^{-18} m^2 with a best estimate of 1×10^{-19} m^2. The model assumes no spatial heterogeneity (i.e., permeability represents a spatially averaged value). However, there are indications of a high degree of lateral variability in permeability in some units, which could have a significant effect on the simulated gas migration distances. Particularly important may be lateral variability within the interbeds. Nonetheless, the gas migration distance performance measure still provides a reasonable comparison for parameter sensitivity, but results should be used with caution.

The best estimate of 0.01 for Salado Formation porosity is derived from electro-magnetic and DC resistivity measurements made in the WIPP underground (Skokan et al., 1989). The halite porosities are expected to range from 0.001 (Powers et al., 1978) to 0.03 (Skokan et al., 1989), while the interbeds porosities range from 0.0006 (see Appendix A) to 0.03 (Skokan et al., 1989).

Rock (bulk) compressibility of the porous matrix for both the halite and the anhydrite interbeds was computed directly from elastic properties (Green and Wang, 1990):

$$\alpha = \frac{1}{K + 4G/3} \tag{3-5}$$

where:

α = rock (bulk) compressibility [Pa^{-1}],
K = drained bulk modulus of rock [Pa], and
G = drained shear modulus of rock [Pa].

The pore volume compressibility, α_p, required by TOUGH2/EOS8, was calculated using α and the porosity, ϕ, from (de Marsily, 1986):

$$\alpha_p = \frac{\alpha}{\phi} \tag{3-6}$$

Krieg (1984) and Beauheim et al. (1991) suggest best estimates of 20.7 GPa for halite bulk modulus, 12.4 GPa for halite shear modulus, 83.4 GPa for anhydrite bulk modulus and 27.8 GPa for anhydrite shear modulus. The best estimates for rock compressibility, calculated from Equation 3-5, were 2.7×10^{-11} Pa^{-1} for halite and 8.3×10^{-12} Pa^{-1} for the interbeds. The best estimates for pore volume compressibility, calculated from Equation 3-6 with a best-estimate porosity of 0.01, were 2.7×10^{-9} Pa^{-1} for halite and 8.3×10^{-10} Pa^{-1} for the interbeds.

Krieg (1984) and Beauheim et al. (1991) also suggest a range of 15.0 GPa to 21.7 GPa for halite bulk modulus and 8.1 GPa to 15.6 GPa for halite shear modulus. Substituting these maximum and minimum K and G values into Equation 3-5 produces a range of 2.4×10^{-11} Pa^{-1} to 3.9×10^{-11} Pa^{-1} for halite rock compressibility. Equation 3-5 assumes that the compressibility of the rock grains is negligible relative to the compressibility of the rock pores. Beauheim et al. (1991) suggest that, for halite, rock grain compressibility may not be negligible. This assumption results in an alternative minimum halite rock compressibility of 5.6×10^{-12} Pa^{-1} (see Appendix A).

The range for anhydrite compressibility was calculated from specific storage values reported by Beauheim et al. (1991). The specific storage, S_s, is (Freeze and Cherry, 1979):

$$S_s = \rho_f g(\alpha + \phi\beta) \tag{3-7}$$

where:

ρ_f = fluid density [1,200 kg/m^3],
g = acceleration of gravity [9.81 N/kg],

β = fluid compressibility [2.5×10^{-10} Pa^{-1}].

The minimum specific storage of 9.7×10^{-8} corresponds to a minimum anhydrite rock compressibility of 5.7×10^{-12} Pa^{-1} and the maximum specific storage of 2.5×10^{-7} corresponds to a maximum anhydrite rock compressibility of 1.9×10^{-11} Pa^{-1}.

3.1.2.2 SALADO FORMATION MULTIPHASE FLOW PROPERTIES

There are no measured relative permeability or capillary pressure data for the Salado Formation halite or anhydrite. In the absence of WIPP-specific data, the multiphase flow properties were based on actual measurements on an approximate analogue material. A low-permeability sandstone (Morrow et al., 1986), characterized by very fine sand interbedded with coals and shale, was selected as an analogue because it was the lowest permeability material for which relative permeability and capillary pressure measurements were available.

The analogue material was a fine sandstone with thin bedding, a porosity of 0.12, moderate sorting, subangular quartz grains, and dolomitic cementation. The dominant pore geometry consisted of intergranular cracks between abutting quartz grains and solution pores partially filled with dolomite (Morrow et al., 1986; Soeder and Randolph, 1984). The measured permeability of the sample to brine ranged from 2.4×10^{-17} m^2 to 4.3×10^{-17} m^2. Measured data from the analogue sandstone were fit to the modified Brooks and Corey (1964) model (described in Section 3.1.1.2) to obtain the following parameter values: $S_{br} = 0.20$; $S_{gr} = 0.20$; $\lambda = 0.7$; and $p_t = 0.30$ MPa. The data and methodology used to determine these parameters are presented in Appendix A.

The relative permeability relationships, calculated from Equations 3-1, 3-2, and 3-3 using the analogue sandstone parameter values, are shown in Figure 3-3. These relative permeabilities were assumed to describe both the halite and the anhydrite interbeds. To examine the sensitivity of system behavior to Salado Formation multiphase flow properties, the residual brine and gas saturations were varied from 0.0 to 0.4 and the pore-size λ was varied from 0.2 to 10.0, as suggested by Webb (1992b). Alternative relationships for relative permeability (Parker et al., 1987) and capillary pressure (Van Genuchten, 1980) were also simulated. These alternative relationships were proposed by Webb (1992b) and are discussed in Sections 5.1.2.2 and 5.1.3.2.

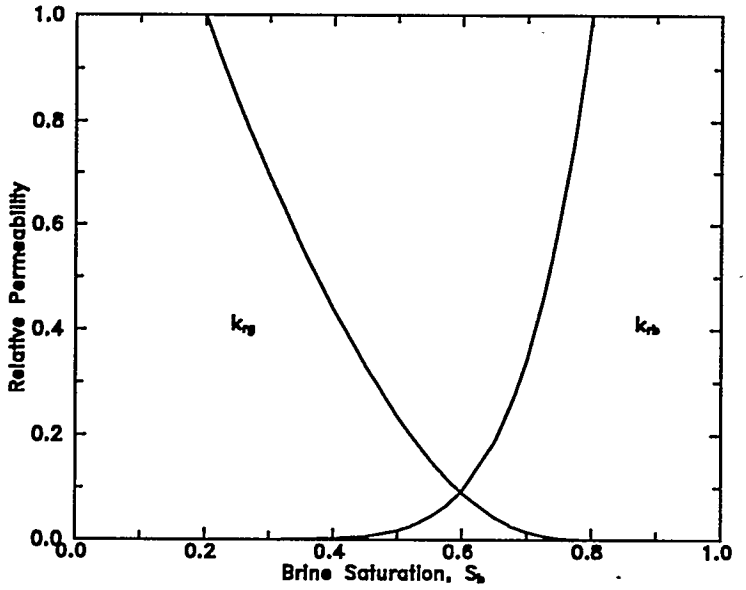

Figure 3-3. Simulated relative permeability relationships for the Salado Formation halite and interbeds.

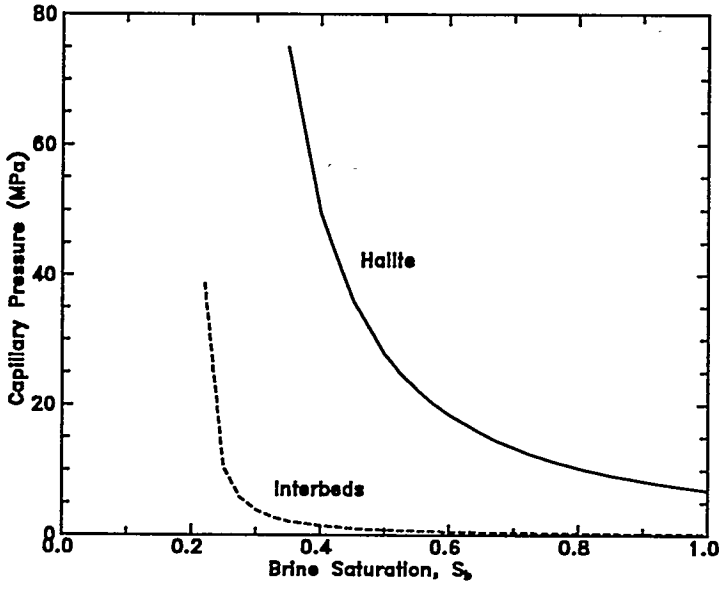

Figure 3-4. Simulated gas-brine capillary pressure relationships for the Salado Formation halite and interbeds.

The permeability of the analogue sandstone was within a few orders of magnitude of the estimated range for anhydrite permeability (1×10^{-18} m^2 to 1×10^{-21} m^2). Therefore, the threshold pressure for the analogue sandstone was assumed to be representative of anhydrite. The permeability of the analogue sandstone was about four orders of magnitude higher than the best-estimate halite permeability (1×10^{-21} m^2). Because this permeability difference might indicate different pore structure, the threshold pressure for halite was estimated from a permeability-threshold pressure correlation for consolidated lithologies presented by Davies (1991):

$$p_t = (5.6 \times 10^{-7})(k^{-0.346}) \qquad (3\text{-}8)$$

where:

p_t = threshold pressure (MPa), and
k = intrinsic permeability (m^2).

The threshold pressure calculated from Equation 3-8, corresponding to the best- estimate halite intrinsic permeability, was 10.3 MPa. Capillary pressures for halite and the anhydrite interbeds (Figure 3-4) were calculated from Equation 3-4 using the best-estimate threshold pressures.

The presence of excavation-related and pre-existing fractures in the anhydrite interbeds will result in a reduction in threshold pressure of the total rock mass (Davies, 1991). For this reason, the threshold pressure for the analogue sandstone (0.3 MPa) was taken as the best estimate for the anhydrite interbeds rather than the 2.1 MPa value calculated using the permeability-threshold pressure correlation and the best-estimate interbed permeability (1×10^{-19} m^2). An interbed threshold pressure of 2.1 MPa was examined in sensitivity simulations.

Halite threshold pressure was assumed to range from a minimum of 2.1 MPa (corresponding to $k = 1 \times 10^{-19}$ m^2) to a maximum of 22.9 MPa (corresponding to $k = 1 \times 10^{-22}$ m^2). For the interbeds, a minimum of 0.2 MPa (corresponding to $k = 1 \times 10^{-16}$ m^2) and a maximum of 4.7 MPa (corresponding to $k = 1 \times 10^{-20}$ m^2) were assumed. The lower bound for interbed threshold pressure corresponds to an excavation-disturbed permeability measured by Beauheim et al. (1993a) and is assumed to be representative of a fractured interbed.

Gas penetration into brine-saturated rock can occur when:

$$p_g > p_t + p_b \tag{3-9}$$

where:

p_g = gas pressure in the disposal room,
p_t = threshold pressure in Salado Formation, and
p_b = brine pressure in Salado Formation.

If gas pressures in the room reach lithostatic pressure (15 MPa) and the far-field brine pressure is 12 MPa, gas penetration into the Salado will not occur unless the threshold pressure is 3 MPa or less. The estimated threshold pressures suggest that gas will flow into the interbeds in response to room pressurization but that gas penetration into the halite under far-field pressure is unlikely. However, brine pressures are likely to be significantly lower within the first few meters of an excavation. Assuming that brine pressure falls to near atmospheric (0.1 MPa) adjacent to an excavation, gas penetration into the depressurized zone of halite may occur for threshold pressures of 15 MPa or less. Pressure-induced fracturing, particularly in the interbeds, will result in lower threshold pressures and will further facilitate gas entry.

The sandstone analogue and the permeability-threshold pressure correlation provide the best estimates for the relative permeability and threshold pressure relationships in the halite and anhydrite interbeds. Howver, their applicability to the Salado Formation has not been determined. It should be emphasized that, in the absence of any WIPP-specific data, both the best estimates and the variations of the two-phase relationships remain highly uncertain.

3.1.2.3 SALADO FORMATION INITIAL CONDITIONS

The undisturbed pore pressure in the Salado Formation at the elevation of the repository is expected to be bounded by hydrostatic (6 MPa) and lithostatic (15 MPa) (Peterson et al., 1987; Nowak and McTigue, 1987; Lappin et al., 1989). Pore pressures extrapolated from pressure recovery trends from in-situ hydraulic testing provide the best estimates of Salado Formation pressure. The extrapolated values have some uncertainty depending on the quality and duration of the tests and may be influenced to some extent by excavation-related depressurization. Based on hydraulic testing performed by Beauheim et al. (1991) and Howarth et al. (1991), the undisturbed brine pore pressure at the repository level was assumed to be 12.0 MPa to 12.5 MPa. A best estimate of 12.0 MPa was used in baseline simulations and a range

of 11.0 MPa to 15.0 MPa was selected for sensitivity analysis. The low end of the range corresponds to measured (not extrapolated), undisturbed pore pressures while the high end of the range corresponds to the highest theoretical value (lithostatic, approximately 15 MPa).

The vertical pore-pressure distribution above and below the repository level was referenced to a 12.0 MPa pressure at the vertical center of the repository. Because gravitational effects were not included in the baseline simulations, an initial brine pressure of 12.0 MPa was specified for the entire fluid-flow continuum (halite and interbeds). While this simplification had some effect on phase segregation within the disposal room, it had little effect on brine and gas flow in the halite and interbeds. In simulations with gravitational effects, a hydrostatic pressure distribution above and below the repository was simulated.

The undisturbed Salado Formation halite and interbeds were assumed to have an initial gas saturation of 0.0 and an initial brine saturation of 1.0. To examine the effects of exsolved gas, as observed in depressurized test zones (Beauheim et al., 1991), a non-zero initial gas saturation in the Salado Formation was tested in a sensitivity simulation.

3.1.3 Fluid [Brine and Gas] Properties

Fluid properties are determined internally by TOUGH2/EOS8 from equation of state relationships. A detailed summary of the TOUGH2/EOS8 fluid properties is contained in Appendix A. With the modified EOS8H module, the gas is assumed to be hydrogen, behaving as an ideal gas with a viscosity of 9×10^{-6} Pa•s. The brine has a density of 1,200 kg/m^3, a viscosity of 1.6×10^{-3} Pa•s, and a compressibility of 2.4×10^{-10} Pa^{-1}. The solubility of hydrogen in brine is described by a Henry's Law Constant, K_H, of 2.9×10^{10} Pa. The properties presented here are approximate values. Actual values vary as a function of temperature and pressure.

3.2 Gas-Generation Parameters

In TOUGH2/EOS8, gas generation is simulated with specified gas sources within the disposal room. Source rates are specified in units of kg/s. Tables 2-1 and 2-2 present gas-generation rate histories in terms of moles per drum per year. The conversion from moles per

drum per year makes the following assumptions; 6,804 drums per room; 365.25 days per year; and 2.016×10^{-3} kg per mole of H_2. Furthermore, each room has six gas sources, located in the six elements (grid blocks) nearest the room center. Simulated gas generation was scaled down to account for the half-width and unit length of the simulated room. However, simulation results were re-scaled to represent a full room (full width, 91.44 m length).

Based on the experimental results of Brush (1991), four specified gas-generation rate histories, listed in Table 2-1, were simulated. These specified rates were not dependent on the simulated brine volume in the room. The sensitivity of system behavior to specified gas-generation rates was examined with two additional sets of simulations. Based on more recent experimental results (Brush, 1995), a revised set of specified rate histories was simulated: 105/5; 1.6/0.6; and 0.1/0. As discussed in Section 2.4.1, these designations represent first phase/second phase gas-generation rates in moles per drum per year. The second set of sensitivity simulations used constant (one phase) gas-generation rates. The following constant rates, in moles per drum per year, were simulated: 1.5; 1.0; 0.5; 0.2; and 0.1.

For brine-dependent rate simulations (Table 2-2), gas-generation rates were a composite of experimentally-determined brine-inundated and vapor-limited rates. The composite rate was based on local brine saturation conditions in the room. A brine saturation of 0.3 (approximately equal to the residual brine saturation) was assumed to represent the threshold between brine-inundated and vapor-limited conditions, as described in Section 2.4.2.1. A sensitivity simulation with a brine saturation threshold of 0.1 was also performed.

All of the aforementioned simulations (both specified and brine-dependent rate) assumed a total gas-generation potential of 1,600 moles per drum (1.09×10^7 moles per room), which is comprised of 1,050 moles per drum for anoxic corrosion and 550 moles per drum for microbial degradation. This baseline gas potential corresponds to a gas mass of about 22,000 kg. By using the same gas potential, each different gas-generation rate history resulted in a different gas-generation duration. The sensitivity to gas-generation potential was examined by simulating a constant 0.5 moles per drum per year rate under the following five potentials (moles per drum): 600; 900; 1,600; 2,500; and 3,700. The lowest potential corresponds to gas from microbial degradation (corrosion is assumed limited by passivation) of CH TRU waste. The highest potential corresponds to gas from CH and RH TRU waste and assumes complete degradation of plastics and rubbers.

3.3 Room Closure Parameters

TOUGH2/EOS8 is a fluid and heat flow code and does not directly simulate mechanical deformation. The geomechanics of salt creep and room closure and consolidation are approximated by two flow and closure coupling methods, both which are based on results from the SANCHO mechanical deformation code. Room closure calibration was performed for each of the coupling methods by comparing TOUGH2/EOS8 simulation results of gas generation in a sealed room (i.e., no brine inflow and no gas release) with results from the SANCHO f-series simulations performed by Stone (1995a). A detailed discussion of the room closure calibration simulations is presented by Freeze et al. (1995); a short summary is given here.

With the pressure lines method (Section 2.3.1), room closure was determined by interpolating between SANCHO-produced gas-time-porosity relationships. A comparison of the TOUGH2/EOS8 porosity function results with SANCHO f-series results was somewhat redundant, as the pressure lines were able to exactly reproduce the room closure and room pressure data from which they were derived.

With the boundary backstress method (Section 2.3.2), calibration of TOUGH2/EOS8 room closure was an iterative process to determine the combination of salt phase flow properties and backstress control (artificial boundary) parameters that most closely reproduced the SANCHO f-series results. Initial salt phase pressures of 15.0 MPa in salt-flow continuum and 0.1 MPa in the disposal room, which were selected to be consistent with the initial conditions used by Stone (1995a), produced a flow of salt phase fluid from the salt-flow continuum into the room that was representative of room closure. A set of salt phase flow parameters and artificial boundary parameters were determined through an empirical calibration process to produce TOUGH2/EOS8 results that closely matched the room closure and room pressure results from the SANCHO f-series. Where practical, the physical properties of salt and the theoretical relationships between potential flow parameters and mechanical salt creep parameters were preserved. However, the differences between the processes of salt flow modeled as a fluid flow process and salt flow modeled as a creep deformation process precluded a rigorous adherence to physically identifiable processes.

Boundary backstress calibration results are shown in Figure 3-5. The boundary backstress method slightly underestimates room pressure at high gas-generation rates ($f \geq 0.6$) and slightly overestimates room pressure at low rates ($f \leq 0.2$). However, the boundary backstress provides

a slightly better approximation of room closure than the pressure lines method in simulations where the gas-generation rate history deviates from the SANCHO f-series rates (Freeze et al., 1995). Implications of these calibration results on coupled flow and closure simulations are discussed in Sections 4 and 5 where pertinent.

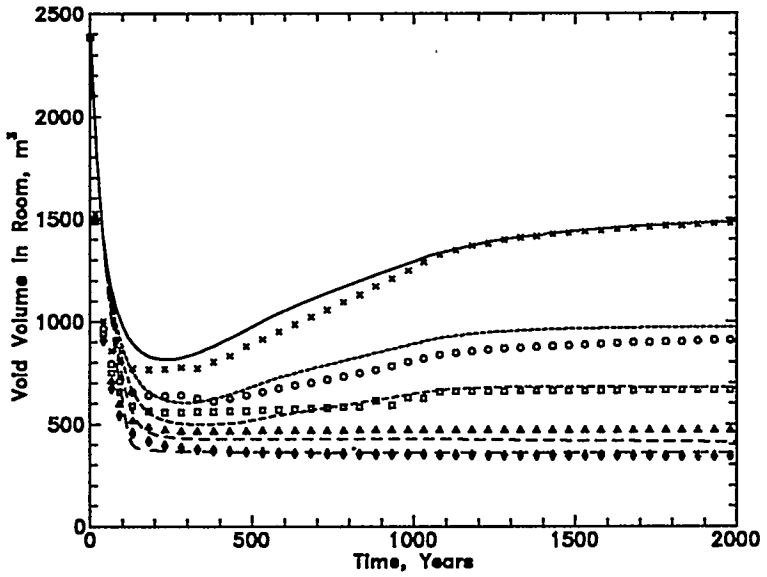

(a) Void Volume

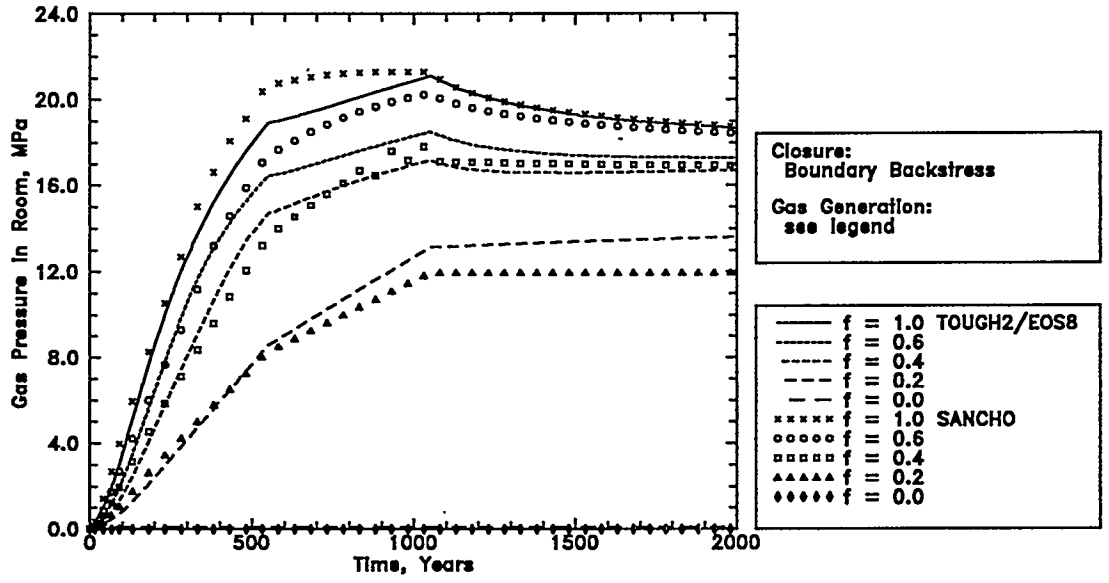

(b) Room Pressure

Figure 3-5. Room closure calibration of TOUGH2/EOS8 boundary backstress method to SANCHO simulated closure of a sealed room (Stone, 1992) under five different gas-generation rate histories.

4.0 BASELINE SIMULATION RESULTS

Baseline simulations examined system behavior under best-estimate conditions. All baseline simulations used the best-estimate hydrologic parameters (Section 3.1 and Appendix A). Four specified gas-generation rate histories (Table 2-1) and three brine-dependent rate histories (Table 2-2) were selected to approximate the expected range of production of waste-generated gas at the WIPP (Section 2-4). The specified 2/1 rate history represents the best estimate of gas generation under brine-inundated conditions and is equivalent to the f=1.0 rate history of Stone (1995a). The specified 0.2/0.1 rate history represents the best estimate of gas generation under vapor-limited conditions.

Simulation results from the 2/1 and 0.2/0.1 specified gas-generation rate histories are discussed in Section 4.1, an examination of system behavior under best-estimate conditions. Simulation results using best-estimate brine-dependent rates are compared with 2/1 and 0.2/0.1 specified rate history results in Section 4.2. Simulation results examining sensitivity to other specified and brine-dependent gas-generation rates are presented in Section 5.2.

For each simulation, eight attributes were analyzed: room void volume; room gas phase pressure; brine flow (inflow and expulsion) between the room and the Salado Formation; gas phase flow out of the room (gas expulsion); gas phase saturation and migration in the upper composite interbed; gas phase saturation and migration in the lower composite interbed; mass of gas generated; and mass of gas in the room. Some of these attributes are interdependent. For example, gas mass in the room is equal to gas mass generated minus gas mass expelled. Also, while gas migration in the upper and lower interbeds is quantitatively different, in most cases the response to variations in system parameters is similar in both interbeds. The effects of gravity, which were not simulated, might produce a greater difference between interbeds.

All of the baseline rate histories assumed a total gas-generation potential of 1,600 moles per drum (1,050 moles per drum for anoxic corrosion and 550 moles per drum for microbial activity). Under all of the baseline rate histories, gas was still being released from the room after 2,000 years, which was the duration of the SANCHO room closure simulations performed by Stone (1995a). For the 0.2/0.1 rate history, gas generation continued for 10,500 years. Because these TOUGH2/EOS8 simulations were performed to examine system behavior and the sensitivity of system performance to variations in system parameters, and not to provide a

comparison with regulatory standards, the TOUGH2/EOS8 simulations were extended beyond the 10,000-year regulatory time frame to 12,000 years. This time period was selected because by 12,000 years gas expulsion from the room had nearly ceased, room pressures had stabilized, and gas generation was complete under all of the baseline rate histories.

Eight methods for coupling multiphase flow with room closure in TOUGH2/EOS8 were examined by Freeze et al. (1995). The pressure lines method and the boundary backstress method were identified as the most accurate and robust methods under expected repository conditions. Each of the baseline gas-generation rate histories was simulated with both of these closure coupling methods.

The baseline simulation results indicated that: (1) the two specified rate histories, 2/1 and 0.2/0.1, tested system behavior over a range of conditions that could be considered representative of most brine-dependent conditions; and (2) under best-estimate conditions, limited brine availability produced very little mobile brine in the room, and the resulting brine-dependent gas-generation rate history was very similar to the specified 0.2/0.1 rate history.

4.1 System Behavior Under Best-Estimate Conditions

The baseline simulation results provide an estimate of system performance under best-estimate conditions. TOUGH2/EOS8 results for the 2/1 and 0.2/0.1 specified gas-generation rate histories are presented in Figure 4-1 for the boundary backstress method and in Figure 4-2 for the pressure lines method. These specified rate histories produced a range of system behavior that was sufficient to qualitatively describe the performance of the WIPP repository under the expected range of brine-dependent conditions (see Section 4.2 for discussion). The best-estimate brine-dependent gas-generation rate history did not produce system behavior under best-estimate conditions that was significantly different from the specified 0.2/0.1 rate history.

There are slight differences between the results of simulations using the boundary backstress method (Figure 4-1) and those using the pressure lines method (Figure 4-2), as discussed by Freeze et al. (1995). The following discussions of system behavior make reference to boundary backstress results but are equally pertinent to pressure lines results.

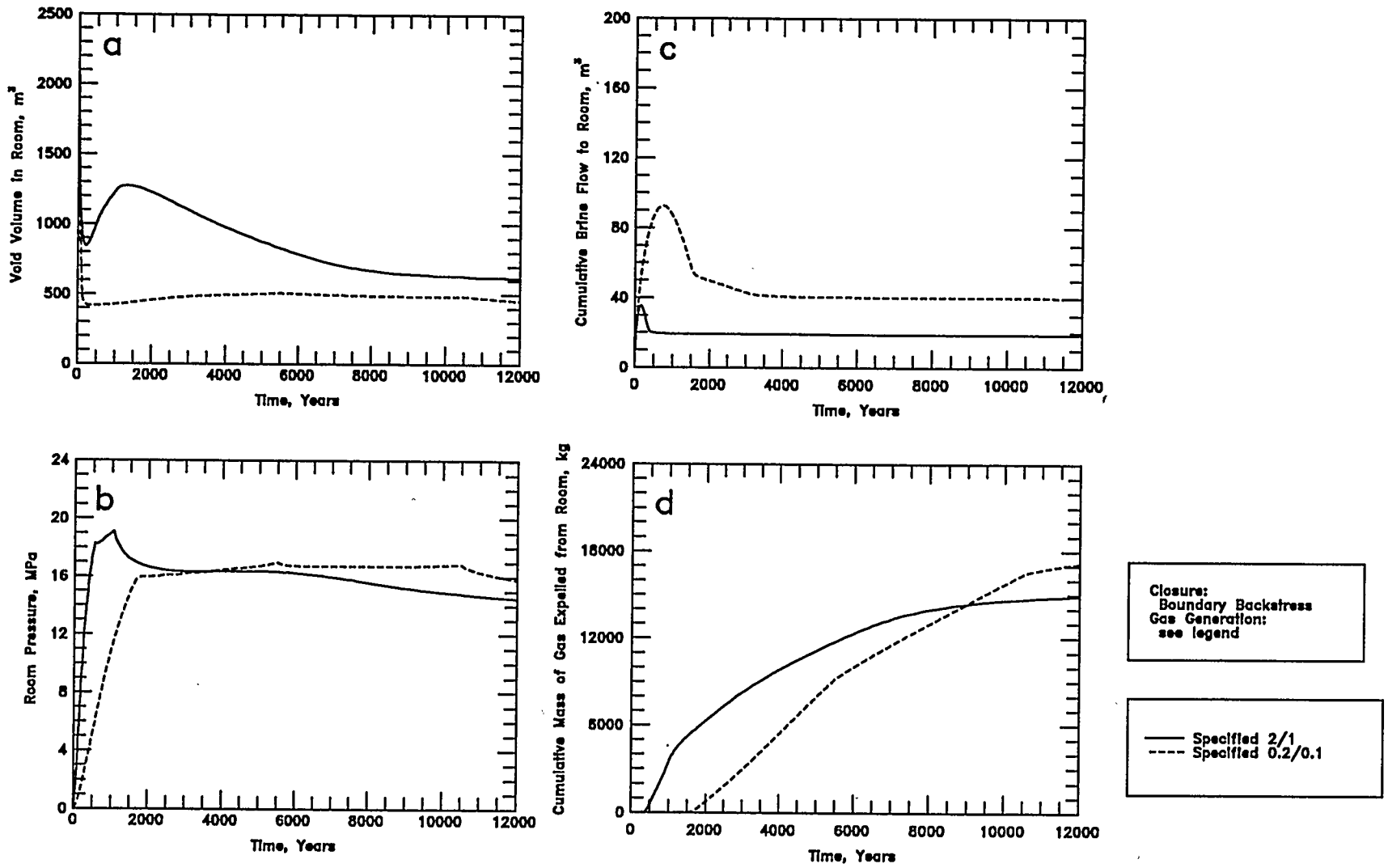

Figure 4-1 (a-d). TOUGH2/EOS8 boundary backstress simulation results for coupled flow and closure under best estimate conditions: a - Void Volume; b - Gas Pressure; c - Brine Flow; d - Gas Expulsion.

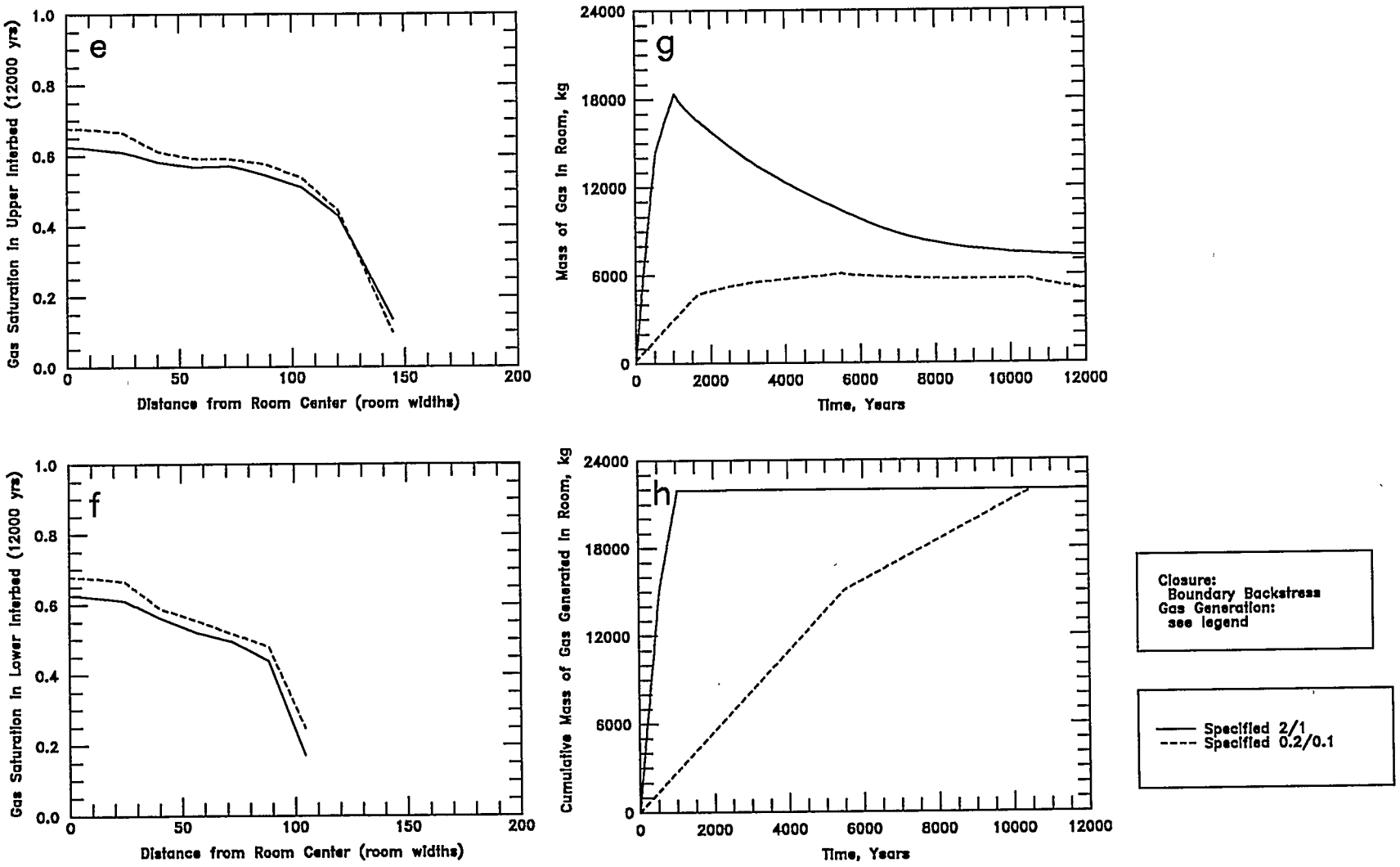

Figure 4-1 (e-h). TOUGH2/EOS8 boundary backstress simulation results for coupled flow and closure under best estimate conditions: e - Upper Interbed Gas Profile; f - Lower Interbed Gas Profile; g - Room Gas Mass; h - Gas Generation.

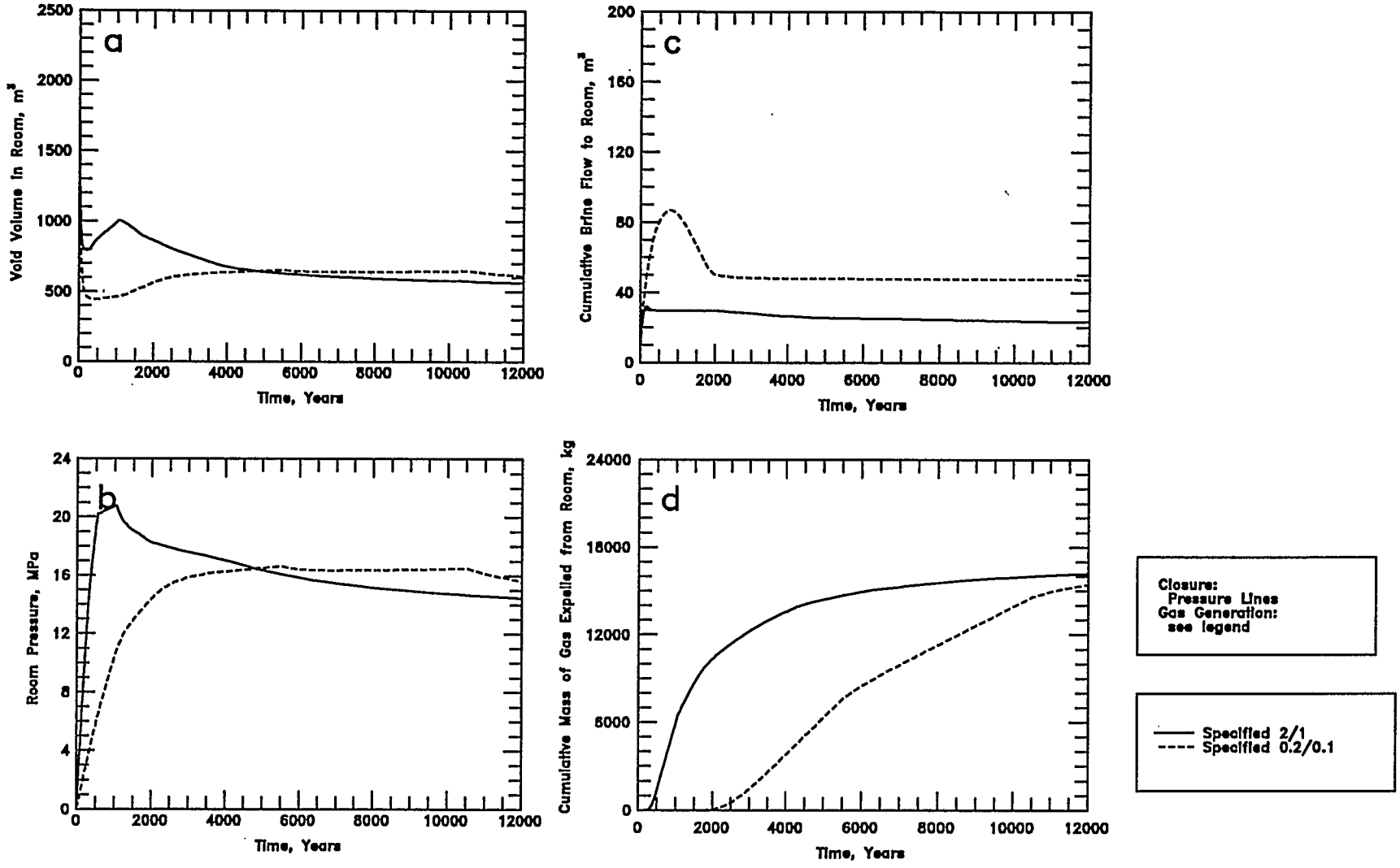

Figure 4-2 (a-d). TOUGH2/EOS8 pressure lines simulation results for coupled flow and closure under best estimate conditions: a - Void Volume; b - Gas Pressure; c - Brine Flow; d - Gas Expulsion.

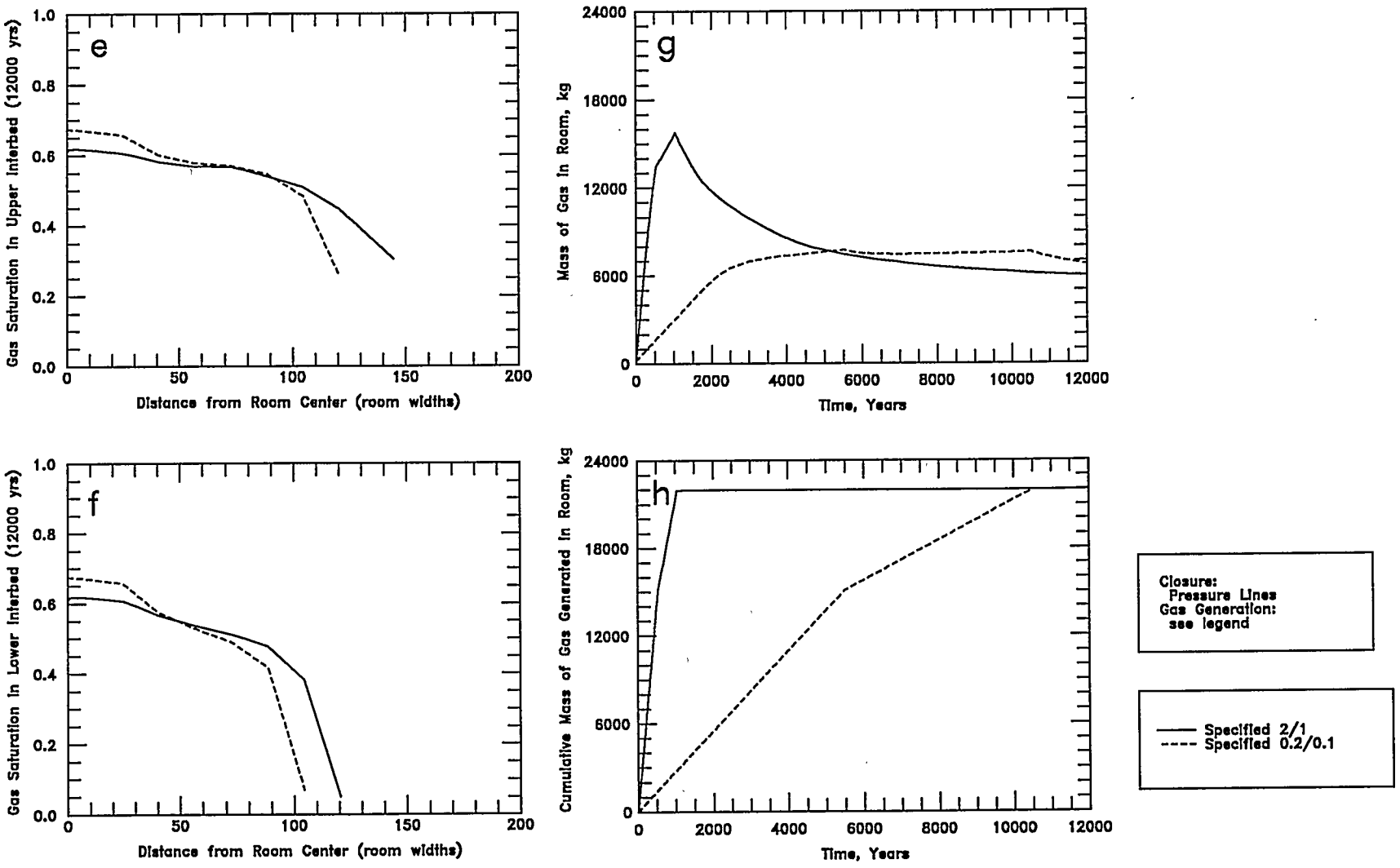

Figure 4-2 (e-h). TOUGH2/EOS8 pressure lines simulation results for coupled flow and closure under best estimate conditions: e - Upper Interbed Gas Profile; f - Lower Interbed Gas Profile; g - Room Gas Mass; h - Gas Generation.

In the first few hundred years subsequent to the backfilling and sealing of a disposal room, pressure gradients were inward, room closure was rapid (Figure 4-1a), and brine flow was from the Salado Formation into the room (Figure 4-1c). During this time, both simulated room closure and brine inflow were moderated somewhat by gas pressures resulting from the higher 2/1 gas-generation rate. With the 2/1 rate (2 moles per drum per year for the first 550 years) the minimum early time room void volume was 844 m^3 as compared with a minimum void volume of 415 m^3 for the 0.2/0.1 rate (0.2 moles per drum per year for the first 5,500 years) (Figure 4-1a). The peak cumulative brine inflow was 35 m^3 with the 2/1 rate as compared with 92 m^3 for the 0.2/0.1 rate (Figure 4-1c).

In the baseline simulations, brine inflow was predominantly through the interbeds. Brine in the halite near the interbeds flowed into the depressurized interbeds, which responded more quickly than the halite to near-atmospheric room pressure. Brine then flowed into the room through the high-transmissivity room-interbed connections. About 60% of the total brine inflow was through the lower interbed into the bottom of the room. Approximately 35% of the brine inflow was through the upper interbed while only about 5% flowed directly from the near-field halite into the room. The brine inflow was greater into the bottom of the room because the lower interbed was three times thicker than the upper interbed. This brine inflow behavior produced brine saturation conditions in the room that were similar to what would be expected with gravity-driven phase segregation within the room. For the 2/1 rate, only about 2 m^3 brine flowed into the room directly from the surrounding halite. This predicted brine inflow is consistent with the peak brine inflow of 2.5 m^3 from a SANTOS f=1.0 simulation (Stone, 1995b), which did not include interbeds. SANTOS is an enhanced version of SANCHO that includes the capability to model single-phase brine flow through a deforming salt matrix.

The simulated brine inflow volumes in TOUGH2/EOS8 (and SANTOS) are for a single, isolated disposal room. For a disposal room with the interior of a waste panel, brine inflow would only be available from a lateral distance of approximately 15 m (distance to the salt pillar centerline). Therefore, these single, isolated room simulations provide an upper bound on brine inflow.

Rising room pressures (Figure 4-1b), resulting from the combined effects of gas generation and room closure, eventually produced both a reversal of room closure (Figure 4-1a) and a reversal of the brine-pressure gradient. The higher 2/1 gas-generation rate accelerated room

pressurization, resulting in an earlier onset of room expansion and brine expulsion relative to the lower 0.2/0.1 rate case.

Immediately following the reversal of the pressure gradient, brine expulsion occurred to both the interbeds and the near-field halite. Gas expulsion was delayed until the capillary resistance in the interbeds was overcome. For the 2/1, rate the average room brine saturation at the time of pressure gradient reversal was only 0.07. For the 0.2/0.1 rate, the average saturation was higher, 0.28, because of greater brine inflow and greater room closure. Brine saturations at the room edges and at the bottom of the room were greater than the room-average value. Brine expulsion was limited to about 50% of the brine inflow volume because brine saturations in the room were reduced to the residual brine saturation before all of the brine was expelled. The lack of brine expulsion beyond about 4,000 years (Figure 4-1c) is a result of all brine in the room being at or below residual brine saturation.

With the baseline conceptual model, gas expulsion did not start until brine expulsion was completed (Figures 4-1c and 4-1d illustrate this point). Brine and gas expulsion are interrelated through the multiphase flow relationships (Section 1.1.3). In TOUGH2/EOS8 simulations, gas movement through the interbeds required the displacement of brine into the halite surrounding the interbeds. Gas expulsion occurred first to the upper interbed because of the lower brine saturations at the top of room (resulting from less brine inflow). However, approximately 70% of the total gas mass expelled was to the lower interbed because of its greater thickness. Because brine inflow behavior produced brine saturation conditions in the room that were similar to gravity-driven phase segregation, gas expulsion behavior was not significantly altered by gravitational effects (Section 5.3.2.3).

Room expansion was most rapid prior to gas expulsion, although the rate of expansion was always significantly slower than the initial rate of room closure. Room pressurization and room expansion slowed in response to gas release. In certain cases, the specified gas-generation rate was less than the rate of gas expulsion and the room started to close again (Figure 4-1a). Re-closure of the room was proportional to the degree of expansion that occurred. With the 2/1 rate there was much more room expansion and re-closure than with the 0.2/0.1 rate.

With the 2/1 rate history, a peak room pressure of about 19 MPa was reached at the end of gas generation, declining towards the far-field brine pressure (12 MPa) by the end of 12,000 years. With the 0.2/0.1 rate history, room pressure rose to about 16 MPa by

1,500 years and then stayed relatively constant despite continued gas generation. By 12,000 years it was also declining towards the far-field pressure. In both cases, room pressures above lithostatic were maintained for several thousand years. Baseline simulations did not consider fracturing or alteration of hydrologic properties. An alternative fractured interbed conceptualization was used to examine the effects of fracturing (Section 5.3.2.1).

Despite the transitory differences in room closure and expansion, room pressure, and brine inflow, caused by differences in the gas-generation rate histories, the simulations achieved a relatively common final state. The final (12,000 year) mass of gas released (Figure 4-1d) and gas migration distances in the upper and lower interbeds (Figures 4-1e and 4-1f, respectively) were quite similar, apparently influenced little by differences in gas-generation rate history. The mass of gas released ranged from approximately 15,000 kg (2/1 rate) to 17,000 kg (0.2/0.1 rate) of H_2, which is 70 to 80% of the total gas generated (Figure 4-1g). The gas phase migrated approximately 150 room widths (1500 m) in the upper composite interbed and 115 room widths (1150 m) in the lower composite interbed. Gas migration distance was greater in the upper interbed because, although it received only 30% of the expelled gas, it only had 25% of the total interbed thickness (i.e, the lower interbed was three times thicker than the upper interbed). The impact of gravitational effects on gas migration behavior was examined in sensitivity simulations (Section 5.3.2.3).

A series of gas saturation profiles for times ranging from 2,000 to 12,000 years are shown in Figure 4-3a for the upper interbed and Figure 4-3b for the lower interbed. These profiles show how the gas phase migrates with time under the specified 2/1 rate history. Gas migration was negligible between 10,000 and 12,000 years. This corresponds to the time at which the rate of gas expulsion is reduced to near zero (Figure 4-1d).

4.2 Comparison of Gas-Generation Rate Histories

To understand the influence of a brine-dependent gas-generation rate history on repository performance, simulation results using the best-estimate brine-dependent rates (Table 2-2) were compared with results from the 2/1 and 0.2/0.1 specified rate histories. Two different methods of coupling gas generation with brine availability, the capillary fringe method (Section 2.4.2.1) and the linear correlation method (Section 2.4.2.2), were used in brine-dependent simulations.

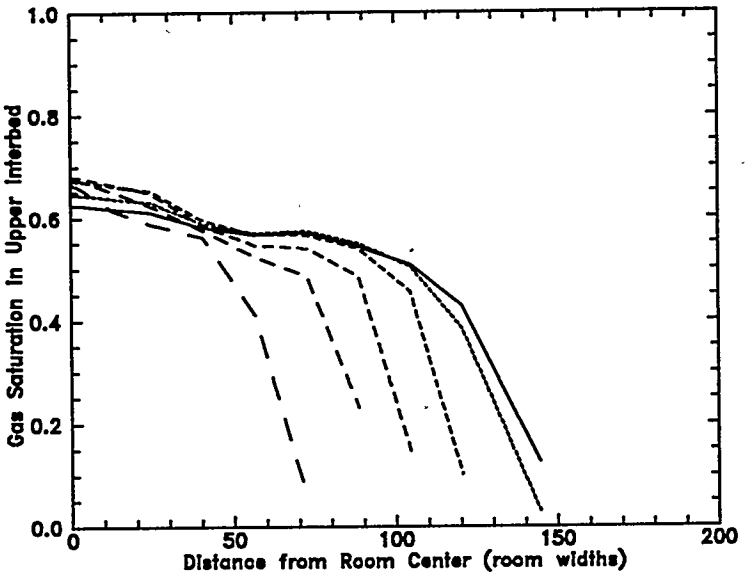

(a) Upper Interbed

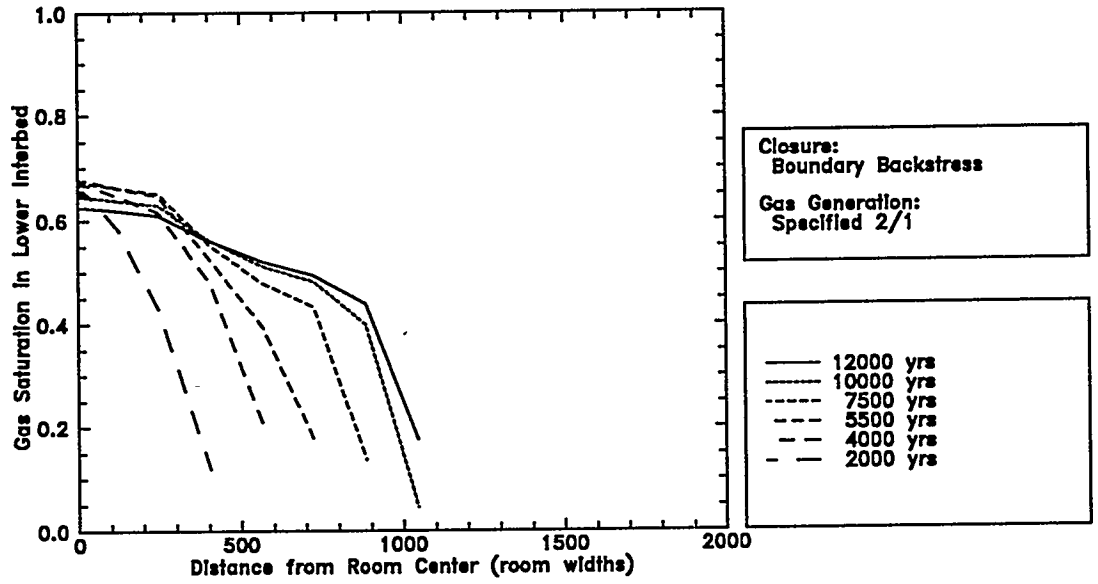

(b) Lower Interbed

Figure 4-3. Simulated interbed gas saturation profiles under the specified 2/1 gas-generation rate history.

Simulation results are compared in Figure 4-4. All simulations used the boundary backstress method. The pressure lines results yielded similar comparisons and are not presented.

The relative system responses were influenced by both the magnitude and the duration of gas generation (Figure 4-4h). In the specified rate simulations, gas-generation rates changed only at pre-specified times, independent of the amount of brine in the room. In the brine-dependent rate simulations, gas-generation rates were variable, changing in response to changes in the amount of brine in the room. The specified 2/1 history had the highest early rate, resulting in (1) the least early-time closure (Figure 4-4a), (2) the least brine inflow and subsequent expulsion (Figure 4-4c), (3) the fastest room pressurization (Figure 4-4b), (4) the earliest gas expulsion (Figure 4-4d), and (5) the greatest rate of room expansion (Figure 4-4a).

Room expansion ceased when the gas-generation rate became either very small or zero. As a result, the specified 2/1 rate actually had the shortest expansion period because its gas potential was exhausted earlier than in the other cases. The time of peak room pressure also corresponded to a time of significant reduction in gas-generation rate. The highest peak room pressure (19 MPa) was reached under the specified 2/1 rate history. However, at times beyond 5,000 years, room pressures were highest for the specified 0.2/0.1 rate and the two brine-dependent rate methods because they had slow, long-duration gas generation. The total mass of gas expelled was greatest for these three cases (Figure 4-4d), because a high room pressure was maintained for a relatively long duration. A high early-time pressure does not necessarily result in maximum gas release if the high pressure is not maintained. Final (12,000 year) gas migration distance in the interbeds (Figures 4-4e and 4-4f) was not sensitive to differences in either the magnitude or duration of gas generation, as long as the total mass of gas generated was constant.

The brine-dependent rate histories were selected to examine system response to gas generation that was driven by brine availability. The baseline brine-dependent rate simulations specified gas generation to be at the best-estimate brine-inundated rate (analogous to the 2/1 rates) for brine-inundated room conditions and at the best-estimate vapor-limited rate (analogous to the 0.2/0.1 rate) for vapor-limited room conditions. The differences between the capillary fringe method and the linear correlation method are described in Section 2.4.2. Using best-estimate properties, there was not enough brine inflow to produce brine-inundated effects with the capillary fringe method. Consequently, the capillary fringe results were identical to the specified 0.2/0.1 results (Figure 4-4). Because of the formulation of the linear correlation

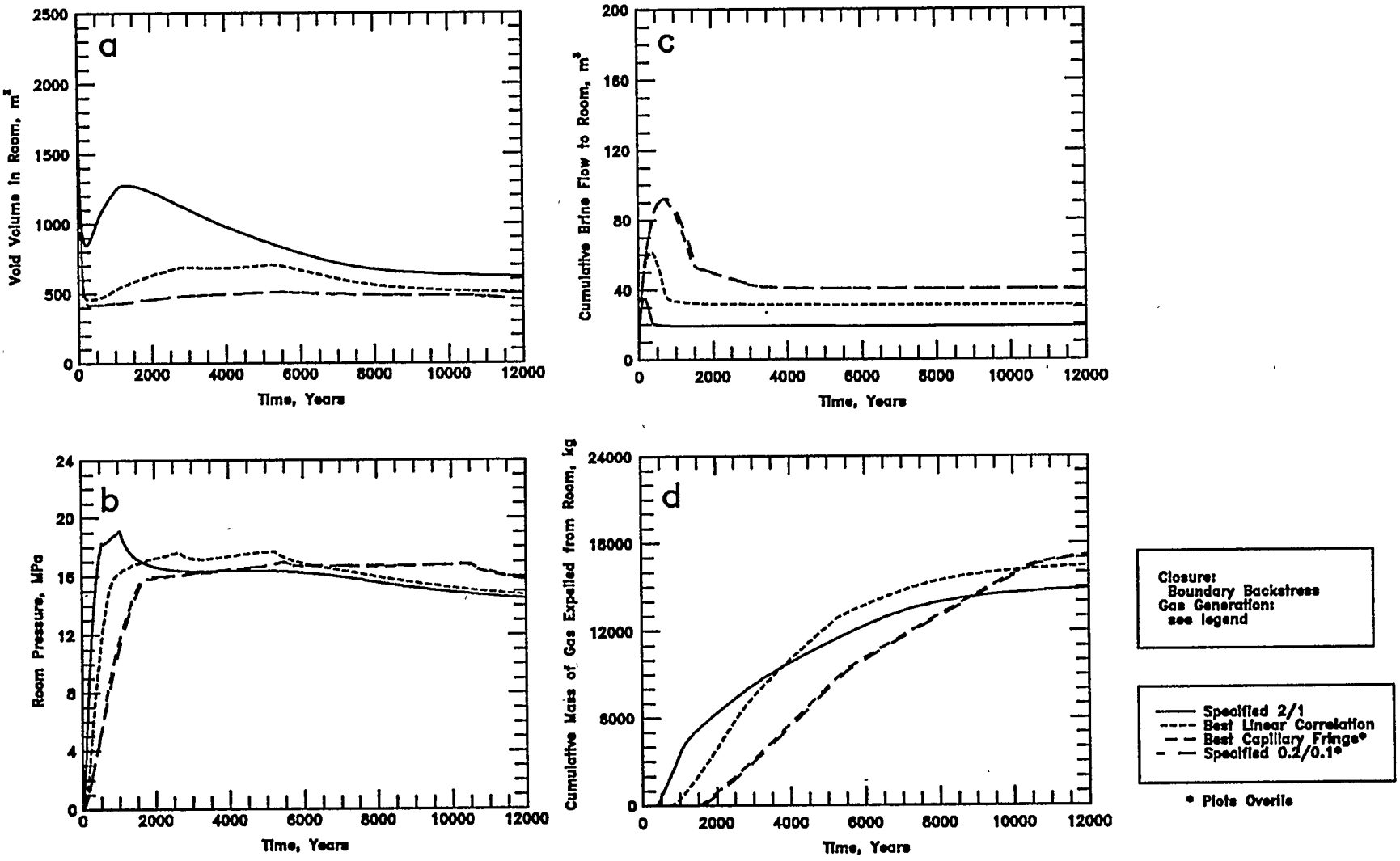

Figure 4-4 (a-d). Comparison of TOUGH2/EOS8 boundary backstress simulation results for specified and brine-dependent gas-generation rate histories: a - Void Volume; b - Gas Pressure; c - Brine Flow; d - Gas Expulsion.

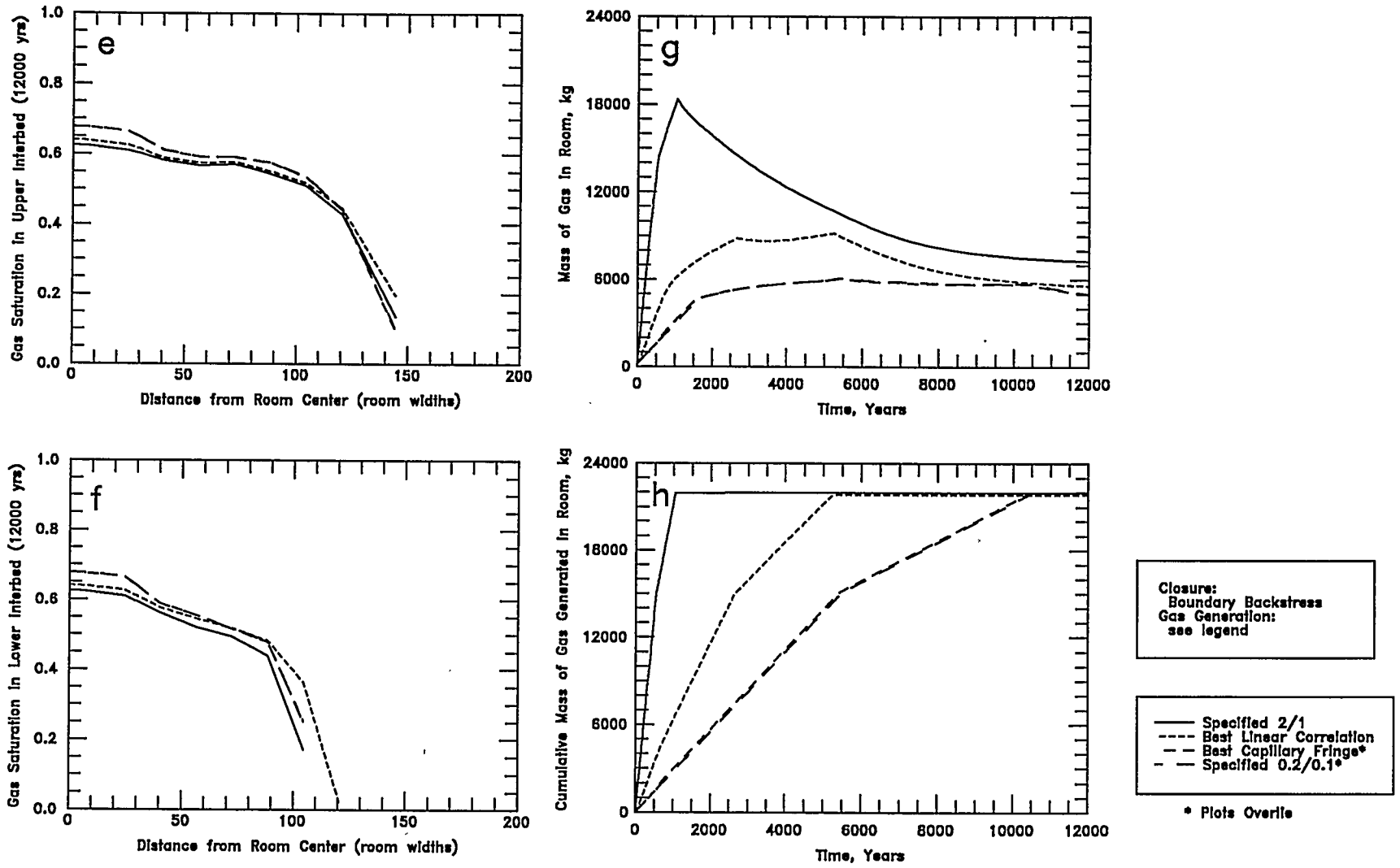

Figure 4-4 (e-h). Comparison of TOUGH2/EOS8 boundary backstress simulation results for specified and brine-dependent gas-generation rate histories: e - Upper Interbed Gas Profile; f - Lower Interbed Gas Profile; g - Room Gas Mass; h - Gas Generation.

method, any non-zero brine saturation in the room was sufficient to produce some brine-inundated effects. Using best-estimate parameters, brine inflow was about 60 m^3 (Figure 4-4c) and gas generation was at about twice the 0.2/0.1 rate (Figure 4-4h). The resulting room closure and expansion (Figure 4-4a), room pressurization (Figure 4-4b), and gas expulsion (Figure 4-4d), were different from the capillary fringe results and were bounded by the specified 2/1 and 0.2/0.1 results.

An important observation is that, in the absence of sufficient brine to drive brine-inundated gas generation, brine-dependent gas generation proceeds at near the vapor-limited rates. Under these conditions, brine-dependent simulation results are very sensitive to the estimates of vapor-limited rates. The results from the brine-dependent rate baseline simulations were not significantly different from the baseline specified 0.2/0.1 rate results. Therefore, only the two specified rate histories, 2/1 and 0.2/0.1, were used in sensitivity simulations (Section 5) to examine system behavior. The sensitivity of system response to gas-generation rate is quantified in Section 5.2.

The hypothesis that gas generation may be a self-limiting or at least a self-regulating process (Section 1.2.3) is supported by these results. Approximately 100 m^3 to 200 m^3 of brine is required to generate the anoxic corrosion potential of 1,050 moles per drum in a disposal room (Section 1.2.3). Under best-estimate conditions (24 m^3 of brine initially in the room), the maximum brine volume in the room was only about 59 m^3 with the specified 2/1 rate, not enough to drive gas generation to the complete exhaustion of potential. With the specified 0.2/0.1 rate history, the maximum brine in the room was about 116 m^3. Without considering additional brine that might be present in downdip rooms, the volume of brine inflow required to assure potential-limited rather than brine-limited gas generation under best-estimate conditions might only be achieved with very low (less than the 0.2/0.1 rates) gas-generation rates in the room. Under this scenario, a large gas-generation rate is only likely for a short period of time, after which the brine supply is exhausted and cannot be replenished by inflow due to high room pressures.

5.0 SENSITIVITY SIMULATION RESULTS

Sensitivity simulations were performed to examine the effect on system behavior of varying the model input system parameters over their expected range of uncertainty (see Section 3.1 and Appendix A). Sensitivities were obtained by varying one parameter at a time to its minimum and maximum expected value while holding all other parameters at best-estimate values. Sensitivity simulations were performed for hydrologic parameters (Section 5.1), gas-generation parameters (Section 5.2), and model conceptualizations (Section 5.3). The system response to parameter changes was evaluated using parameter sensitivity and importance coefficients as outlined in Section 2.6. All sensitivity simulation results are summarized in this Section, but because of the large number of sensitivity simulations performed, only selected results are presented graphically. A complete set of sensitivity simulation results is presented graphically in Appendix B.

The baseline simulations identified two specified gas-generation rate histories, 2/1 and 0.2/0.1, that together provided a representation of the range of system behavior for best-estimate hydrologic parameters. Most sensitivity simulations use the specified 2/1 gas-generation rate history. However, because parameter sensitivity may be different with relatively high gas-generation rates and moderate room closure (as with the 2/1 rates) than with lower gas-generation rates and more room closure (as with the 0.2/0.1 rates), some sensitivity simulations were also performed using the specified 0.2/0.1 rate history.

Because many of the parameter values are not well known, the sensitivity simulations provided: (1) an estimate of the possible range of system behavior; (2) an indication of the relative sensitivity and importance of the parameters to system behavior; and (3) guidance in selecting which parameter values and ranges should be investigated with further experimental work.

Four performance measures were selected to evaluate parameter sensitivity and importance: maximum gas phase pressure in the room; maximum brine volume in the room; total gas expelled from the room; and maximum gas migration distance in an interbed. These performance measures are described in Section 2.6.3. A typical uncertainty range included three parameter values, minimum, best estimate, and maximum. The best-estimate value represents a most likely value, but has no statistical significance (i.e., it is not a calculated mean, median, average, or expected value). The minimum and maximum values define the most likely extreme

values based on an evaluation of available data. In some cases, additional simulations were performed with intermediate values to better delineate parameter sensitivity.

Two parameter sensitivity coefficients were calculated for each performance measure, S^- applicable between the minimum and best-estimate parameter values, and S^+ applicable between the best-estimate and maximum values. Two importance coefficients were also calculated for each performance measure, I^- corresponding to the range from minimum to best estimate (as with S^-), and I^+ corresponding to the range from best estimate to maximum (as with S^+). Importance coefficients are additive, such that a total parameter importance over the expected parameter range can be determined from the sum of I^+ and I^-. Sensitivity coefficients are not additive. As discussed in Section 2.6.4, parameter importance is dependent on both the parameter sensitivity and range. A change in a parameter range (e.g., as a result of new experimental information) will produce a change in parameter importance. Therefore, a ranking of parameters must consider not only the importance, but also the sensitivity, which is independent of the range.

Parameter sensitivity and importance coefficients generally vary over the expected range of parameter uncertainty. To illustrate this non-linearity, sensitivities are also presented graphically in the form of dimensionless sensitivity plots which give a better indication of the changing parameter sensitivity and importance over the range of uncertainty. These plots use dimensionless parameters (P/P_o) on the x-axis to compare the sensitivity of several different parameters for the same performance measure. Following the convention of Section 2.6.4, P represents an input parameter, subscript o represents a best-estimate value, and Ψ represents a performance measure. The comparison is possible with dimensionless parameters because each baseline (best estimate) parameter value is equivalent to 1 on the dimensionless x-axis. The slope of the sensitivity curve is indicative of parameter sensitivity. The use of dimensionless performance measures (Ψ/Ψ_o) on the y-axis allows for a direct comparison between different performance measures. The dimensionless performance measure value is indicative of parameter importance. Based on Equation 2-15, the importance coefficients can be calculated from $I^- = 1 - (\Psi/\Psi_0)$ and $I^+ = (\Psi/\Psi_0) - 1$.

For each parameter there are eight sensitivity and eight importance coefficients (S^-, S^+, I^-, I^+, for each of four performance measures). Because different processes were important for different performance measures, a separate parameter ranking was performed for each performance measure. For each performance measure, parameters were ranked in order of total importance. These rankings, presented in Section 6, also make note of which parameters have

high sensitivity coefficients and which parameters are sensitive and/or important over only a portion of their expected range.

Sensitivity simulations primarily used the boundary backstress method to couple flow and closure, but the pressure lines method was used in certain simulations where long execution times were expected. Parameter sensitivity was found to be very similar regardless of the closure methodology used. This similarity is illustrated with a comparison of parameter sensitivity for halite intrinsic permeability using both the boundary backstress method and the pressure lines method (Figure 5-1). For all four performance measures, parameter sensitivity (represented by the slope of the lines) and total importance (represented by the difference between minimum and maximum dimensionless performance measure values) are nearly identical.

A comparison of the importance coefficients for hydrologic and gas-generation parameters with the importance coefficients for model conceptualization provides an indication of the direction for future work. High parameter importance suggests that refinement of parameter best estimates and ranges may be necessary. High conceptual model importance suggests that a better understanding of process coupling is required and that the coupled process model should be improved. Low conceptual model importance suggests that simplified models may adequately capture the important dynamics of process coupling.

5.1 Hydrologic Parameters

Discussion of sensitivity simulations for hydrologic parameters is divided into three parts: disposal room parameters (Section 5.1.1); halite parameters (Section 5.1.2); and interbed parameters (Section 5.1.3). In each Section, a separate discussion of parameter sensitivity is provided for physical properties (intrinsic permeability, porosity, compressibility), initial conditions (pressure, phase saturations), and multiphase flow properties (relative permeability, capillary pressure). Preliminary simulations indicated that performance measures were not sensitive to variations in fluid properties. Therefore, sensitivity to fluid properties was not examined formally.

In each Section, sensitivity (S^- and S^+) and importance (I^- and I^+) coefficients are tabulated and dimensionless sensitivity plots for physical properties, initial conditions, and

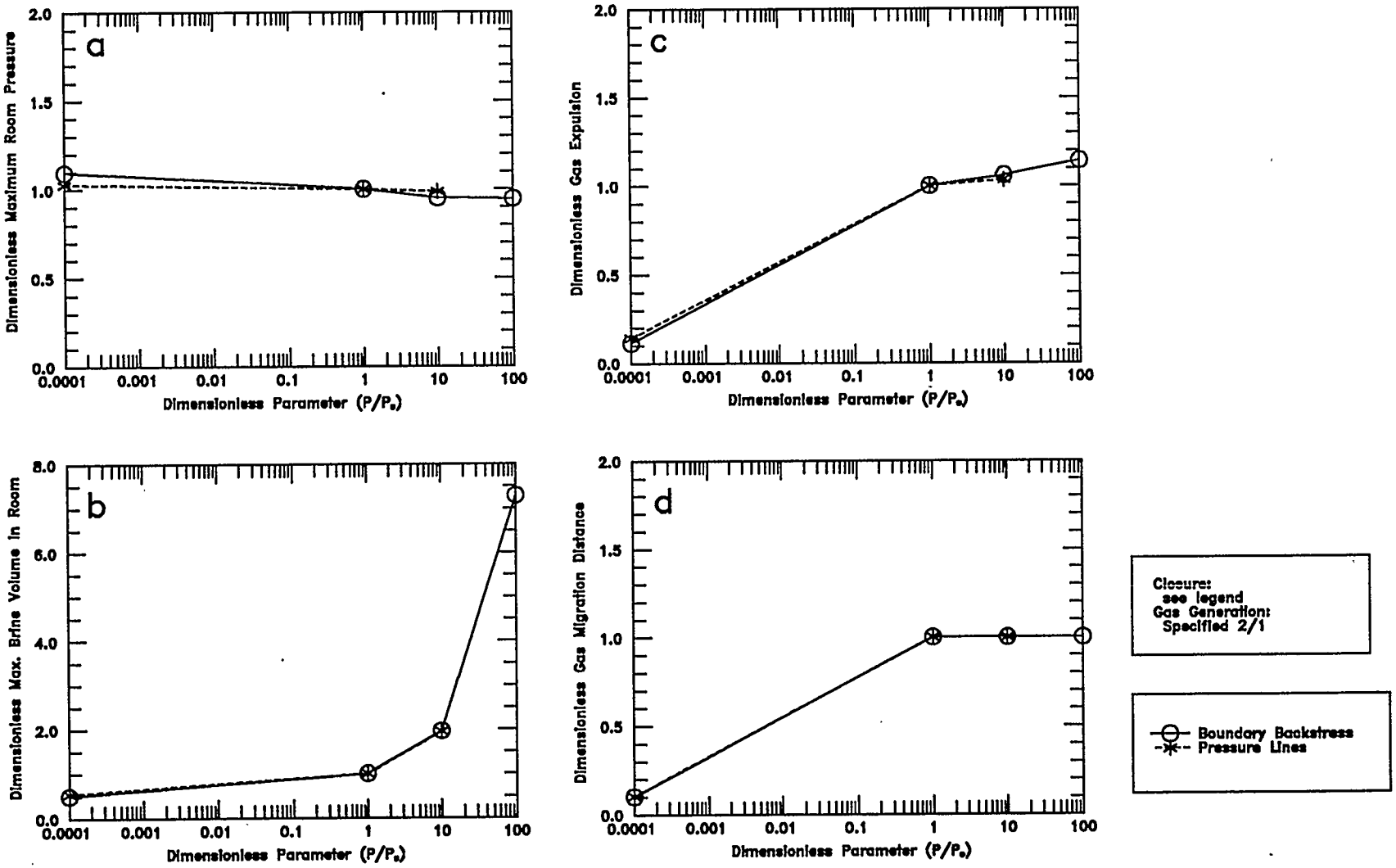

Figure 5-1 (a-d). Comparison of system sensitivity under the boundary backstress and pressure lines flow and closure coupling methods: a - Maximum Room Pressure; b - Maximum Brine in Room; c - Gas Expulsion; d - Gas Migration Distance.

multiphase flow properties are presented. Sensitivity and importance calculations are based on specified 2/1 gas-generation rate history simulations. In most cases, parameter sensitivity and importance was similar under the specified 0.2/0.1 rate history. Significant differences in sensitivity and importance between the two specified rate histories are noted in the sensitivity discussion. Detailed sensitivity simulation results, for both rate histories, are included in Appendix B.

5.1.1 Disposal Room

Parameter ranges for the disposal room hydrologic parameters are listed in Table 3.1. Sensitivity and importance coefficients for each performance measure under the specified 2/1 rate history are presented in Tables 5-1 and 5-2, respectively. Dimensionless parameter sensitivity and importance plots are presented in Figure 5-2 for the physical properties and initial conditions and in Figure 5-3 for the multiphase flow properties.

5.1.1.1 DISPOSAL ROOM PHYSICAL PROPERTIES AND INITIAL CONDITIONS

Because changes to disposal room porosity and compressibility were included in the baseline model conceptualization through closure coupling, a sensitivity to those disposal room rock properties was not performed. Room porosity changed due to room closure and resulting porosity changes were much larger than any uncertainty in initial room porosity. The backstress resulting from the consolidation of the waste and backfill within the room was directly dependent on the changing compressibility of the room contents.

Intrinsic permeability was the only disposal room physical property for which sensitivity simulations were performed. Simulations considered a baseline value of 1×10^{-17} m^2 and a maximum value of 1×10^{-14} m^2. The minimum room permeability corresponded to the baseline value, so only S^+ and I^+ coefficients could be calculated. Sensitivity and importance coefficients were zero for all four performance measures, indicating that system behavior was insensitive to this change in room permeability. This lack of sensitivity is in part an artifact of a coarse vertical room discretization and the absence of gravitational effects in the model. With the baseline model, segregation of the gas phase to the top of the room and the brine phase to the bottom of the room does not occur. With gravity and a finer vertical room discretization, a high room permeability would be expected to increase phase segregation within the room and

Table 5-1. Sensitivity Coefficients for Disposal Room Parameters Under Specified 2/1 Gas-Generation Rate History

	Performance Measure							
	Max. Room Pressure		Max. Brine in Room		Gas Expelled from Room		Gas Migration Distance	
Parameter	S^-	S^+	S^-	S^+	S^-	S^+	S^-	S^+
Physical								
Intrinsic Permeability	---	0.00	---	0.00	---	0.00	---	0.00
Porosity	---	---	---	---	---	---	---	---
Rock Compressibility	---	---	---	---	---	---	---	---
Initial								
Initial Brine Saturation	0.00	0.00	0.40	0.40	0.00	0.00	0.00	0.00
Multiphase								
Residual Brine Saturation	0.00	---	-0.01	---	0.08	---	0.00	---
Residual Gas Saturation	0.00	0.00	0.00	0.00	-0.02	-0.02	0.00	0.00
Pore-Size Lambda (λ)	0.00	0.00	0.00	0.00	-0.08	-0.01	0.00	0.00
Threshold Pressure	---	---	---	---	---	---	---	---

Table 5-2. Importance Coefficients for Disposal Room Parameters Under Specified 2/1 Gas-Generation Rate History

	Performance Measure							
	Max. Room Pressure		Max. Brine in Room		Gas Expelled from Room		Gas Migration Distance	
Parameter	I^-	I^+	I^-	I^+	I^-	I^+	I^-	I^+
Physical								
Intrinsic Permeability	---	0.00	---	0.00	---	0.00	---	0.00
Porosity	---	---	---	---	---	---	---	---
Rock Compressibility	---	---	---	---	---	---	---	---
Initial								
Initial Brine Saturation	0.00	0.01	0.39	2.25	0.00	0.01	0.00	0.00
Multiphase								
Residual Brine Saturation	0.00	---	-0.01	---	0.07	---	0.00	---
Residual Gas Saturation	0.00	0.00	0.00	0.00	-0.02	-0.09	0.00	0.00
Pore-Size Lambda (λ)	0.00	0.00	0.00	0.00	-0.07	-0.02	0.00	0.00
Threshold Pressure	---	---	---	---	---	---	---	---

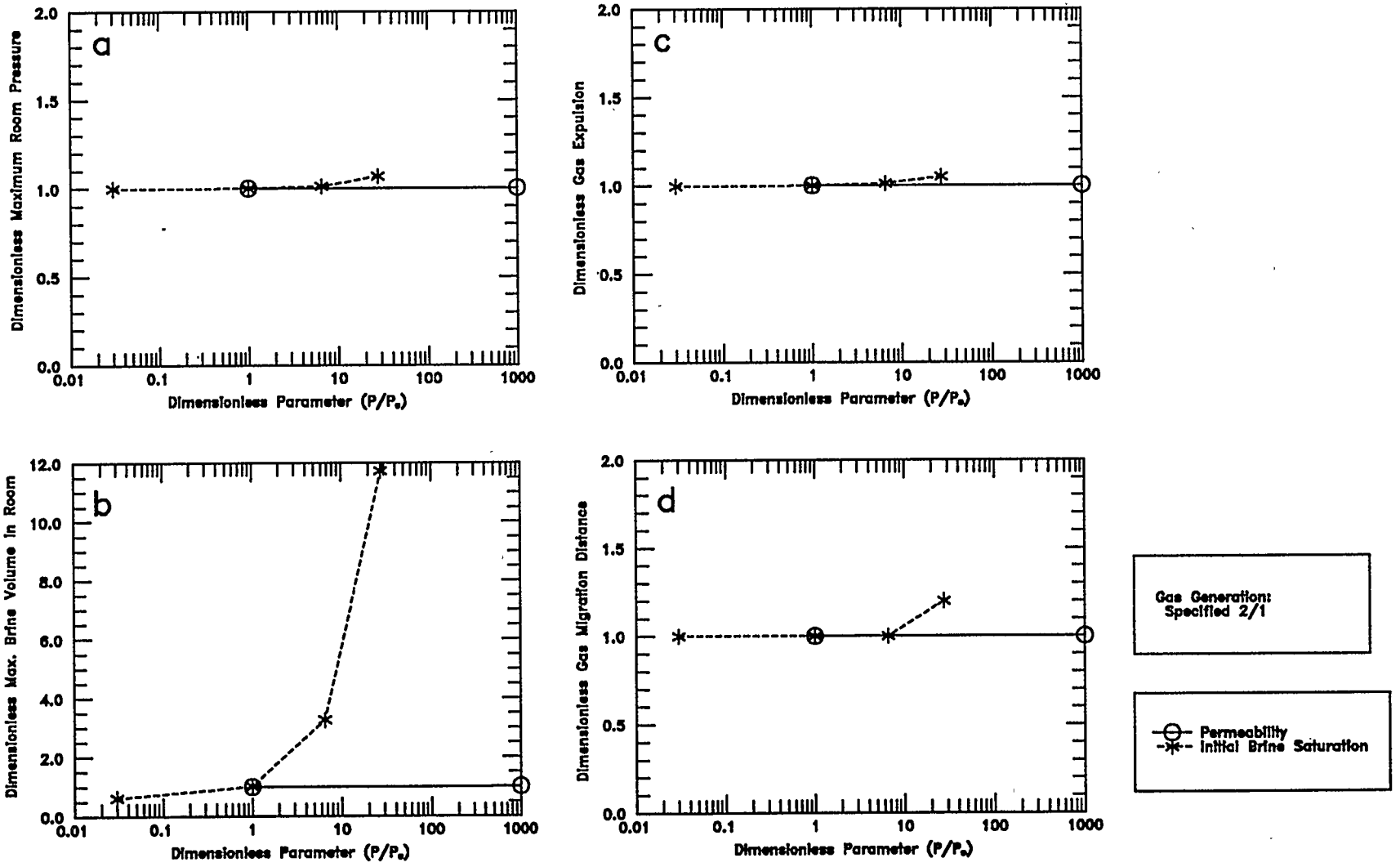

Figure 5-2 (a-d). Dimensionless plots of performance measure sensitivity to disposal room intrinsic permeability and initial brine saturation: a - Maximum Room Pressure; b - Maximum Brine in Room; c - Gas Expulsion; d - Gas Migration Distance.

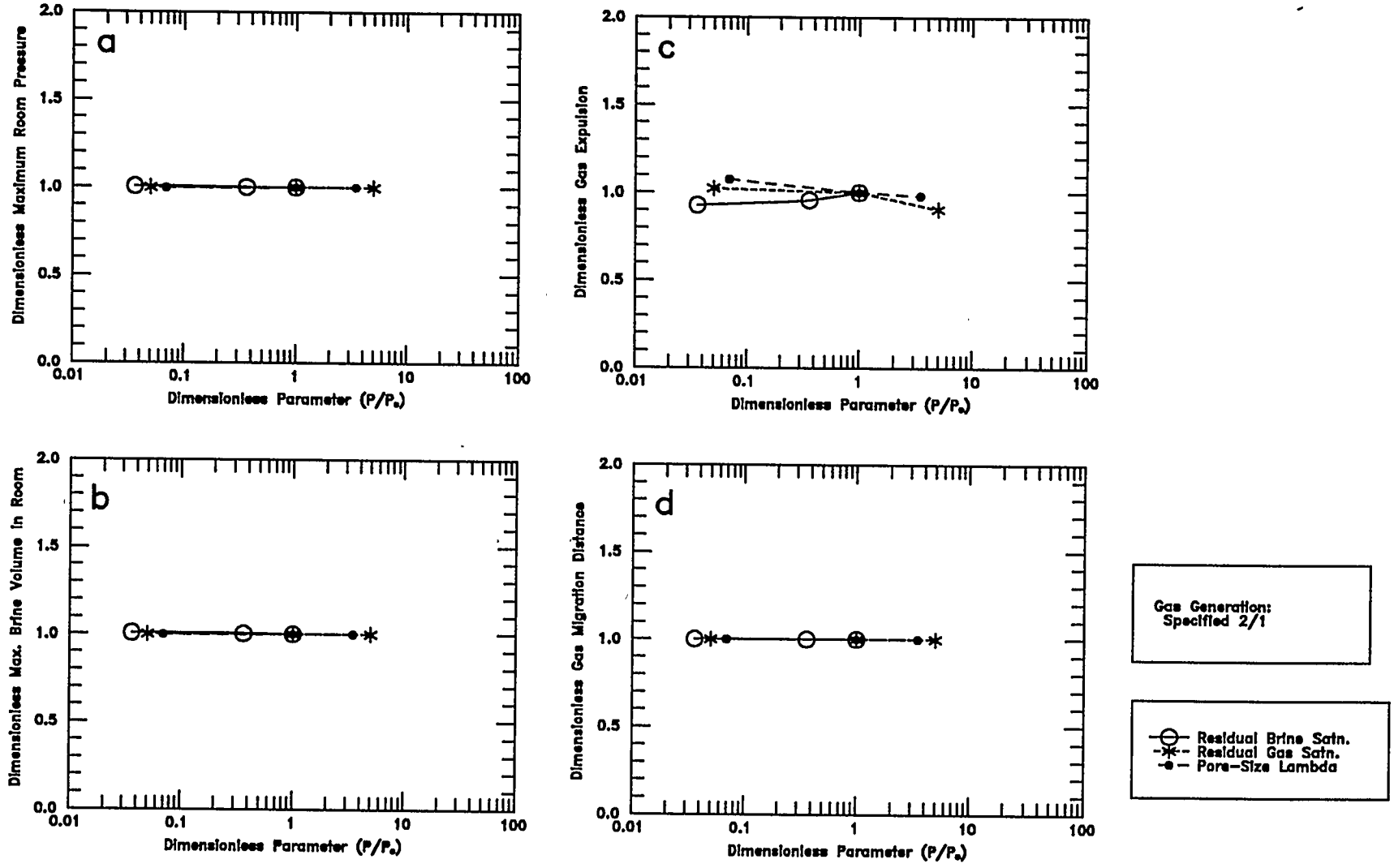

Figure 5-3 (a-d). Dimensionless plots of performance measure sensitivity to disposal room multiphase flow properties: a - Maximum Room Pressure; b - Maximum Brine in Room; c - Gas Expulsion; d - Gas Migration Distance.

change the relative gas releases to the upper and lower interbeds with some impact on overall gas release. This hypothesis was tested using an alternative conceptual model (Section 5.3.2.3).

One further consideration is the relationship between room permeability and interbed permeability. Although not likely under the current estimates of permeability ranges, if the room permeability were lower than the interbed permeability, gas release would be limited by the rate at which gas could flow out of the room and room permeability could be a very important parameter. The room permeability sensitivity simulation was performed in part to demonstrate that the baseline room permeability was large enough not to restrict the flow of brine and gas between the room and the Salado Formation.

The initial brine saturation in the room was varied from a minimum of 0.0003 to a maximum of 0.066, with a best estimate of 0.01. An initial brine saturation of 0.276, equivalent to the residual brine saturation, was also simulated, but was not considered in the calculation of sensitivity and importance coefficients because it was outside the expected range (Section 3.1.1.3). The inclusion of 0.276 would increase parameter importance because of the increase in parameter range. Results from the initial room brine saturation sensitivity simulations are shown in Figure 5-4. Simulation results indicated that (1) there is a direct correlation between initial brine saturation and maximum brine volume in the room, and (2) increasing the initial brine saturation in the room results in a reduction in room closure that is roughly equivalent to the additional room void volume occupied by brine. The initial brine volume in the room was 1 m^3, 24 m^3, and 159 m^3, for the minimum, best-estimate, and maximum initial brine saturations, respectively. An initial saturation of 0.276 produced an initial brine volume in the room of 667 m^3. Because brine inflow with the specified 2/1 rate was relatively low (35 m^3), the maximum brine volume in the room was very sensitive to the initial brine saturation (Figure 5-2b). The maximum brine volume performance measure had a maximum sensitivity coefficient of 0.40 and a total importance of 2.64. Initial brine saturation in the room was one of the most important parameters for this performance measure.

The other performance measures, maximum room pressure (Figure 5-2a), gas expulsion (Figure 5-2c), and gas migration distance (Figure 5-2d), were not sensitive to initial brine saturation over the range (0.0003 to 0.066) simulated. The performance measures were slightly sensitive at an initial brine saturation of 0.276, which corresponds to a dimensionless parameter value of 27.6 in Figure 5-2. The insensitivity of these three performance measures to initial brine saturation is partly due to the use of specified gas-generation rates, which are not

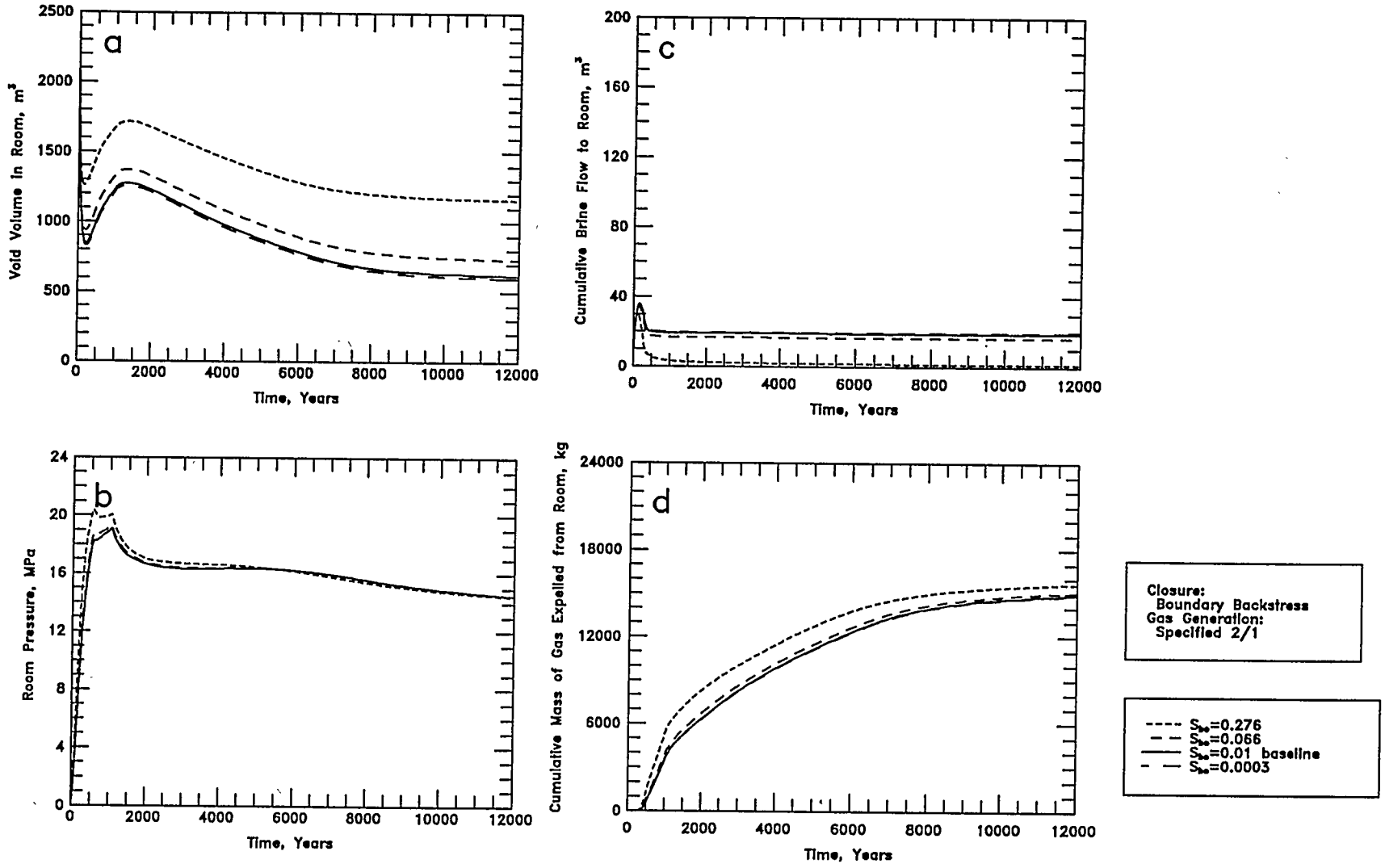

Figure 5-4 (a-d). Sensitivity to disposal room initial brine saturation: a - Void Volume; b - Gas Pressure; c - Brine Flow; d - Gas Expulsion.

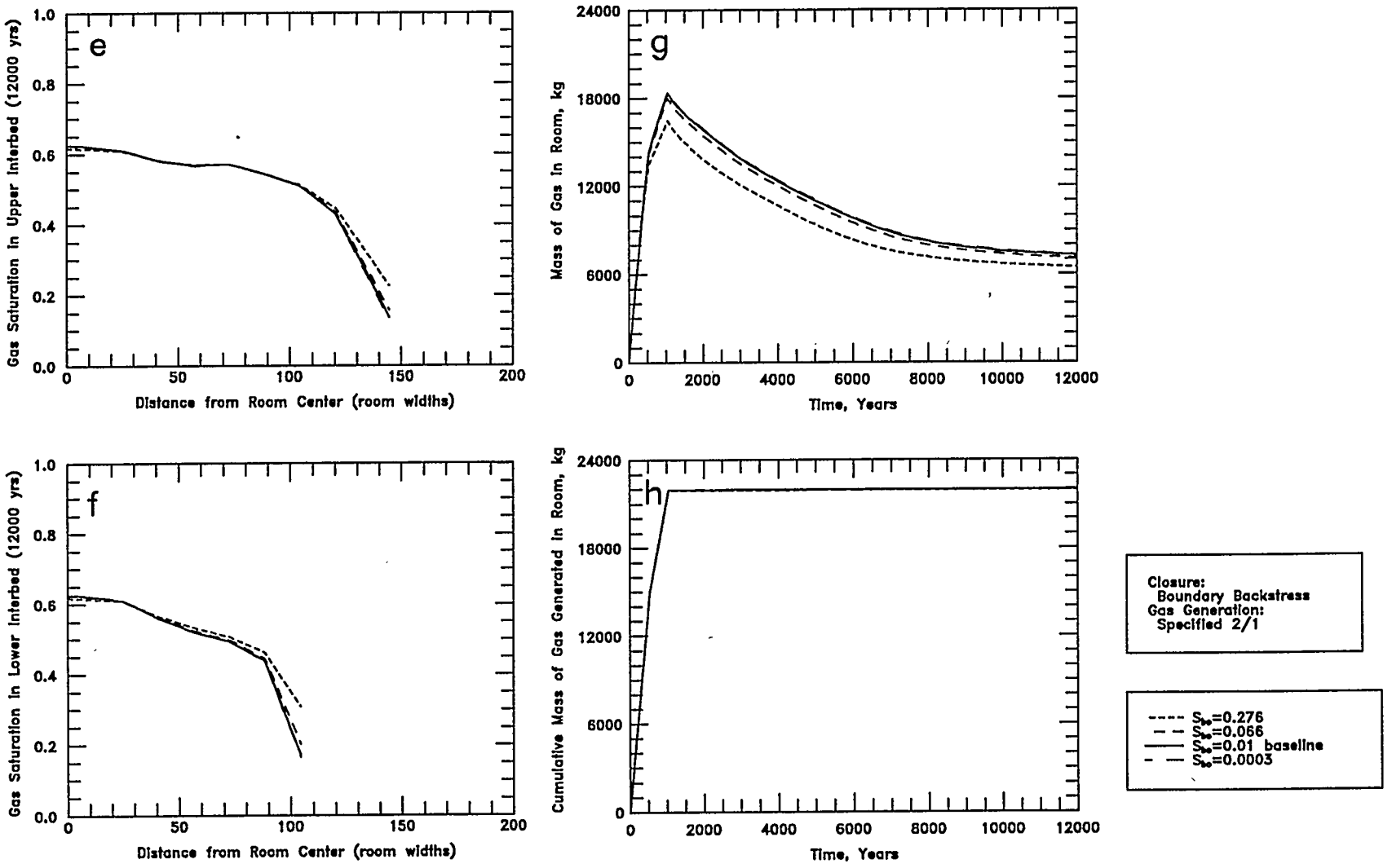

Figure 5-4 (e-h). Sensitivity to disposal room initial brine saturation: e - Upper Interbed Gas Profile; f - Lower Interbed Gas Profile; g - Room Gas Mass; h - Gas Generation.

dependent on brine availability, and to the fact that brine saturations remained below residual saturation in most simulations. The sensitivity to brine-dependent gas-generation parameters is presented in Section 5.2.4

All of the performance measures were slightly less sensitive under the specified 0.2/0.1 rates, primarily because there was greater brine inflow under the lower gas-generation rates. The sensitivity of all performance measures to initial brine saturation is expected to decrease as gas-generation rates decrease.

5.1.1.2 DISPOSAL ROOM MULTIPHASE FLOW PROPERTIES

The relative permeability and capillary pressure relationships used in the baseline TOUGH2/EOS8 model are defined by the Brooks and Corey (1964) model, modified to account for a non-zero residual gas saturation (Section 3.1.1.2). They are dependent on the following parameters: residual brine saturation, S_{br}; residual gas saturation, S_{gr}; pore-size distribution index, λ; and threshold pressure, p_t. Threshold pressure can be used to vary capillary pressure independent of relative permeability, the other three parameters vary both capillary pressure and relative permeability concurrently. No information is available concerning actual values for these parameters in a WIPP disposal room. The parameter database (Appendix A) provides only best estimates for the multiphase flow parameters, S_{br}, S_{gr}, λ, and p_t. The parameter ranges used in the sensitivity simulations were selected somewhat arbitrarily based on estimates from Webb (1992b). The effects of these changes on the relative permeability and capillary pressure relationships in the room are shown in Figure 5-5 for residual brine saturation, Figure 5-6 for residual gas saturation, and Figure 5-7 for pore-size λ.

The residual brine saturation was varied from a minimum of 0.01 to a best estimate of 0.276, with an intermediate value of 0.10 also simulated. A decrease in the residual brine saturation resulted in an increase in the relative permeability to brine in the room, a decrease in the saturation at which brine becomes mobile, and a decrease in the relative permeability to gas (Figure 5-5a). As a result, the volume and duration of brine expulsion increased and the mass of gas expelled was reduced. Gas migration distance was also reduced slightly. The reduction in gas expulsion and migration was due to both the decreased relative permeability to gas and the increased brine expulsion. For the gas expulsion performance measure, the sensitivity coefficient S^- was 0.08 and the total importance coefficient was 0.07. Sensitivity and importance coefficients for the other performance measures were approximately zero.

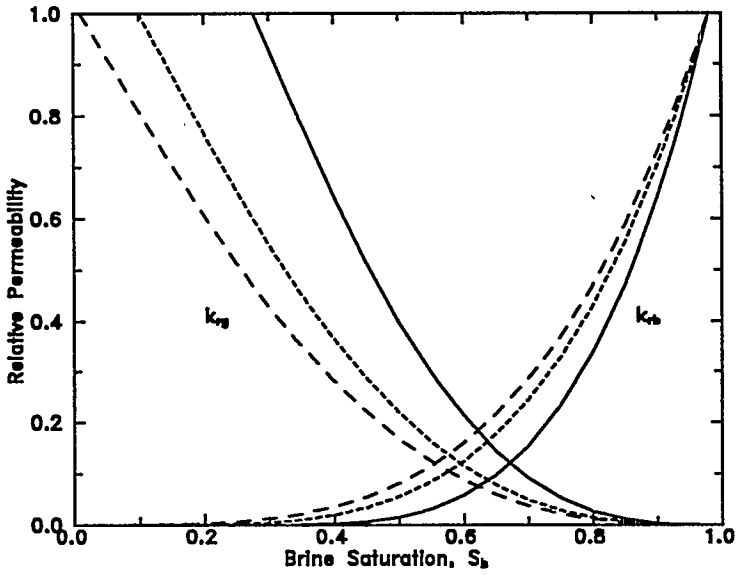

(a) Relative Permeability

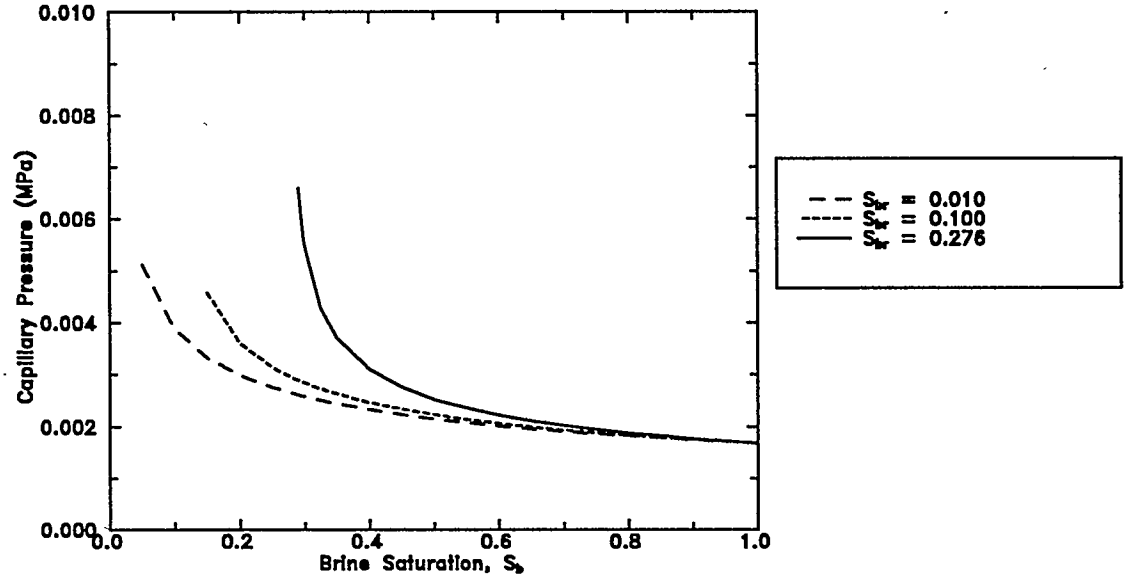

(b) Capillary Pressure

Figure 5-5. Effects of variations in residual brine saturation on disposal room relative permeability and capillary pressure relationships.

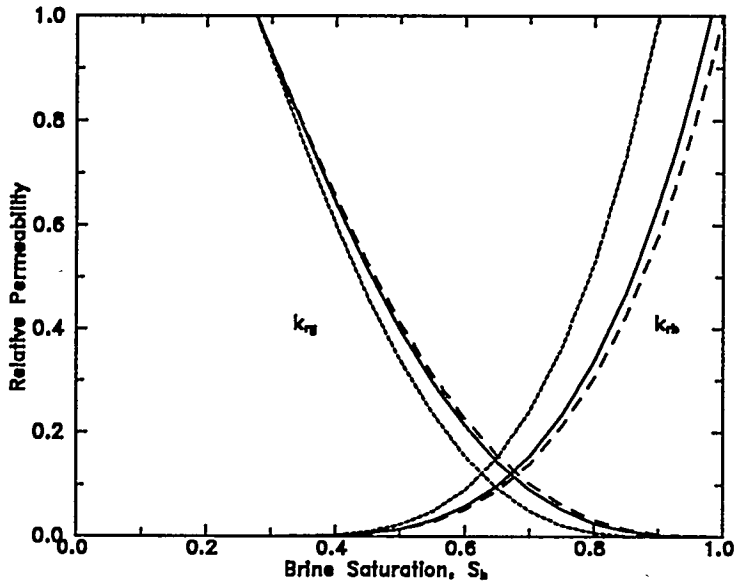

(a) Relative Permeability

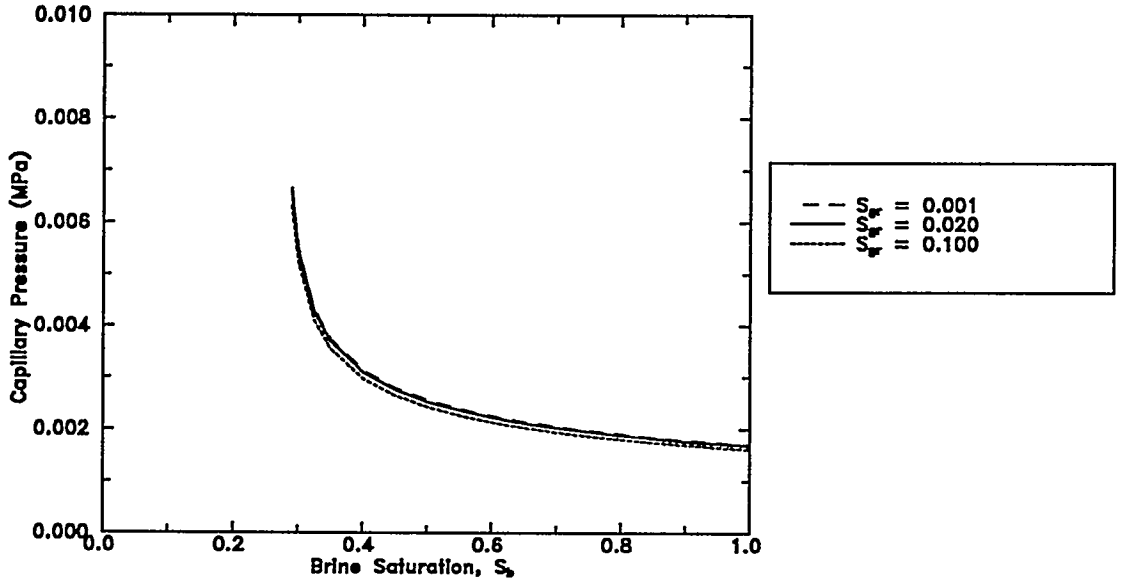

(b) Capillary Pressure

Figure 5-6. Effects of variations in residual gas saturation on disposal room relative permeability and capillary pressure relationships.

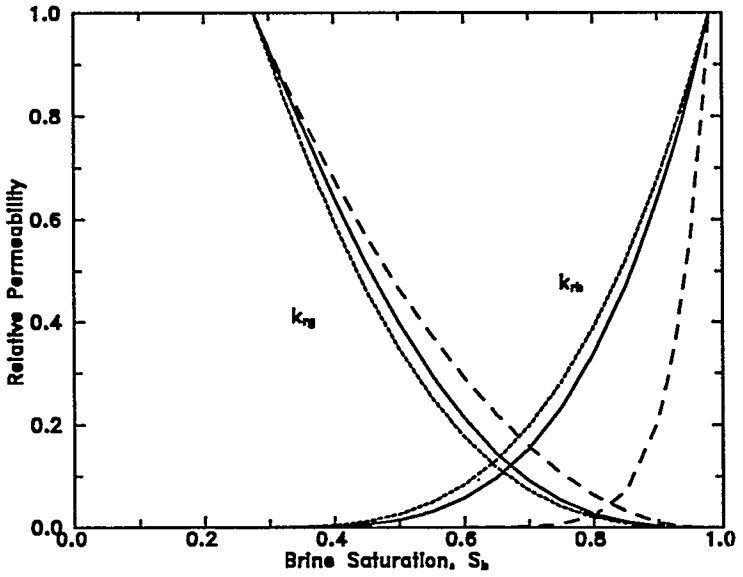

(a) Relative Permeability

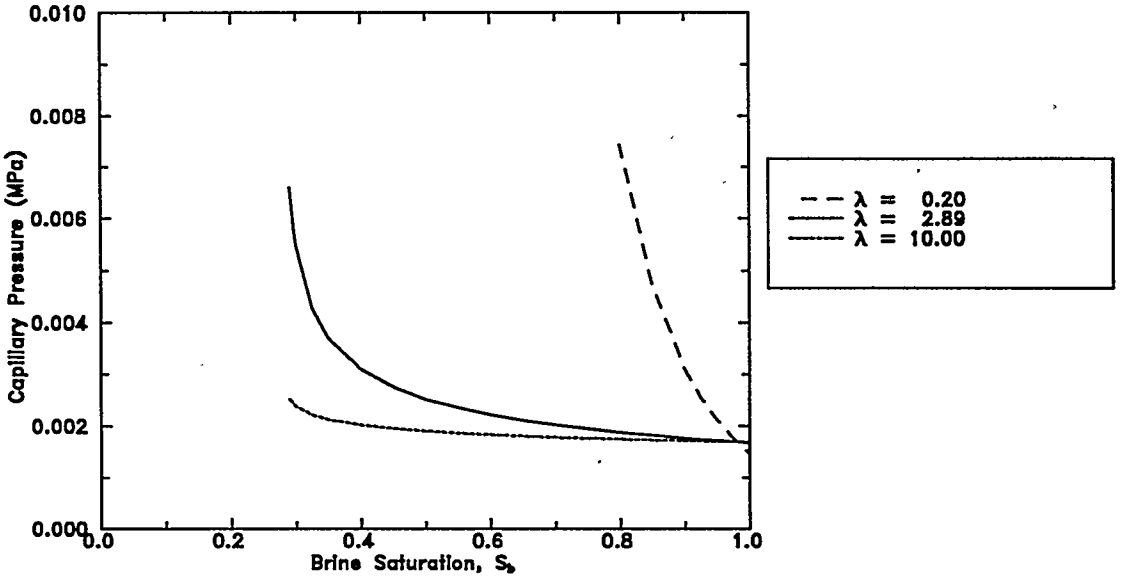

(b) Capillary Pressure

Figure 5-7. Effects of variations in pore-size distribution index (λ) on disposal room relative permeability and capillary pressure relationships.

The residual gas saturation was varied from a minimum of 0.001 to a maximum of 0.10, with a best estimate of 0.02. An increase in the residual gas saturation decreased the relative permeability to gas in the room, increased the saturation at which gas becomes mobile, and increased the relative permeability to brine (Figure 5-6a). Because of these effects, the mass of gas expelled from the room decreased with increasing residual gas saturation. Brine expulsion was not affected, but the gas migration distance decreased slightly. For the gas expulsion performance measure, the maximum sensitivity coefficient was 0.02 and the total importance coefficient was 0.11. Gas expulsion was more sensitive to an increase in residual gas saturation than to a decrease ($I^+ = 0.09$, $I^- = 0.02$). Sensitivity and importance coefficients for the other performance measures were zero.

The pore-size distribution index, λ, was varied from a minimum of 0.2 to a maximum of 10, with a best estimate of 2.89. A decrease in the pore-size λ reduced the relative permeability to brine and increased the relative permeability to gas (Figure 5-7a). These changes in relative permeability resulted in a decrease in the volume of brine expelled and an increase in the mass of gas expelled from the room. The gas migration distance also increased slightly. For the gas expulsion performance measure, the maximum sensitivity coefficient was 0.08 and the total importance coefficient was 0.09. Sensitivity and importance coefficients for the other performance measures were zero.

Sensitivity simulations were not performed for disposal room threshold pressure because it was not expected to change significantly from the best-estimate value of approximately zero. Only the gas expulsion performance measure had any non-zero sensitivity and importance coefficients in response to changes in the disposal room multiphase flow parameters. This insensitivity may be partly an artifact of the room conceptualization. Movement of brine and gas within a disposal room is a complex process. The simplified room model used here cannot capture that complexity. Until a more complex disposal room hydrologic model is incorporated, the effects of variations the room multiphase flow properties on system behavior such as gas release cannot be fully evaluated.

The insensitivity of the performance measures to the disposal room multiphase flow properties may be misleading. Given the complete lack of WIPP-specific data, it is uncertain whether the modified Brooks and Corey (1964) model is appropriate, let alone whether the assumed parameter ranges are representative. However, given the insensitivity of the performance measures to variations in room intrinsic permeability over three orders of

magnitude, the multiphase flow properties might be expected to produce low sensitivities over a similar range.

5.1.2 Salado Formation Halite

Parameter ranges for the hydrologic parameters of the Salado Formation halite are listed in Table 3.2. Sensitivity and importance coefficients for each performance measure are presented in Tables 5-3 and 5-4, respectively, for the specified 2/1 rate history.

Dimensionless parameter sensitivity and importance plots are presented in Figure 5-8 for the physical properties and initial conditions and in Figure 5-9 for the multiphase flow properties.

5.1.2.1 HALITE PHYSICAL PROPERTIES AND INITIAL CONDITIONS

For the halite, physical property sensitivity simulations were performed for intrinsic permeability, porosity, and compressibility. Initial condition sensitivity was examined for the initial brine pressure. The halite intrinsic permeability, k, was varied from a minimum of 1×10^{-25} m^2 to a maximum of 1×10^{-19} m^2, with a best estimate of 1×10^{-21} m^2. An intermediate value of 1×10^{-20} m^2 was also simulated. Results from the halite permeability sensitivity simulations are shown in Figure 5-10.

Variations in halite permeability affected system behavior by varying brine flow between the interbeds and the surrounding halite. Simulation results showed that changing the halite intrinsic permeability directly impacted (1) the volume of brine inflow and expulsion, (2) the mass of gas expelled from the room, and (3) gas migration distance. The peak brine inflow to the room ranged from 6 m^3 (for $k = 1 \times 10^{-25}$ m^2) to 408 m^3 (for $k = 1 \times 10^{-19}$ m^2). The relative volumes of brine inflow through the upper and lower interbeds were sensitive to halite permeability although the duration of brine inflow and expulsion was not. The large volume of brine inflow for the maximum permeability case was significant enough to reduce room closure relative the other cases. The pore space required for gas migration in the interbeds is created when brine is displaced from the interbeds and expelled into the surrounding halite. Both the mass of gas expelled and the gas migration distances were similar for the best-estimate and maximum permeability cases but were less for the minimum permeability case. Room void

Table 5-3. Sensitivity Coefficients for Halite Parameters Under Specified 2/1 Gas-Generation Rate History

	Performance Measure							
	Max. Room Pressure		Max. Brine in Room		Gas Expelled from Room		Gas Migration Distance	
Parameter	S^-	S^+	S^-	S^+	S^-	S^+	S^-	S^+
Physical								
Intrinsic Perm. (constant p_f)	-0.09	0.00	0.50	0.06	0.89	0.00	0.90	0.00
Intrinsic Perm. (variable p_f)	-0.10	0.00	0.50	0.06	0.89	0.00	0.90	0.00
Porosity (constant α_p)	-0.07	-0.02	0.31	0.13	0.24	0.02	0.15	0.00
Porosity (constant α)	0.00	-0.01	0.05	0.03	0.01	0.01	0.00	0.00
Rock Compressibility	-0.05	-0.03	0.19	0.13	0.08	0.03	0.00	0.00
Initial								
Initial Brine Pressure	0.20	0.19	0.85	0.92	-0.35	-1.41	-2.39	-1.59
Multiphase								
Residual Brine Saturation	0.00	0.00	0.00	0.00	0.00	0.00	0.00	0.00
Residual Gas Saturation	0.00	0.00	0.01	0.00	0.00	0.00	0.00	0.00
Pore-Size Lambda (λ)	0.00	0.00	-0.01	0.00	-0.01	0.00	0.00	0.00
Threshold Pressure	0.00	0.00	0.00	0.00	-0.01	0.00	0.00	0.00

Table 5-4. Importance Coefficients for Halite Parameters Under Specified 2/1 Gas-Generation Rate History

	Performance Measure							
	Max. Room Pressure		Max. Brine in Room		Gas Expelled from Room		Gas Migration Distance	
Parameter	I^-	I^+	I^-	I^+	I^-	I^+	I^-	I^+
Physical								
Intrinsic Perm. (constant p_f)	-0.09	-0.05	0.50	6.28	0.89	0.14	0.90	0.00
Intrinsic Perm. (constant p_f)	-0.10	-0.14	0.50	6.28	0.89	0.19	0.90	-0.27
Porosity (constant α_p)	-0.06	-0.04	0.28	0.26	0.21	0.04	0.13	0.00
Porosity (constant α)	-0.00	-0.01	0.04	0.07	0.01	0.01	0.00	0.00
Rock Compressibility	-0.04	-0.01	0.15	0.06	0.06	0.01	0.00	0.00
Initial								
Initial Brine Pressure	0.02	0.05	0.07	0.23	-0.03	-0.35	-0.20	-0.40
Multiphase								
Residual Brine Saturation	0.00	0.00	0.00	0.00	0.00	0.00	0.00	0.00
Residual Gas Saturation	0.00	0.00	0.01	0.00	0.00	0.00	0.00	0.00
Pore-Size Lambda (λ)	0.00	0.00	0.00	-0.01	0.00	0.00	0.00	0.00
Threshold Pressure	0.00	0.00	0.00	0.00	0.00	0.00	0.00	0.00

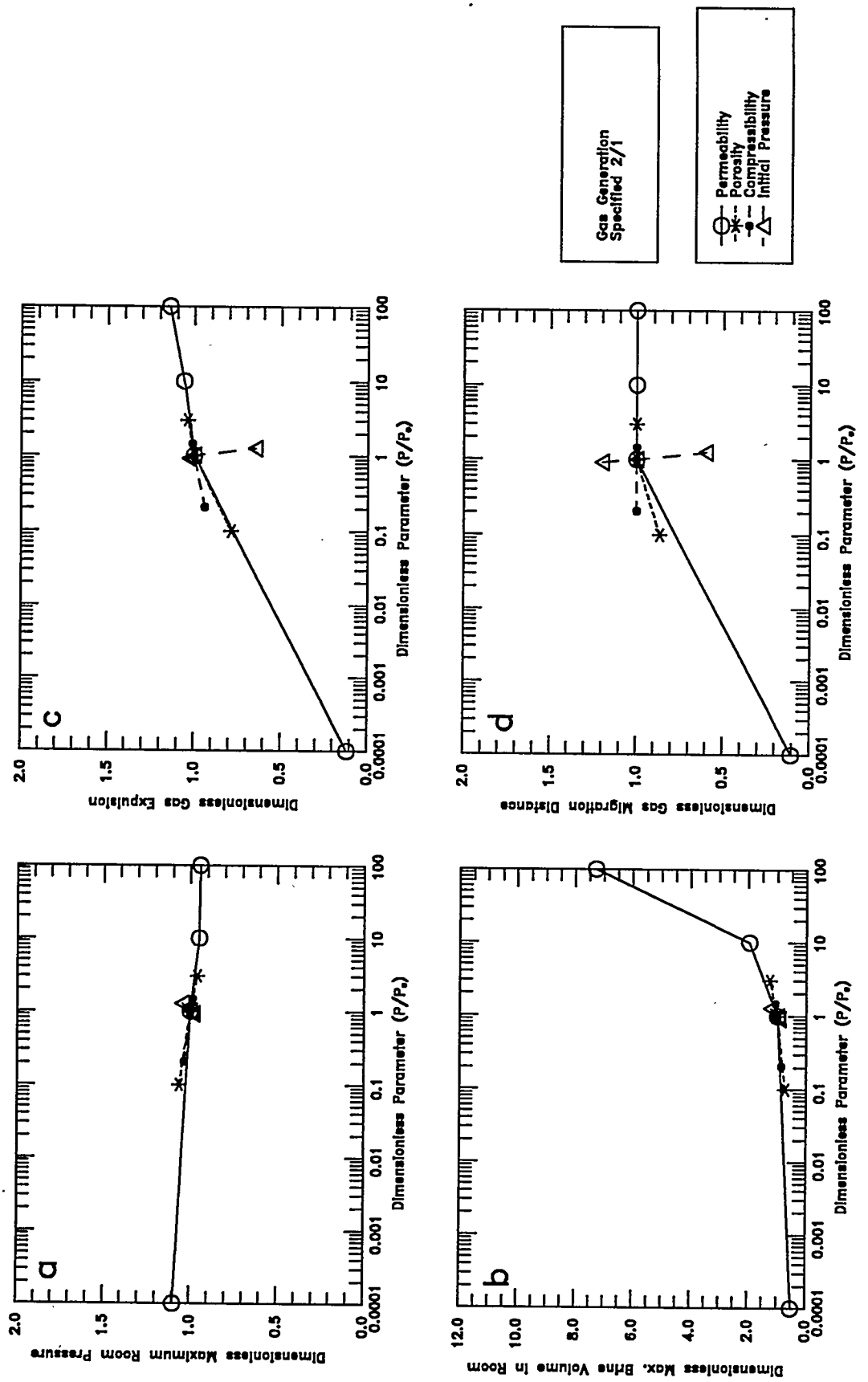

Figure 5-8 (a-d). Dimensionless plots of performance measure sensitivity to halite physical properties and initial pressure: a - Maximum Room Pressure; b - Maximum Brine in Room; c - Gas Expulsion; d - Gas Migration Distance.

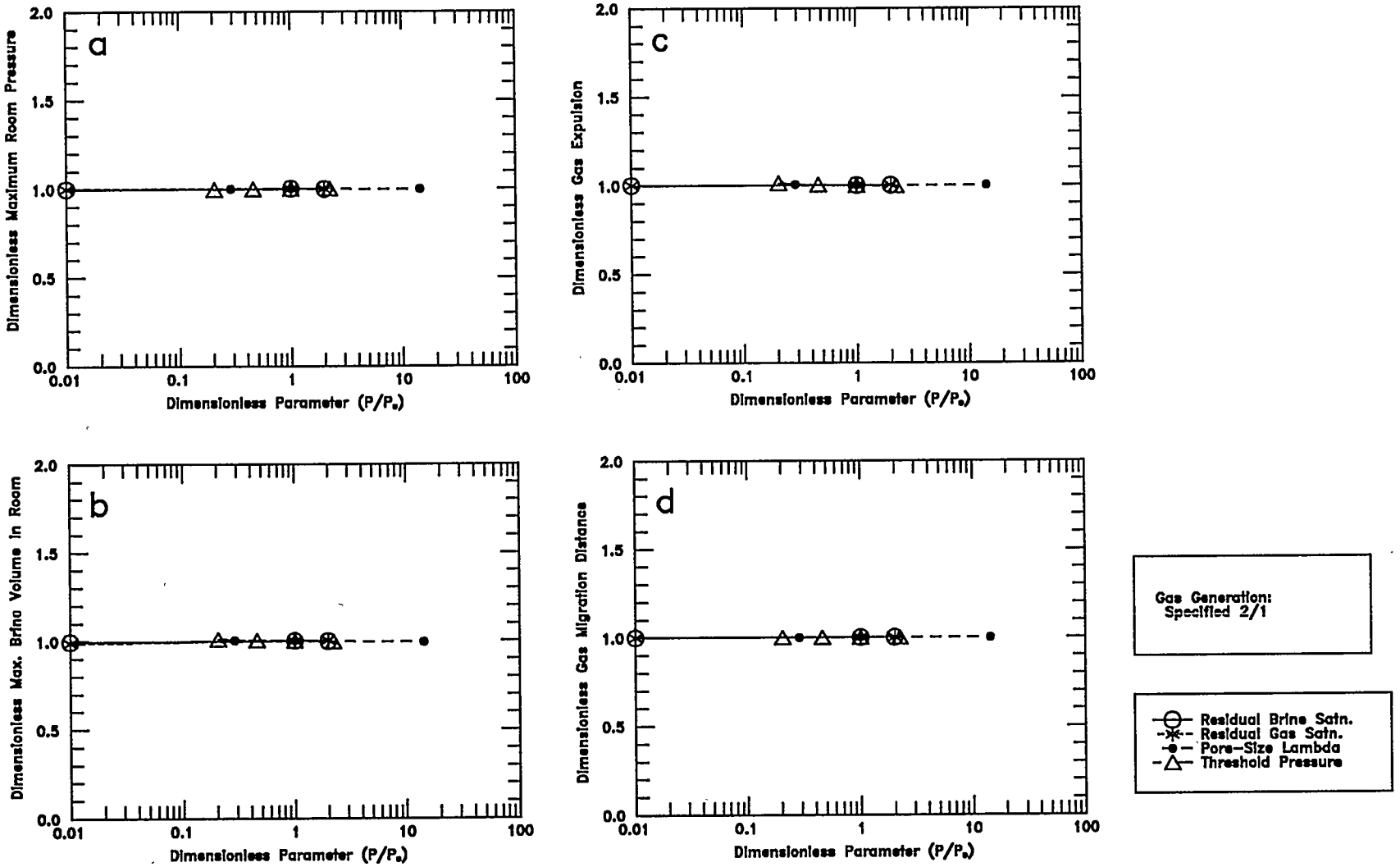

Figure 5-9 (a-d). Dimensionless plots of performance measure sensitivity to halite multiphase flow properties: a - Maximum Room Pressure; b - Maximum Brine in Room; c - Gas Expulsion; d - Gas Migration Distance.

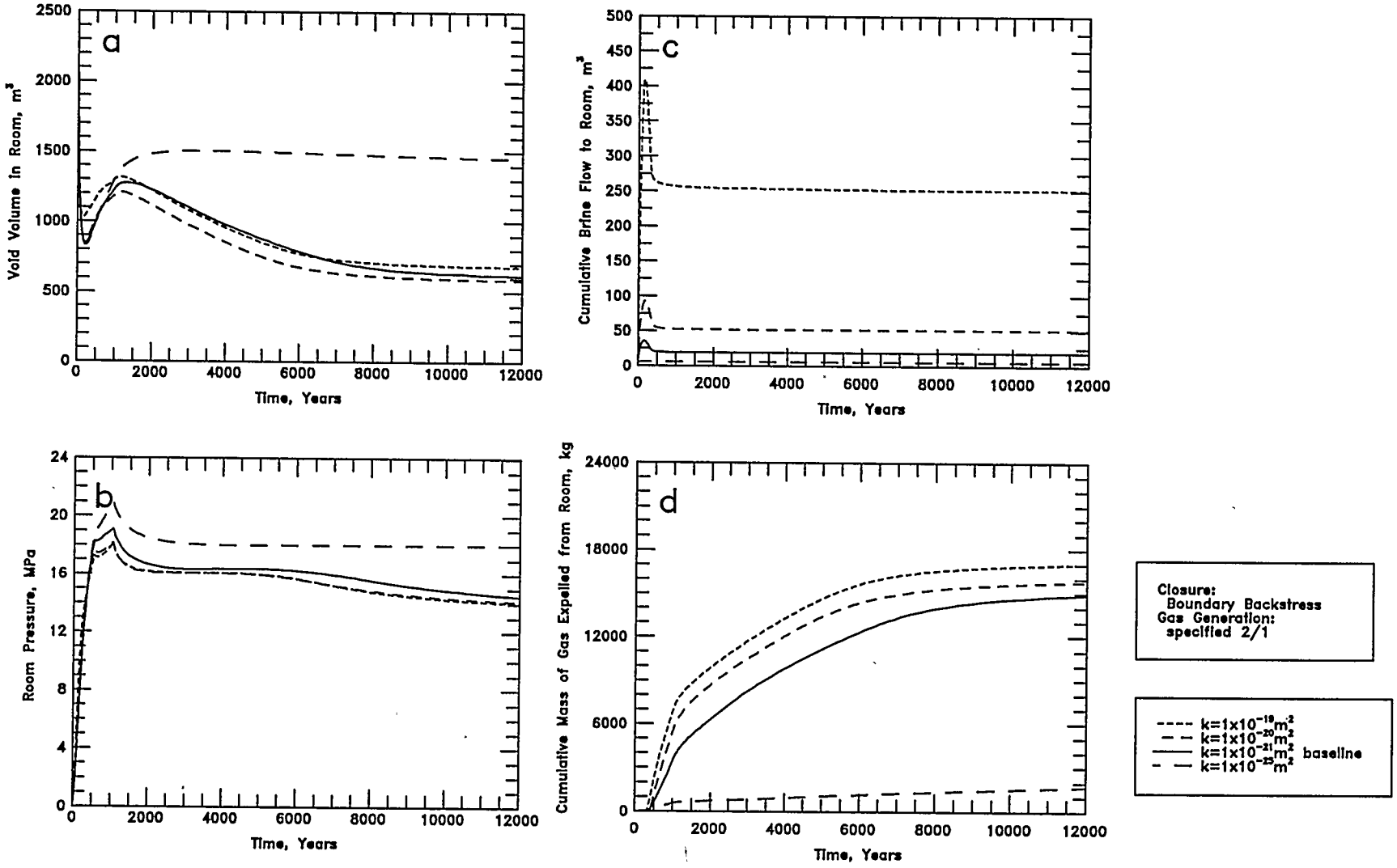

Figure 5-10 (a-d). Sensitivity to halite intrinsic permeability (constant threshold pressure): a - Void Volume; b - Gas Pressure; c - Brine Flow; d - Gas Expulsion.

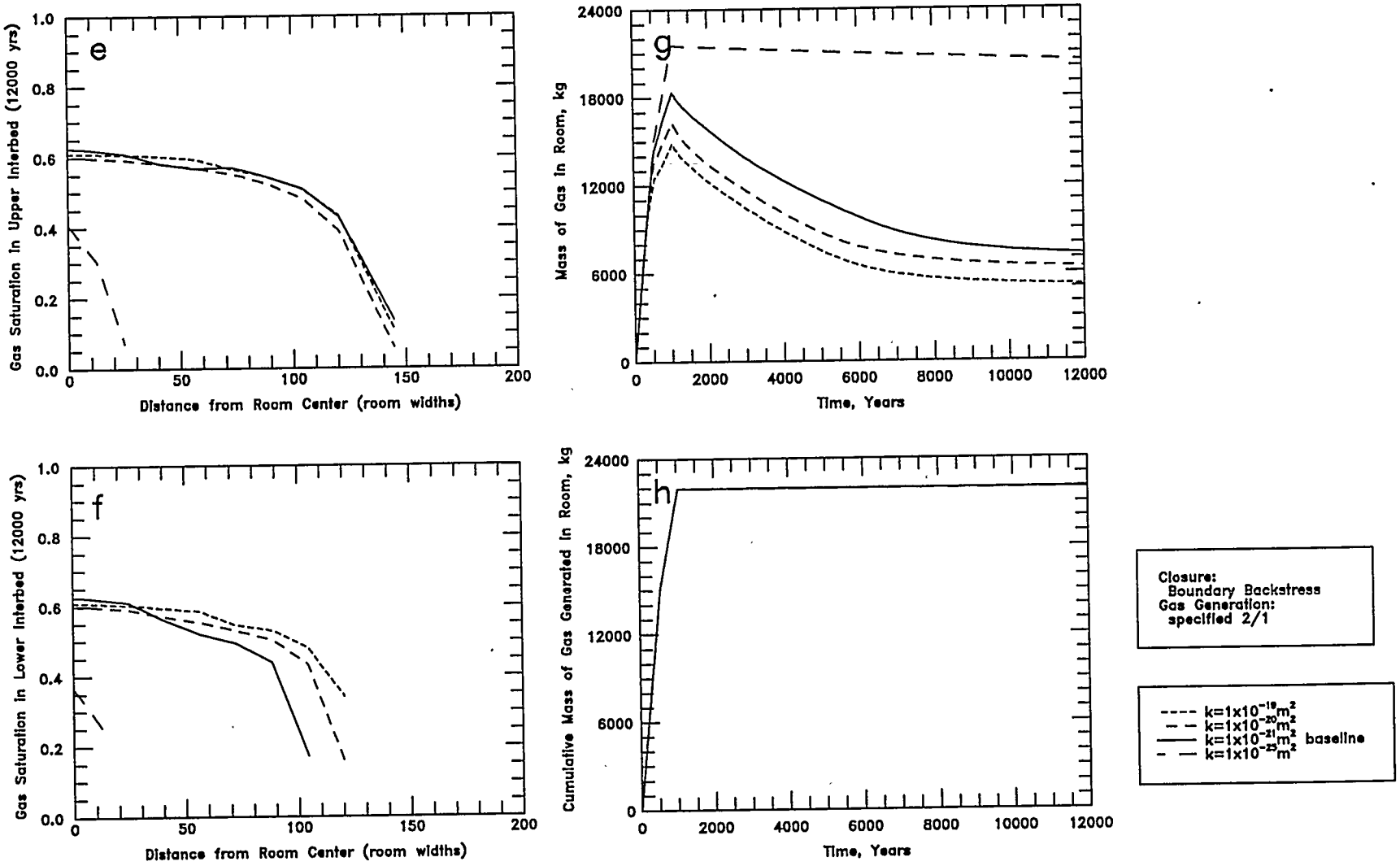

Figure 5-10 (e-h). Sensitivity to halite intrinsic permeability (constant threshold pressure): e - Upper Interbed Gas Profile; f - Lower Interbed Gas Profile; g - Room Gas Mass; h - Gas Generation.

volume and pressure behavior was similar for the maximum and best-estimate halite permeabilities because the gas expulsion and mass of gas in the room were similar. However, reduced gas expulsion in the minimum permeability case resulted in higher room pressure and greater room expansion.

These results suggest that the displacement of brine from the interbeds into the halite by gas is a limiting condition on gas movement in the interbeds when halite permeability is less than about 1×10^{-21} m^2. At higher halite permeabilities, gas migration is limited by other factors. Because of the direct correlation between brine inflow and halite permeability, the performance measure maximum brine volume in the room (Figure 5-8b) had large sensitivity and importance coefficients, particularly at higher permeabilities. The performance measures gas expulsion (Figure 5-8c) and gas migration distance (Figure 5-8d) also had large sensitivity and importantcoefficients, especially at lower permeabilities. Halite permeability was one of the most important parameters for each of these three performance measures. Only the maximum room pressure performance measure was not particularly sensitive to halite permeability. In brine-dependent rate simulations the room pressure might be more sensitive, given the correlation between brine inflow and halite intrinsic permeability.

The sensitivity and importance coefficients of the performance measures to halite intrinsic permeability under the specified 0.2/0.1 gas-generation rate history were all similar to the sensitivity and importance coefficients observed with the 2/1 rate history. The halite intrinsic permeability sensitivity simulations presented here were all run using the boundary backstress method. Similar sensitivity and importance coefficients were obtained under both specified gas-generation rate histories using the pressure lines method (see Figure 5-1).

Davies (1991) derived a correlation between intrinsic permeability and threshold pressure, p_t (Equation 3-8). To account for this correlation, the halite intrinsic permeability simulations were also run with gas-brine threshold pressures in the halite adjusted to be consistent with intrinsic permeability. The previously discussed uncorrelated threshold pressure simulations all used the best-estimate threshold pressure of 10.3 MPa, which corresponds to a permeability of 1×10^{-21} m^2. The permeability-correlated threshold pressures, calculated from Equation 3-8, were 250 MPa for $k = 1 \times 10^{-25}$ m^2, 4.7 MPa for $k = 1 \times 10^{-20}$ m^2, and 2.1 MPa for $k = 1 \times 10^{-19}$ m^2.

Results from the permeability-correlated threshold pressure simulations were similar to the uncorrelated simulation results in all cases except for $k = 1 \times 10^{-19}$ m^2. The difference shows up in the I^+ importance coefficients (Table 5-4). The permeability-correlated sensitivities are not included in Figure 5-8. In the uncorrelated simulations, the 10.3 MPa threshold pressure prevented gas expulsion to the halite for all permeabilities. However, the 2.1 MPa threshold pressure used in the 1×10^{-19} m^2 permeability-correlated simulation was low enough that there was (1) gas expulsion from the room to the halite, and (2) gas expulsion from the interbeds to the surrounding halite. The additional gas-storage volume in the halite resulted in reduced room pressures and a 30% decrease in gas migration distance.

While threshold pressure in the halite is expected to be high (10.3 MPa) based on theoretical considerations, it has never been measured in the Salado Formation halite or any other halite. The heightened importance of the 2.1 MPa halite threshold pressure in the 1×10^{-19} m^2 permeability-correlated simulation indicates that, if the estimated halite threshold pressure is unrealistically high, then enhanced gas storage in the halite could have a significant beneficial impact on gas migration performance measures.

Halite porosity, ϕ, was varied from a minimum of 0.001 to a maximum of 0.03, with a best estimate of 0.01. Sensitivity simulations were performed in which it was assumed that pore volume compressibility, α_p, was equivalent to the best-estimate value of 2.7×10^{-9} Pa^{-1} and did not change with porosity. Simulation results are shown in Figure 5-11. The pore volume compressibility is calculated as the rock (bulk) compressibility, α, divided by the porosity. The assumption of a constant pore volume compressibility implies that the rock compressibility varies in proportion to the porosity. The corresponding specific storage in the halite was 3.5×10^{-8} m^{-1} for $\phi = 0.001$, 3.5×10^{-7} m^{-1} for $\phi = 0.01$, and 1.0×10^{-6} m^{-1} for $\phi = 0.03$. Halite specific storage is considered because the storage of brine in the halite is important to system behavior.

Increased porosity produces increased storativity, resulting in an increase in the volume of brine that can be released from storage in the halite and made available for inflow to the room. Changes in brine inflow were directly correlated with changes in halite porosity and halite specific storage. Gas expulsion was also correlated with halite porosity. The increased storativity due to increased porosity provided additional storage volume for brine displaced from the interbeds by expelled gas.

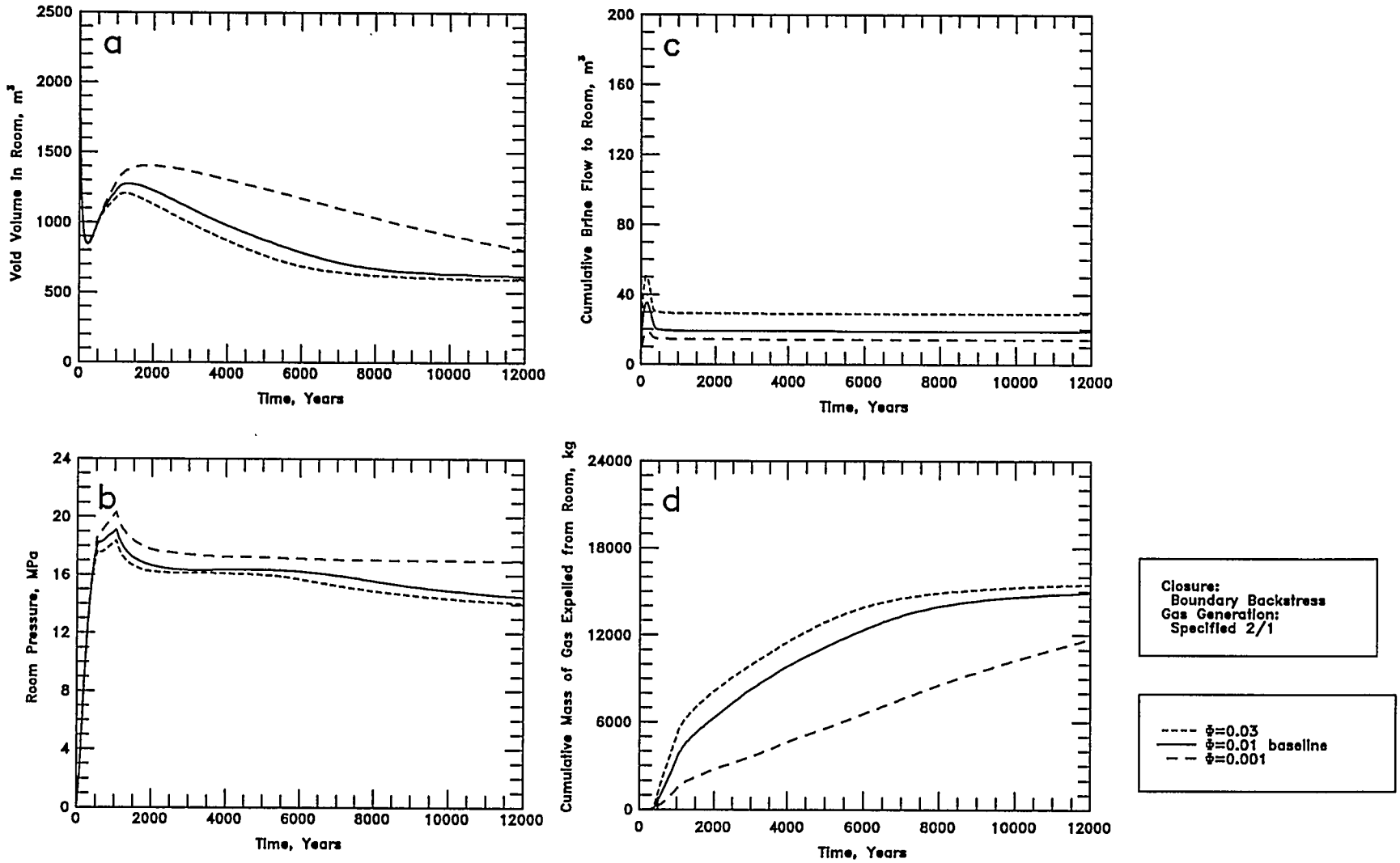

Figure 5-11 (a-d). Sensitivity to halite porosity (constant pore volume compressibility): a - Void Volume; b - Gas Pressure; c - Brine Flow; d - Gas Expulsion.

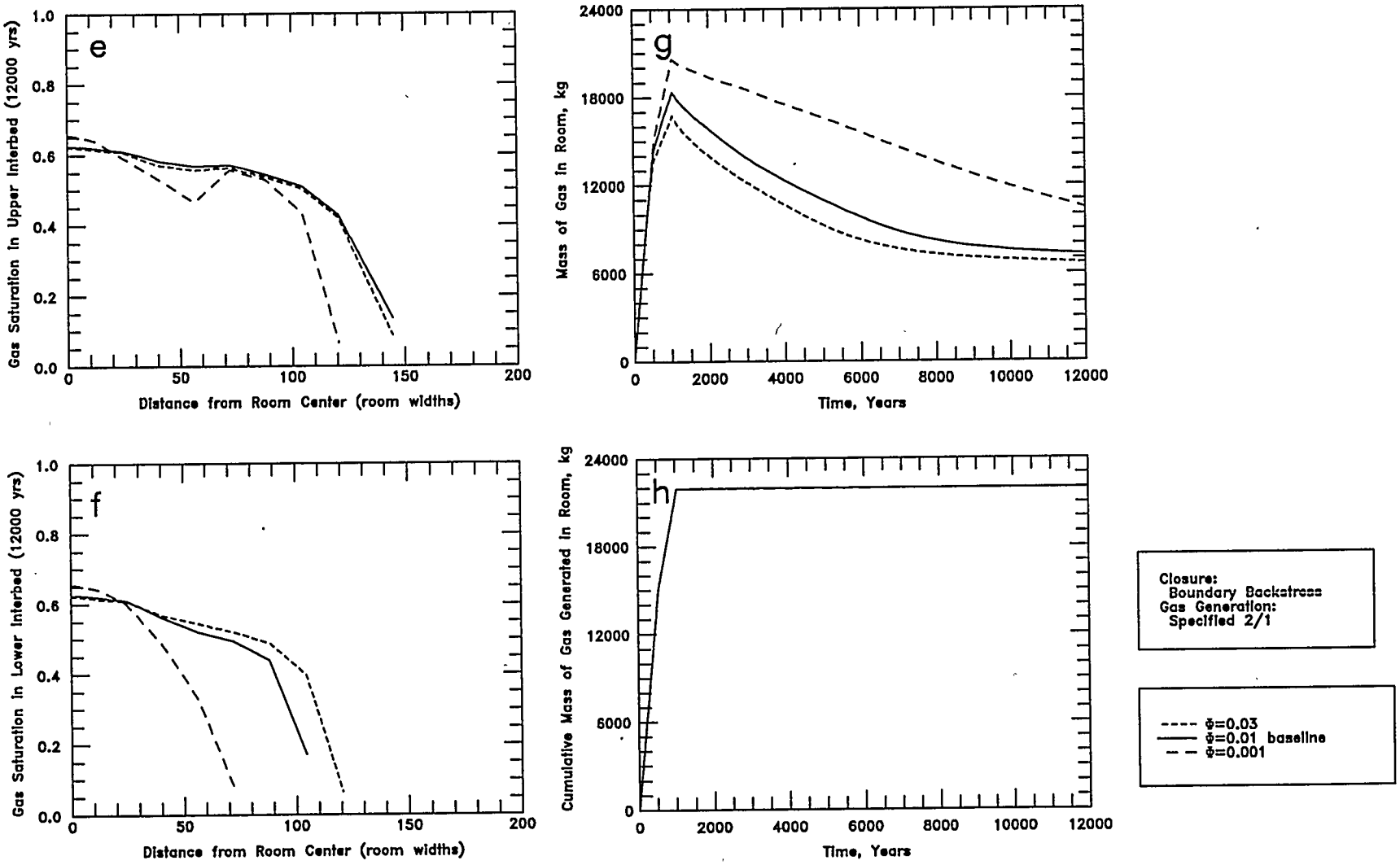

Figure 5-11 (e-h). Sensitivity to halite porosity (constant pore volume compressibility): e - Upper Interbed Gas Profile; f - Lower Interbed Gas Profile; g - Room Gas Mass; h - Gas Generation.

The performance measures, maximum brine volume in the room (Figure 5-8b), gas expulsion (Figure 5-8c), and gas migration distance (Figure 5-8d) all had moderately high sensitivity and importance coefficients for halite porosity. Only maximum room pressure was relatively insensitive to halite porosity. In brine-dependent rate simulations the room pressure might be more sensitive, given the correlation between brine inflow and halite porosity. The sensitivity and importance coefficients of the performance measures to halite porosity under the specified 0.2/0.1 rates were all similar to the sensitivity and importance coefficients calculated with the specified 2/1 rate history. Similar sensitivity and importance coefficients were obtained using the pressure lines method.

As an alternative to the constant pore volume compressibility assumption, simulations were also performed with a constant rock compressibility, α, equivalent to the best-estimate value of 2.7×10^{-11} Pa^{-1}. A constant rock compressibility presumes that the pore volume compressibility varies inversely with the porosity. The corresponding specific storage values for the constant-rock-compressibility halite porosity simulations were 3.2×10^{-7} m^{-1} for $\phi = 0.001$, 3.5×10^{-7} m^{-1} for $\phi = 0.01$, and 4.1×10^{-7} m^{-1} for $\phi = 0.03$. Because this range of specific storage is much smaller than for the constant pore volume compressibility simulations, importance coefficients were also much smaller. The constant rock compressibility simulations are not shown in Figure 5-8.

The halite rock compressibility was varied from a minimum of 5.6×10^{-12} Pa^{-1} to a maximum of 3.9×10^{-11} Pa^{-1}, with a best-estimate value of 2.7×10^{-11} Pa^{-1}. An intermediate value of 2.4×10^{-11} Pa^{-1} was also simulated. As with halite porosity, halite compressibility directly influences brine storage in the halite. The corresponding range for specific storage was 9.5×10^{-8} m^{-1} for the minimum compressibility to 4.9×10^{-7} m^{-1} for the maximum compressibility. The performance measures were somewhat sensitive to halite compressibility (Figure 5-8), with sensitivity coefficients similar to halite porosity. The importance coefficients for halite compressibility were smaller than for porosity because the range of specific storage was smaller.

The initial brine pressure in the Salado Formation was varied from 11.0 MPa to 15.0 MPa, with a best estimate of 12.0 MPa. Initial pressures were changed in both the halite and the interbeds. Simulation results are shown in Figure 5-12. A high formation pressure produced a higher initial inward pressure gradient, resulting in increased brine inflow. A low

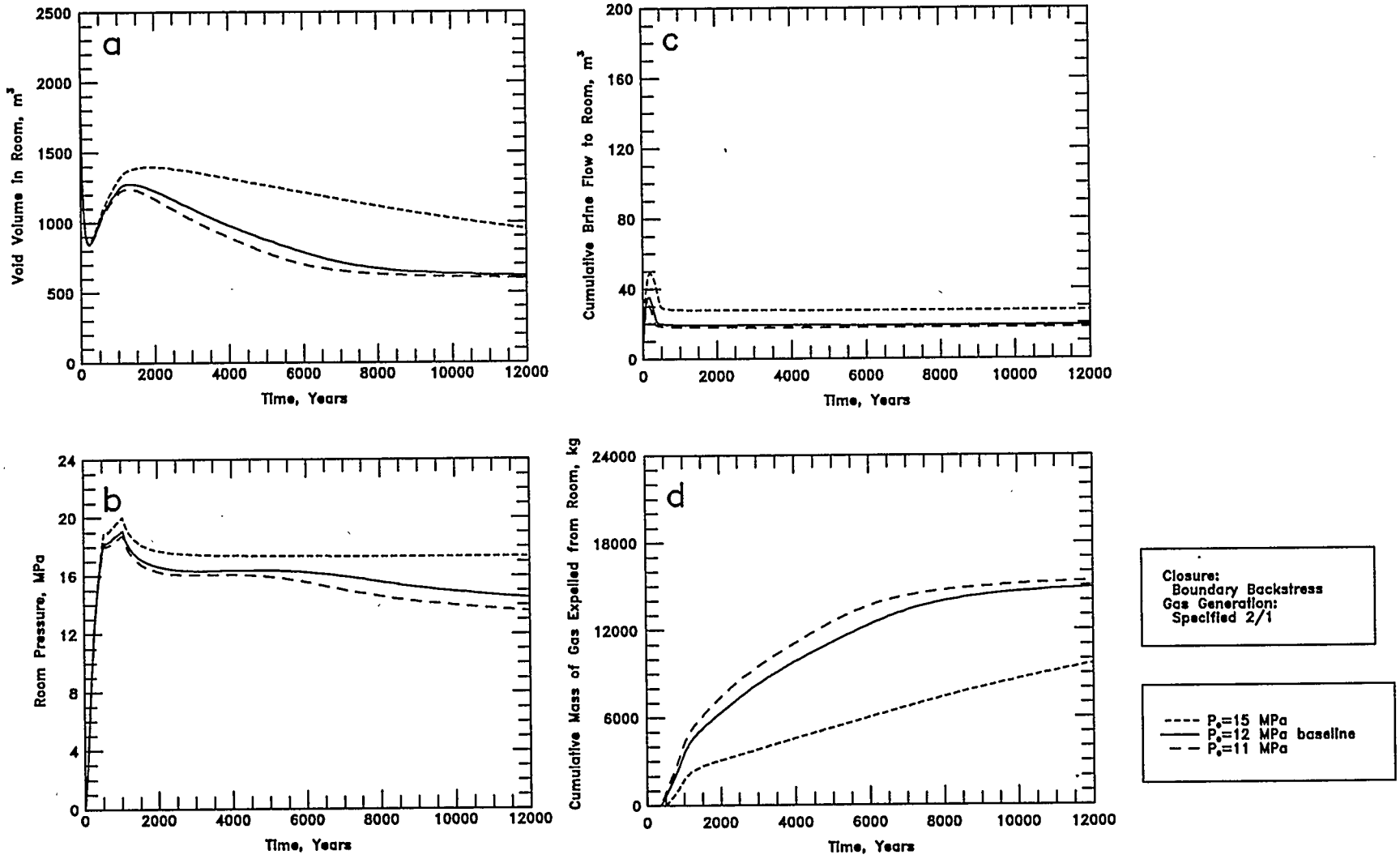

Figure 5-12 (a-d). Sensitivity to initial Salado Formation pressure: a - Void Volume; b - Gas Pressure; c - Brine Flow; d - Gas Expulsion.

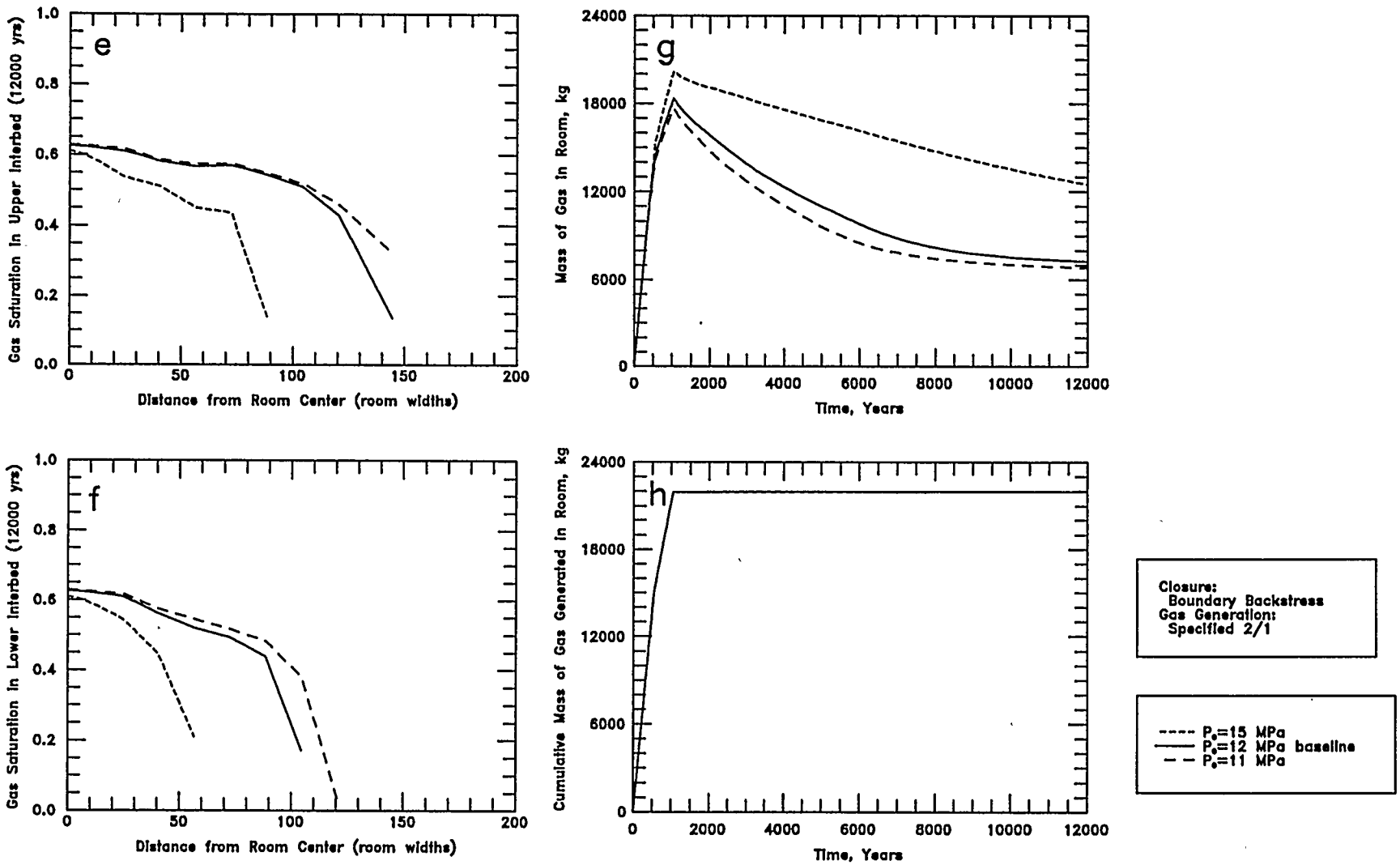

Figure 5-12 (e-h). Sensitivity to initial Salado Formation pressure: e - Upper Interbed Gas Profile; f - Lower Interbed Gas Profile; g - Room Gas Mass; h - Gas Generation

formation pressure resulted in the greatest gas expulsion because the lower far-field pressure resulted in a higher outward pressure gradient. Gas migration was also increased by a low formation pressure.

All of the performance measures were sensitive to the initial brine pressure, however because of the small range, the importance coefficients were moderated somewhat. Nonetheless, the importance coefficients were still significant for the maximum brine volume in the room, gas expulsion, and gas migration distance. Sensitivity and importance coefficients were similar with the specified 0.2/0.1 rate history.

5.1.2.2 HALITE MULTIPHASE FLOW PROPERTIES

saturation (Section 3.1.1.2), are dependent on residual brine saturation, residual gas saturation, pore-size λ, and threshold pressure. No information is available concerning actual parameter values for these multiphase flow properties in Salado Formation halite. Parameter ranges selected for the sensitivity simulations were based on estimates from Webb (1992b). Both the residual brine saturation and residual gas saturation were varied from a minimum of 0.00 to a maximum of 0.40, with best estimates of 0.20. The pore-size λ was varied from a minimum of 0.2 to a maximum of 10, with a best estimate of 0.7.

Under baseline conditions there is very little multiphase flow in the halite. Initially the halite is fully brine-saturated and there is no gas expulsion from the room into the halite. As a result, the system behavior and performance measures were not sensitive to variations in the halite residual saturations and pore-size λ. In the dimensionless sensitivity plots (Figure 5-9) the minimum residual brine and gas saturations are zero, but are plotted at a dimensionless parameter value of 0.01 because of the logarithmic axis.

The threshold pressure in the halite was varied from a minimum of 2.1 MPa to a maximum of 22.9 MPa, with a best estimate of 10.3 MPa. An intermediate threshold pressure of 4.7 MPa was also simulated. The performance measures were not sensitive to halite threshold pressure even for the minimum value. A higher threshold pressure (corresponding to the minimum permeability of 1×10^{-25} m^2) would produce the same results as with 22.9 MPa because gas cannot enter the halite in either case. Threshold pressure may be more sensitive at values low enough to permit significant gas expulsion to the halite.

The halite threshold pressure simulation results appear contradictory to the results from the variable-threshold-pressure halite permeability simulations, where the performance measures were sensitive to a threshold pressure of 2.1 MPa. The apparent contradiction emphasizes the importance of the combination of permeability and threshold pressure to gas expulsion. In the minimum halite threshold pressure simulation, the halite had an intrinsic permeability of 1×10^{-21} m^2 and a threshold pressure of 2.1 MPa. Because the permeability was significantly higher (1×10^{-19} m^2) and the threshold pressure was lower (0.3 MPa) in the interbeds than in the halite, all gas expulsion was to the interbeds and was insensitive to the change in halite threshold pressure from 10.3 MPa to 2.1 MPa. The variable-threshold-pressure, maximum halite permeability simulation had a halite permeability of 1×10^{-19} m^2 and a threshold pressure of 2.1 MPa. Because the halite permeability was the same as the interbed permeability, the system was much more sensitive to changes in halite threshold pressure, particularly as it approached the interbed threshold pressure.

The insensitivity of the performance measures to the halite multiphase flow properties may be misleading. Given the complete lack of WIPP-specific data, it is uncertain whether the modified Brooks and Corey (1964) model is appropriate, let alone whether the assumed parameter ranges are reasonable. To further examine the sensitivity of the system to changes in the multiphase flow properties, alternative capillary pressure and relative permeability relationships were tested, as suggested by Webb (1992b). The van Genuchten (1980) model, modified for a non-zero residual gas saturation, was used to define the capillary pressure and brine phase relative permeability relationships. The gas phase relative permeability relationship was taken from Parker et al. (1987). A comparison of these alternative relationships with the modified Brooks and Corey (1964) relationships are shown in Figure 5-13a for relative permeability and Figure 5-13b for capillary pressure. Simulation results are shown in Figure 5-14. The use of the van Genuchten (1980) and Parker et al. (1987) relationships in the halite resulted in a reduction in the mass of gas expelled from the room and a decrease in gas migration distance. These results were caused by a reduction in the relative permeability to brine in the halite (Figure 5-13a), making it more difficult for brine to be expelled by gas from the interbeds to the halite. A second factor was the decrease in the capillary pressure at high brine saturations (Figure 5-13b) which allowed some gas to flow from the interbeds to the halite. Gas saturations in the interbeds were correspondingly lower, resulting in a lower relative permeability to gas in the interbeds. These sensitivity results are not shown in Figure 5-9 because the parameter change (difference in methods) cannot be quantified. However, importance coefficients of 0.80 for gas migration distance and 0.09 for gas expulsion were

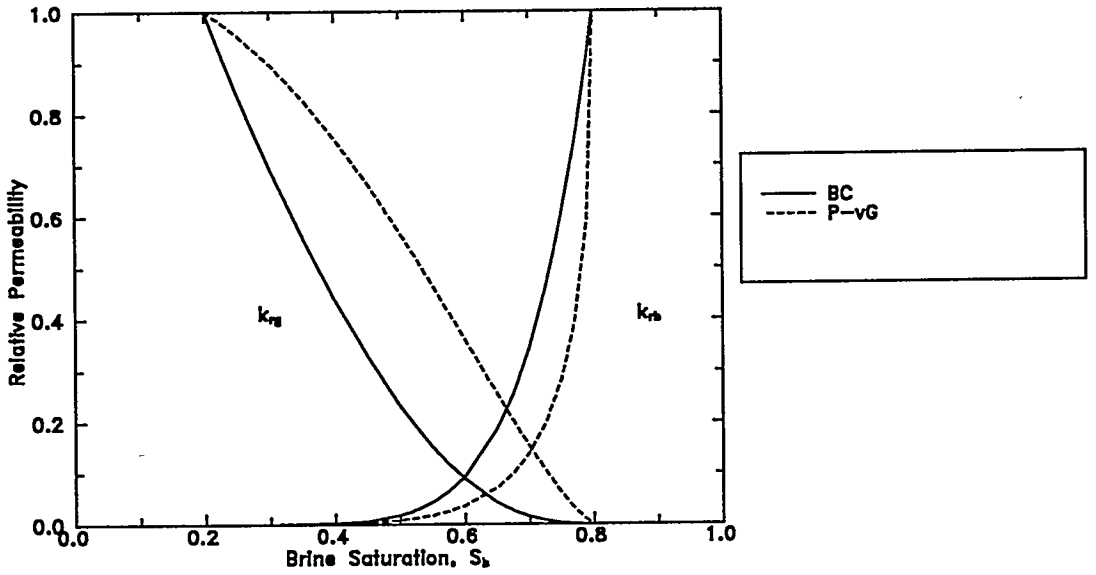

(a) Relative Permeability

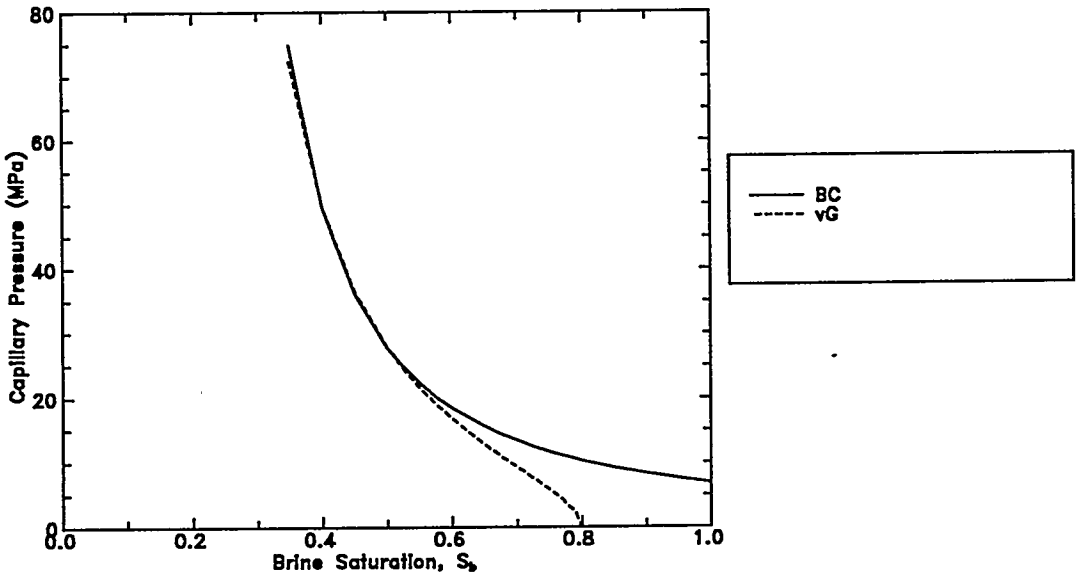

(b) Capillary Pressure

Figure 5-13. Effects of two-phase characteristic relationships on halite relative permeability and capillary pressure: BC - Brooks and Corey (1964); P - Parker et al., (1987); vG - van Genuchten (1980).

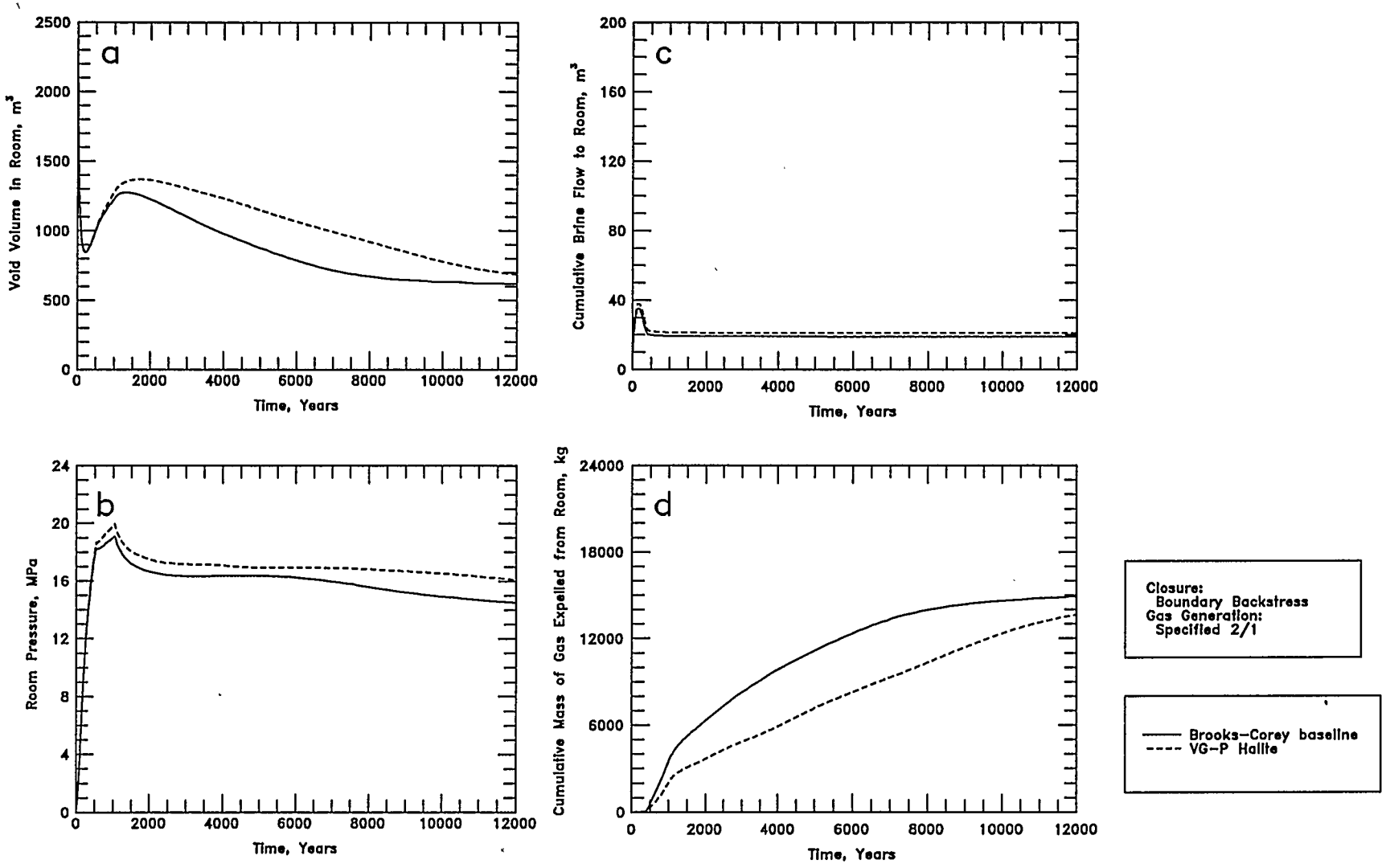

Figure 5-14 (a-d). Sensitivity to halite two-phase characteristic relationship: a - Void Volume; b - Gas Pressure; c - Brine Flow; d - Gas Expulsion.

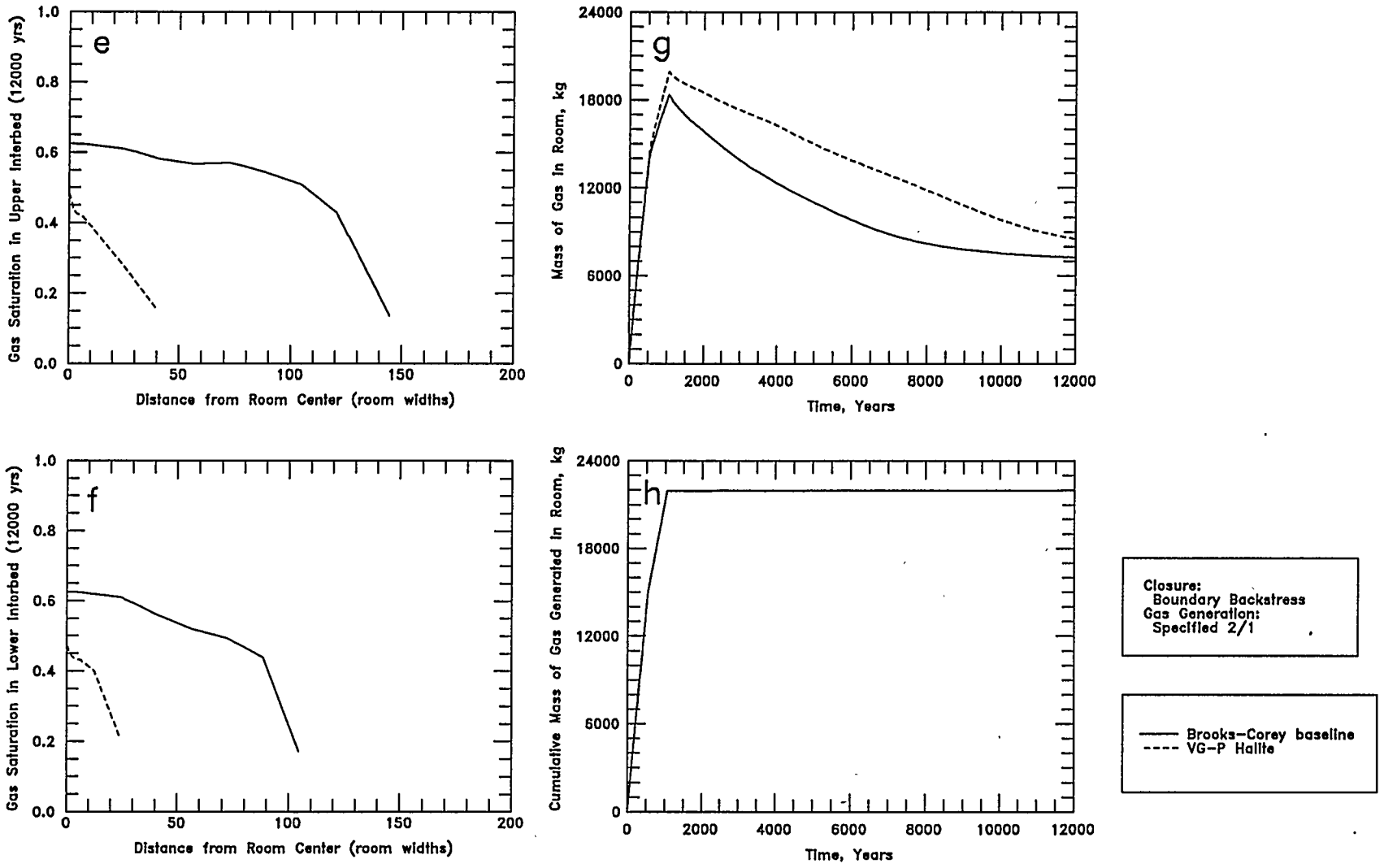

Figure 5-14 (e-h). Sensitivity to halite two-phase characteristic relationship: e - Upper Interbed Gas Profile; f - Lower Interbed Gas Profile; g - Room Gas Mass; h - Gas Generation.

calculated using Equation 2-15. The large importance coefficient for gas migration distance suggests that the uncertainty in the halite multiphase flow properties produces significant uncertainty in gas migration distance.

5.1.3 Salado Formation Interbeds

Parameter ranges for the hydrologic parameters of the Salado Formation anhydrite interbeds are listed in Table 3.3. Sensitivity and importance coefficients for each performance measure are presented in Tables 5-5 and 5-6, respectively, for the specified 2/1 gas-generation rate history. Dimensionless parameter sensitivity and importance plots are presented in Figure 5-15 for the physical properties and initial conditions and in Figure 5-16 for the multiphase flow properties. Note that minimum residual saturations of 0.0 are plotted as 0.01 in Figure 5-16 because of the logarithmic axis.

5.1.3.1 INTERBED PHYSICAL PROPERTIES AND INITIAL CONDITIONS

Physical property sensitivity simulations were performed for interbed intrinsic permeability, porosity, and compressibility. Sensitivity to the initial brine pressure in the interbeds was examined in conjunction with the halite initial pressure and is discussed in Section 5.1.2.1. Sensitivity to interbed thickness was also examined.

The interbed intrinsic permeability, k, was varied from a minimum of 1×10^{-21} m^2 to a maximum of 1×10^{-18} m^2, with a best estimate of 1×10^{-19} m^2. An intermediate value of 1×10^{-20} m^2 was also simulated as was an alternative maximum of 1×10^{-16} m^2. The alternative maximum permeability was assumed to represent an excavation-disturbed value (Beauheim et al., 1993a) and was not included in sensitivity and importance calculations. A comparison of interbed permeability simulation results under the specified 2/1 rate history is shown in Figure 5-17.

The volume of brine inflow and expulsion were increased by high interbed permeability and decreased by low interbed permeability. The peak inflow ranged from 15 m^3 (for $k = 1 \times 10^{-21}$ m^2) to 93 m^3 (for $k = 1 \times 10^{-18}$ m^2). At early time, the distance of depressurization within the interbed increased with increasing interbed permeability. As a result, more interbed contact area with the halite was available and brine inflow was increased. The

Table 5-5. Sensitivity Coefficients for Interbed Parameters Under Specified 2/1 Gas-Generation Rate History

	Performance Measure							
	Max. Room Pressure		Max. Brine in Room		Gas Expelled from Room		Gas Migration Distance	
Parameter	S^-	S^+	S^-	S^+	S^-	S^+	S^-	S^+
Physical								
Intrinsic Perm. (constant p_f)	-0.10	-0.01	0.35	0.11	0.83	0.01	0.91	0.07
Intrinsic Perm. (variable p_f)	-0.11	-0.01	0.35	0.11	1.00	0.01	1.01	0.07
Porosity (constant α_p)	-0.05	0.02	0.01	0.01	0.43	-0.02	-5.15	-0.27
Porosity (constant α)	-0.05	0.02	0.01	0.00	0.42	-0.02	-5.15	-0.27
Rock Compressibility	0.00	0.00	0.00	0.00	0.00	0.00	0.00	0.00
Interbed Thickness	0.03	0.03	0.00	0.00	-0.02	0.01	-1.11	0.51
Multiphase								
Residual Brine Saturation	0.00	0.00	0.00	0.00	0.00	-0.01	0.17	0.00
Residual Gas Saturation	0.00	0.00	0.02	0.00	0.00	0.01	0.00	-0.17
Pore-Size Lambda (λ)	-0.05	0.00	0.00	0.00	0.36	0.00	0.19	0.02
Threshold Pressure	0.01	0.01	0.01	0.00	-0.03	-0.06	0.00	-0.06

Table 5-6. Importance Coefficients for Interbed Parameters Under Specified 2/1 Gas-Generation Rate History

	Performance Measure							
	Max. Room Pressure		Max. Brine in Room		Gas Expulsion from Room		Gas Migration Distance	
Parameter	I^-	I^+	I^-	I^+	I^-	I^+	I^-	I^+
Physical								
Intrinsic Perm. (constant p_f)	-0.10	-0.10	0.35	0.97	0.82	0.09	0.90	0.61
Intrinsic Perm. (variable p_f)	-0.11	-0.06	0.35	0.97	0.99	0.05	1.00	0.61
Porosity (constant α_p)	-0.05	0.03	0.01	0.01	0.41	-0.03	-4.84	-0.53
Porosity (constant α)	-0.05	0.03	0.00	0.01	0.39	-0.03	-4.84	-0.53
Rock Compressibility	0.00	0.00	0.00	0.00	0.00	0.00	0.00	0.00
Interbed Thickness	0.01	0.01	0.00	0.00	-0.01	0.00	-0.61	0.20
Multiphase								
Residual Brine Saturation	0.00	0.00	0.00	0.00	0.00	-0.01	0.17	0.00
Residual Gas Saturation	0.00	0.00	0.02	0.00	0.00	0.01	0.00	-0.17
Pore-Size Lambda (λ)	-0.04	0.00	0.00	0.00	0.26	0.02	0.13	0.20
Threshold Pressure	0.00	0.09	0.00	0.00	-0.01	-0.92	0.00	-0.90

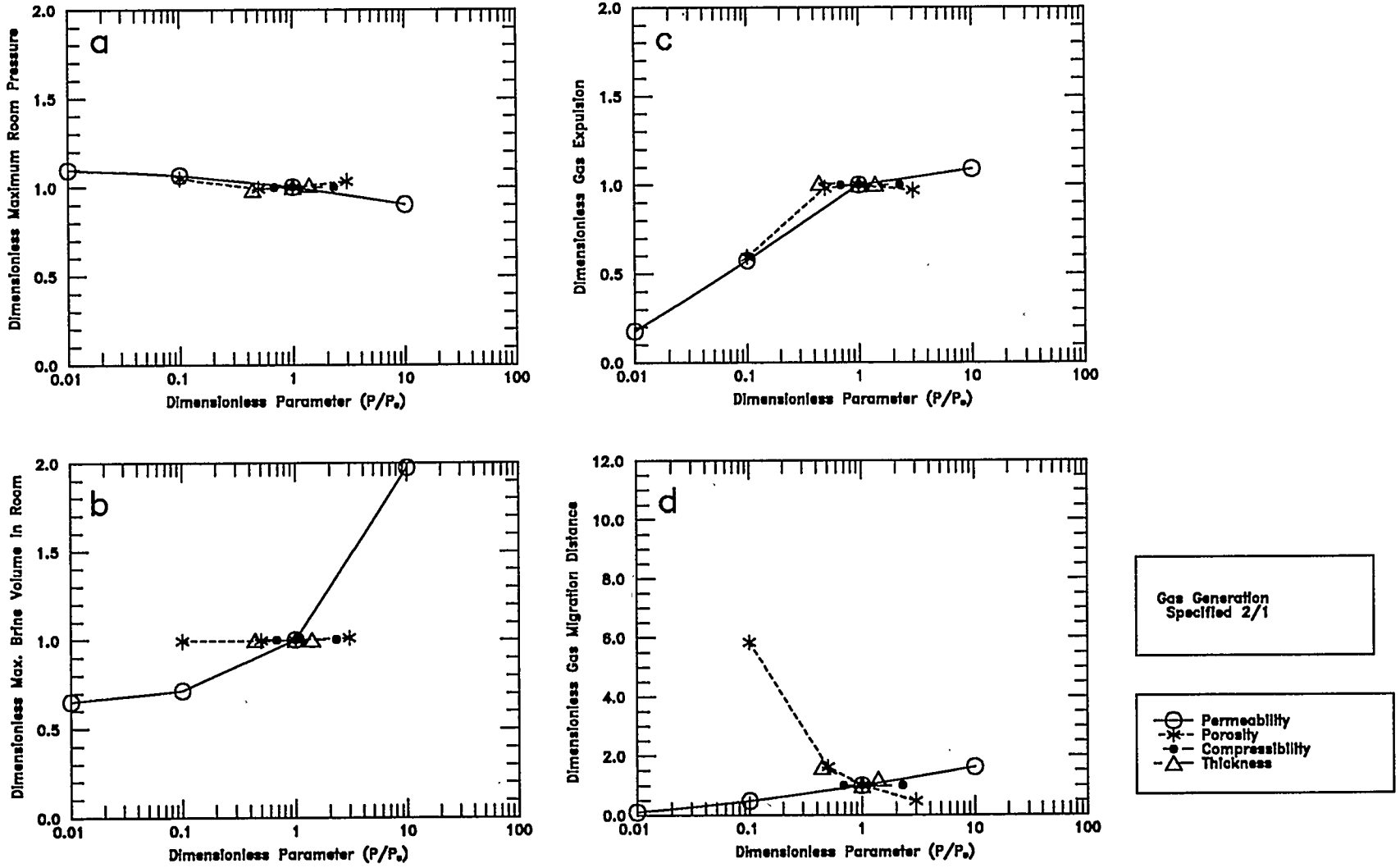

Figure 5-15 (a-d). Dimensionless plots of performance measure sensitivity to interbed physical properties: a - Maximum Room Pressure; b - Maximum Brine in Room; c - Gas Expulsion; d - Gas Migration Distance.

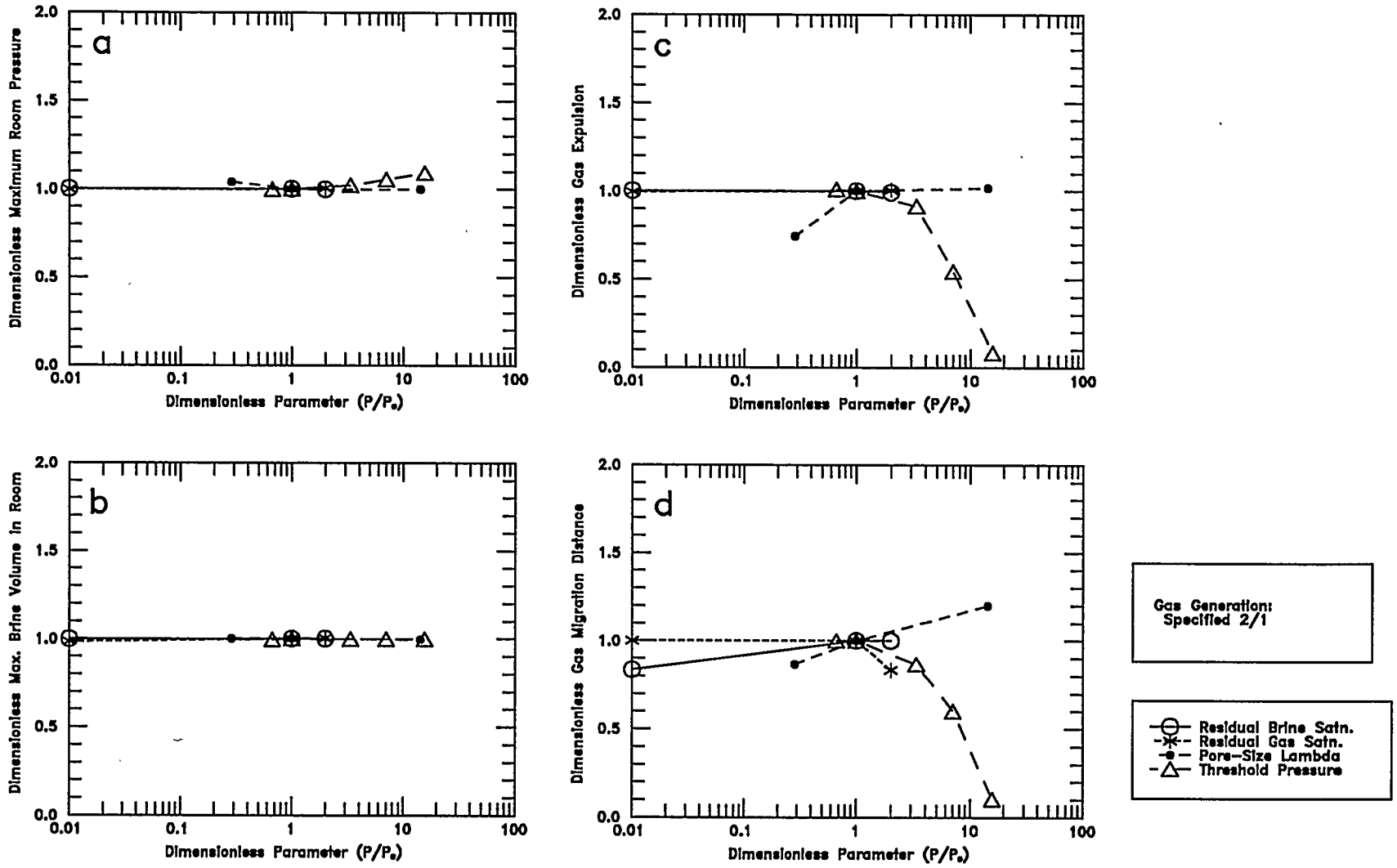

Figure 5-16 (a-d). Dimensionless plots of performance measure sensitivity to interbed multiphase flow properties: a - Maximum Room Pressure; b - Maximum Brine in Room; c - Gas Expulsion; d - Gas Migration Distance.

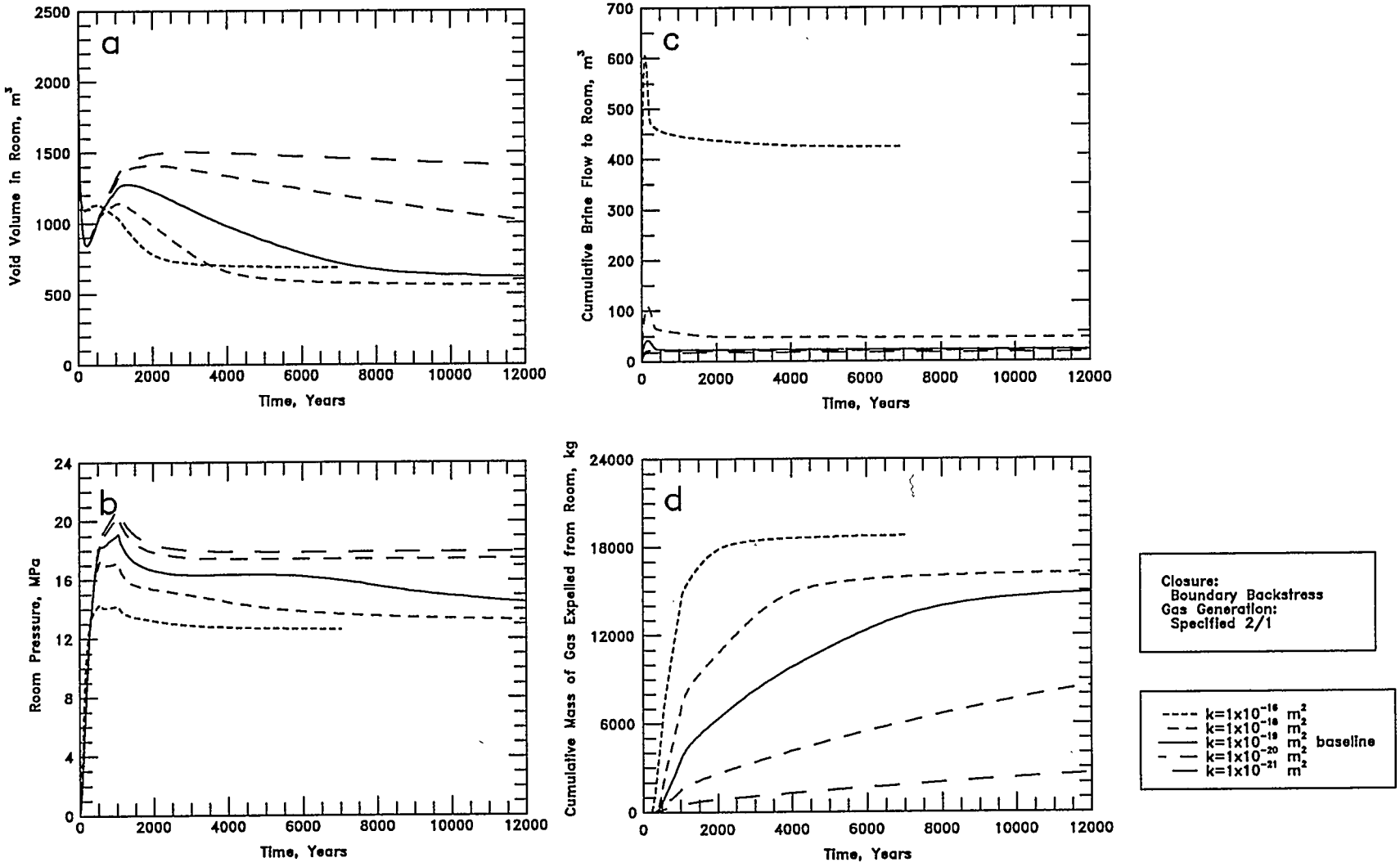

Figure 5-17 (a-d). Sensitivity to interbed intrinsic permeability: a - Void Volume; b - Gas Pressure; c - Brine Flow; d - Gas Expulsion.

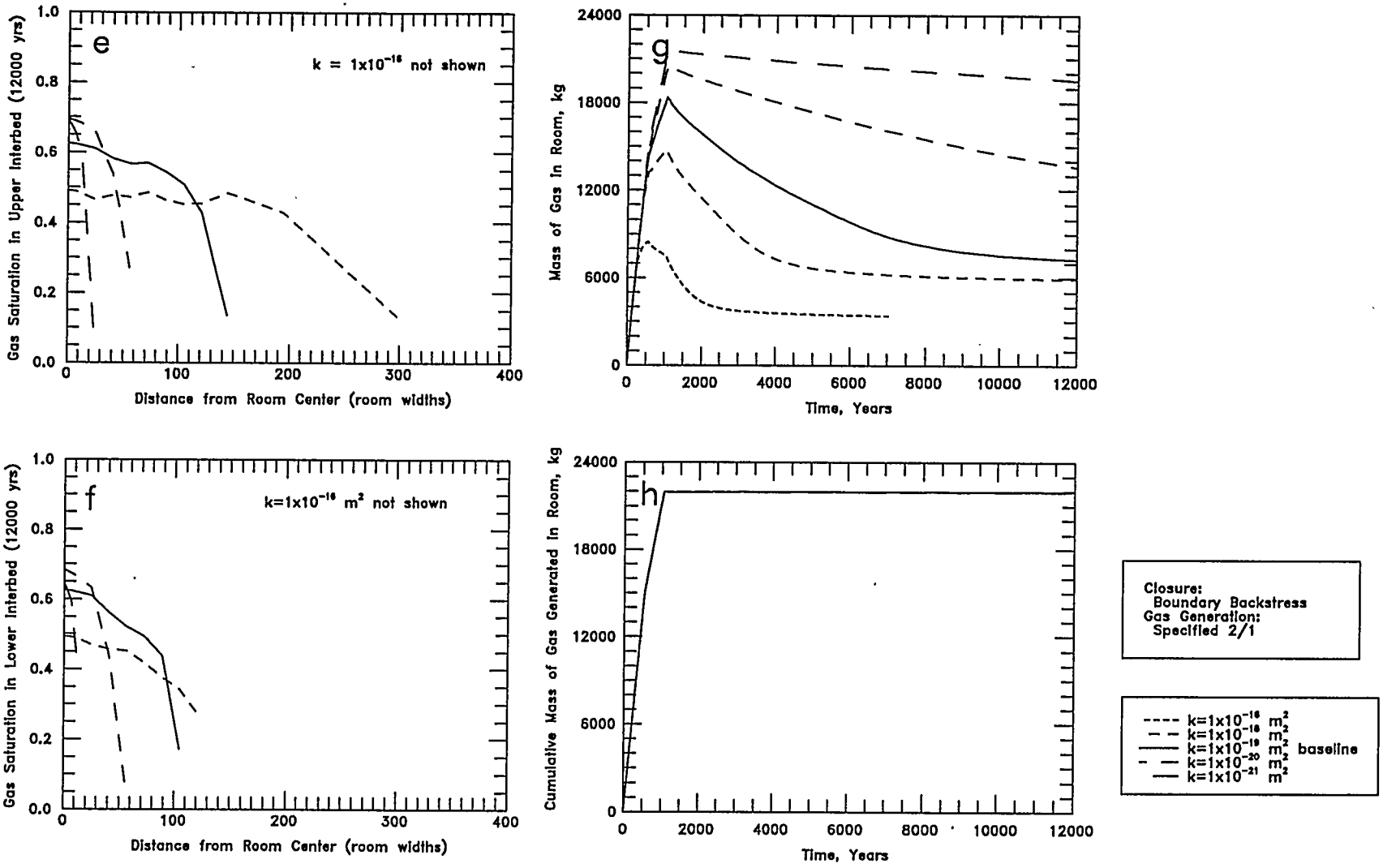

Figure 5-17 (e-h). Sensitivity to interbed intrinsic permeability: e - Upper Interbed Gas Profile; f - Lower Interbed Gas Profile; g - Room Gas Mass; h - Gas Generation.

duration of brine inflow and expulsion was not affected by changes in interbed permeability. The mass of gas expelled from the room was increased by high interbed permeability and decreased by low interbed permeability. Gas migration distance in the interbeds also increased with higher interbed permeability. The increase in gas expulsion and migration with increasing interbed permeability was at least partially due to an increased distance of interbed pressurization at late time, which made more interbed contact area available for the displacement of brine from the interbeds into the surrounding halite. Disposal room void volume and pressure behavior was consistent with brine and gas flow. With increased gas expulsion, room pressures were lower and room closure was greater.

The performance measures maximum brine volume in the room (Figure 5-15b), gas expulsion (Figure 5-15c), and gas migration distance (Figure 5-15d) were quite sensitive to changes in interbed intrinsic permeability. The large sensitivity and importance coefficients were similar to those for halite intrinsic permeability. The maximum room pressure performance measure was not as sensitive to interbed permeability (Figure 5-15a).

The sensitivity and importance coefficients of the performance measures to interbed intrinsic permeability using the specified 0.2/0.1 gas-generation rate history were similar to the sensitivity and importance coefficients with the specified 2/1 rate history. The interbed intrinsic permeability sensitivity simulations discussed here were all run using the boundary backstress method. Similar sensitivity and importance coefficients were obtained with both specified gas-generation rates using the pressure lines method.

These simulations all used the best-estimate threshold pressure of 0.3 MPa, which corresponds to the threshold pressure for the interbed analogue material. To examine the correlation between intrinsic permeability and threshold pressure, p_t, the interbed intrinsic permeability simulations were also run with the following gas-brine threshold pressures in the interbeds, calculated from Equation 3-8: 10.3 MPa for $k = 1 \times 10^{-21}$ m^2; 3.7 MPa for $k = 1 \times 10^{-20}$ m^2; 2.1 MPa for $k = 1 \times 10^{-19}$ m^2; 1.0 MPa for $k = 1 \times 10^{-18}$ m^2; and 0.2 MPa for $k = 1 \times 10^{-16}$ m^2. These permeability-correlated threshold pressures are larger than the best-estimate analogue-based value (0.3 MPa) in all cases except for $k = 1 \times 10^{-16}$ m^2.

In the uncorrelated simulations, the 0.3 MPa threshold pressure was low enough to produce gas expulsion to the interbeds for all permeabilities. The increased permeability-correlated threshold pressures resulted in a significant reduction in gas expulsion and gas migration

distance. The permeability-correlated threshold pressure simulations are not included in Figure 5-15.

Interbed porosity, ϕ, was varied from a minimum of 0.0006 to a maximum of 0.03, with a best estimate of 0.01. An intermediate porosity of 0.005 was also simulated. It was assumed that pore volume compressibility, α_p, was equivalent to the best-estimate value of 8.3×10^{-10} Pa^{-1} and did not change with porosity. A comparison of interbed porosity simulation results is shown in Figure 5-18 for the specified 2/1 rate history.

Because the interbeds do not contain a significant brine storage volume relative to the halite, brine inflow and expulsion were not sensitive to changes in interbed porosity (Figure 5-15b). The brine source is the halite while the interbeds act as a conduit. Changing the porosity of the interbeds did not change the volume of brine available, it only changed the distance from which brine was collected by the interbeds. In the case of minimum porosity, brine was collected from a greater distance and at a greater velocity than with the best-estimate porosity. However, less brine was collected per unit length of interbed because of the lower porosity, resulting in the same total volume of brine collection (inflow).

Gas migration distance increased as interbed porosity decreased (Figure 5-15d). However, some anomalous gas expulsion behavior occurred at low porosities (Figure 5-15c). With the maximum porosity, both gas migration distance and the mass of gas expelled were less than for the baseline case. With porosities less than the best estimate, gas migration distance was increased and early-time gas expulsion was increased relative to the baseline case. However, the rate of gas expulsion dropped unexpectedly at about 500 years for $\phi = 0.0006$ and at 1,000 years for $\phi = 0.005$. Because of the drop in gas expulsion, the total (12,000 year) mass of gas expelled was actually lower in both reduced porosity cases than with the best-estimate porosity. This anomalous gas expulsion behavior is not fully understood. One possible explanation is that, due to gas saturation in the interbeds being highest in low porosity cases (Figures 5-18e and 5-18f), the corresponding low relative permeability to brine makes brine displacement from the interbeds to the halite increasingly difficult, impeding gas expulsion.

The gas migration performance measure was very sensitive to changes in interbed porosity, with a maximum sensitivity coefficient of 5.15 and a total importance of 5.37. Gas expulsion had a maximum sensitivity coefficient of 0.43 and a total importance coefficient of 0.41. System behavior, including the sharp drop in gas expulsion for the low interbed porosities, was similar with the specified 0.2/0.1 rate history and with the pressure lines method.

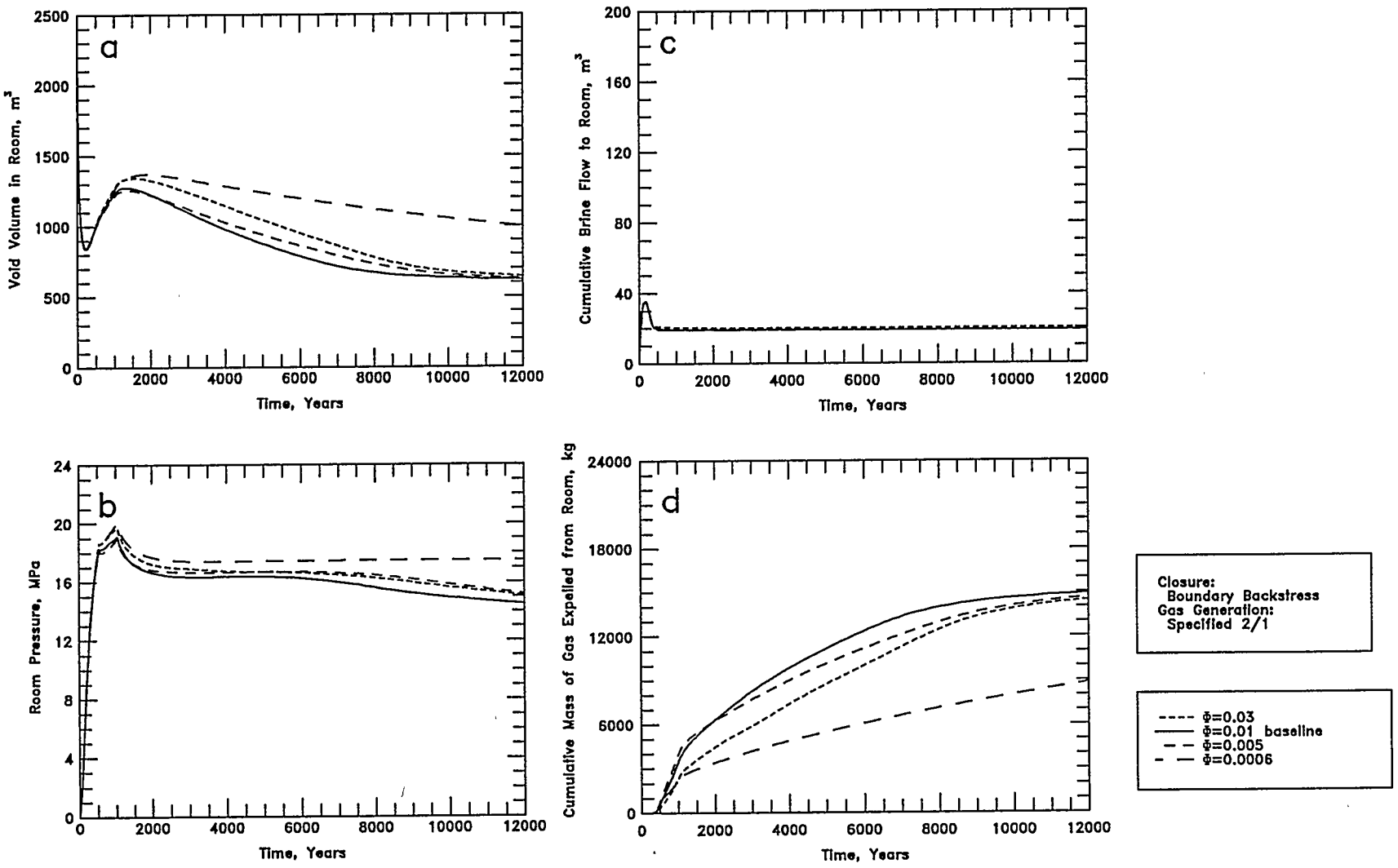

Figure 5-18 (a-d). Sensitivity to interbed porosity (constant pore volume compressibility): a - Void Volume; b - Gas Pressure; c - Brine Flow; d - Gas Expulsion.

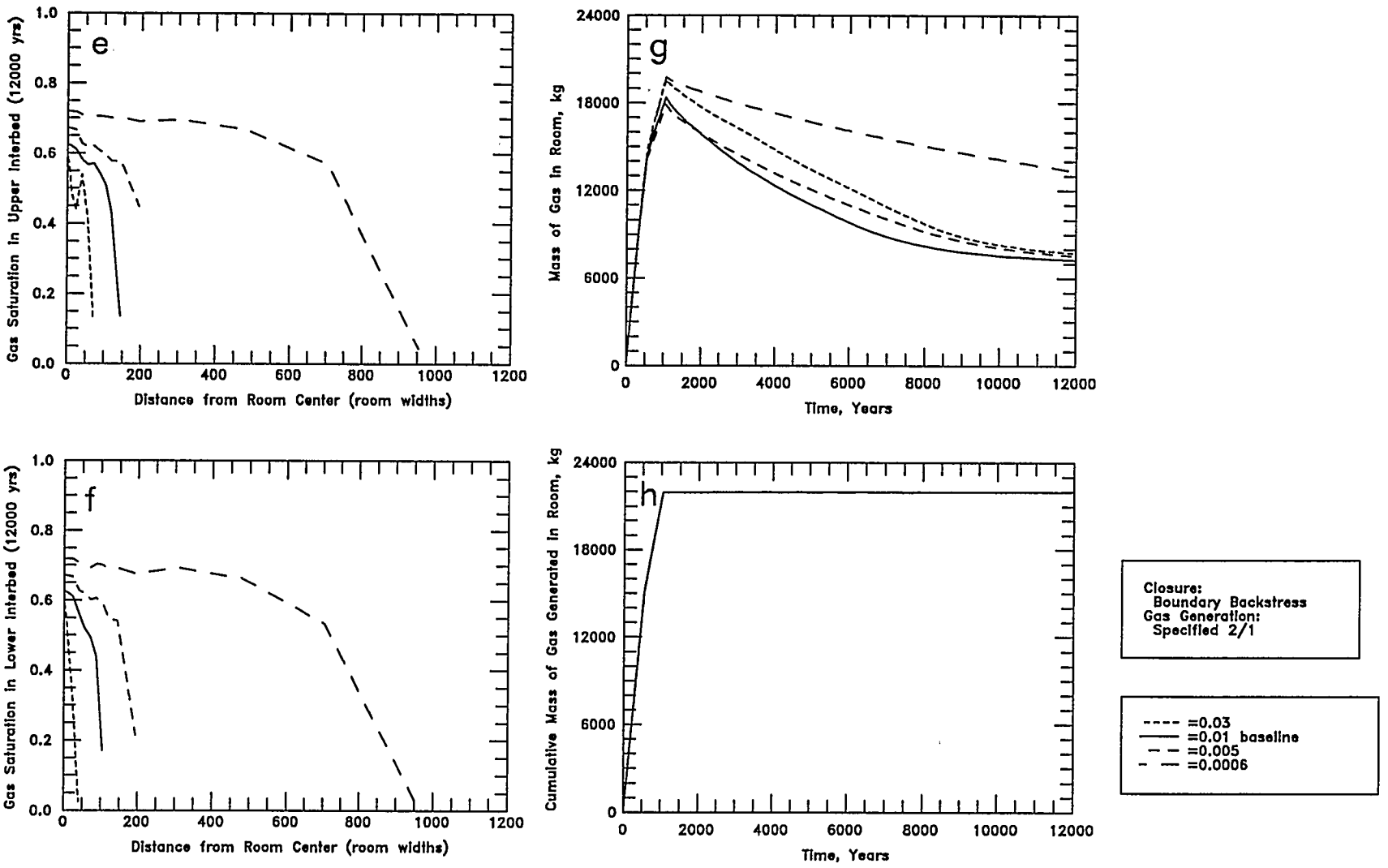

Figure 5-18 (e-h). Sensitivity to interbed porosity (constant pore volume compressibility): e - Upper Interbed Gas Profile; f - Lower Interbed Gas Profile; g - Room Gas Mass; h - Gas Generation.

As an alternative to the constant pore volume compressibility assumption, simulations were also performed with a constant rock compressibility, α, equivalent to the best-estimate value of 8.3×10^{-12} Pa^{-1}. The corresponding range of specific storage was much smaller than for the constant pore volume compressibility simulations. Simulation results were nearly identical to the constant pore volume compressibility simulations, suggesting that the unexpected gas expulsion behavior at low interbed porosity was not due to interbed gas storage considerations or to changes in the compressibility.

The interbed rock compressibility was varied from a minimum of 5.7×10^{-12} Pa^{-1} to a maximum of 1.9×10^{-11} Pa^{-1}, with a best-estimate value of 8.3×10^{-12} Pa^{-1}. Interbed compressibility directly influences storage in the interbeds. The performance measures were not sensitive to interbed compressibility (Figure 5-15). These results are consistent with the interbed porosity simulations, which showed no sensitivity to interbed storage volume. The interbed compressibility simulations used the pressure lines method.

The thickness of the lower composite interbed was varied from 0.40 m to 1.25 m, with a best estimate of 0.90 m. This range corresponds to the assumed range in Marker Bed 139 thickness (Krieg, 1984). Simulation results showed that only the gas migration distance in the lower interbed was affected significantly by changes in the lower interbed thickness. Gas migration distance increased with a thinner interbed and decreased with a thicker interbed.

5.1.3.2 INTERBED MULTIPHASE FLOW PROPERTIES

As with the disposal room and the halite, there are no WIPP-specific data for interbed multiphase flow properties. The parameter ranges used in the sensitivity simulations were selected somewhat arbitrarily based on estimates from Webb (1992b). Both the residual brine saturation and residual gas saturation were varied from a minimum of 0.00 to a maximum of 0.40, with best estimates of 0.20. The pore-size λ was varied from a minimum of 0.2 to a maximum of 10, with a best estimate of 0.7. The effects of these variations on the relative permeability and capillary pressure relationships in the room are shown in Figure 5-19 for residual brine saturation, Figure 5-20 for residual gas saturation, and Figure 5-21 for pore-size λ.

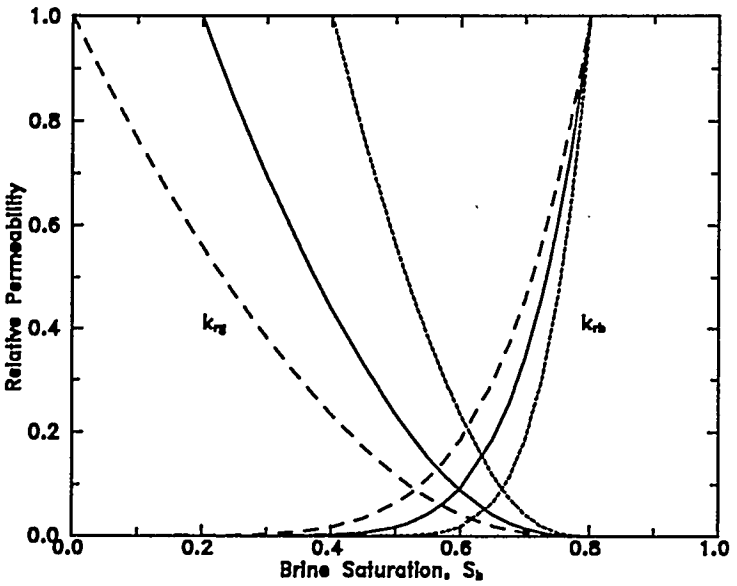

(a) Relative Permeability

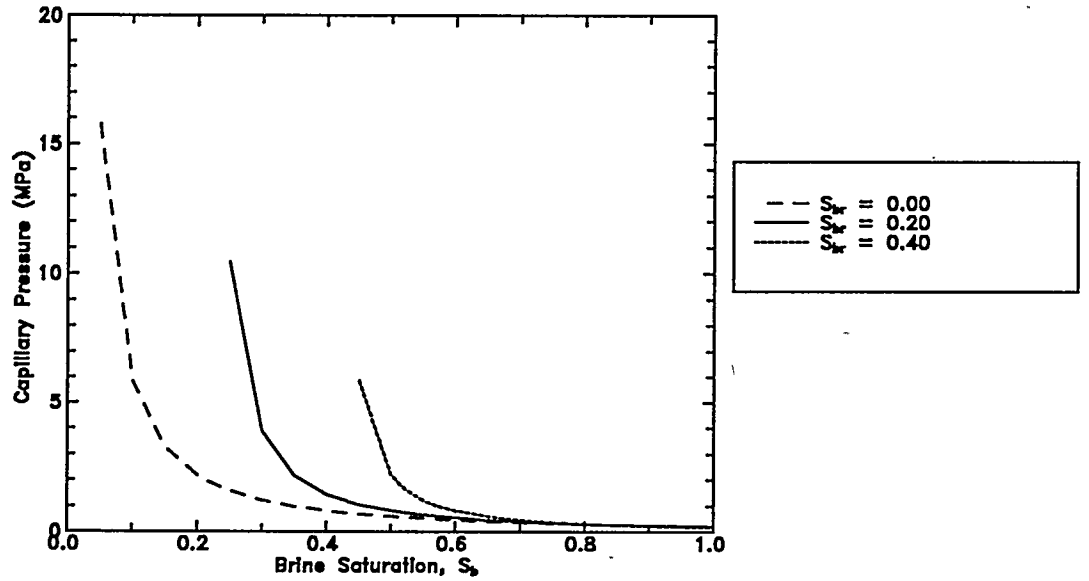

(b) Capillary Pressure

Figure 5-19. Effects of variations in residual brine saturation on interbed relative permeability and capillary pressure relationships.

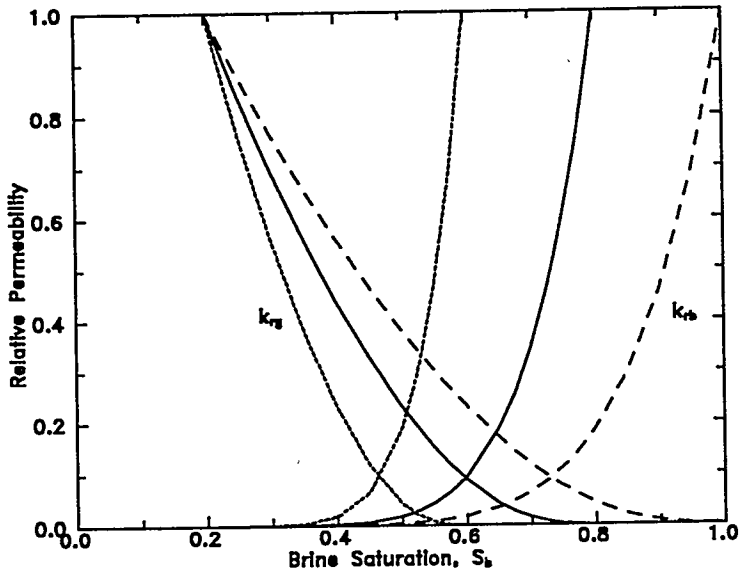

(a) Relative Permeability

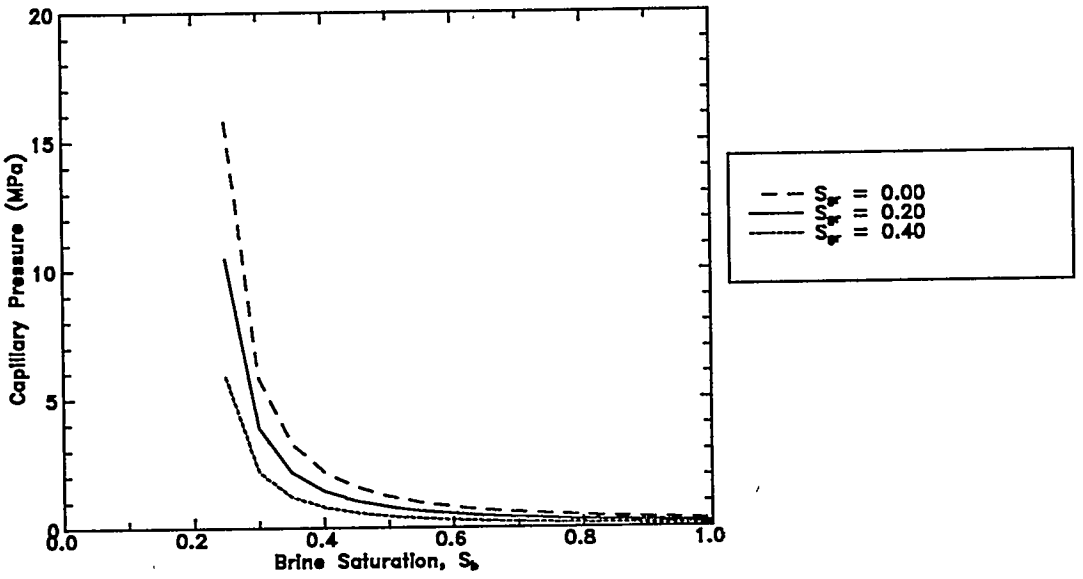

(b) Capillary Pressure

Figure 5-20. Effects of variations in residual gas saturation on interbed relative permeability and capillary pressure relationships.

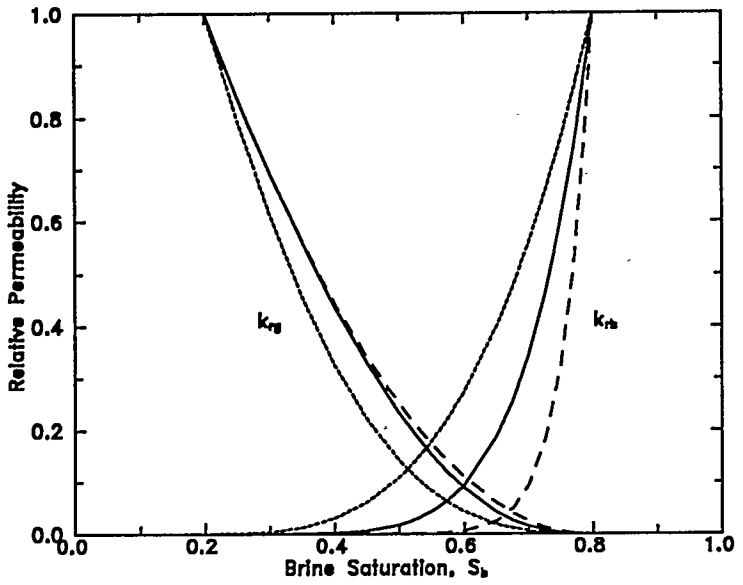

(a) Relative Permeability

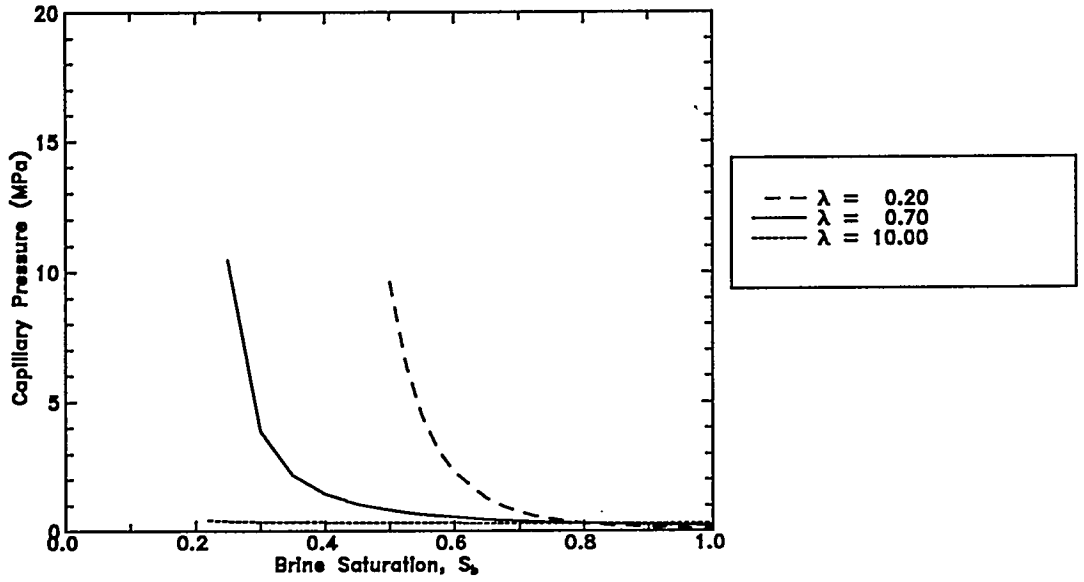

(b) Capillary Pressure

Figure 5-21. Effects of variations in pore-size distribution index (λ) on interbed relative permeability and capillary pressure relationships.

The interbed residual brine saturation sensitivity simulations were run using the pressure lines method. An increase in the residual brine saturation resulted in an increase in the relative permeability to gas in the interbed and a decrease in the gas-accessible volume. As a result, gas migration distance was increased with increasing residual brine saturation. For the gas migration distance performance measure, the maximum sensitivity coefficient was 0.17 and the total importance coefficient was 0.17. The other performance measures were not sensitive to changes in residual brine saturation.

The increase in relative permeability to gas with increasing residual brine saturation resulted from two offsetting effects. As residual brine saturation is increased, the relativepermeability to gas at a given saturation is increased (Figure 5-19a), but the gas saturation in the interbeds is decreased in response to increased capillary pressure (Figure 5-19b). Despite the low interbed gas saturation ($S_g = 0.5$) with the maximum residual brine saturation, the corresponding relative permeability to gas ($k_{rg} = 0.55$) was still greater than for the baseline case ($k_{rg} = 0.40$), which had an interbed gas saturation of 0.6.

The interbed residual gas saturation sensitivity simulations were also run using the pressure lines method. A decrease in the residual gas saturation increased the relative permeability to gas in the interbed and reduced the saturation at which gas becomes mobile (Figure 5-20a). Because of these effects, gas migration distance was increased with decreasing residual gas saturation. For the gas migration distance performance measure, the maximum sensitivity coefficient was 0.17 and the total importance coefficient was 0.17. The other performance measures were not sensitive to changes in residual gas saturation.

The increase in relative permeability to gas with decreasing residual gas saturation resulted from the same two counteractive effects that were described for the residual brine saturation sensitivity. At the minimum residual gas saturation, the low interbed gas saturation ($S_g = 0.55$) still corresponded to a relative permeability to gas ($k_{rg} = 0.45$) that was greater than for the baseline case ($k_{rg} = 0.40$).

Despite the fact that the relative permeability to gas at a given saturation increased with decreasing pore-size λ (Figure 5-21a), the gas saturation in the interbeds decreased with decreasing λ and the relative permeability to gas in the interbeds actually increased with increasing λ. At the maximum λ, the high interbed gas saturation ($S_g = 0.8$) corresponded to a relative permeability to gas ($k_{rg} = 1.00$) that was greater than for the baseline case ($k_{rg} =$

0.40). Because of this combination of factors, gas migration distance was increased with increasing pore-size λ. For the gas migration distance performance measure, the maximum sensitivity coefficient was 0.19 and the total importance coefficient was 0.33.

For the minimum λ case, the relative permeability to gas was low enough ($k_{rg} = 0.2$) and the capillary pressure was high enough (5 MPa) that gas expulsion was actually reduced relative to the other cases. For the gas expulsion performance measure, the maximum sensitivity coefficient was 0.36 and the total importance coefficient was 0.28. The other two performance measures were not sensitive to changes in pore-size λ.

The threshold pressure was varied from a minimum of 0.2 MPa to a maximum of 4.7 MPa, with a best estimate of 0.3 MPa. Intermediate threshold pressures of 1.0 MPa and 2.1 MPa were also simulated. A comparison of interbed threshold pressure sensitivity simulations is shown in Figure 5-22. An increase in interbed threshold pressure resulted in an increase the capillary resistance to be overcome to force gas into the interbeds. As a result, simulations with increased threshold pressure exhibited (1) decreased gas expulsion, (2) decreased gas migration distance, (3) increased room pressure, and (4) increased room expansion and minimal re-closure. System behavior did not change significantly in response to decreased threshold pressure because the baseline value (0.3 MPa) was already small. The maximum sensitivity and total importance coefficients were 0.06 and 0.90, respectively, for the gas migration distance performance measure and 0.06 and 0.93, respectively, for the gas expulsion performance measure. Interbed threshold pressure was one of the most important parameters for these two performance measures, despite its small range. The other two performance measures were insensitive to changes in interbed threshold pressure.

Given the complete lack of WIPP-specific data, it is uncertain whether the modified Brooks and Corey (1964) model is appropriate, let alone whether the assumed parameter ranges are reasonable. To further examine the sensitivity of the system to changes in the multiphase flow properties, alternative capillary pressure and relative permeability relationships were tested, as suggested by Webb (1992b). The van Genuchten (1980) model, modified for a non-zero residual gas saturation, was used to define the capillary pressure and brine phase relative permeability relationships. The gas phase relative permeability relationship was taken from Parker et al. (1987). A comparison of these alternative relationships with the modified Brooks and Corey (1964) relationships are shown in Figure 5-23a for relative permeability and Figure 5-23b for capillary pressure. Simulation results are shown in Figure B-27 (Appendix B). Use of the

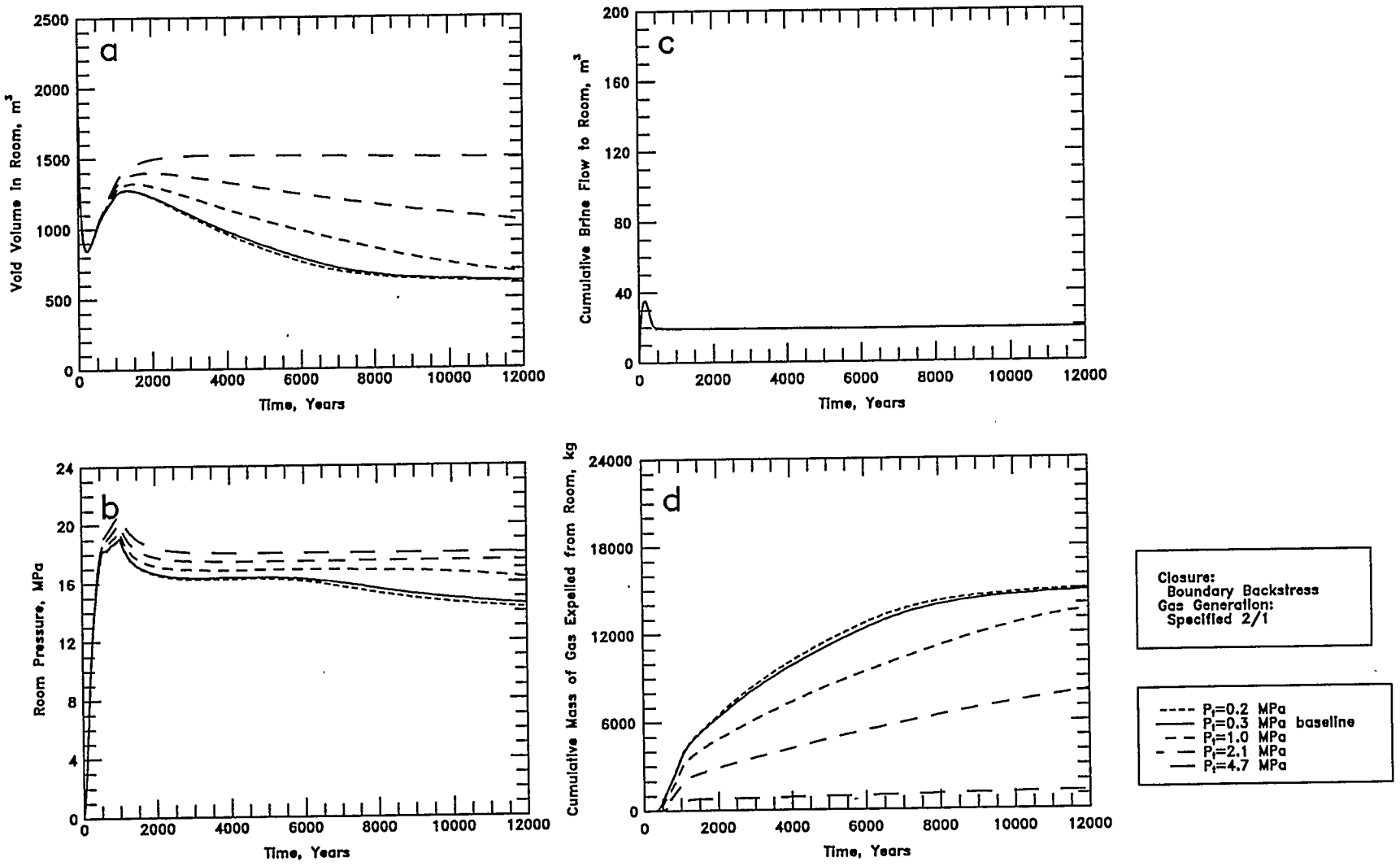

Figure 5-22 (a-d). Sensitivity to interbed threshold pressure: a - Void Volume; b - Gas Pressure; c - Brine Flow; d - Gas Expulsion.

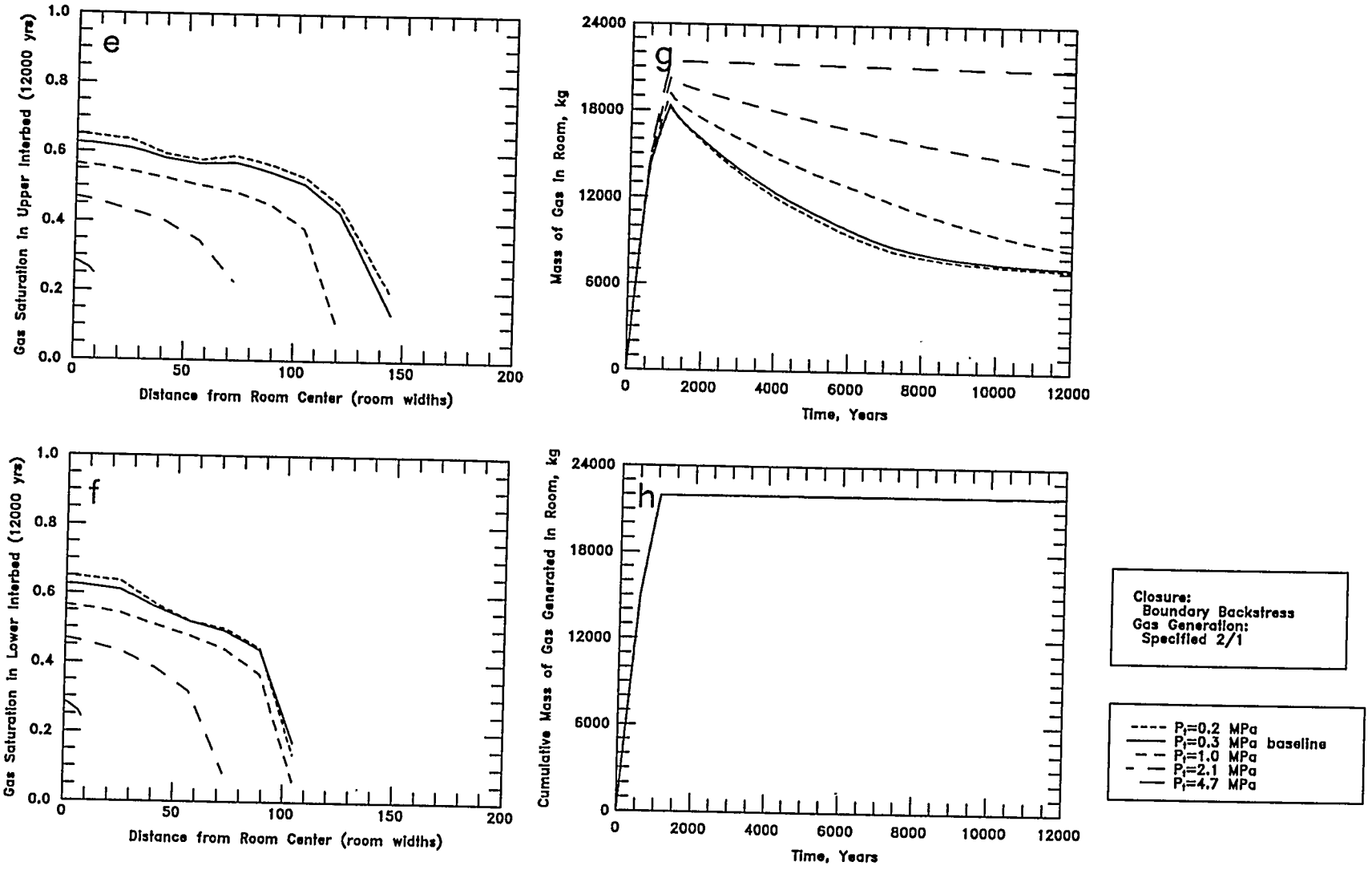

Figure 5-22 (e-h).. Sensitivity to interbed threshold pressure: e - Upper Interbed Gas Profile; f - Lower Interbed Gas Profile; g - Room Gas Mass; h - Gas Generation.

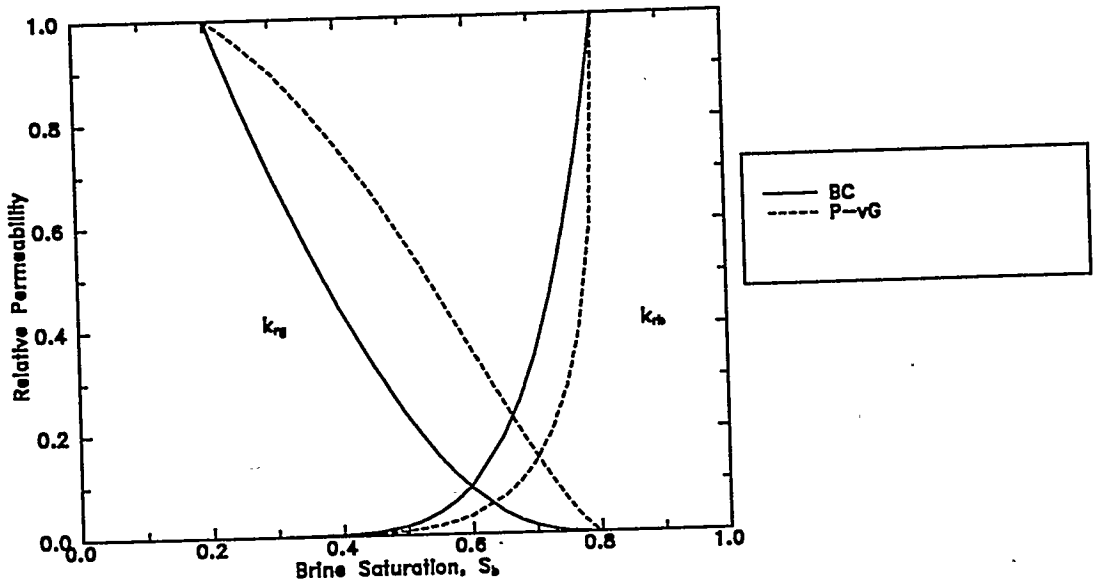

(a) Relative Permeability

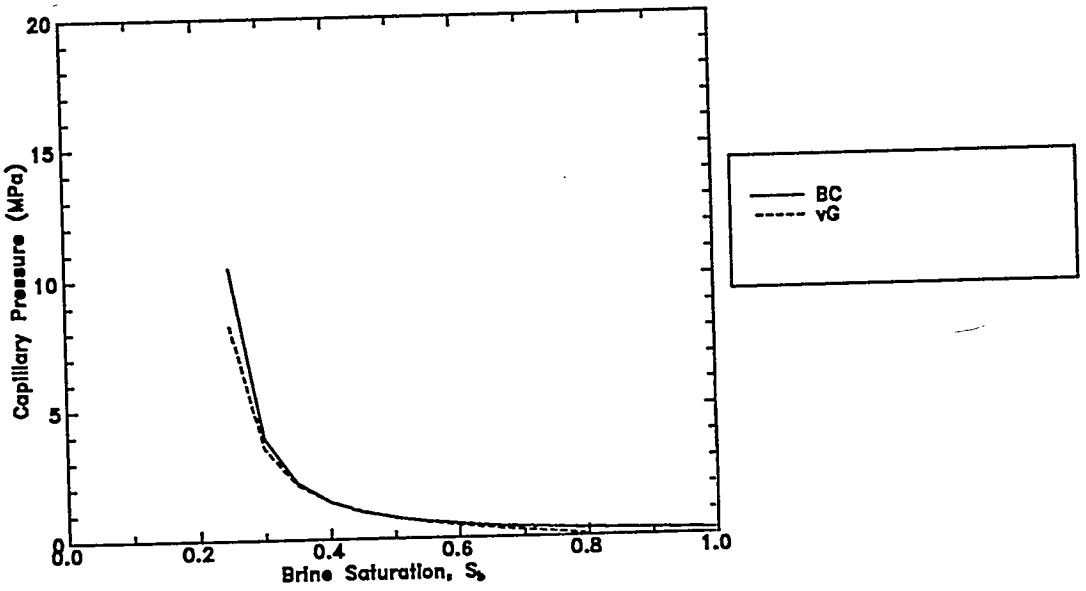

(b) Capillary Pressure

Figure 5-23. Effects of two-phase characteristic relationships on interbed relative permeability and capillary pressure: BC - Brooks and Corey (1964); P - Parker et al. (1987); vG - van Genuchten (1980).

modified van Genuchten (1980) and Parker et al. (1987) relationships increased the gas expulsion to the interbeds and increased the gas migration distance relative to the modified Brooks and Corey (1964) model. In turn, the room pressure was decreased and room closure was more rapid once gas release commenced. These results are commensurate with the difference between the Brooks and Corey and the van Genuchten/Parker relationships. At low gas saturation, relative permeability to gas is higher and capillary pressure is lower for the van Genuchten/Parker relationships. Gas can enter the interbeds under less driving pressure and move more rapidly once there. Importance coefficients, calculated from Equation 2-15, were 0.20 for the gas migration distance performance measure and 0.03 for the gas expulsion performance measure. Variations in the van Genuchten/Parker parameters were not examined. The sensitivity results are not shown in Figure 5-16 because the parameter change (difference in method) cannot be quantified.

5.2 Gas-Generation Parameters

Sensitivity to the rate and duration of gas generation was examined by varying specified rate histories (Section 5.2.1), constant rates (Section 5.2.2), and gas-generation potentials (Section 5.2.3). Sensitivity to the brine-dependent rate methods and parameters is examined in Section 5.2.4. Sensitivity and importance coefficients for each performance measure were calculated for the range of constant rates and the range of gas potentials simulated. Dimensionless parameter sensitivity and importance plots of these two quantifiable gas-generation parameters are presented in Figure 5-24.

5.2.1 Specified Gas-Generation Rate Histories

Four specified gas-generation rate histories were identified in Section 2.4.1, based on experiment results from Brush (1991). These rate histories, listed in Table 2-1, are: 7/2; 2/1; 0.2/0.1; and 0/0. The rate histories are designated by two stages of gas generation. The first stage corresponds to the time period when gas is generated from both anoxic corrosion and microbial activity. The second stage, with a lower gas-generation rate, corresponds to the time period when gas is generated only by anoxic corrosion because the potential for microbial degradation has been depleted. During the course of this investigation, revised gas-generation rate estimates became available (Brush, 1995). Three revised rate histories resulted: 105/5; 1.6/0.6; and 0.1/0.

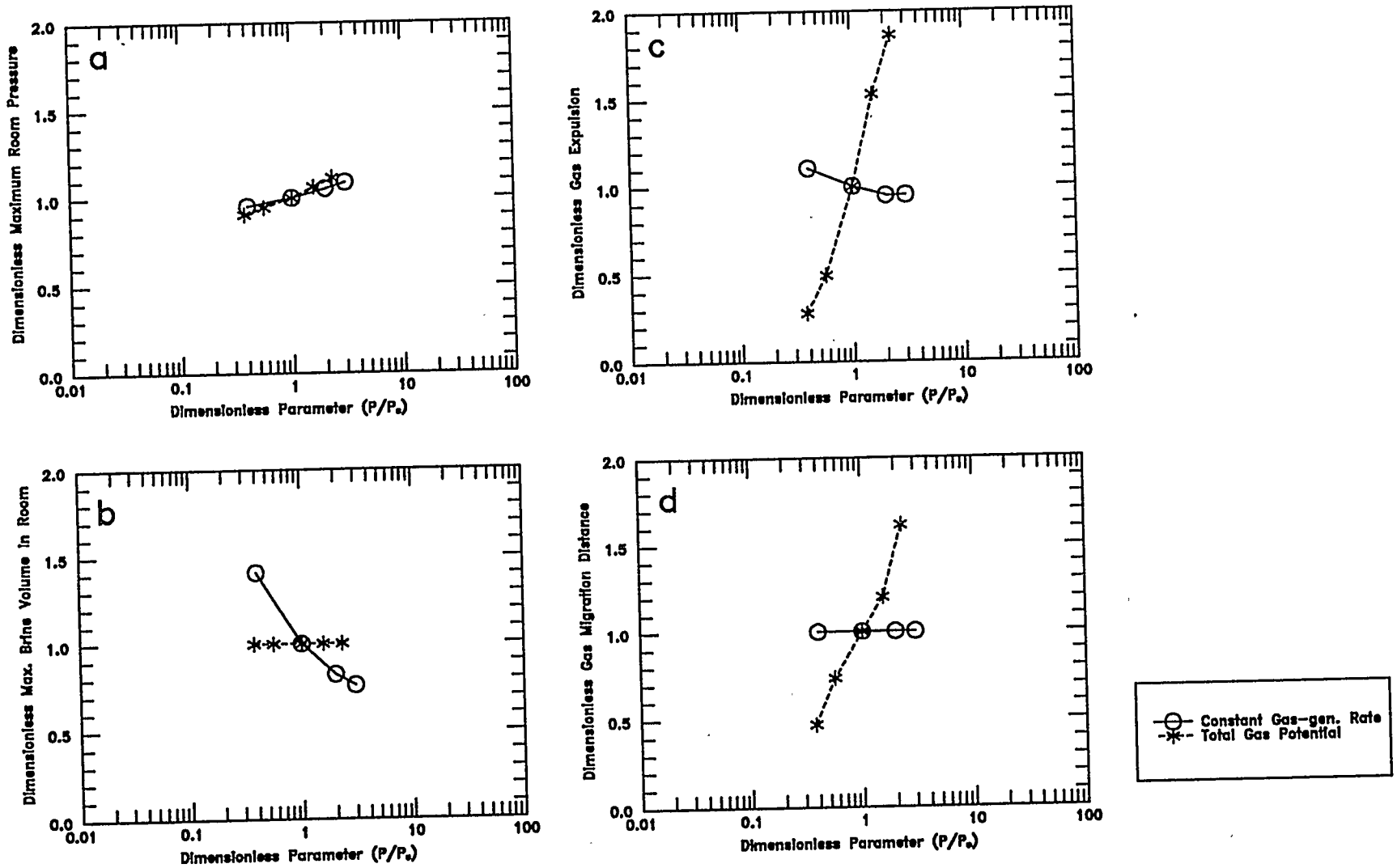

Figure 5-24. Dimensionless plots of performance measure sensitivity to gas-generation rate and potential: a - Maximum Room Pressure; b - Maximum Brine in Room; c - Gas Expulsion; d - Gas Migration Distance.

These seven specified gas-generation rate histories were simulated with best-estimate system parameters using the boundary backstress method. The specified 2/1 and 0.2/0.1 rate histories were used in baseline simulations (Figure 4-1). Simulation results for the other five rate histories are shown in Figure 5-25. All seven specified rate histories assumed the same total potential for gas generation, 1,050 moles per drum from corrosion and 550 moles per drum from microbial activity. The total mass of gas generated was nearly 22,000 kg of H_2. A comparison of the different gas-generation rate histories is shown in Figures 4-1h and 5-25h. Note that for the 0.1/0 rate history the total gas potential was not exhausted, as only about 7,500 kg of H_2 were generated.

There was a wide range in room closure behavior (Figure 5-25a), room pressure (Figure 5-25b), brine inflow and expulsion (Figure 5-25c), and rate of gas expulsion (Figure 5-25d) depending upon the gas-generation rate history. However, with the exception of the 0.1/0 case, there was little variation in the total mass of gas expelled (Figure 5-25d) and gas migration distance (Figures 5-25e and 5-25f) for the different rate histories. These results suggest that while the gas-generation rate affects the closure and pressurization history of the room and host rock, it has little effect on the long-term distribution of gas and brine between the room, halite, and interbeds. The 0.1/0 simulation, which had less gas generation than with the other rate histories, had less gas expelled and less gas migration. This result suggests that gas expulsion and gas migration may be more sensitive to the total mass of gas generated than to the gas-generation rate (see Section 5.2.3).

Room closure behavior for the specified 7/2, 1.6/0.6, and 0.1/0 rate histories (Figure 5-25a) was similar to the room closure behavior in baseline simulations (Section 4.1). Initial room closure was followed by a period of room expansion in response to high gas pressures in the room. A combination of gas expulsion and the end of gas generation resulted in subsequent re-closure of the room. The maximum room pressures (Figure 5-25b) always occurred when the mass of gas in the room increased so rapidly that the room expanded in response. The mass of gas in the room is distinct from gas-generation rate, because if a rate of gas expulsion can be maintained that is greater than or equal to the gas-generation rate, the mass of gas in the room will not increase and gas pressure will not rise.

With the 105/5 rate history, gas was generated so rapidly that most of the gas-generation potential was realized in the first 10 years and there was relatively little room closure (Figure 5-25a). Gas generation was complete by 110 years. Because a large room void volume was

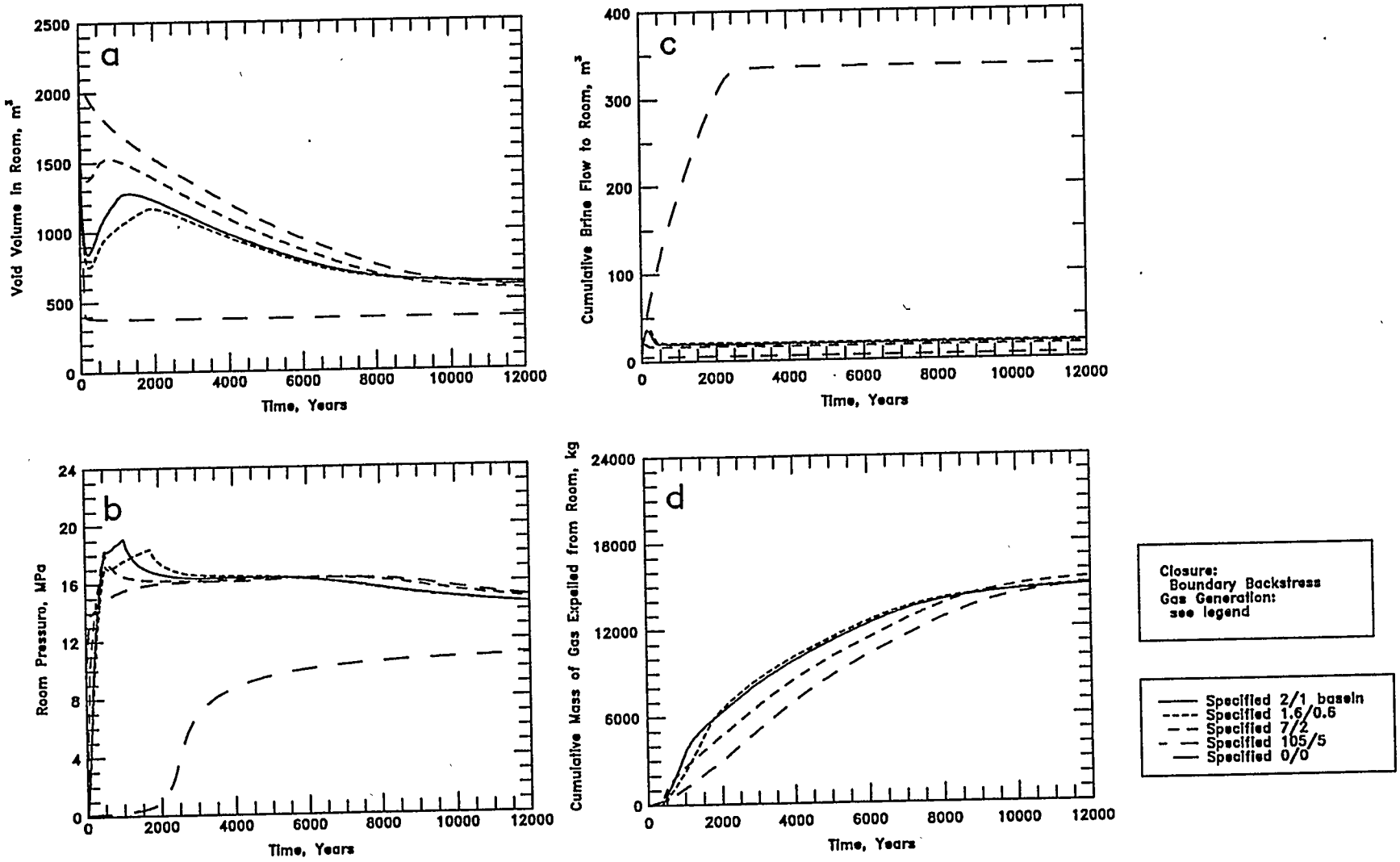

Figure 5-25 (a-d). Sensitivity to specified gas-generation rate history: a - Void Volume; b - Gas Pressure; c - Brine Flow: d - Gas Expulsion.

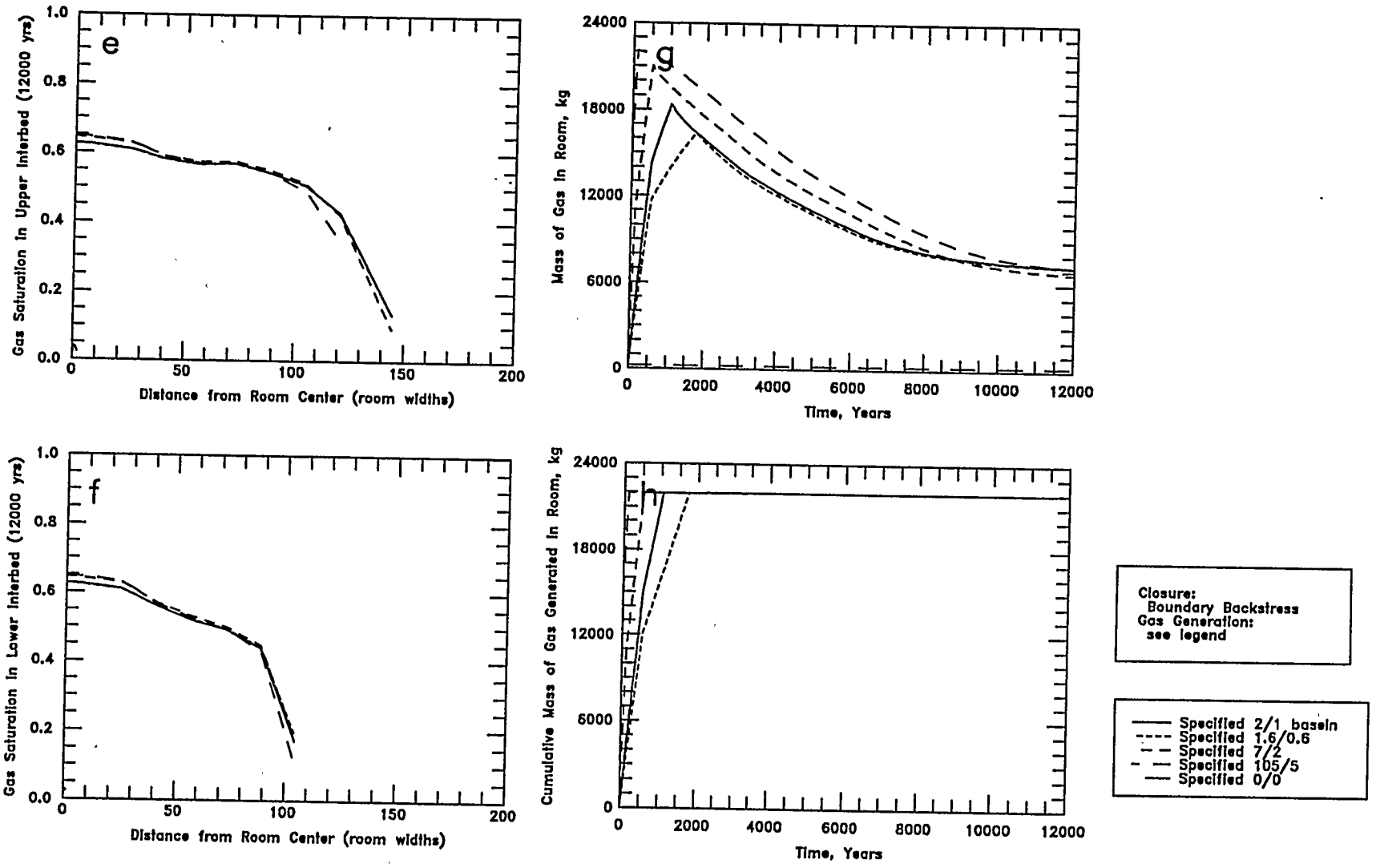

Figure 5-25 (e-h). Sensitivity to specified gas-generation rate history: e - Upper Interbed Gas Profile; f - Lower Interbed Gas Profile; g - Room Gas Mass; h - Gas Generation.

maintained, extreme room pressures were never attained (Figure 5-25b) and room expansion did not occur. There was very little brine inflow because of the rapid room pressurization. The rate of gas expulsion was actually lower with the 105/5 rates than with lower gas-generation rate histories because of the lower room pressure.

The 0/0 rate history (no gas generation) bounds the lower limit of gas generation. While the 0/0 rate was not important relative to gas expulsion and migration, it did produce several interesting results. Brine inflow was significantly greater than for the 0.1/0 case (Figure 5-25c), even though the 0.1/0 rate was very low (0.1 moles per drum per year for 5,500 years). By 2,000 years in the 0/0 case the room void volume (342 m^3) was almost entirely filled with brine (brine inflow was about 340 m^3), at which time room pressures started to rise (Figure 5-25b) due to compression of the gas by inflowing brine and room closure. The gas pressure in the room rose to about 11 MPa over 12,000 years. It is presumed that the room gas pressure would eventually approach 12 MPa, the far-field brine pressure, because the gas-brine capillary pressure in the room is zero.

Some of these specified rate simulations were also run using the pressure lines method. However, for the 7/2 rate history there was an obvious discrepancy in early-time room closure behavior between the boundary backstress results and the pressure lines results. The pressure lines results showed two distinct room expansion and re-closure sequences in the first 1,000 years. These pressure line results appeared to be skewed towards the SANCHO f-series results (see discussion in Freeze et al. (1995)) and were considered to be less accurate than the boundary backstress results for this rate history that differed significantly from the SANCHO f-series.

5.2.2 Constant Gas-Generation Rate

System behavior was compared for five different fixed gas-generation rates. Each constant rate was assumed to have a total gas potential of 1,600 moles per drum (1,050 moles per drum anoxic corrosion, 550 moles per drum microbial activity) or about 22,000 kg per room. Therefore, each simulation had a different duration of gas generation. The five constant gas-generation rates were 1.5 moles per drum per year (for 1,067 years), 1.0 moles per drum per year (for 1,600 years), 0.5 moles per drum per year (for 3,200 years), 0.2 moles per drum per year (for 8,000 years), and 0.1 moles per drum per year (for 16,000 years). Because the

simulations only extended to 12,000 years, the total gas potential was not exhausted at the rate of 0.1 moles per drum per year. For comparison, the specified 2/1 rate was 2.0 moles per drum per year (from 0 to 550 years) and 1.0 moles per drum per year (from 550 to 1,050 years) and the specified 0.2/0.1 rate was 0.2 moles per drum per year (from 0 to 5,500 years) and 0.1 moles per drum per year (from 5,500 to 10,500 years).

Simulation results are shown in Figure 5-26. As expected, room pressurization was fastest and peak pressure was greatest with the highest gas-generation rate (Figure 5-26b). However, room pressures approached similar values following the end of gas generation regardless of rate and duration. Room void volume behavior was consistent with room pressure; room expansion occurred sooner with higher gas-generation rates (Figure 5-26a). Gas expulsion (Figure 5-26d) and migration (Figures 5-26e and 5-26f) were similar for all constant rate simulations in which the total gas potential was exhausted. Brine inflow and expulsion (Figure 5-26c) increased with an decreased gas-generation rate because the lower rates produced slower room pressurization.

Performance measure sensitivities to constant gas-generation rate are shown in Figure 5-24. The results suggest that while brine inflow and room pressure are sensitive to the gas-generation rate, the total mass of gas expelled and the gas migration distance are sensitive to gas potential rather than to gas rate.

5.2.3 Gas-Generation Potential

System behavior was compared for a constant 0.5 moles-per-drum-per-year gas-generation rate under five gas potentials. The five gas potentials corresponded to five different durations of gas generation. Simulated gas potentials were 600 moles per drum (in 1,200 years), 900 moles per drum (in 1,800 years), 1,600 moles per drum (in 3,200 years), 2,500 moles per drum (in 5,000 years), and 3,700 moles per drum (in 7,400 years). For comparison, the baseline total potential was 1,600 moles per drum. The simulated gas potentials are representative of waste-limited gas potentials. These potentials can only be realized if sufficient brine is available to drive the gas-generation reactions. The mass of gas generated would be lower if brine availability or brine consumption limited the gas potentials.

Simulation results are shown in Figure 5-27. Results were identical for all potentials for the first 1,200 years because the gas-generation rates were the same. Since all brine flow occurred within the first 1,200 years (Figure 5-27c) brine flow was not sensitive to changes in gas potential. After gas potentials were exhausted, room pressures (Figure 5-27b) and the

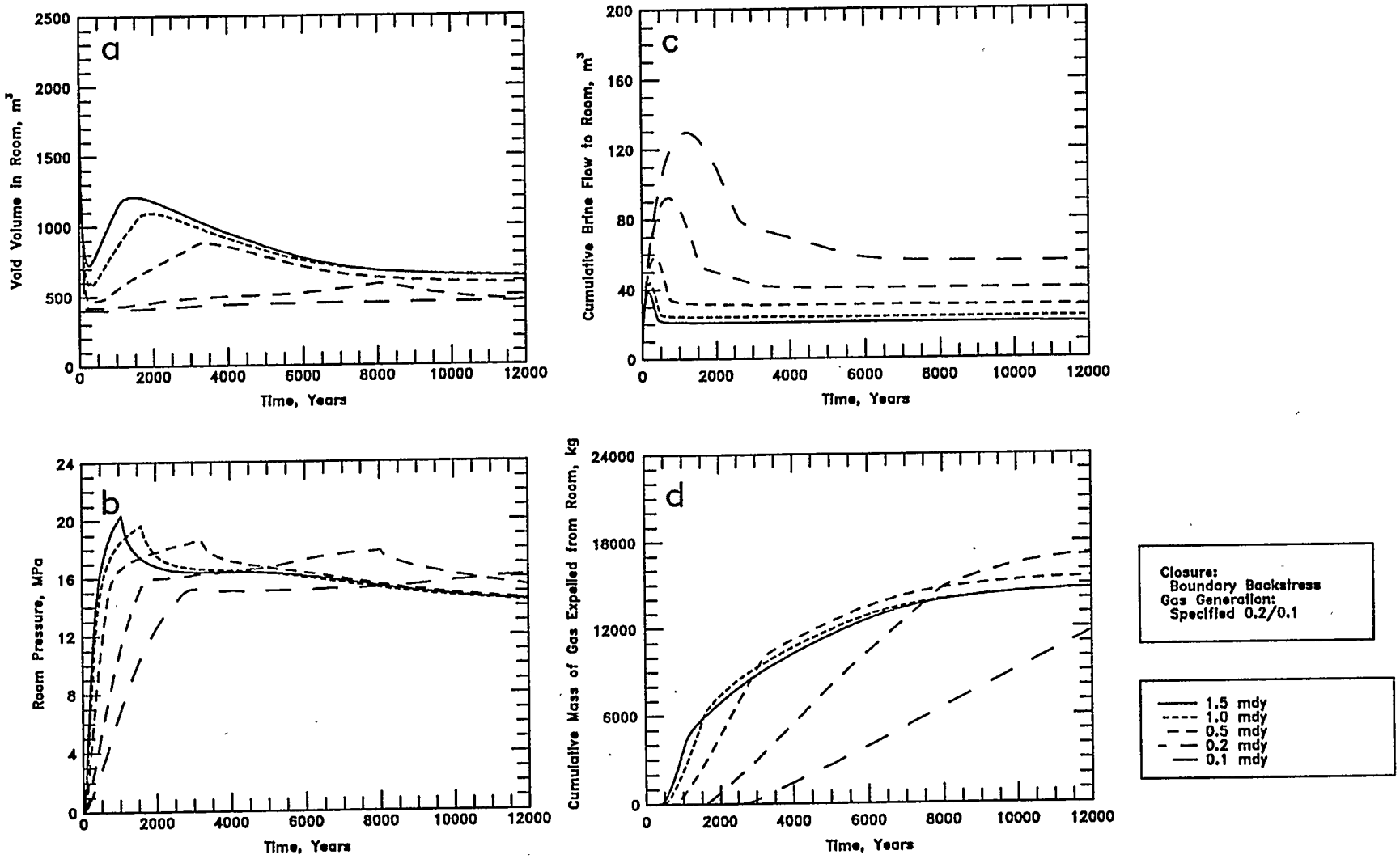

Figure 5-26 (a-d). Sensitivity to constant gas-generation rate: a - Void Volume; b - Gas Pressure; c - Brine Flow; d - Gas Expulsion.

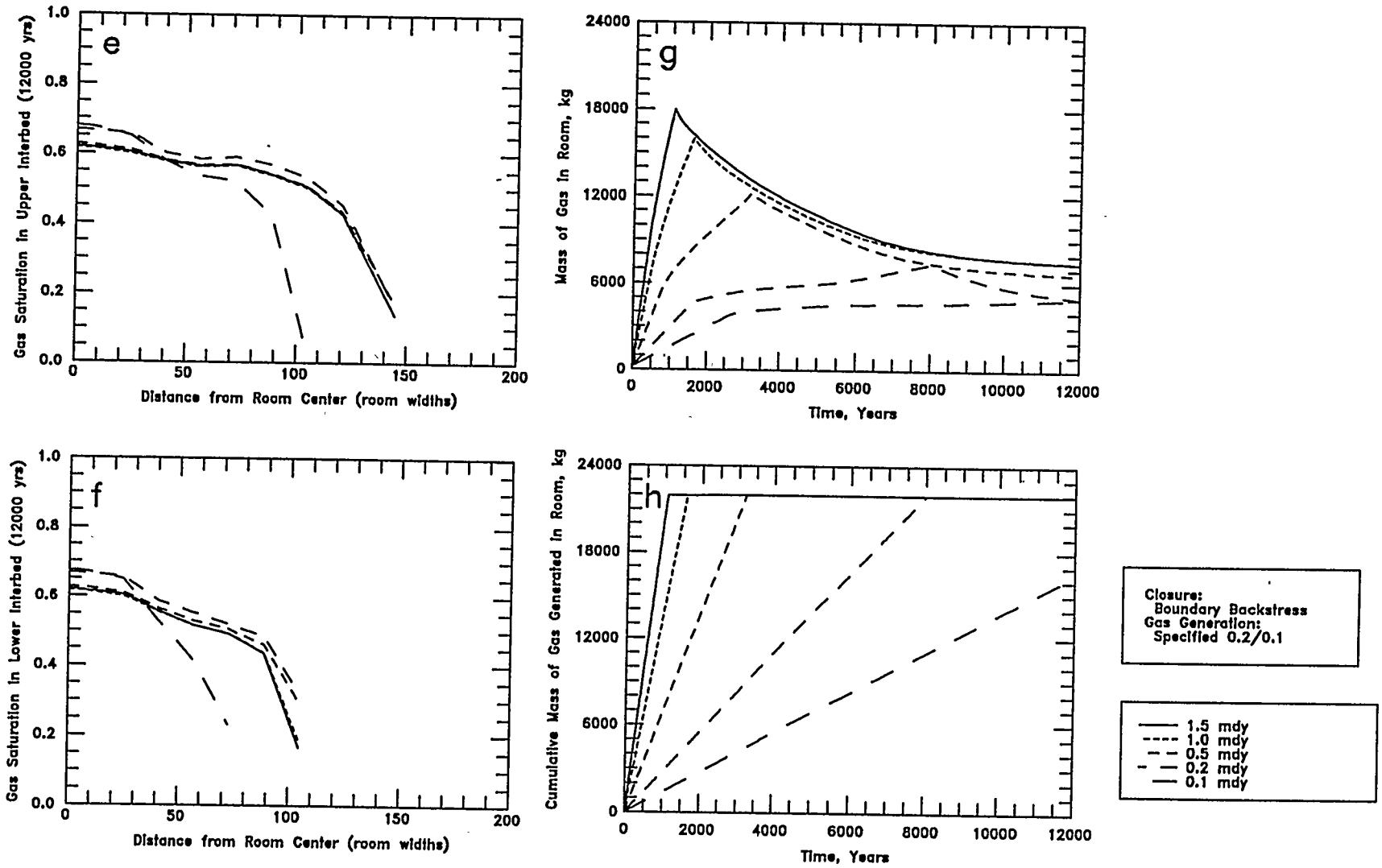

Figure 5-26 (e-h). Sensitivity to constant gas-generation rate: e - Upper Interbed Gas Profile; f - Lower Interbed Gas Profile; g - Room Gas Mass; h - Gas Generation.

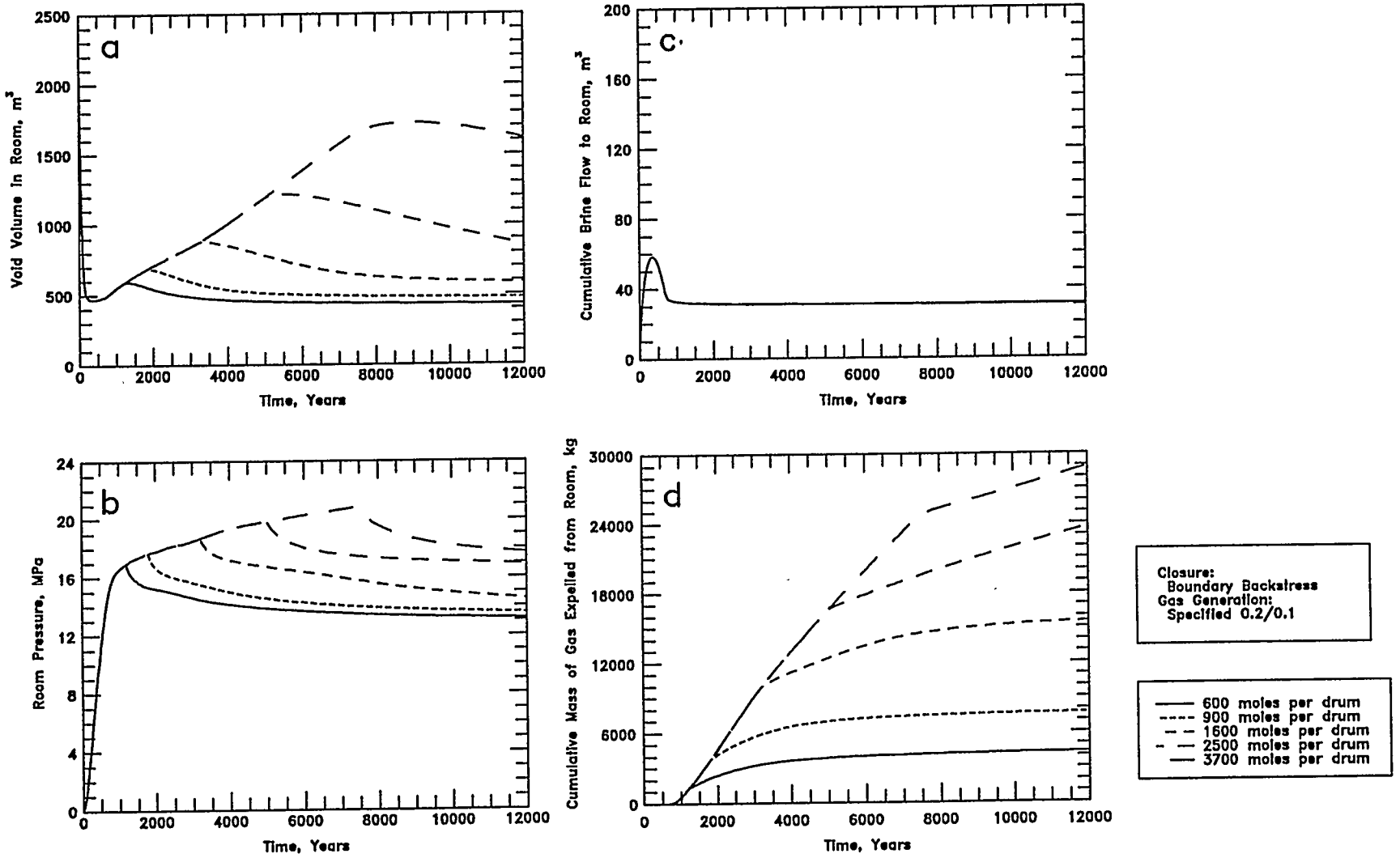

Figure 5-27 (a-d). Sensitivity to gas-generation potential: a - Void Volume; b - Gas Pressure; c - Brine Flow; d - Gas Expulsion.

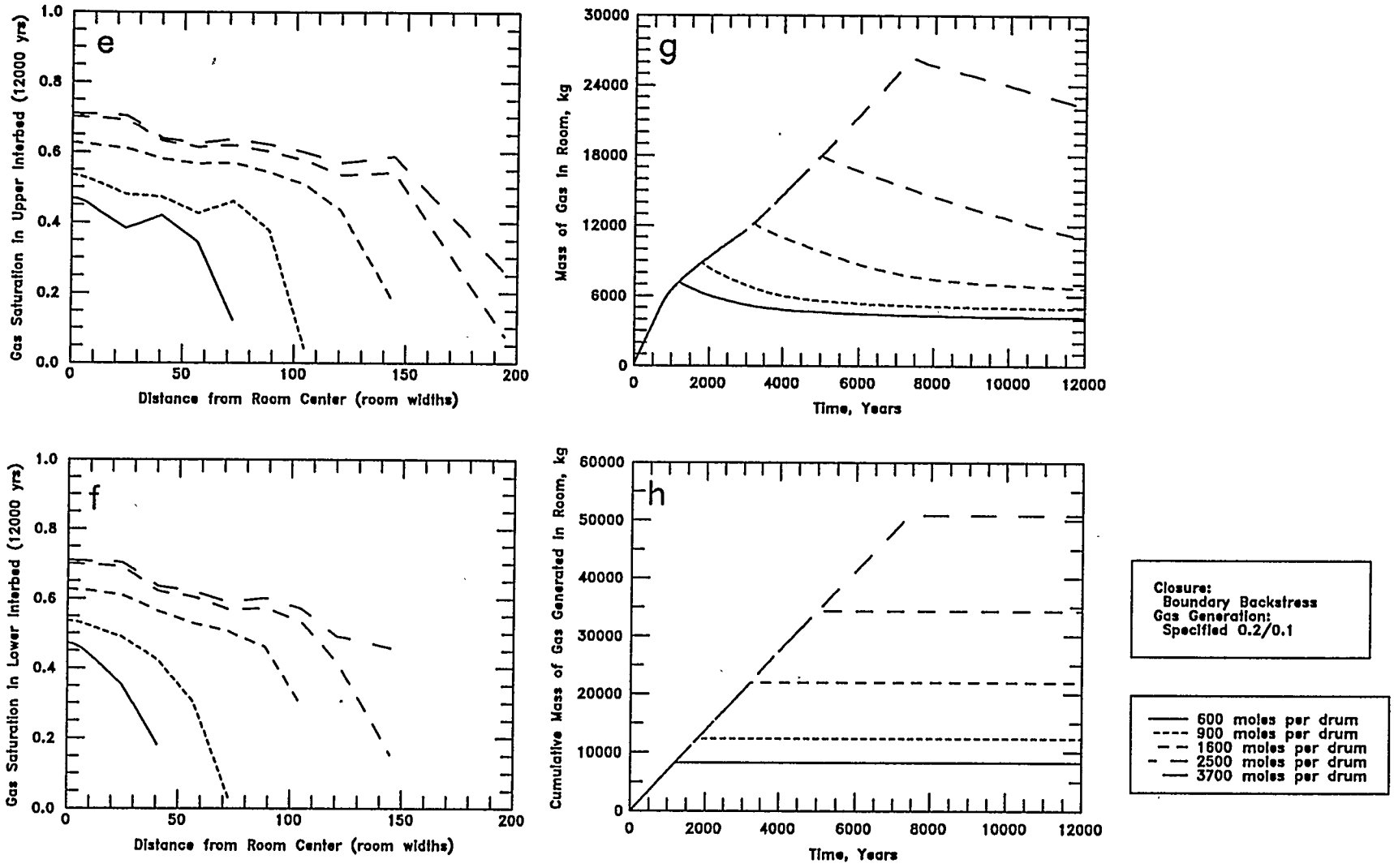

Figure 5-27 (e-h). Sensitivity to gas-generation potential: e - Upper Interbed Gas Profile; f - Lower Interbed Gas Profile; g - Room Gas Mass; h - Gas Generation.

rate of gas expulsion (Figure 5-27d) declined. Correspondingly, the mass of gas generated (Figure 5-27h) and gas expelled (Figure 5-27d) were greatest for the largest gas potential.

Performance measure sensitivities to total gas potential are shown in Figure 5-24. Total importance coefficients were 1.59 for the gas expulsion performance measure and 1.14 for the gas migration distance performance measure. All performance measures (except brine volume in room) were more sensitive to the mass of gas generated than to gas-generation rate. This is because every increase in the mass of gas generated increases the amount of brine that must be displaced to make way for storage of gas at equilibrium pore pressure. The rate of gas generation makes little difference: if rates are low, brine is displaced at near equilibrium pressure, if rates are rapid, gas is stored initially at higher pressure in the room until, as time passes, it is released more slowly into the interbeds. The long-term saturation state and pressure of gas is similar for similar masses of gas generated, with only minor dependence on rate. An important caveat to this conclusion is that if fracturing of the interbeds is sensitive to peak room pressure, then the final conditions might become very dependant on the pressure history of the room.

5.2.4 Brine-Dependent Gas-Generation Rate

In brine-dependent gas generation simulations, the simulated gas-generation rate was determined as a function of the brine saturation in the room. In regions with brine-dominated conditions a specified brine-inundated rate (assumed to be the 2/1 rate) was used, while regions with gas-dominated conditions used a specified vapor-limited rate (assumed to be the 0.2/0.1 rate). Two different methods of coupling gas generation with brine availability were utilized, the capillary fringe method (Section 2.4.2.1) and the linear correlation method (Section 2.4.2.2). The two methods are differentiated by the way in which brine-dominated and gas-dominated conditions are determined. Results from baseline simulations, which used best estimates of brine-inundated and vapor-limited rates, are discussed in Section 4.2 and presented graphically in Figure 4-4. As noted in Section 2.4.2.2, the linear correlation method predicts gas-generation rates that are equivalent to brine pooling on the floor of the room (no capillary fringe), where the brine pool produces gas at the brine-inundated rate and the overlying portion of the room produces gas at the vapor-limited rate.

The capillary fringe method approximates gravity-driven phase segregation in the room. It was developed to minimize the need for simulations with finely discretized rooms and gravitational effects. This method uses the simulated volume of brine in the room and the waste

and backfill properties to calculate the theoretical extent of a capillary fringe. A threshold brine saturation was defined such that room segments where the theoretical brine saturation was above the threshold were assumed to generate gas at the specified brine-inundated rate and room segments where the theoretical brine saturation was below the threshold were assumed to generate gas at the slower, vapor-limited rate. For the baseline capillary fringe simulation, the threshold brine saturation was 0.3, corresponding approximately to the residual brine saturation. With this implementation, vapor-limited conditions correspond to room segments where brine is immobile because relative permeability to brine is at or near zero. Under baseline conditions, the volume of brine in the room was small enough that theoretical brine saturations were below the threshold saturation in the entire room, and gas was generated at the specified vapor-limited rate. Simulation results were therefore identical to the specified 0.2/0.1 rate history.

To examine the effect of brine-inundated conditions in the room, a capillary fringe sensitivity simulation was performed with the threshold brine saturation set to 0.1 (the residual brine saturation was not changed). The sensitivity simulation results are compared with the baseline capillary fringe results in Figure 5-28. Conditions were identical to the baseline capillary fringe simulation until 60 years. At that time, the simulated brine volume in the room produced a theoretical brine saturation (calculated from Equation 2-6) above 0.1 in at least part of the capillary fringe. The resulting gas-generation rate in the room, influenced by the theoretical brine-inundated conditions in part of the room, increased. The room remained at least partly brine-inundated for about 200 years, at which time theoretical brine saturations dropped below 0.1 everywhere in the room due to brine expulsion. Gas generation progressed at vapor-limited rates from 260 years until the gas potential was exhausted.

The 200-year interval of high gas-generation rate affected results significantly. Room pressure (Figure 5-28b) increased rapidly, driving out brine until partly brine-inundated conditions no longer existed and the high rate decreased. Thereafter, room pressure rose slowly to about 16 MPa, where it remained for the rest of the simulation, similar to the baseline case. Room closure (Figure 5-28a) was briefly reversed during the high rate interval, after which it declined slowly toward a final state. Brine inflow (Figure 5-28c) was much less than for the baseline case because of the higher room pressure. Gas expulsion (Figure 5-28d) began earlier than the in the baseline case, but at a similar rate of expulsion. Finally, gas migration distance (Figures 5-28e and 5-28f) was similar to the baseline case.

The sensitivity simulation for the capillary fringe method demonstrates how gas generation may be limited by brine availability. Initially, the nearly-dry room generates gas at vapor-limited rates. Due to brine inflow, gas generation increases to near brine-inundated rates,

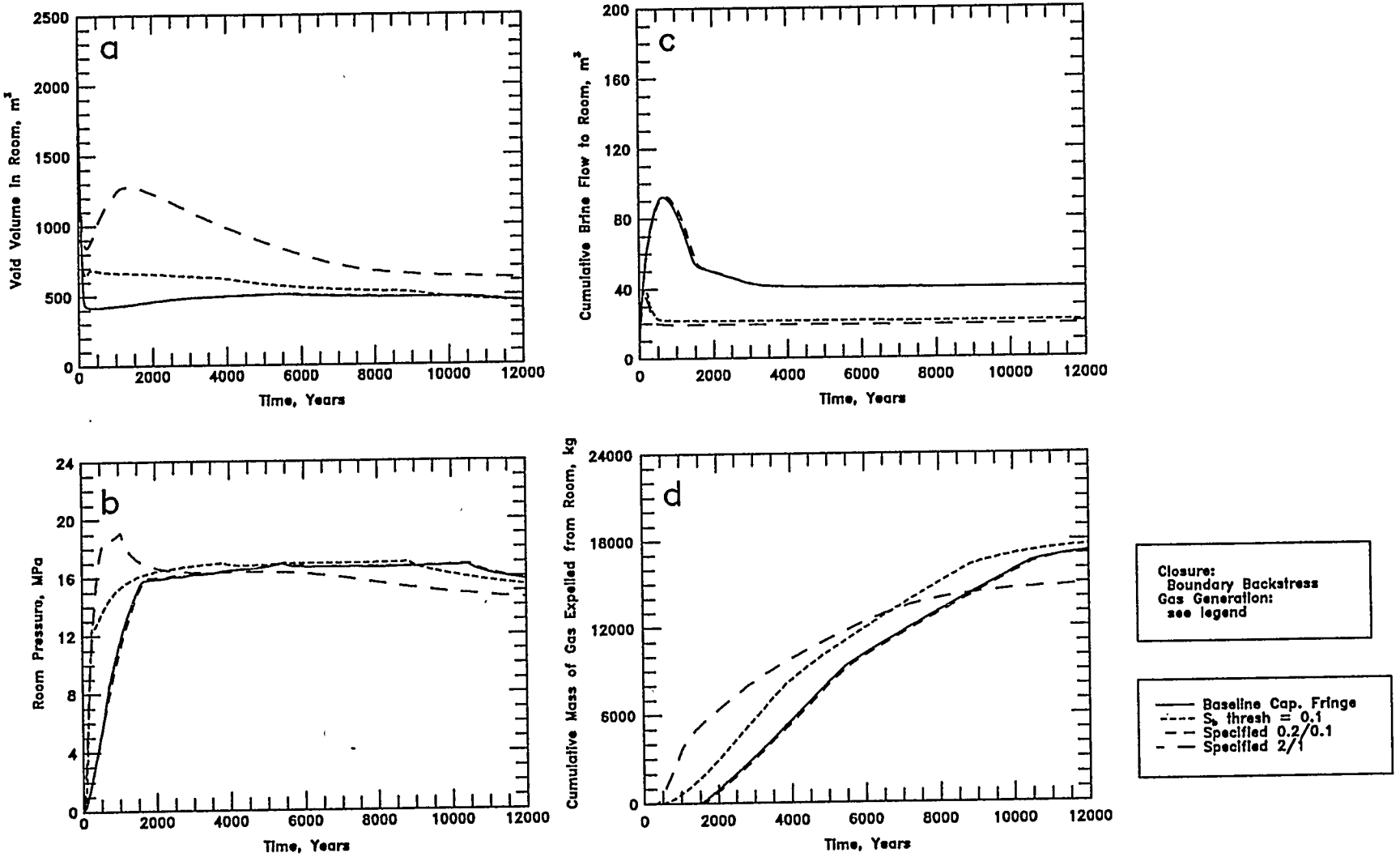

Figure 5-28 (a-d). Sensitivity to capillary fringe threshold brine saturation: a - Void Volume; b - Gas Pressure; c - Brine Flow; d - Gas Expulsion.

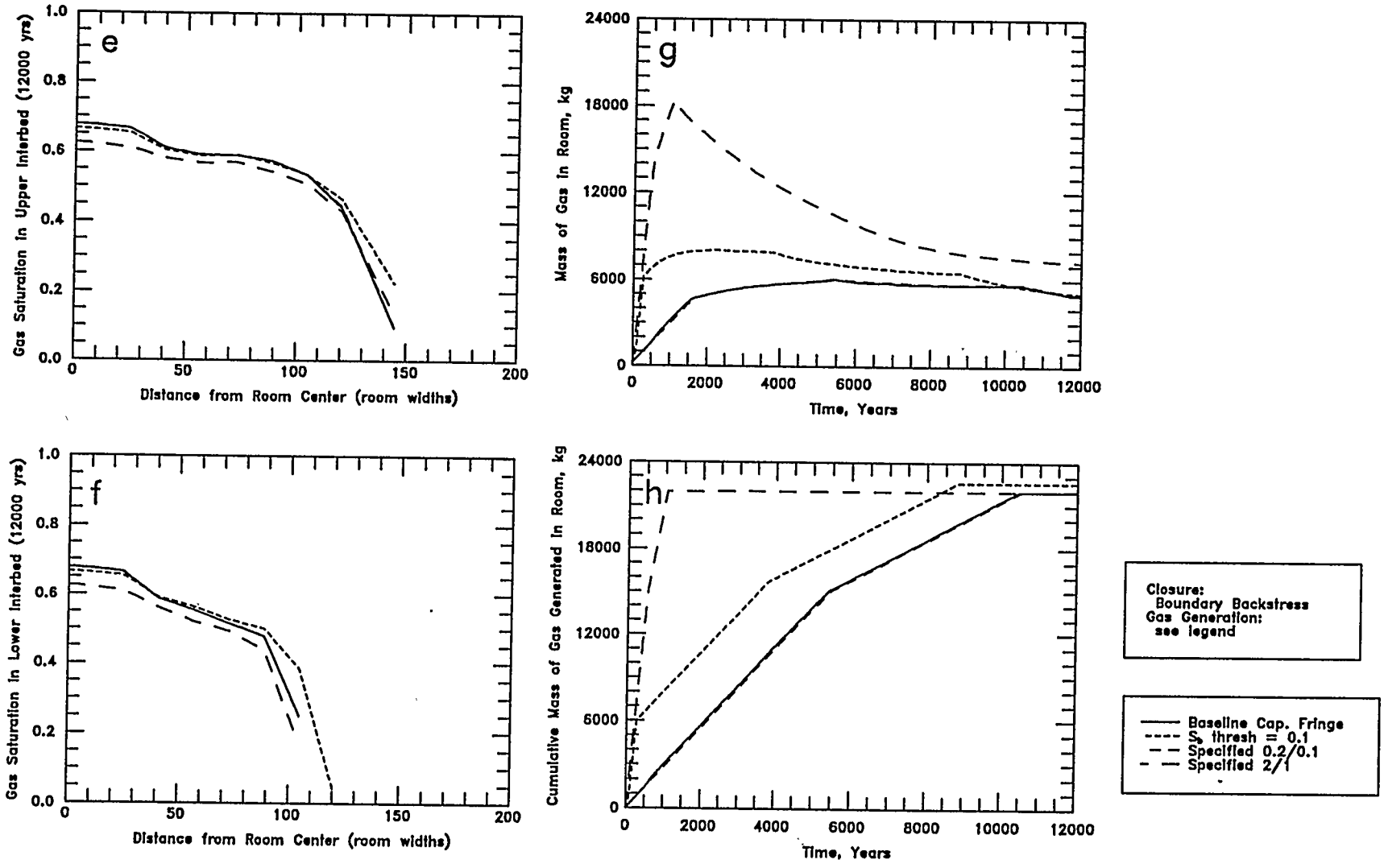

Figure 5-28 (e-h). Sensitivity to capillary fringe threshold brine saturation: e - Upper Interbed Gas Profile; f - Lower Interbed Gas Profile; g - Room Gas Mass; h - Gas Generation.

which pressurizes the room, reverses the brine pressure gradient, and expels brine back to the halite and interbeds. In response to brine expulsion, gas generation drops to vapor-limited rates. Pressures remain relatively low and approach lithostatic gradually, and gas expulsion generally proceeds at the same rate as gas generation except during the high generation rate stage.

Similar behavior would be expected from a capillary fringe simulation with a threshold saturation of 0.3 and a higher initial brine saturation in the room. As the brine volume in the room increases due to brine inflow, theoretical brine saturations in the capillary fringe would exceed 0.3 and gas generation rates would increase.

The brine-dependent rate simulations are sensitive to brine saturation in the room. The baseline and sensitivity simulations shown in Figures 4-4 and 5-28, respectively, show that the simulations are also highly sensitive to (1) the brine-dependent rate method: capillary fringe or linear correlation (or puddle on the floor), and (2) the parameters used to define the method. However, all the brine-dependent rate simulations presented here are bounded by the 2/1 and 0.2/0.1 specified rate simulations. Thus, while the uncertainties in the brine-dependent rate methods may be important, the bounding specified rate histories were sufficient to determine the TOUGH2/EOS8 parameter sensitivities presented in this report.

5.3 Model Conceptualization

5.3.1 Flow and Closure Coupling Methods

Eight alternative methods for coupling multiphase flow and room closure were evaluated by Freeze et al. (1995). Only two methods were found to be accurate and robust enough to approximate the effects of room closure under most conditions, the boundary backstress method and pressure-time-porosity line interpolation (pressure lines method). The boundary backstress method is thought to be a more reliable indicator of system behavior due to a theoretical basis for modeling salt deformation as a viscous process. It is a complex method and a detailed calibration process is required. The pressure lines method is thought to be less reliable because the results were skewed towards SANCHO f-series results for gas-generation rate histories that differed from the SANCHO f-series histories that were used for calibration. Due to its relative simplicity, the pressure lines method is easier to implement in multiphase flow codes and simulations have a shorter execution time (10 to 20 times faster than boundary backstress).

Baseline and sensitivity simulation results, described in the previous sections, were similar with both methods. Differences between results were small and were primarily due to differences between the calibration processes of the two methods. The importance coefficients, calculated using Equation 2-15, for the comparison of the two closure coupling methods were less than 0.10 for all performance measures. These importance coefficients are small relative to the differences caused by most parameter variations.

As discussed previously in Section 5, the sensitivity of performance measures to parameter value changes is similar regardless of whether the simulations used the boundary backstress method or the pressure lines method (see Figure 5-1 for an example), further indicating that the behavior of flow and closure process coupling is relatively insensitive to the choice of coupling method.

5.3.2 Alternative Conceptual Models

5.3.2.1 INTERBED FRACTURE

The implementation of a conceptual model to simulate the effects of fracture dilatation was discussed in Section 2.5.1. This model is based on a preliminary model developed by WIPP PA and used in preliminary PA calculations (Stoelzel et al., 1995). The baseline interbed fracture simulation used the same parameter values and gas-generation rate history as the baseline specified 2/1 rate simulation, except that the interbed fracture model (Equations 2-8 to 2-10) was implemented with the following parameter values:

p_o	=	12.0 MPa
p_{if}	=	12.6 MPa
p_{ff}	=	15.0 MPa
α_{po}	=	8.3×10^{-10} Pa^{-1}
ϕ_o	=	0.01
ϕ_{max}	=	0.10
k_o	=	1×10^{-19} m^2
k_{max}	=	1×10^{-16} m^2
n	=	3

These values were selected, somewhat arbitrarily, as best estimates for the anhydrite interbeds. No development of actual parameter values was undertaken. For example, the maximum

fracture porosity of 0.10 may be quite high for the corresponding maximum fracture permeability of 1 x 10^{-16} m^2. The intention was to corroborate with the preliminary WIPP PA implementation, however, Stoelzel et al. (1995) used an updated set of interbed fracture parameters that were not available at the time the TOUGH2/EOS8 study was performed. Hydrofracturing test results (Beauheim et al., 1993b) and/or planned pressure-dependent permeability testing (including fracture dilatation measurement) may provide additional parameter information.

Results from the baseline interbed fracture simulation are compared to the baseline specified 2/1 rate results in Figure 5-29. The baseline interbed fracture affected all performance measures except for the maximum brine volume in the room, which was unaffected only because brine inflow ceases before pressures rise enough to initiate changes to interbed properties. The rates of gas flow to the interbeds increased, the total mass of gas expelled increased, maximum pressures were diminished, but gas migration distance was decreased. The somewhat counter-intuitive decrease in gas migration distance under enhanced fracture conditions is discussed in the following paragraph.

The interbed fracture model alters both porosity and permeability, which impacts both the storage and transmissive properties of interbeds. Because the permeability changes are dependent on the porosity change (Figure 2-5), the model will be referred to as the porosity model. The maximum pressure attained during the baseline fracture simulation was approximately 16 MPa, about 1 MPa higher than necessary to increase interbed porosity and permeability to their maximum attainable values, ϕ_{max} and k_{max}. The maximum interbed permeability is determined from Equation 2-10, with ϕ set equal to ϕ_{max}. Near the room, the porosity of the interbeds was increased from 0.01 to 0.10, while the permeability was increased about three orders of magnitude to about 1 x 10^{-16} m^2. With the selected baseline interbed fracture parameters, the increased interbed storativity had a greater effect than the increased transmissivity and gas migration distance was actually less than in the comparative unfractured simulation. If a different set of fracture parameters were used (i.e., smaller ϕ_{max} or larger k_{max}), gas migration distance might increase under interbed fracture conditions.

Similar relative effects of changing interbed porosity and permeability were observed in the interbed sensitivity simulations (Section 5.1.3.1). A factor-of-three increase in porosity from 0.01 to 0.03 decreased gas migration distance by about a factor of three (Figures 5-18e and 5-18f), while a factor-of-ten increase in permeability from 1 x 10^{-19} m^2 to 1 x 10^{-18} m^2 increased gas migration distance by only about a factor of two (Figures 5-17e and 5-17f).

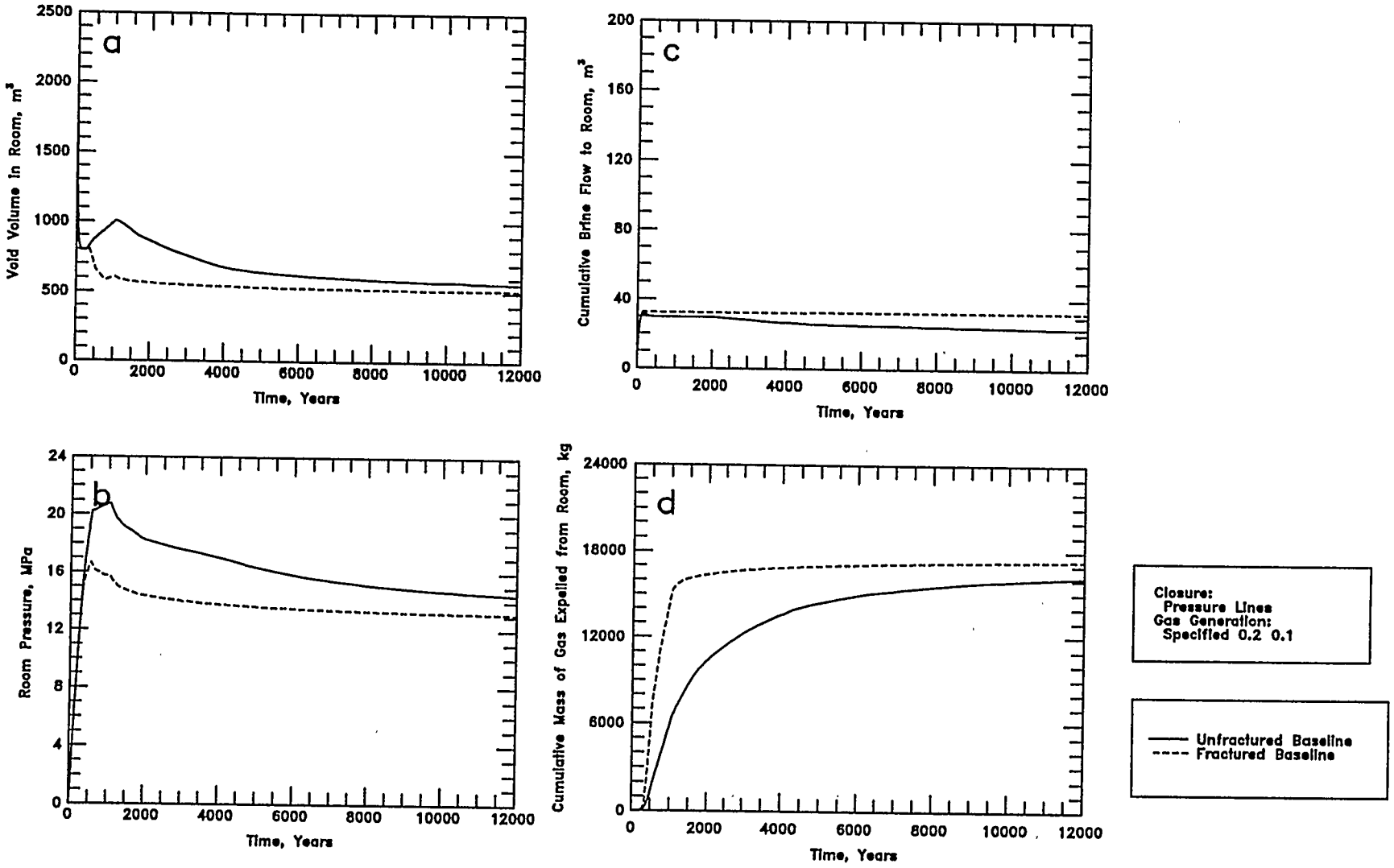

Figure 5-29 (a-d). Results from interbed fracture alternative conceptual model: a - Void Volume; b - Gas Pressure; c - Brine Flow; d - Gas Expulsion.

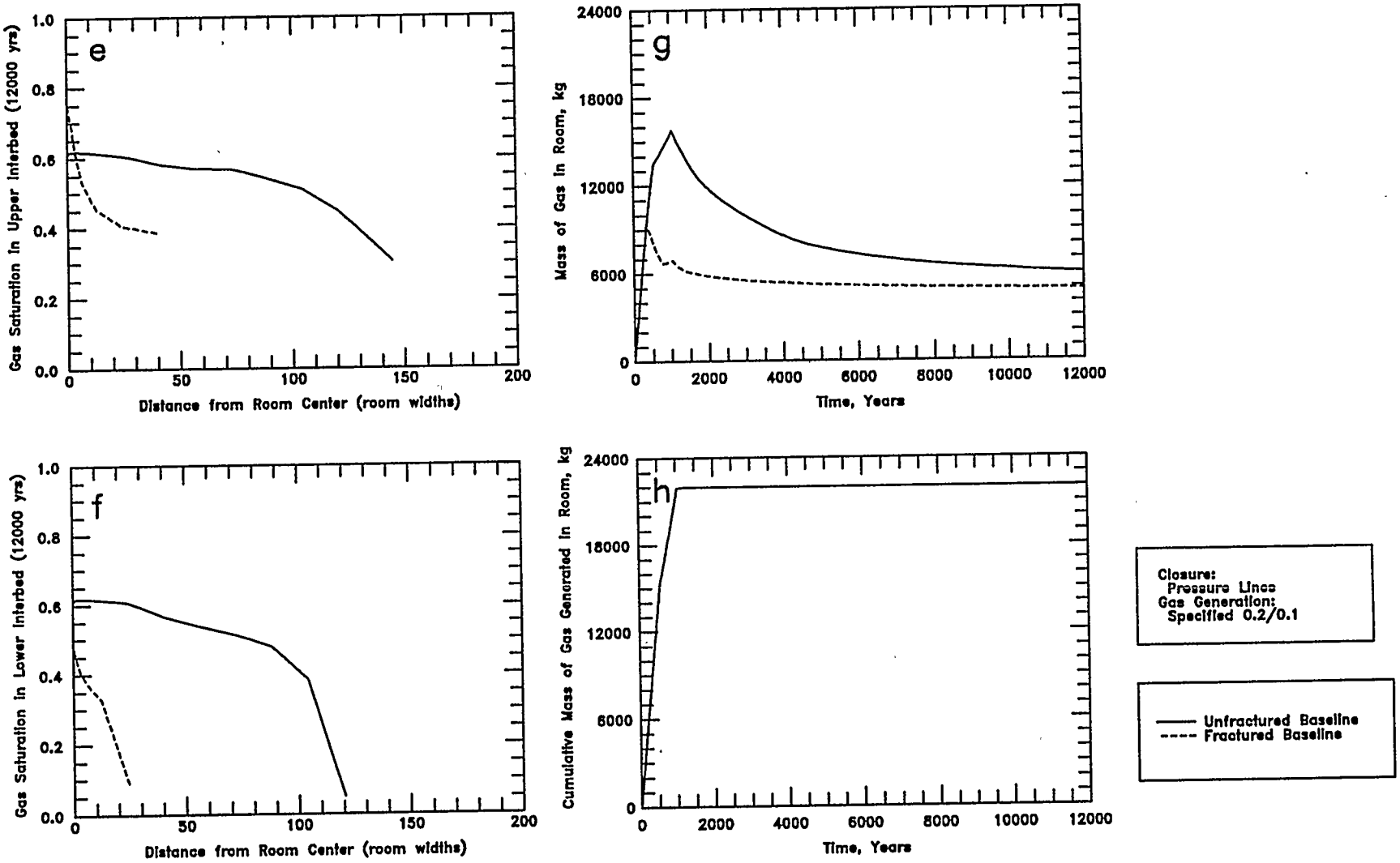

Figure 5-29 (e-h). Results from interbed fracture alternative conceptual model: e - Upper Interbed Gas Profile; f - Lower Interbed Gas Profile; c - Room Gas Mass; d - Gas Expulsion.

The sensitivity of system behavior to changes in interbed fracture storativity was examined by varying the maximum interbed fracture porosity, ϕ_{max}, from 0.05 to 0.20. The baseline value was 0.10. With decreasing ϕ_{max}, gas expulsion decreased, the maximum room pressure increased, and migration distance increased. In all cases the maximum room pressure attained was high enough that the interbed porosity and permeability reached their maximum attainable values. In no case did gas migration distance exceed that observed for the baseline unfractured (specified 2/1 rate) simulation. However, it is possible that even a ϕ_{max} of 0.05 is not low enough to be representative of a k_{max} of 1×10^{-16} m^2 (see discussion is following paragraphs). The maximum sensitivity coefficient for the gas migration distance performance measure was 3.16, which is comparable to the high sensitivity (maximum coefficient of 5.15) to interbed porosity in the baseline specified 2/1 rate simulations. Although these simulation results suggest that gas migration distance may decrease under interbed fracture conditions, they are not rigorously defensible because of the absence of WIPP-specific experimental data. Rather, these simulation results underscore the criticality of understanding interbed porosity and porosity changes if predictions of gas migration distance are desired.

The counter-intuitive decrease in gas migration distance with fractures may also be caused in part by inaccuracy within the permeability correlation of the interbed fracture model. To examine this effect, the permeability exponent, n, was varied between 2 and 4. The baseline value was 3. With the baseline interbed fracture parameters, the resulting variation in k_{max} was 1×10^{-15} m^2 to 1×10^{-17} m^2. With increasing n, gas expulsion increased, room pressure declined, and gas migration distances showed a slight increase. In all cases the maximum allowable changes to porosity and permeability were applied to the interbeds. Sensitivity coefficients to changes in n were lower than the corresponding sensitivities to interbed permeability.

With the conceptual model implemented in this study, the permeability in the fractured element is dependent on porosity (Equation 2-10). However, theoretical evaluation of the permeability of fractures suggests that permeability should vary as a function of fracture aperture. It is likely that the relative magnitude of aperture change is much greater than corresponding porosity changes in a fractured element. The fracture permeability might be larger if the correlation were based on changes in fracture aperture rather than changes in porosity due to fracture dilation. A simple way to evaluate the effects of a more rapidly changing fracture permeability would be to increase the permeability exponent, n, in the permeability-porosity correlation to a much larger value which would produce a larger permeability increase for a given increase in porosity, resulting in increased gas migration distance.

A more rigorous relationship between porosity and permeability considers changes in the fracture aperture due to fracture dilatation. The Navier-Stokes equations, applied to a parallel plate model of viscous flow, suggests that intrinsic permeability in a fracture, k_f, varies as a function of the fracture aperture, b, squared (Bear, 1972):

$$k = \frac{b^2}{12} \tag{5-1}$$

This aperture model could be applied in TOUGH2/EOS8 by calculating thickness-averaged values for permeability, k_e, and porosity, ϕ_e, that apply to the model grid blocks representing the total thickness of the interbed. The thickness-averaged values include contributions from both fracture (assume a number of fractures, N, having a total thickness of Nb) and matrix (assume a total matrix thickness of h). Assuming horizontal fractures, horizontal flow, and the same potential gradient across the fractures and the matrix, the thickness-averaged permeability is:

$$k_e = \frac{(Nb)k_f + (h)k_m}{(Nb+h)} \tag{5-2}$$

and the thickness-averaged porosity is:

$$\phi_e = \frac{Nb + (h)\phi_m}{(Nb+h)} \tag{5-3}$$

where subscripts f and m represent fracture and matrix, respectively.

The permeability-porosity relationship for the aperture model is compared with the porosity model in Figure 5-30. The aperture model predicts a rapid increase in permeability once fracture dilatation begins, regardless of the number of fractures, whereas the porosity model predicts a more gradual increase in permeability. Because the behavior of the two models is inherently different, there is no permeability exponent value, n, that can make the porosity model behave similarly to the aperture model. Because of higher predicted permeabilities, the aperture model will propagate fracture-altered properties further away from the repository, and will likely increase gas migration distance.

In summary, the current porosity model implementation of interbed fracture, which relates permeability changes to porosity changes, may underestimate the effects of increased permeability on gas migration distance. To overcome this deficiency, a new fracture model,

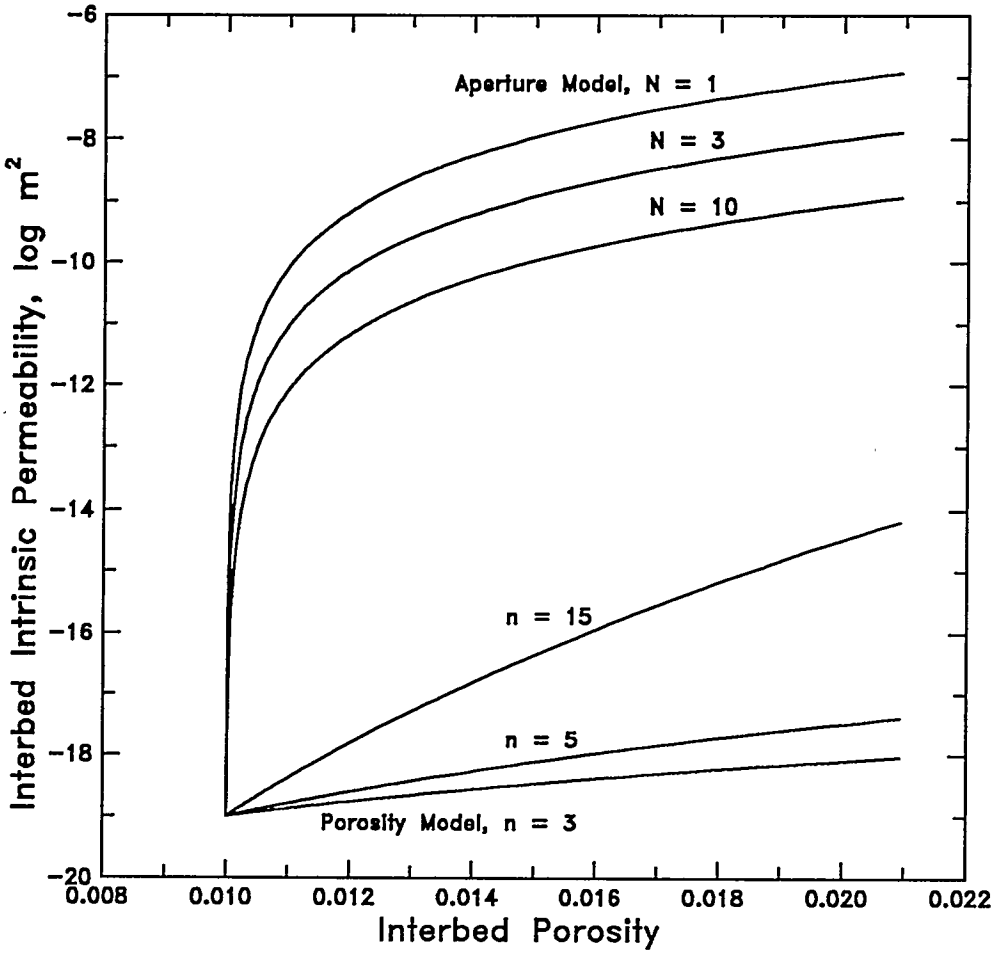

Figure 5-30. Comparison of change in interbed permeability with respect to change in interbed porosity for two different interbed fracture models.

relating permeability changes to changes in fracture aperture, has been proposed. The new aperture model can be implemented in a future version of TOUGH2/EOS8 for comparative simulations.

5.3.2.2 DISTURBED ROCK ZONE

The baseline model assumed that fracture connections, characteristic of a DRZ, existed between the disposal room and the interbeds. However, no other adjustments were made to the rock properties to reflect the presence of a DRZ. Section 2.5.2 describes a conceptual model for the DRZ in which the intrinsic permeability, rock compressibility, and initial pressure are altered from baseline values in a 10 m thick section of the Salado Formation surrounding a room. These altered properties are representative of the enhanced permeability and storativity expected near the excavation.

Permeabilities were increased three orders of magnitude, from 1×10^{-21} m^2 to 1×10^{-18} m^2 for halite and from 1×10^{-19} m^2 to 1×10^{-16} m^2 for the interbeds. Compressibilities were increased about an order of magnitude, from 2.7×10^{-11} Pa^{-1} to 1.2×10^{-10} Pa^{-1} for halite and from 8.3×10^{-12} Pa^{-1} to 8.2×10^{-11} Pa^{-1} for the interbeds. The initial brine pressure was reduced from 12.0 MPa to 7.5 MPa in the DRZ, while the initial brine saturation was unchanged at 1.0. High permeabilities and compressibilities were maintained for 200 years, at which time they were restored to undisturbed (baseline) values, representative of DRZ healing. Porosity and multiphase flow properties in the DRZ were not altered from baseline values.

Simulation results are presented in Figure 5-31. The increased transmissivity of the disturbed near-field Salado Formation resulted in increased brine inflow for 200 years relative to the baseline specified 2/1 rate simulation (Figure 5-31b). After 200 years, brine flow trends were similar to those of the baseline simulation. The additional brine inflow (about 30 m^3) was due to increased flow rates in and to the near-field interbeds. Only about 8 m^3 of brine, or four times the baseline simulation amount, flowed into the room directly from the halite. Because of the short duration of the DRZ, the other performance measures and system behavior were similar to baseline results. With a brine-dependent gas-generation rate, the increased brine inflow may result in a larger impact on other performance measures.

The conceptual model set up for the disturbed rock zone tests the importance of near-field brine mobility in the years immediately after the operational phase, but ignores the effects of

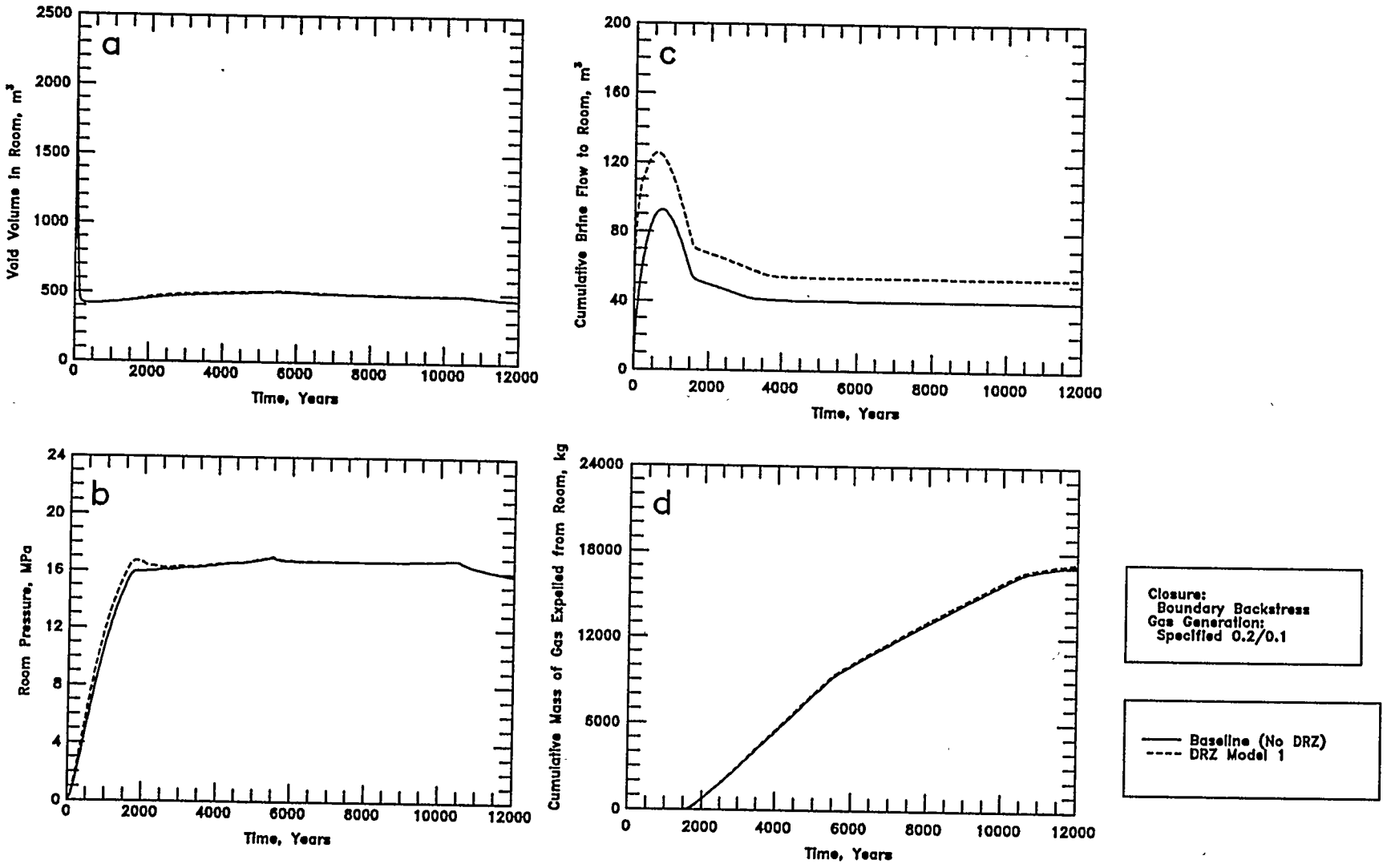

Figure 5-31 (a-d). Results from Disturbed Rock Zone alternative conceptual model: a - Void Volume; b - Gas Pressure; c - Brine Flow; d - Gas Expulsion.

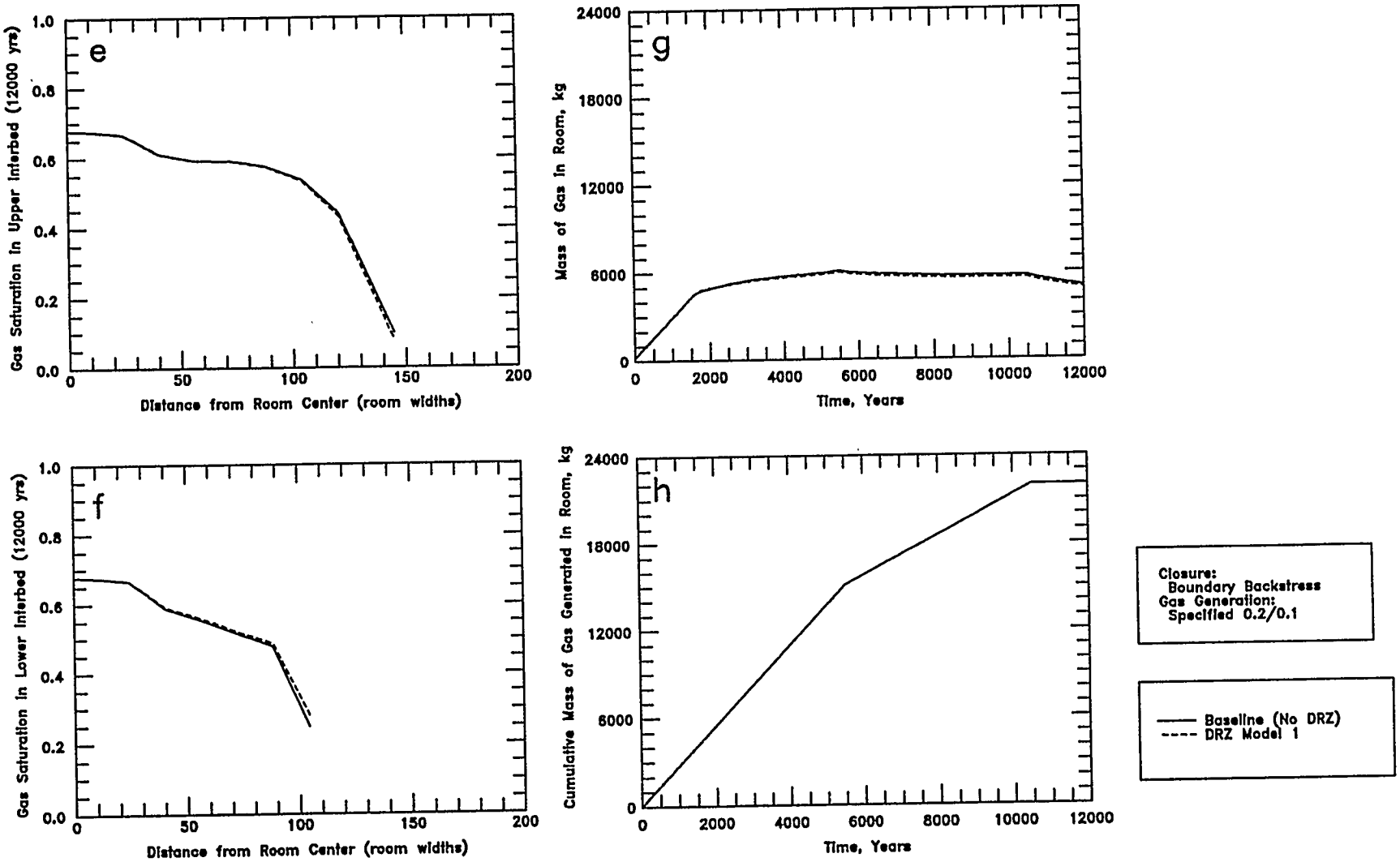

Figure 5-31 (e-h). Results from Disturbed Rock Zone alternative conceptual model: e - Upper Interbed Gas Profile; f - Lower Interbed Gas Profile; g - Room Gas Mass; h - Gas Expulsion.

possible non-zero gas mobility in halite due to decreasing gas-brine threshold pressure, the uncertain initial condition for brine saturation, and the effects of post-closure deformation on DRZ pressures and volumes. The effects of these additional processes could be important. For example, during excavation and the operational phase, pore pressures and porosity in the DRZ are expected to change. This will alter the saturation of brine and gas in an as-yet undetermined manner. An incorrect assumption about either the initial porosity or brine saturation in the disturbed rock zone could lead to misleading inferences about the brine availability in the room. Conceptualizing and implementing a hydrologically meaningful disturbed rock zone process model remains for future work.

5.3.2.3 EFFECTS OF GRAVITY

The effects of gravity, implemented as described in Section 2.5.3, had only a small effect on the system performance measures relative to the baseline specified 2/1 rate simulation (Figure 5-32). Gravity did produce phase segregation within the room, which resulted in nearly all brine expulsion going to the lower interbed. However, the total volume of brine expelled was similar to the baseline case. Gravity also resulted in earlier gas expulsion to the upper interbed and delayed gas expulsion to the lower interbed, but the total mass of gas expelled was unaffected. Gas migration distance was slightly increased in the upper interbed (Figure 5-32e) and slightly decreased in the lower interbed (Figure 5-32f) with gravitational effects.

If the natural dip of the Salado Formation were incorporated, flow of brine and gas in opposite directions in the interbeds could occur due to density-driven flow (Webb, 1995). Brine could flow towards the room in response to gravity while gas flowed away under a pressure gradient. Under these conditions, rising gas pressure would not necessarily prevent brine flow to the room. As the conceptual representation of hydrologic coupling of the room and the Salado Formation becomes more complex, it will be increasingly important to determine and model how gravity affects flow in the system. Numerical simulations incorporating stratigraphic dip are the subject of follow-on studies to this report.

5.3.2.4 GAS EXSOLUTION FROM THE SALADO FORMATION

Gas exsolution from brine in the Salado Formation is expected in response to excavation-related depressurization. To approximate the effects of gas exsolution, TOUGH2/EOS8

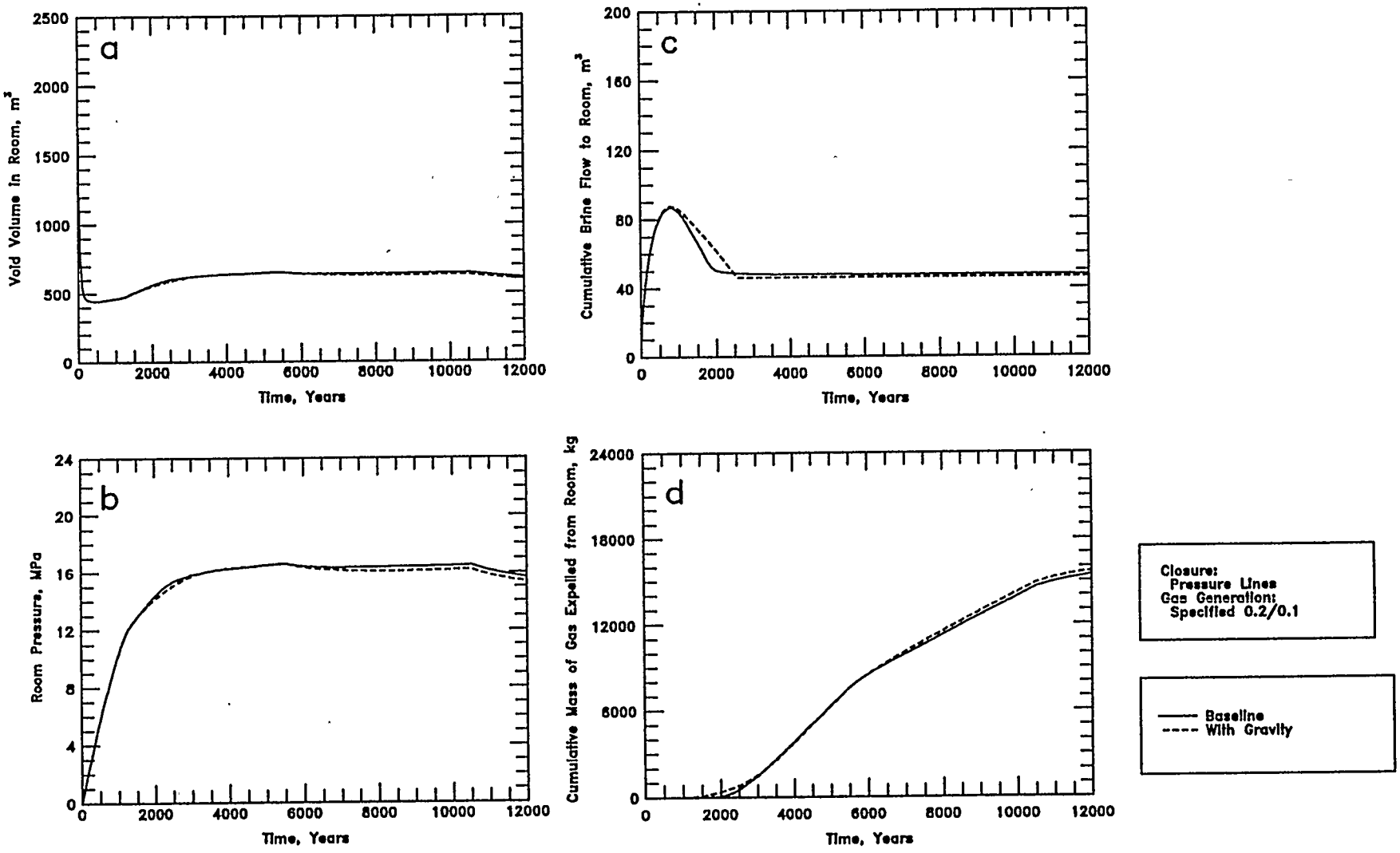

Figure 5-32 (a-d). Results from gravity alternative conceptual model: a - Void Volume; b - Gas Pressure; c - Brine Flow; d - Gas Expulsion.

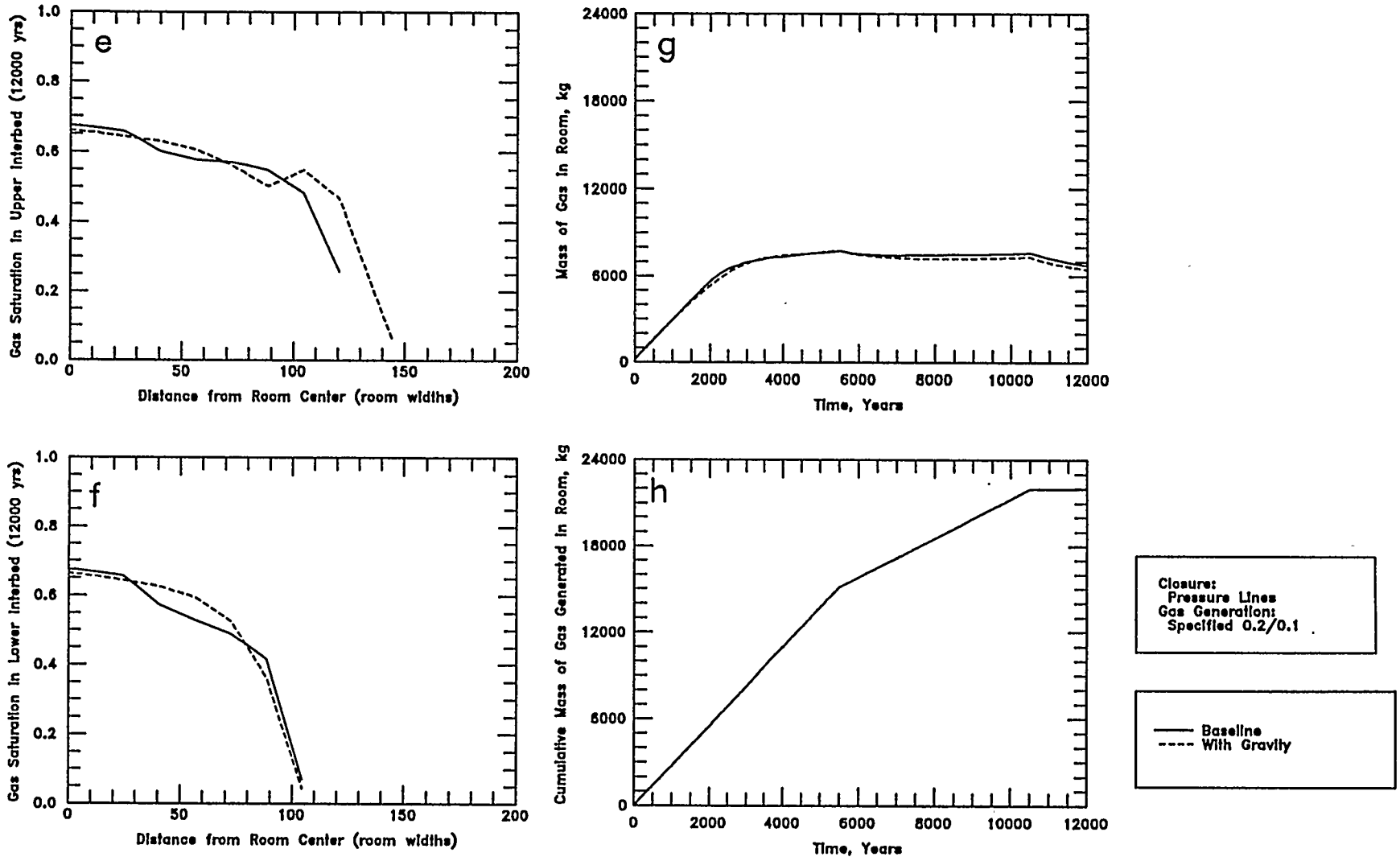

Figure 5-32 (e-h). Results from gravity alternative conceptual model: e - Upper Interbed Gas Profile; f - Lower Interbed Gas Profile; g - Room Gas Mass; h - Gas Generation.

simulations were performed with elevated initial gas saturations throughout the Salado Formation as described in Section 2.5.4. Initial gas saturations of 0.10 and 0.20 were simulated. The baseline simulations had zero initial gas saturation.

Sensitivity simulation results are shown in Figure 5-33. The increase in the initial gas saturation produced a corresponding increase in the relative permeability to gas. As a result, both gas expulsion (Figure 5-33d) and gas migration distance (Figures 5-33e and 5-33f) increased with increasing initial gas saturation. Sensitivity and importance coefficients were similar to those obtained with residual gas saturation (Section 5.1.3.2). These results emphasize the importance of interbed relative permeability to gas on gas migration distance.

As noted in Section 2.5.4, simulating increased gas saturations everywhere in the Salado Formation produces the maximum effects of gas exsolution. For example, based on gas solubility values for air in brine (Appendix A), depressurization from 12 MPa to 0.1 MPa would produce a gas saturation due to exsolution of about 0.30. However, Figure 2-6 suggests that a pressure of 0.1 MPa will only be present within a few meters of a disposal room. Depressurization to 1 MPa and 5 MPa would produce gas saturations of 0.02 and 0.002, respectively. Pressures of 1 MPa may exist as far as 5 m a room, while pressures of 5 MPa may exist as far as 10 m from a room (Figure 2-6). The simulated gas saturations of 0.10 and 0.20 are reasonable within a few meters of the room, but are too high at a distances of greater than 5 m from the room. As a result, relative permeability to gas is overestimated at distances of greater than 5 m from the room in these gas exsolution simulations.

5.3.2.5 INSTANTANEOUS ROOM DEPRESSURIZATION

The instantaneous room depressurization alternative conceptual model was described in Section 2.5.5. A rapid room depressurization, as would occur due to a borehole penetration, was simulated at 1,000 years for both the specified 2/1 and specified 0.2/0.1 gas-generation rate histories. In both cases, the room was depressurized instantaneously to 7.7 MPa by the removal of a mass of gas, and was immediately sealed afterwards. There was no instantaneous change in brine or gas saturation in the room coincident with the depressurization, which is similar to the effect of a breach borehole venting gas. Subsequent to the depressurization, gas and brine flow is between the room and the Salado Formation.

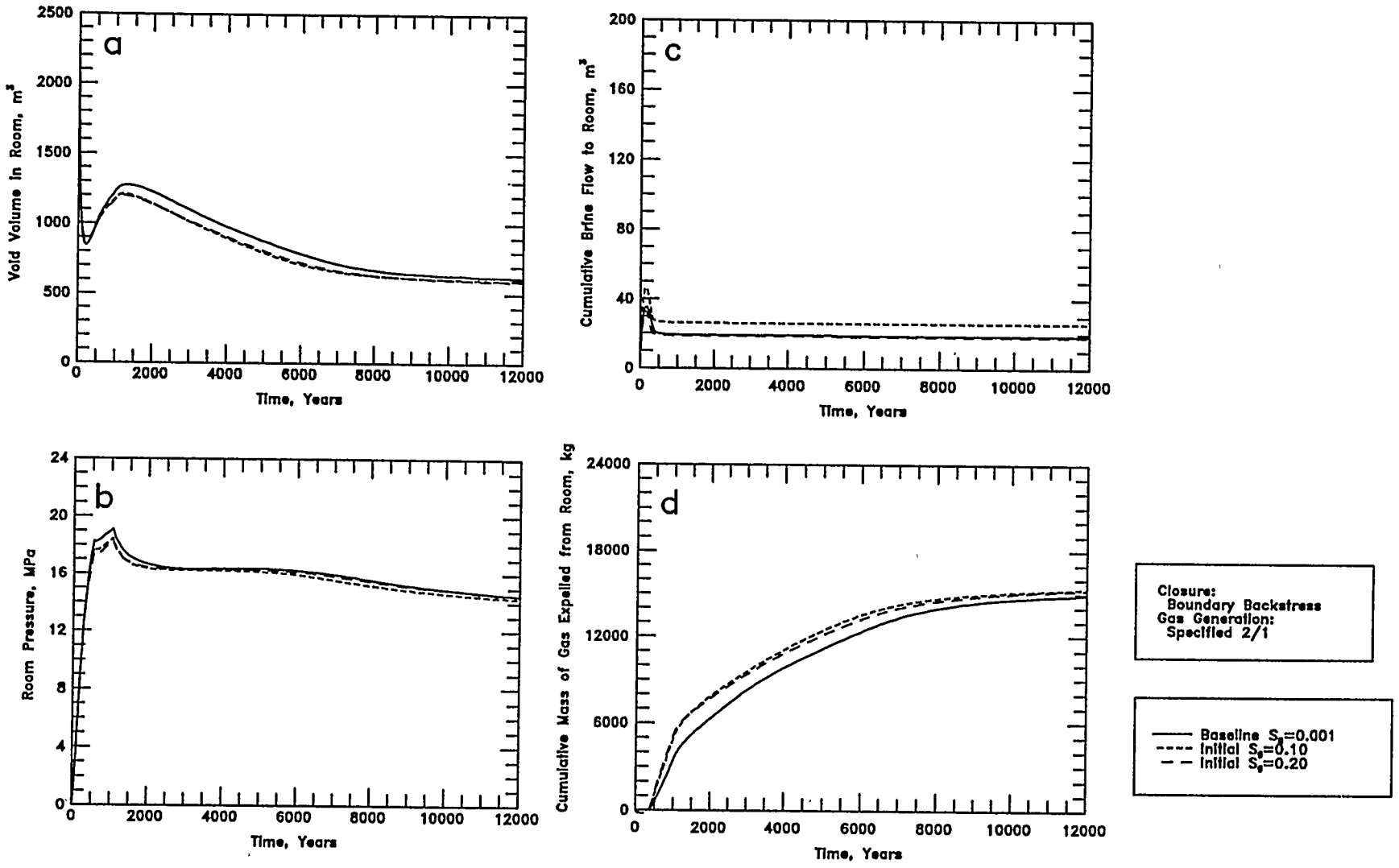

Figure 5-33 (a-d). Results from gas exsolution alternative conceptual model: a - Void Volume; b - Gas Pressure; c - Brine Flow; d - Gas Expulsion.

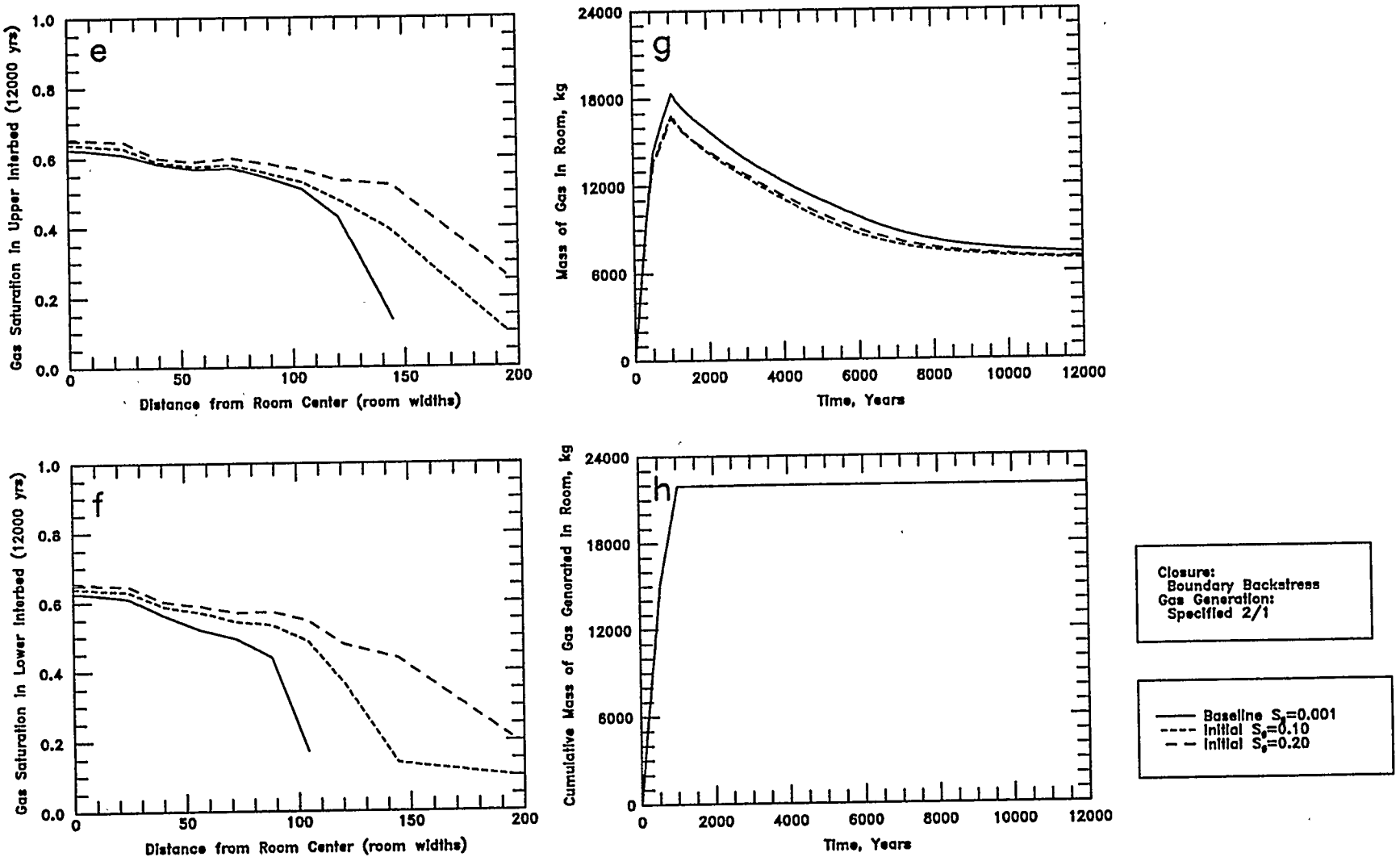

Figure 5-33 (e-h). Results from gas exsolution alternative conceptual model: e - Upper Interbed Gas Profile; f - Lower Interbed Gas Profile; g - Room Gas Mass; h - Gas Generation.

Simulation results are shown in Figure 5-34. The effect on system behavior was highly dependent upon the mass of gas removed to produce the instantaneous depressurization to 7.7 MPa. For the specified 2/1 rates, depressurization at 1,000 years is late in the generation history and the room has pressurized and expanded considerably. The peak room pressure occurred at the moment of depressurization. Because a large mass of gas was released up the borehole to drop the pressure to 7.7 MPa, the expanded room void volume could not be maintained and rapid room closure occurred. Gas expulsion to the interbeds slowed dramatically, and the gas migration distance was decreased relative to the baseline simulation.

For the specified 0.2/0.1 rate history, results from the instantaneous depressurization at 1,000 years under were quite similar to the baseline (non-intruded) specified 0.2/0.1 simulation except for some slight differences immediately following depressurization. Because gas pressures were low at the time of the depressurization, very little gas was removed from the room to drop the pressure to 7.7 MPa. Interestingly, the depressurization event took place soon after brine expulsion had started. The instantaneous drop in pressure reversed the brine pressure gradient and caused a brief period of renewed brine inflow to the room. There was little change in subsequent room pressurization, gas expulsion, and gas migration distance.

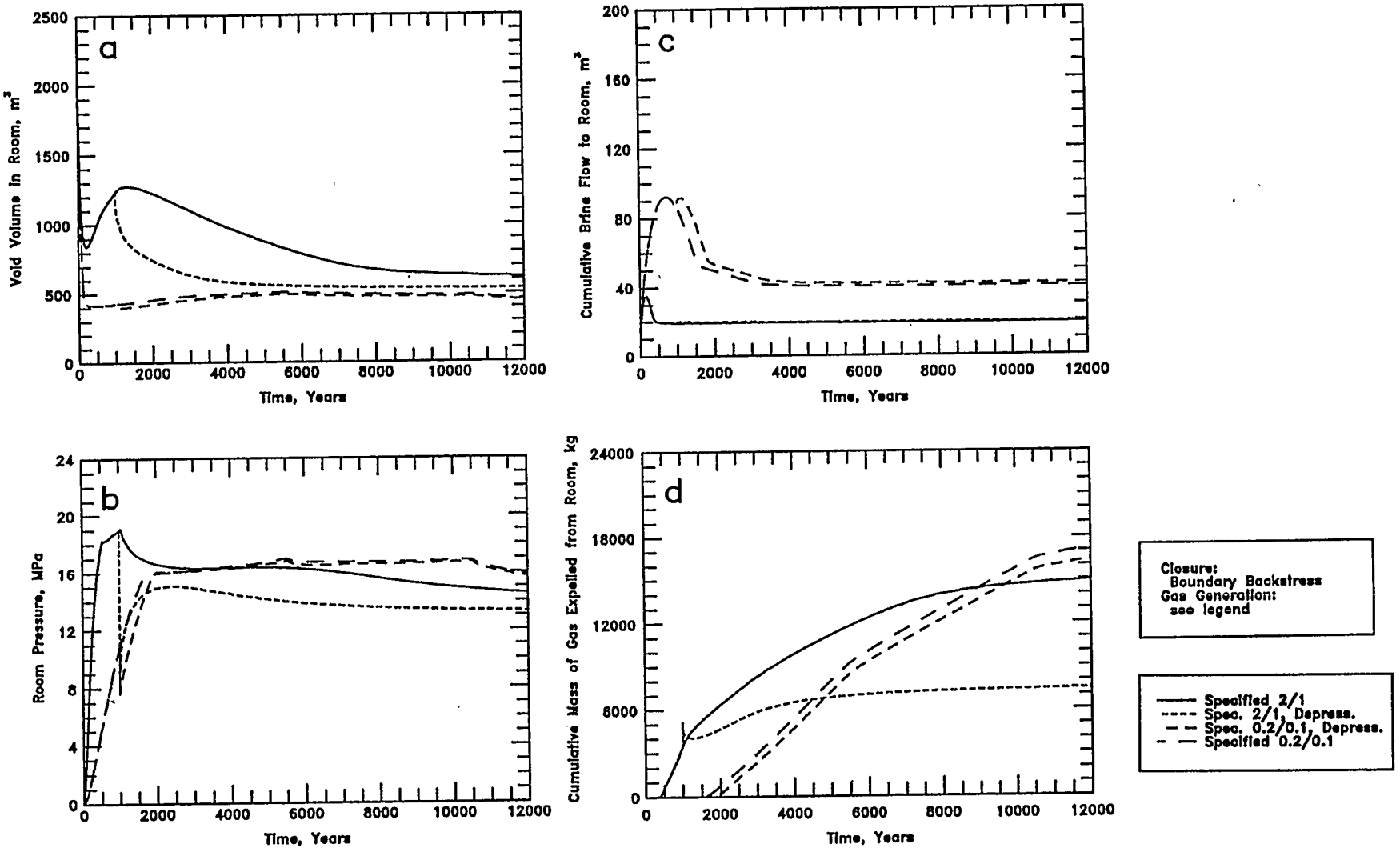

Figure 5-34 (a-d). Results from instantaneous room depressurization alternative conceptual model: a - Void Volume; b - Gas Pressure; c - Brine Flow; d - Gas Expulsion.

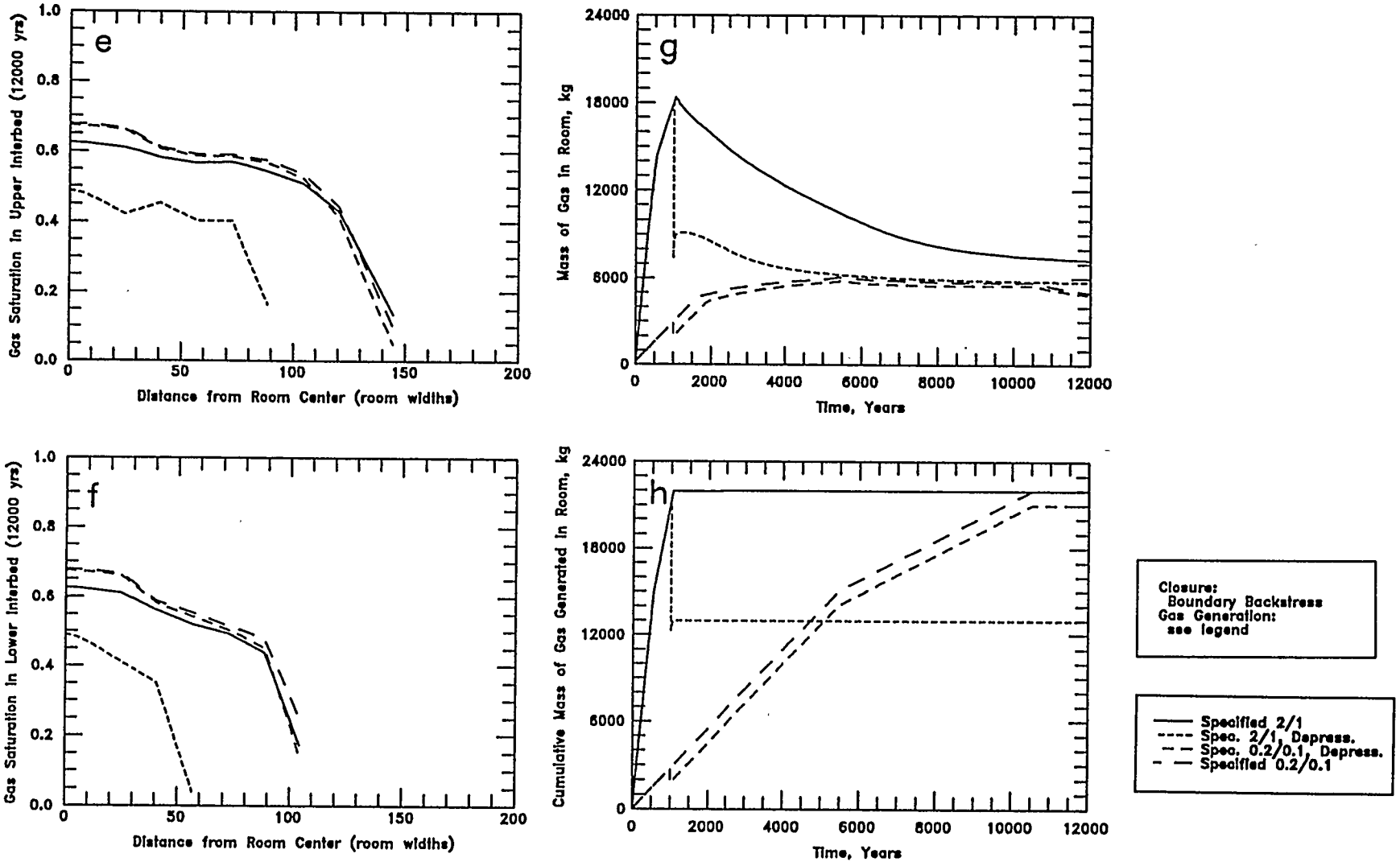

Figure 5-34 (e-h). Results from instantaneous room depressurization alternative conceptual model: e - Upper Interbed Gas Profile; f - Lower Interbed Gas Profile; g - Room Gas Mass; h - Gas Generation.

This page intentionally left blank

6.0 SUMMARY OF RESULTS AND CONCLUSIONS

A numerical model, TOUGH2/EOS8, was utilized to simulate the coupled processes of gas generation, room closure and expansion, and multiphase fluid flow. System response to gas generation was simulated with a two-dimensional vertical cross-section of a single, isolated disposal room. The disposal room was surrounded by homogeneous halite containing two anhydrite interbeds, one above and one below the room. The interbeds were assumed to have flow connections to the room through high-permeability, excavation-induced fractures.

TOUGH2/EOS8 was used to simulate system behavior under best-estimate (baseline) system parameters (Section 4.1) and to examine the sensitivity of system behavior to variations in gas-generation rate history and potential (Sections 4.2 and 5.2) and hydrologic parameters (Section 5.1). This model analysis used a deterministic approach, in which a single best-estimate value was selected for each parameter through an evaluation of available data. The best-estimate parameter values represent most likely values, but were not determined statistically (i.e., they were not mean, median, average, or expected values). Parameter uncertainty was characterized by selecting a minimum and maximum value for each parameter, representative of the extreme expected values. The selection of best- estimate parameter values and expected ranges was based on data available as of June, 1993.

Baseline simulations used two different specified gas-generation rate histories, 2/1 and 0.2/0.1. The 2/1 specified rate history (2 moles per drum per year to 550 years followed by 1 mole per drum per year to 1,050 years) assumed that gas generation was at rates estimated for brine-inundated conditions, while the 0.2/0.1 specified rate history (0.2 moles per drum per year to 5500 years followed by 0.1 moles per drum per year to 10,500 years) was consistent with estimated vapor-limited rates. These specified rates were not dependent on brine availability. A total gas potential of 1600 moles per drum was assumed for both cases.

Because these TOUGH2/EOS8 simulations were performed to examine system behavior and the sensitivity of system performance to variations in system parameters, and not to provide a comparison with regulatory standards, the TOUGH2/EOS8 simulations were extended beyond the 10,000-year regulatory time frame to 12,000 years. By 12,000 years, gas expulsion from the room had nearly ceased, room pressures had stabilized, and gas generation was complete. System behavior was evaluated by tracking four performance measures: (1) peak room pressure;

(2) maximum brine volume in the room; (3) total mass of gas expelled from the room over 12,000 years; and (4) the maximum gas migration distance in an interbed.

Sensitivity simulations were performed in which a single parameter value was varied to its minimum and maximum values with all other parameters held at best-estimate values. The effects of parameter uncertainty on simulation results were quantified by evaluating the change in the performance measures in response to parameter variations. Conceptual models for fracture formation and/or dilatation in the interbeds, a disturbed rock zone, density-driven phase segregation in the room, gas exsolution due to depressurization of the near-room brine, and instantaneous room depressurization representative of human intrusion, were also examined with TOUGH2/EOS8.

Simulation results provided conclusions about system behavior (Section 6.1), parameter sensitivity and importance rankings (Section 6.2), and modeling process coupling (Section 6.3). Conclusions were also drawn about how these simulation results can support the efforts to include these processes in WIPP performance assessment models and guide future experimental work (Section 6.4).

6.1 System Behavior

The baseline simulation results estimated system performance under best-estimate conditions (Section 4). TOUGH2/EOS8 results for the 2/1 and 0.2/0.1 specified gas-generation rate histories were presented in Figure 4-1. These specified rate histories produced a range of system behavior that was sufficient to qualitatively describe the performance of the WIPP repository under the expected range conditions. Simulations with brine-dependent gas-generation rates did not produce system behavior under best-estimate conditions that was significantly different from the specified 0.2/0.1 rate history.

In the first few hundred years subsequent to the backfilling and sealing of a disposal room, brine pressure gradients were inward, room closure was rapid, and brine flow was from the Salado Formation into the room. During this time, rising room pressures, which resulted from the combined effects of gas generation and room closure, eventually produced both a reversal of room closure and a reversal of the brine pressure gradient. The higher 2/1 gas-generation rate accelerated room pressurization, resulting in less room closure and an earlier onset of room

expansion and brine expulsion relative to the lower 0.2/0.1 rate case. The minimum early time void volume was 844 m^3 for the 2/1 rate history and 415 m^3 for the 0.2/0.1 rate history.

Brine inflow was also moderated somewhat by the higher 2/1 gas-generation rate. The peak cumulative brine inflow was 35 m^3 with the 2/1 rate as compared with 92 m^3 for the 0.2/0.1 rate. Brine inflow was greater into the bottom of the room because the lower composite interbed was three times thicker than the upper composite interbed. This brine inflow behavior produced brine saturation conditions in the room that were similar to what would be expected with gravity-driven phase segregation, even though gravitational effects were not simulated. Under gravity-driven phase segregation conditions, brine would migrate to the bottom of the room and gas would rise to the top of the room. With an initial brine volume of 24 m^3, the corresponding maximum brine volumes in the room were 59 m^3 and 116 m^3 for the 2/1 and 0.2/0.1 rates, respectively. Although the source rock for brine was the halite, brine inflow was predominantly through the interbeds. Brine in the halite near the interbeds flowed into the depressurized interbeds, which responded more quickly than the halite to near-atmospheric room pressure, and then into the room through the high-transmissivity room-interbed connections.

Immediately following the reversal of the brine pressure gradient, brine expulsion occurred to both the interbeds and the near-field halite. Gas expulsion was delayed until the capillary resistance in the interbeds was overcome. Brine expulsion was limited to about 50% of the brine inflow volume because brine saturations in the room were reduced to the residual brine saturation before all of the brine was expelled (at saturations below residual, brine is not mobile). Beyond 4,000 years there was no brine expulsion because all brine in the room was at or below residual brine saturation.

Gas expulsion did not start until brine expulsion was completed. In TOUGH2/EOS8 simulations, gas movement through the interbeds required the displacement of brine into the halite surrounding the interbeds. Gas expulsion occurred first to the upper interbed because of the lower brine saturations at the top of room that resulted from brine inflow. However, approximately 70% of the total gas mass expelled was to the lower interbed because of its greater thickness. The total mass of gas expelled ranged from approximately 15,000 kg (for the 2/1 rate) to 17,000 kg (for the 0.2/0.1 rate) of H_2, which was 70 to 80% of the approximately 22,000 kg of gas generated.

Room expansion was most rapid prior to gas expulsion, although the rate of expansion was always slower than the initial rate of room closure. Room pressurization and room expansion slowed at the onset of gas expulsion from the room. As the rate of gas expulsion exceeded the specified gas-generation rate, expansion ceased and the room started to close again. Re-closure of the room was proportional to the degree of previous expansion. With the 2/1 rate there was much more room expansion and re-closure than with the 0.2/0.1 rate.

The highest peak room pressure (19 MPa) was reached with the specified 2/1 rate history. However, at times beyond 5,000 years, room pressures were higher for the specified 0.2/0.1 rate because of the slow, long-duration gas generation. The total mass of gas expelled was actually greater for the lower 0.2/0.1 rates, because a high room pressure was maintained for a relatively long duration. A high early-time pressure does not necessarily result in maximum gas release if the high pressure is not maintained.

In TOUGH2/EOS8 baseline simulations, the effects of interbed fracture were not included and pore pressures above lithostatic were not mitigated by fracturing. With both the 2/1 and 0.2/0.1 specified rate histories, room pressures above lithostatic were maintained for several thousand years. Actual repository pressures will likely be limited to near-lithostatic due to interbed fracturing. The greater than lithostatic simulated pressures indicate that there is the possibility that existing fractures will dilate or new fractures will form if a significant portion of the 1,600 moles per drum gas-generation potential is realized.

Despite the differences in gas-generation rate history, room closure and expansion, brine inflow, and room pressure history between the specified 2/1 and 0.2/0.1 cases, the simulations achieved a relatively common final state. The final (12,000 year) mass of gas expelled released and gas migration distances in the interbeds were quite similar. In both cases, the gas phase migrated approximately 150 room widths in the upper composite interbed and 115 room widths in the lower composite interbed. The difference between the two interbeds is due differences in the thickness and in the mass of gas expelled to each interbed. These simulated gas migration distances compare favorably with estimates from mass-balance calculations made in Section 1.2.2 for the fully-consolidated room geometry (83 to 130 room widths). Gas migration was negligible between 10,000 and 12,000 years. This corresponds to the time at which the rate of gas expulsion declined to near zero. The gas migration distance was not sensitive to differences in either the magnitude or duration of gas generation, as long as the total mass of gas generated was constant.

In brine-dependent rate simulations using best-estimate properties, there was not enough brine inflow to produce brine-inundated conditions in the room (i.e., brine saturation never reached the threshold saturation of 0.3). The maximum average room brine saturation of 0.28 was barely larger than the residual brine saturation of 0.276. Consequently, brine-dependent gas generation proceeded at near the vapor-limited rates and results were very similar to the specified 0.2/0.1 results.

The hypothesis that gas generation may be a self-limiting or at least a self-regulating process (Section 1.2.3) is supported by these results. Approximately 100 m^3 to 200 m^3 of brine is required to generate the anoxic corrosion potential of 1,050 moles per drum in a disposal room. Under best-estimate conditions, the maximum brine volume in the room was only 59 m^3 with the specified 2/1 rate, not enough to drive gas generation to the complete exhaustion of potential. With the specified 0.2/0.1 rate history, the maximum brine in the room was 116 m^3. Even without considering the effects of brine consumption by the corrosion reactions, the volume of brine inflow required to assure potential-limited rather than brine-limited gas generation requires very low (less than the 0.2/0.1 rates) gas-generation rates in the room. Under this scenario, a large gas-generation rate is only likely for a short period of time, after which the brine supply is exhausted and cannot be replenished by inflow due to high room pressures.

The difference in brine inflow between very low gas-generation rates (i.e., specified 0.2/0.1) and no gas generation is significant. Only in the case of no gas generation does the brine volume in the room exceed 200 m^3. However, many factors that could impact these brine volume estimates (and the brine-dependent rate predictions) were not included in the TOUGH2/EOS8 model. It is likely that rooms at the ends of panels will have more brine inflow than other rooms due to their increased capture zone. There could be brine saturation gradients across the repository, causing local differences in gas-generation rate. This in turn would cause local pressure gradients and flow within the repository. Brine may accumulate in the downdip portion of the repository, resulting in higher brine saturations in downdip rooms. Finally, there is a large uncertainty in the multiphase flow characteristics in the room and in the Salado Formation.

The baseline simulation results indicated that: (1) the two specified rate histories, 2/1 and 0.2/0.1, tested system behavior over a range of conditions that could be considered representative of most brine-dependent conditions; and (2) under best-estimate conditions, limited

brine availability resulted in little mobile brine in the room, and the corresponding brine-dependent gas-generation rate history was very similar to the specified 0.2/0.1 rate history.

6.2 Parameter Sensitivity and Importance Rankings

Sensitivity and importance coefficients for each system parameter were calculated for each of the four system performance measures (Section 5). Parameter sensitivity and importance coefficients for the specified 2/1 rate history for all hydrologic parameters were presented in Tables 5-1 through 5-6. Discussion in this Section focuses on the 2/1 rate history results. Sensitivity and importance coefficients were similar for the 0.2/0.1 rate simulations; significant differences are noted. Importance coefficients were also calculated for gas-generation parameters and alternative model conceptualizations. A total importance coefficient quantifies the change in a performance measure relative to its baseline value over the expected range of a system parameter. The total importance coefficient can be used to rank which system parameters have the greatest effect on a given performance measure. Total importance coefficients and the associated parameter rankings are influenced by the parameter ranges and the baseline values of the performance measures.

Parameter rankings by importance coefficient are presented for each of the four performance measures: maximum room pressure (Table 6-1); maximum brine volume in the room (Table 6-2); mass of gas expelled (Table 6-3); and maximum gas migration distance (Table 6-4). Note that the importance coefficients are normalized to the baseline value of the performance measure (Equation 2-15). For the baseline specified 2/1 rate histories, these values are: maximum room pressure = 19.1 MPa; maximum brine volume in the room = 59 m^3; mass of gas expelled = 14,900 kg; and maximum gas migration distance = 150 room widths (120 room widths is maximum extent of gas saturation above residual). Tables 6-1 through 6-4 also include maximum sensitivity coefficients.

Table 6-1. Importance Rankings for Maximum Room Pressure

Rank	Parameter	Maximum Sensitivity Coefficient	Total Importance Coefficient
1	Gas-Generation Potential	0.15	0.20
1	Interbed Permeability	0.10	0.20
3	Interbed Fracture	--	0.19
4	Halite Permeability	0.09	0.14
4	Gas-Generation Rate	0.08	0.14
6	Halite Porosity	0.09	0.10
7	Interbed Threshold Pressure	0.01	0.09
8	Initial Salado Brine Pressure	0.20	0.07
9	Closure Coupling Method	--	0.06
10	Halite Rock Compressibility	0.05	0.05
10	Interbed Porosity	0.05	0.05
12	Interbed Pore-Size λ	0.05	0.04
12	Gas Exsolution	--	0.04
12	Halite van Genuchten/Parker	--	0.04
15	Interbed van Genuchten/Parker	--	0.03
16	Interbed Thickness	0.03	0.02
17	Initial Brine in Room	0.00	0.01
18	Disturbed Rock Zone	--	0.00
	Interbed Rock Compressibility	0.00	0.00
	Interbed Residual Brine Saturation	0.00	0.00
	Interbed Residual Gas Saturation	0.00	0.00
	Halite Residual Brine Saturation	0.00	0.00
	Halite Residual Gas Saturation	0.00	0.00
	Halite Pore-Size λ	0.00	0.00
	Halite Threshold Pressure	0.00	0.00
	Room Permeability	0.00	0.00
	Room Residual Brine Saturation	0.00	0.00
	Room Residual Gas Saturation	0.00	0.00
	Room Pore-Size λ	0.00	0.00
	Gravitational Effects	--	0.00

Table 6-2. Importance Rankings for Maximum Brine Volume in Room

Rank	Parameter	Maximum Sensitivity Coefficient	Total Importance Coefficient
1	Halite Permeability	0.50	6.78
2	Initial Brine in Room	0.40	2.64
3	Interbed Permeability	0.35	1.32
4	Gas-Generation Rate	0.68	0.65
5	Halite Porosity	0.31	0.54
6	Initial Salado Brine Pressure	0.92	0.30
7	Disturbed Rock Zone	--	0.28
8	Halite Rock Compressibility	0.19	0.21
9	Closure Coupling Method	--	0.06
10	Gas Exsolution	--	0.04
10	Halite van Genuchten/Parker	--	0.04
12	Interbed Residual Gas Saturation	0.02	0.02
12	Interbed Porosity	0.01	0.02
14	Halite Residual Gas Saturation	0.01	0.01
14	Halite Pore-Size λ	0.01	0.01
14	Room Residual Brine Saturation	0.01	0.01
14	Gravitational Effects	--	0.01
18	Gas-Generation Potential	0.00	0.00
	Interbed Fracture	--	0.00
	Interbed van Genuchten/Parker	--	0.00
	Interbed Threshold Pressure	0.01	0.00
	Interbed Thickness	0.00	0.00
	Interbed Rock Compressibility	0.00	0.00
	Interbed Residual Brine Saturation	0.00	0.00
	Interbed Pore-Size λ	0.00	0.00
	Halite Residual Brine Saturation	0.00	0.00
	Halite Threshold Pressure	0.00	0.00
	Room Permeability	0.00	0.00
	Room Residual Gas Saturation	0.00	0.00
	Room Pore-Size λ	0.00	0.00

Table 6-3. Importance Rankings for Mass of Gas Expelled from Room

Rank	Parameter	Maximum Sensitivity Coefficient	Total Importance Coefficient
1	Gas-Generation Potential	1.16	1.58
2	Halite Permeability	0.89	1.03
3	Interbed Threshold Pressure	0.06	0.93
4	Interbed Permeability	0.83	0.91
5	Interbed Porosity	0.43	0.41
6	Initial Salado Brine Pressure	1.41	0.38
7	Interbed Pore-Size λ	0.36	0.28
8	Halite Porosity	0.24	0.25
9	Gas-Generation Rate	0.17	0.15
10	Interbed Fracture	--	0.13
11	Room Residual Gas Saturation	0.02	0.11
12	Closure Coupling Method	--	0.10
13	Halite van Genuchten/Parker	--	0.09
13	Room Pore-Size λ	0.01	0.09
15	Halite Rock Compressibility	0.08	0.07
15	Room Residual Brine Saturation	0.00	0.07
17	Gas Exsolution	--	0.04
18	Interbed van Genuchten/Parker	--	0.03
19	Gravitational Effects	--	0.02
20	Disturbed Rock Zone	--	0.01
20	Interbed Thickness	0.02	0.01
20	Interbed Residual Brine Saturation	0.01	0.01
20	Interbed Residual Gas Saturation	0.01	0.01
20	Initial Brine in Room	0.00	0.01
25	Halite Pore-Size λ	0.01	0.00
	Halite Threshold Pressure	0.01	0.00
	Interbed Rock Compressibility	0.00	0.00
	Halite Residual Brine Saturation	0.00	0.00
	Halite Residual Gas Saturation	0.00	0.00
	Room Permeability	0.00	0.00

Table 6-4. Importance Rankings for Maximum Gas Migration Distance

Rank	Parameter	Maximum Sensitivity Coefficient	Total Importance Coefficient
1	Interbed Porosity	5.15	5.37
2	Interbed Permeability	0.91	1.51
3	Gas-Generation Potential	0.85	1.14
4	Halite Permeability	0.90	0.90
4	Interbed Threshold Pressure	0.06	0.90
6	Halite van Genuchten/Parker	--	0.80
7	Interbed Fracture	--	0.66
8	Interbed Thickness	1.11	0.61
9	Initial Salado Brine Pressure	2.39	0.60
10	Interbed Pore-Size λ	0.19	0.33
11	Interbed van Genuchten/Parker	--	0.20
11	Gas Exsolution	--	0.20
13	Interbed Residual Brine Saturation	0.17	0.17
13	Interbed Residual Gas Saturation	0.17	0.17
15	Halite Porosity	0.15	0.13
16	Closure Coupling Method	--	0.10
17	Disturbed Rock Zone	--	0.00
	Gas-Generation Rate	0.00	0.00
	Initial Brine in Room	0.00	0.00
	Interbed Rock Compressibility	0.00	0.00
	Halite Rock Compressibility	0.00	0.00
	Halite Residual Brine Saturation	0.00	0.00
	Halite Residual Gas Saturation	0.00	0.00
	Halite Pore-Size λ	0.00	0.00
	Halite Threshold Pressure	0.00	0.00
	Room Permeability	0.00	0.00
	Room Residual Brine Saturation	0.00	0.00
	Room Residual Gas Saturation	0.00	0.00
	Room Pore-Size λ	0.00	0.00
	Gravitational Effects	--	0.00

While a large sensitivity coefficient is indicative that the system is sensitive to a certain parameter, a small sensitivity coefficient is not necessarily indicative of an insensitive parameter. A small sensitivity coefficient can also be caused by a parameter value (P) that is much lower than the baseline value (P_o), because sensitivity is proportional to $P/(P_o-P)$ as indicated by Equation 2-13. This effect can produce contradictorily low S^- sensitivity coefficients in certain cases where the system is actually quite sensitive to variations in a parameter at less than the baseline value. This effect is not present in importance coefficients because the importance coefficient is based on changes in performance measures (Equation 2-15), not on changes in parameter values. Therefore, a parameter ranking by sensitivity coefficient may be misleading if the corresponding importance coefficients are not also considered. A high importance coefficient with a small sensitivity coefficient may indicate a parameter that is important only due to an extended range, but it may also indicate a parameter that is sensitive to variations at less than the baseline value.

A total of 30 parameters are ranked in Tables 6-1 through 6-4. These include: 5 disposal room parameters (see Table 3-1); 8 halite parameters (see Table 3-2), 8 anhydrite interbed parameters (see Table 3-3); 2 alternative multiphase relationships (van Genuchten/Parker in both the halite and the interbeds); 2 gas-generation parameters (rate and potential); 4 alternative conceptual models (interbed fracture, disturbed rock zone, gravitational effects, and gas exsolution); and the selection of closure coupling method (boundary backstress or pressure lines).

Maximum room pressure is dependent on the coupled effects of gas generation, room closure and expansion, and brine and gas flow between the room and the Salado Formation. Total importance coefficients for the maximum room pressure performance measure (Table 6-1) were much smaller than for the other performance measures, indicating that maximum room pressure does not change very significantly from the baseline value of 19.1 MPa. In most simulations maximum room pressures were above lithostatic, a condition expected to initiate fracturing in the interbeds and alter interbed properties. The low importance coefficients suggest that, with the TOUGH2/EOS8 conceptualization, less-than-lithostatic maximum pressures are not likely to occur in response to variations of parameters over the expected range of uncertainty. This conclusion is supported by the fact that the interbed fracture conceptual model, which does limit pressures to near-lithostatic, was one of the most important parameters to maximum room pressure. Other important parameters were: gas-generation rate, which influences early-time pressures; gas-generation potential, which influences late-time pressures;

and halite and interbed permeability, which control the rate of gas and brine flow into and out of the room.

Maximum brine volume in the room is dependent on the initial brine in the waste and backfill, and on the brine inflow, which is driven by the Salado physical properties and the brine pressure gradient. By far the most important parameter influencing maximum brine volume in the room (Table 6-2) was halite permeability (I=6.78). Even though brine inflow occurs predominantly through the interbeds, the halite provides the source for the brine, and halite permeability, halite porosity (I=0.54), and halite rock compressibility (I=0.21) were important parameters. The importance of the near-field halite was also shown by the large importance coefficient for the disturbed rock zone model (I=0.28). The initial brine in the room was very important (I=2.64) due to the direct correlation between maximum brine in the room and initial brine in the room. The interbed permeability (I=1.32) was important because interbeds are a conduit for brine inflow, while the gas-generation rate (I=0.65) and initial Salado brine pressure (I=0.30) were important because they influenced the brine pressure gradient.

Both the maximum room pressure and maximum brine in the room performance measures were influenced by how gas-generation was implemented in TOUGH2/EOS8 and by the room conceptualization. Because the sensitivity and importance coefficients were calculated from specified gas-generation rate results, the importance of parameters controlling brine availability in the room may have been underestimated. For example, the initial brine volume in the room influences brine availability and brine-dependent gas generation rates, which would likely have an effect on room pressurization. However, in the specified rate simulations, maximum room pressure was not sensitive to initial brine.

The mass of gas expelled from the room performance measure (Table 6-3) identifies several processes that are important to system behavior. The most important parameter was the gas-generation potential (I=1.58). Its importance is based on the assumption that all of the gas potential is exhausted and is not limited by brine availability. The high importance of gas potential supports the observation in Section 6.1 that the total mass of gas expelled is strongly influenced by the mass of gas generated (potential), but is not overly dependent on the gas-generation rate (I=0.15). Gas expulsion was also sensitive to several interbed parameters (threshold pressure (I=0.93), permeability (I=0.91), porosity (I=0.41), and pore-size λ (I=0.28)) and to initial Salado brine pressure (I=0.38). An interesting result is the high importance of halite permeability (I=1.03) and, to a lesser extent, halite porosity (I=0.25). The

high importance coefficients of these halite parameters emphasizes that the displacement of brine from the interbeds into the surrounding halite is a controlling process for gas expulsion and gas migration.

For the gas migration distance performance measure (Table 6-4), the most important parameter was interbed porosity (I=5.37). The interbed porosity is important because it controls the gas storage volume. A low porosity results in a large gas migration distance. Other important interbeds parameters were: interbed permeability (I=1.51), interbed threshold pressure (I=0.90), the interbed fracture model (I=0.66), and interbed thickness (I=0.61). The gas-generation potential (I=1.14) was an important parameter because a greater mass of gas generated results in greater gas expulsion and further gas migration. Halite permeability (I=0.90) and halite van Genuchten/Parker multiphase relationships (I=0.80) were important because, as with gas expulsion, a limiting condition on gas movement in the interbeds was the displacement of brine into the halite. The initial Salado brine pressure (I=0.60) and the other interbed multiphase parameters (residual brine and gas saturation, pore-size λ, van Genuchten/Parker relationships) were of moderate importance.

The total importance coefficients listed in Tables 6-1 through 6-4 are also presented in graphical form. Importance coefficients for each performance measure are shown in Figure 6-1 for the disposal room parameters, Figure 6-2 for the halite physical parameters, Figure 6-3 for the halite multiphase parameters, Figure 6-4 for the interbed physical parameters, and Figure 6-5 for the halite multiphase parameters. Figure 6-6 shows importance coefficients for gas-generation parameters and closure coupling method, while Figure 6-7 shows importance coefficients for the alternative conceptual models. These Figures are useful to identify the relative importance of each parameter to all performance measures.

The importance coefficients for the gas expulsion and gas migration distance performance measures provide the most guidance to system sensitivity with respect to regulatory standards (particularly 40 CFR 268.6). With respect to gas migration distance the most important parameters were: interbed porosity; interbed permeability; gas-generation potential; halite permeability; and interbed threshold pressure. These same five parameters were most important to gas expulsion. The following parameters were of moderate importance to these two performance measures: initial Salado brine pressure; interbed fracture model; interbed thickness; and halite van Genuchten/Parker relationships. The moderate importance of the interbed fracture and halite van Genuchten/Parker models are noteworthy because neither model is supported by WIPP-specific data.

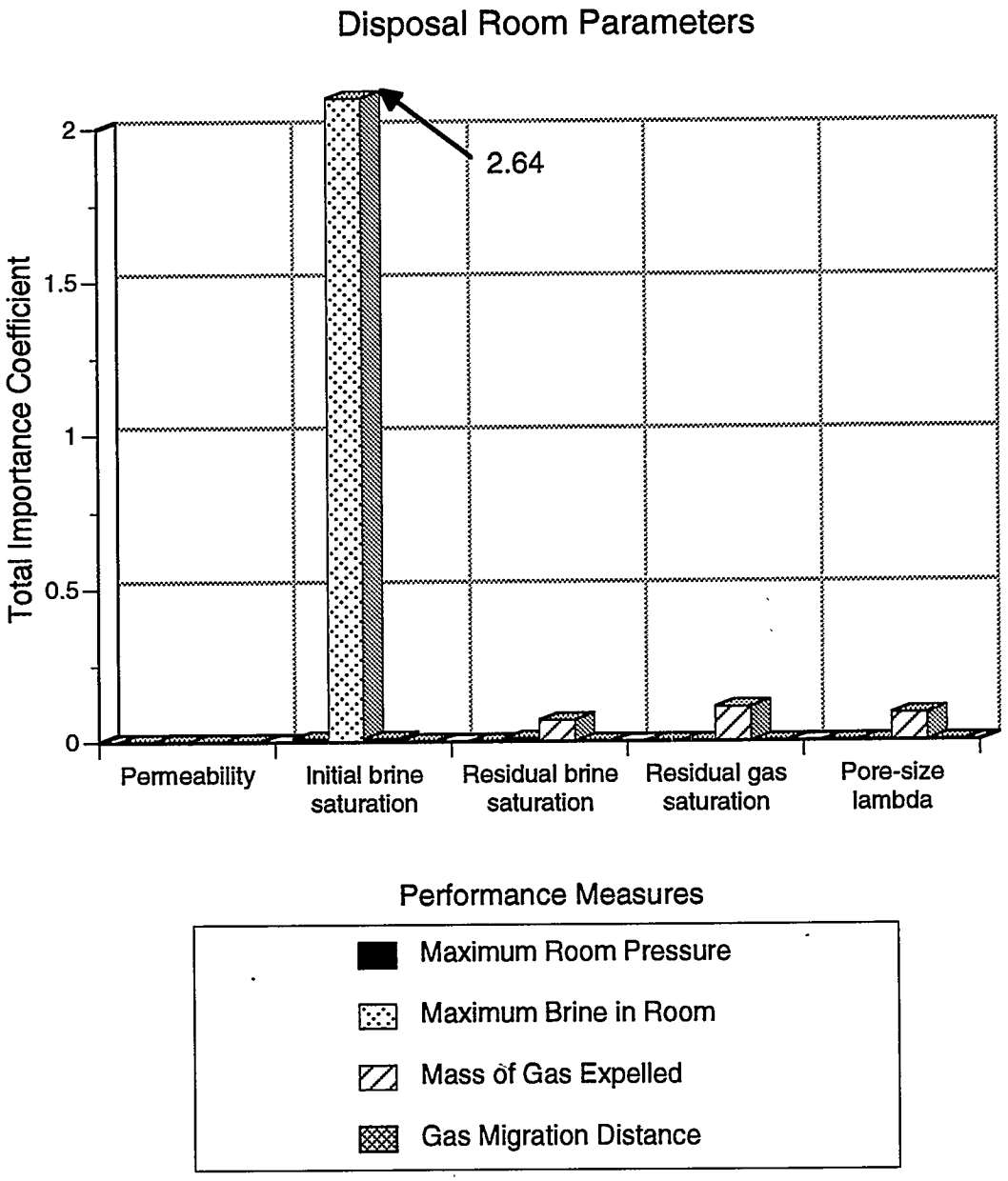

Figure 6-1. Total importance coefficients for each performance measure for disposal room parameters.

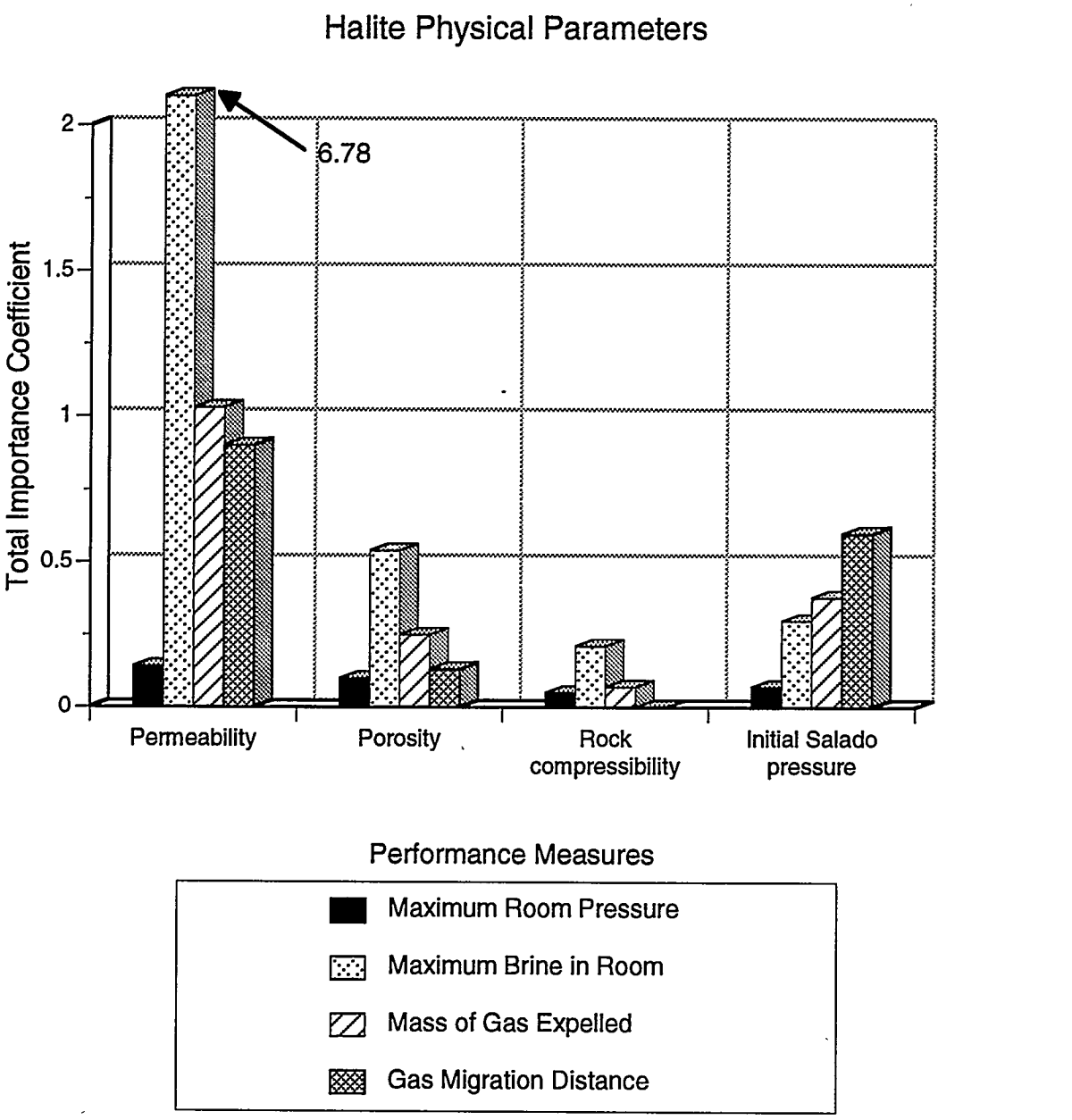

Figure 6-2. Total importance coefficients for each performance measure for halite physical parameters.

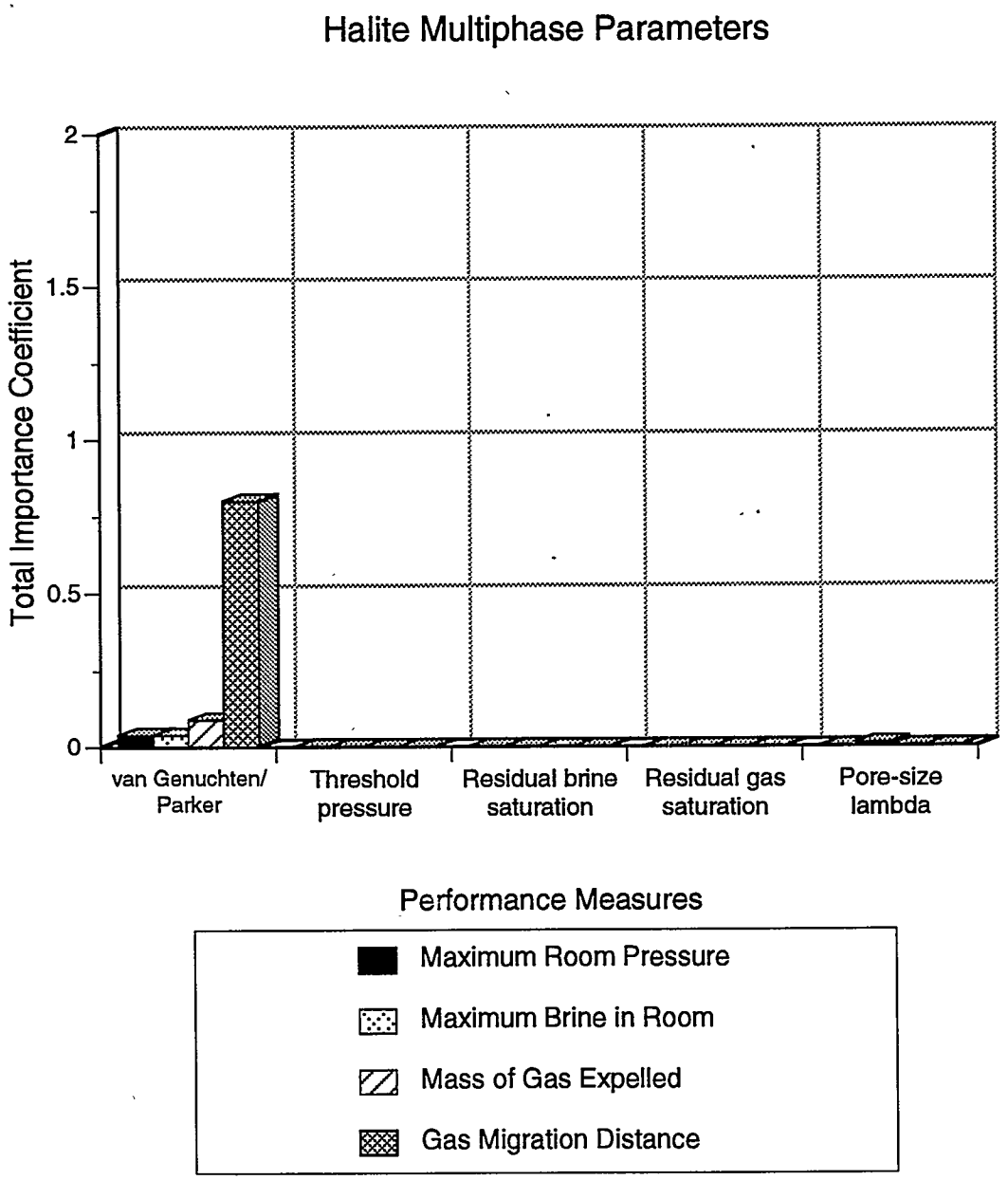

Figure 6-3. Total importance coefficients for each performance measure for halite multiphase flow parameters.

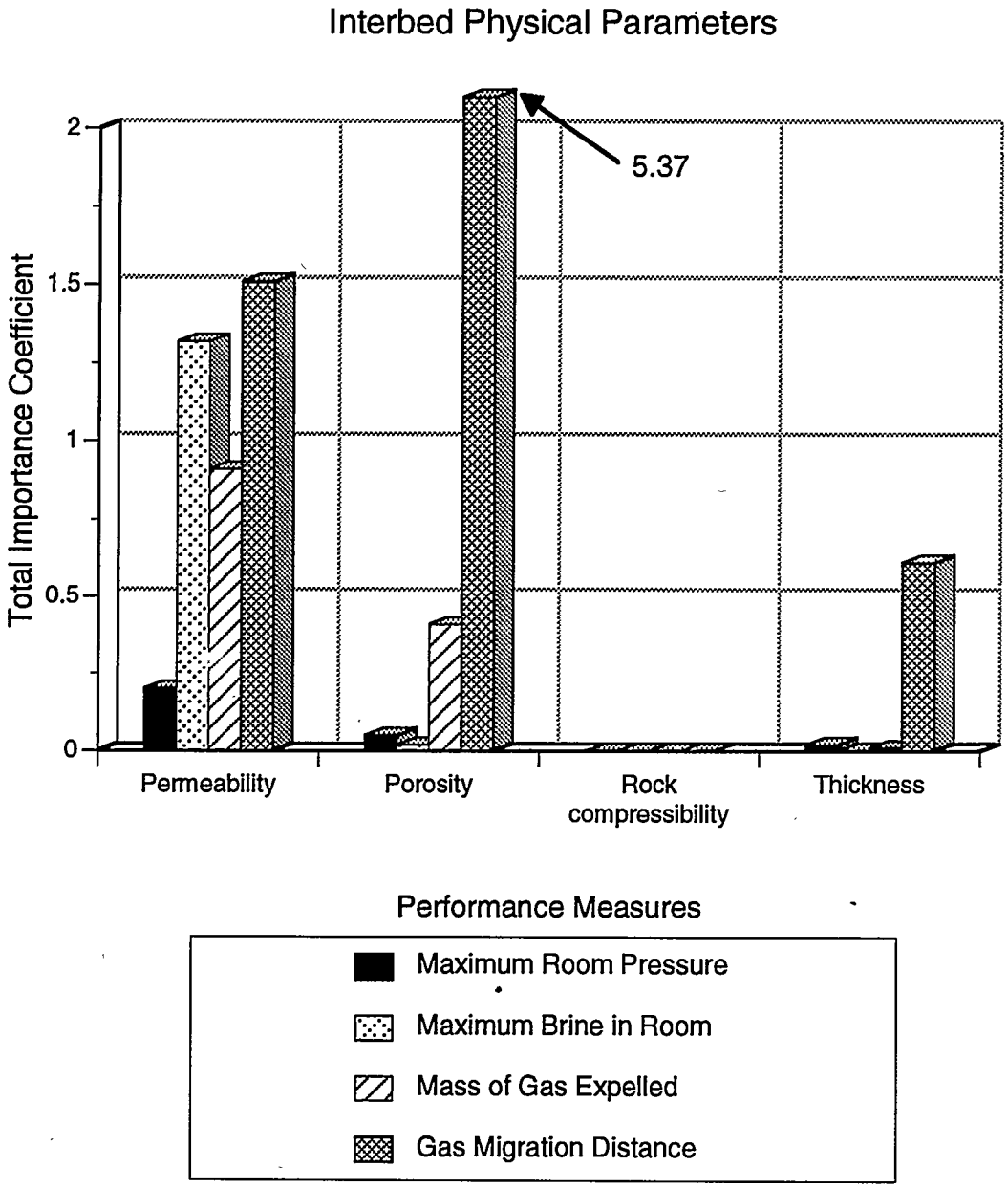

Figure 6-4. Total importance coefficients for each performance measure for interbed physical parameters.

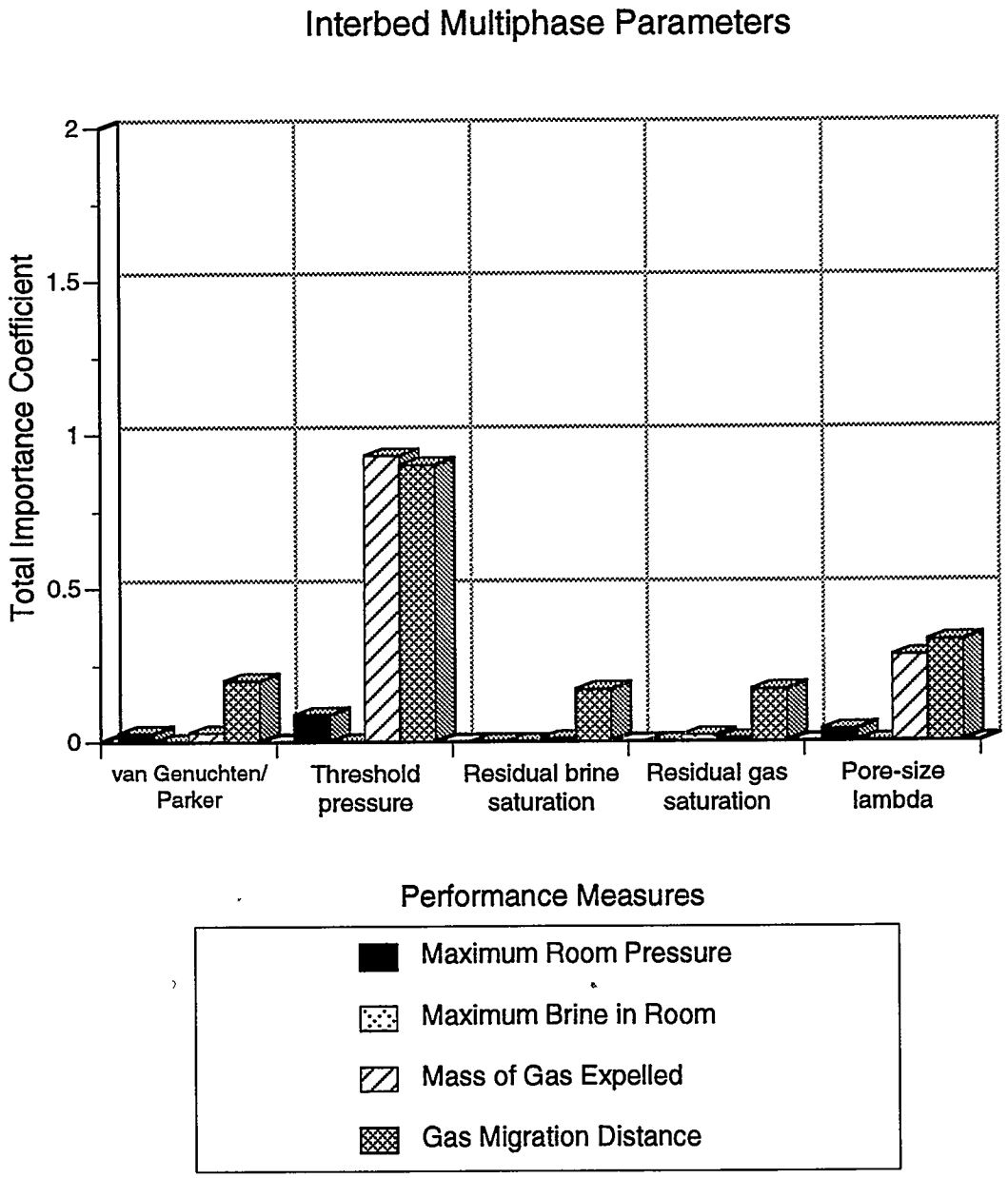

Figure 6-5. Total importance coefficients for each performance measure for interbed multiphase flow parameters.

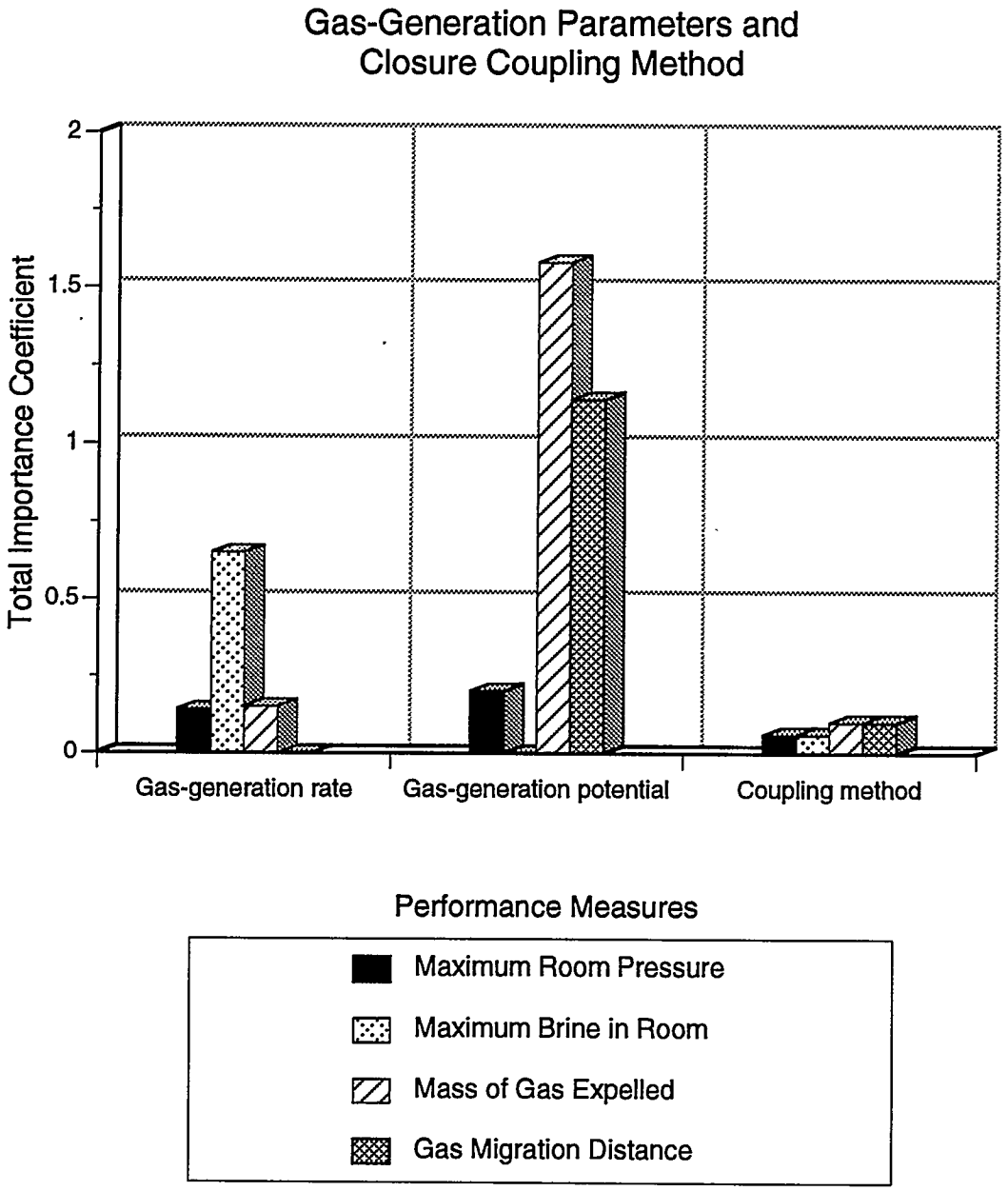

Figure 6-6. Total importance coefficients for each performance measure for gas-generation parameters and closure coupling method.

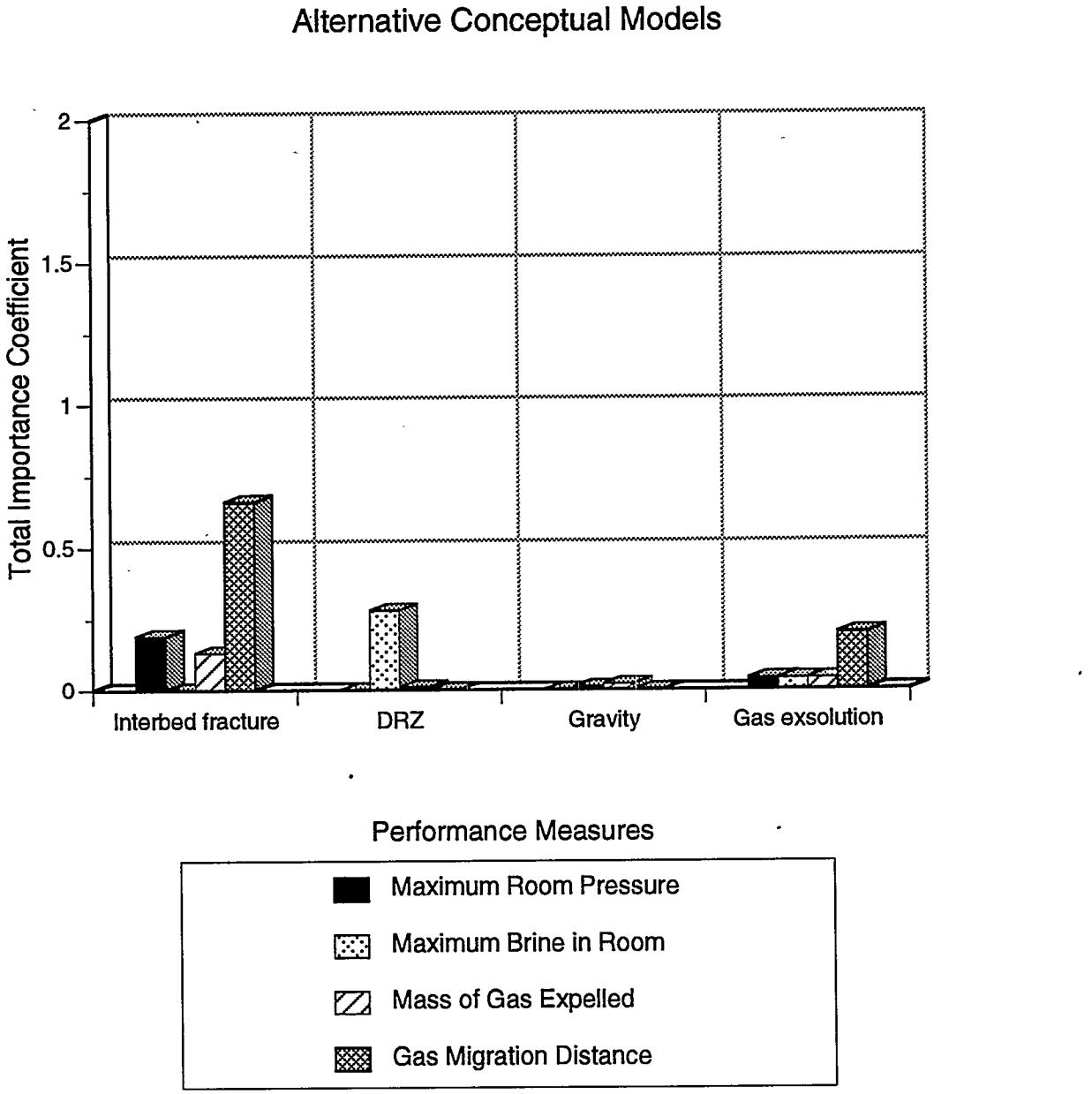

Figure 6-7. Total importance coefficients for each performance measure for alternative conceptual models.

Also of interest are the following parameters, which were completely insensitive for all of the performance measures: gravitational effects; room permeability; interbed compressibility; and halite multiphase parameters (residual brine and gas saturation, pore-size λ, and threshold pressure). These parameters with zero importance may identify limitations of the TOUGH2/EOS8 model. For example, the distribution of brine and gas within the room is dependent on room permeability and on the heterogeneous nature of the waste and backfill. In TOUGH2/EOS8, a homogeneous room is simulated and gravitational effects are ignored, effectively eliminating the importance of room permeability to system response.

The zero importance of the halite multiphase parameters may also be misleading. Given the complete lack of WIPP-specific measurements of multiphase parameters, there is some concern as to whether the uncertainty in these parameters is adequately captured in the TOUGH2/EOS8 importance coefficients. The current parameters are based solely upon analogue materials and theoretical considerations. It is not known if the sensitivity evaluation encompassed the range of uncertainty that is present in the two-phase characteristic curves. As an example, halite threshold pressure is expected to be high (10.3 MPa) based on theoretical considerations, but it has never been measured. Simulations which combined a lower (2.1 MPa) threshold pressure with an increased halite permeability resulted in significant gas expulsion to the halite and a significant decrease in gas migration distance in the interbeds (Section 5.1.2.1). If the measured halite threshold pressure turns out to be low, and there are zones (i.e., a DRZ) of higher permeability present, then enhanced gas storage in the halite could have a significant beneficial impact on gas migration. This uncertainty was not captured in the TOUGH2/EOS8 importance coefficients.

Similarly, the use of the van Genuchten/Parker multiphase model in the halite had moderate importance and resulted in a decrease in the mass of gas expelled from the room and a decrease in gas migration distance (Section 5.1.2.2), while the use of the van Genuchten/Parker model in the interbeds had low importance and increased gas expulsion and gas migration distance (Section 5.1.3.2). Given the complete lack of WIPP-specific van Genuchten/Parker parameters, its importance for the gas migration performance measures is somewhat uncertain and may be underestimated.

WIPP PA simulations using the BRAGFLO code (WIPP PA Department, 1993b) identified the following parameters as being very important to gas and brine migration for undisturbed performance: initial brine saturation in the waste; interbed permeability; gas-generation rate

controls; and shaft seal permeability (> 200 years). They also identified the following important parameters: interbed porosity; halite permeability; shaft seal permeability (0-200 years); Brooks-Corey/van Genuchten-Parker pointer (described below); and DRZ porosity. There are some conceptual differences between the WIPP PA Department (1992b) model and the TOUGH2/EOS8 model. The WIPP PA model calculates a brine-dependent gas-generation rate and considers a repository scale including shafts. Despite these conceptual differences, there is agreement between the important parameters in the two models.

Both models identified interbed permeability, interbed porosity, and halite permeability as the most important physical parameters. The TOUGH2/EOS8 gas-generation potential and the WIPP PA gas-generation controls were both important because they influence the mass of gas generated. The WIPP PA Brooks-Corey/van Genuchten-Parker pointer, which identifies the relative permeability and capillary pressure relationships to be used, influences multiphase flow as does the TOUGH2/EOS8 interbed threshold pressure. The high importance of the initial brine saturation in the room was not reproduced with TOUGH2/EOS8 because the importance coefficients were calculated from specified gas-generation rate simulations. However, the initial brine saturation in the room does have a large TOUGH2/EOS8 importance coefficient for the maximum brine volume in the room performance measure. If brine-inundated conditions were present in the room, brine-dependent rate simulations might produce similarly large importance coefficients for other performance measures.

6.3 Conclusions

TOUGH2/EOS8 was used in a deterministic framework to simulate the interdependent processes of gas generation, room closure and expansion, and multiphase brine and gas flow. Repository simulations were performed at a disposal room scale. TOUGH2/EOS8 simulation and sensitivity results were similar to the WIPP PA Department (1993b) stochastic results using BRAGFLO, suggesting that the TOUGH2/EOS8 deterministic approach can be used to evaluate system performance and alternative conceptual models in support of WIPP PA, and in addition can provide useful physical insight as to why certain parameters are important to various repository performance measures.

The methodology allows conceptual models to be quantitatively evaluated at a sub-system level using specific mechanistically-based performance measures, rather than at the level of overall repository performance, as is required of the WIPP PA model.

TOUGH2/EOS8 baseline simulations identified the following important processes:

(1) two specified gas-generation rate histories, 2/1 (representative of rates under brine-inundated conditions) and 0.2/0.1 (representative of rates under vapor-limited conditions) tested system behavior over a range of conditions considered to bound the range of expected brine-dependent conditions;

(2) the linear correlation brine-dependent method (analogous to the method used by WIPP PA) predicts brine-dependent rates that are similar to what would be expected from a puddle of brine on the floor but are greater than the rates predicted if brine forms a capillary fringe in the room;

(3) limited brine availability under best-estimate conditions resulted in brine-dependent gas-generation rate histories, predicted assuming a capillary fringe, that were very similar to the specified 0.2/0.1 rate history;

(4) under best-estimate conditions, room pressures in excess of lithostatic could theoretically be maintained for thousands of years, providing there is no alteration of the interbed properties (however, alteration is likely to occur under such high pressures);

(5) very low gas-generation rates (less than 0.1 moles per drum per year) are required to keep room pressures below lithostatic if there is no alteration of the interbed properties in response to interbed fracturing.

(6) both the total mass of gas expelled from the room and the long-term gas migration distance are very dependent on the total mass of gas generated but are not particularly sensitive to the rate or duration of gas-generation; and

(7) an important limitation to gas movement in the interbeds is the displacement of brine by gas into the surrounding halite.

The TOUGH2/EOS8 sensitivity simulations identified the following parameters as important to gas expulsion and migration away from a disposal room: interbed porosity; interbed permeability; gas-generation potential; halite permeability; and interbed threshold pressure. In addition, there is some concern as to whether the uncertainty in multiphase flow parameters is adequately captured in the TOUGH2/EOS8 importance coefficients, given the lack of WIPP-specific data. Simulations also showed that the inclusion of an interbed fracture model and a disturbed rock zone model would influence system performance.

A comparison of the importance coefficients for hydrologic and gas-generation parameters with the importance coefficients for the alternative conceptual models and closure coupling methodology provides an indication of the direction for future work. In these simulations, the physical parameters had a high importance relative to the conceptual models, suggesting that uncertainty can be reduced by refining parameter best estimates and ranges. A high relative importance for the conceptual models would suggest that uncertainty can be reduced by improving the conceptual models. The low importance for the conceptual models in this study (except for the interbed fracture and DRZ models) suggests that the conceptual models in TOUGH2/EOS8 adequately capture the important dynamics of system behavior.

The following conclusions, with implications for future work, are drawn from the TOUGH2/EOS8 simulation results:

(1) The deterministic approach used with TOUGH2/EOS8 can be used to support WIPP PA sensitivity and uncertainty simulations, to make choices between alternative conceptual models, and to provide insight to controlling physical processes in a completely coupled system. However, it can not be used to address regulatory compliance.

(2) The fluid flow and closure coupling methodologies currently implemented in TOUGH2/EOS8 and BRAGFLO are important (see Freeze et al., 1995) and adequately model the coupled processes.

(3) A fundamental difference between the TOUGH2/EOS8 and WIPP PA conceptual models is the treatment of gas generation. TOUGH2/EOS8 uses a simplified approach with bounding specified gas-generation rates. Given that the mass of gas generated is one of the most important model parameters, further study of gas-

generation and multiphase flow processes must be performed to determine whether this simplified approach would be defensible in the WIPP PA model.

(4) Refinement of parameter estimates for the other important parameters: interbed porosity and permeability; halite permeability; and interbed threshold pressure; should continue. In-situ permeability testing is ongoing (see Beauheim et al., 1991 and Beauheim et al., 1993a). Threshold pressure testing is also being initiated.

(5) A conceptual model for formation and propagation of fractures in the interbeds must be developed, given the TOUGH2/EOS8 simulated pressures that were greater than lithostatic. Due to the high importance of interbed permeabilty and porosity to gas migration, a defensible model for fracture permeability and porosity must be developed. In addition to the simplified porosity model used in TOUGH2/EOS8, a model similar to the aperture model (Section 5.3.2.1) and a dual-porosity-based model should be considered.

(6) The WIPP-specific two-phase characteristic relationships must be investigated. Laboratory studies (Howarth, 1993) have already been planned to address this issue. Alterations to the interbed two-phase properties may be particularly important with interbed fracturing.

(7) Additional conceptual models may be needed to simulate the effects of detailed heterogeneous halite stratigraphy, repository scale behavior, a stratigraphically dipping repository, and interbed heterogeneity. These conceptual models as well as interbed fracture and DRZ models, could be tested deterministically at a sub-system level with TOUGH2/EOS8 (or a conceptually equivalent BRAGFLO setup) to evaluate whether or not these additional conceptual complexities should be implemented into overall repository performance model.

This page intentionally left blank

7.0 REFERENCES

Bear, J. 1972. *Dynamics of Fluids in Porous Media.* New York, NY: American Elsevier.

Beauheim, R.L., G.J. Saulnier, Jr., and J.D. Avis. 1991. *Interpretation of Brine-Permeability Tests of the Salado Formation at the Waste Isolation Pilot Plant Site: First Interim Report.* SAND90-0083. Albuquerque, NM: Sandia National Laboratories.

Beauheim, R.L., R.M. Roberts, T.F. Dale, M.D. Fort, and W.A. Stensrud. 1993a. *Hydraulic Testing of Salado Formation Evaporites at the Waste Isolation Pilot Plant Site: Second Interpretive Report.* SAND92-0533. Albuquerque, NM: Sandia National Laboratories.

Beauheim, R.L., W.W. Wawersik, and R.M. Roberts. 1993b. "Coupled Permeability and Hydrofracture Tests to Assess the Waste-Containment Properties of Fractured Anhydrite," *International Journal of Rock Mechanics and Mining Sciences & Geomechanics Abstracts.* Vol. 30, no. 7, 1159-1163.

Beraun, R., and P.B. Davies. 1992. "Baseline Design Input Data Base to be used During Calculations Effort to be Performed by Division 1514 in Determining the Mechanical Creep Closure Behavior of Waste Disposal Rooms in Bedded Salt," *Preliminary Performance Assessment for the Waste Isolation Pilot Plant, December 1992 - Volume 3: Model Parameters.* SAND92-0700/3. Albuquerque, NM: Sandia National Laboratories. A-5 through A-13.

Borns, D.J., and J.C. Stormont. 1988. *An Interim Report on Excavation Effect Studies at the Waste Isolation Pilot Plant: The Delineation of the Disturbed Rock Zone.* SAND87-1375. Albuquerque, NM: Sandia National Laboratories.

Borns, D.J., and J.C. Stormont. 1989. "The Delineation of the Disturbed Rock Zone Surrounding Excavations in Salt," *Rock Mechanics as a Guide for Efficient Utilization of Natural Resources: Proceedings of the 30th U.S. Symposium, West Virginia University, Morgantown, WV, June 19-22, 1989.* Ed. A.W. Khair. Brookfield, VT: A.A. Balkema. 353-360.

Brooks, R.H., and A.T. Corey. 1964. *Hydraulic Properties of Porous Media.* Hydrology Paper. No. 3. Fort Collins, CO: Colorado State University.

Brush, L.H. 1990. *Test Plan for Laboratory and Modeling Studies of Repository and Radionuclide Chemistry for the Waste Isolation Pilot Plant.* SAND90-0266. Albuquerque, NM: Sandia National Laboratories.

Brush, L.H. 1991. "Appendix A: Current Estimates of Gas Production Rates, Gas Production Potentials, and Expected Chemical Conditions Relevant to Radionuclide Chemistry for the Long-Term WIPP Performance Assessment," *Preliminary Comparison with 40 CFR Part 191, Subpart B for the Waste Isolation Pilot Plant, December 1991 - Volume 3: Reference Data.* Eds. R.P. Rechard, A.C. Peterson, J.D. Schreiber, J.H. Iuzzolino, M.S. Tierney, and J.S. Sandha. SAND91-0893/3. Albuquerque, NM: Sandia National Laboratories. A-25 through A-36.

Brush, L.H. 1995. "Likely Gas-Generation Reactions and Current Estimates of Gas-Generation Rates for the Long-Term WIPP Performance Assessment," *A Summary of Methods for Approximating Salt Creep and Disposal Room Closure in Numerical Methods of Multiphase Flow.* G.A. Freeze, K.W. Larson, and P.B. Davies. SAND94-0251. Albuquerque, NM: Sandia National Laboratories. C-5 through C-45.

Burdine, N.T. 1953. "Relative Permeability Calculations From Pore-Size Distribution Data," *Transactions of the American Institute of Mining and Metallurgical Engineers. Petroleum Branch.* Vol. 198, 71-78

Butcher, B.M. 1989. *Waste Isolation Pilot Plant Simulated Waste Compositions and Mechanical Properties.* SAND89-0372. Albuquerque, NM: Sandia National Laboratories.

Butcher, B.M., and R.C. Lincoln. 1995a. "The Initial Brine Saturation of Waste and Backfill Within WIPP Disposal Rooms (WBS 1.1.1.2.3)," *Coupled Multiphase Flow and Closure Analysis of Repository Response to Waste-Generated Gas at the Waste Isolation Pilot Plant (WIPP).* G.A. Freeze, K.W. Larson, and P.B. Davies. SAND93-1986. Albuquerque, NM: Sandia National Laboratories. C-5 through C-6.

Butcher, B.M., and R.C. Lincoln. 1995b. "Upper limit of initial brine saturation in waste and backfill," *Coupled Multiphase Flow and Closure Analysis of Repository Response to Waste-Generated Gas at the Waste Isolation Pilot Plant (WIPP).* G.A. Freeze, K.W. Larson, and P.B. Davies. SAND93-1986. Albuquerque, NM: Sandia National Laboratories. C-7 through C-8.

Butcher, B.M., and F.T. Mendenhall. 1993. *A Summary of the Models Used for the Mechanical Response of Disposal Rooms in the Waste Isolation Pilot Plant with Regard to Compliance with 40 CFR 191, Subpart B.* SAND92-0427. Albuquerque, NM: Sandia National Laboratories.

Butcher, B.M., C.F. Novak, and M. Jercinovic. 1991a. *The Advantages of a Salt/Bentonite Backfill for Waste Isolation Pilot Plant Disposal Rooms.* SAND90-3074. Albuquerque, NM: Sandia National Laboratories.

Butcher, B.M., T.W. Thompson, R.G. Van Buskirk, and N.C. Patti. 1991b. *Mechanical Compaction of Waste Isolation Pilot Plant Simulated Waste.* SAND90-1206. Albuquerque, NM: Sandia National Laboratories.

Davies, P.B. 1991. *Evaluation of the Role of Threshold Pressure in Controlling Flow of Waste-Generated Gas into the Bedded Salt at the Waste Isolation Pilot Plant.* SAND90-3246. Albuquerque, NM: Sandia National Laboratories.

Davies, P.B., L.H. Brush, and F.T. Mendenhall. 1992. "Assessing the Impact of Waste-Generated Gas from the Degradation of Transuranic Waste at the Waste Isolation Pilot Plant: An Overview of Strongly Coupled Chemical, Hydrologic, and Structural Processes," *Gas Generation and Release From Radioactive Repositories, 3rd Organisation for Economic Co-Operation and Development/Nuclear Energy Agency (OECD/NEA) Gas Workshop, Aix-en-Provence, France, September 23-26, 1991.* SAND90-0707C. Paris, France: Organisation for Economic Co-Operation and Development. 54-74.

de Marsily, G. 1986. *Quantitative Hydrogeology.* Orlando, FL: Academic Press.

Deal, D.E., and R.M. Roggenthen. 1991. "Evolution of Hydrologic Systems and Brine Geochemistry in a Deforming Salt Medium: Data from WIPP Brine Seeps," *Waste Management '91, Waste Processing, Transportation, Storage and Disposal, Technical Programs and Public Education, Tucson, AZ, February 24-28, 1991.* Ed. R.G. Post. Tucson, AZ: University of Arizona. Vol. II, 507-516.

Demond, A.H., and P.V. Roberts. 1987. "An Examination of Relative Permeability Relations for Two-Phase Flow in Porous Media," *Water Resources Bulletin.* Vol. 23, no. 4, 617-628.

Freeze, G.A., K.W. Larson, and P.B. Davies. 1995. *A Summary of Methods for Approximating Salt Creep and Disposal Room Closure in Numerical Models of Multiphase Flow.* SAND94-0251. Albuquerque, NM: Sandia National Laboratories.

Freeze, R.A., and J.A. Cherry. 1979. *Groundwater.* Englewood Cliffs, NJ: Prentice Hall.

Golden Software, Inc. 1994. *SURFER for Windows User's Guide.* Golden, CO: Golden Software, Inc. (Available from Golden Software, Inc., 809 14th St., Golden, CO (303) 279-1021.)

Gray, W.G., and S.M. Hassanizadeh. 1991. "Paradoxes and Realities in Unsaturated Flow Theory," *Water Resources Research.* Vol. 27, no. 8, 1847-1854.

Green, D.H., and H.F. Wang. 1990. "Specific Storage as a Poroelastic Coefficient," *Water Resources Research.* Vol. 26, no. 7, 1631-1637.

Howarth, S.M. 1993. *Conceptual Plan: Two-Phase Flow Laboratory Program for the Waste Isolation Pilot Plant.* SAND93-1197. Albuquerque, NM: Sandia National Laboratories.

Howarth, S.M., E.W. Peterson, P.L. Lagus, K.H. Lie, S.J. Finley, and E.J. Nowak. 1991. "Interpretation of In-Situ Pressure and Flow Measurements of the Salado Formation at the Waste Isolation Pilot Plant," *Rocky Mountain Regional Meeting and Low-Permeability Reservoirs Symposium, Denver, CO, April 15-17, 1991.* SAND90-2334C; SPE 21840. Richardson, TX: Society of Petroleum Engineers. 355-369.

Hunter, T.O., comp. 1979. *Summary of Research and Development Activities in Support of Waste Acceptance Criteria for WIPP.* SAND79-1305. Albuquerque, NM: Sandia National Laboratories.

Jones, C.L., C.G. Bowles, and K.G. Bell. 1960. *Experimental Drill Hole Logging in Potash Deposits of the Carlsbad District, New Mexico.* USGS Open-File Report 60-84. Washington, DC: US GPO.

Krieg, R.D. 1984. *Reference Stratigraphy and Rock Properties for the Waste Isolation Pilot Plant (WIPP) Project.* SAND83-1908. Albuquerque, NM: Sandia National Laboratories.

Lappin, A.R., R.L. Hunter, D.P. Garber, and P.B. Davies, eds. 1989. *Systems Analysis, Long-Term Radionuclide Transport, and Dose Assessments, Waste Isolation Pilot Plant (WIPP), Southeastern New Mexico; March 1989.* SAND89-0462. Albuquerque, NM: Sandia National Laboratories.

Lappin, A.R., R.L. Hunter, P.B. Davies, D.J. Borns, M. Reeves, J.F. Pickens, and H.J. Iuzzolino. 1990. *Systems Analysis, Long-Term Radionuclide Transport, and Dose Assessments, Waste Isolation Pilot Plant (WIPP), Southeastern New Mexico; September 1989.* SAND89-1996. Albuquerque, NM: Sandia National Laboratories.

McTigue, D.F., S.J. Finley, and E.J. Nowak. 1989. "Brine Transport in Polycrystalline Salt: Field Measurements and Model Considerations," *EOS Transactions.* Vol. 70, no. 43, 1111.

Molecke, M.A. 1979. *Gas Generation From Transuranic Waste Degradation: Data Summary and Interpretation.* SAND79-1245. Albuquerque, NM: Sandia National Laboratories.

Morrow, N.R., J.S. Ward, and K.R. Brower. 1986. *Rock Matrix and Fracture Analysis of Flow in Western Tight Gas Sands. 1985 Annual Report.* DOE/MC/21179-2032 (DE86001055). Morgantown, WV: U.S. Department of Energy; Socorro, NM: New Mexico Institute of Mining and Technology, New Mexico Petroleum Recovery Center.

Munson, D.E., A.F. Fossum, and P.E. Senseny. 1989. "Approach to First Principles Model Prediction of Measured WIPP In Situ Room Closure in Salt," *Rock Mechanics as a Guide for Efficient Utilization of Natural Resources: Proceedings of the 30th U.S. Symposium, West Virginia University, Morgantown, WV, June 19-22, 1989.* Ed. A.W. Khair. Brookfield, VT: A.A. Balkema. 673-680.

Nowak, E.J., and D.F. McTigue. 1987. *Interim Results of Brine Transport Studies in the Waste Isolation Pilot Plant (WIPP).* SAND87-0880. Albuquerque, NM: Sandia National Laboratories.

Nowak, E.J., D.F. McTigue, and R. Beraun. 1988. *Brine Inflow to WIPP Disposal Rooms: Data, Modeling, and Assessment.* SAND88-0112. Albuquerque, NM: Sandia National Laboratories.

Nowak, E.J., J.R. Tillerson, and T.M. Torres. 1990. *Initial Reference Seal System Design: Waste Isolation Pilot Plant.* SAND90-0355. Albuquerque, NM: Sandia National Laboratories.

Parker, J.C., R.J. Lenhard, and T. Kuppusamy. 1987. "A Parametric Model for Constitutive Properties Regarding Multiphase Flow in Porous Media," *Water Resources Research.* Vol. 23, no. 4, 618-624.

Peterson, E.W., P.L. Lagus, and K. Lie. 1987. *WIPP Horizon Free Field Fluid Transport Characteristics.* SAND87-7164. Albuquerque, NM: Sandia National Laboratories.

Pfeifle, T.W. 1987. *Backfill Material Specifications and Requirements for the WIPP Simulated DHLW and TRU Waste Technology Experiments.* SAND85-7209. Albuquerque, NM: Sandia National Laboratories.

Powers, D.W., S.J. Lambert, S.E. Shaffer, L.R. Hill, and W.D. Weart, eds. 1978. *Geological Characterization Report for the Waste Isolation Pilot Plant (WIPP) Site, Southeastern New Mexico.* SAND78-1596. Albuquerque, NM: Sandia National Laboratories.

Pruess, K. 1987. *TOUGH User's Guide.* NUREG/CR-4645, SAND86-7104, LBL-20700. Berkeley, CA: Lawrence Berkeley Laboratory.

Pruess, K. 1991. *TOUGH2 - A General-Purpose Numerical Simulator for Multiphase Fluid and Heat Flow.* LBL-29400. Berkeley, CA: Lawrence Berkeley Laboratory.

Reeves, M., G.A. Freeze, V.A. Kelley, J.F. Pickens, D.T. Upton, and P.B. Davies. 1991. *Regional Double-Porosity Solute Transport in the Culebra Dolomite under Brine-Reservoir-Breach Release Conditions: An Analysis of Parameter Sensitivity and Importance.* SAND89-7069. Albuquerque, NM: Sandia National Laboratories.

Sjaardema, G.D., and R.D. Krieg. 1987. *A Constitutive Model for the Consolidation of WIPP Crushed Salt and Its Use in Analyses of Backfilled Shaft and Drift Configurations.* SAND87-1977. Albuquerque, NM: Sandia National Laboratories.

Skokan, C.K., M.C. Pfeifer, G.V. Keller, and H.T. Andersen. 1989. *Studies of Electrical and Electromagnetic Methods for Characterizing Salt Properties at the WIPP Site, New Mexico.* SAND87-7174. Albuquerque, NM: Sandia National Laboratories.

Soeder, D.J., and P.L. Randolph. 1984. *Special Dry Core Analysis of the Mesa Verde Formation U.S. DOE Multiwell Experiment Garfield County, Colorado.* DOE/MC/20342-4. Morgantown, WV: U.S. Department of Energy.

Stoelzel, D., P. Vaughn, J. Bean, and J. Schreiber. 1995. "Summary of 1993-94 WIPP Preliminary Undisturbed Repository Calculations," *Coupled Multiphase Flow and Closure Analysis of Repository Response to Waste-Generated Gas at the Waste Isolation Pilot Plant (WIPP).* G.A. Freeze, K.W. Larson, and P.B. Davies, SAND93-1986. Albuquerque, NM: Sandia National Laboratories. C-25 through C-47.

Stone, C.M. 1995a. "Creep Closure Behavior of Waste Disposal Rooms in Bedded Salt Due to Gas Generation Produced by Several Alternatives of the Engineered Alternatives Task Force," *A Summary of Methods for Approximating Salt Creep and Disposal Room Closure in Numerical Methods of Multiphase Flow.* G.A. Freeze, K.W. Larson, and P.B. Davies. SAND94-0251. Albuquerque, NM: Sandia National Laboratories. C-85 through C-105.

Stone, C.M. 1995b. "Application of SANTOS to Waste Disposal Room Problems Including a Demonstration of Coupled Structural/Porous Flow Capability," *A Summary of Methods for Approximating Salt Creep and Disposal Room Closure in Numerical Methods of Multiphase Flow.* G.A. Freeze, K.W. Larson, and P.B. Davies. SAND94-0251. Albuquerque, NM: Sandia National Laboratories. C-107 through C-133.

Stone, C.M., R.D. Krieg, and Z.E. Beisinger. 1985. *SANCHO, A Finite Element Computer Program for the Quasistatic, Large Deformation, Inelastic Response of Two-Dimensional Solids.* SAND84-2618. Albuquerque, NM: Sandia National Laboratories.

Stormont, J.C. 1990. *Summary of 1988 WIPP Facility Horizon Gas Flow Measurements.* SAND89-2497. Albuquerque, NM: Sandia National Laboratories.

Stormont, J.C., E.W. Peterson, and P.L. Lagus. 1987. *Summary of and Observations About WIPP Facility Horizon Flow Measurements Through 1986.* SAND87-0176. Albuquerque, NM: Sandia National Laboratories.

U.S. DOE (Department of Energy). 1980. *Final Environmental Impact Statement: Waste Isolation Pilot Plant.* DOE/EIS-0026. Washington, DC: U.S. DOE. Vols. 1-2.

U.S. DOE (Department of Energy). 1986. *Design Validation Final Report.* DOE/WIPP 86-010. San Francisco, CA: Bechtel National, Inc.

U.S. DOE (Department of Energy). 1989. *Draft Supplement Environmental Impact Statement, Waste Isolation Pilot Plant.* DOE/EIS-0026-DS. Washington, DC: U.S. DOE.

U.S. DOE (Department of Energy). 1990. *Final Supplement Environmental Impact Statement, Waste Isolation Pilot Plant.* DOE/EIS-0026-FS. Washington, DC: U.S. Department of Energy, Office of Environmental Restoration and Waste Management.

U.S. DOE (Department of Energy). 1991. *Waste Acceptance Criteria for the Waste Isolation Pilot Plant, December 1991.* DOE/WIPP-069, Rev. 4. Carlsbad, NM: Westinghouse Electric Corporation.

U.S. EPA (Environmental Protection Agency). 1978. "40 CFR Parts 1500-1508: Regulations for Implementing the Procedural Provisions of the National Environmental Policy Act," in the most recent *Code of Federal Regulations*. Washington, DC: Office of the Federal Register, National Archives and Records Administration.

U.S. EPA (Environmental Protection Agency). 1985. "40 CFR Part 191: Environmental Standards for the Management and Disposal of Spent Nuclear Fuel, High-Level and Transuranic Radioactive Wastes; Final Rule," *Federal Register*. Vol. 50, no. 182, 38066-38089.

U.S. EPA (Environmental Protection Agency). 1986. "40 CFR Part 268: Land Disposal Restrictions," in the most recent *Code of Federal Regulations*. Washington, DC: Office of the Federal Register, National Archives and Records Administration.

van Genuchten, M.Th. 1980. "A Closed-Form Equation for Predicting the Hydraulic Conductivity of Unsaturated Soils," *Soil Science Society of America Journal.* Vol. 44, no. 5, 892-898.

Webb, S.W. 1992a. "Sensitivity Studies for Gas Release from the Waste Isolation Pilot Plant (WIPP)," *Gas Generation and Release from Radioactive Repositories, 3rd Organisation for Economic Co-Operation and Development/Nuclear Energy Agency (OECD/NEA) Gas Workshop, Aix-en-Provence, France, September 23-26, 1991*. SAND91-1872C. Paris, France: Organisation for Economic Co-Operation and Development. 309-326.

Webb, S.W. 1992b. "Uncertainty Estimates for Two-Phase Characteristic Curves for 1992 40 CFR 191 Calculations," *Preliminary Performance Assessment for the Waste Isolation Pilot Plant, December 1992 - Volume 3: Model Parameters.* Sandia WIPP Project. SAND92-0700/3. Albuquerque, NM: Sandia National Laboratories. A-147 through A-155.

Webb, S.W. 1995. "Countercurrent Flow in a Marker Bed and Implications for Gas Migration - Brine Inflow," *Coupled Multiphase Flow and Closure Analysis of Repository Response to Waste Generated Gas at the Waste Isolation Pilot Plant (WIPP).* G.A. Freeze, K.W. Larson, and P.B. Davies. SAND93-1986. Albuquerque, NM: Sandia National Laboratories. C-9 through C-10.

WIPP PA (Performance Assessment) Department. 1992a. *Preliminary Performance Assessment for the Waste Isolation Pilot Plant, December 1992 - Volume 1: Third Comparison with 40 CFR 191, Subpart B.* SAND92-0700/1. Albuquerque, NM: Sandia National Laboratories.

WIPP PA (Performance Assessment) Department. 1992b. *Preliminary Performance Assessment for the Waste Isolation Pilot Plant, December 1992 - Volume 2: Technical Basis.* SAND92-0700/2. Albuquerque, NM: Sandia National Laboratories.

WIPP PA (Performance Assessment) Department. 1992c. *Preliminary Performance Assessment for the Waste Isolation Pilot Plant, December 1992 - Volume 3: Model Parameters.* SAND92-0700/3. Albuquerque, NM: Sandia National Laboratories.

WIPP PA (Performance Assessment) Department. 1992d. *Long-Term Gas and Brine Movement at the Waste Isolation Pilot Plant: Preliminary Sensitivity Analyses for Post-Closure 40 CFR 268 (RCRA), May 1992.* SAND92-1933. Albuquerque, NM: Sandia National Laboratories.

WIPP PA (Performance Assessment) Department. 1993a. *Preliminary Performance Assessment for the Waste Isolation Pilot Plant, December 1992 - Volume 4: Uncertainty and Sensitivity Analyses for 40 CFR 191, Subpart B.* SAND92-0700/4. Albuquerque, NM: Sandia National Laboratories.

WIPP PA (Performance Assessment) Department. 1993b. *Preliminary Performance Assessment for the Waste Isolation Pilot Plant, December 1992 - Volume 5: Uncertainty and Sensitivity Analyses of Gas and Brine Migration for Undisturbed Performance.* SAND92-0700/5. Albuquerque, NM: Sandia National Laboratories.

WIPP PA (Performance Assessment) Division. 1991. *Preliminary Comparison with 40 CFR Part 191, Subpart B for the Waste Isolation Pilot Plant, December 1991 - Volume 1: Methodology and Results.* SAND91-0893/1. Albuquerque, NM: Sandia National Laboratories.

APPENDIX A: PARAMETER DATABASE

This page intentionally left blank

PARAMETER DATA BASE FOR TOUGH2/EOS8 SIMULATIONS OF BRINE AND GAS FLOW TO AND FROM A WIPP WASTE DISPOSAL ROOM

Peter B. Davies
Geohydrology Department 6115
Sandia National Laboratories
Albuquerque, NM 87185

Geoff A. Freeze
INTERA, Inc.
1650 University Blvd. NE, Suite 300
Albuquerque, NM 87102

Toya L. Jones
INTERA, Inc.
6850 Austin Center Blvd, Suite 300
Austin, TX 78731

January 1994

097B-36E-007E

This page intentionally left blank

CONTENTS

PREFACE

This Appendix documents the status of the parameter data base as of January 1994. The data contained herein was used in the simulations of brine flow and gas migration to and from a WIPP waste disposal room with gas generation that are discussed in this report. This data base has evolved using the following approach to updating data and information for each parameter. At the time any change is made to a parameter entry, the date is updated. Any editorial change to a parameter rationale, comment, and/or reference is indicated by incrementing the rationale number by a letter. Any value change to a parameter is indicated by a numeric increment in the rationale number. This data base may continue to evolve in future simulations are warranted.

I. MODEL CONFIGURATION

DATE :	08/31/93	RATIONALE NUMBER :	002A
PARAMETER :	Vertical Model Dimension		
VALUE :	262.5 m		
KEYWORD :	ELEME, CONNE		

RATIONALE : In order to minimize boundary effects from the upper and lower model boundaries, it is desirable to have a relatively thick salt section above and below the waste disposal room. Because the focus of the simulations is the room and immediately adjacent portions of the Salado, it is not essential that the upper and lower model boundaries correspond precisely with formation boundaries. Therefore, the total vertical dimension of the model is specified at 262.5 m, with 130.0 m of salt above the room and 128.5 m of salt below the room.

COMMENTS : In certain sensitivity simulations (i.e. high halite permeabilty), a larger vertical dimension is required to minimize boundary effects.

Because of the integral finite difference method used for discretization, it is possible to maintain a constant total vertical dimension for all three fixed room geometries (initial, intermediate, and fully consolidated) despite the different room heights.

Since the repository excavations follow gently dipping stratigraphic units, repository depth varies somewhat with location. The general repository depth is specified as 655.0 m below ground surface (Lappin et al., 1989; p. 1-1). This depth corresponds to the vertical mid-point of the room in all three fixed room geometries.

REFERENCES :

Lappin, A.R., R.L. Hunter, D.P. Garber, and P.B. Davies, eds. 1989. *Systems Analysis, Long-Term Radionuclide Transport, and Dose Assessments, Waste Isolation Pilot Plant (WIPP), Southeastern New Mexico; March 1989.* SAND89-0462. Albuquerque, NM: Sandia National Laboratories.

DATE :	08/31/93	RATIONALE NUMBER :	003A
PARAMETER :	Horizontal Model Dimension		
VALUE :	2285 m		
KEYWORD :	ELEME, CONNE		
RATIONALE :	For simulations that examine an isolated room in an infinite salt, it is desirable to have a relatively thick horizontal salt section in order to minimize boundary effects, particularly in the interbeds. Therefore, the total horizontal model dimension is specified at 2285 m, with 2280 m of salt outside the room.		
COMMENTS :	In certain sensitivity simulations (i.e. high permeabilty), a larger horizontal dimension is required to minimize boundary effects. Because of the integral finite difference method used for discretization, it is possible to maintain a constant total horizontal dimension for all three fixed room geometries (initial, intermediate, and fully consolidated) despite the different room half-widths. For simulations that examine a room in a panel, it is assumed that the distance from the room centerline to the centerline of the adjacent salt pillar is a constant. Therefore, as horizontal room closure occurs, the half room width decreases and the half salt pillar width increases. A total horizontal dimension of 20.3 m is based on the design dimensions of 10.06 m (33 ft) wide rooms and 30.48 m (100 ft) wide salt pillars (U.S. Department of Energy, 1986; p.12-2).		
REFERENCES :	U.S. Department of Energy. 1986. *Design Validation Final Report.* DOE/WIPP 86-010. San Francisco, CA: Bechtel National Inc.		

DATE :	08/31/93	RATIONALE NUMBER :	001D
PARAMETER :	Room Geometry		
VALUE :	Room Height4.0 m Room 1/2 Width 5.0 m		
KEYWORD :	ELEME, CONNE		

RATIONALE : The initial room dimensions are taken from the original design document (U.S. Department of Energy, 1986; p. 12-8) and are 3.96 m (13 ft) by 10.06 m (33 ft) by 91.44 m (300 ft). These dimensions correspond to an initial room volume of 3644 m^3.

Given the variability in room dimensions at any given time due to variations in actual excavation dimensions, room dimensions for the model are rounded to two significant figures.

COMMENTS : The model room dimensions imply an initial room volume of (2)(5.0)(4.0)(91.44) = 3658 m^3.

The actual excavation dimensions for Panel 1 are larger than the original design dimensions [4.06 m (13'4") by 10.16 m (33'4") by 91.44 m (300')] (U.S. Department of Energy, 1989; p. 2-299). These larger dimensions were used to provide additional closure leeway for retrievability [February 9, 1990 personal communication with S. Pickering (Division 6340) and C. Franke (Westinghouse)]. However, it is not clear that all future waste disposal rooms will be excavated to these larger dimensions. Therefore, all calculations use the original room dimensions given in U.S. Department of Energy (1986).

The following rationale was used to determine the three fixed room geometries.

The initial fixed room dimensions and volume is assumed to be equivalent to the room geometry described above:

Initial fixed room height	= 4.0 m
Initial fixed room half-width	= 5.0 m
Initial fixed room volume	= 3658 m^2

The intermediate room volume is taken from the minimum void volume state reached in the baseline (f = 1.0) room closure simulation conducted by Stone (1995). The minimum void volume of 766 m^3 was reached at about 185 years for a gas generation rate of 2 moles/drum/yr (f = 1.0). The simulation

PARAMETER (cont'd) :	Room Geometry

COMMENTS (cont'd):

assumed a constant solids volume of 432 m^3 for waste and 797 m^3 for backfill, for a total constant solids volume of 1229 m^3 for a room. These volumes are calculated from the initial volumes and porosities for waste and backfill (Beraun and Davies, 1992; p. 1-2). The sum of void and solids volumes yields an intermediate room volume of 1995 m^3.

The vertical and horizontal closures presented by Stone (1995, p. 12-13) are for the room wall mid-points and therefore represent maximum closure. At the time of minimum void volume (185 years), maximum vertical closure was 1.64 m and maximum horizontal closure was 1.60 m. To estimate the intermediate room dimensions, vertical and horizontal closure distances were selected to produce approximately the estimated intermediate room volume (1995 m^3) while maintaining the 1.64/1.60 ratio of vertical to horizontal closure. The closure distances presented by Stone (1995) are for room walls that have maximum closure (sag) at the wall mid-point. The fixed room geometries assume rooms to have flat walls. The selected closure distances are:

vertical closure = 1.44 m
horizontal closure = 1.41 m

This gives:

Intermed. fixed room height = 3.96 - 1.44 = 2.52 m
Intermed. fixed room half-width = 5.03 - 0.71 = 4.32 m
Intermed. fixed room volume = (2)(4.32)(2.52)(91.44)
= 1991 m^2

Although room dimensions should be rounded to two significant figures, a third significant figure is retained to maintain an intermediate room volume that is close to the estimated volume of 1995 m^3 .

The fully consolidated room volume is taken from the final void volume state reached in the no gas generation (f=0.0) room closure simulation conducted by Stone (1995). The final void volume was 343 m^3 (at 2000 years) for zero gas generation rate (f=0.0). The simulation assumed a constant solids volume of of 1229 m^3 for a room. The sum of void and solids volumes yields an intermediate room volume of 1572 m^3.

PARAMETER (cont'd) :	Room Geometry
COMMENTS (cont'd):	At the time of minimum void volume (2000 years), maximum vertical closure was 2.17 m and maximum horizontal closure was 2.09 m (Stone, 1995; p. 12-13). To estimate the fully consolidated room dimensions, vertical and horizontal closure distances were selected to produce approximately the estimated fully consolidated room volume (1572 m^3) while maintaining the 2.17/2.09 ratio of vertical to horizontal closure. The selected closure distances are: vertical closure = 1.88 m horizontal closure = 1.81 m This gives: Fully Cons. fixed room height = 3.96 - 1.88 = 2.08 m Fully Cons. fixed room half-width = 5.03 - 0.91 = 4.12 m Fully Cons. fixed room volume = (2)(4.12)(2.08)(91.44) = 1567 m^2 To maintain an intermediate room volume that is close to the estimated volume of 1572 m^3 a third significant figure is retained.
REFERENCES:	Beraun, R., and P.B. Davies. 1992. "Baseline Design Input Data Base to be Used During Calculations Effort to be Performed by Division 1514 in Determining the Mechanical Creep Closure Behavior of Waste Disposal Rooms in Bedded Salt," *Preliminary Performance Assessment for the Waste Isolation Pilot Plant, December 1992 - Volume 3: Model Parameters.* SAND92-0700/3. Albuquerque, NM: Sandia National Laboratories. A-5 through A-13. Stone, C.M. 1995. "Creep Closure Behavior of Waste Disposal Rooms in Bedded Salt Due to Gas Generation Produced by Several Alternatives of the Engineered Alternatives Task Force," *A Summary of Methods for Approximating Salt Creep and Disposal Room Closure in Numerical Methods of Multiphase Flow.* G.A. Freeze, K.W. Larson, and P.B. Davies. SAND94-0251. Albuquerque, NM: Sandia National Laboratories. C-85 through C-105. U.S. Department of Energy. 1986. *Design Validation Final Report.* DOE/WIPP 86-010. San Francisco, CA: Bechtel National, Inc. U.S. Department of Energy. 1989. *Geotechnical Field Data and Analysis Report, July 1987 - June 1988.* DOE/WIPP 89-009, Vol. II. Carlsbad, NM: Westinghouse Electric Corporation.

DATE :	08/31/93	RATIONALE NUMBER :	003A
PARAMETER :	Stratigraphic Thicknesses		
VALUE :	Stratigraphic Unit		Thickness (m)
	With Individual Interbeds		
	Halite		127.5
	Marker Bed 138		0.2
	Halite		6.7
	Anhydrite "a"		0.2
	Halite		2.0
	Anhydrite "b"		0.1
	Halite		2.1
	Room		
	Halite		1.6
	Marker Bed 139		0.9
	Halite		7.7
	Anhydrite "c"		0.1
	Halite		127.7
	With Composite Interbeds		
	Halite		127.6
	Upper Composite Interbed (Anhydrite a + b)		0.3
	Halite		2.1
	Room		
	Halite		1.6
	Lower Composite Interbed (Marker Bed 139)		0.9
	Halite		126.0
KEYWORD:	ELEME, CONNE		
RATIONALE:	Stratigraphic thicknesses with individual interbeds are based on the reference stratigraphy presented in U.S. Department of Energy (1989; p. 2-2 to 2-5). With the exception of a minor (4 cm) difference in the thickness of Marker Bed 139, this reference stratigraphy is identical over the pertinent interval to the reference stratigraphy presented in U.S. Department of Energy (1986; p. 6-26 to 6-28). Given the somewhat variable nature of the individual stratigraphic units, stratigraphic thicknesses are specified to the nearest 0.1 m.		

PARAMETER (cont'd) :	Stratigraphic Thicknesses
RATIONALE (cont'd) :	The thickness of the upper composite interbed is equal to the sum of the thicknesses of anhydrite "a" and anhydrite "b". The thickness of the lower composite interbed is equal to the thickness of Marker Bed 139. Composite interbeds are considered to simplify the problem for computational efficiency. The room position within the stratigraphic section is based on the specification that the tops of the rooms are to be located approximately 7 ft (2.1 m) below "clay seam G" at the base of "anhydrite b" (U.S. Department of Energy, 1986; p. 3-6). The reference stratigraphic thickness from the base of "clay seam G" to the top of Marker Bed 139 is 7.7 m. Given the 2.1 m thickness above the room and an initial room height of 4.0 m, this leaves a thickness of 1.6 m between the floor of the room and the top of Marker Bed 139.
COMMENTS :	The thickness of Marker Bed 139 varies from 0.4 m to 1.25 m (Krieg, 1984). The use of composite interbeds reduces the surface area for brine flow from the interbeds into the intact salt. This flow is important because gas that flows into the interbeds must displace brine. The creep closure process may cause a small increase in the thickness of the halite between the top of the room and anhydrite "b" and between the floor and Marker Bed 139. However, this change in thickness is expected to be very small compared to room closure. Therefore, these halite thicknesses are held constant for all fixed room geometries.
REFERENCES :	Krieg, R.D. 1984. *Reference Stratigraphy and Rock Properties for the Waste Isolation Pilot Plant (WIPP) Project.* SAND83-1908. Albuquerque, NM: Sandia National Laboratories. U.S. Department of Energy. 1986. *Design Validation Final Report.* DOE/WIPP 86-010. San Francisco, CA: Bechtel National, Inc. U.S. Department of Energy. 1989. *Geotechnical Field Data and Analysis Report, July 1987 - June 1988.* DOE/WIPP 89-009. Carlsbad, NM: Westinghouse Electric Corporation.

IIA. PHYSICAL PROPERTIES

DATE :	08/31/93	RATIONALE NUMBER :	003B
PARAMETER :	Salado Permeability		
VALUE :	1.0E-21 m^2 - Salado halite 1.0E-19 m^2 - Marker Bed 138 1.0E-19 m^2 - Anhydrite "a" 1.0E-19 m^2 - Anhydrite "b" 1.0E-19 m^2 - Marker Bed 139 1.0E-19 m^2 - Anhydrite "c" 1.0E-19 m^2 - Composite Interbeds		
KEYWORD :	ROCKS		
RATIONALE :	The permeabilities reported here are undisturbed values (i.e., they do not reflect excavation effects). These values are based on analyses of the in-situ permeability tests (Beauheim et al., 1991).		
COMMENTS :	Permeability in the Salado varies significantly in different lithologic units. The permeability distribution given here is highly simplified. The reported range of Salado halite permeabilities is 6E-20 m^2 to 9E-22 m^2 (Beauheim et al., 1991). McTigue (1992) reported a range of 3E-21 m^2 to 1E-22 m^2. All of these permeability values were measured close (3-6 m) to excavations. A single value of 3E-18 m^2 was reported at ~2 m from an excavation and a test of pure halite further (9 m) from the excavation showed no measurable (~zero) permeability (Beauheim et al., 1991). Howarth et al. (1991) reported far-field (> 20 m from room) Salado halite permeabilities ranging from 2E-21 m^2 to ~zero. For most Salado halite, 1.0E-21 m^2 is considered to be a reasonable undisturbed value for simplified calculations. A range of 1.0E-19 m^2 to 1.0E-25 m^2 (approximately zero) has been selected for sensitivity analysis.		

PARAMETER (cont'd) :	Salado Permeability
COMMENTS (cont'd) :	The reported range of anhydrite permeabilities is 6E-18 m^2 to 3E-20 m^2 (Beauheim et al., 1991). These measurements are taken from MB138, MB139, and anhydrite "c" at distances of about 10 m from an excavation. For all Marker Beds and anhydrite interbeds, 1.0E-19 m^2 is considered a representative permeability. A range of 1.0E-21 m^2 to 1.0E-18 m^2 has been selected for sensitivity analysis. The composite interbeds are assigned a permeability which is consistent with the permeabilities used for the individual interbeds. There are indications of a high degree of lateral variability in permeability in some units which will not be captured in the simulations. Particularly important may be lateral variability within the interbeds.
REFERENCES :	Beauheim, R.L., G.J. Saulnier, Jr., and J.D. Avis. 1991. *Interpretation of Brine-Permeability Tests of the Salado Formation at the Waste Isolation Pilot Plant Site: First Interim Report.* SAND90-0083. Albuquerque, NM: Sandia National Laboratories. Howarth, S.M., E.W. Peterson, P.L. Lagus, K.H. Lie, S.J. Finley, and E.J. Nowak. 1991. "Interpretation of In-Situ Pressure and Flow Measurements of the Salado Formation at the Waste Isolation Pilot Plant," *Rocky Mountain Regional Meeting and Low-Permeability Reservoirs Symposium, Denver, CO, April 15-17, 1991.* SAND90-2334C; SPE 21840. Richardson, TX: Society of Petroleum Engineers. 355-369. McTigue, D.F. 1992. *Permeability and Hydraulic Diffusivity of Waste Isolation Pilot Plant Repository Salt Inferred from Small-Scale Brine Inflow Experiments.* SAND92-1911. Albuquerque, NM: Sandia National Laboratories.

DATE :	08/31/93	RATIONALE NUMBER :	003
PARAMETER :	Room Permeability		
VALUE :	1.0E-17 m^2		
KEYWORD :	ROCKS		

RATIONALE : The permeabilty in a WIPP disposal room is expected to vary spatially due to the heterogeneous nature of the waste and backfill, and temporally due to creep closure. The permeability is expected to range from a maximum of 1E-11 m^2 for initially unconsolidated backfill and waste, to a minimum of 1E-17 m^2 for fully consolidated sludge waste.

In simulations, a room permeability of 1E-17 m^2 was used to minimize execution time.

COMMENTS : The initial room contains unconsolidated backfill and waste. Both of these materials are expected to be characterized by high void volumes. The permeability is likely to be high and difficult to quantify. Holcomb and Shields (1987; Figure 4) present a relationship between permeability and fractional density of intact Salado halite. For a fractional density of 0.6 for crushed salt backfill (Nowak et al., 1990), the extrapolated backfill permeability is 1E-11 m^2. This permeability is considered representative of the initial room filled with backfill and waste. As an upper bound, the initial room permeability may be assumed to be approximately equivalent to that of gravel. Freeze and Cherry (1979; p. 24) report a permeability of 1.0E-09 m^2 for gravel.

Butcher et al. (1991) estimate the following permeabilities from flow experiments at 14 MPa:

4E-14 m^2 to 1E-12 m^2 for metallic/glass waste,
2E-15 m^2 to 2E-13 m^2 for combustible (cellulosic) waste,
1E-17 m^2 to 2E-16 m^2 for sludge waste.

These experiments are representative of near fully consolidated conditions for the waste. There is uncertainty in whether the flow paths in the room are governed by the high (parallel flow paths) or low (series flow paths) permeability materials.

PARAMETER (cont'd) :	Room Permeability
COMMENTS (cont'd):	Lappin et al. (1989; p. 4-56) select a value of 1E-13 m^2 for a fully consolidated room. This value assumes that the fully consolidated backfill, which has a low permeability similar to that of Salado halite (1.0E-21 m^2), does not form a continuous phase, and therefore, does not control the fully consolidated room permeability [personal communication between P. Davies (Division 6344) and B. Butcher (Division 6345) on January 26, 1990].
REFERENCES :	Butcher, B.M., T.W. Thompson, R.G. VanBuskirk, and N.C. Patti. 1991. *Mechanical Compaction of Waste Isolation Pilot Plant Simulated Waste.* SAND90-1206. Albuquerque, NM: Sandia National Laboratories. Freeze, R.A., and J.A. Cherry. 1979. *Groundwater.* Englewood Cliffs, NJ: Prentice-Hall, Inc. Holcomb, D.J., and M. Shields. 1987. *Hydrostatic Creep Consolidation of Crushed Salt with Added Water.* SAND87-1990. Albuquerque, NM: Sandia National Laboratories. Lappin, A.R., R.L. Hunter, D.P. Garber, and P.B. Davies, eds. 1989. *Systems Analysis, Long-Term Radionuclide Transport, and Dose Assessments, Waste Isolation Pilot Plant (WIPP), Southeastern New Mexico; March 1989.* SAND89-0462. Albuquerque, NM: Sandia National Laboratories. Nowak, E.J., J.R. Tillerson, and T.M. Torres. 1990. *Initial Reference Seal System Design: Waste Isolation Pilot Plant.* SAND90-0355. Albuquerque, NM: Sandia National Laboratories.

DATE :	08/31/93	RATIONALE NUMBER :	002
PARAMETER :	Salado Porosity		
VALUE :	0.01		
KEYWORD :	ROCKS		

RATIONALE :

Salado Halite

The value of 0.01 for the porosity of Salado halite is estimated from electro-magnetic and DC resistivity measurements made underground at the WIPP site (Skokan et al., 1989; p. 15). To place this value in context, the low end of the Salado halite porosity is estimated to be on the order of 0.001, based on drying experiments (Powers et al., 1978; p. 7-30); the high end of the Salado halite porosity is estimated to be approximately 0.03, based on the low end (10 ohm) of the DC resistivity measurements made underground (Skokan et al., 1989; p.6,13).

Salado Interbeds

The interbeds are assumed to have the same estimated (0.01) and maximum (0.03) porosity as the Salado halite. Fracturing, diagenetic changes, and dual porosity behavior may impact the effective porosity of the anhydrite interbeds. A local porosity of 0.0006 was estimated based on observed tracer migration between two boreholes during in-situ testing [personal communication between R. Roberts (INTERA) and G. Freeze]. This porosity was assumed to be minimum for simulation.

REFERENCES :

Powers, D.W., S.J. Lambert, S.E. Shaffer, L.R. Hill, and W.D. Weart, eds. 1978. *Geological Characterization Report for the Waste Isolation Pilot Plant (WIPP) Site, Southeastern New Mexico.* SAND78-1596, Vol. II. Albuquerque, NM: Sandia National Laboratories.

Skokan, C.K., M.C. Pfeifer, G.V. Keller, and H.T. Andersen. 1989. *Studies of Electrical and Electromagnetic Methods for Characterizing Salt Properties at the WIPP Site, New Mexico.* SAND87-7174. Albuquerque, NM: Sandia National Laboratories.

DATE :	08/31/93	RATIONALE NUMBER :	002B
PARAMETER :	Room Porosity		
VALUE :	0.66		
KEYWORD :	ROCKS		

RATIONALE : The initial room porosity is based on a volume average of the porosities of the room contents. The volumes and porosities of the contents are taken from Beraun and Davies (1992). The porosity is calculated using:

$$\phi_{room} = \frac{V_{drums}\phi_{drums} + V_{backfill}\phi_{backfill} + V_{vent.}\phi_{vent.}}{V_{room}} \qquad (1)$$

The initial room volume is calculated to be 3644 m^3 based on the initial room dimensions [3.96 m (13 ft) by 10.06 m (33 ft) by 91.44 m (300 ft)] from the original design document (U.S. Department of Energy, 1986; p. 12-8). There are 6804 drums in each waste disposal room (Lappin et al., 1989; p. 4-50) which yields a total drum volume of 1663 m^3 (Beraun and Davies, 1992; p. 1). In each room there are 2722 drums of solid organic waste (cellulosics) having an initial porosity of 0.8, 2722 drums of solid inorganic waste (metals and glass) having an initial porosity of 0.8, and 1360 drums of sludges having an initial porosity of 0.5 (Beraun and Davies, 1992; p. 2). The average initial porosity of all waste drums is 0.74 . The initial room has 1328 m^3 of backfill with an initial porosity of 0.4 (Beraun and Davies, 1992; p. 1-2). The ventilation gap is 0.71 m (28 inches) high for a total volume of 654 m^3 (Beraun and Davies, 1992; p. 1).

Using equation (1), the initial room porosity is:

$$\phi_{initial\ room} = \frac{(1663 m^3 \cdot 0.74) + (1328 m^3 \cdot 0.40) + (654 m^3 \cdot 1.00)}{3644 m^3}$$

$$= 0.66$$

COMMENTS : The initial room porosity corresponds to an initial void volume of 2415 m^3 and an initial solids volume of 1229 m^3.

PARAMETER (cont'd) :	Room Porosity
COMMENTS (cont'd):	The model initial room has a total volume of 3658 m^2 (see room geometry rationale). To model an initial void volume of 2415 m^2, consistent with Beraun and Davies (1991), an initial room porosity of 0.6603 is used in simulations. The model initial room porosity corresponds to a void volume of 2415 m^3 and a initial solids volume of 1243 m^3. The following rationale was used to determine porosities for fixed intermediate and fixed fully consolidated room geometries. The intermediate room porosity is derived from the minimum void volume state reached in the baseline (f=1.0) room closure simulation conducted by Stone (1995). Porosity is calculated from total room volume and room void volume at this intermediate state. Based on the Stone (1995) calculations, this yields: $$\phi = \frac{V_v}{V_v + V_s} = \frac{766 m^3}{766 m^3 + 1229 m^3} = 0.38$$ The model intermediate room has a total volume of 1991 m^2 (see room geometry rationale). To model an intermediate void volume of 766 m^2 and solids volume of 1229 m^2, consistent with Stone (1995), an intermediate room porosity of 0.3840 is used in simulations. The model intermediate room porosity corresponds to a void volume of 765 m^3 and a solids volume of 1226 m^3. The fully consolidated room porosity is derived from the final void volume state reached in the no gas generation (f=0.0) room closure simulation conducted by Stone (1995): $$\phi = \frac{V_v}{V_v + V_s} = \frac{343 m^3}{343 m^3 + 1229 m^3} = 0.22$$ The model fully consolidated room has a total volume of 1567 m^2 (see room geometry rationale). To model a fully consolidated void volume of 343 m^2 and solids volume of 1229 m^2, consistent with Stone (1995), a fully consolidated room porosity of 0.2180 is used in simulations. The model fully consolidated room porosity corresponds to a void volume of 342 m^3 and a solids volume of 1225 m^3.

PARAMETER (cont'd) :	Room Porosity
COMMENTS (cont'd):	Beraun and Davies (1992; Figure 2) estimate a fully consolidated (i.e., at 15 MPa stress) waste porosity of about 0.2, which is close to the fully consolidated room porosity.
REFERENCES :	Beraun, R., and P.B. Davies. 1992. "Baseline Design Input Data Base to be Used During Calculations Effort to be Performed by Division 1514 in Determining the Mechanical Creep Closure Behavior of Waste Disposal Rooms in Bedded Salt," *Preliminary Performance Assessment for the Waste Isolation Pilot Plant, December 1992 - Volume 3: Model Parameters.* SAND92-0700/3. Albuquerque, NM: Sandia National Laboratories. A-5 through A-13. Lappin, A.R., R.L. Hunter, D.P. Garber, and P.B. Davies, eds. 1989. *Systems Analysis, Long-Term Radionuclide Transport, and Dose Assessments, Waste Isolation Pilot Plant (WIPP), Southeastern New Mexico; March 1989.* SAND89-0462. Albuquerque, NM: Sandia National Laboratories. Stone, C.M. 1995. "Creep Closure Behavior of Waste Disposal Rooms in Bedded Salt Due to Gas Generation Produced by Several Alternatives of the Engineered Alternatives Task Force," *A Summary of Methods for Approximating Salt Creep and Disposal Room Closure in Numerical Methods of Multiphase Flow.* G.A. Freeze, K.W. Larson, and P.B. Davies. SAND94-0251. Albuquerque, NM: Sandia National Laboratories. C-85 through C-105. U.S. Department of Energy. 1986. *Design Validation Final Report.* DOE/WIPP 86-010. San Francisco, CA: Bechtel National, Inc.

DATE :	08/31/93	RATIONALE NUMBER :	002B
PARAMETER :	Salado Compressibility		
VALUE :		Compressibility	
		α (bulk) Pa^{-1}	α_p (pore volume) Pa^{-1}
	Halite	2.7E-11	2.7E-09
	Interbeds	8.3E-12	8.3E-10
KEYWORD :	ROCKS		

RATIONALE : Compressibility of the porous matrix for both the Salado halite and the anhydrite interbeds can be computed directly from elastic properties (Green and Wang, 1990; p. 1632):

$$\alpha = \frac{1}{K + 4G/3} \qquad (1)$$

where:

α = rock compressibility [Pa^{-1}],
K = drained bulk modulus of rock [Pa],
G = drained shear modulus of rock [Pa],

The pore volume compressibility, α_p, which is required in most multiphase flow codes, can be calculated using α and the porosity, ϕ, from (de Marsily, 1986; pp. 103-105):

$$\alpha_p = \frac{\alpha}{\phi} \qquad (2)$$

Salado Halite

Beauheim et al. (1991; p. 37) gives the following ranges for halite elastic properties:

	Min.	Base	Max.
Young's Modulus (E) [GPa]	20.7	31.0	36.5
Poisson's Ratio (ν)	0.17	0.25	0.31
Bulk Modulus (K) [GPa]	15.0	20.7	21.7
Shear Modulus (G) [GPa]	8.1	12.4	15.6

PARAMETER (cont'd) :	Salado Compressibility

COMMENTS : The halite rock compressibility, α, is calculated from equation (1) using the base values for K and G:

$$\alpha = \frac{1}{(20.7\times10^{9}\text{Pa}) + (4)(12.4\times10^{9}\text{Pa})/(3)} = 2.7\times10^{-11}\ \text{Pa}^{-1}$$

Using the specified Salado porosity, ϕ, of 0.01 (see porosity rationale), α_p is calculated from equation (2):

$$\alpha_p = \frac{\alpha}{\phi} = 2.7 \times 10^{-9}\ \text{Pa}^{-1}$$

Salado Interbeds

Beauheim et al. (1991; p. 37) gives the following ranges for anhydrite elastic properties:

	Min.	Base	Max.
Young's Modulus (E) [GPa]	59.0	75.1	78.9
Poisson's Ratio (ν)	0.31	0.35	0.42
Bulk Modulus (K) [GPa]	68.1	83.4	85.0
Shear Modulus (G) [GPa]	21.4	27.8	30.4

These anhydrite properties are assumed representative of the interbeds. The anhydrite interbed rock compressibility, α, is calculated from equation (1) using the base values for K and G:

$$\alpha = \frac{1}{(83.4\times10^{9}\text{Pa}) + (4)(27.8\times10^{9}\text{Pa})/(3)} = 8.3\times10^{-12}\ \text{Pa}^{-1}$$

Using an interbed porosity, ϕ, of 0.01 (see porosity rationale) the interbed pore volume compressibility is calculated from equation (2) as:

$$\alpha_p = \frac{\alpha}{\phi} = 8.3 \times 10^{-10}\ \text{Pa}^{-1}$$

PARAMETER (cont'd) :	Salado Compressibility

COMMENTS : The compressibility of the rock pores is proportional to 1/K. The compressibility of the solids or rock grains is proportional to $1/K_s$, where K_s is defined as the unjacketed bulk modulus of the rock or the grain modulus. The rock compressibility, α, defined by equation (1) assumes that the rock pores are much more compressible than the solids or rock grains (i.e., $K/K_s \approx 0$). In this case, the specific storage, S_s, can be calculated as follows (Freeze and Cherry, 1979; p. 59):

$$S_s = \rho_f g(\alpha + \phi\beta) \quad (3)$$

where (based on Beauheim et al., 1991):

ρ_f = fluid density [1200 kg/m^3],
g = acceleration of gravity [9.81 N/kg],
ϕ = porosity [0.01],
β = fluid (brine) compressibility [2.5E-10 Pa^{-1}],

Specific storage calculated from rock compressibilities using equation (3) is 3.5E-7 m^{-1} for halite and 1.3E-7 m^{-1} for the interbeds.

A parameter range is determined by substituting the maximum and minimum K and G values into equation (1). For halite, the range of rock compressibility is 2.4E-11 Pa^{-1} to 3.9E-11 Pa^{-1} with a corresponding specific storage range of 3.2E-7 m^{-1} to 4.9E-7 m^{-1}.

Green and Wang (1991; p. 1632) give the following relationship for specific storage when the compressibility of the rock grains is not negligible (i.e., $K/K_s \neq 0$):

$$S_s = \rho_f g \left[\left(\frac{1}{K} - \frac{1}{K_s} \right) \left(1 - \frac{4G(1 - K/K_s)/3}{K + 4G/3} \right) + \phi \left(\frac{1}{K_f} - \frac{1}{K_s} \right) \right] \quad (4)$$

where:

K_f = bulk modulus of fluid [Pa],

Beauheim et al. (1991; p. 39) suggest that, for halite, K_s = 23.4 GPa and that specific storage, calculated from equation (4) because K/K_s is not zero, is 9.5E-8 m^{-1}. A corresponding effective halite rock compressibility of 5.6E-12 Pa^{-1} can be backed out using equation (3). This value is used as an alternative minimum value.

PARAMETER (cont'd) :	Salado Compressibility
COMMENTS (cont'd) :	For the anhydrite interbeds, substituting the maximum and minimum K and G values into equation (1) yields a range for rock compressibility of 8.0E-12 Pa^{-1} to 1.0E-11 Pa^{-1} with a corresponding range for specific storage of 1.2E-7 m^{-1} to 1.5E-7 m^{-1}. Beauheim et al. (1991) reported a range of 9.7E-8 m^{-1} to 2.5E-7 m^{-1} interbed specific storage. Using equation (3), an alternative range for anhydrite interbed rock compressibility of 5.7E-12 m^{-1} to 1.9E-11 m^{-1} is calculated. Beauheim et al. (1991; p. 100) also suggest that fracturing might result in a fourfold increase in interbed rock compressibility, α.
REFERENCES :	Beauheim, R.L., G.J. Saulnier, Jr., and J.D. Avis. 1991. *Interpretation of Brine-Permeability Tests of the Salado Formation at the Waste Isolation Pilot Plant Site: First Interim Report.* SAND90-0083. Albuquerque, NM: Sandia National Laboratories. de Marsily, G. 1986. *Quantitative Hydrogeology.* Orlando, FL: Academic Press. Freeze, R.A., and J.A. Cherry. 1979. *Groundwater.* Englewood Cliffs, NJ: Prentice-Hall, Inc. Green, D.H., and H.F. Wang. 1990. "Specific Storage as a Poroelastic Coefficient," *Water Resources Research*. Vol. 26, no. 7, 1631-1637.

DATE :	08/31/93	RATIONALE NUMBER :	003A
PARAMETER :	Room Compressibility		
VALUE :	0.0 Pa^{-1}		
KEYWORD :	ROCKS		

RATIONALE : The waste-backfill mixture within the waste disposal rooms is heterogeneous and has physical characteristics that will change as the room closes. Thus, quantifying the compressibility of the waste-backfill mixture that fills a room is a difficult task.

In coupled flow and closure simulations, the effects of room pore volume compressibility are incorporated indirectly through the coupling methods, and the simulated room (waste and backfill) compressibility is zero.

COMMENTS : For the fixed room geometry simulations, room compressiblity considers only backfill compressibility. Estimates of backfill compressibility are based on laboratory tests of crushed salt backfill at varying states of consolidation (Holcomb and Hannum, 1982; Sjaardema and Kreig, 1987). The laboratory test consists of consolidating crushed salt under hydrostatic pressure up to 21 MPa, interrupted by several depressurization-repressurization cycles. Elastic properties have been determined for each depressurization-repressurization cycle, which correspond to a specific consolidation state and density.

Based on these tests, empirically derived expressions for elastic bulk modulus and elastic shear modulus were developed by Sjaardema and Krieg (1987; p. 59):

$$K = 1.76 \times 10^4 \cdot e^{(6.53E-3)(\rho)} \quad (1)$$

$$G = 1.06 \times 10^4 \cdot e^{(6.53E-3)(\rho)} \quad (2)$$

where:

K = bulk modulus [Pa],
G = shear modulus [Pa],
ρ = backfill density [kg/m^3].

PARAMETER (cont'd) :	Room Compressibility

COMMENTS (cont'd) :

The bulk compressibility of the backfill, $\alpha_{backfill}$, which has units of Pa^{-1}, can be computed directly from the elastic properties (Green and Wang, 1990; p. 1632):

$$\alpha_{backfill} = \frac{1}{K + 4G/3} \quad (3)$$

Most multiphase flow codes use pore volume compressibility, α_p, which can be calculated from the bulk compressibility, α, and the room porosity, ϕ, using (de Marsily, 1986; pp. 103-105):

$$\alpha_p = \frac{\alpha}{\phi} \quad (4)$$

Initial Room

Under initial room conditions most of the compaction will be in the backfill surrounding the waste. The initial emplacement density of the backfill is assumed to be 1280 kg/m^3 (Nowak et al., 1990). Equation (1) yields:

$$K = 1.76 \times 10^4 \cdot e^{(6.53E-3)(1280 kg/m^3)} = 7.51 \times 10^7 \text{ Pa}$$

Equation (2) yields:

$$G = 1.06 \times 10^4 \cdot e^{(6.53E-3)(1280 kg/m^3)} = 4.52 \times 10^7 \text{ Pa}$$

The bulk compressibility, α, is calculated from equation (3):

$$\alpha = \frac{1}{(7.51 \times 10^7 Pa) + (4)(4.52 \times 10^7 Pa)/(3)} = 7.4 \times 10^{-9} \text{ Pa}^{-1}$$

The initial room porosity is 0.66 (see porosity rationale). From equation (4):

$$\alpha_p = \frac{\alpha}{\phi} = 1.1 \times 10^{-8} \text{ Pa}^{-1}$$

PARAMETER (cont'd) :	Room Compressibility

COMMENTS (cont'd) :

Intermediate Room

Under intermediate room conditions the backfill is assumed to be compacted to its final density and the waste is assumed to be undergoing some compaction. The final fractional density of backfill is 0.95 (Lappin et al., 1989; p. 4-59) and the density of intact WIPP salt is 2140 kg/m^3 (Sjaardema and Krieg, 1987; p. 11). Therefore:

$$\rho_{\text{intermediate backfill}} = (0.95)(\rho_{\text{intact salt}}) = (0.95)(2140\ \text{kg/m}^3) = 2.03\text{x}10^3\ \text{kg/m}^3$$

Substituting this density into equations (1) and (2) yields:

$$K = 1.76\text{x}10^4 \cdot e^{(6.53\text{E-}3)(2030\text{kg/m}^3)} = 1.01\text{x}10^{10}\ \text{Pa}$$

$$G = 1.06\text{x}10^4 \cdot e^{(6.53\text{E-}3)(2030\text{kg/m}^3)} = 6.06\text{x}10^9\ \text{Pa}$$

The bulk compressibility, α, is calculated from equation (3):

$$\alpha = \frac{1}{(1.01\text{x}10^{10}\text{Pa}) + (4)(6.06\text{x}10^9\text{Pa})/(3)} = 5.5\text{x}10^{-11}\ \text{Pa}^{-1}$$

The intermediate room porosity is assumed to be 0.38 (see porosity rationale). From equation (4):

$$\alpha_p = \frac{\alpha}{\phi} = 1.4 \times 10^{-10}\ \text{Pa}^{-1}$$

Fully Consolidated Room

Under fully consolidated room conditions both the backfill and waste are assumed to be compacted to their final density. The backfill density (2030 kg/m^3) and bulk compressibility (5.5E-11 Pa^{-1}) are the same as in the intermediate room state. The fully consolidated room porosity is assumed to be 0.22 (see porosity rationale). From equation (4):

$$\alpha_p = \frac{\alpha}{\phi} = 2.5 \times 10^{-10}\ \text{Pa}^{-1}$$

PARAMETER (cont'd) :	Room Compressibility

COMMENTS (cont'd) : The bulk compressibility of the waste can be estimated from the relationship between waste porosity, ϕ, and stress (assumed equivalent to effective stress, σ_e) presented by Beraun and Davies (1992, p. 4) using the relationship (Freeze and Cherry, 1979; p. 54):

$$\alpha_{waste} = -\frac{d\phi}{d\sigma_e} \qquad (5)$$

At early time (stress < 4 MPa, initial room state) the bulk compressibility of the waste is:

$$\alpha_{waste} = -\frac{(0.44-0.78)}{(4.0\times10^{6}-0.1\times10^{6})} = 8.7\times10^{-8}\ Pa^{-1}$$

At late time (stress > 8 MPa, fully consolidated room state):

$$\alpha_{waste} = -\frac{(0.19-0.31)}{(15.0\times10^{6}-8.0\times10^{6})} = 1.7\times10^{-8}\ Pa^{-1}$$

These results suggest that the waste is much more compressible than the backfill.

These room compressibility values are regarded as having a very large uncertainty. Sources of uncertainty include:

i) Assumption of using backfill to approximate what will in reality be a mixture of backfill and waste.

ii) Uncertainty in the estimate of backfill density at any given point in a room's closure history.

iii) Selection of appropriate room porosity for converting to pore volume compressibility from the bulk compressibility. For these calculations, the estimated porosity for a waste-backfill mixture is used.

PARAMETER (cont'd) :	Room Compressibility

REFERENCES :

Beraun, R., and P.B. Davies. 1992. "Baseline Design Input Data Base to be Used During Calculations Effort to be Performed by Division 1514 in Determining the Mechanical Creep Closure Behavior of Waste Disposal Rooms in Bedded Salt," *Preliminary Performance Assessment for the Waste Isolation Pilot Plant, December 1992 - Volume 3: Model Parameters.* SAND92-0700/3. Albuquerque, NM: Sandia National Laboratories. A-5 through A-13.

de Marsily, G. 1986. *Quantitative Hydrogeology.* Orlando, FL: Academic Press.

Freeze, R.A., and J.A. Cherry. 1979. *Groundwater.* Englewood Cliffs, NJ: Prentice-Hall, Inc.

Green, D.H., and H.F. Wang. 1990. "Specific Storage as a Poroelastic Coefficient," *Water Resources Research.* Vol. 26, no. 7, 1631-1637.

Holcomb, D.J., and D.W. Hannum. 1982. *Consolidation of Crushed Salt Backfill Under Conditions Appropriate to the WIPP Facility.* SAND82-0630. Albuquerque, NM: Sandia National Laboratories.

Lappin, A.R., R.L. Hunter, D.P. Garber, and P.B. Davies, eds. 1989. *Systems Analysis, Long-Term Radionuclide Transport, and Dose Assessments, Waste Isolation Pilot Plant (WIPP), Southeastern New Mexico; March 1989.* SAND89-0462. Albuquerque, NM: Sandia National Laboratories.

Nowak, E.J., J.R. Tillerson, and T.M. Torres. 1990. *Initial Reference Seal System Design: Waste Isolation Pilot Plant.* SAND90-0355. Albuquerque, NM: Sandia National Laboratories.

Sjaardema, G.D., and R.D. Krieg. 1987. *A Constitutive Model for the Consolidation of WIPP Crushed Salt and Its Use in Analyses of Backfilled Shaft and Drift Configurations.* SAND87-1977. Albuquerque, NM: Sandia National Laboratories.

IIB. TWO-PHASE PROPERTIES

DATE :	08/31/93	RATIONALE NUMBER :		002B	
PARAMETER :	Relative Permeability and Capillary Pressure Curves for Halite				
VALUE :	S_b	k_{rb}	k_{rg}	P_c	
				MPa	bars
	0.200	0.000E+0	1.000E+0		
	0.220	2.230E-9	9.344E-1	1332.	13320
	0.250	4.776E-7	8.402E-1	359.6	3596
	0.300	2.769E-5	6.938E-1	133.6	1336
	0.350	2.976E-4	5.598E-1	74.86	748.6
	0.400	1.605E-3	4.380E-1	49.64	496.4
	0.450	5.930E-3	3.287E-1	36.09	360.9
	0.500	1.725E-2	2.327E-1	27.81	278.1
	0.525	2.757E-2	1.903E-1	24.81	248.1
	0.550	4.255E-2	1.519E-1	22.31	223.1
	0.575	6.374E-2	1.177E-1	20.22	202.2
	0.600	9.303E-2	8.785E-2	18.44	184.4
	0.650	1.854E-1	4.189E-2	15.58	155.8
	0.675	2.545E-1	2.578E-2	14.43	144.3
	0.700	3.437E-1	1.403E-2	13.41	134.1
	0.725	4.574E-1	6.290E-3	12.50	125.0
	0.750	6.007E-1	1.980E-3	11.70	117.0
	0.770	7.405E-1	4.488E-4	11.12	111.2
	0.790	9.062E-1	1.744E-5	10.58	105.8
	0.800	1.000E+0	0.000E+0	10.33	103.3
	0.900	1.000E+0	0.000E+0	8.290	82.90
	1.000	1.000E+0	0.000E+0	6.850	68.50
KEYWORD :	ROCKS, RPCAP				

RATIONALE : There are no measured relative permeability or capillary pressure curves for the Salado halite. A literature search failed to locate either measured or theoretically based curves for the halite. In the absence of site-specific or halite-specific data, two-phase properties are based on data from actual measurements on analogue materials. A "tight" gas sand core (Sample MWX 67-35) from the multi-well experiment (Morrow et al., 1986) was selected as an analogue to determine the relative permeability characteristics of halite.

PARAMETER (cont'd) :	Relative Permeability and Capillary Pressure Curves for Halite

RATIONALE (cont'd) :

The "tight" gas sand sample is from the Williams Fork Formation of the Mesa Verde Group. The environment of deposition is a lower delta plain referred to as a paludal zone characterized by very fine sand interbedded with coals and shale. Sample 67-35 is a fine sandstone with thin bedding, 12 percent porosity, moderate sorting, subangular quartz grains, and dolomitic cementation. The dominant pore geometry consists of intergranular cracks between abutting quartz grains and solution pores partially filled with dolomite (Morrow et al., 1986; Soeder and Randolph, 1984). The permeability of this sample to brine is 43 μd (4.3E-17 m^2) at 3.4 MPa confining pressure and 24 μd (2.4E-17 m^2) at 34.0 MPa confining pressure.

The two-phase properties are derived from the relationships of Brooks and Corey (1964):

Wetting Phase (brine) Relative Permeability

$$k_{rb} = k_{rw} = S_e^{(2+3\lambda)/\lambda} \quad (1)$$

Non-Wetting Phase (gas) Relative Permeability

$$k_{rg} = k_{rnw} = (1 - S_e)^2 \quad (1 - S_e^{(2+\lambda)/\lambda}) \quad (2)$$

where the effective wetting phase (brine) saturation, S_e, is defined as:

$$S_e = \frac{S_b - S_{br}}{1 - S_{gc} - S_{br}} \quad (3)$$

and

λ = pore-size distribution index,
S_b = wetting phase (brine) saturation,
S_{br} = residual brine saturation, and
S_{gc} = critical gas saturation.

Equation (3) for effective wetting phase saturation differs slightly from the form presented in Brooks and Corey (1964), however, they do discuss this form briefly in Appendix I (p. 23). This formulation is similar to an equation presented by Burdine (1953), whose work provides a basis for the Brooks and Corey

PARAMETER (cont'd) :	Relative Permeability and Capillary Pressure Curves for Halite

RATIONALE (cont'd) :

(1964) model. Equation (3) is selected because it satisfies the bounding conditions of the relative permeability relationships of equations (1) and (2). At the point of zero brine mobility, $S_b = S_{br}$, equation (3) yields $S_e = 0$ and equation (1) yields $k_{rb} = 0$. At the point of zero gas mobility, $S_b = 1 - S_{gc}$, equation (3) yields $S_e = 1$ and equation (2) yields $k_{rg} = 0$.

The Brooks and Corey (1964) model is fit to the measured data from the "tight" gas sand. From this fit, the following parameter values are estimated:

$$S_{br} = 0.20 \quad S_{gc} = 0.20 \quad \lambda = 0.7$$

The S_{gc} value was estimated from the observed non-wetting phase relative permeability versus saturation data shown in Figures 1 and 2. The method used to determine S_{br} is described in Brooks and Corey (1964; p. 24). Determining S_{br} is a trial and error procedure that involves fitting calculated curves to the observed capillary pressure versus saturation data shown in Figures 3 and 4.

The λ value used in the Brooks and Corey (1964) model is obtained by determining the slope of a line through the observed capillary pressure for the "tight" gas sand plotted logrithmically as a function of effective brine saturation, S_e (Figure 4). A threshold pressure for the sand (0.3 MPa) is also determined from Figure 4. The run 2 and run 3 data points on Figures 3 and 4 are taken from Morrow et al. (1986; Fig. 19).

Because the "tight" gas sand permeability (4E-17 m^2) was about four orders of magnitude higher than the halite permeability (1E-21 m^2), the threshold pressure, P_t, for halite was estimated from a permeability-threshold pressure correlation. The threshold pressure is defined as the capillary pressure at the point gas forms a continuous phase (i.e., at $S_g = S_{gc}$).

Halite threshold pressures, P_t (in MPa), are calculated from the following permeability correlation (k in m^2) for consolidated lithologies (Davies, 1991; p. 25):

$$P_t = (5.6 \times 10^{-7})(k^{-0.346}) \qquad (4)$$

and: $P_t = 10.3$ MPa (for $k = 1E\text{-}21$ m^2)

PARAMETER (cont'd) :	Relative Permeability and Capillary Pressure Curves for Halite
RATIONALE (cont'd) :	The capillary pressure, P_c, is calculated from the threshold pressure (Brooks and Corey, 1964): $$P_c = \frac{P_t}{S_e^{1/\lambda}} \quad (5)$$ Figure 5 shows the calculated capillary pressure curve for halite with a permeability of 1E-21 m^2. The wetting (brine) and non-wetting (gas) phase relative permeability curves, calculated from equations (1) and (2), respectively, are indicated by solid lines in Figures 1 and 2. The calculated sand capillary pressure curves, calculated from equation (5), are indicated by solid lines in Figures 3 and 4. The calculated relative permeability and sand capillary pressure curves closely approximate the observed data in all four figures. Therefore, the S_{gc}, S_{br}, and λ values selected are considered representative of the "tight" gas sand and are assumed to provide an analogue for halite relative permeability. Measurements of relative permeability for the wetting phase were not obtained by Morrow et al. (1986) for the multi-well borehole cores because of the length of time required and the difficulty in obtaining accurate measurements. The calculated wetting phase curve using the Brooks and Corey (1964) model provides the best available estimate for this parameter.
COMMENTS :	To examine the sensitivity of system behavior to halite multiphase flow properties, the residual brine and gas saturations were varied from 0.0 to 0.4 and the pore-size λ was varied from 0.2 to 10.0, as suggested by Webb (1992). A range of threshold pressures was calculated from equation (4): P_t = 250. MPa (for k = 1E-25 m^2) = 22.9 MPa (for k = 1E-22 m^2) = 4.7 MPa (for k = 1E-20 m^2) = 2.1 MPa (for k = 1E-19 m^2)

PARAMETER (cont'd) :	Relative Permeability and Capillary Pressure Curves for Halite
COMMENTS (cont'd) :	Gas penetration into brine saturated halite can occur when: $$P_g > P_t + P_b$$ where: P_g = gas pressure in the disposal room, P_t = threshold pressure in halite, P_b = brine pressure in halite. Given the likelihood of high threshold pressures in the halite (Davies, 1991; p. 28), gas penetration may not occur under repository conditions. If gas pressures in the room reach lithostatic pressure (15 MPa) and the far field brine pressure is 12 MPa, gas penetration into halite will not occur unless $P_t \approx 3$ MPa or less. However, brine pressures are likely to be significantly lower within the first few meters of an excavation. Assuming that brine pressure falls to near atmospheric ($\sim$ 0.1 MPa) adjacent to an excavation, gas penetration into at least the depressurized zone of halite is likely to occur for $P_t \approx 15$ MPa or less. In summary, for these estimated threshold pressures, gas penetration may be restricted to a narrow zone of depressurized rock directly adjacent to the excavation. The gas sand sample has an intrinsic permeability of approximately 4.0E-17 m^2 whereas the intrinsic permeability of the Salado halite ranges from 1.0E-20 m^2 to 1.0E-22 m^2. However, the gas sand is the closest analogue found for the Salado halite. Demond and Roberts (1987) suggest that relative permeability curves are insensitive to intrinsic permeability, in which case the difference in the permeabilities may not be a major issue. However, the degree to which this gas sand sample represents the pore size distribution and pore structure likely to exist in the Salado halite is of importance. The three to five order of magnitude difference in permeabilities between the gas sand and the Salado halite may suggest a different pore structure. Nonetheless, until a more representative sample can be identified, the relative permeability and capillary pressure curves for the gas sand are assumed suitable for the Salado halite.

PARAMETER (cont'd) :	Relative Permeability and Capillary Pressure Curves for Halite

REFERENCES :

Brooks, R.H., and A.T. Corey. 1964. *Hydraulic Properties of Porous Media.* Hydrology Papers No. 3. Fort Collins, CO: Colorado State University.

Burdine, N.T. 1953. "Relative Permeability Calculations From Pore-Size Distribution Data," *Transactions of the American Institute of Mining and Metallurgical Engineers: Petroleum Branch.* Vol. 198, 71-78.

Davies, P.B. 1991. *Evaluation of the Role of Threshold Pressure in Controlling Flow of Waste-Generated Gas into the Bedded Salt Surrounding the WIPP Repository.* SAND90-3246. Albuquerque, NM: Sandia National Laboratories.

Demond, A.H., and P.V. Roberts. 1987. "An Examination of Relative Permeability Relations for Two-Phase Flow in Porous Media," *Water Resources Bulletin.* Vol. 23, no. 4, 617-628.

Morrow, N.R., J.S. Ward, and K.R. Brower. 1986. *Rock Matrix and Fracture Analysis of Flow in Western Tight Gas Sands. 1985 Annual Report.* DOE/MC/21179-2032 (DE86001055). Morgantown, WV: U.S. Department of Energy; Socorro, NM: New Mexico Institute of Mining and Technology, New Mexico Petroleum Recovery Center.

Soeder, D.J., and P.L. Randolph. 1984. *Special Dry Core Analysis of the Mesa Verde Formation U.S. DOE Multiwell Experiment Garfield County, Colorado.* DOE/MC/20342-4. Morgantown, WV: U.S. Department of Energy.

Webb, S.W. 1992. "Uncertainty Estimates for Two-Phase Characteristic Curves for 1992 40 CFR 191 Calculations," *Preliminary Performance Assessment for the Waste Isolation Pilot Plant, December 1992 - Volume 3: Model Parameters.* Sandia WIPP Project. SAND92-0700/3. Albuquerque, NM: Sandia National Laboratories. A-147 through A-155.

PARAMETER (cont'd) :	Relative Permeability and Capillary Pressure Curves for Halite

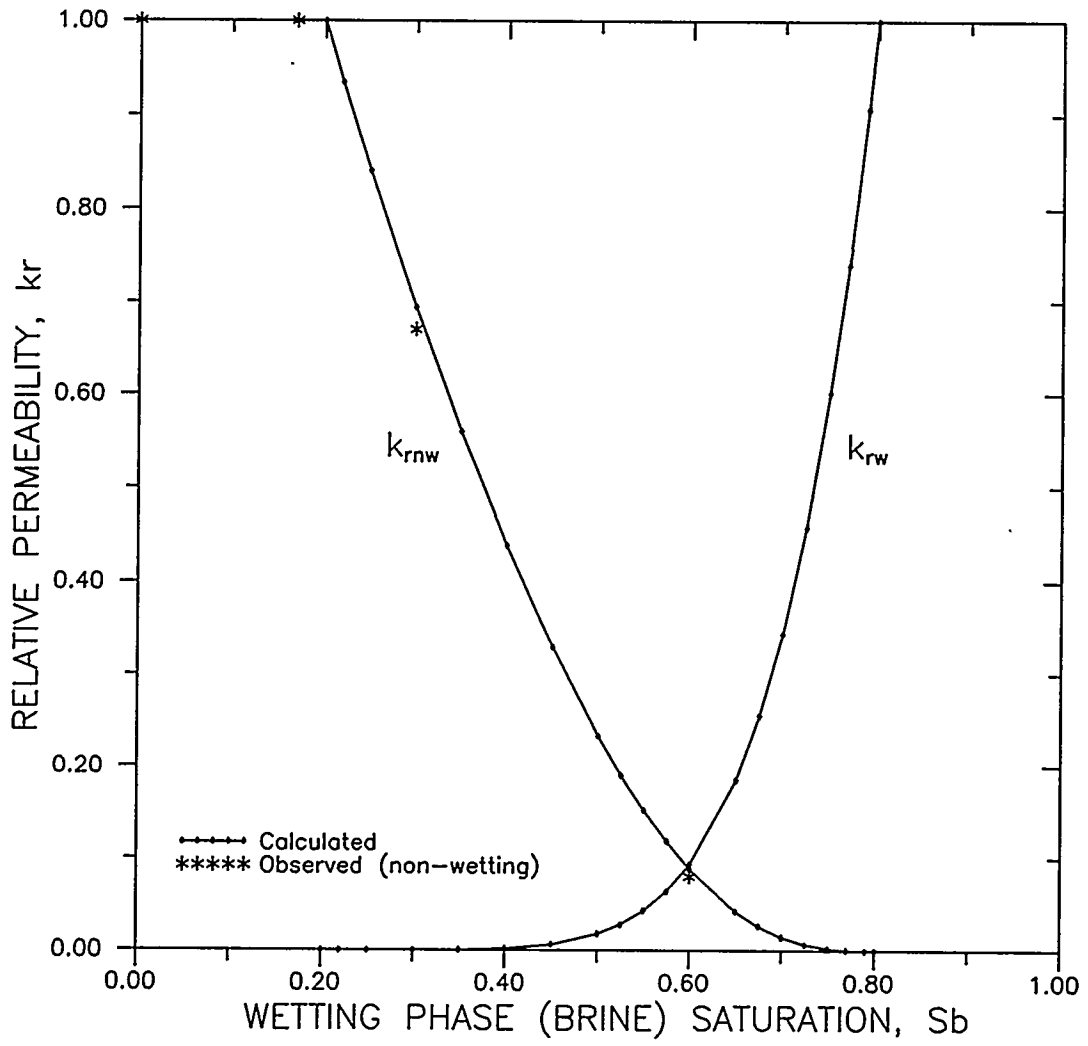

Figure 1. Observed relative permeabilities for the "tight" gas sand and calculated relative permeabilities.

PARAMETER (cont'd) :	Relative Permeability and Capillary Pressure Curves for Halite

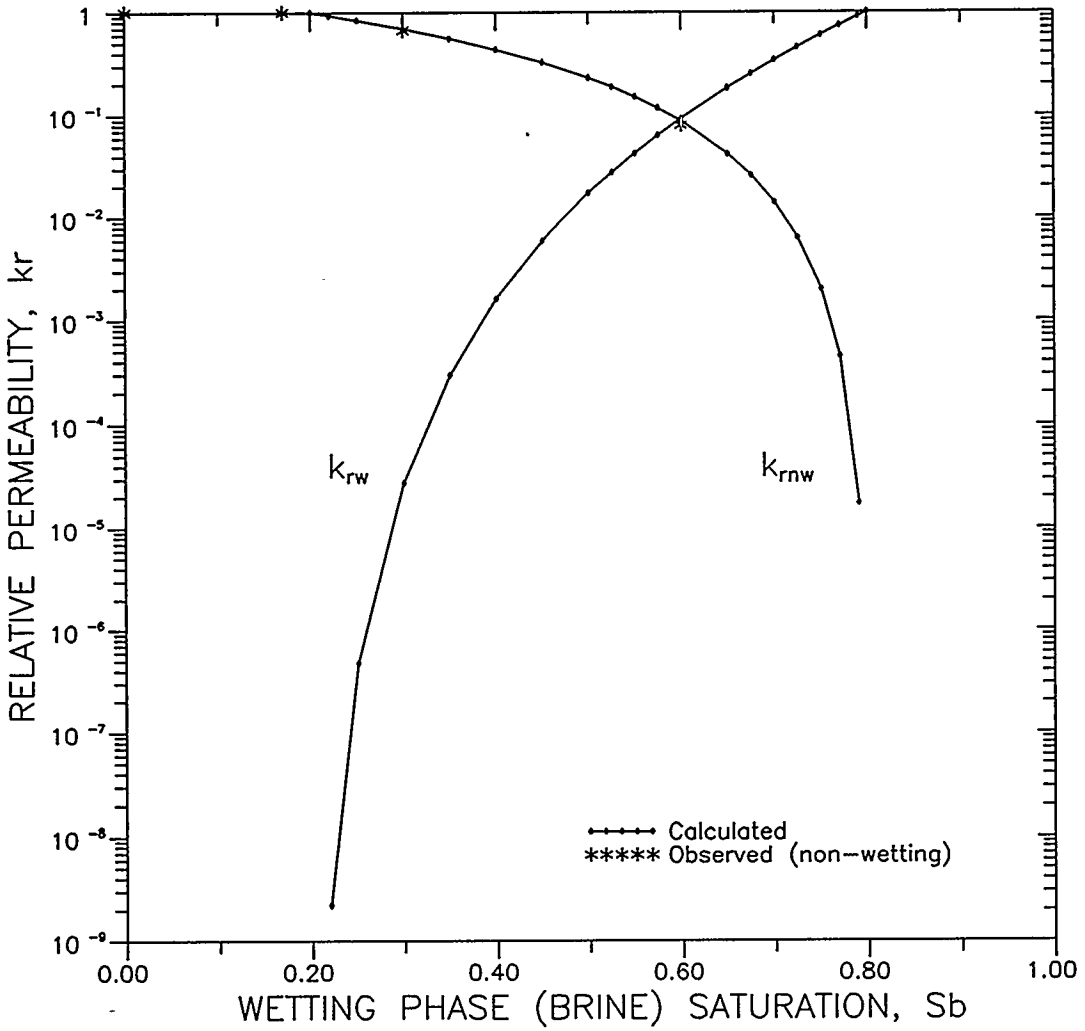

Figure 2. Observed relative permeabilities for the "tight" gas sand and calculated relative permeabilities (log scale).

PARAMETER (cont'd) :	Relative Permeability and Capillary Pressure Curves for Halite

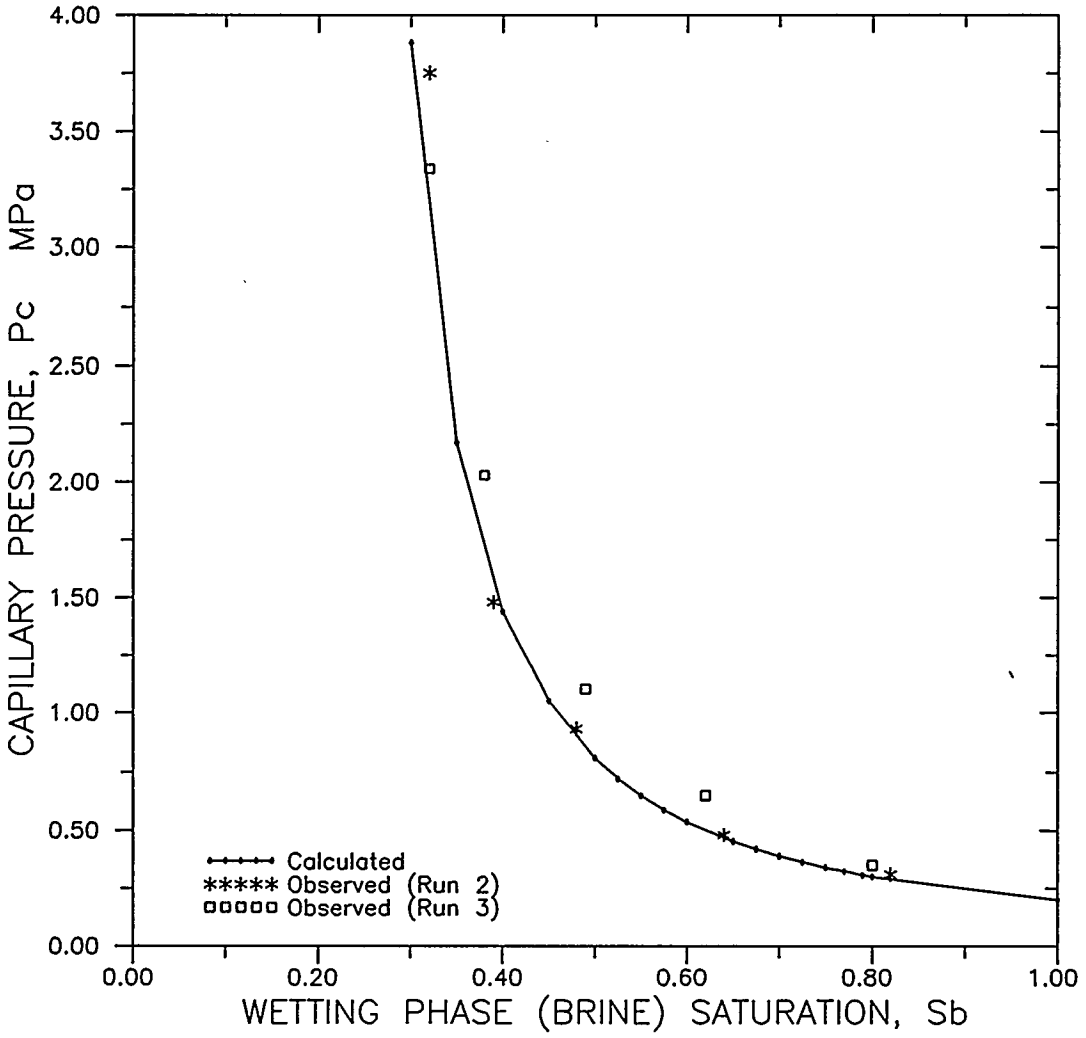

Figure 3. Observed and calculated capillary pressure for the "tight" gas sand.

PARAMETER (cont'd) :	Relative Permeability and Capillary Pressure Curves for Halite

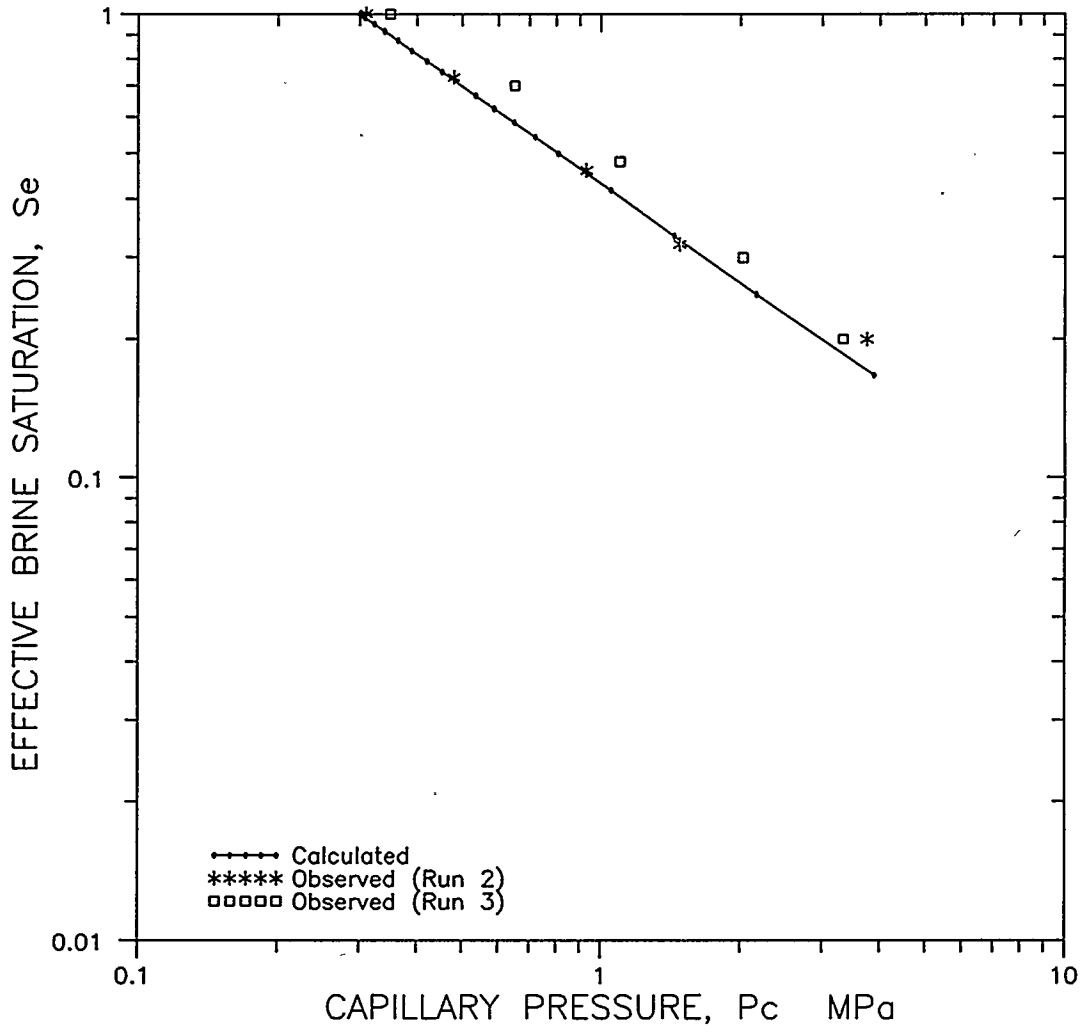

Figure 4. Observed and calculated effective saturation vs. capillary pressure used to determine the Brooks and Corey (1964) model parameters, λ (slope) and P_t (intercept at $S_e = 1$).

PARAMETER (cont'd) :	Relative Permeability and Capillary Pressure Curves for Halite

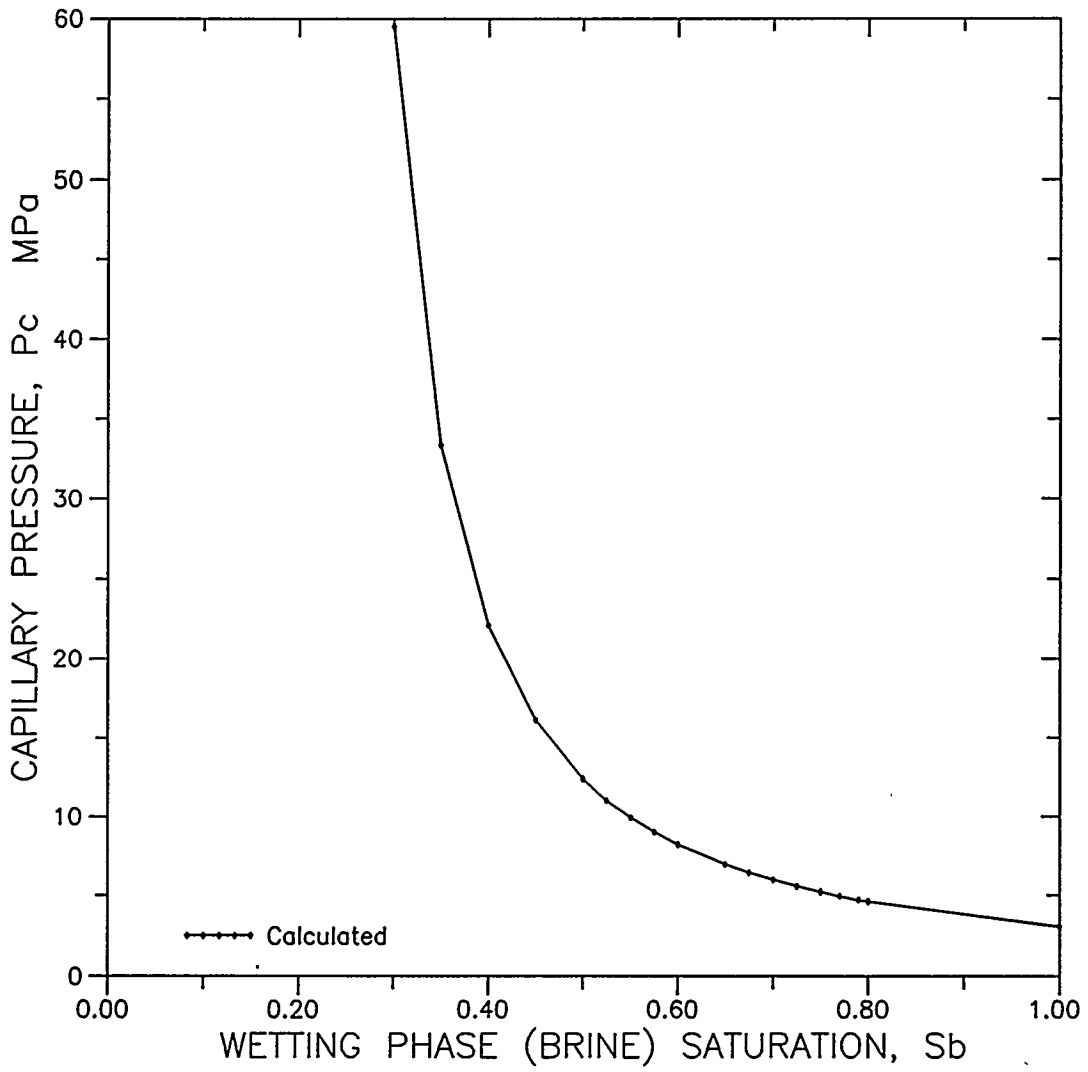

Figure 5. Calculated capillary pressure for halite.

DATE :	08/31/93	RATIONALE NUMBER :		001D	
PARAMETER :	Relative Permeability and Capillary Pressure Curves for the Salado Interbeds				
VALUE :	S_b	k_{rb}	k_{rg}	P_c MPa	P_c bars
	0.200	0.000E+0	1.000E+0		
	0.220	2.230E-9	9.344E-1	38.66	386.6
	0.250	4.776E-7	8.402E-1	10.44	104.4
	0.300	2.769E-5	6.938E-1	3.879	38.79
	0.350	2.976E-4	5.598E-1	2.174	21.74
	0.400	1.605E-3	4.380E-1	1.441	14.41
	0.450	5.930E-3	3.287E-1	1.048	10.48
	0.500	1.725E-2	2.327E-1	.8075	8.075
	0.525	2.757E-2	1.903E-1	.7203	7.203
	0.550	4.255E-2	1.519E-1	.6479	6.479
	0.575	6.374E-2	1.177E-1	.5871	5.871
	0.600	9.303E-2	8.785E-2	.5354	5.354
	0.650	1.854E-1	4.189E-2	.4525	4.525
	0.675	2.545E-1	2.578E-2	.4189	4.189
	0.700	3.437E-1	1.403E-2	.3893	3.893
	0.725	4.574E-1	6.290E-3	.3631	3.631
	0.750	6.007E-1	1.980E-3	.3397	3.397
	0.770	7.405E-1	4.488E-4	.3228	3.228
	0.790	9.062E-1	1.744E-5	.3073	3.073
	0.800	1.000E+0	0.000E+0	.3000	3.000
	0.900	1.000E+0	0.000E+0	.2407	2.407
	1.000	1.000E+0	0.000E+0	.1989	1.989
KEYWORD :	ROCKS, RPCAP				
RATIONALE :	There are no measured relative permeability or capillary pressure curves for the Salado interbeds. A literature search failed to locate either measured or theoretically based curves for the Salado interbeds. In the absence of site-specific data, two-phase properties are based on data from actual measurements on analogue materials. A "tight" gas sand core (Sample MWX 67-35) from the multi-well experiment (Morrow et al., 1986) was selected as an analogue to determine the				

PARAMETER (cont'd) :	Relative Permeability and Capillary Pressure Curves for the Salado Interbeds

RATIONALE (cont'd) : relative permeability characteristics and threshold pressure of the anhydrite interbeds.

The "tight" gas sand sample is from the Williams Fork Formation of the Mesa Verde Group. The environment of deposition is a lower delta plain referred to as a paludal zone characterized by very fine sand interbedded with coals and shale. Sample 67-35 is a fine sandstone with thin bedding, 12 percent porosity, moderate sorting, subangular quartz grains, and dolomitic cementation. The dominant pore geometry consists of intergranular cracks between abutting quartz grains and solution pores partially filled with dolomite (Morrow et al., 1986; Soeder and Randolph, 1984). The permeability of this sample to brine is 43 μd (4.3E-17 m^2) at 3.4 MPa confining pressure and 24 μd (2.4E-17 m^2) at 34.0 MPa confining pressure.

The two-phase properties are derived from the relationships of Brooks and Corey (1964):

Wetting Phase (brine) Relative Permeability

$$k_{rb} = k_{rw} = S_e^{(2+3\lambda)/\lambda} \quad (1)$$

Non-Wetting Phase (gas) Relative Permeability

$$k_{rg} = k_{rnw} = (1 - S_e)^2 \quad (1 - S_e^{(2+\lambda)/\lambda}) \quad (2)$$

where the effective wetting phase (brine) saturation, S_e, is defined as:

$$S_e = \frac{S_b - S_{br}}{1 - S_{gc} - S_{br}} \quad (3)$$

and

λ = pore-size distribution index,
S_b = wetting phase (brine) saturation,
S_{br} = residual brine saturation, and
S_{gc} = critical gas saturation.

Equation (3) for effective wetting phase saturation differs slightly from the form presented in Brooks and Corey (1964), however, they do discuss this form briefly in Appendix I (p. 23). This

PARAMETER (cont'd) :	Relative Permeability and Capillary Pressure Curves for the Salado Interbeds

RATIONALE (cont'd) :

formulation is similar to an equation presented by Burdine (1953), whose work provides a basis for the Brooks and Corey (1964) model. Equation (3) is selected because it satisfies the bounding conditions of the relative permeability relationships of equations (1) and (2). At the point of zero brine mobility, $S_b = S_{br}$, equation (3) yields $S_e = 0$ and equation (1) yields $k_{rb} = 0$. At the point of zero gas mobility, $S_b = 1 - S_{gc}$, equation (3) yields $S_e = 1$ and equation (2) yields $k_{rg} = 0$.

The Brooks and Corey (1964) model is fit to the measured data from the "tight" gas sand. From this fit, the following parameter values are estimated:

$$S_{br} = 0.20 \quad S_{gc} = 0.20 \quad \lambda = 0.7$$

The S_{gc} value was estimated from the observed non-wetting phase relative permeability versus saturation data shown in Figures 1 and 2. The method used to determine S_{br} is described in Brooks and Corey (1964; p. 24). Determining S_{br} is a trial and error procedure that involves fitting calculated curves to the observed capillary pressure versus saturation data shown in Figures 3 and 4.

The λ value used in the Brooks and Corey (1964) model is obtained by determining the slope of a line through the observed capillary pressure for the "tight" gas sand plotted logrithmically as a function of effective brine saturation, S_e
(Figure 4). A threshold pressure for the sand (0.30 MPa) is also determined from Figure 4. The run 2 and run 3 data points on Figures 3 and 4 are taken from Morrow et al. (1986; Fig. 19).

Because the "tight" gas sand permeability (4E-17 m^2) was within two orders of magnitude of the anhydrite interbed permeability (1E-19 m^2), the threshold pressure, P_t, for the sand (0.30 MPa) was assumed to be representative of the Salado interbeds. The threshold pressure is defined as the capillary pressure at the point gas forms a continuous phase (i.e., at $S_g = S_{gc}$). The capillary pressure, P_c, is calculated from the threshold pressure (Brooks and Corey, 1964):

$$P_c = \frac{P_t}{S_e^{1/\lambda}} \qquad (4)$$

PARAMETER (cont'd) :	Relative Permeability and Capillary Pressure Curves for the Salado Interbeds
RATIONALE (cont'd) :	The capillary pressure curve for the "tight" gas sand (Figure 3), calculated from equation (4), is representative of the interbeds. This threshold pressure is slightly lower than the value (2.1 MPa) found by Davies (1991; p. 25) using a permeability correlation. A lower threshold pressure is consistent with fracturing . The wetting (brine) and non-wetting (gas) phase relative permeability curves, calculated from equations (1) and (2), respectively, are indicated by solid lines in Figures 1 and 2. The calculated sand capillary pressure curves, calculated from equation (4), are indicated by solid lines in Figures 3 and 4. The calculated relative permeability and sand capillary pressure curves closely approximate the observed data in all four figures. Therefore, the S_{gc}, S_{br}, and λ values selected are considered representative of the "tight" gas sand and are assumed to provide an analogue for halite relative permeability and capillary pressure. Measurements of relative permeability for the wetting phase were not obtained by Morrow et al. (1986) for the multi-well borehole cores because of the length of time required and the difficulty in obtaining accurate measurements. The calculated wetting phase curve using the Brooks and Corey (1964) model provides the best available estimate for this parameter.
COMMENTS :	This core is selected because it has permeability close to the range believed to exist in the interbeds. Although intrinsic permeability does not have a direct effect upon the relative permeability and capillary pressure curves, the pore structure and pore size do. These also directly affect intrinsic permeability. Therefore, a sample with low permeability is used with the assumption that at extremely low permeabilities, the pore characteristics would not be radically different from that which exists in the interbeds. This sample contains visible fractures but, because of the nature of dominant pore geometry (i.e. intergranular cracks between quartz grains), the data from this sample is still considered to represent the characteristics which might be found in the Salado interbeds. To examine the sensitivity of system behavior to the interbed multiphase flow properties, the residual brine and gas saturations were varied from 0.0 to 0.4 and the pore-size λ was varied from 0.2 to 10.0, as suggested by Webb (1992).

PARAMETER (cont'd) :	Relative Permeability and Capillary Pressure Curves for the Salado Interbeds
COMMENTS (cont'd) :	A range of threshold pressures was calculated from equation (4): P_t = 4.7 MPa (for k = 1E-20 m^2) = 2.1 MPa (for k = 1E-19 m^2) = 1.0 MPa (for k = 1E-18 m^2) = 0.2 MPa (for k = 1E-16 m^2) The relative permeability and capillary pressure data obtained in "tight" gas sands provides a reasonable first estimate of the two-phase parameters needed to characterize the relative permeability and capillary pressure curves for the WIPP interbeds. The gas sands have intrinsic permeabilities close to the range believed characteristic of the interbeds. However, a question that remains to be answered originates from the differences in pore geometries between the gas sands and the interbeds and the effect this difference would have on the relative permeability and capillary pressure curves.
REFERENCES :	Brooks, R.H., and A.T. Corey. 1964. *Hydraulic Properties of Porous Media.* Hydrology Papers No. 3. Fort Collins, CO: Colorado State University. Burdine, N.T. 1953. "Relative Permeability Calculations From Pore-Size Distribution Data," *Transactions of the American Institute of Mining and Metallurgical Engineers. Petroleum Branch.* Vol 198, 71-78. Davies, P.B. 1991. *Evaluation of the Role of Threshold Pressure in Controlling Flow of Waste-Generated Gas into the Bedded Salt at the Waste Isolation Pilot Plant.* SAND90-3246. Albuquerque, NM: Sandia National Laboratories. Morrow, N.R., J.S. Ward, and K.R. Brower. 1986. *Rock Matrix and Fracture Analysis of Flow in Western Tight Gas Sands. 1985 Annual Report.* DOE/MC/21179-2032 (DE86001055). Morgantown, WV: U.S. Department of Energy; Socorro, NM: New Mexico Institute of Mining and Technology, New Mexico Petroleum Recovery Center. Soeder, D.J., and P.L. Randolph. 1984. *Special Dry Core Analysis of the Mesa Verde Formation U.S. DOE Multiwell Experiment Garfield County, Colorado.* DOE/MC/20342-4. Morgantown, WV: U.S. Department of Energy. Webb, S.W. 1992. "Uncertainty Estimates for Two-Phase Characteristic Curves for 1992 40 CFR 191 Calculations," *Preliminary Performance Assessment for the Waste Isolation Pilot Plant, December 1992 - Volume 3: Model Parameters.* Sandia WIPP Project. SAND92-0700/3. Albuquerque, NM: Sandia National Laboratories. A-147 through A-155.

PARAMETER (cont'd) :	Relative Permeability and Capillary Pressure Curves for the Salado Interbeds

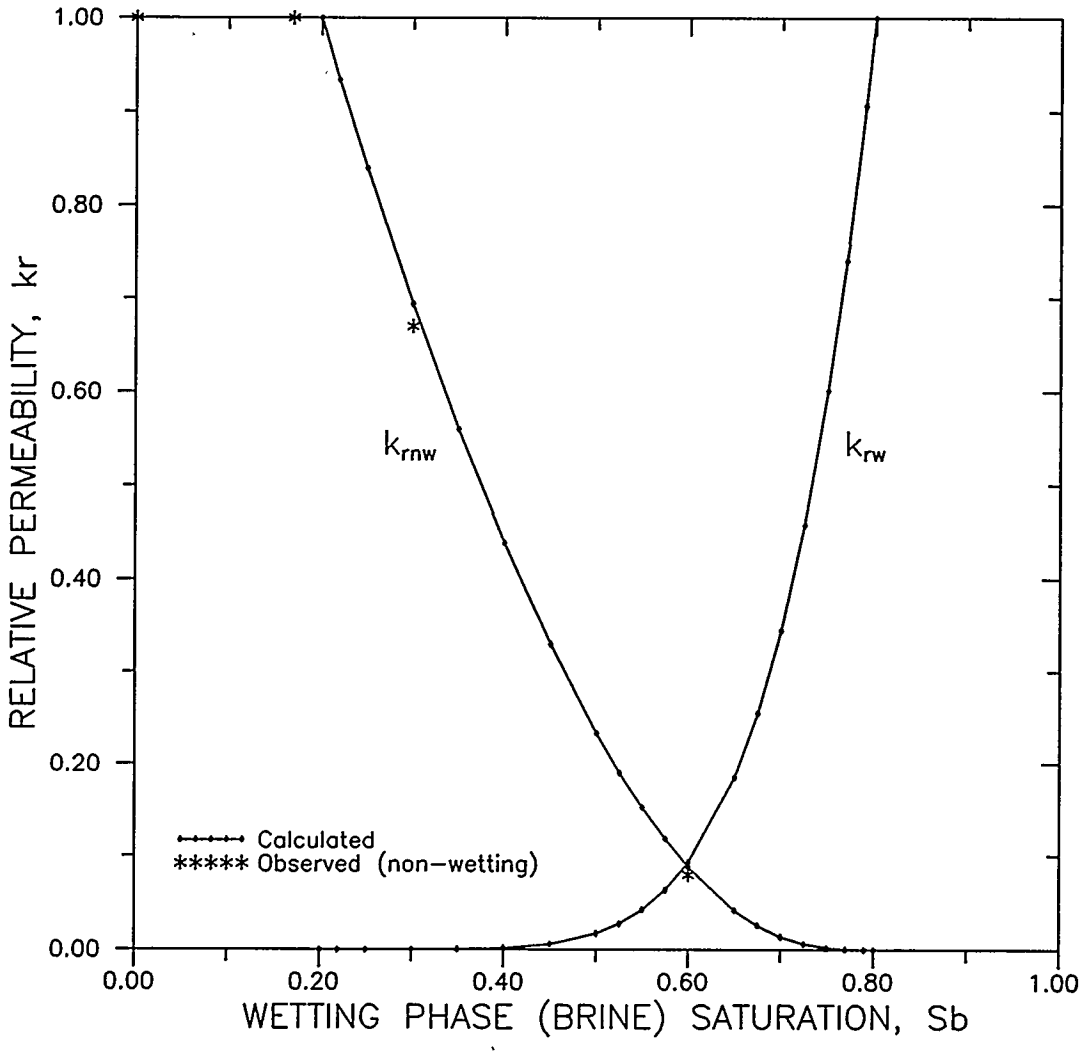

Figure 1. Observed relative permeabilities for the "tight" gas sand and calculated relative permeabilities for the WIPP interbeds.

PARAMETER (cont'd) :	Relative Permeability and Capillary Pressure Curves for the Salado Interbeds

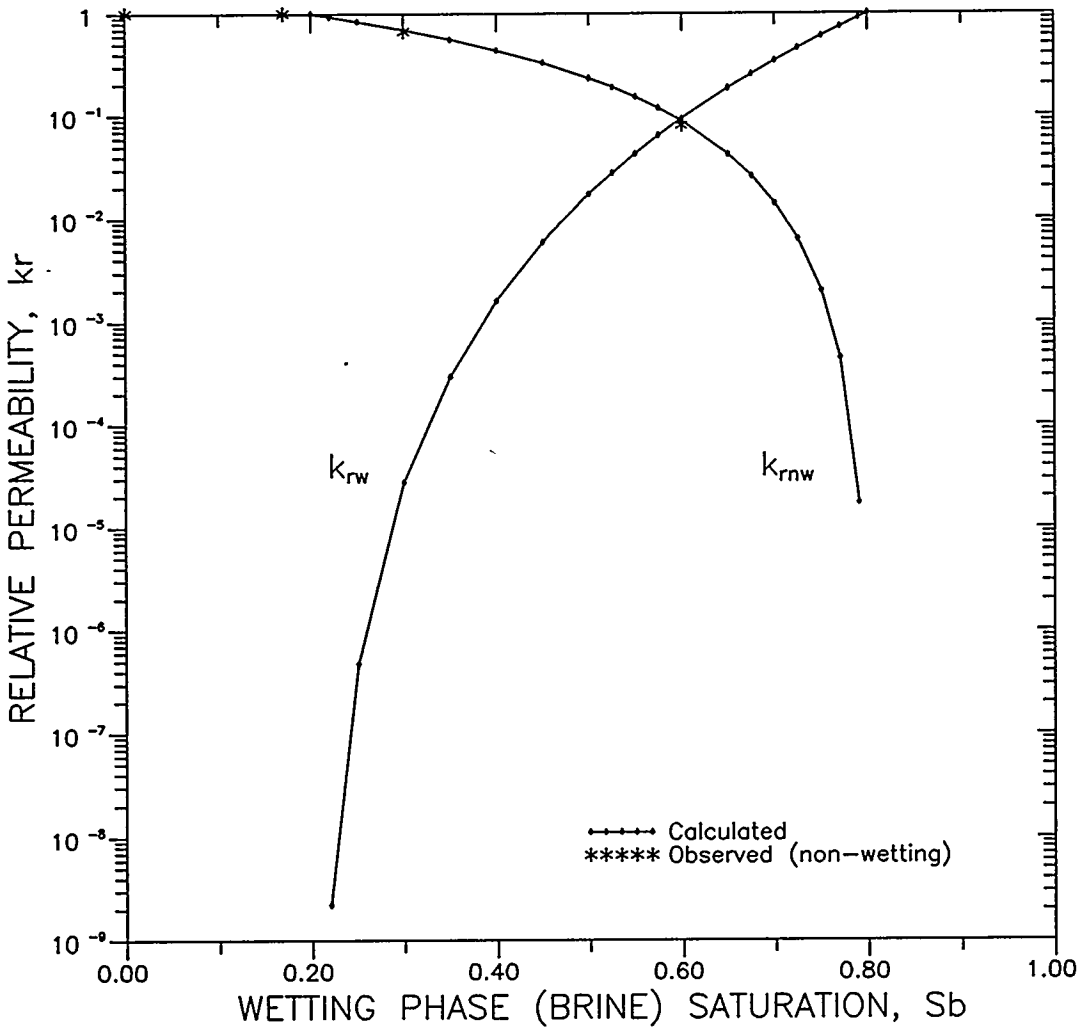

Figure 2. Observed relative permeabilities for the "tight" gas sand and calculated relative permeabilities for the WIPP Interbeds (log scale).

PARAMETER (cont'd) :	Relative Permeability and Capillary Pressure Curves for the Salado Interbeds

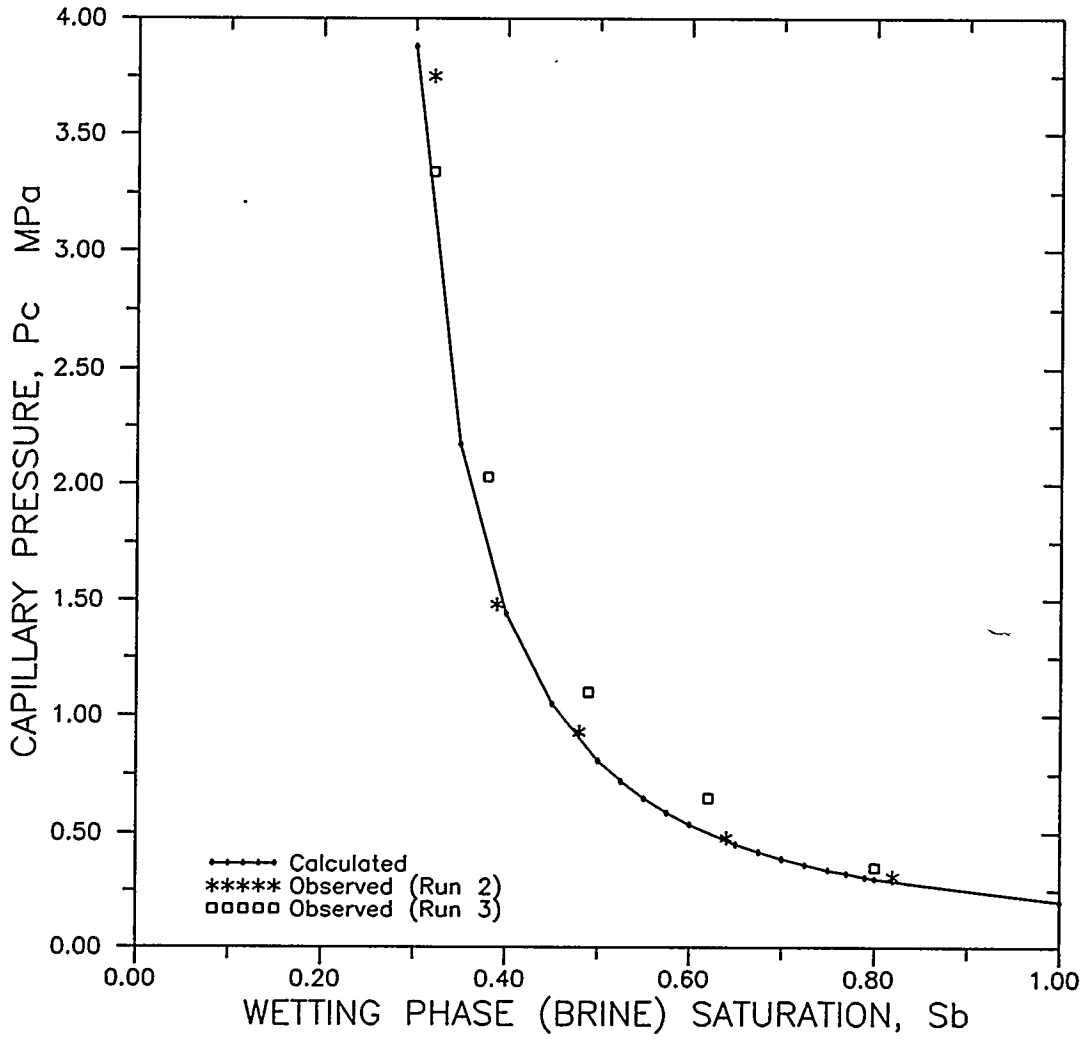

Figure 3. Observed capillary pressure for the "tight" gas sand and calculated capillary pressure for the WIPP Interbeds.

PARAMETER (cont'd) :	Relative Permeability and Capillary Pressure Curves for the Salado Interbeds

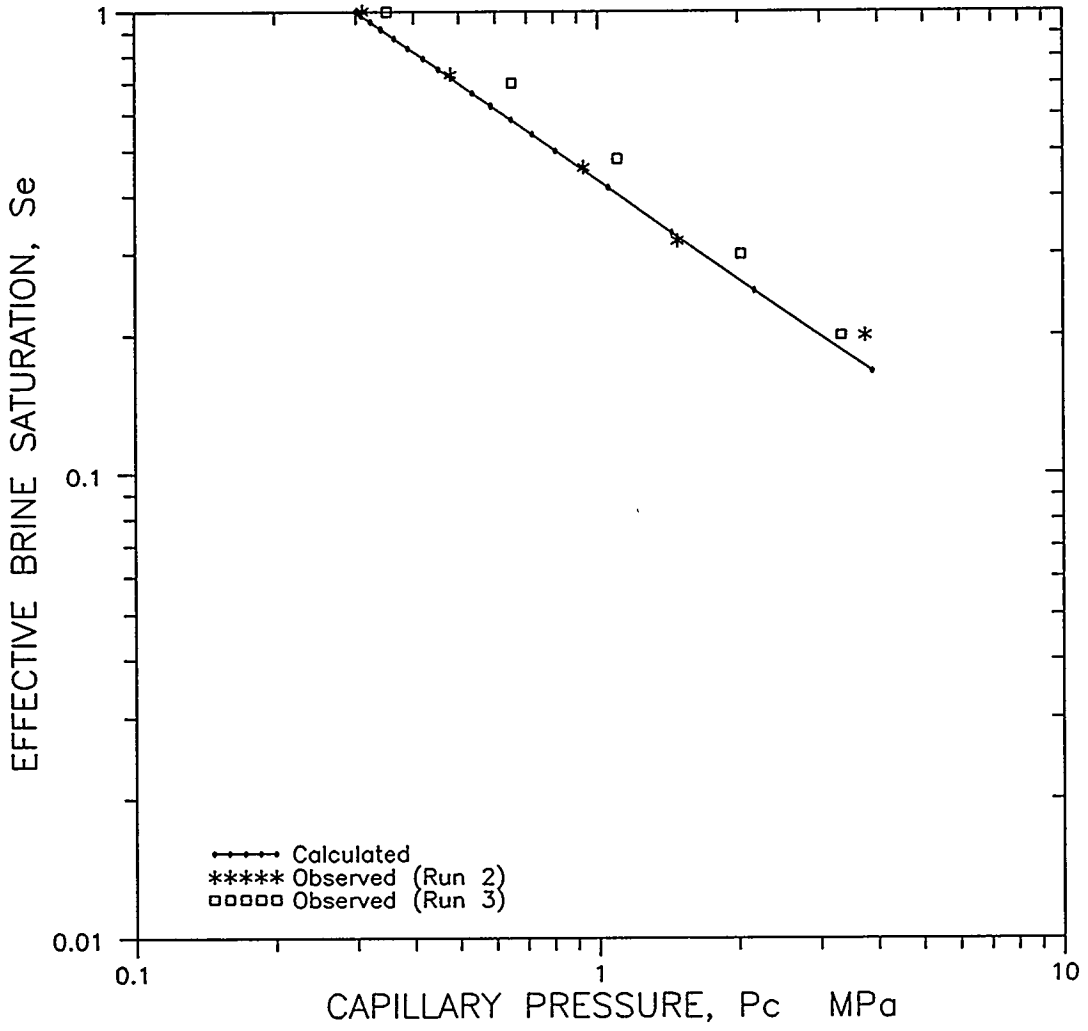

Figure 4. Observed and calculated effective saturation vs. capillary pressure used to determine the Brooks and Corey (1964) model parameters, λ (slope) and P_t (intercept at $S_e = 1$).

DATE :	08/31/93	RATIONALE NUMBER :	003	
PARAMETER :	Relative Permeability and Capillary Pressure Curves for the Waste Disposal Room			
VALUE :	S_b	k_{rb}	k_{rg}	P_c (MPa)	P_c (bars)
	0.276	0.000E+0	1.000E+0		
	0.290	5.226E-7	9.594E-1	6.595E-3	6.595E-2
	0.300	3.823E-6	9.299E-1	5.473E-3	5.473E-2
	0.325	5.332E-5	8.561E-1	4.275E-3	4.275E-2
	0.350	2.443E-4	7.831E-1	3.707E-3	3.707E-2
	0.400	1.643E-3	6.428E-1	3.100E-3	3.100E-2
	0.450	5.739E-3	5.135E-1	2.757E-3	2.757E-2
	0.500	1.458E-2	3.979E-1	2.527E-3	2.527E-2
	0.550	3.068E-2	2.975E-1	2.356E-3	2.356E-2
	0.600	5.697E-2	2.130E-1	2.224E-3	2.224E-2
	0.650	9.678E-2	1.444E-1	2.116E-3	2.116E-2
	0.700	1.538E-1	9.111E-2	2.026E-3	2.026E-2
	0.750	2.321E-1	5.208E-2	1.949E-3	1.949E-2
	0.800	3.361E-1	2.571E-2	1.883E-3	1.883E-2
	0.850	4.706E-1	9.960E-3	1.824E-3	1.824E-2
	0.900	6.406E-1	2.384E-3	1.772E-3	1.772E-2
	0.925	7.406E-1	7.848E-4	1.749E-3	1.749E-2
	0.950	8.515E-1	1.290E-4	1.726E-3	1.726E-2
	0.970	9.486E-1	4.826E-6	1.708E-3	1.708E-2
	0.980	1.000E+0	0.000E+0	1.700E-3	1.700E-2
	0.990	1.000E+0	0.000E+0	1.692E-3	1.692E-2
	1.000	1.000E+0	0.000E+0	1.684E-3	1.684E-2
KEYWORD :	ROCKS, RPCAP				
RATIONALE :	There are no measured relative permeability or capillary pressure curves for waste disposal rooms at the WIPP site. A literature search failed to locate either measured or theoretically based curves for the waste disposal rooms. In the absence of site-specific or room-specific data, two-phase properties are based on data from actual measurements on analogue materials. A heterogeneous mix of unconsolidated				

PARAMETER (cont'd) :	Relative Permeability and Capillary Pressure Curves for the Waste Disposal Room

RATIONALE (cont'd) : fragmented clay, sandstone, and volcanic sand (Brooks and Corey, 1964) was selected as an analogue to determine the relative permeability characteristics and threshold pressure of the waste disposal rooms.

The analogue material was created to simulate a soil characterized by a well aggregated structure with secondary as well as primary porosity. Aggregates created by crushing oven-dried clay and consolidated sandstone were combined with volcanic sand to obtain this mixture. The mixture had a porosity of 0.44 and an intrinsic permeability of 1.5E-05 m^2. This porosity is near the middle of the range expected for the various waste disposal room states (see room porosity rationale). The permeability is higher than expected in the room by at least six orders of magnitude (see room permeability rationale).

The two-phase properties are derived from the relationships of Brooks and Corey (1964):

Wetting Phase (brine) Relative Permeability

$$k_{rb} = k_{rw} = S_e^{(2+3\lambda)/\lambda} \quad (1)$$

Non-Wetting Phase (gas) Relative Permeability

$$k_{rg} = k_{rnw} = (1 - S_e)^2 \ (1 - S_e^{(2+\lambda)/\lambda}) \quad (2)$$

where the effective wetting phase (brine) saturation, S_e, is defined as:

$$S_e = \frac{S_b - S_{br}}{1 - S_{gc} - S_{br}} \quad (3)$$

and

λ = pore-size distribution index,
S_b = wetting phase (brine) saturation,
S_{br} = residual brine saturation, and
S_{gc} = critical gas saturation.

Equation (3) for effective wetting phase saturation differs slightly from the form presented in Brooks and Corey (1964), however, they do discuss this form briefly in Appendix I (p. 23). This

PARAMETER (cont'd) :	Relative Permeability and Capillary Pressure Curves for the Waste Disposal Room

RATIONALE (cont'd) :

formulation is similar to an equation presented by Burdine (1953), whose work provides a basis for the Brooks and Corey (1964) model. Equation (3) is selected because it satisfies the bounding conditions of the relative permeability relationships of equations (1) and (2). At the point of zero brine mobility, $S_b = S_{br}$, equation (3) yields $S_e = 0$ and equation (1) yields $k_{rb} = 0$. At the point of zero gas mobility, $S_b = 1 - S_{gc}$, equation (3) yields $S_e = 1$ and equation (2) yields $k_{rg} = 0$.

The Brooks and Corey (1964) model is fit to the measured data from the fragmented mixture. From this fit, the following parameter values are estimated:

$$S_{br} = 0.276 \qquad S_{gc} = 0.02 \qquad \lambda = 2.89$$

The S_{gc} value of 0.02 was estimated from the observed non-wetting phase relative permeability versus saturation data shown in Figures 1 and 2. The method used to determine S_{br} is described in Brooks and Corey (1964; p. 24). They determined S_{br} for the fragmented mixture to be 0.276.

Brooks and Corey (1964) obtained a λ value of 2.89 by determining the slope of a line through the observed capillary pressure for the fragmented mixture plotted logrithmically as a function of effective brine saturation, S_e (Figure 3). A threshold pressure, P_t, for the fragmented mixture was determined by Brooks and Corey (1964) to be 1.7E-3 MPa based on Figure 3.

The threshold pressure is defined as the capillary pressure at the point gas forms a continuous phase (i.e., at $S_g = S_{gc}$). The capillary pressure, P_c, is calculated from the threshold pressure (Brooks and Corey, 1964):

$$P_c = \frac{P_t}{S_e^{1/\lambda}} \qquad (4)$$

The capillary pressure curve for the fragmented mixture, calculated from equation (4), is shown in Figure 4.

However, because the heterogeneous waste and backfill is not expected to have a consistent pore structure, zero capillary pressure was assumed for the room.

PARAMETER (cont'd) :	Relative Permeability and Capillary Pressure Curves for the Waste Disposal Room
RATIONALE : (cont'd) :	The wetting (brine) and non-wetting (gas) phase relative permeability curves, calculated from equations (1) and (2), respectively, are indicated by solid lines in Figures 1 and 2. The calculated relative permeability curves closely approximate the observed data in both figures. Therefore, the S_{gc}, S_{br}, and λ values selected are considered representative of the fragmented mixture and are assumed to provide an analogue for the waste disposal room relative permeability.
COMMENTS :	To examine the sensitivity of system behavior to disposal room multiphase flow properties, the residual brine saturation lowered to 0.01, the residual gas saturation was varied from 0.01 to 0.10, and the pore-size λ was varied from 0.2 to 10.0. Brooks and Corey (1964) used a variation of equation (3) to calculate effective wetting phase saturation, S_e. They assumed that S_{gc} was equal to zero for their calculations. Thus, the values of S_{br}, λ, and P_t they present are slightly different than if $S_{gc}=0.02$ had been used. These differences are insignificant, given the overall uncertainty in the parameters. The disposal rooms are expected to contain a heterogenous mix of partially crushed drums and backfill. The backfill will consist of crushed salt or a mixture of crushed salt and bentonite. The fragmented mixture used as an analogue for the disposal room contents was selected because of its high degree of heterogeneity. While this representation of the disposal room contents may be useful from the standpoint of capturing some of the heterogenous character of a room, it may underestimate the capacity of the backfill to adsorb and immobilize a significant quantity of water. Alternative analogues for the room contents that focus on imbibition behavior are required to examine this aspect of room behavior. Demond and Roberts (1987) suggest that the relative permeability and capillary pressure curves are insensitive to intrinsic permeability, in which case the difference in the permeability of the analogue material and the permeability of the waste disposal room may not be a major issue. However, the degree to which the fragmented sample represents the pore size distribution and pores structure likely to exist in the room is of importance. The greater than four order of magnitude difference in permeabilities between the fragmented mixture and

PARAMETER (cont'd) :	Relative Permeability and Capillary Pressure Curves for the Waste Disposal Room
COMMENTS (cont'd) :	the room may suggest a different pore structure. Nonetheless, until a more representative sample can be identified, the relative permeability and capillary pressure curves for the fragmented mixture are assumed suitable for the waste disposal room.
REFERENCES :	Brooks, R.H., and A.T. Corey. 1964. *Hydraulic Properties of Porous Media.* Hydrology Paper No. 3. Fort Collins, CO: Colorado State University. Burdine, N.T. 1953. "Relative Permeability Calculations From Pore-Size Distribution Data," *Transactions of the American Institute of Mining and Metallurgical Engineers. Petroleum Branch.* Vol. 198, 71-78. Demond, A.H., and P.V. Roberts. 1987. "An Examination of Relative Permeability Relations for Two-Phase Flow in Porous Media," *Water Resources Bulletin.* Vol. 23, no. 4, 617-628.

PARAMETER (cont'd) :	Relative Permeability and Capillary Pressure Curves for the Waste Disposal Room

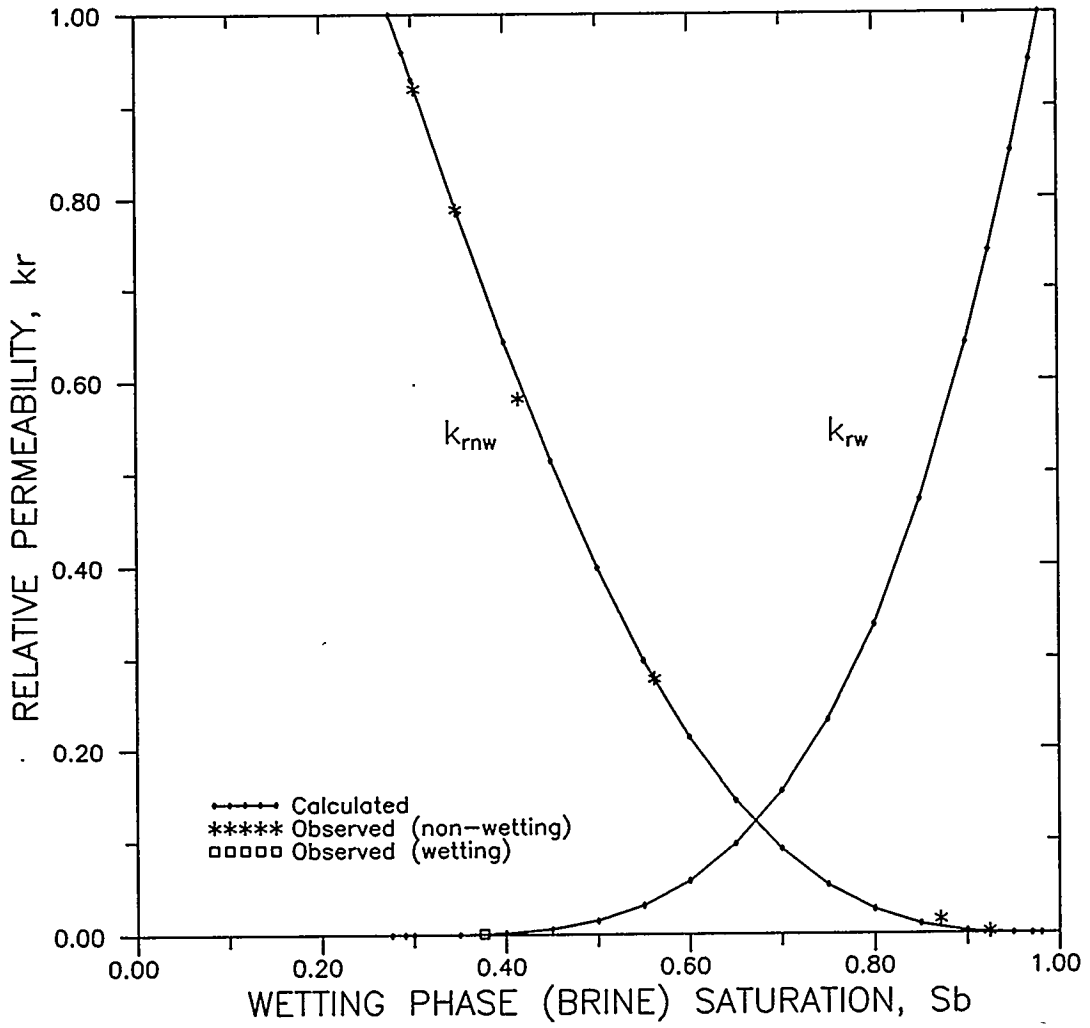

Figure 1. Observed relative permeabilities for the fragmented mixture and calculated relative permeabilities for the waste disposal room.

PARAMETER (cont'd) :	Relative Permeability and Capillary Pressure Curves for the Waste Disposal Room

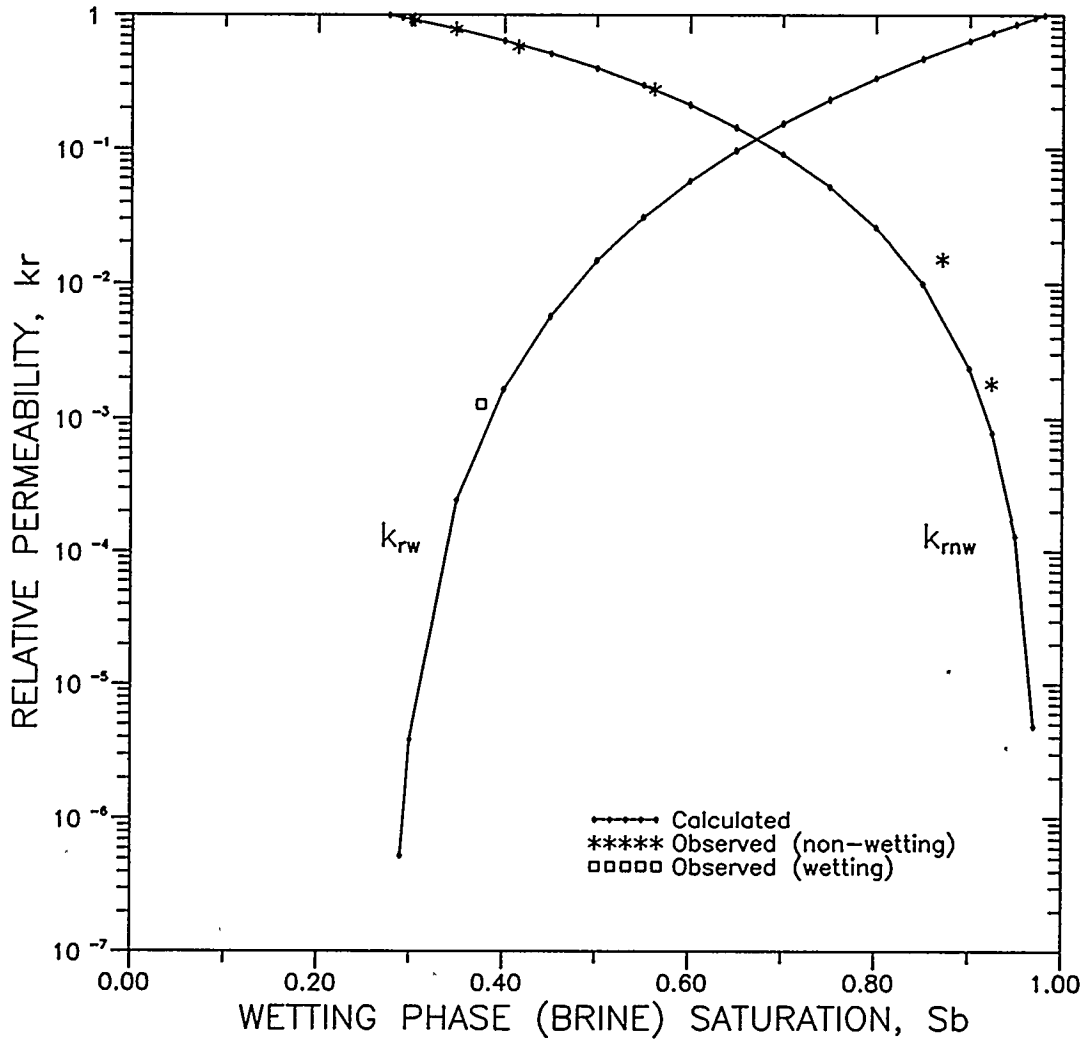

Figure 2. Observed relative permeabilities for the fragmented mixture and calculated relative permeabilities for the waste disposal room (log scale).

PARAMETER (cont'd) :	Relative Permeability and Capillary Pressure Curves for the Waste Disposal Room

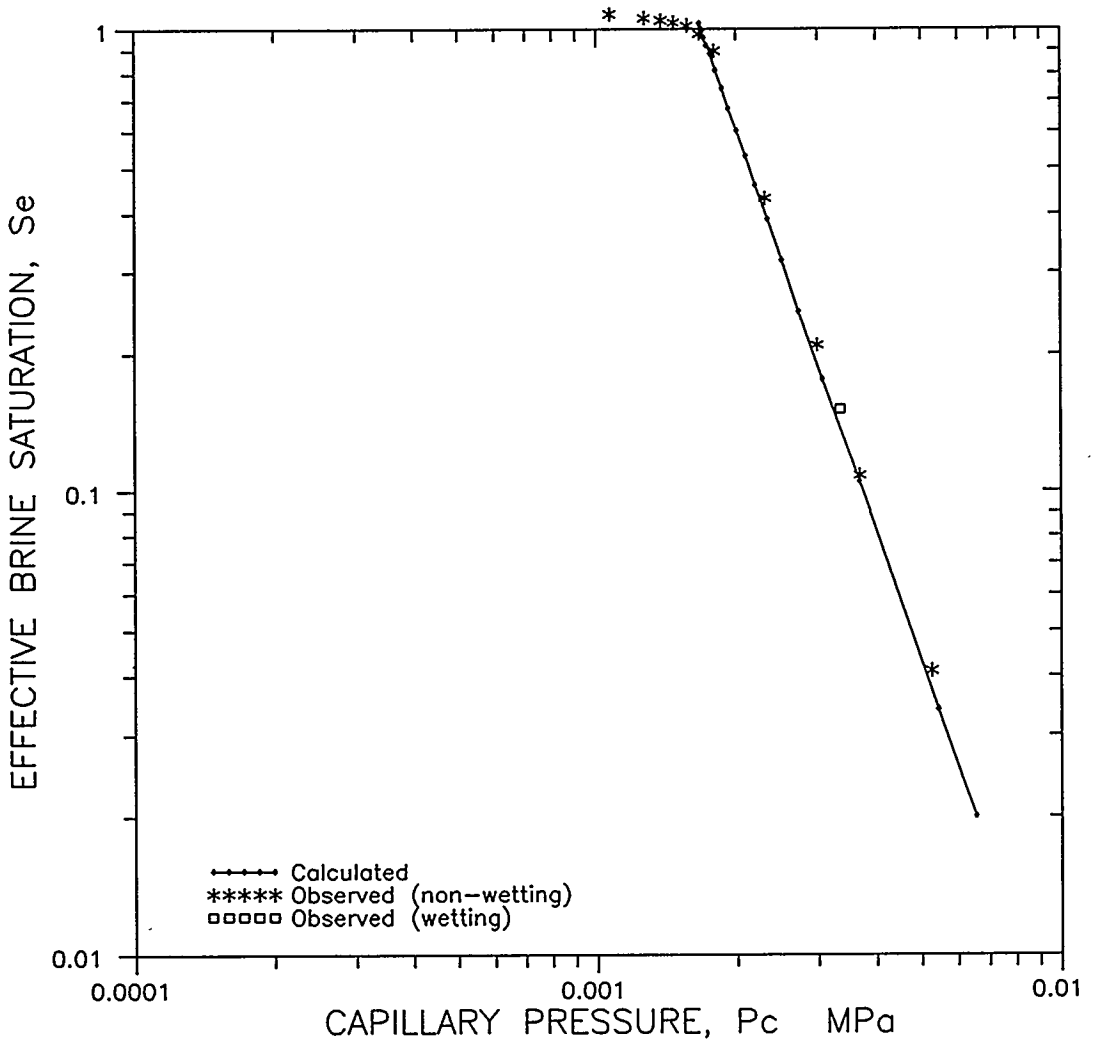

Figure 3. Observed and calculated effective saturation vs. capillary pressure used to determine the Brooks and Corey (1964) model parameters, λ (slope) and P_t (intercept at $S_e = 1$).

PARAMETER (cont'd) :	Relative Permeability and Capillary Pressure Curves for the Waste Disposal Room

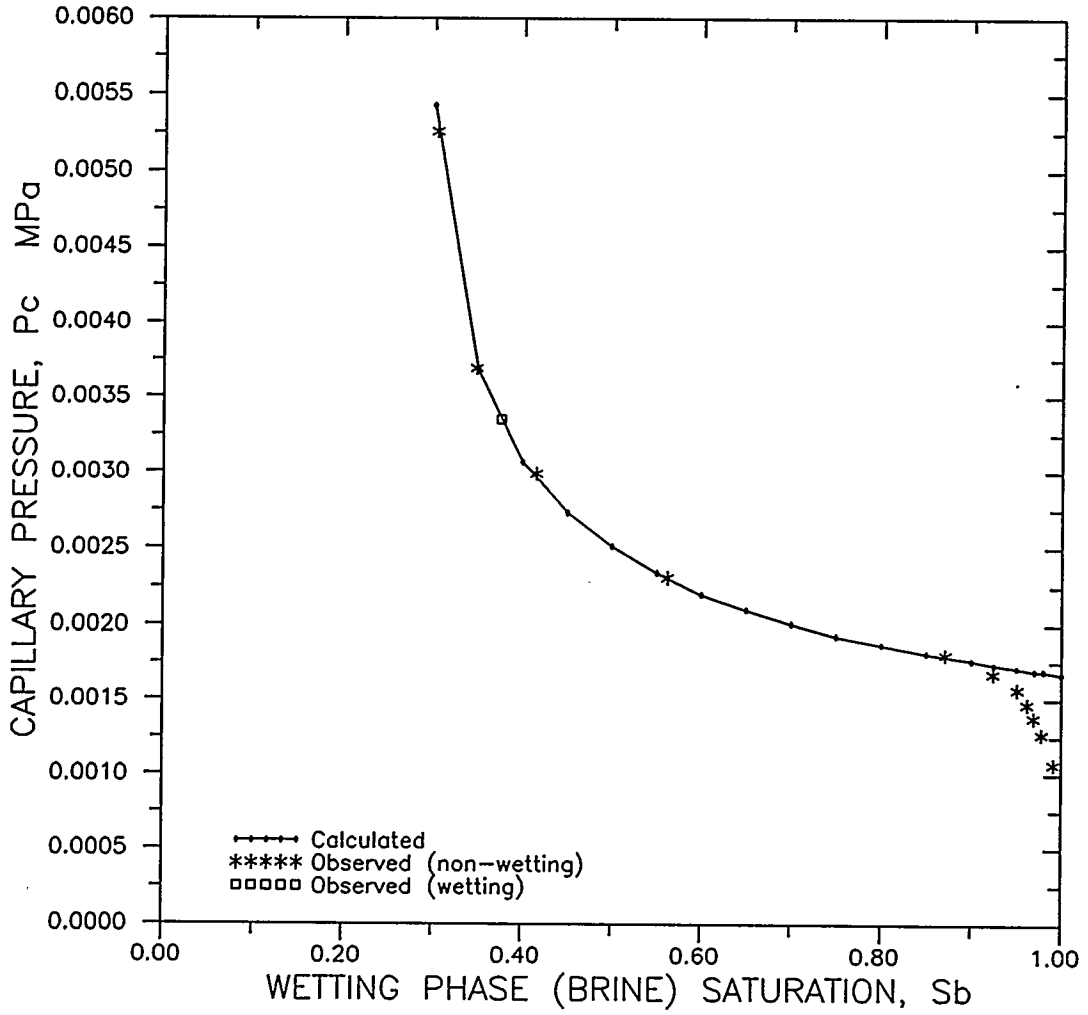

Figure 4. Observed capillary pressure for the fragmented mixture and calculated capillary pressure for the waste disposal room.

III. FLUID PROPERTIES

DATE :	06/09/93	RATIONALE NUMBER:	002
PARAMETER :	Gas Density		
VALUE :	Pressure (MPa)	Air Density at 30°C (kg/m^3)	Hydrogen Density at 30°C (kg/m^3)
	0.1	1.15	0.08
	1.0	11.5	0.8
	5.0	57.4	4.0
	10.0	114.9	8.0
	15.0	172.3	12.0
	20.0	229.8	16.0
	50.0	574.5	40.0
KEYWORD :	(Air): None. SUBROUTINE EOS8 (Hydrogen): None. SUBROUTINE EOS8H		

RATIONALE : The density of the gas component (either air or hydrogen) is calculated internally by TOUGH28 as a function of temperature and pressure. Density calculations assume a temperature of 30°C.

Gas density is calculated assuming ideal gas behavior (Z=1) which is described by (Aziz and Settari, 1979; p. 15):

$$\rho = \frac{PM}{ZRT} \qquad (1)$$

where:

ρ = gas density (g/L = kg/m^3)
P = gas pressure (Pa),
M = molecular weight of gas (g/mole),
Z = real gas deviation factor,
R = gas constant (8314.56 Pa·L/°K·mole),
T = absolute temperature (303.15 °K)

The molecular weight for air is 28.96 g/mole and for H_2 gas is 2.016 g/mole.

PARAMETER (cont'd) :	Gas Density
COMMENTS :	Simulations assume that H_2 is the only gas in the system and that the H_2 density is representative of the total gas component density in and around the waste disposal rooms. Calculation of non-ideal gas behavior based on critical pressures and temperatures from Nordstrom and Munoz (1986) and gas compressibility relations from Reynolds (1968) indicate that waste-generated gas begins to deviate from ideal pressure, volume behavior at approximately 20 MPa. Because most realistic repository pressure estimates suggest pressures less than 20 MPa, ideal gas behavior is assumed. However, if important scenarios emerge with gas pressure well in excess of 20 MPa, the non-ideal gas behavior should be implemented.
REFERENCES :	Aziz, K., and A. Settari. 1979. *Petroleum Reservoir Simulation.* New York: Elsevier. Nordstrom, D.K., and J.L. Munoz. 1986. *Geochemical Thermodynamics.* Palo Alto, CA: Blackwell Scientific Publications. Reynolds, W.C. 1968. *Thermodynamics.* New York, NY: McGraw- Hill.

DATE :	06/09/93	RATIONALE NUMBER :	002
PARAMETER :	Gas Viscosity		
VALUE :	Pressure (MPa)	Air Viscosity at 30°C (Pa·s)	Hydrogen Viscosity at 30°C (Pa·s)
	0.1	18.6E-6	8.99E-6
	1.0	18.6E-6	9.00E-6
	5.0	18.6E-6	9.06E-6
	10.0	18.6E-6	9.14E-6
	15.0	18.6E-6	9.27E-6
	0.0	18.6E-6	9.40E-6
	50.0	18.6E-6	9.72E-6
KEYWORD :	(Air): None. SUBROUTINE VISCO (air) (Hydrogen): None. SUBROUTINE VISCO (H_2)		
RATIONALE :	The viscosity of the gas component (either air or hydrogen) is calculated internally by TOUGH28 as a function of temperature and pressure. Viscosity calculations assume a temperature of 30°C.		
COMMENTS :	Simulations assume that H_2 is the only gas in the system and that the H_2 viscosity is representative of the total gas viscosity in and around the waste disposal rooms. A viscosity of 0.0089 cp for H_2 at 25°C (77°F) and 1 atm was taken from Perry (1963; Fig. 3-42 and Table 3-263; p. 3-196, 3-197). The variation of viscosity with pressure is presented by Katz et al. (1959; Fig. 4-102, p. 173). This figure gives viscosity ratios (μ/μ_1) as a function of pseudoreduced pressure (P_R) and pseudoreduced temperature (T_R) where μ is the gas viscosity at T_R and P_R and μ_1 is the gas viscosity at T_R and 1 atm. Using pseudocritical values for hydrogen gas (H_2) from Weast et al. (1989; p. F-70), viscosity ratios are effectively equal to 1 for all pressures from 1 to 500 atm, indicating that gas viscosity does not vary significantly over the range of pressures encountered in and around the WIPP waste disposal rooms.		

PARAMETER (cont'd) :	Gas Viscosity
REFERENCES :	Katz, D.L., D. Cornell, R. Kobayashi, F.H. Poettmann, J.A. Vary, J.R. Elenbaas, and C.F. Weinaug. 1959. *Handbook of Natural Gas Engineering.* New York, NY: McGraw-Hill. Perry, R.H., C.H. Chilton, and S.D. Kirkpatrick, eds. 1963. *Chemical Engineers Handbook.* New York, NY: McGraw-Hill. Weast, R.C., D.C. Lide, M.J. Astle, and W.H. Beyer, eds. 1989. *CRC Handbook of Chemistry and Physics.* 70th ed. Boca Raton, FL: CRC Press.

DATE :	06/09/93	RATIONALE NUMBER :	002
PARAMETER :	Gas Compressibility		
VALUE :	Pressure MPa	Air Compressibility Pa^{-1}	H_2 Compressibility Pa^{-1}
	0.1	1E-3	1E-3
	1.0	1E-5	1E-5
	5.0	1E-6	1E-6
	10.0	2E-7	2E-7
	15.0	1E-7	1E-7
	20.0	7E-8	7E-8
	50.0	5E-8	5E-8
KEYWORD :	(Air): None. SUBROUTINE EOS8 (Hydrogen): None. SUBROUTINE EOS8H		

RATIONALE : Gas compressibility, β_g, is calculated from (Freeze and Cherry, 1979; p. 52):

$$\beta_g = -\frac{1}{V}\frac{dV}{dp} \qquad (1)$$

where:

V = gas volume (m^3)
p = gas pressure (Pa)

Recognizing that $V \propto 1/\rho$, gas compressibility is computed internally by TOUGH28 from equation (1) using the pressure-density relationships presented in the gas density rationale for gas (air and hydrogen) at 30°C.

COMMENTS : Simulations assume that H_2 is the only gas in the system and that the H_2 compressibility is representative of the total gas compressibility in and around the waste disposal rooms.

Calculation of non-ideal gas behavior based on critical pressures and temperatures from Nordstrom and Munoz (1986) and gas compressibility relations from Reynolds (1968) indicate that waste-generated gas begins to deviate from ideal pressure, volume behavior at approximately 20 MPa. Because most realistic repository pressure estimates suggest pressures less than 20 MPa, ideal gas behavior is assumed. However, if important scenarios emerge with gas pressure well in excess of 20 MPa, the non-ideal gas behavior should be implemented.

PARAMETER (cont'd) :	Gas Compressibility
REFERENCES :	Freeze, R.A., and J.A. Cherry. 1979. *Groundwater.* Englewood Cliffs, NJ: Prentice-Hall, Inc. Nordstrom, D.K., and J.L. Munoz. 1986. *Geochemical Thermodynamics.* Palo Alto, CA: Blackwell Scientific Publications. Reynolds, W.C. 1968. *Thermodynamics.* New York, NY: McGraw- Hill.

DATE :	06/09/93	RATIONALE NUMBER :	004
PARAMETER :	Gas Solubility		
		Henry's Law Constant, K_H (Pa)	
	Air in Water	1.0E10	
	Air in Brine	4.0E10	
	Hydrogen in Brine	2.9E10	
KEYWORD :	(Air/Water): None. SUBROUTINE EOS8 (Air/Brine): None. SUBROUTINE EOS8B (Hydrogen/Brine): None. SUBROUTINE EOS8H		

RATIONALE : The solubility of gas in the fluid phase can be expressed using Henry's Law (Cygan, 1991; p. 10):

$$K_H = \frac{p_g}{X} \qquad (1)$$

where:

K_H = Henry's constant (Pa)
p_g = gas partial pressure (Pa)
X = mole fraction solubility

The mole fraction solubility, X, is defined as:

$$X = \frac{\text{moles of gas}}{\text{moles solution}} \qquad (2)$$

Henry's Law constants for air in water (1.0E10 Pa) and hydrogen in water (1.379E-10) are calculated internally by TOUGH28. Henry's Law constants for air in brine and hydrogen in brine are specified in TOUGH28 based on the observations of Cygan (1991) that solubilities of gases in brine are about four times lower than in water. The solubility constant used by TOUGH28 is equivalent to $1/K_H$.

COMMENTS : Simulations assume that H_2 is the only gas in the system and that the H_2 solubility in brine is representative of the total gas solubility in and around the waste disposal rooms. Depending on waste content and which gas generation processes are active, waste-generated gas is expected to range from 50-80% hydrogen.

PARAMETER (cont'd) :	Gas Solubility

COMMENTS (cont'd) : Henry's Law constant shows some pressure and temperature dependence, however, TOUGH28 uses a constant value for K_H. Cygan (1991; p. 55-56) presents the following data for nitrogen solubility (representative of air) in pure water and in 4-5 N NaCl brine solution.

Table 1. Nitrogen Solubilities

Gas Pressure (MPa)	Mole Fraction		Henry's Constant, K_H	
	Water	Brine	Water	Brine
1.0	1.0E-4	3.0E-5	1.0E10	3.3E10
5.0	5.4E-4	1.6E-4	0.9E10	3.1E10
10.0	8.0E-4	2.9E-4	1.3E10	3.5E10
15.0	1.1E-3	3.5E-4	1.4E10	4.3E10
20.0	1.4E-3	4.0E-4	1.4E10	5.0E10
50.0	3.0E-3	8.0E-4	1.7E10	6.3E10
TOUGH28 Air			1.0E10	4.0E10

Cygan (1991; p. 72) determined the following relationship for hydrogen solubility in pure water and in 5 N NaCl brine solution:

$$X = D_0 + D_1 \ln(p_g) \qquad (3)$$

The values for D_0 and D_1 are:

	in pure water	in 5 N NaCl brine
D_0	-8.8980	-10.0789
D_1	0.9538	0.8205

The hydrogen solubilities, calculated using equation (3) are given in Table 2.

PARAMETER (cont'd) :	Gas Solubility

COMMENTS (cont'd) :

Table 2. Hydrogen Solubilities

Gas Pressure (MPa)	Mole Fraction Water	Mole Fraction Brine	Henry's Constant, K_H Water	Henry's Constant, K_H Brine
0.1	1.52E-5	6.34E-6	0.66E10	1.6E10
1.0	1.37E-4	4.20E-5	0.73E10	2.4E10
5.0	6.34E-4	1.57E-4	0.79E10	3.2E10
10.0	1.23E-3	2.78E-4	0.81E10	3.6E10
15.0	1.81E-3	3.87E-4	0.83E10	3.9E10
20.0	2.38E-3	4.90E-4	0.84E10	4.1E10
50.0	5.70E-3	1.04E-3	0.88E10	4.8E10
TOUGH28 H_2			0.73E10	2.7E10

REFERENCES :

Cygan, R.T. 1991. *The Solubility of Gases in NaCl Brine and a Critical Evaluation of Available Data.* SAND90-2848. Albuquerque, NM: Sandia National Laboratories.

DATE :	06/09/93	RATIONALE NUMBER :	003
PARAMETER :	Brine Density		
VALUE :	Pressure (MPa)	Pure Water Density at 30°C (kg/m^3)	Brine Density at 30°C (kg/m^3)
	0.1	995.75	1194.90
	1.0	996.15	1195.38
	5.0	997.92	1197.50
	10.0	1000.10	1200.12
	15.0	1002.26	1202.71
	20.0	1004.40	1205.28
	50.0	1016.79	1220.15
KEYWORD :	None. SUBROUTINE COWAT		

RATIONALE : The density of pure water is calculated internally by TOUGH28 as a function of temperature and pressure. Pure water densities are multiplied by 1.2 to represent brine. Density calculations assume a temperature of 30°C.

COMMENTS : Salado brine densities reported by Deal et al. (1987) range from 1215 to 1224 kg/m^3. A Salado brine density at the WIPP site was estimated to be 1222 kg/m^3 (specific gravity = 1.222) by Beauheim et al. (1991; p. 38). Other reported values include 1200 kg/m^3 (Lappin et al., 1989; p. 3-20), 1200 kg/m^3 (Stein and Krumhansl,1986; 1.2 g/cm^3), and 1200 kg/m^3 at 28°C (Kaufmann, 1960; p. 612). The range of TOUGH28 values is consistent with these reported values.

The assumed brine density corresponds to a brine that is nearly saturated with NaCl. If a nearly saturated brine is assumed to be 25% NaCl by weight (Perry, 1963; p. 3-77), then it will have about 300,000 ppm NaCl based on the following calculation:

$$\left[\frac{1.2\ \text{g brine}}{1\ \text{cm}^3\ \text{brine}}\right]\left[\frac{25\ \text{g NaCl}}{100\ \text{g brine}}\right]\left[\frac{1000\ \text{cm}^3\ \text{brine}}{1\ \ell\ \text{brine}}\right]$$

$$= 300\ \frac{\text{g NaCl}}{\ell\ \text{brine}} = 300{,}000\ \text{mg}/\ell = 300{,}000\ \text{ppm}$$

PARAMETER (cont'd) :	Brine Density
REFERENCES :	Beauheim, R.L., G.J. Saulnier, Jr., and J.D. Avis. 1991. *Interpretation of Brine-Permeability Tests of the Salado Formation at the Waste Isolation Pilot Plant Site: First Interim Report.* SAND90-0083. Albuquerque, NM: Sandia National Laboratories. Deal, D.E., J.B. Case, R.M. Deshler, P.E. Drez, J. Myers, and J.R. Tyburski. 1987. *Brine Sampling and Evaluation Program Phase II Report.* DOE/WIPP 87-010. Carlsbad, NM: Westinghouse Electric Corporation. Kaufmann, D.W., ed. 1960. *Sodium Chloride, The Production and Properties of Salt and Brine.* American Chemical Society Monograph No. 145. New York, NY: Reinhold Publishing Corp. Lappin, A.R., R.L. Hunter, D.P. Garber, and P.B. Davies, eds. 1989. *Systems Analysis, Long-Term Radionuclide Transport, and Dose Assessments, Waste Isolation Pilot Plant (WIPP), Southeastern New Mexico; March 1989.* SAND89-0462. Albuquerque, NM: Sandia National Laboratories. Perry, R.H., C.H. Chilton, and S.D. Kirkpatrick, eds. 1963. *Chemical Engineers Handbook.* New York, NY: McGraw-Hill. Stein, C.L., and J.L. Krumhansl. 1986. *Chemistry of Brines in Salt from the Waste Isolation Pilot Plant (WIPP), Southeastern New Mexico: A Preliminary Investigation.* SAND85-0897. Albuquerque, NM: Sandia National Laboratories.

DATE :	06/09/93	RATIONALE NUMBER :	001B
PARAMETER :	Brine Viscosity		
VALUE :	1.6E-3 Pa·s (1.6 cp)		
KEYWORD :	None. SUBROUTINE VISW		

RATIONALE : The viscosity of pure water is calculated internally by TOUGH28 as a function of temperature and pressure. The viscosity of Salado brine at 30°C at the WIPP site is taken to be 1.6E-3 Pa·s (1.6 cp). This is based on the data of Kaufmann (1960; p. 622) and Ezrokhi (1952) for a brine at 28°C. Pure water viscosities at 30°C are 0.8E-3 Pa·s (0.8 cp).

Earlougher (1977; p. 241) presents a figure showing a brine viscosity correction factor as a function of pressure. The correction factor ranges from 1.00 at 0 psi (0 MPa) to 1.01 at 10,000 psi (68.9 MPa). These small correction factors produce a negligible increase in viscosity and, as a result, brine viscosity is assumed constant with pressure.

COMMENTS : Earlougher (1977; p. 241) indicates that for a 25% NaCl brine (approximately WIPP brine) at 25°C (77°F) the viscosity is 1.66 cp. Dorsey (1968; p. 183) shows that the viscosity of fresh water at 25°C is about 7% higher than at 28°C. The viscosity of pure water at 20°C, as calculated by TOUGH28, is 1.0 cp. These references indicate that brine viscosity has a small temperature dependence.

The presence of dissolved gas generally results in a negligible effect on water viscosity (Bradley, 1987; p. 24-16).

REFERENCES : Bradley, H.B. ed. 1987. *Petroleum Engineering Handbook.* Richardson, TX: Society of Petroleum Engineers.

Dorsey, N.E. 1968. *Properties of Ordinary Water-Substance in All Its Phases.* American Chemical Society Monograph Series. New York: Hafner Publishing Company.

Earlougher, R.C. 1977. *Advances in Well Test Analysis.* Monograph Volume 5. Dallas, TX: Society of Petroleum Engineers of AIME.

PARAMETER (cont'd) :	Brine Viscosity
REFERENCES (cont'd) :	Ezrohki, L.L. 1952. "Viscosity of Aqueous Solutions of the Individual Salts of Sea Water Systems," *The Journal of Applied Chemistry of the USSR.* Vol. 25, 917-926. Kaufmann, D.W., ed. 1960. *Sodium Chloride, The Production and Properties of Salt and Brine.* American Chemical Society Monograph No. 145. New York, NY: Reinhold Publishing Corp.

DATE:	08/31/93	RATIONALE NUMBER :	005
PARAMETER :	Brine Compressibility		
VALUE :	Brine Pressure MPa	Pure Water Compressibility Pa^{-1}	Brine Compressibility Pa^{-1}
	0.1	4.5E-10	2.5E-10
	1.0	4.5E-10	2.5E-10
	5.0	4.4E-10	2.4E-10
	10.0	4.4E-10	2.4E-10
	15.0	4.3E-10	2.3E-10
	20.0	4.3E-10	2.3E-10
	50.0	4.1E-10	2.1E-10
KEYWORD :	(Pure Water): None. SUBROUTINE COWAT (Brine correction): ROCKS		

RATIONALE : Fluid compressibility, β, is calculated from (Freeze and Cherry, 1979; p. 52):

$$\beta = - \frac{1}{V} \frac{dV}{dp} \qquad (1)$$

where:

V = fluid volume (m^3)
p = fluid pressure (Pa)

Recognizing that $V \propto 1/\rho$, pure water compressibility, β_w, is computed from equation (1) using the pressure-density relationships presented in the brine density rationale for brine at 30°C. Brine compressibility, β_b, is calculated from:

$$\beta_b = \beta_w - 2.0E{-}10 \qquad (2)$$

The brine correction in equation (2) is based on measured compressibilities ranging from 2.40E-10 Pa^{-1} to 2.54E-10 Pa^{-1} for WIPP Room Q brine at atmospheric pressure and temperatures from 20 to 40°C (McTigue et al.,1991; p. 1).

Because compressibility is determined internally by TOUGH28, the brine correction is achieved by adjusting the pore volume (rock) compressibility for all domains containing brine.

PARAMETER (cont'd) :	Brine Compressibility

COMMENTS : Beauheim et al. (1991; p. 36-37) assumed a compressibility of 3.1E-10 Pa^{-1} for in-situ Salado brine. Earlougher (1977; p. 231) presents several plots of compressibility for brine without solution gas as a function of temperature, pressure, and brine density. The Salado brine at the WIPP site is assumed to have a density of 1200 kg/m^3 (equivalent to 300,000 ppm NaCl), as indicated in the brine density rationale. Table 1 gives the compressibility versus pressure for brine at a temperature of 25°C (77°F) using the relationship developed using Earlougher (1977; Fig. D.19)

Table 1. Compressibility versus Pressure Relationship For Gas-Free Brine

Fluid Pressure		Compressibility of Gas-Free Brine	
(psi)	(MPa)	(psi^{-1})	(Pa^{-1})
14.5	0.1	2.20E-6	3.2E-10
145.0	1.0	2.15E-6	3.1E-10
725.0	5.0	1.99E-6	2.9E-10
1450.0	10.0	1.90E-6	2.8E-10
2900.0	20.0	1.82E-6	2.6E-10
5800.0	40.0	1.72E-6	2.5E-10

These brine compressibilities are similar to the values measured by McTigue et al. (1991)

The specific storage, S_s, can be calculated as follows (de Marsily, 1986; p. 108):

$$S_s = \rho_f g \phi (C_R + \beta) \quad (3)$$

where:

ρ_f = fluid density,
g = acceleration of gravity,
ϕ = porosity,
C_R = pore volume (rock) compressibility,
β = fluid compressibility,

Because specific storage is dependent only on the sum of C_R and β, the correction for brine compressibility (equation (2)) is entered through the C_R term.

PARAMETER (cont'd) :	Brine Compressibility
REFERENCES :	Beauheim, R.L., G.J. Saulnier, Jr., and J.D. Avis. 1991. *Interpretation of Brine-Permeability Tests of the Salado Formation at the Waste Isolation Pilot Plant Site: First Interim Report.* SAND90-0083. Albuquerque, NM: Sandia National Laboratories. de Marsily, G. 1986. *Quantitative Hydrogeology.* Orlando, FL: Academic Press. Earlougher, R.C. 1977. *Advances in Well Test Analysis.* Monograph Volume 5. Dallas, TX: Society of Petroleum Engineers of AIME. Freeze, R.A., and J.A. Cherry. 1979. *Groundwater.* Englewood Cliffs, NJ: Prentice-Hall, Inc. McTigue, D.F., S.J. Finley, J.H. Gieske, and K.L. Robinson. 1991. "Compressibility Measurements on WIPP Brines," *Preliminary Comparison with 40 CFR Part 191, Subpart B for the Waste Isolation Pilot Plant, December 1991. Volume 3: Reference Data.* WIPP Performance Assessment Division. Eds. R.P. Rechard, A.C. Peterson, J.D. Schreiber, H.J. Iuzzolino, M.S. Tierney, and J.S. Sandha. SAND91-0893/3. Albuquerque, NM: Sandia National Laboratories. A-79 through A-98.

IV. GAS GENERATION RATES

DATE :	08/31/93	RATIONALE NUMBER :	003B
PARAMETER :	Gas Generation Rates		
VALUE :	Gas Generation Rate (mole/drum/year)		
	Brine Inundated		Vapor-Limited	
	0-550 years	550-1050 years	0-5500 years	5500-10500 years
	2.0	1.0	0.2	0.1
KEYWORD :	GENER		

RATIONALE : Gas generation rates are based on the combined gas generation rates for anoxic corrosion of the steel waste containers and Fe and Fe-base alloys and for microbial degradation of cellulosics in the waste. Due to the uncertainty of the rates, all values are rounded to one significant figure. Estimates are made for both brine-inundated and vapor-limited (humid) conditions. Brine-inundated rates are based on laboratory experiments with steel immersed in brine while vapor-limited rates are based on laboratory experiments with steel suspended above brine (Brush, 1991).

The total gas production potential is 1050 moles/drum for anoxic corrosion and 550 moles/drum for microbial degradation (Beraun and Davies, 1992; p. 5).

Brine-Inundated Room Conditions

Brush (1991; p. 9) gives best estimates of gas generation under brine-inundated conditions of 1 mole/drum/year due to anoxic corrosion and 1 mole/drum/year due to microbial degradation. Based on the assumed total potentials, gas generation by microbial degradation will occur for 550 years and by anoxic corrosion for 1050 years under brine-inundated conditions. Brush (1991; p. 9) estimates minimum rates of 0 moles/drum/year for anoxic corrosion and 0 moles/drum/year for microbial degradation and maximum rates of 2 moles/drum/year for anoxic corrosion and 5 moles/drum/year for microbial degradation. Table 1 summarizes the gas generation rates for brine-inundated room conditions.

PARAMETER (cont'd) :	Gas Generation Rates

RATIONALE (cont'd) :

Table 1. Gas Generation Rates (moles/drum/year) for Brine-Inundated Room Conditions

		Rate	Rate	Rate
Minimum	(years)	(0+)		
Anoxic Corrosion		0		
Microbial Degradation		0		
Total		0		
Best	(years)	(0-550)	(550-1050)	(1050+)
Anoxic Corrosion		1	1	0
Microbial Degradation		1	0	0
Total		2	1	0
Maximum	(years)	(0-110)	(110-525)	(525+)
Anoxic Corrosion		2	2	0
Microbial Degradation		5	0	0
Total		7	2	0

Gas generation is simulated using gas injection wells in selected disposal room elements (grid blocks). Gas generation rates must be converted to kg/s/well for input to TOUGH28. There are 6804 drums per room (Lappin et al.,1989; p. 4-50). This number assumes that each room is filled with the maximum number of ideally packed drums. The following conversion is used:

$$\frac{\text{kg gas}}{\text{room} \cdot \text{s}} = \left[\frac{\text{moles}}{\text{drum} \cdot \text{yr}}\right]\left[2.016\text{E-}3\frac{\text{kg}}{\text{mole}}\right]\left[6804\frac{\text{drums}}{\text{room}}\right]\left[\frac{1\ \text{yr}}{3.15576\text{E7 s}}\right]$$

$$= (4.3466\text{E-}7)\left[\frac{\text{moles}}{\text{drum} \cdot \text{yr}}\right] \qquad (1)$$

Simulations use 6 wells per room and each model room is half-width and unit length relative to an actual 91.44 m long room. Therefore an additional conversion is required:

$$\frac{\text{kg gas}}{\text{s} \cdot \text{well}} = \left[\frac{\text{kg gas}}{\text{room} \cdot \text{s}}\right]\left[\frac{1\ \text{room}}{6\ \text{wells}}\right]\left[\frac{1}{(2)(91.44)}\right] \qquad (2)$$

PARAMETER (cont'd) :	Gas Generation Rates

RATIONALE (cont'd) : Using equations (1) and (2), the gas generation rates under brine-inundated room conditions are converted and are listed in Table 2.

Table 2. Gas Generation Rates (kg/s/well) for Brine-Inundated Room Conditions

		Rate	Rate	Rate
	(years)	(0+)		
Minimum	(rate)	0		
	(years)	(0-550)	(550-1050)	(1050+)
Best Estimate	(rate)	7.9225E-10	3.9613E-10	0
	(years)	(0-110)	(110-525)	(525+)
Maximum	(rate)	2.7729E-09	7.9225E-10	0

Vapor-Limited Room Conditions

Brush (1991; p. 9) gives best estimates of gas generation under vapor-limited conditions of 0.1 mole/drum/year due to anoxic corrosion and 0.1 mole/drum/year due to microbial degradation. Based on the assumed total potentials, gas generation by microbial degradation will occur for 5500 years and by anoxic corrosion for 10500 years under vapor-limited conditions. Brush (1991; p. 9) estimates minimum rates of 0 moles/drum/year for anoxic corrosion and 0 moles/drum/year for microbial degradation and maximum rates of 1 moles/drum/year for anoxic corrosion and 1 moles/drum/year for microbial degradation. Table 3 summarizes the gas generation rates for vapor-limited room conditions.

PARAMETER (cont'd) :	Gas Generation Rates

RATIONALE (cont'd) :

Table 3. Gas Generation Rates (moles/drum/year) for Vapor-Limited Room Conditions

		Rate	Rate	Rate
Minimum	(years)	(0+)		
Anoxic Corrosion		0		
Microbial Degradation		0		
Total		0		
Best	(years)	(0-5500)	(5500-10500)	(10500+)
Anoxic Corrosion		0.1	0.1	0.0
Microbial Degradation		0.1	0.0	0.0
Total		0.2	0.1	0.0
Maximum	(years)	(0-550)	(550-1050)	(1050+)
Anoxic Corrosion		1	1	0
Microbial Degradation		1	0	0
Total		2	1	0

Gas generation is simulated using gas injection wells in selected disposal room elements (grid blocks). The same conversion factors are used as for the brine-inundated rates. Using equations (1) and (2), the gas generation rates under vapor-limited room conditions are converted and are listed in Table 4.

Table 4. Gas Generation Rates (kg/s/well) for Vapor-Limited Room Conditions

		Rate	Rate	Rate
	(years)	(0+)		
Minimum	(rate)	0		
	(years)	(0-550)	(550-1050)	(1050+)
Best Estimate	(rate)	7.9225E-11	3.9613E-11	0
	(years)	(0-110)	(110-525)	(525+)
Maximum	(rate)	7.9225E-10	3.9613E-10	0

PARAMETER (cont'd) :	Gas Generation Rates

COMMENTS : It is useful to note that dividing the currently projected waste totals evenly among the rooms produces a somewhat smaller estimate of the number of drums per room. This smaller estimate was not used here on the assumption that, during the operational phase, rooms will be packed to their full capacity rather that leaving each room partially empty based on some assumed total waste volume that will eventually be stored at WIPP.

Brush (1991; p. 9) gives a best estimate of gas generation due radiolysis of brine of 0.0001 mole/drum/year with a range from 0 to 0.1 moles/drum/year. Because these rates are much lower than the anoxic corrosion and microbial degradation rates, radiolysis is not considered in the gas generation totals.

Brush (1995) presents updated estimates for gas generation rates. These updated rates are listed in Tables 5 and 6.

Table 5. Gas Generation Rates (moles/drum/year) for Brine-Inundated Room Conditions

	Rate	Rate	Rate
Minimum (years)	(0+)		
Anoxic Corrosion	0		
Microbial Degradation	0		
Total	0		
Best (years)	(0-550)	(550-1750)	(1750+)
Anoxic Corrosion	0.6	0.6	0
Microbial Degradation	1.0	0.0	0
Total	1.6	0.6	0
Maximum (years)	(0-7)	(7-110)	(525+)
Anoxic Corrosion	150	0	0
Microbial Degradation	5	5	0
Total	155	5	0

PARAMETER (cont'd) :	Gas Generation Rates

COMMENTS (cont'd) :

Table 6. Gas Generation Rates (moles/drum/year) for Vapor-Limited Room Conditions

	Rate	Rate	Rate
Minimum (years)	(0+)		
Anoxic Corrosion	0		
Microbial Degradation	0		
Total	0		
Best (years)	(0-5500)	(5500+)	
Anoxic Corrosion	0.0	0.0	
Microbial Degradation	0.1	0.0	
Total	0.1	0.0	
Maximum (years)	(0-550)	(550-17500)	(17500+)
Anoxic Corrosion	0.06	0.06	0
Microbial Degradation	1.00	0.00	0
Total	1.06	0.06	0

Due to time constraints, these best estimate rates were not incorporated into the baseline simulations, however, because the maximum rates are significantly higher than previously determined, these maximum rates were used in sensitivity simulations.

REFERENCES :

Beraun, R., and P.B. Davies. 1992. "Baseline Design Input Data Base to be Used During Calculations Effort to be Performed by Division 1514 in Determining the Mechanical Creep Closure Behavior of Waste Disposal Rooms in Bedded Salt," *Preliminary Performance Assessment for the Waste Isolation Pilot Plant, December 1992 - Volume 3: Model Parameters.* SAND92-0700/3. Albuquerque, NM: Sandia National Laboratories. A-5 through A-13.

Brush, L.H. 1991. "Appendix A: Current Estimates of Gas Production Rates, Gas Production Potentials, and Expected Chemical Conditions Relevant to Radionuclide Chemistry for the Long-Term WIPP Performance Assessment," *Preliminary Comparison with 40 CFR Part 191, Subpart B for the Waste Isolation Pilot Plant, December 1991 - Volume 3: Reference Data.* Eds. R.P. Rechard, A.C. Peterson, J.D. Schreiber, H.J. Iuzzolino, M.S. Tierney, and J.S. Sandha. SAND91-0893/3. Albuquerque, NM: Sandia National Laboratories. A-25 through A-36.

PARAMETER (cont'd) :	Gas Generation Rates
REFERENCES (cont'd) :	Brush, L.H. 1995. "Likely Gas-Generation Reactions and Current Estimates of Gas-Generation Rates for the Long-Term WIPP Performance Assessment," *A Summary of Methods for Approximating Salt Creep and Disposal Room Closure in Numerical Methods of Multiphase Flow.* G.A. Freeze, K.W. Larson, and P.B. Davies. SAND94-0251. Albuquerque, NM: Sandia National Laboratories. C-5 through C-45. Lappin, A.R., R.L. Hunter, D.P. Garber, and P.B. Davies, eds. 1989. *Systems Analysis, Long-Term Radionuclide Transport, and Dose Assessments, Waste Isolation Pilot Plant (WIPP), Southeastern New Mexico; March 1989.* SAND90-0462. Albuquerque, NM: Sandia National Laboratories.

V. INITIAL CONDITIONS

DATE :	08/31/93	RATIONALE NUMBER:	004A
PARAMETER :	Initial Pressure Distributions		
VALUE :		Brine Pressure MPa	
	Salado	12.0	
	Disposal Room	0.10	
KEYWORD :	INCON, INDOM		

RATIONALE :

Initial Pressure in the Salado Formation

Undisturbed pore pressure in the Salado Formation at the elevation of the repository is expected to be somewhere between hydrostatic (5.9 MPa) and lithostatic (14.8 MPa) (Peterson et al., 1987; Nowak and McTigue, 1987; Lappin et al., 1989). Pore pressures measured during hydraulic testing tend to be less than the assumed undisturbed formation pressure due to excavation related depressurization. Pore pressures extrapolated from pressure recovery trends yield somewhat higher values, however, uncertainty in the extrapolated values varies as a function of the quality and duration of the pressure data and of the extent of the extrapolation. Even the extrapolated values are likely influenced to some extent by excavation related depressurization.

Based on the extrapolated pressures in Table 1, 12.0 MPa is used as a best estimate for undisturbed pore pressure at the repository level. A range of 11.0 MPa to 15.0 MPa has been selected for sensitivity analysis. The low end of the range approximately corresponds to the highest measured pore pressures. The high end of the range corresponds to the highest theoretical value (lithostatic, approximately 15 MPa).

PARAMETER (cont'd) :	Initial Pressure Distributions

RATIONALE (cont'd):

Table 1. Pore Pressures in the Salado Formation

Lithology	Distance from Excavation (m)	Pore Pressure (MPa)	Reference
Halite	27.	9.5	(2)
Anhydrite	9-11.	9.3	(1)
Anhydrite	11-15.	12.4	(1)
Anhydrite	23.	12.5	(2)
Anhydrite	23.	12.6	(2)

(1) Beauheim et al., 1991
(2) Howarth et al., 1991.

The vertical pore-pressure distribution above and below the repository level is assumed to be hydrostatic, referenced to 12.0 MPa pressure at the vertical center of the repository. The hydrostatic pressure distribution assumes a brine density of 1200 kg/m^3 (see brine density rationale) and a gravitational constant of 9.81 N/kg.

This approach was selected because it produces a pressure distribution that is relatively static under undisturbed conditions (i.e., no repository). The disadvantage of using this approach is that it may produce a conceptual pressure discontinuity at the Rustler/Salado interface, as illustrated in Figure 1.

Initial Pressure in the Waste Disposal Rooms

The initial room state represents the room just after it has been backfilled and sealed, therefore, the initial pressure is specified as atmospheric.

$$P_{initial} = 1 \text{ atm} = 1.01325 \text{ bars} = 0.10 \text{ MPa}$$

COMMENTS : Initial room pressures for the fixed room geometries are calculated as follows:

Initial Room Geometry

The initial room pressure is atmospheric.

$$P_{initial} = 1 \text{ atm} = 1.01325 \text{ bars} = 0.10 \text{ MPa}$$

PARAMETER (cont'd) :	Initial Pressure Distributions

COMMENTS (cont'd) :

Intermediate Room Geometry

Initial pressure for the intermediate room is directly proportional to the reduction in void volume due to room closure and consolidation:

$$P_{intermediate} = \left(\frac{V_{initial} \cdot \phi_{initial}}{V_{intermediate} \cdot \phi_{intermediate}} \right) P_{initial}$$

where:

$V_{initial}$ = 3644 m^3 (room geometry rationale)
$\phi_{initial}$ = 0.663 (porosity rationale)
$V_{intermediate}$ = 1995 m^3 (room geometry rationale)
$\phi_{intermediate}$ = 0.384 (porosity rationale)
$P_{initial}$ = 0.10 MPa

Therefore:

$$P_{intermediate} = \frac{(3644)(0.663)}{(1995)(0.384)} (0.10)$$

$$= 0.32 \text{ MPa}$$

Fully Consolidated Room Geometry

Initial pressure for the fully consolidated room is specified using the same approach as for the intermediate room:

$$P_{fully\ consolidated} = \left(\frac{V_{initial} \cdot \phi_{initial}}{V_{fully\ consolidated} \cdot \phi_{fully\ consolidated}} \right) P_{initial}$$

where:

$V_{fully\ consolidated}$ = 1572 m^3 (room geometry rationale)
$\phi_{fully\ consolidated}$ = 0.218 (porosity rationale)

Therefore:

$$P_{fully\ consolidated} = \frac{(3644)(0.663)}{(1572)(0.218)} (0.10)$$

$$= 0.70 \text{ MPa}$$

PARAMETER (cont'd) :	Initial Pressure Distributions
COMMENTS (cont'd):	There is some question as to the best approach for extrapolating the pore pressure above and below the repository level. The primary reason for this uncertainty is that the mechanism for generating a pore pressure above hydrostatic and below lithostatic is not well understood at the present time. An alternative approach to calculating the vertical pore-pressure distribution above and below the repository level is to use a pressure gradient defined by two points, the 12.0 MPa pressure at the repository depth and the pressure at the Rustler/Salado interface predicted by a hydrostatic pressure gradient between that interface and the ground surface (Figure 2). The disadvantage of this approach is that the pressure distribution will not produce a static pressure distribution under undisturbed conditions. This is because the resulting pressure gradient is between hydrostatic and lithostatic.
REFERENCES :	Beauheim, R.L., G.J. Saulnier, Jr., and J.D. Avis. 1991. *Interpretation of Brine-Permeability Tests of the Salado Formation at the Waste Isolation Pilot Plant: First Interim Report.* SAND90-0083. Albuquerque, NM: Sandia National Laboratories. Howarth, S.M., E.W. Peterson, P.L. Lagus, K.H. Lie, S.J. Finley, and E.J. Nowak. 1991. "Interpretation of In-Situ Pressure and Flow Measurements of the Salado Formation at the Waste Isolation Pilot Plant," *Rocky Mountain Regional Meeting and Low-Permeability Reservoirs Symposium, Denver, CO, April 15-17, 1991.* SAND90-2334C; SPE 21840. Richardson, TX: Society of Petroleum Engineers. 355-369. Lappin, A.R., R.L. Hunter, D.P. Garber, and P.B. Davies, eds. 1989. *Systems Analysis, Long-Term Radionuclide Transport, and Dose Assessments, Waste Isolation Pilot Plant (WIPP), Southeastern New Mexico; March 1989.* SAND89-0462. Albuquerque, NM: Sandia National Laboratories. Nowak, E.J., and D.F. McTigue. 1987. *Interim Results of Brine Transport Studies in the Waste Isolation Pilot Plant (WIPP).* SAND87-0880. Albuquerque, NM: Sandia National Laboratories. Peterson, E.W., P.L. Lagus, and K. Lie. 1987. *WIPP Horizon Free Field Fluid Transport Characteristics.* SAND87-7164. Albuquerque, NM: Sandia National Laboratories.

PARAMETER (cont'd) :	Initial Pressure Distributions

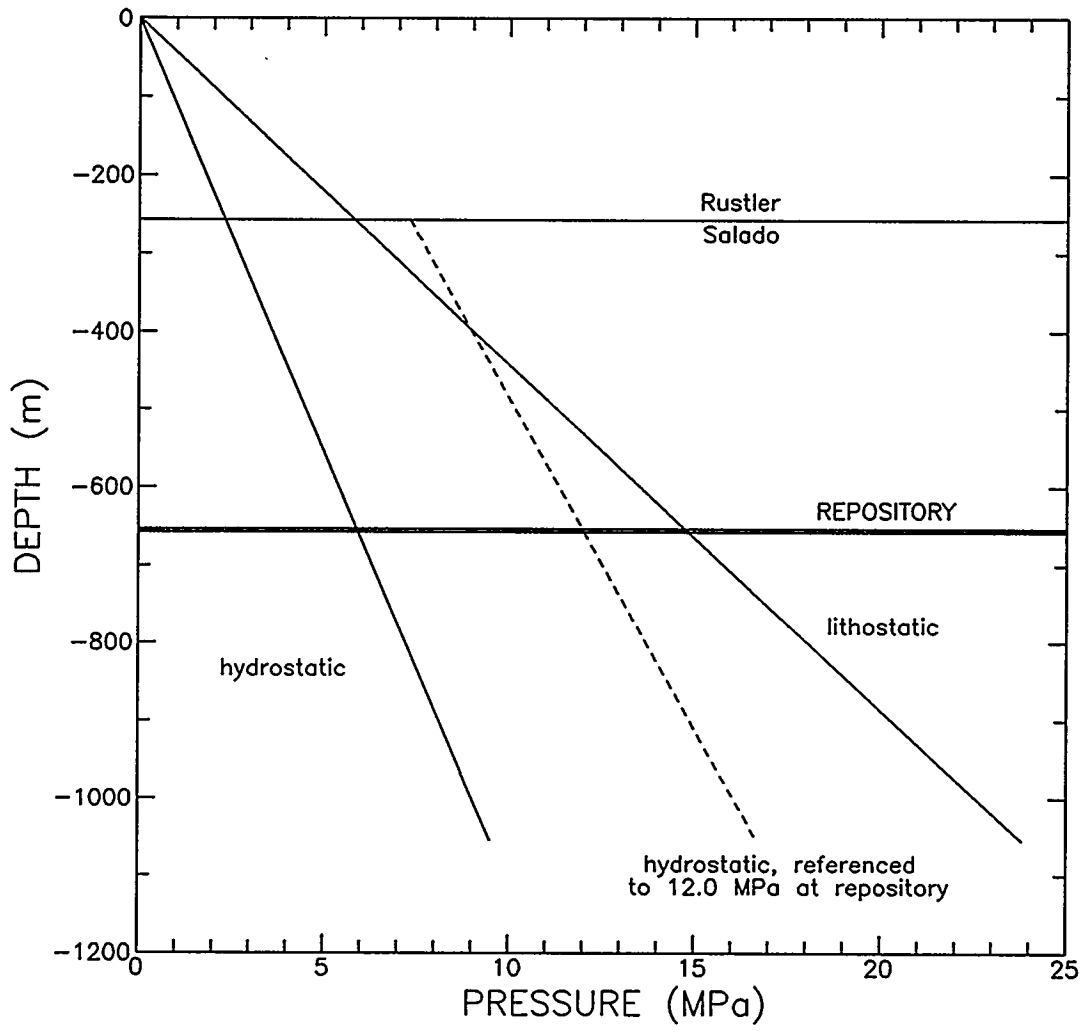

Figure 1. Assumed vertical fluid pressure distribution in the Salado Formation.

PARAMETER (cont'd) :	Initial Pressure Distributions

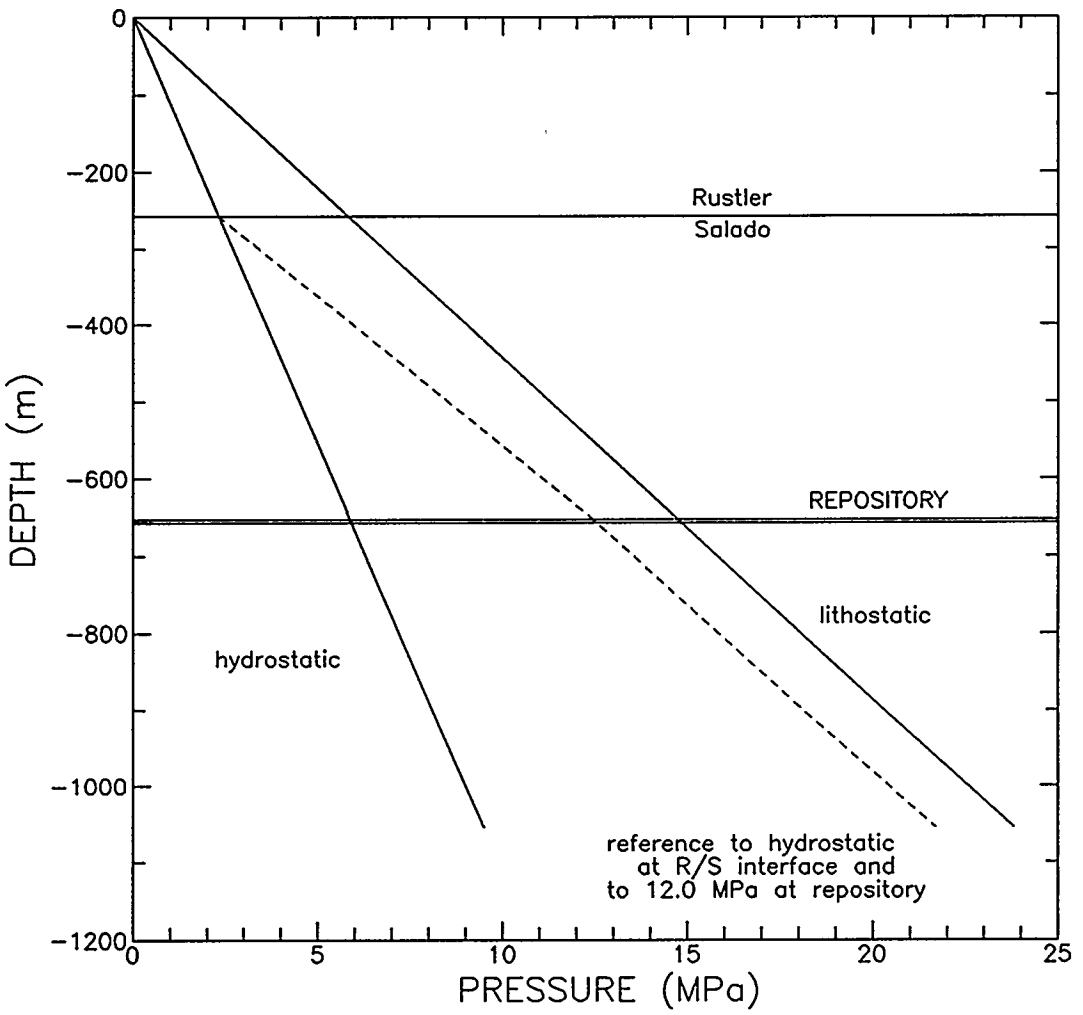

Figure 2. Alternative vertical fluid pressure distribution in the Salado Formation.

DATE :	08/31/93	RATIONALE NUMBER:	004A

PARAMETER : Initial Saturations

VALUE :

	Saturations			
	crushed salt backfill		salt/bentonite backfill	
	S_g	S_b	S_g	S_b
Salado	0.00	1.00	0.00	1.00
Initial	0.99	0.01	0.97	0.03

KEYWORD : INCON, INDOM

RATIONALE : The initial brine saturation, S_b, is calculated using the following equation:

$$S_b = S_w = \frac{V_w}{V_v} = \frac{V_{w\ backfill} + V_{w\ waste}}{V_v} \qquad (1)$$

where:

V_w = initial volume of water (brine) in room [m^3],
V_v = volume of voids in room [m^3],
$V_{w\ backfill}$ = initial volume of water (brine) in backfill [m^3],
$V_{w\ waste}$ = initial volume of water (brine) in waste [m^3].

The initial gas saturation, S_g, is calculated as follows:

$$S_g = 1.0 - S_b \qquad (2)$$

There is some uncertainty in quantifying the amount and mobility of water (brine) that is initially present in the WIPP waste disposal rooms. These two properties are dependent on the amount of water and brine initially present in the waste and the backfill, and on the composition of the waste and backfill in the room. As a result, calculations are made for two different backfill compositions, crushed salt and a 70/30 mixture of crushed salt and bentonite.

Crushed salt is assumed to contain 0.5% water by weight (Pfeifle, 1987; p. 24) and a 70/30 mixture of salt/bentonite backfill is assumed to contain 3.3% water by weight (Pfeifle,

PARAMETER (cont'd) :	Initial Saturations

RATIONALE (cont'd) : 1987; p. 25). The initial volume of water (brine) in the backfill can be computed as follows:

$$V_{w\ backfill} = \frac{\rho_{backfill} \cdot V_{backfill}}{\rho_w \cdot \left[1 + \frac{1}{W_{backfill}}\right]} \qquad (3)$$

where:

$\rho_{backfill}$ = density of backfill
= 1300 kg/m^3 (Lappin et al., 1989; p. 4-58)

$W_{backfill}$ = initial water content (by wt.) of backfill
= 0.005 for crushed salt
= 0.033 for 70/30 salt/bentonite

$V_{backfill}$ = volume of backfill = $V_{init.\ room} - V_{drums} - V_{vent\ gap}$
= 1327 m^3 (room porosity rationale)

ρ_w = density of water (brine)
= 1200 kg/m^3 (brine density rationale)

From equation (3):

$$V_{w\ backfill} = \frac{(1300\ kg/m^3)(1327\ m^3)}{(1200\ kg/m^3)\left[1 + \frac{1}{0.005}\right]}$$

$$= 7.15\ m^3 \quad \text{(for crushed salt backfill)}$$

$$V_{w\ backfill} = \frac{(1300\ kg/m^3)(1327\ m^3)}{(1200\ kg/m^3)\left[1 + \frac{1}{0.033}\right]}$$

$$= 45.92\ m^3 \quad \text{(for salt/bentonite backfill)}$$

The waste is assumed to have an initial water (brine) content of 1% by volume, which is the upper limit specified in the Waste Acceptance Criteria (WAC) (U.S. Department of Energy, 1991). The initial volume of water in the waste can be computed as follows:

PARAMETER (cont'd) :	Initial Saturations

RATIONALE (cont'd) :

$$V_{w\ waste} = V_{waste} * \omega_{waste} \quad (4)$$

where:

V_{waste} = volume of waste
= volume of 6804 drums
= 1663 m^3 (Beraun and Davies, 1992; p. 1)

ω_{waste} = water content (by volume) of waste
= 0.01 (WAC)

From equation (4):

$$V_{w\ waste} = (1663\ m^3)(0.01) = 16.63\ m^3$$

Summing the results from equations (3) and (4), the initial volume of water in a room is:

V_w = 23.78 m^3 (with crushed salt backfill)
= 62.55 m^3 (with salt/bentonite backfill)

The room void volume can be calculated from:

$$V_v = V_{room} \cdot \phi_{room} \quad (5)$$

where:

V_{room} = volume of room [m^3]
ϕ_{room} = porosity of room

For the initial room state:

$V_{initial\ room}$ = 3644 m^3 (room geometry rationale)
$\phi_{initial\ room}$ = 0.663 (room porosity rationale)

Therefore, from equation (1):

$$S_{w\ init.\ room} = \frac{(23.78\ m^3)}{(3644\ m^3)(0.663)}$$

= 0.01 (with crushed salt backfill)

and

PARAMETER (cont'd) :	Initial Saturations

RATIONALE (cont'd):

$$S_{w\ init.\ room} = \frac{(62.55\ m^3)}{(3644\ m^3)(0.663)}$$

$$= 0.03 \quad \text{(with salt/bentonite backfill)}$$

From equation (2):

$S_{g\ init.\ room} = 0.99$ (with crushed salt backfill)
$S_{g\ init.\ room} = 0.97$ (with salt/bentonite backfill)

Salado Formation

The Salado halite and interbeds are assumed to have an initial brine saturation of 1.0 and an initial gas saturation of 0.0.

COMMENTS : Initial saturations for the fixed room geometries are calculated as follows:

Intermediate Room State

For the intermediate room state the void volume has been reduced by room closure and consolidation:

$V_{intermediate\ room} = 1995\ m^3$ (room geometry rationale)
$\phi_{intermediate\ room} = 0.384$ (room porosity rationale)

Therefore, from equation (1):

$$S_{w\ intermed.\ room} = \frac{(23.78\ m^3)}{(1995\ m^3)(0.384)}$$

$$= 0.03 \quad \text{(with crushed salt backfill)}$$

and

$$S_{w\ intermed.\ room} = \frac{(62.55\ m^3)}{(1995\ m^3)(0.384)}$$

$$= 0.08 \quad \text{(with salt/bentonite backfill)}$$

From equation (2):

$S_{g\ intermed.\ room} = 0.97$ (with crushed salt backfill)
$S_{g\ intermed.\ room} = 0.92$ (with salt/bentonite backfill)

PARAMETER (cont'd) :	Initial Saturations

COMMENTS (cont'd) :

Fully Consolidated Room State

For the fully consolidated room state the void volume has been further reduced by room closure and consolidation:

$V_{\text{fully consolidated room}} = 1572\ m^3$ (room geometry rationale)
$\phi_{\text{fully consolidated room}} = 0.218$ (room porosity rationale)

Therefore, from equation (1):

$$S_{w\ \text{fully cons. room}} = \frac{(23.78\ m^3)}{(1572\ m^3)(0.218)}$$

$$= 0.07 \quad \text{(with crushed salt backfill)}$$

and

$$S_{w\ \text{fully cons. room}} = \frac{(62.55\ m^3)}{(1572\ m^3)(0.218)}$$

$$= 0.18 \quad \text{(with salt/bentonite backfill)}$$

From equation (2):

$S_{g\ \text{fully consol. room}} = 0.93$ (with crushed salt backfill)
$S_{g\ \text{fully consol. room}} = 0.82$ (with salt/bentonite backfill)

Initial room saturation is a difficult parameter to characterize in the context of the two phase gas simulations. Sources of complexity include the following.

i) Uncertainty in the initial water (brine) content of the waste. The WAC specifies that the waste will contain <1% water by volume. Some of the waste forms (in particular, sludge material) contain significant amounts of water. However, these materials are packaged with uncured cement, which is intended to extract and chemically bind water from the sludges.

PARAMETER (cont'd) :	Initial Saturations

COMMENTS :

ii) Uncertainty in the initial water content of the backfill. Crushed salt is expected to contain approximately 0.5% water by weight (Pfeifle, 1987; p. 24). If bentonite is used, the bentonite specifications set an upper limit on water content of 10% by weight (Pfeifle, 1987; p. 31). A 70/30 mixed salt/bentonite backfill is expected to have a water content of 3.3% by weight (Pfeifle, 1987; p. 25). The degree of chemical binding of water in bentonite under repository conditions is not well understood at present.

iii) Model limitations of treating the room contents as a homogeneous material with its two-phase properties based on an idealized analogue material. Clearly, the actual waste rooms will contain significant heterogeneities, which are not incorporated into the present model.

To examine the uncertainty in the initial brine saturation in the room, a minimum value of 0.0003 and a maximum value 0.066 were also simulated. The lower bound assumes no free moisture in the waste and minimal brine in the backfill (see Butcher and Lincoln, 1995a). The upper bound was determined from a rudimentary experiment measuring the maximum amount of water retained in waste and backfill (see Butcher and Lincoln, 1995b).

In the model, it is important that the specified initial saturations be consistent with the specified two-phase properties of the room, i.e., the initial water (brine) saturation in the room should not be less than the residual water (brine) saturation, S_{br}. Because the two-phase properties come from idealized analogues, this criteria is not always satisfied. The theoretical initial brine saturation is 0.01 or 0.03 depending on backfill composition, while S_{br} is specified as 0.276 (see the relative permeability and capillary pressure rationale).

The very low initial brine saturations calculated for the room indicate that the room may initially be in a "super-unsaturated" state (i.e., have a saturation that is less than the residual brine saturation). Such a state would be created by the man-made conditions which generated the pore space/structure and fluid

PARAMETER (cont'd) :	Initial Saturations
COMMENTS (cont'd) :	content. This "super-unsaturated" state, if it exists, may require additional laboratory measurements to rigorously model the early time imbibition behavior. However, if the room was initially saturated and then drained, it is highly unlikely that drainage to such low saturations could be achieved. Residual brine saturation is basically a function of pore structure and, because of the crushing of salt, processing of bentonite, and artificial creation of pore space in the waste, the resultant pore structure in the room is probably not capable of draining down to the water contents that have been 'artificially' introduced into this material. Another comment concerns the potential misuse of an initial brine saturation for the room that has been specified to be artificially high (i.e., slightly above 0.276) in order to satisfy criteria that it be above the residual brine saturation. Some gas generation processes may be heavily dependent on "available" water, and therefore, water budget calculations may become an important effort in future calculations. If water budget calculations are to be made, they must: a) recognize the difference between the actual predicted initial water saturation and the residual water saturation used in the simulations, and b) consider the potentially large water-binding capillary forces that may be present under highly unsaturated conditions. If at some point the room analogue material is changed and therefore the residual saturation for the room is changes, then these initial saturations may require re-evaluation.

PARAMETER (cont'd) :	Initial Saturations

REFERENCES :

Beraun, R., and P.B. Davies. 1992 "Baseline Design Input Data Base to be Used During Calculations Effort to be Performed by Division 1514 in Determining the Mechanical Creep Closure Behavior of Waste Disposal Rooms in Bedded Salt," *Preliminary Performance Assessment for the Waste Isolation Pilot Plant, December 1992 - Volume 3: Model Parameters.* SAND92-0700/3. Albuquerque, NM: Sandia National Laboratories. A-5 through A-13.

Butcher, B.M., and R.C. Lincoln. 1995a. "The Initial Brine Saturation of Waste and Backfill Within WIPP Disposal Rooms (WBS 1.1.1.2.3)," *Coupled Multiphase Flow and Closure Analysis of Repository Response to Waste-Generated Gas at the Waste Isolation Pilot Plant (WIPP).* G.A. Freeze, K.W. Larson, and P.B. Davies. SAND93-1986. Albuquerque, NM: Sandia National Laboratories. C-5 through C-6.

Butcher, B.M., and R.C. Lincoln, 1995b. "Upper limit of initial brine saturation in waste and backfill," *Coupled Multiphase Flow and Closure Analysis of Repository Response to Waste-Generated Gas at the Waste Isolation Pilot Plant (WIPP).* G.A. Freeze, K.W. Larson, and P.B. Davies. SAND93-1986. Albuquerque, NM: Sandia National Laboratories. C-7 through C-8.

Lappin, A.R., R.L. Hunter, D.P. Garber, and P.B. Davies, eds. 1989. *Systems Analysis, Long-Term Radionuclide Transport, and Dose Assessments, Waste Isolation Pilot Plant (WIPP), Southeastern New Mexico; March 1989.* SAND89-0462. Albuquerque, NM: Sandia National Laboratories.

Pfeifle, T.W. 1987. *Backfill Material Specifications and Requirements for the WIPP Simulated DHLW and TRU Waste Technology Experiments.* SAND85-7209. Albuquerque, NM: Sandia National Laboratories.

U.S. Department of Energy. 1991. *Waste Acceptance Criteria for the Waste Isolation Pilot Plant, December 1991.* WIPP/DOE-069. Carlsbad, NM: Westinghouse Electric Corporation.

This page intentionally left blank

APPENDIX B: SIMULATION RESULTS

This page intentionally left blank

Figures for Appendix B

Specified 2/1 Gas-Generation Rate History

Disposal Room

Halite

Interbed

Interbed

Other Gas-Generation Rate Histories

Alternative Conceptual Models

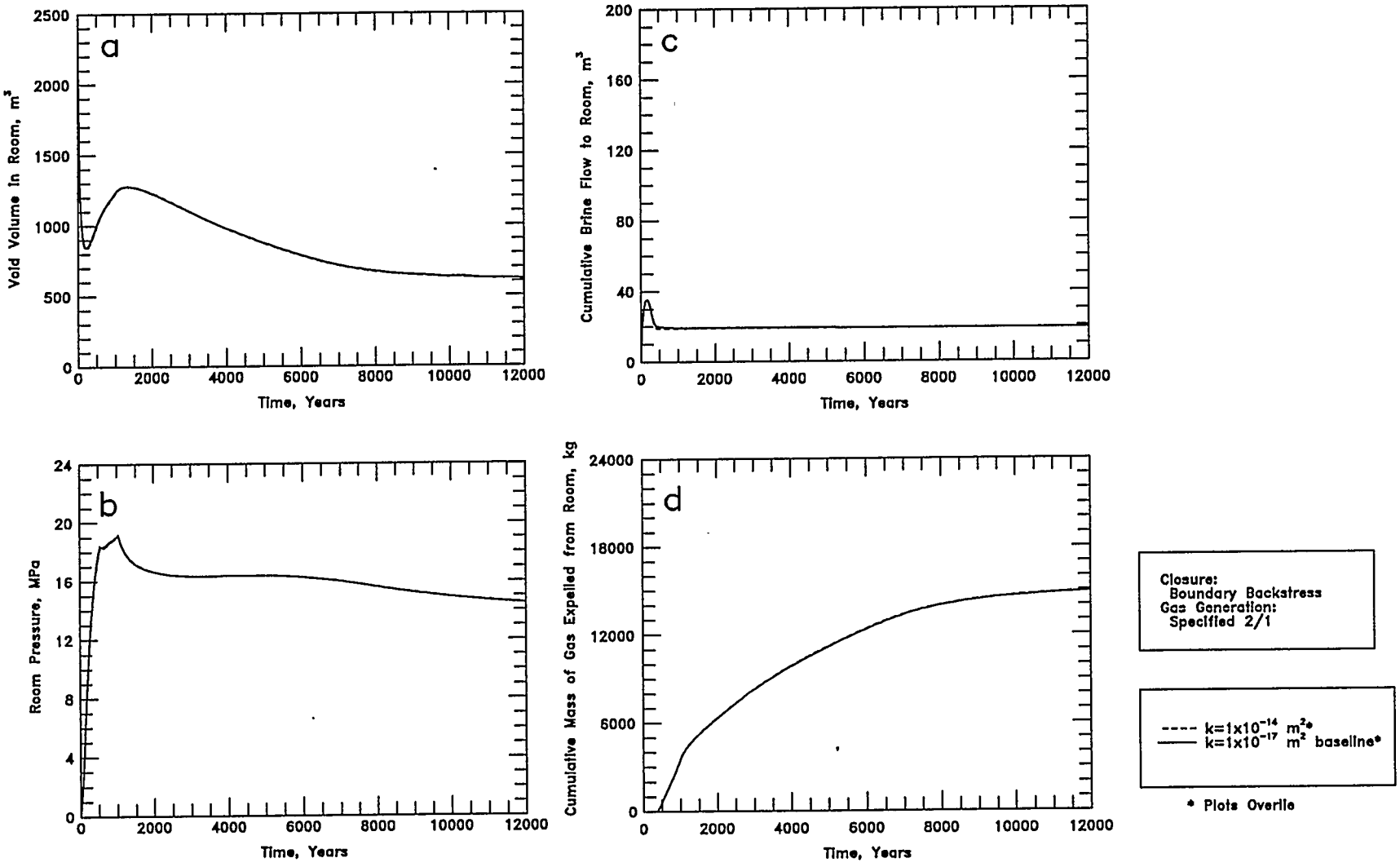

Figure B-1 (a-d). Sensitivity to Disposal Room Intrinsic Permeability: a - Void Volume; b - Gas Pressure; c - Brine Flow; d - Gas Expulsion

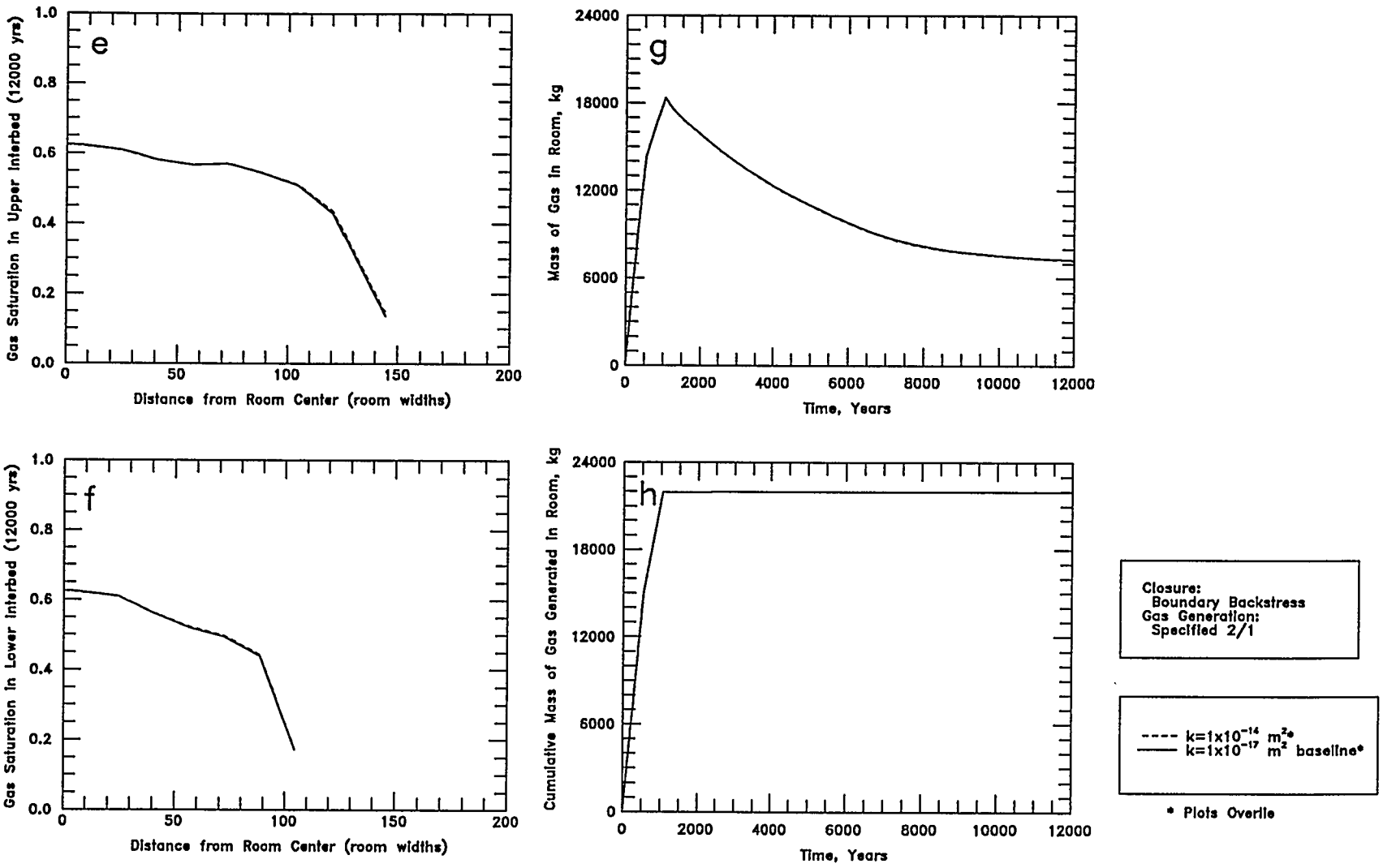

Figure B-1 (e-h). Sensitivity to Disposal Room Intrinsic Permeability:
e - Upper Interbed Gas Profile; f - Lower Interbed Gas Profile;
g - Room Gas Mass; h - Gas Generation

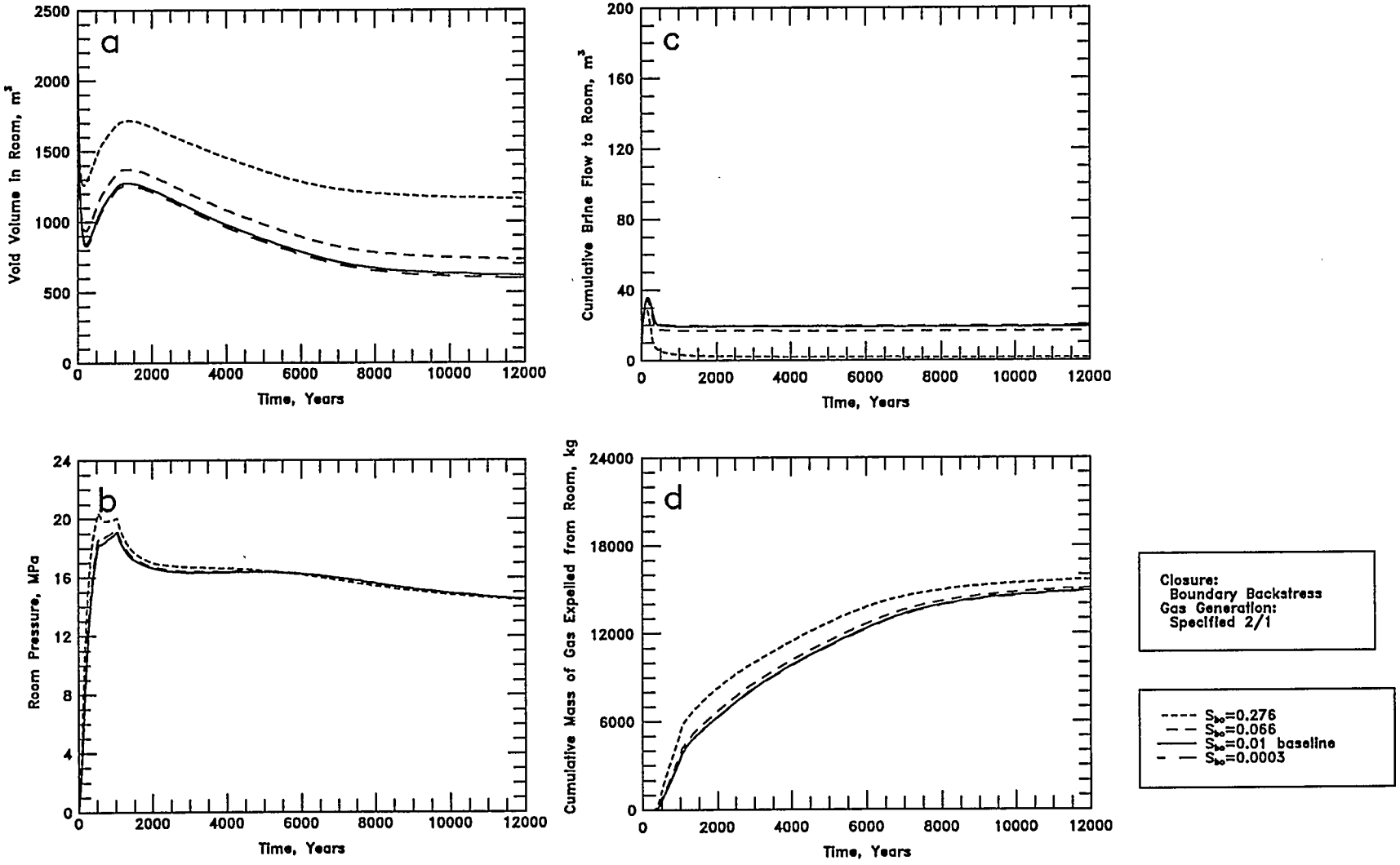

Figure B-2 (a-d). Sensitivity to Disposal Room Initial Brine Saturation: a - Void Volume; b - Gas Pressure; c - Brine Flow; d - Gas Expulsion

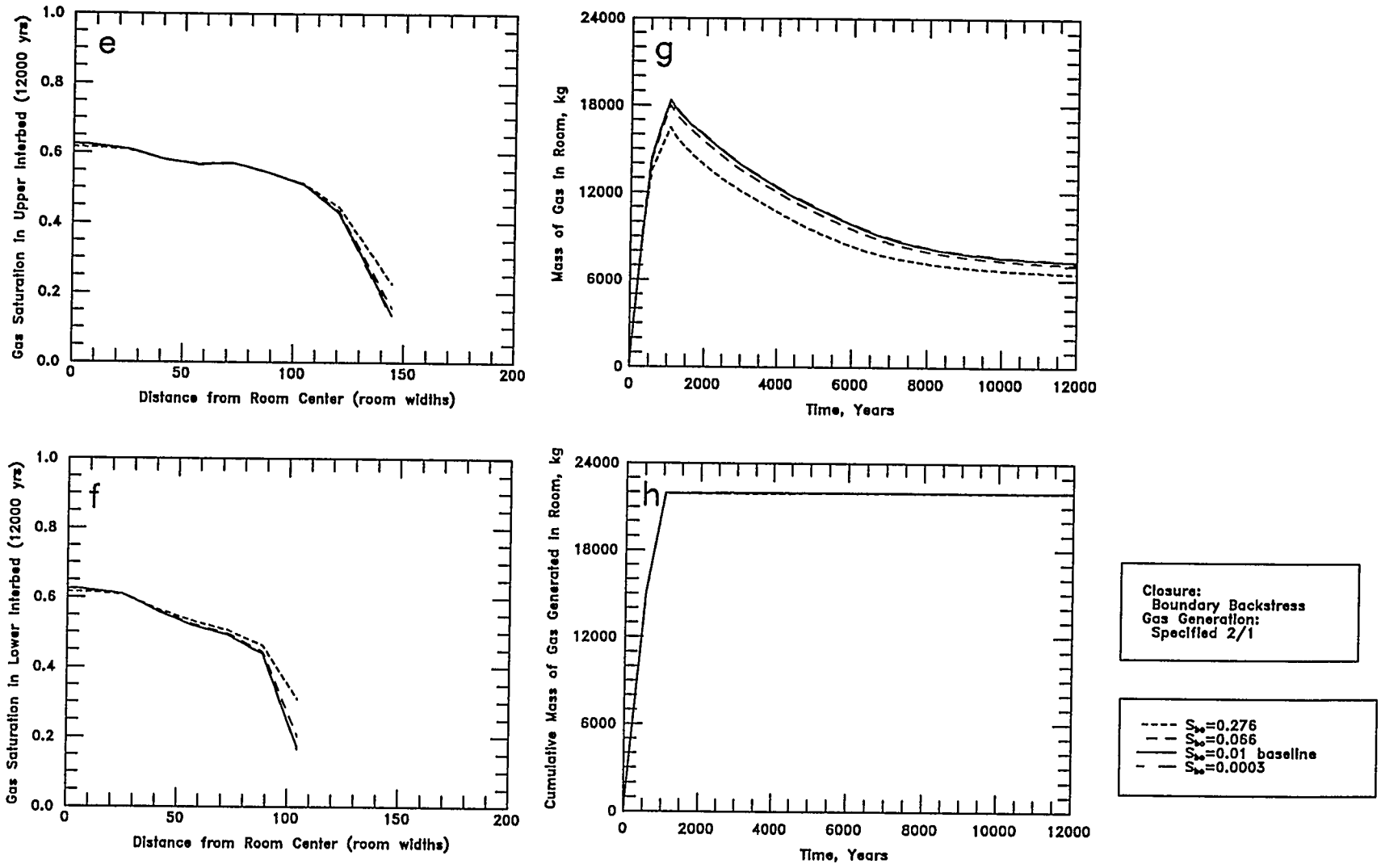

Figure B–2 (e–h). Sensitivity to Disposal Room Initial Brine Saturation: e – Upper Interbed Gas Profile; f – Lower Interbed Gas Profile; g – Room Gas Mass; h – Gas Generation

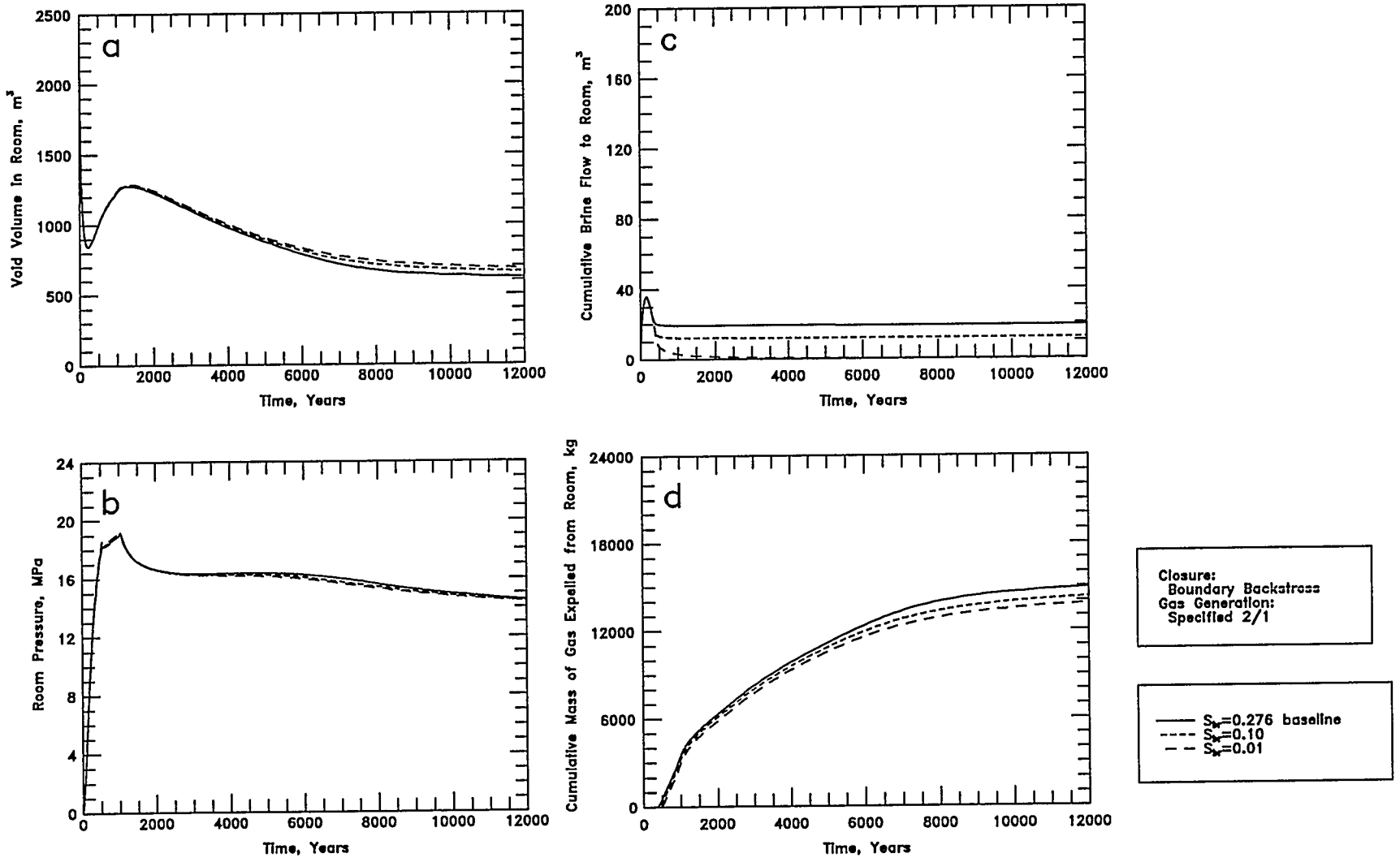

Figure B-3 (a-d). Sensitivity to Disposal Room Residual Brine Saturation: a - Void Volume; b - Gas Pressure; c - Brine Flow; d - Gas Expulsion

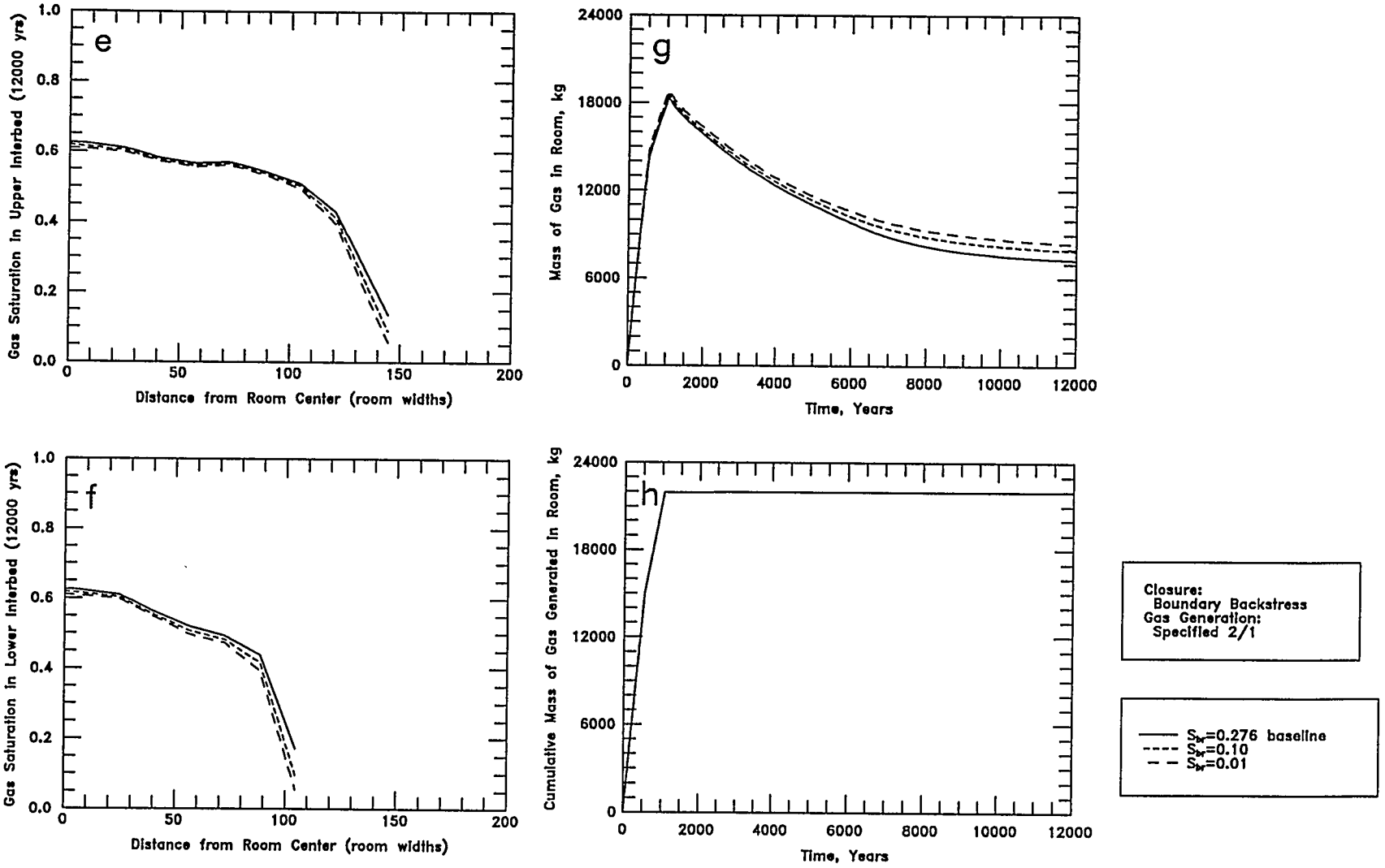

Figure B-3 (e-h). Sensitivity to Disposal Room Residual Brine Saturation: e - Upper Interbed Gas Profile; f - Lower Interbed Gas Profile; g - Room Gas Mass; h - Gas Generation

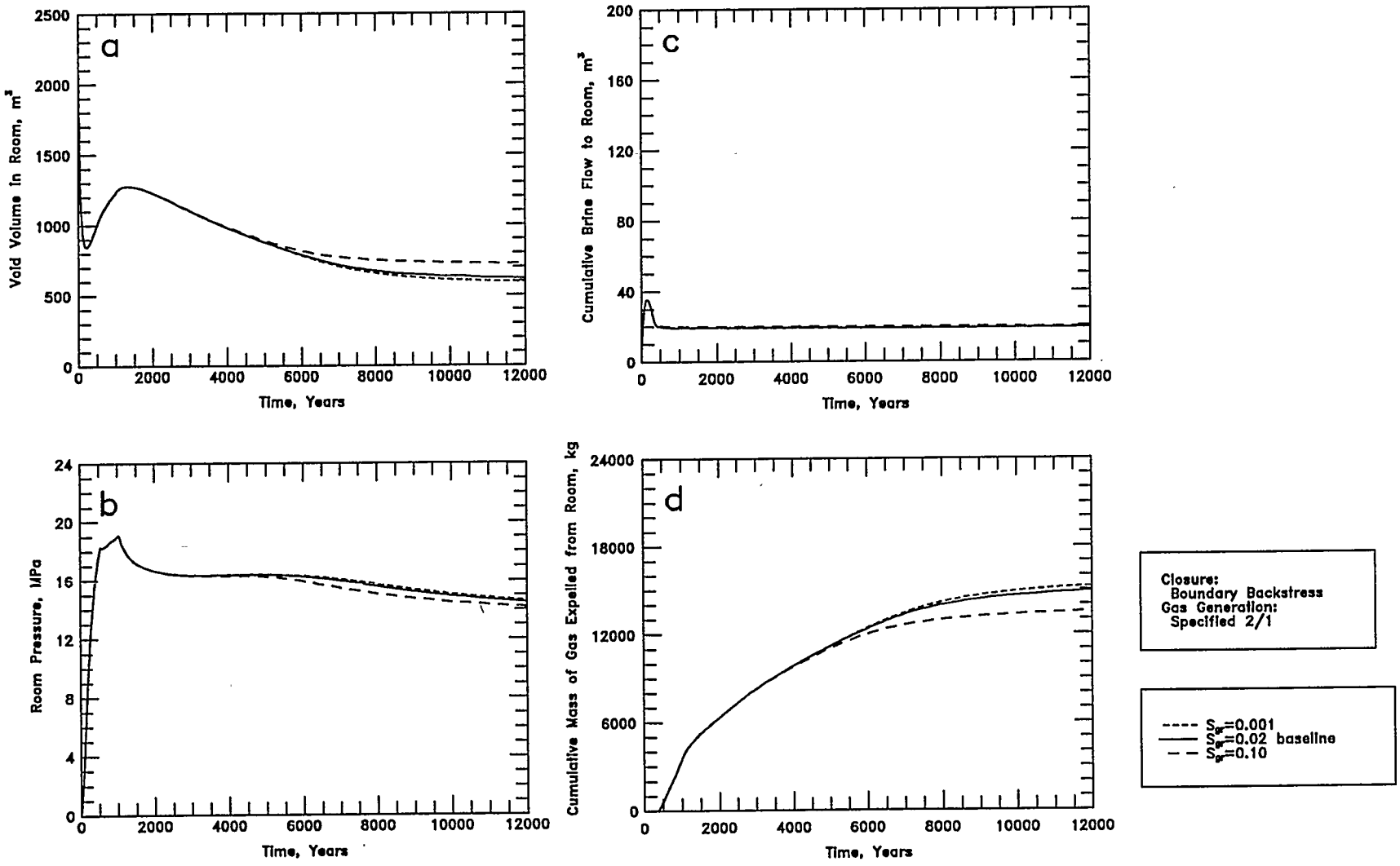

Figure B–4 (a–d). Sensitivity to Disposal Room Residual Gas Saturation: a – Void Volume; b – Gas Pressure; c – Brine Flow; d – Gas Expulsion

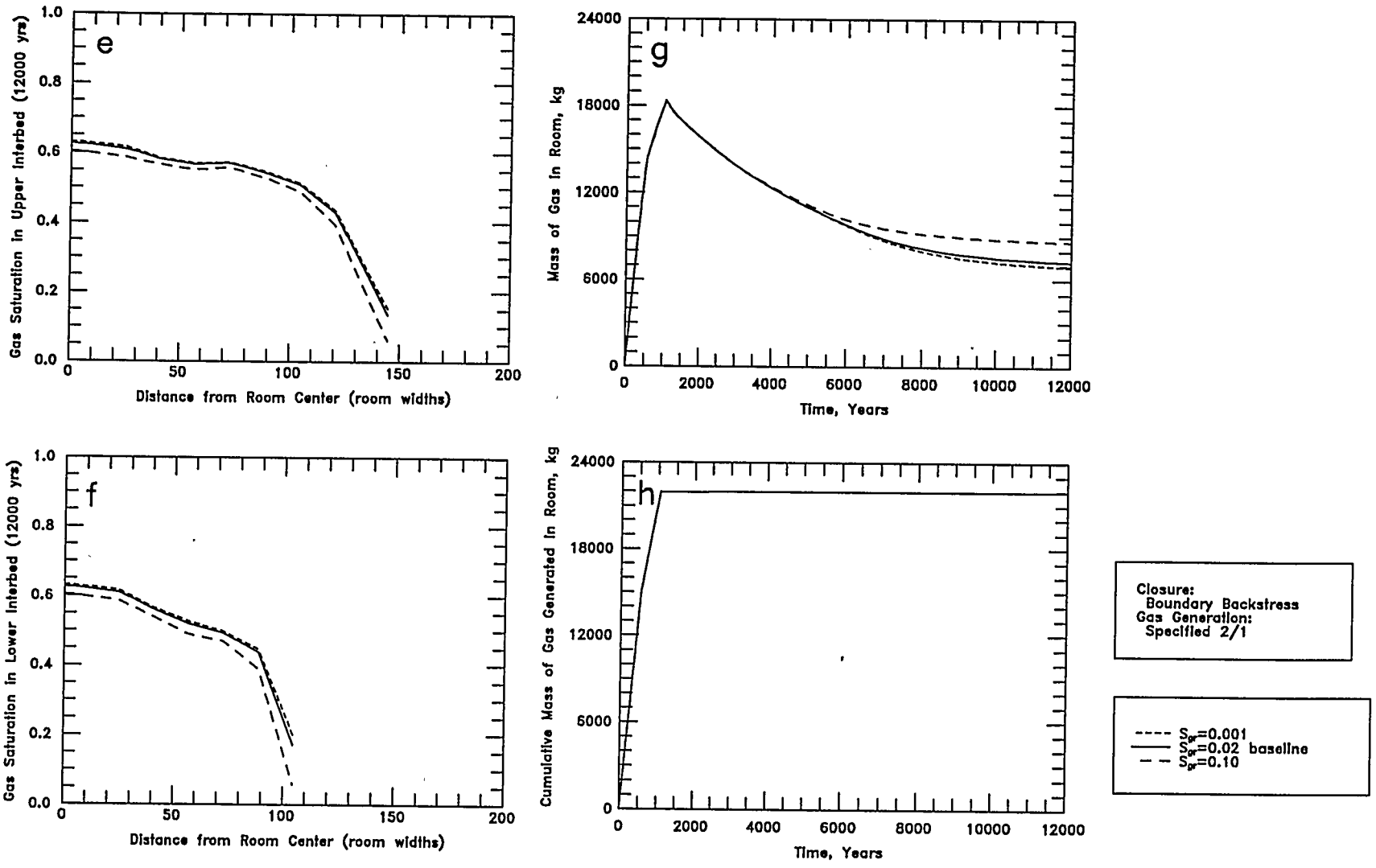

Figure B-4 (e-h). Sensitivity to Disposal Room Residual Gas Saturation: e - Upper Interbed Gas Profile; f - Lower Interbed Gas Profile; g - Room Gas Mass; h - Gas Generation

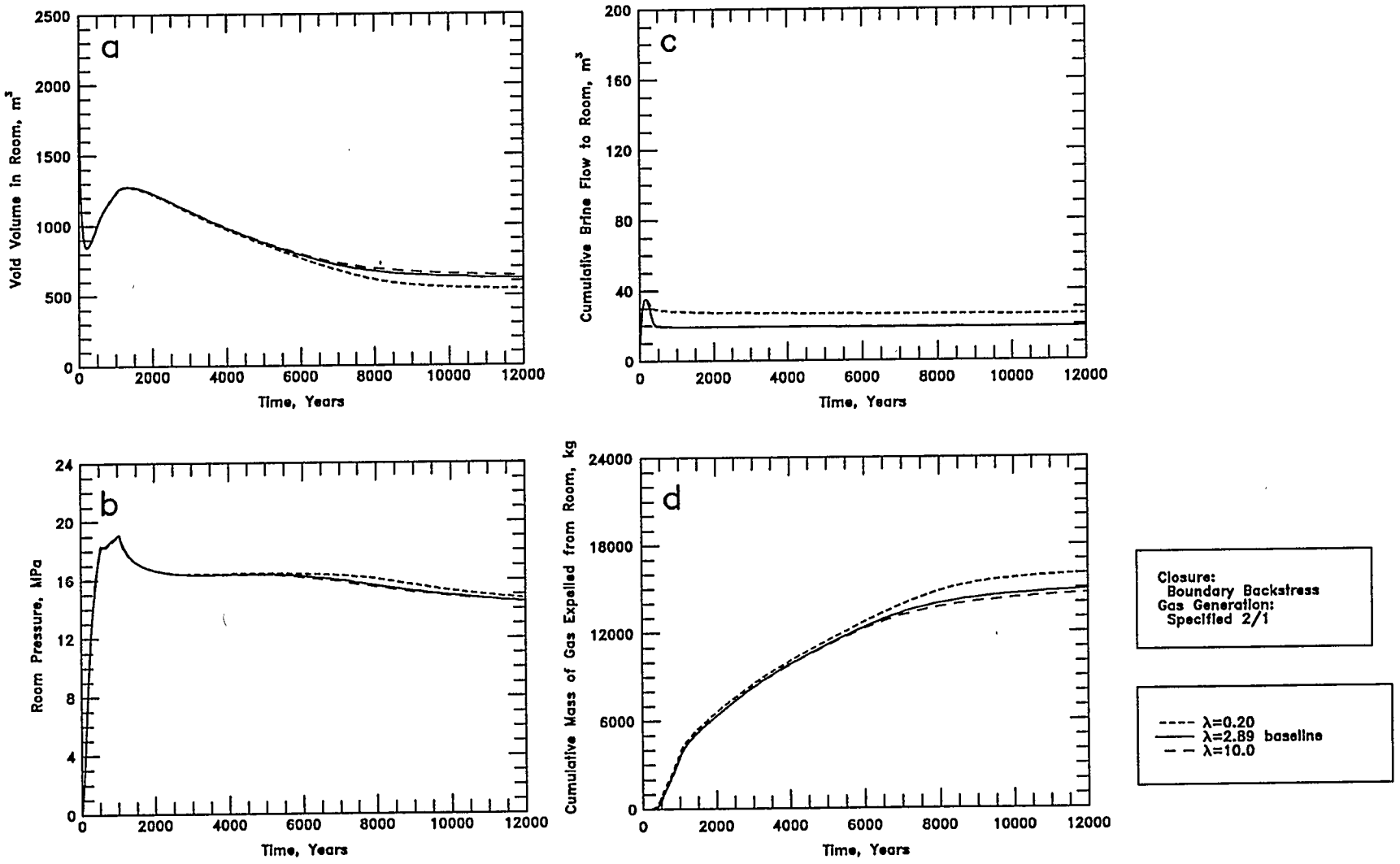

Figure B-5 (a-d). Sensitivity to Disposal Room Pore-Size Lambda:
a - Void Volume; b - Gas Pressure; c - Brine Flow; d - Gas Expulsion

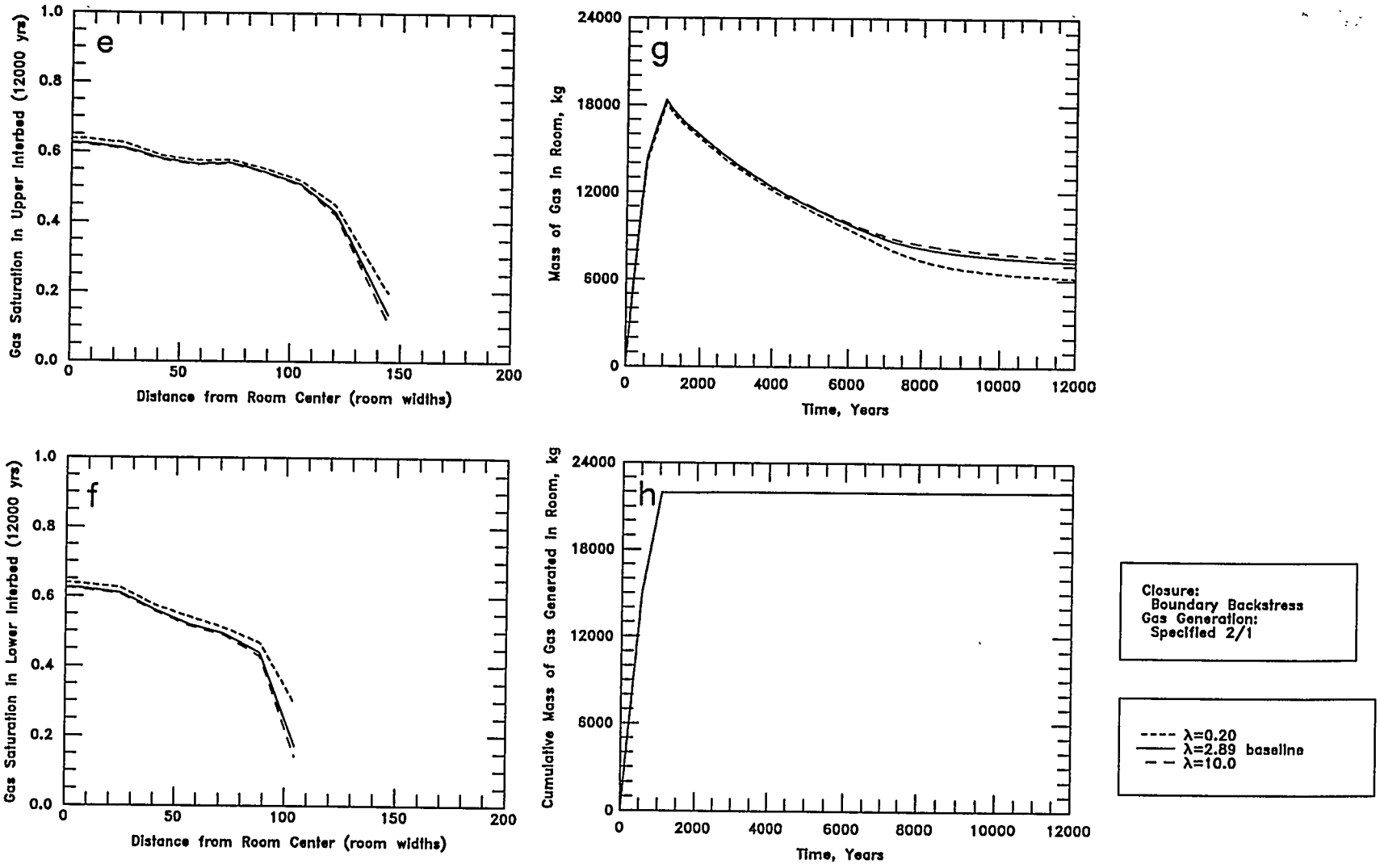

Figure B-5 (e-h). Sensitivity to Disposal Room Pore-Size Lambda:
e - Upper Interbed Gas Profile; f - Lower Interbed Gas Profile;
g - Room Gas Mass; h - Gas Generation

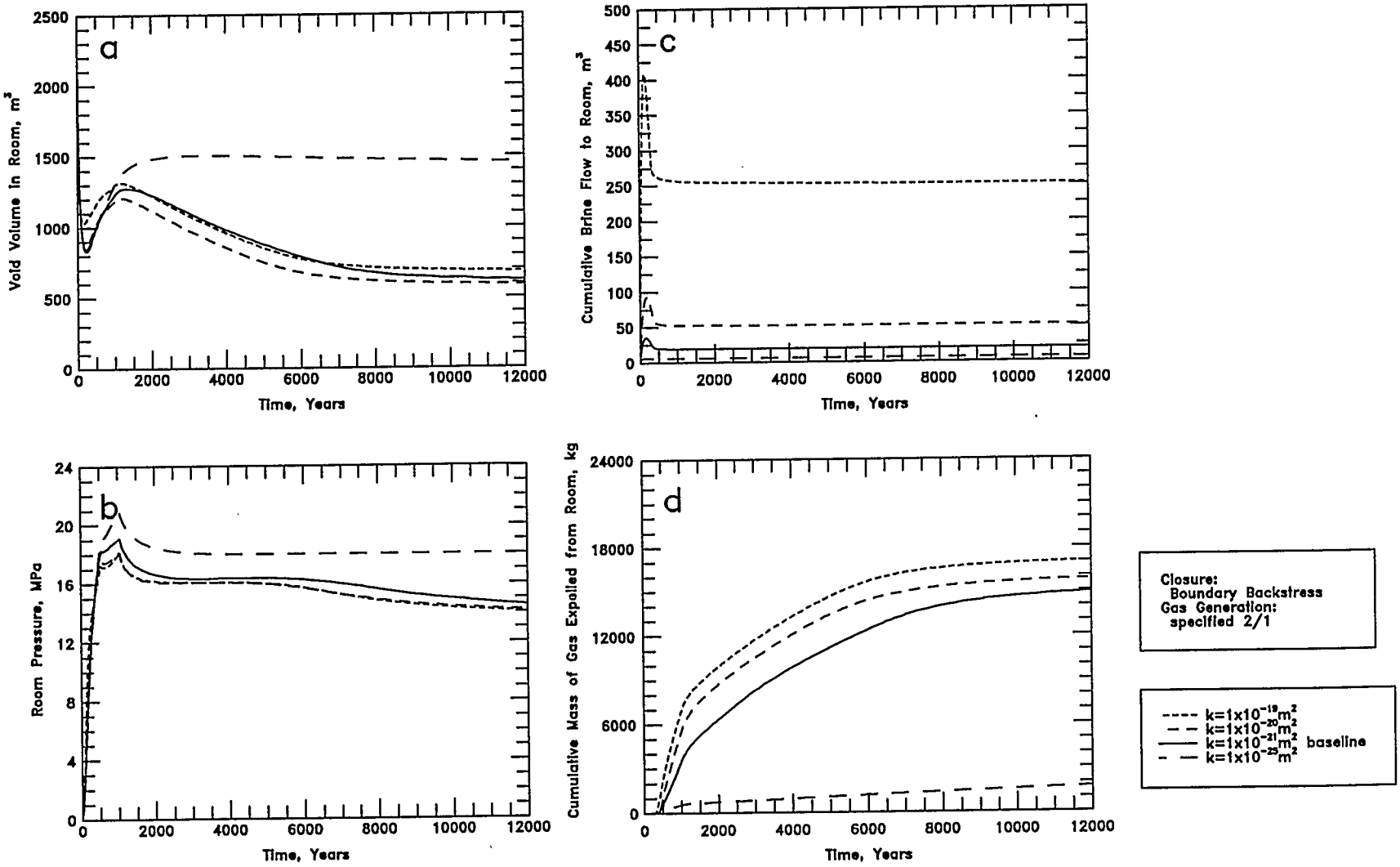

Figure B–6 (a–d). Sensitivity to Halite Intrinsic Permeability (constant threshold pressure): a – Void Volume; b – Gas Pressure; c – Brine Flow; d – Gas Expulsion

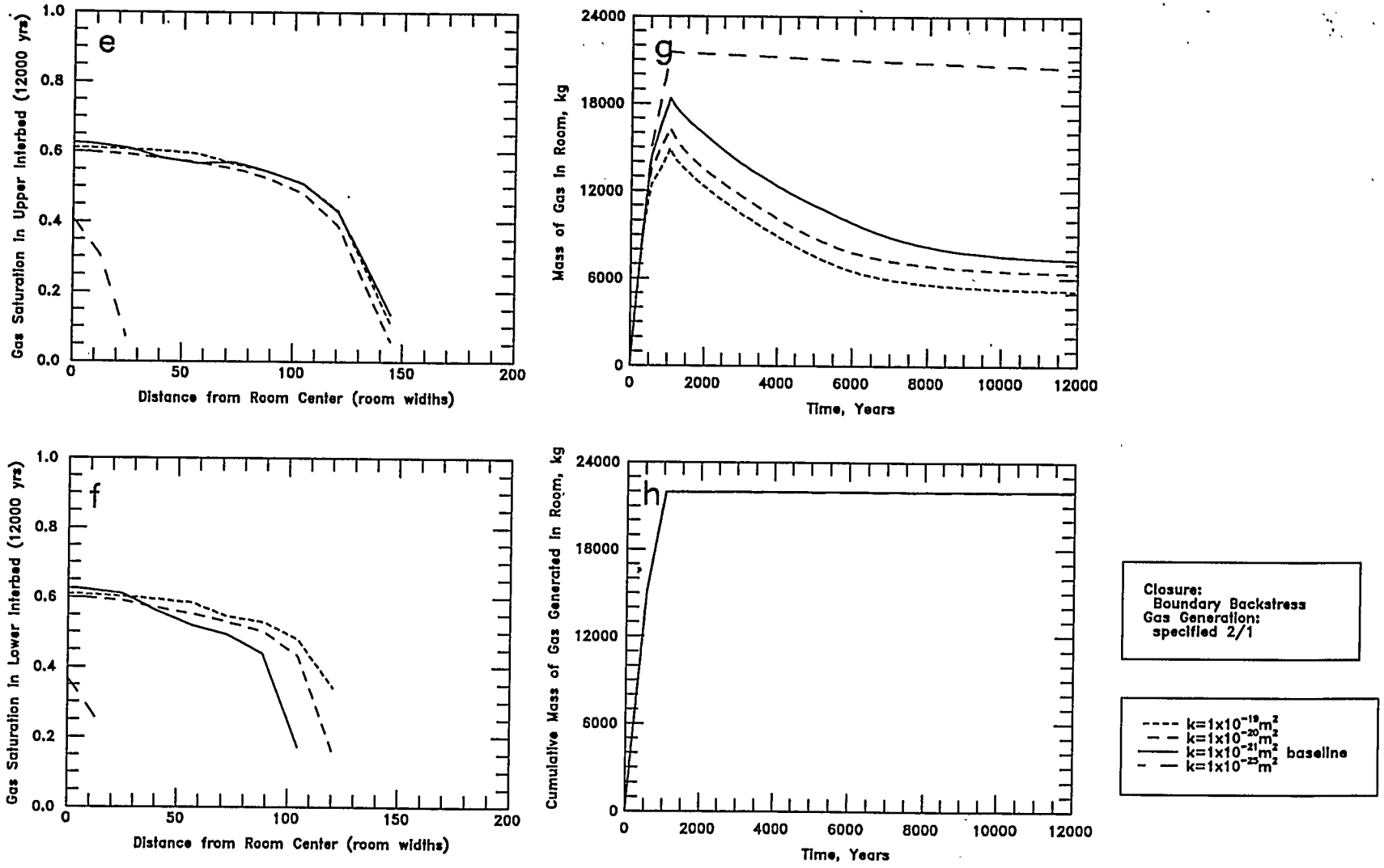

Figure B-6 (e-h). Sensitivity to Halite Intrinsic Permeability (constant threshold pressure): e - Upper Interbed Gas Profile; f - Lower Interbed Gas Profile; g - Room Gas Mass; h - Gas Generation

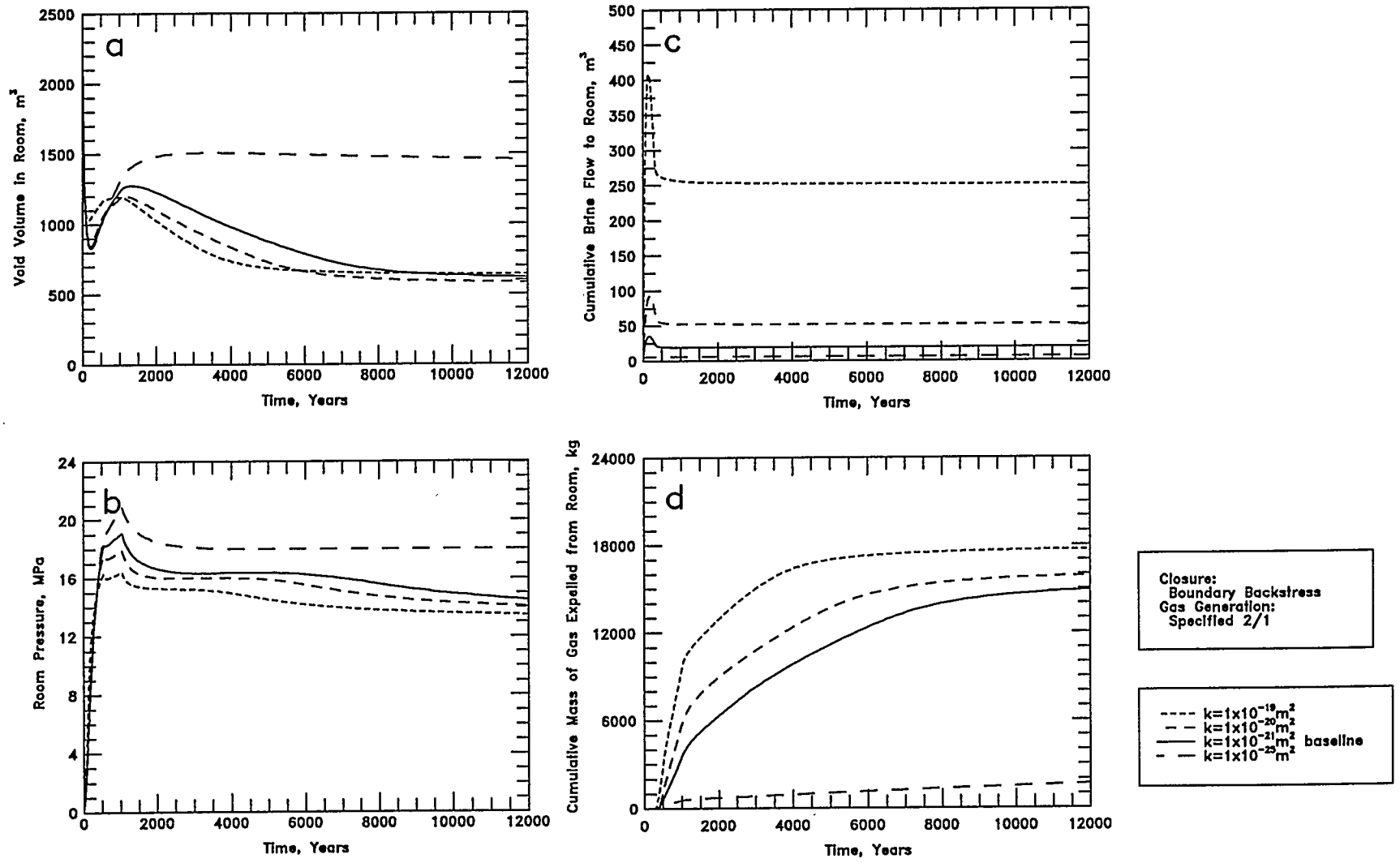

Figure B-7 (a-d). Sensitivity to Halite Intrinsic Permeability (variable threshold pressure): a - Void Volume; b - Gas Pressure; c - Brine Flow; d - Gas Expulsion

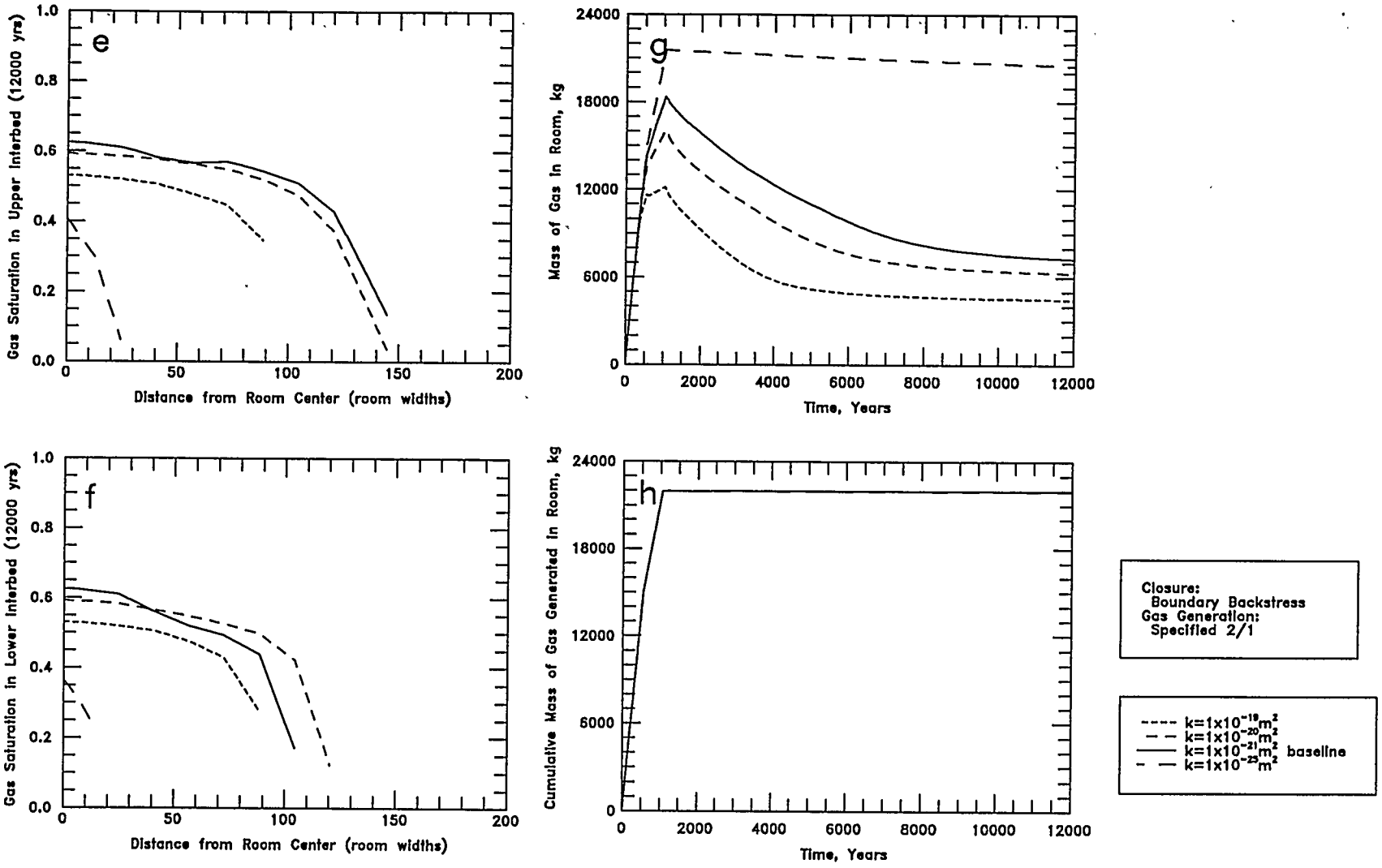

Figure B-7 (e-h). Sensitivity to Halite Intrinsic Permeability (variable threshold pressure): e - Upper Interbed Gas Profile; f - Lower Interbed Gas Profile; g - Room Gas Mass; h - Gas Generation

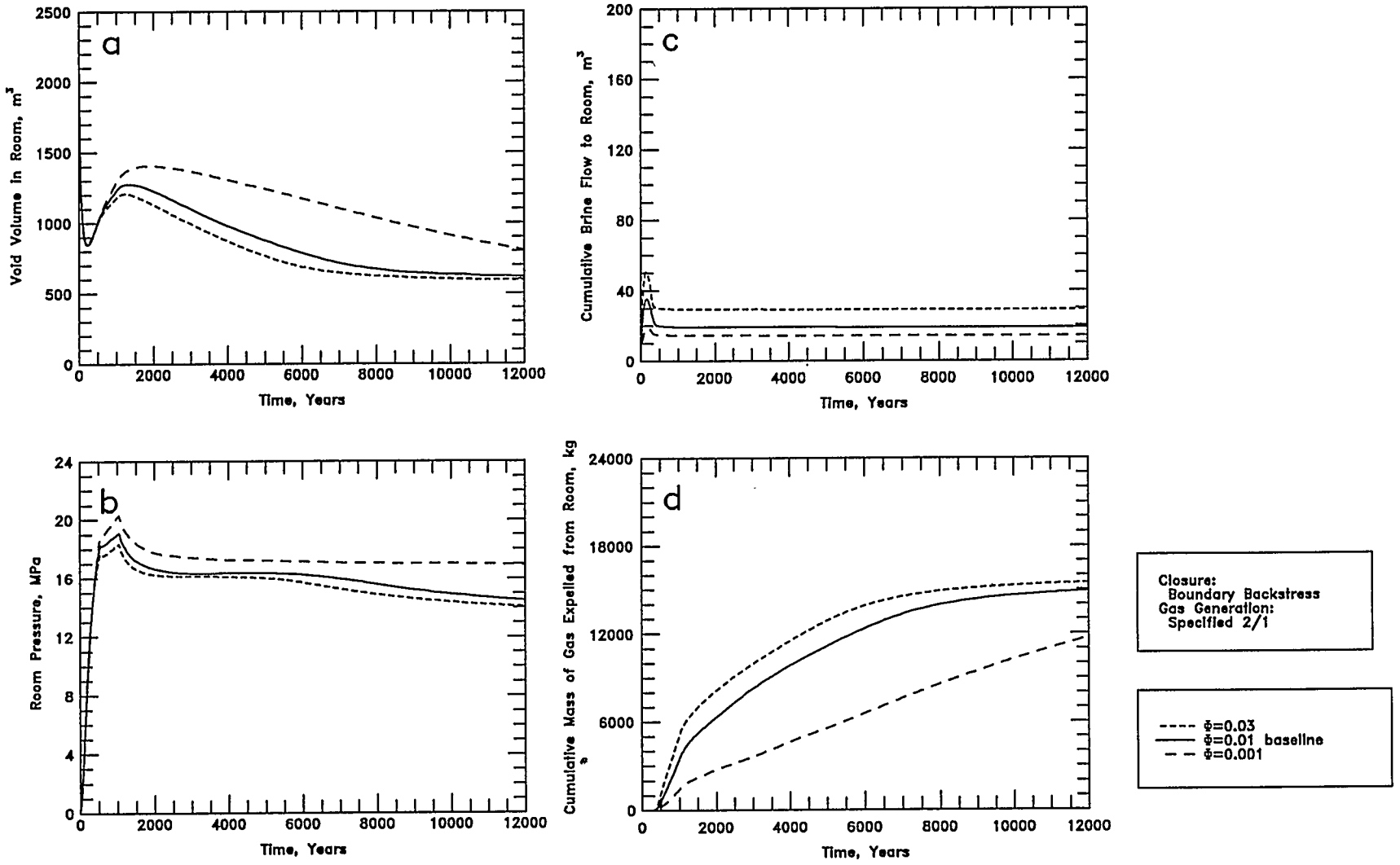

Figure B-8 (a-d). Sensitivity to Halite Porosity (constant pore volume compressibility): a - Void Volume; b - Gas Pressure; c - Brine Flow; d - Gas Expulsion

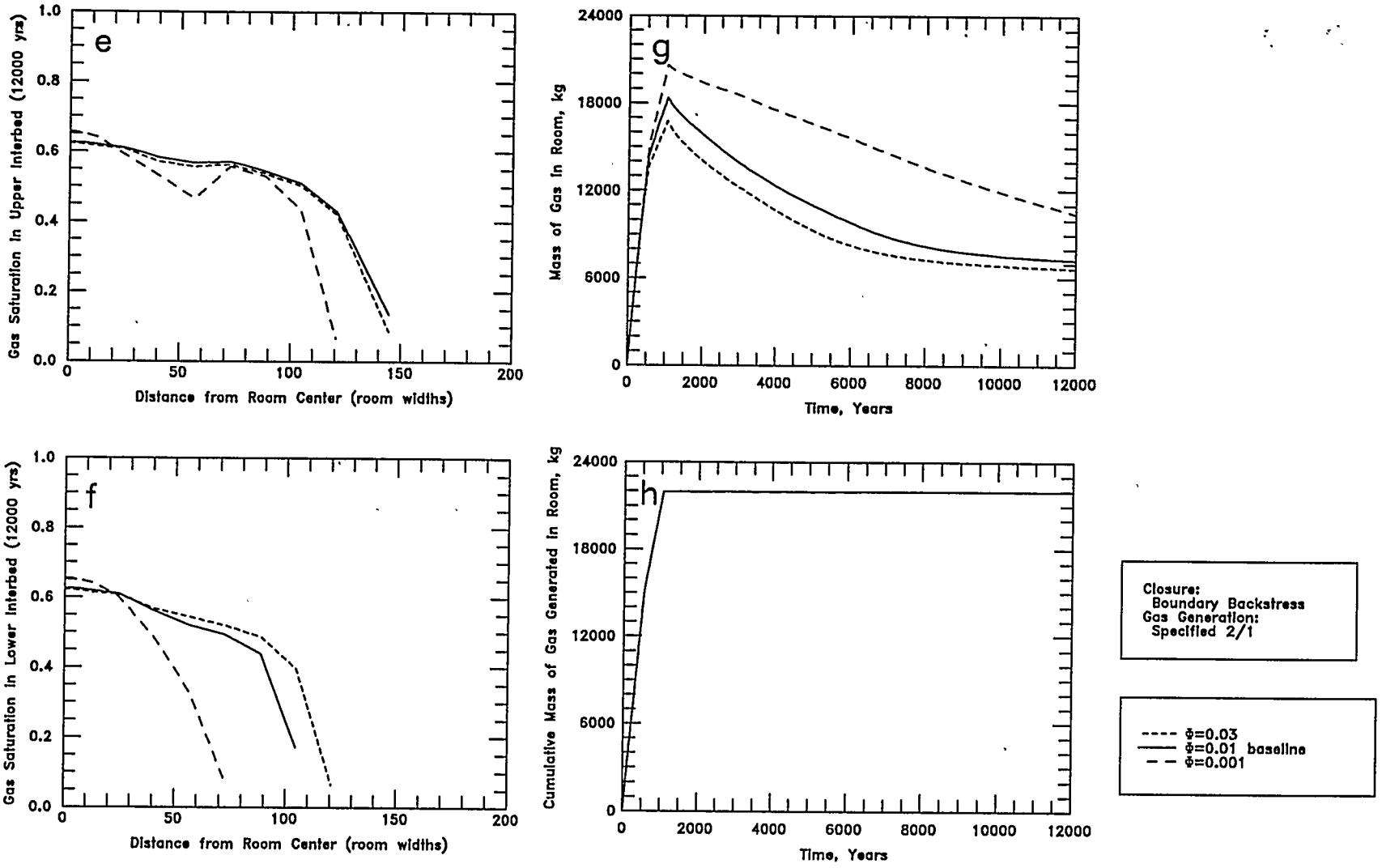

Figure B-8 (e-h). Sensitivity to Halite Porosity (constant pore volume compressibility): e - Upper Interbed Gas Profile; f - Lower Interbed Gas Profile; g - Room Gas Mass; h - Gas Generation

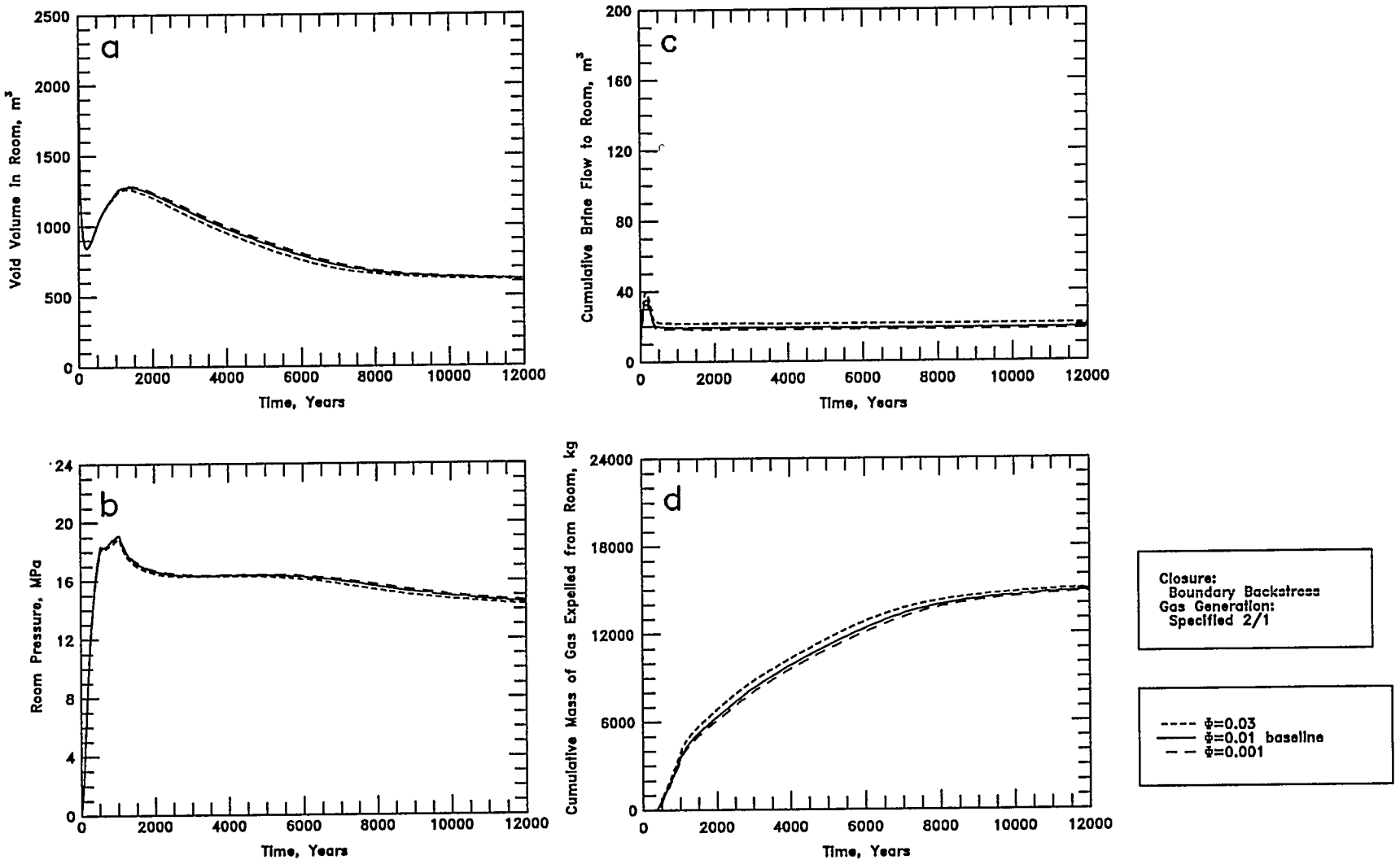

Figure B-9 (a-d). Sensitivity to Halite Porosity (constant rock compressibility): a – Void Volume; b – Gas Pressure; c – Brine Flow; d – Gas Expulsion

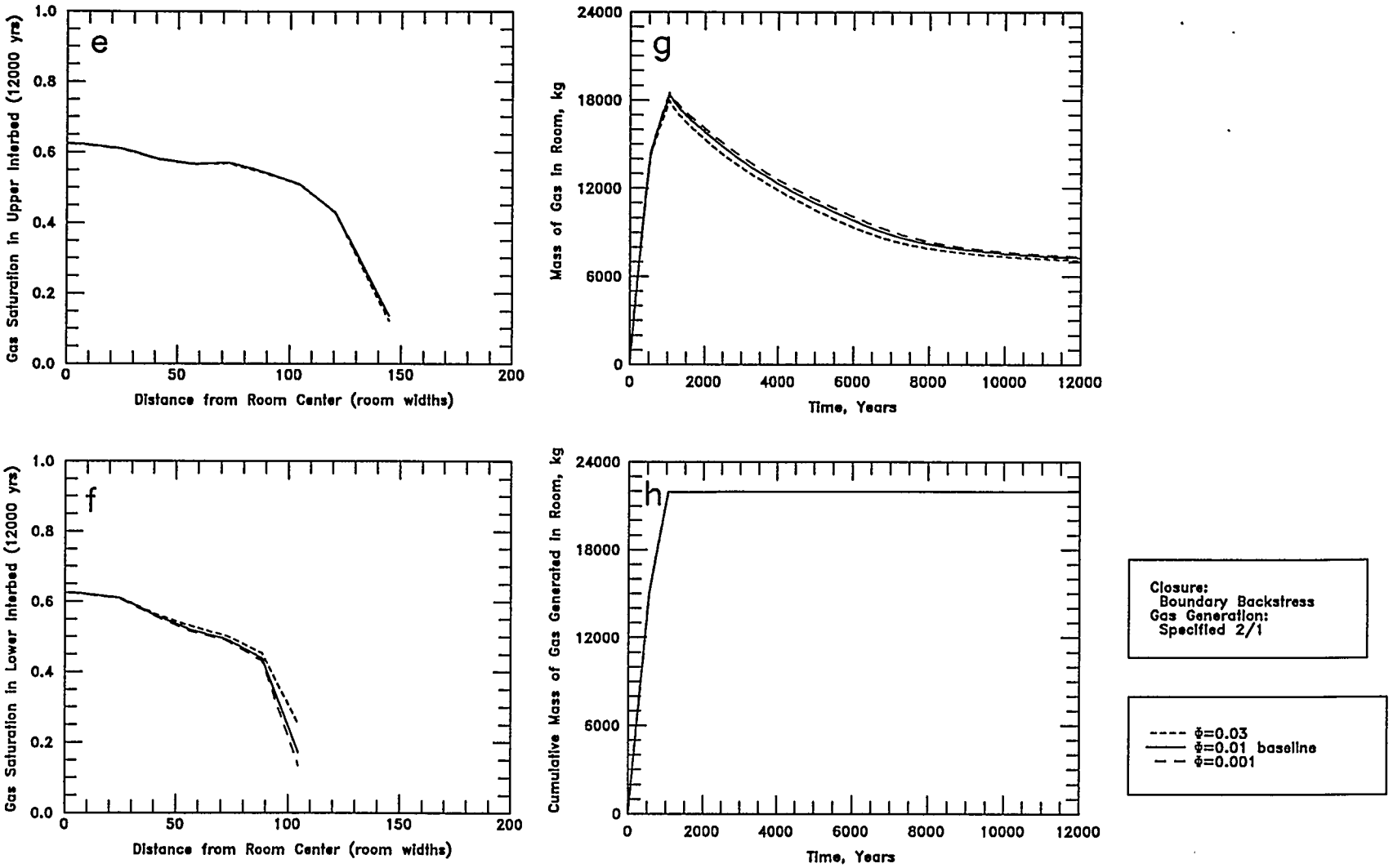

Figure B-9 (e-h). Sensitivity to Halite Porosity (constant rock compressibility): e - Upper Interbed Gas Profile; f - Lower Interbed Gas Profile; g - Room Gas Mass; h - Gas Generation

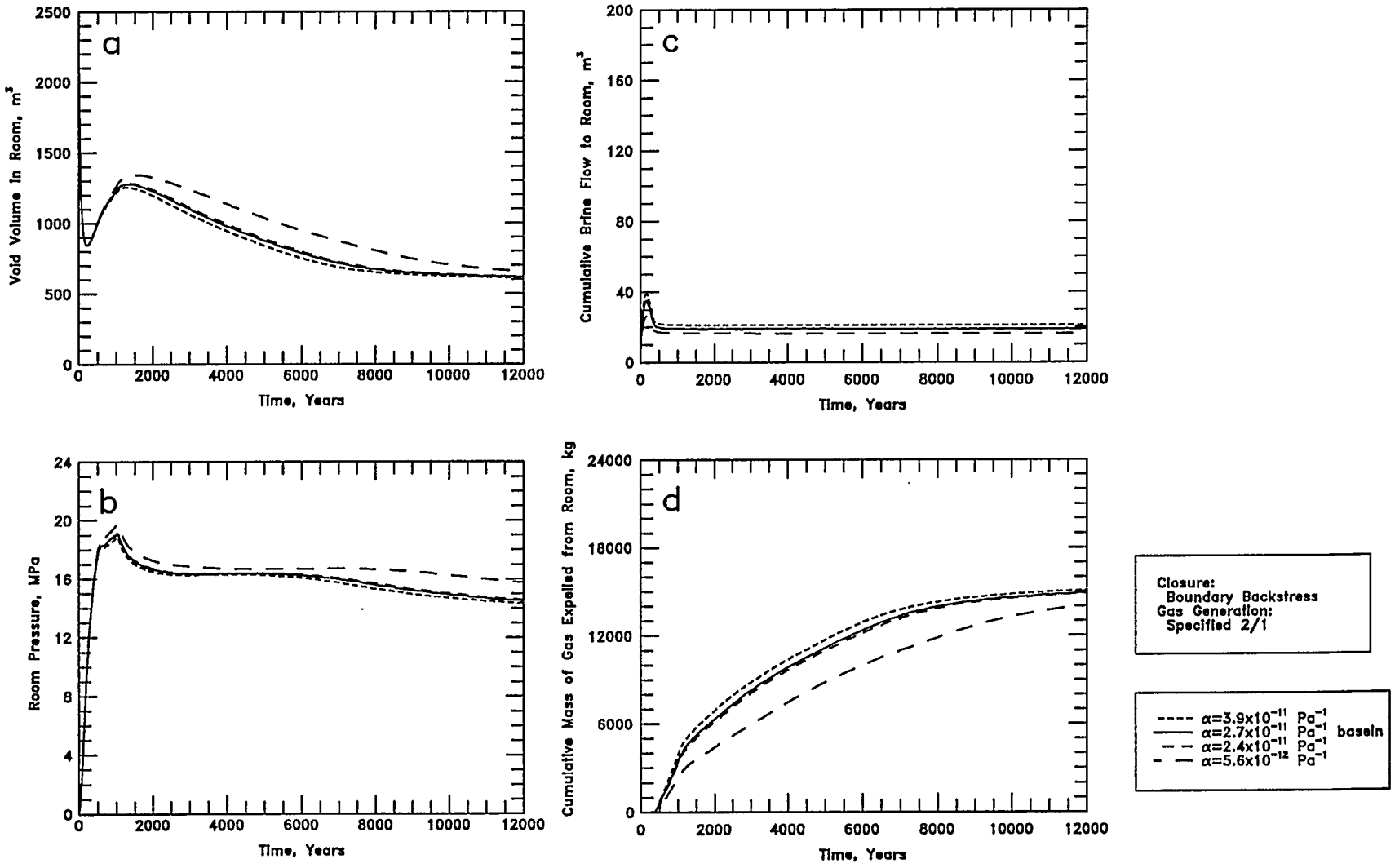

Figure B-10 (a-d). Sensitivity to Halite Rock Compressibility:
a - Void Volume; b - Gas Pressure; c - Brine Flow; d - Gas Expulsion

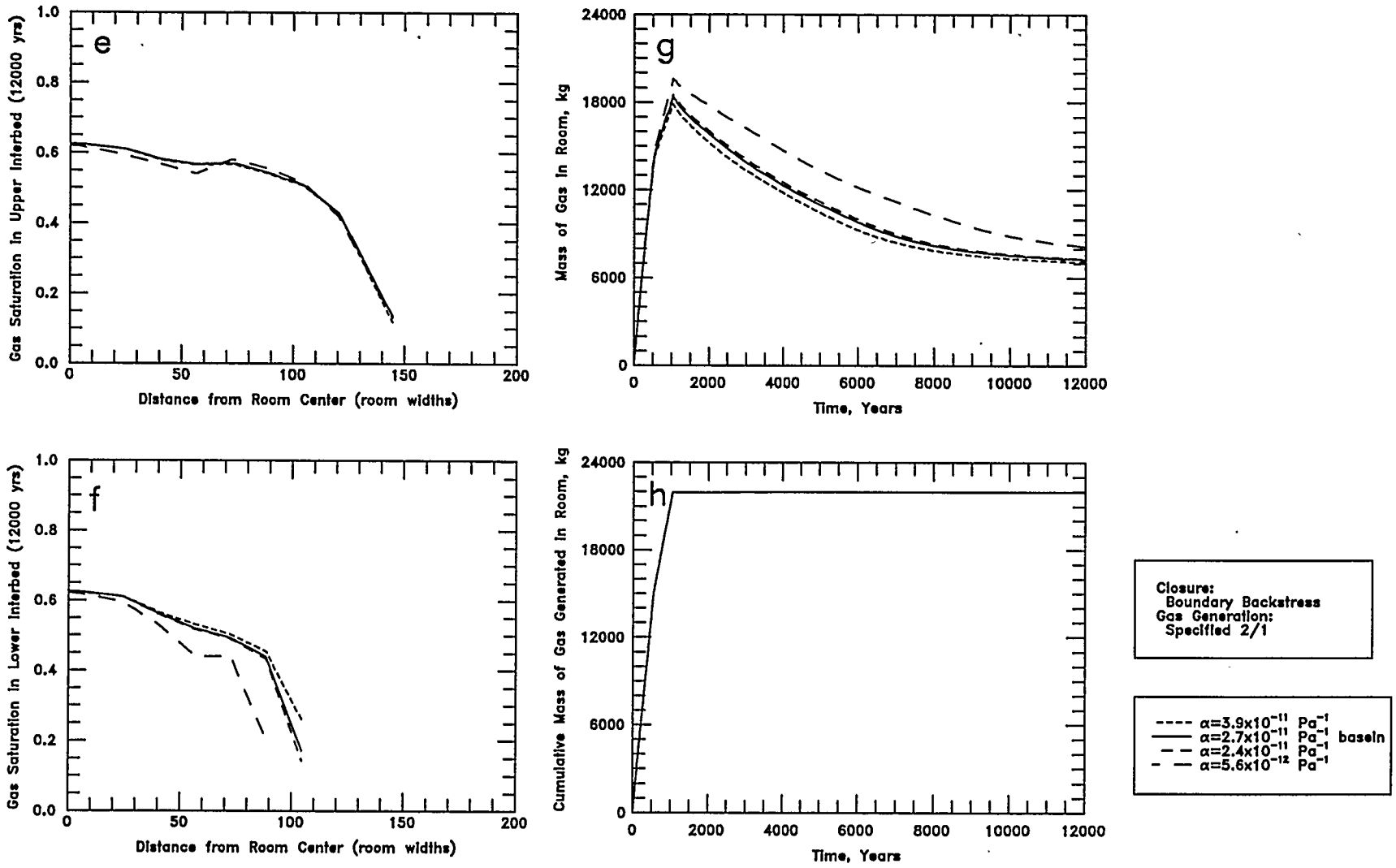

Figure B-10 (e-h). Sensitivity to Halite Rock Compressibility:
e - Upper Interbed Gas Profile; f - Lower Interbed Gas Profile;
g - Room Gas Mass; h - Gas Generation

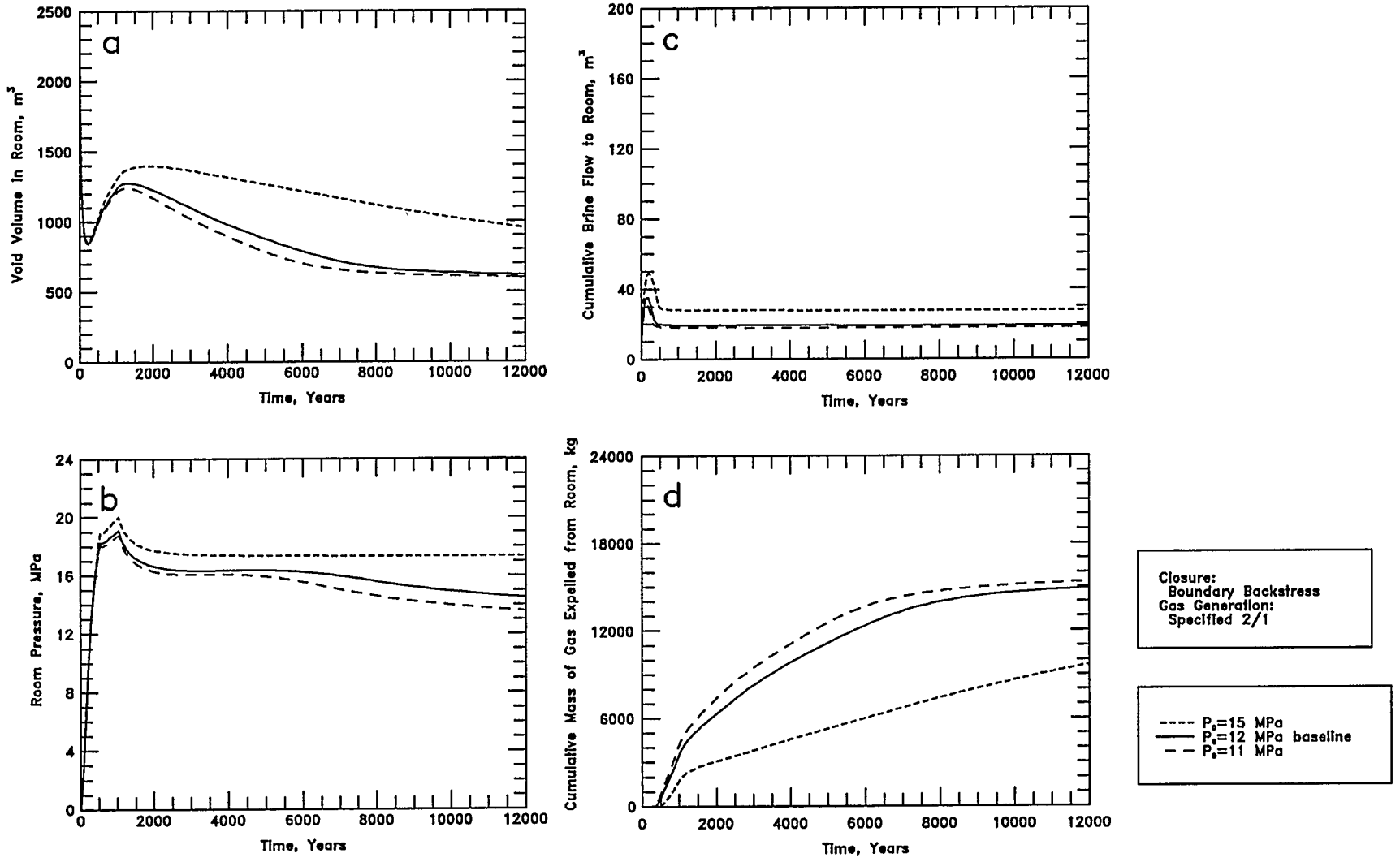

Figure B–11 (a–d). Sensitivity to Initial Salado Formation Pressure:
a – Void Volume; b – Gas Pressure; c – Brine Flow; d – Gas Expulsion

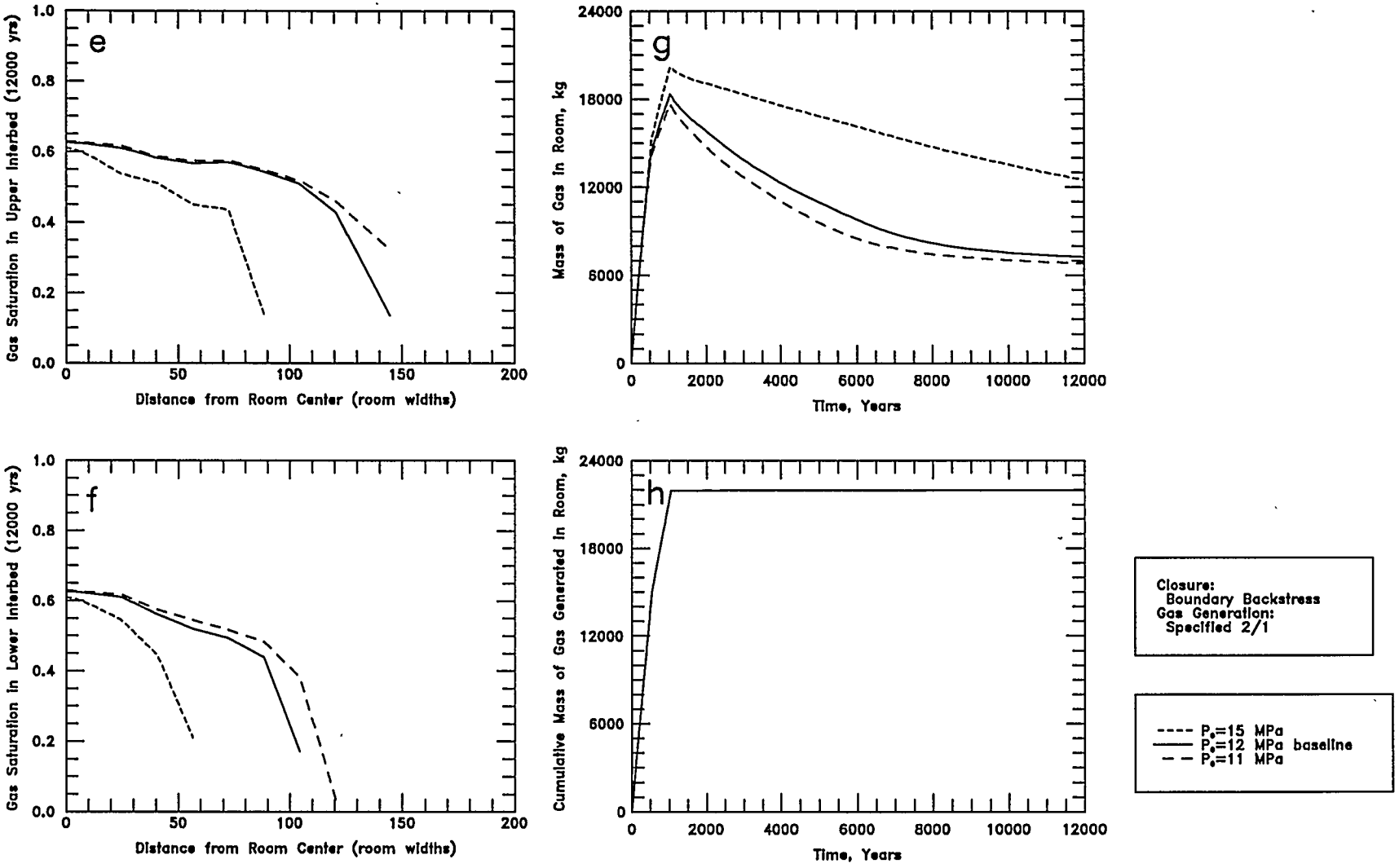

Figure B-11 (e-h). Sensitivity to Initial Salado Formation Pressure:
e - Upper Interbed Gas Profile; f - Lower Interbed Gas Profile;
g - Room Gas Mass; h - Gas Generation

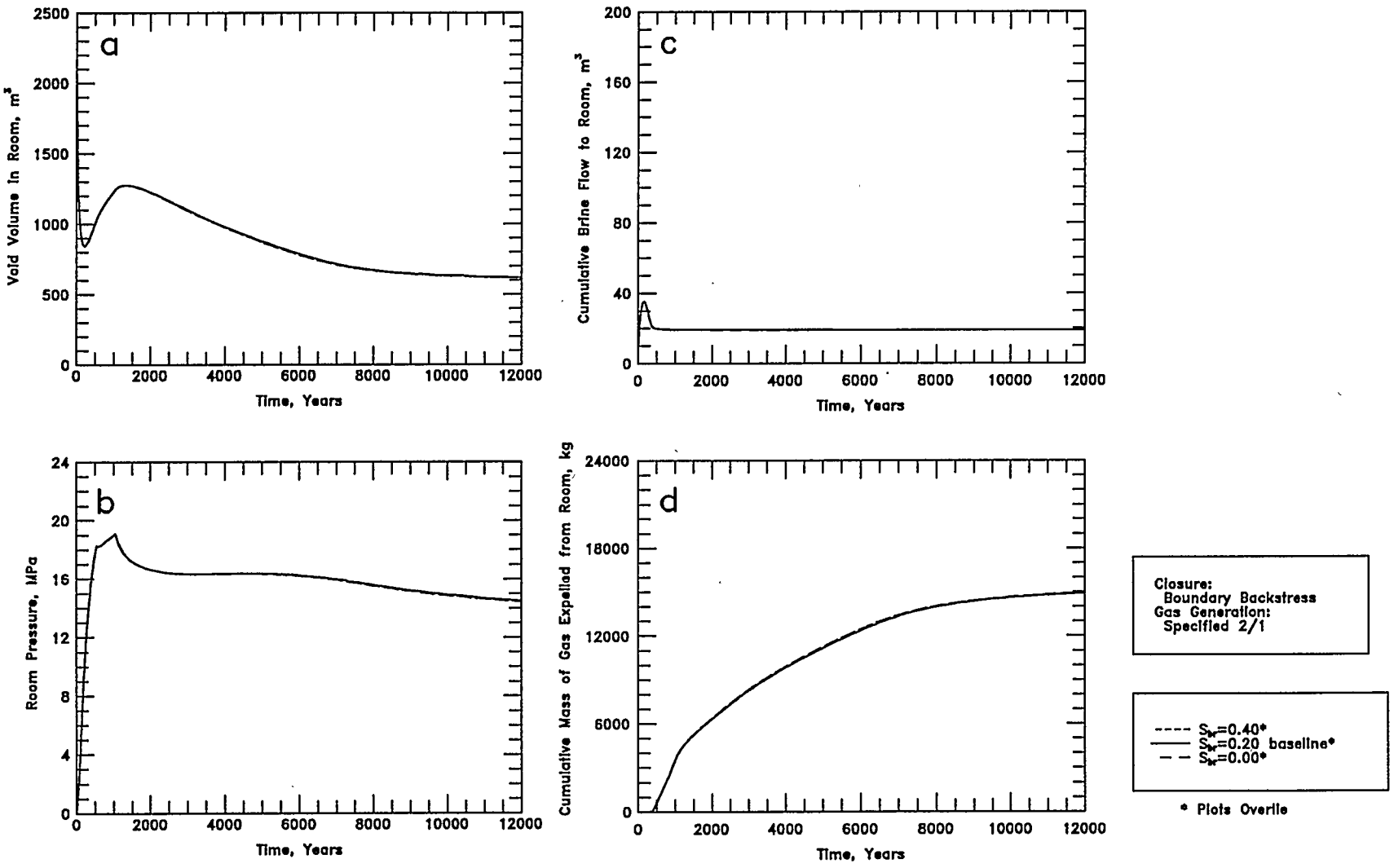

Figure B-12 (a-d). Sensitivity to Halite Residual Brine Saturation:
a - Void Volume; b - Gas Pressure; c - Brine Flow; d - Gas Expulsion

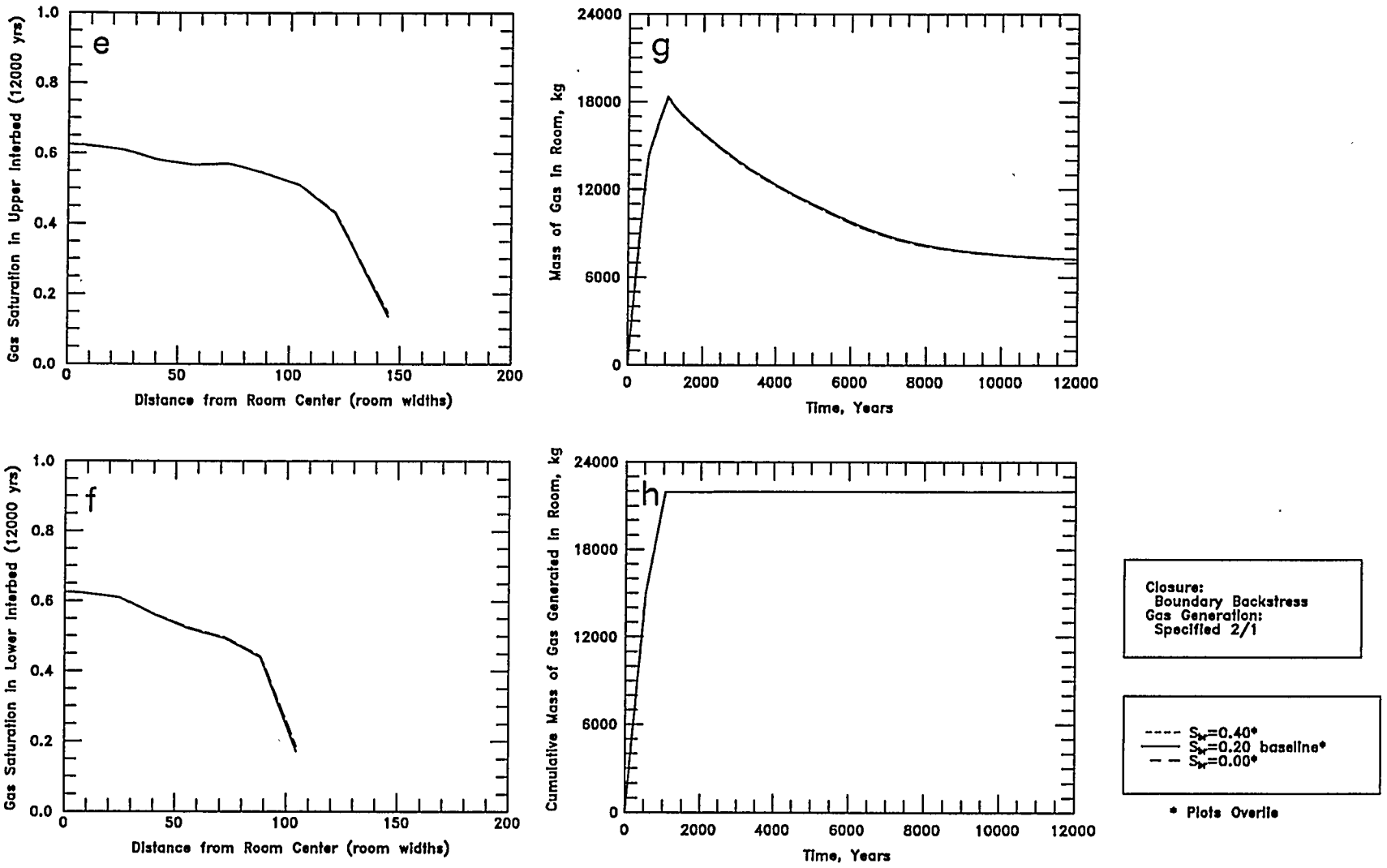

Figure B-12 (e-h). Sensitivity to Halite Residual Brine Saturation:
e - Upper Interbed Gas Profile; f - Lower Interbed Gas Profile;
g - Room Gas Mass; h - Gas Generation

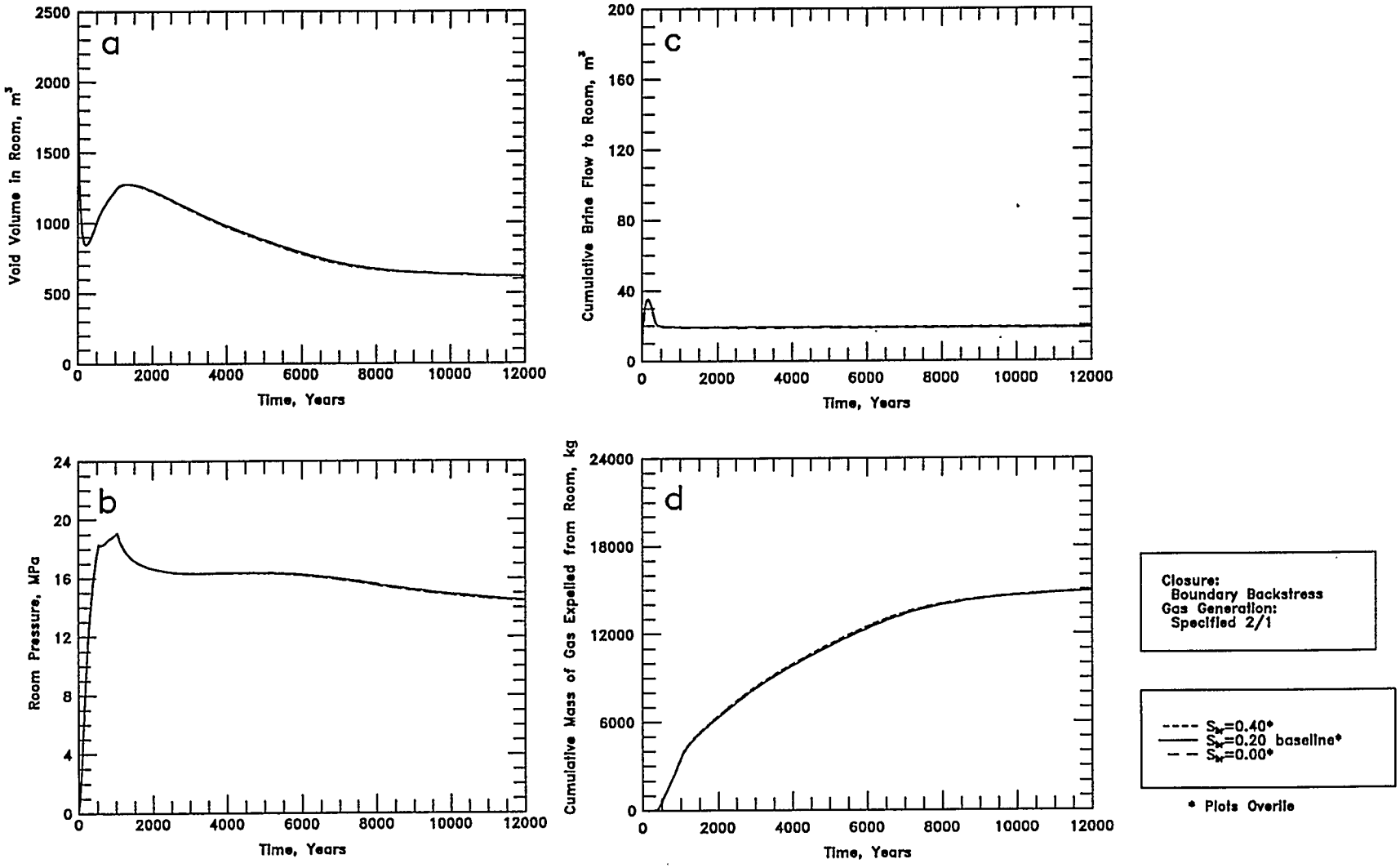

Figure B-13 (a-d). Sensitivity to Halite Residual Gas Saturation:
a - Void Volume; b - Gas Pressure; c - Brine Flow; d - Gas Expulsion

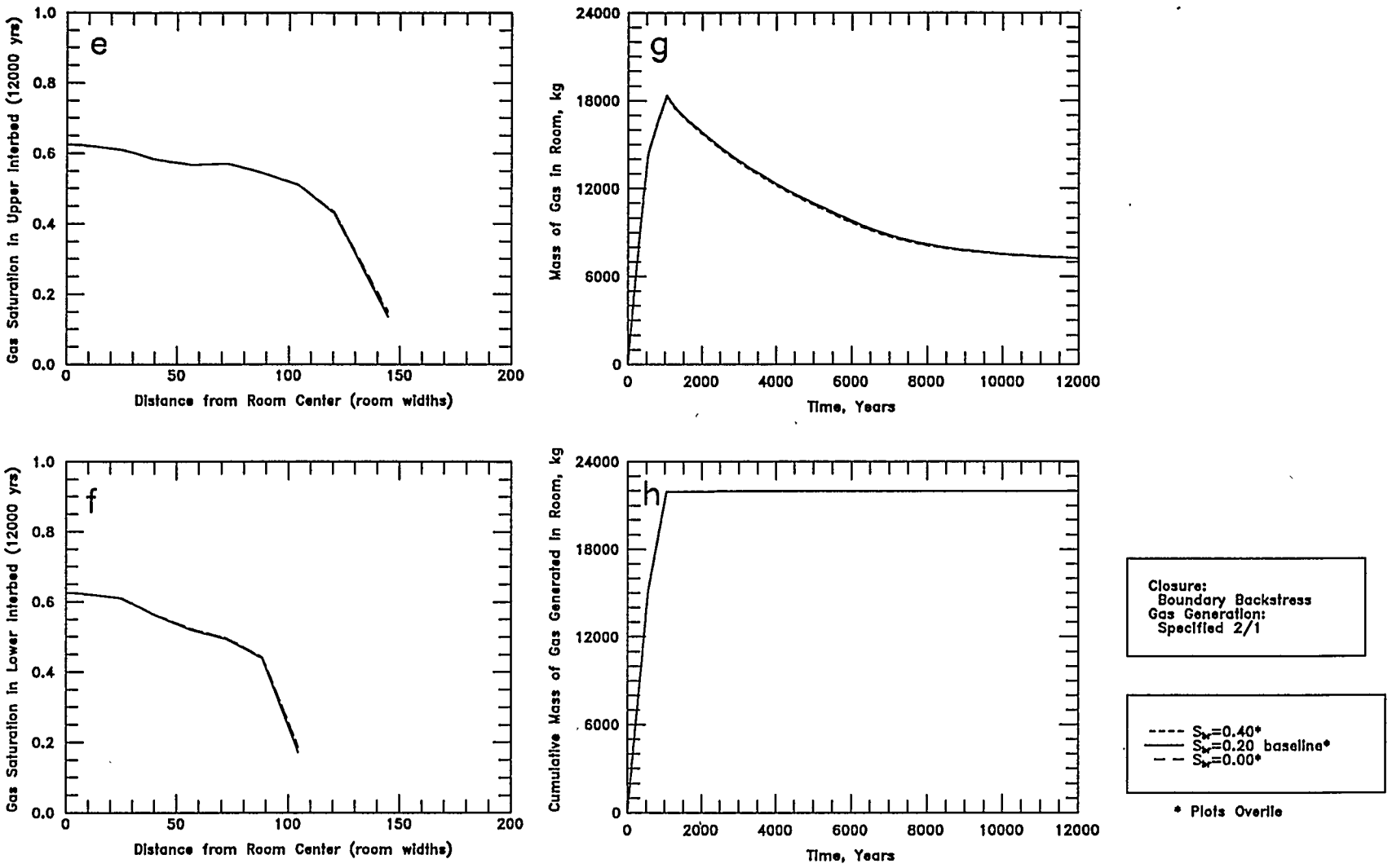

Figure B-13 (e-h). Sensitivity to Halite Residual Gas Saturation:
e - Upper Interbed Gas Profile; f - Lower Interbed Gas Profile;
g - Room Gas Mass; h - Gas Generation

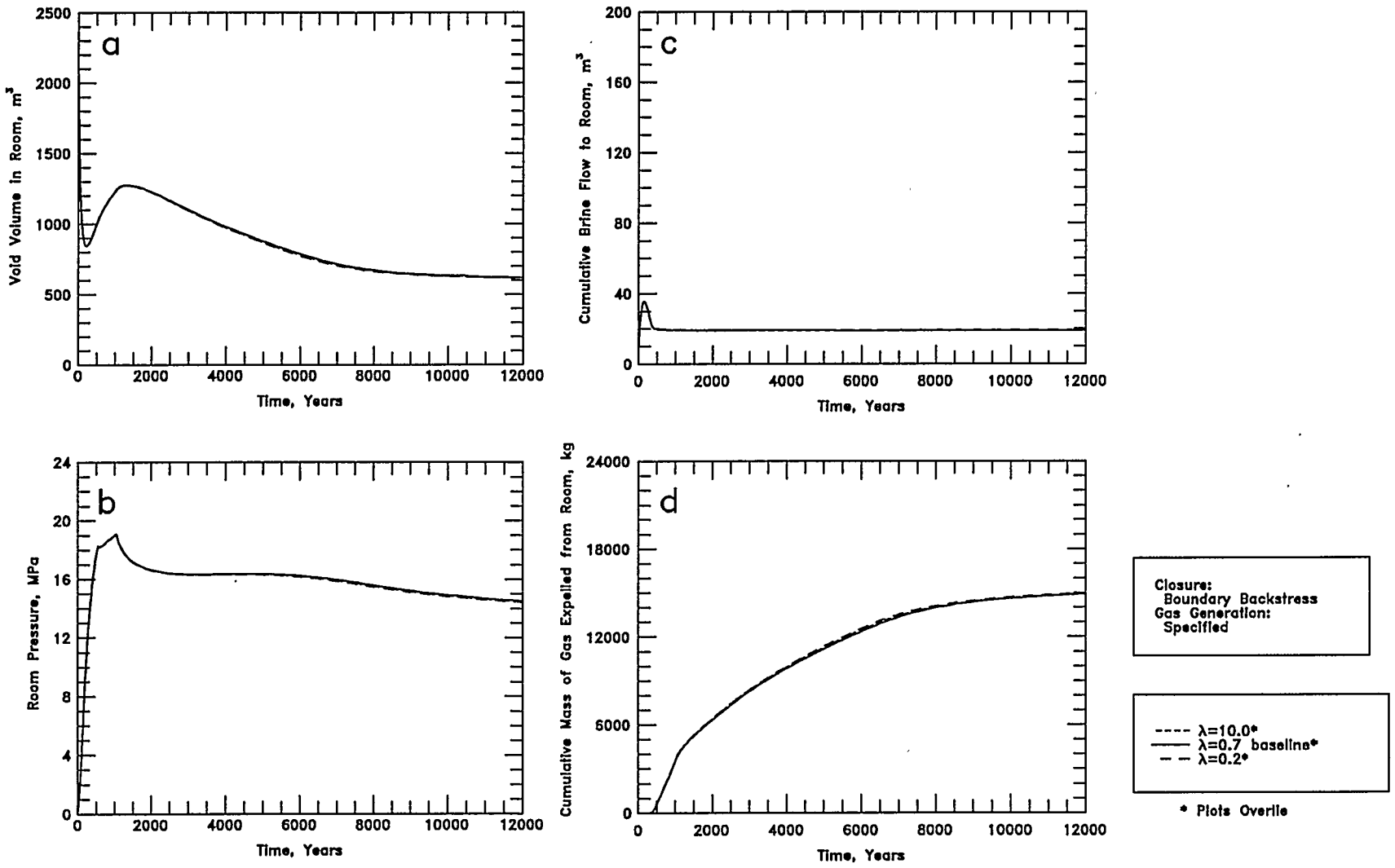

Figure B-14 (a-d). Sensitivity to Halite Pore-Size Lambda:
a - Void Volume; b - Gas Pressure; c - Brine Flow; d - Gas Expulsion

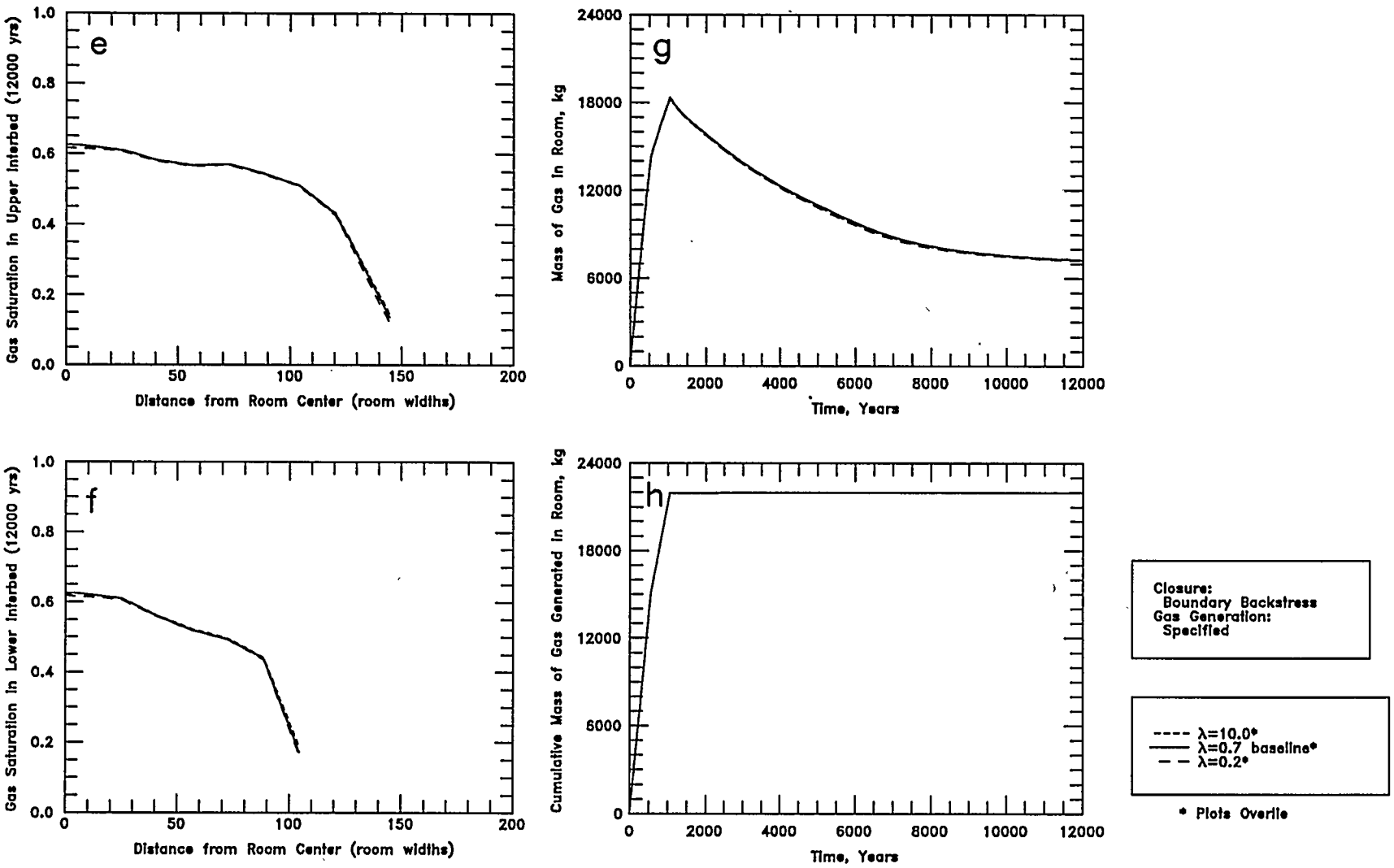

Figure B-14 (e-h). Sensitivity to Halite Pore-Size Lambda:
e - Upper Interbed Gas Profile; f - Lower Interbed Gas Profile;
g - Room Gas Mass; h - Gas Generation

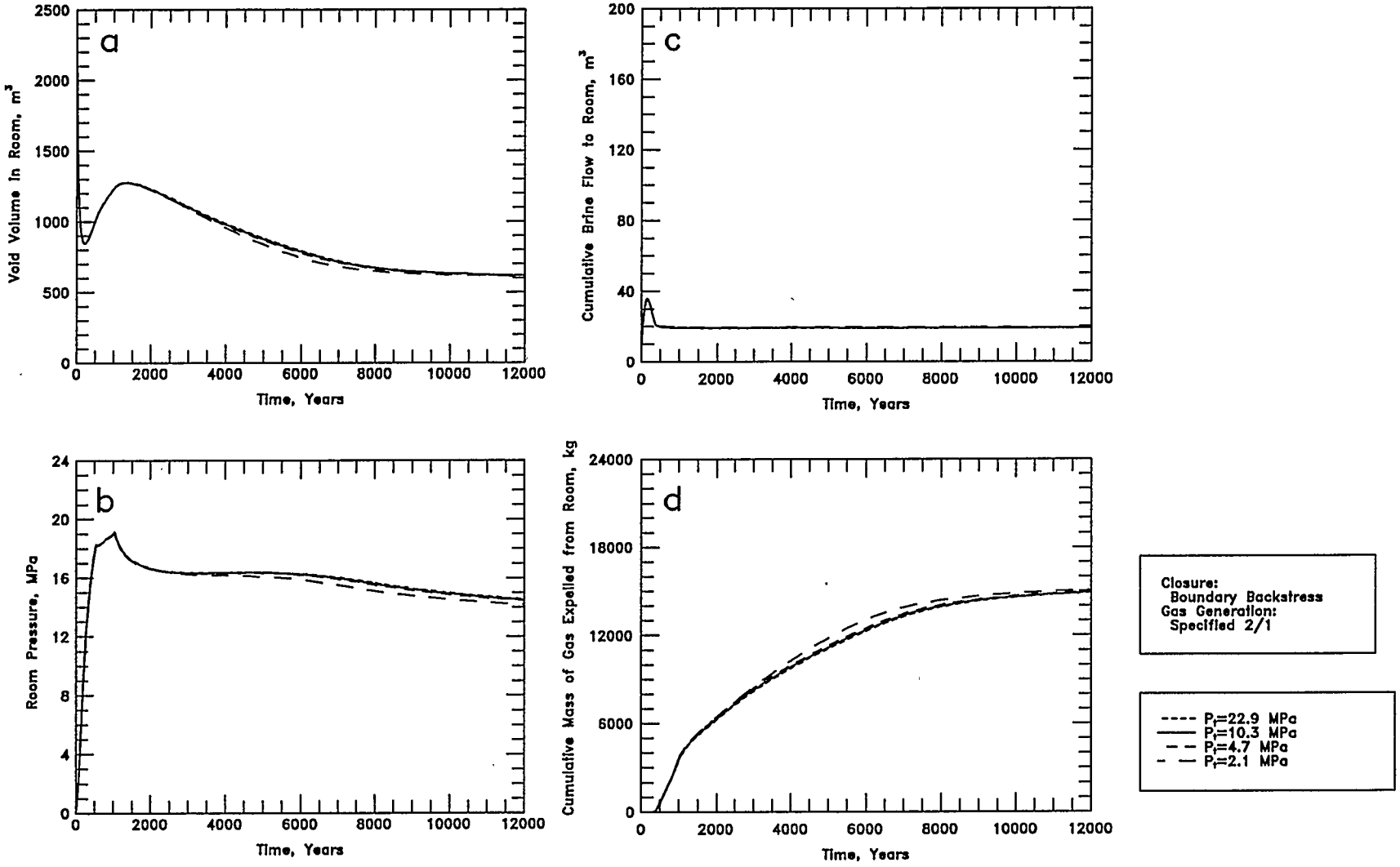

Figure B-15 (a-d). Sensitivity to Halite Threshold Pressure:
a - Void Volume; b - Gas Pressure; c - Brine Flow; d - Gas Expulsion

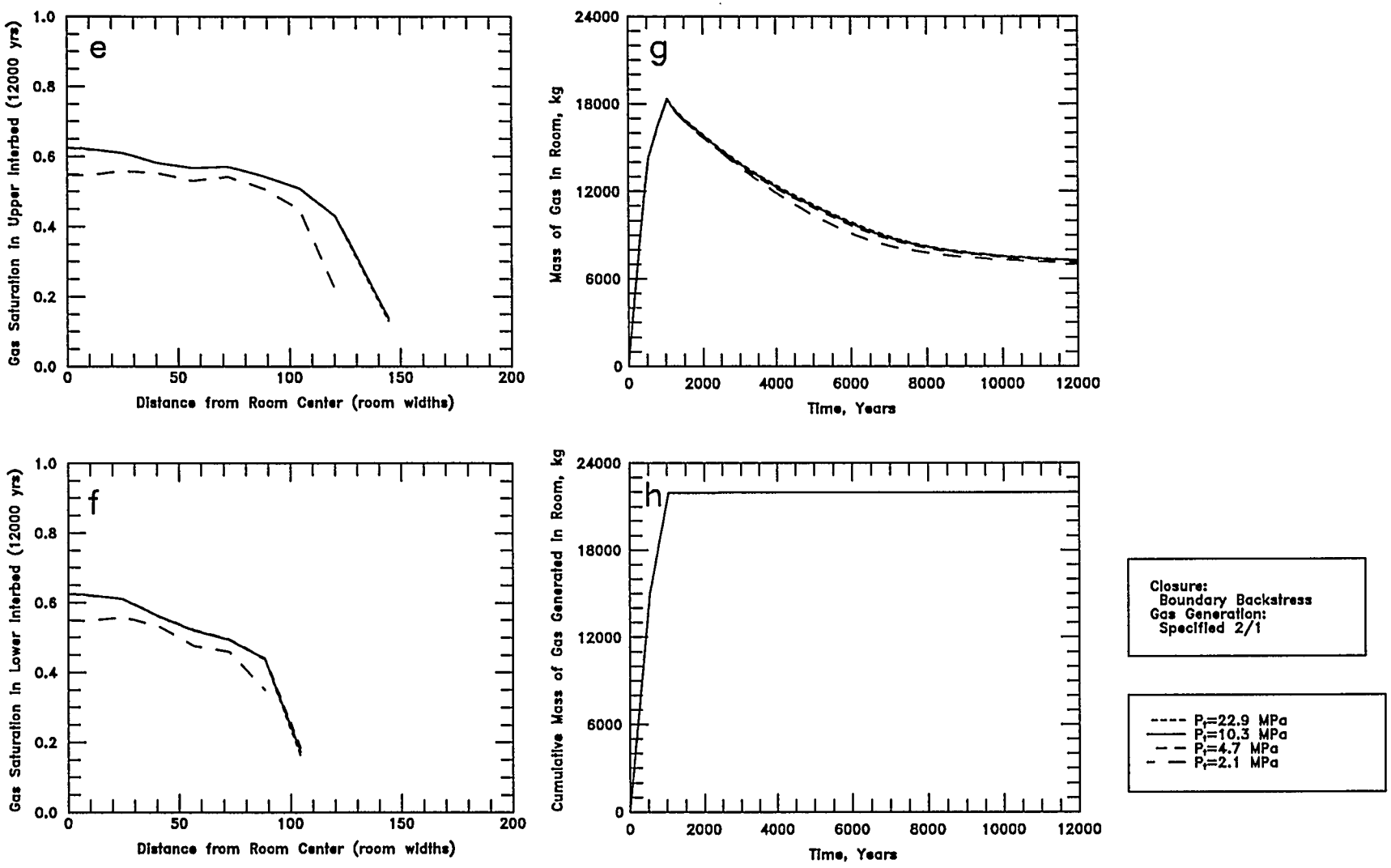

Figure B-15 (e-h). Sensitivity to Halite Threshold Pressure:
e - Upper Interbed Gas Profile; f - Lower Interbed Gas Profile;
g - Room Gas Mass; h - Gas Generation

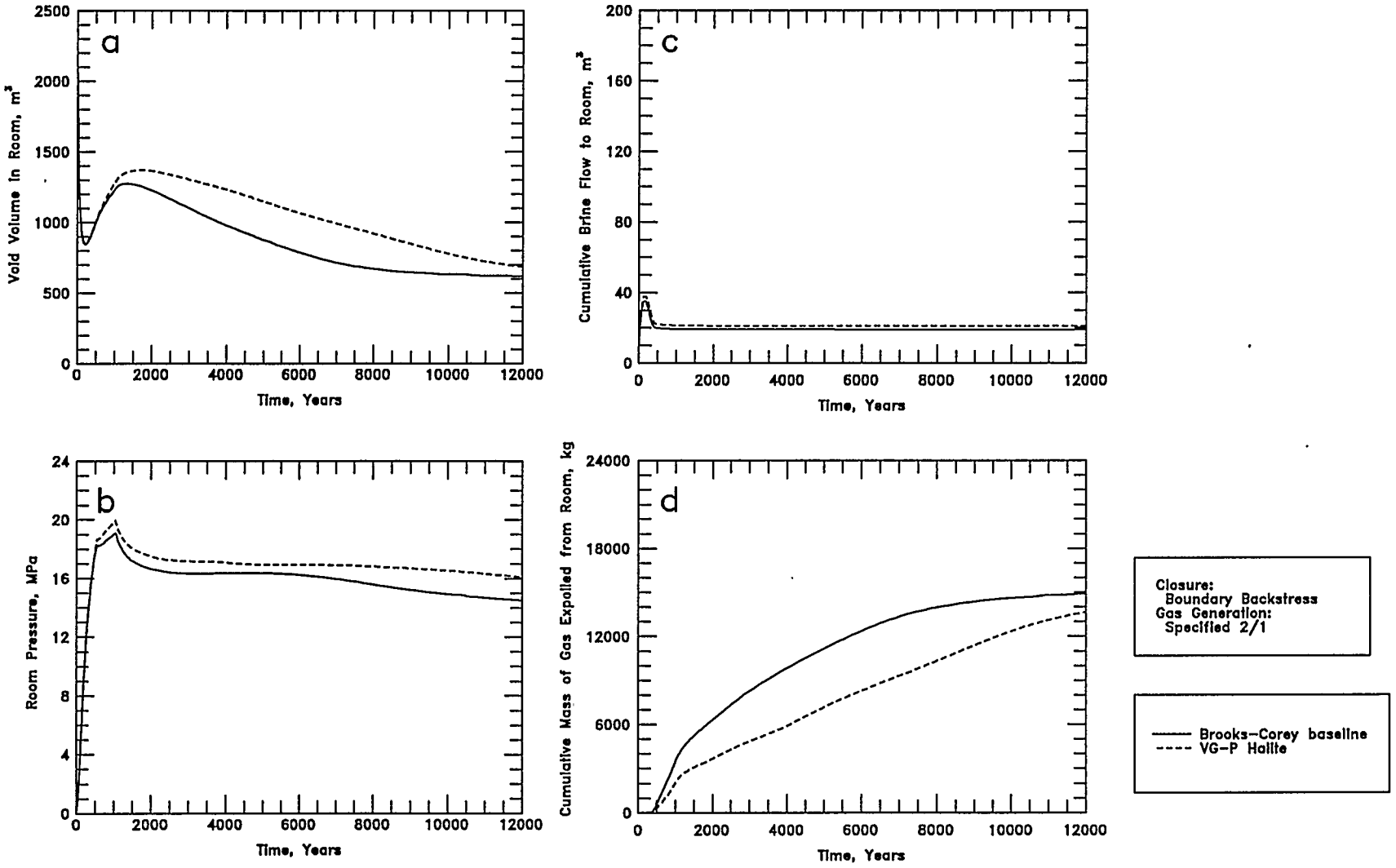

Figure B-16 (a-d). Senstitivity to Halite Two-Phase Characteristic Relationship: a - Void Volume; b - Gas Pressure; c - Brine Flow; d - Gas Expulsion

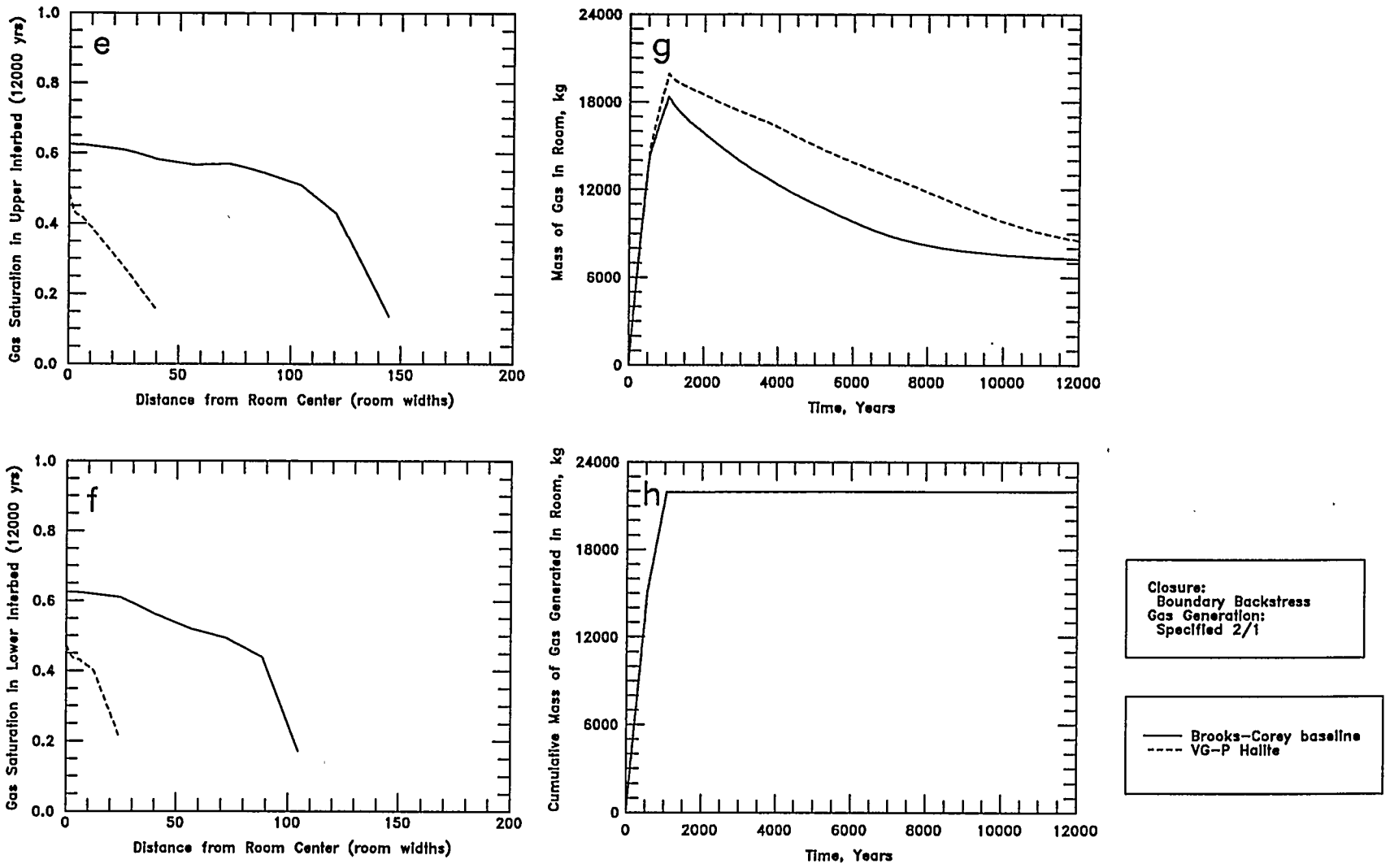

Figure B-16 (e-h). Senstitivity to Halite Two-Phase Characteristic Relationship:
e - Upper Interbed Gas Profile; f - Lower Interbed Gas Profile;
g - Room Gas Mass; h - Gas Generation

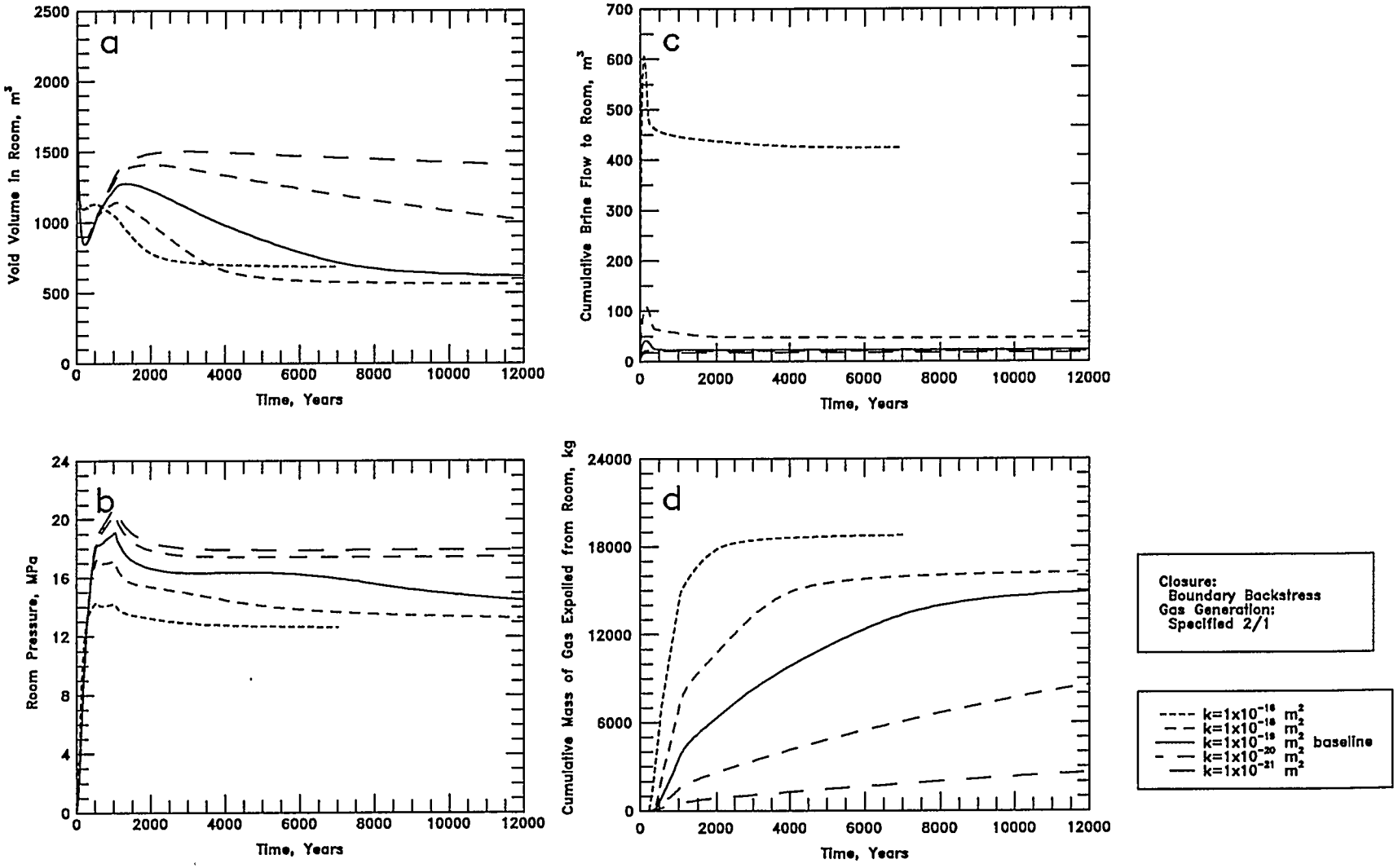

Figure B–17 (a–d). Sensitivity to Interbed Intrinsic Permeability (constant threshold pressure): a – Void Volume; b – Gas Pressure; c – Brine Flow; d – Gas Expulsion

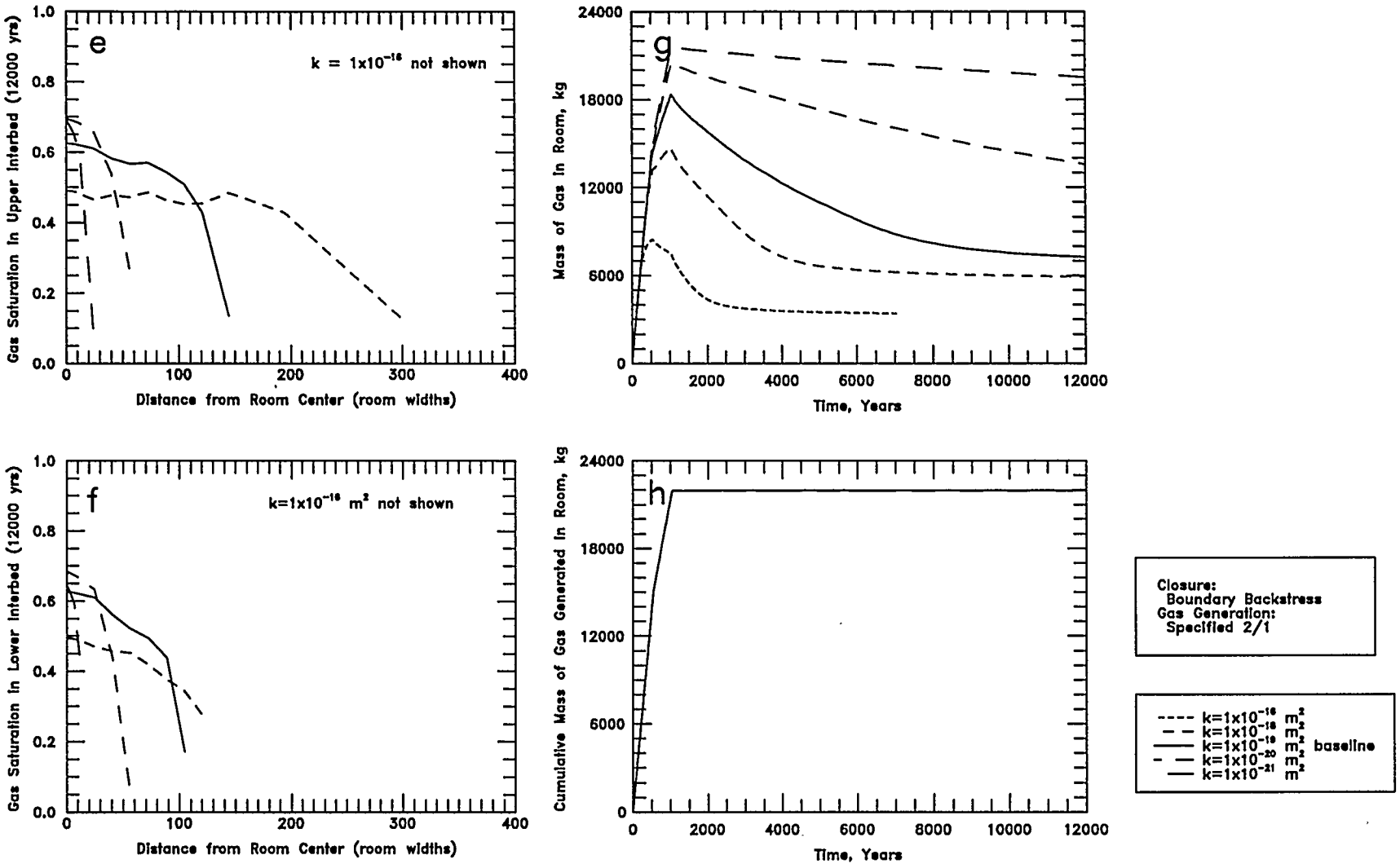

Figure B-17 (e-h). Sensitivity to Interbed Intrinsic Permeability (constant threshold pressure): e - Upper Interbed Gas Profile; f - Lower Interbed Gas Profile; g - Room Gas Mass; h - Gas Generation

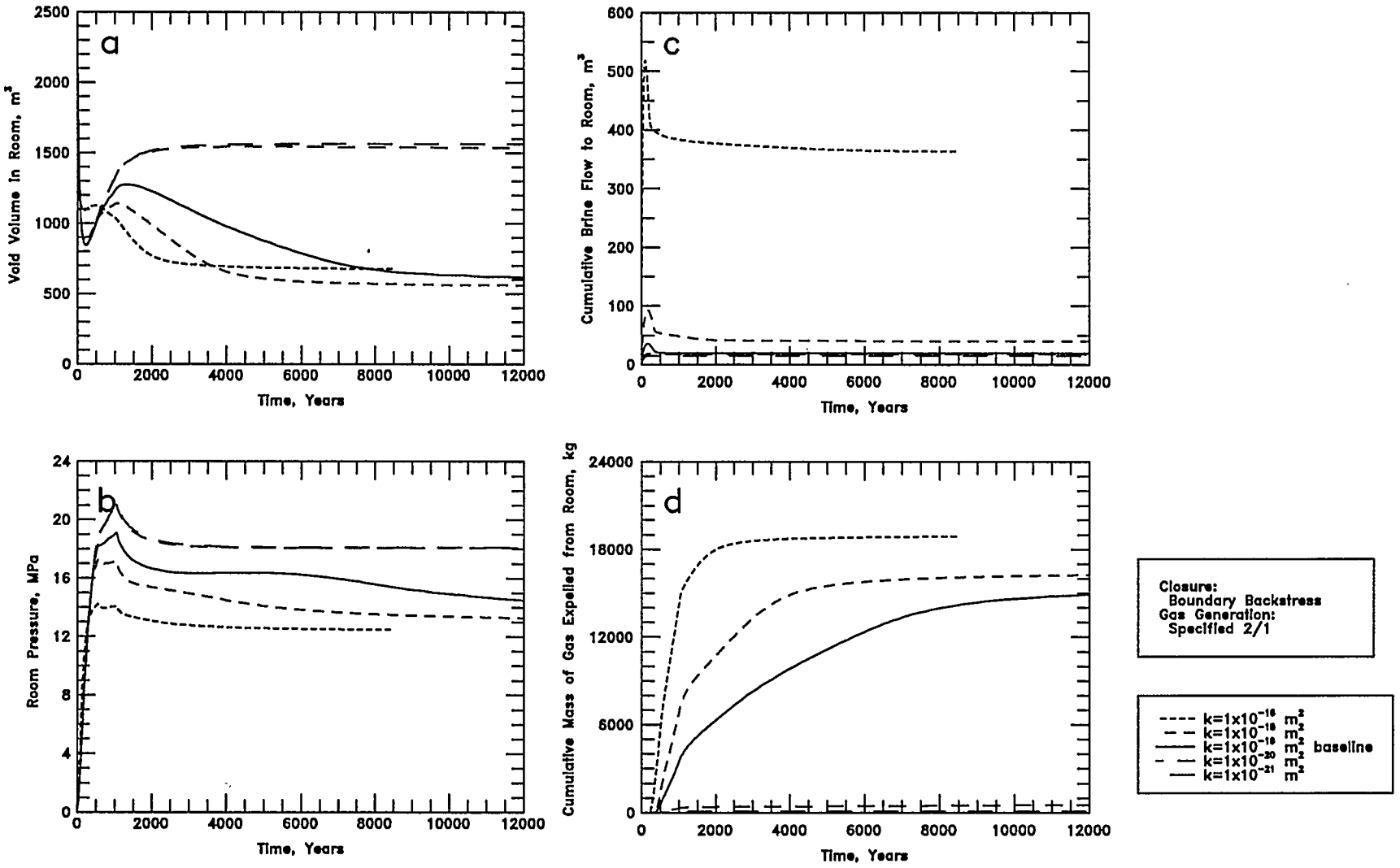

Figure B-18 (a-d). Sensitivity to Interbed Intrinsic Permeability (variable threshold pressure): a - Void Volume; b - Gas Pressure; c - Brine Flow; d - Gas Expulsion

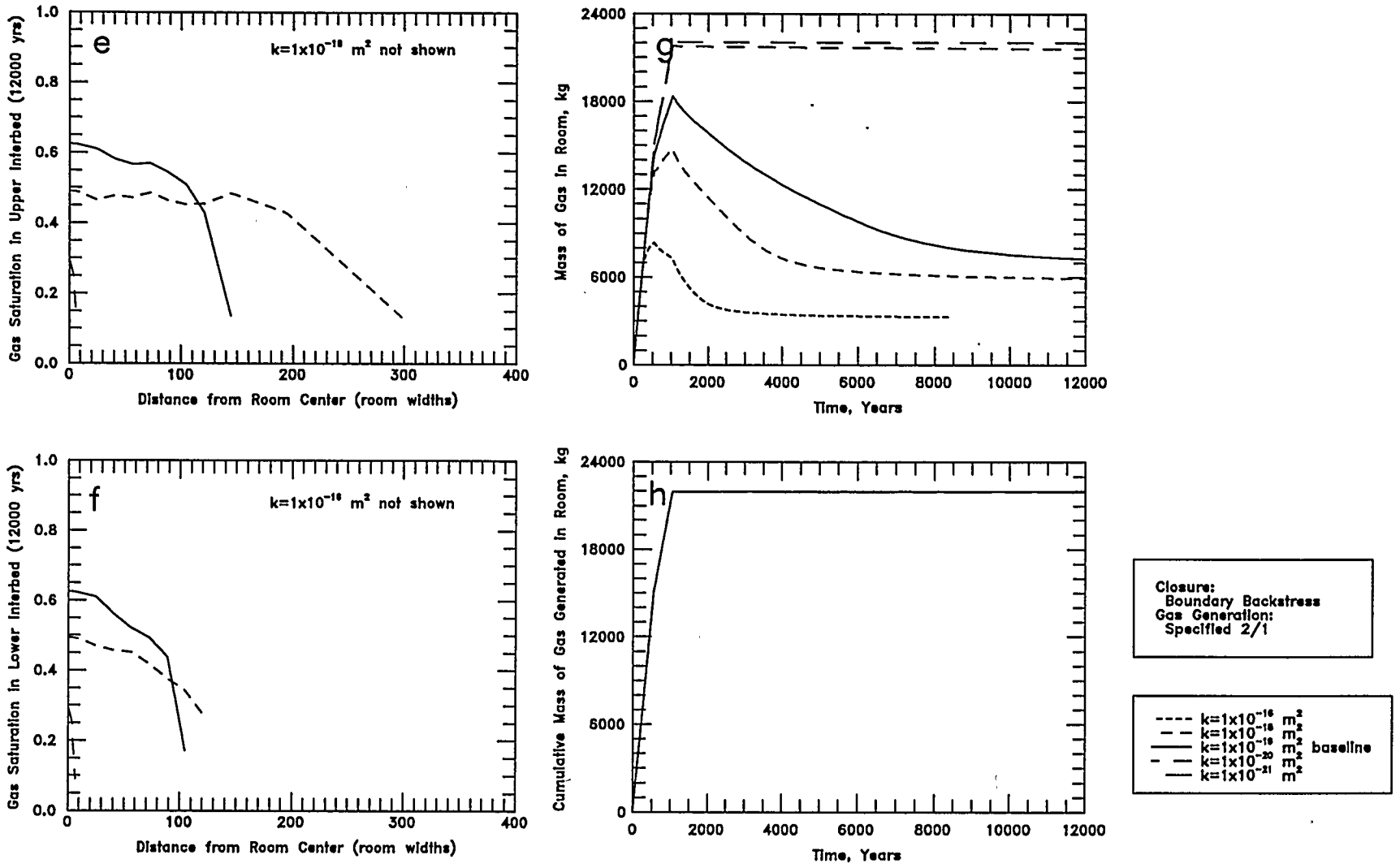

Figure B-18 (e-h). Sensitivity to Interbed Intrinsic Permeability (variable threshold pressure): e - Upper Interbed Gas Profile; f - Lower Interbed Gas Profile; g - Room Gas Mass; h - Gas Generation

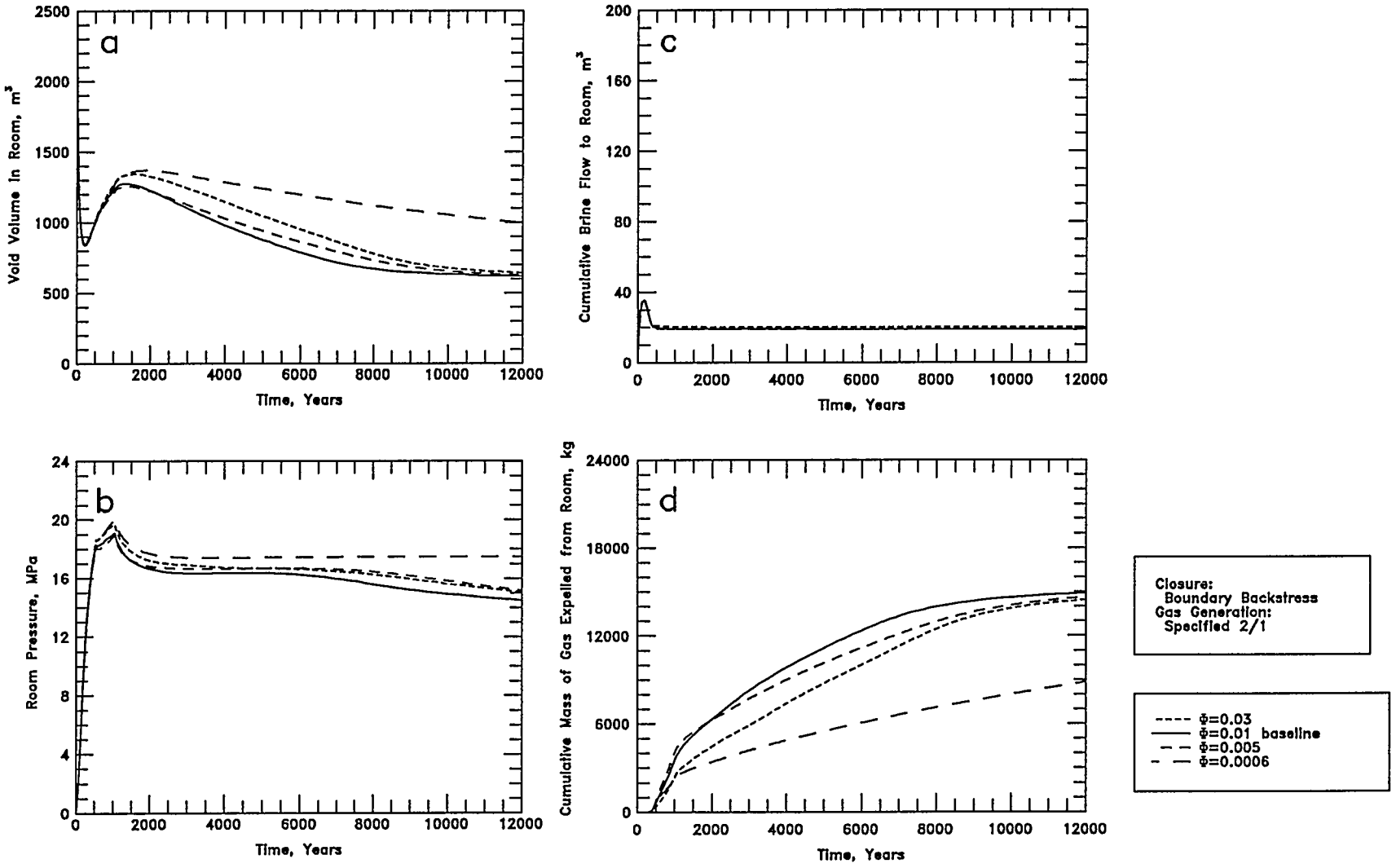

Figure B-19 (a-d). Sensitivity to Interbed Porosity (constant pore volume compressibility: a - Void Volume; b - Gas Pressure; c - Brine Flow; d - Gas Expulsion

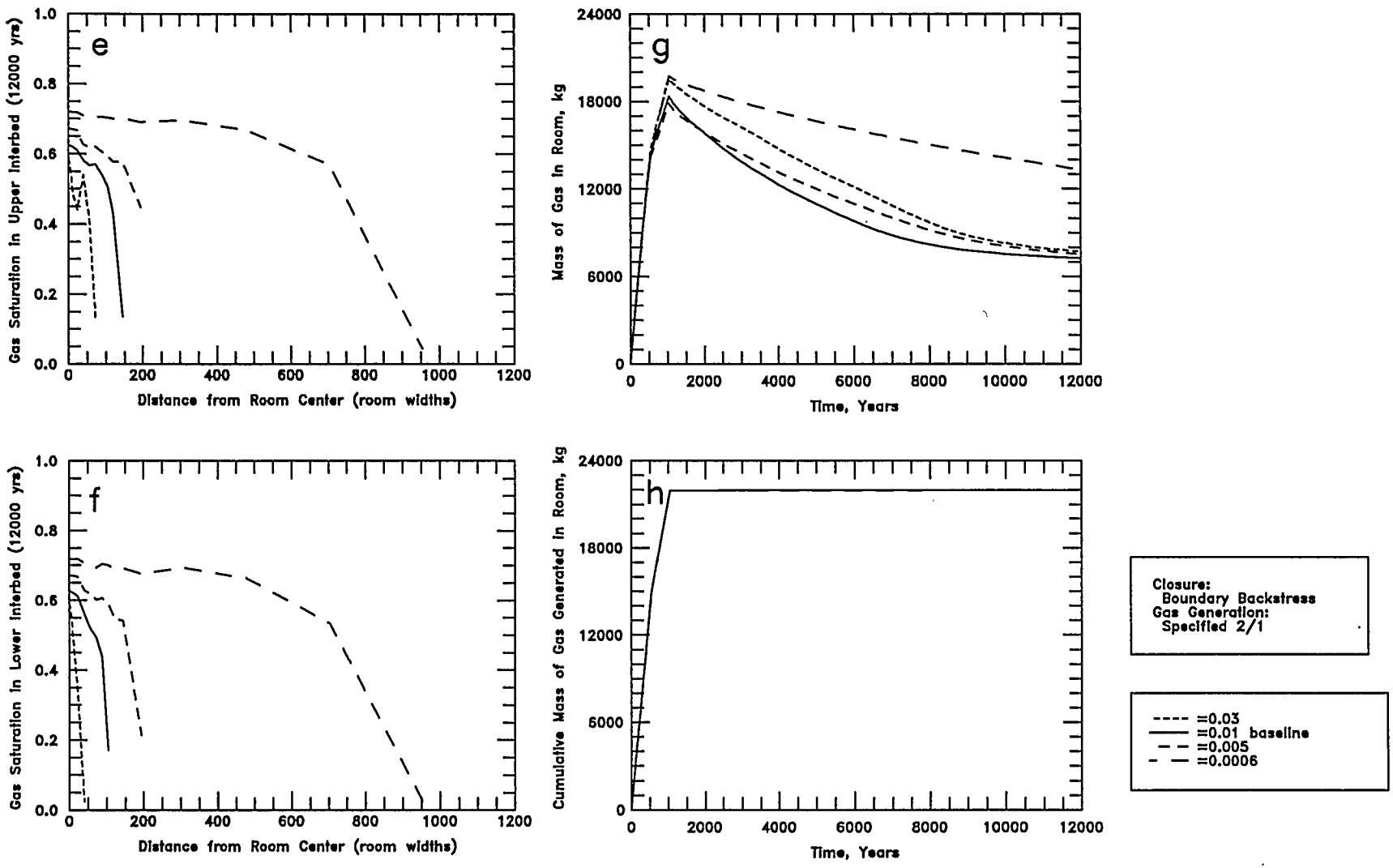

Figure B-19 (e-h). Sensitivity to Interbed Porosity (constant pore volume compressibility): e - Upper Interbed Gas Profile; f - Lower Interbed Gas Profile; g - Room Gas Mass; h - Gas Generation

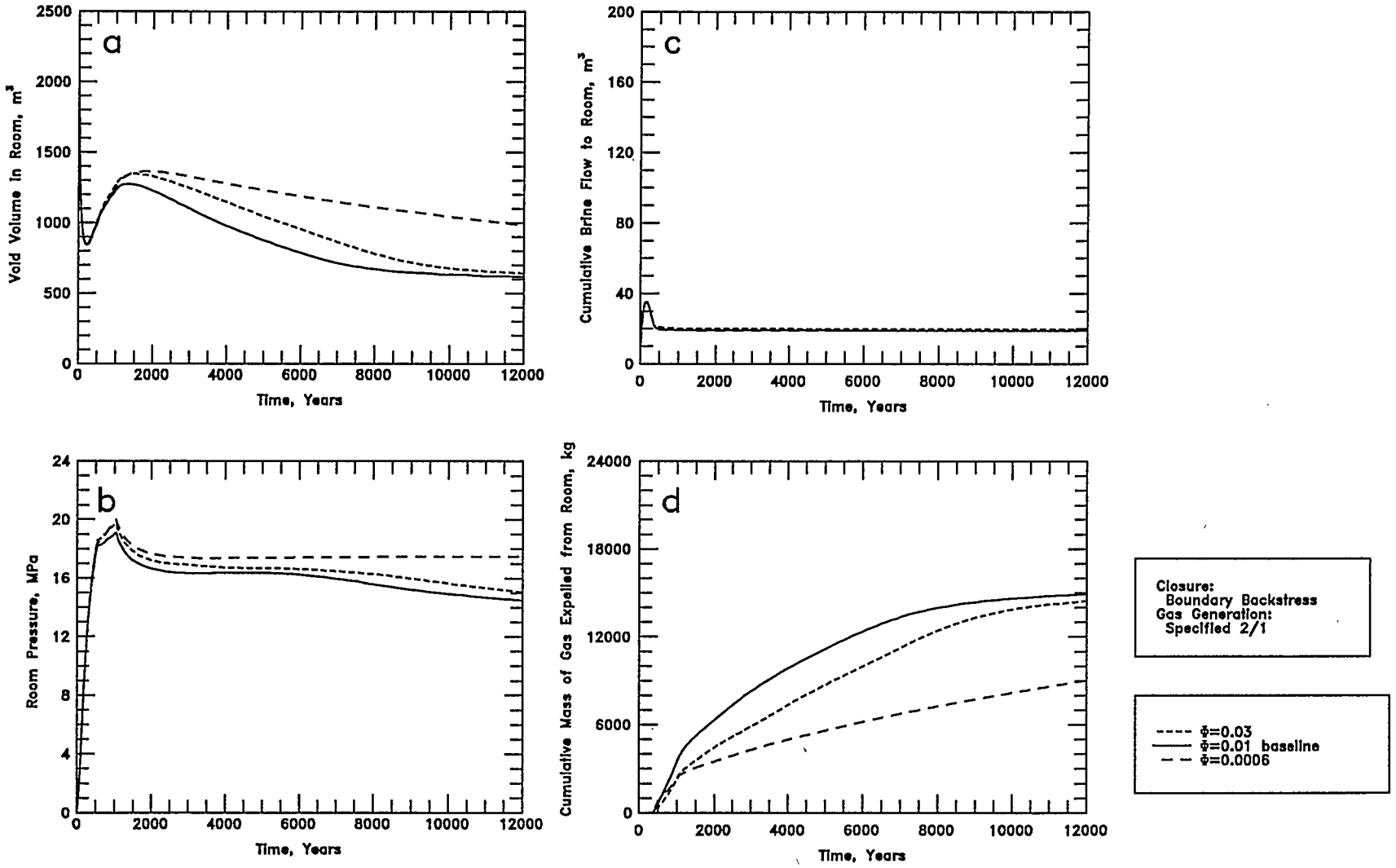

Figure B–20 (a–d). Sensitivity to Interbed Porosity (constant rock compressibility): a – Void Volume; b – Gas Pressure; c – Brine Flow; d – Gas Expulsion

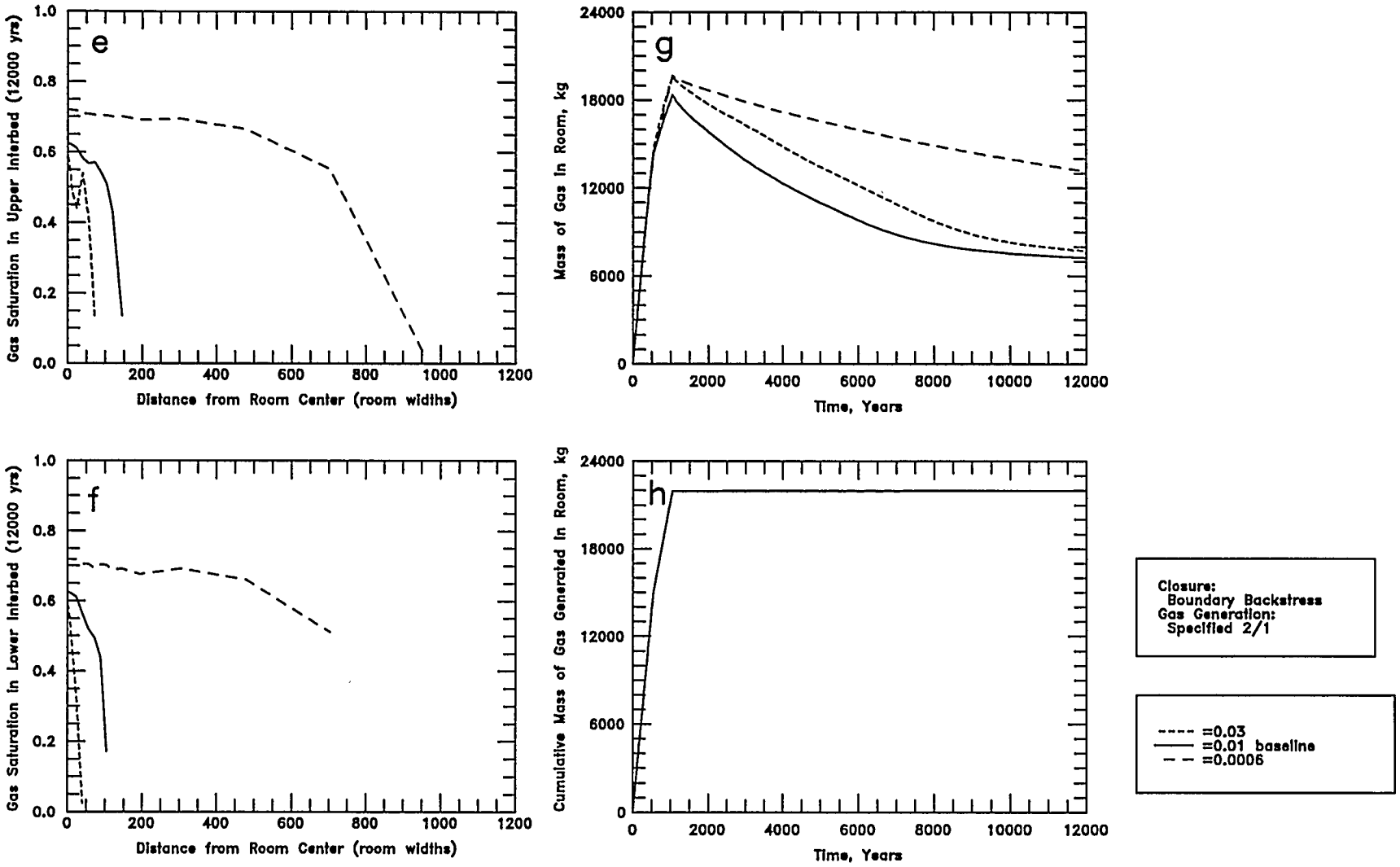

Figure B-20 (e-h). Sensitivity to Interbed Porosity (constant rock compressibility): e - Upper Interbed Gas Profile; f - Lower Interbed Gas Profile; g - Room Gas Mass; h - Gas Generation

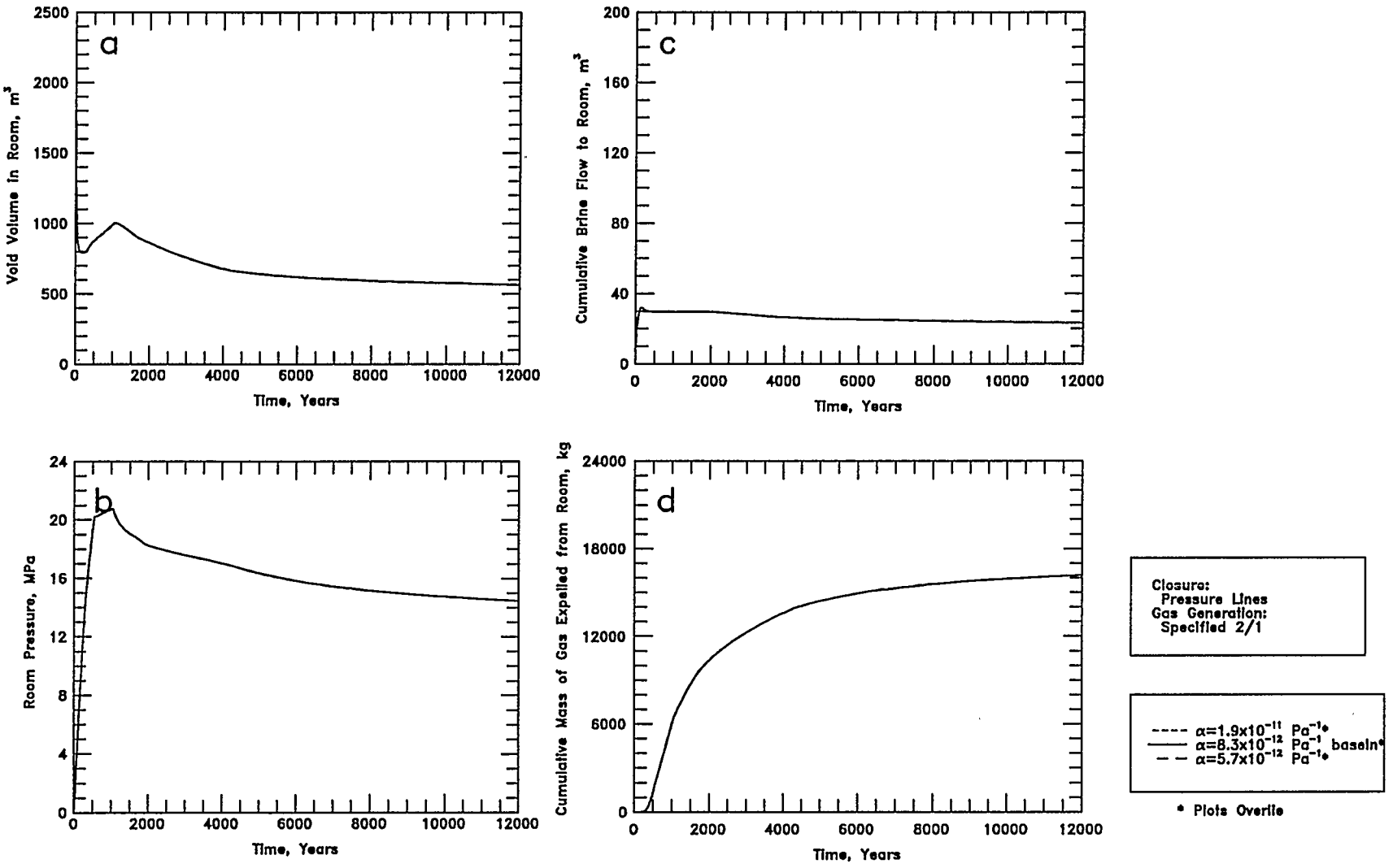

Figure B-21 (a-d). Sensitivity to Interbed Rock Compressibility:
a - Void Volume; b - Gas Pressure; c - Brine Flow; d - Gas Expulsion

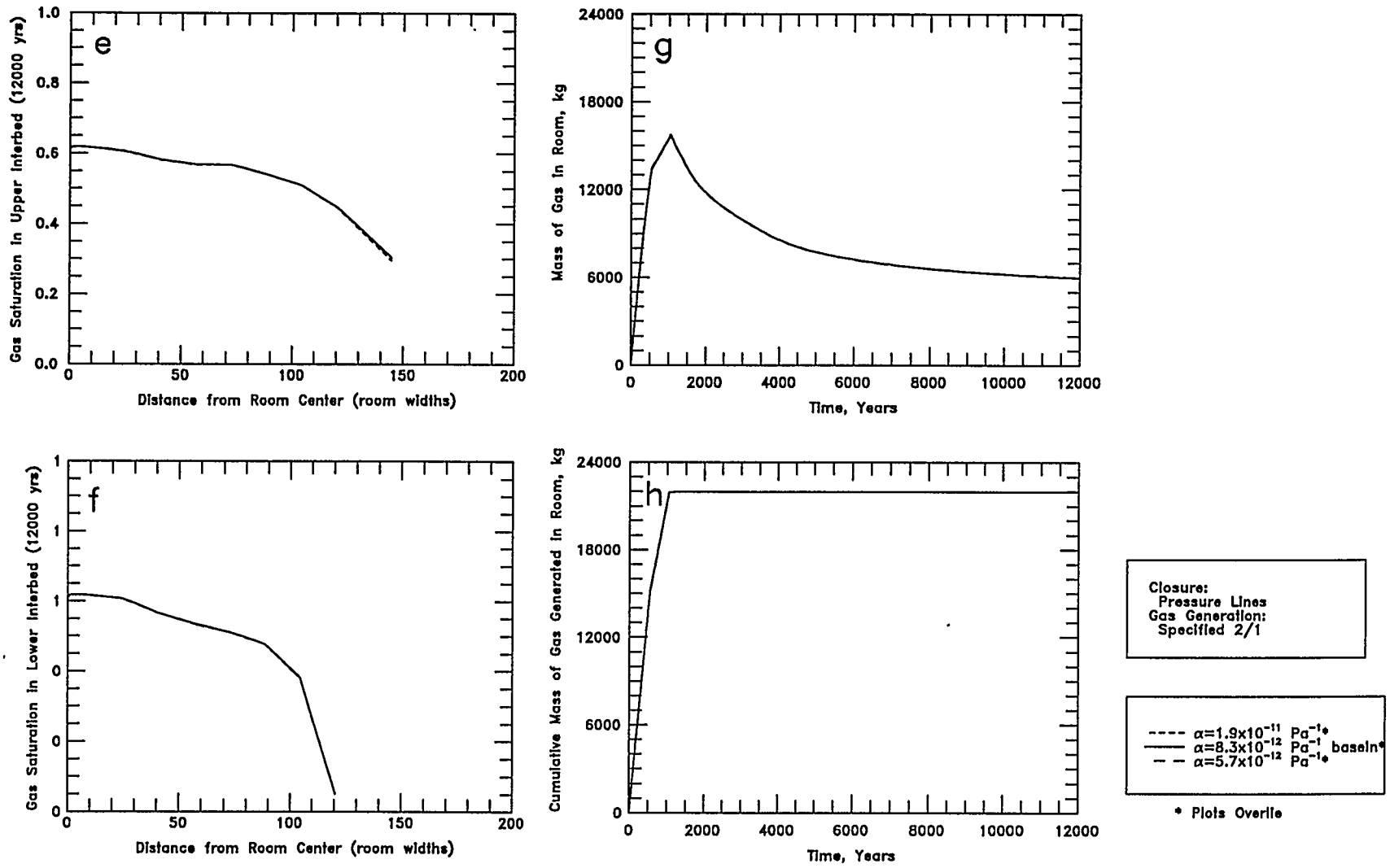

Figure B-21 (e-h). Sensitivity to Interbed Rock Compressibility:
e - Upper Interbed Gas Profile; f - Lower Interbed Gas Profile;
g - Room Gas Mass; h - Gas Generation

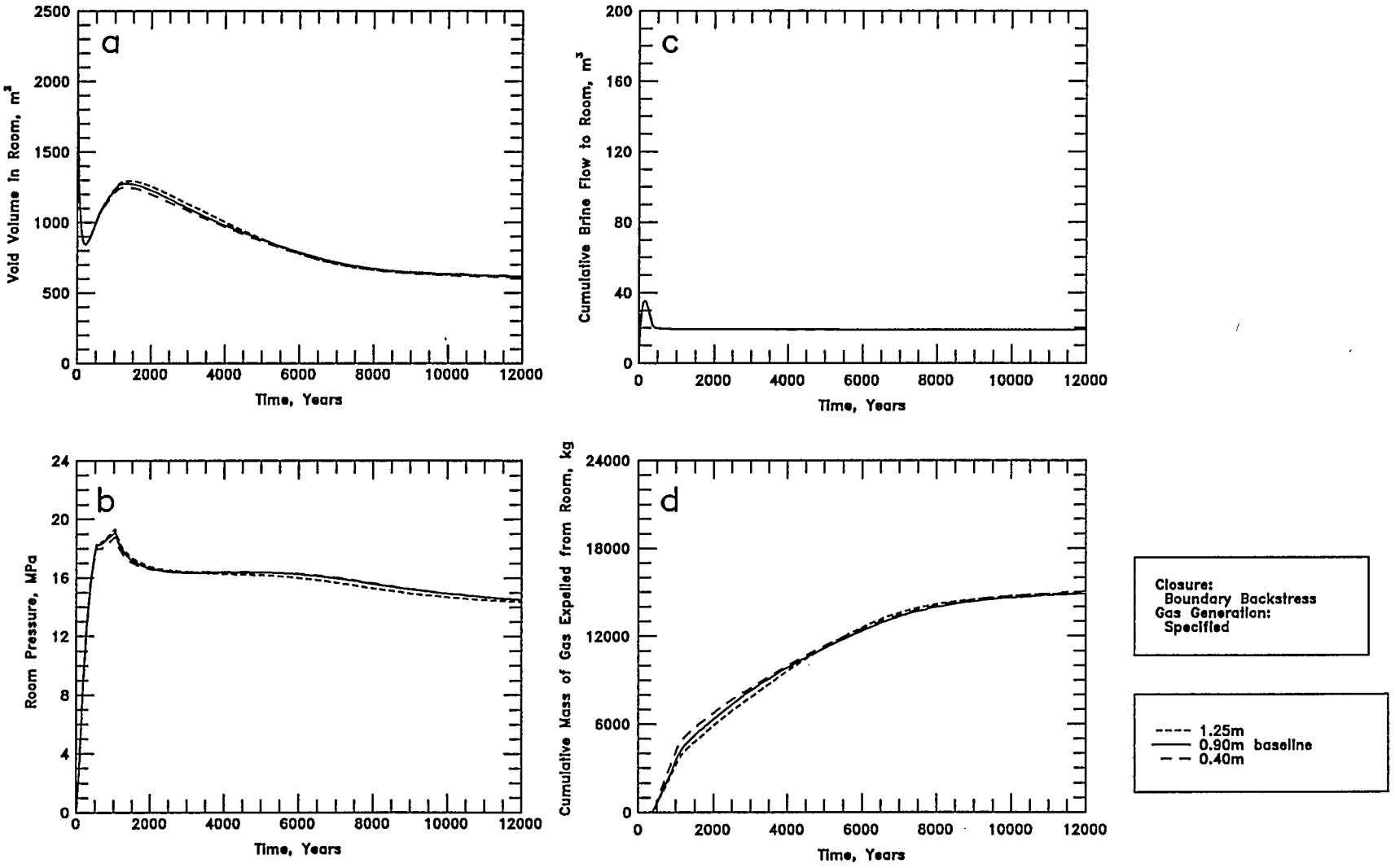

Figure B-22 (a-d). Sensitivity to Lower Interbed Thickness:
a - Void Volume; b - Gas Pressure; c - Brine Flow; d - Gas Expulsion

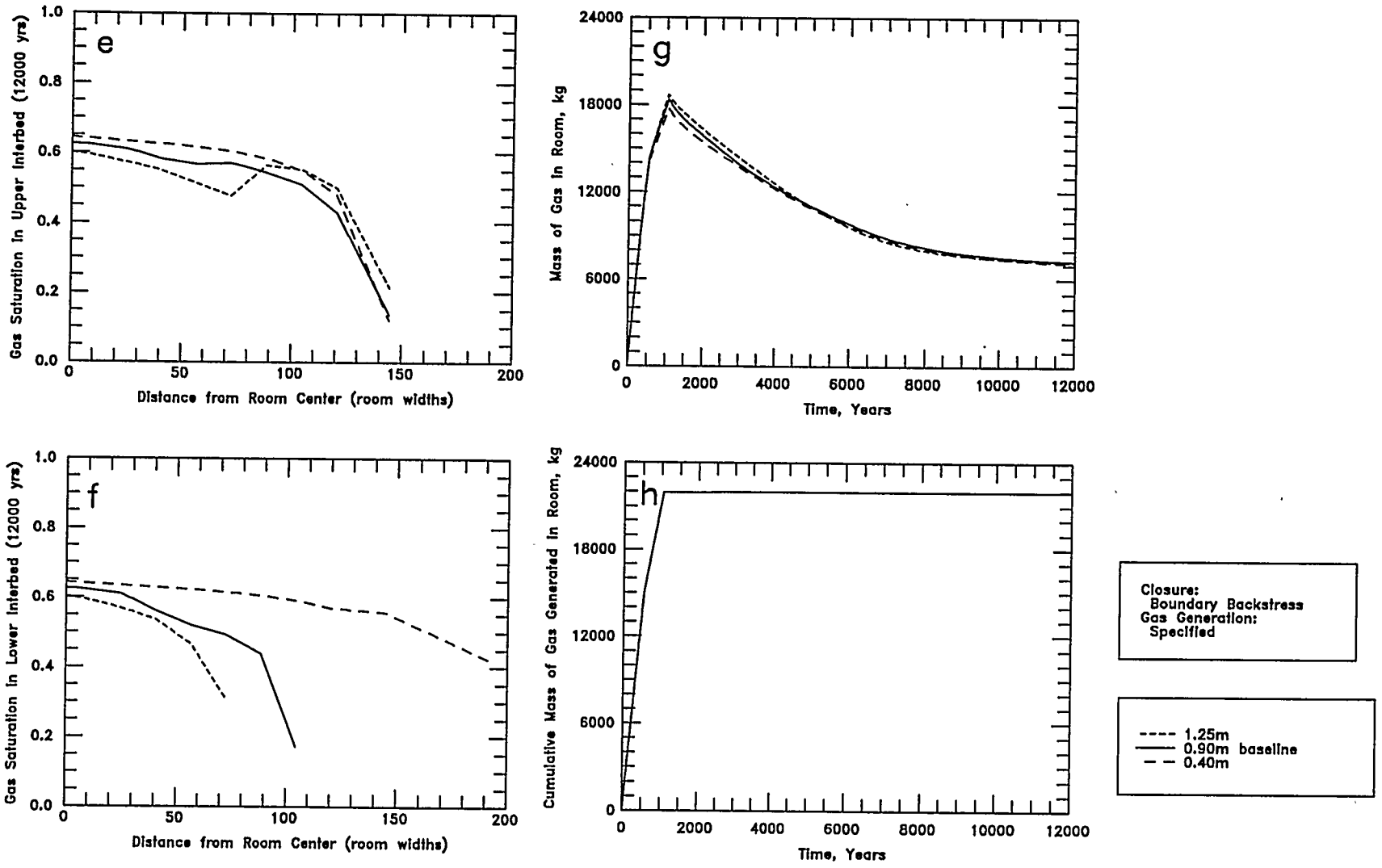

Figure B-22 (e-h). Sensitivity to Lower Interbed Thickness:
e - Upper Interbed Gas Profile; f - Lower Interbed Gas Profile;
g - Room Gas Mass; h - Gas Generation

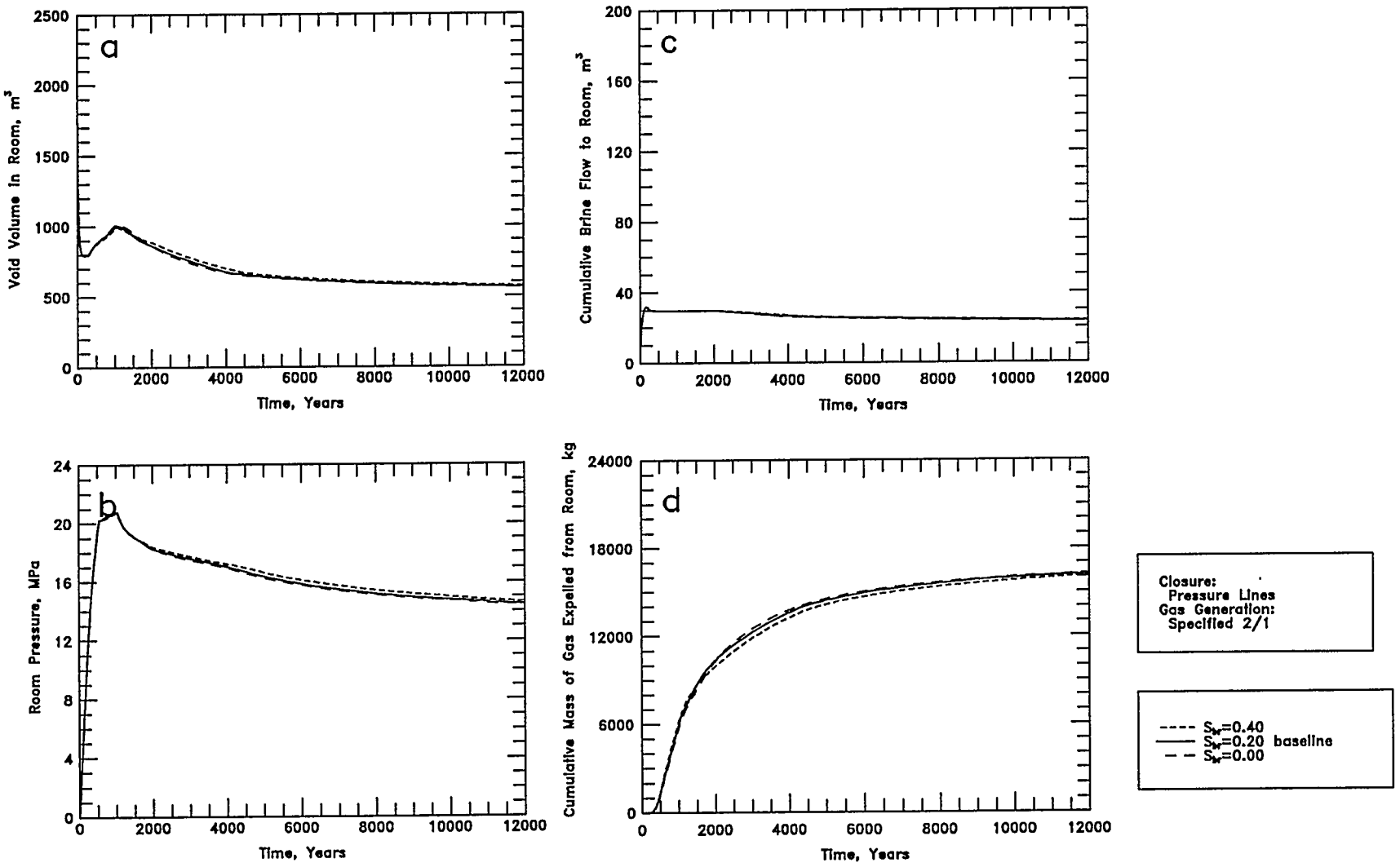

Figure B-23 (a-d). Sensitivity to Interbed Residual Brine Saturation:
a - Void Volume; b - Gas Pressure; c - Brine Flow; d - Gas Expulsion

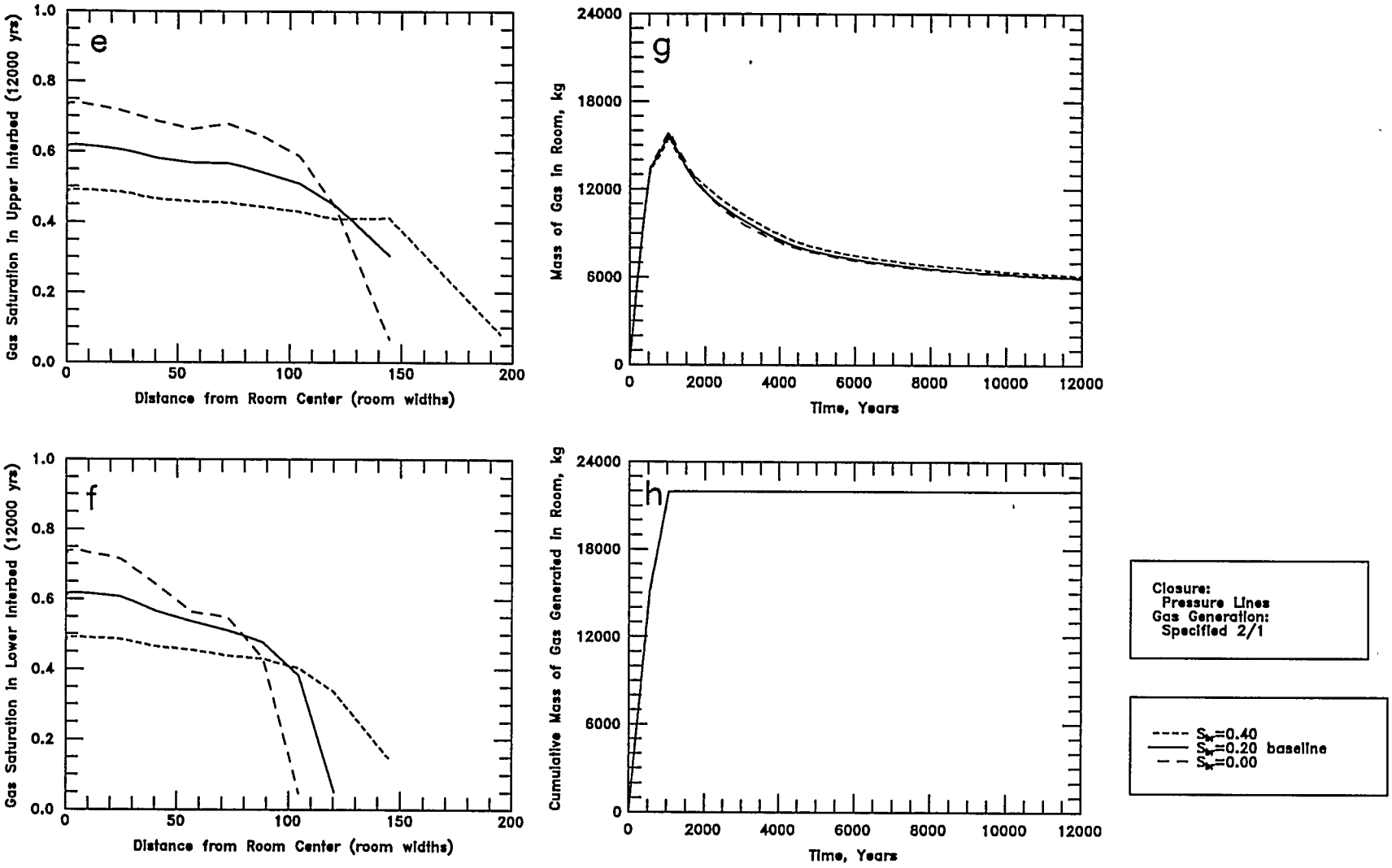

Figure B-23 (e-h). Sensitivity to Interbed Residual Brine Saturation:
e - Upper Interbed Gas Profile; f - Lower Interbed Gas Profile;
g - Room Gas Mass; h - Gas Generation

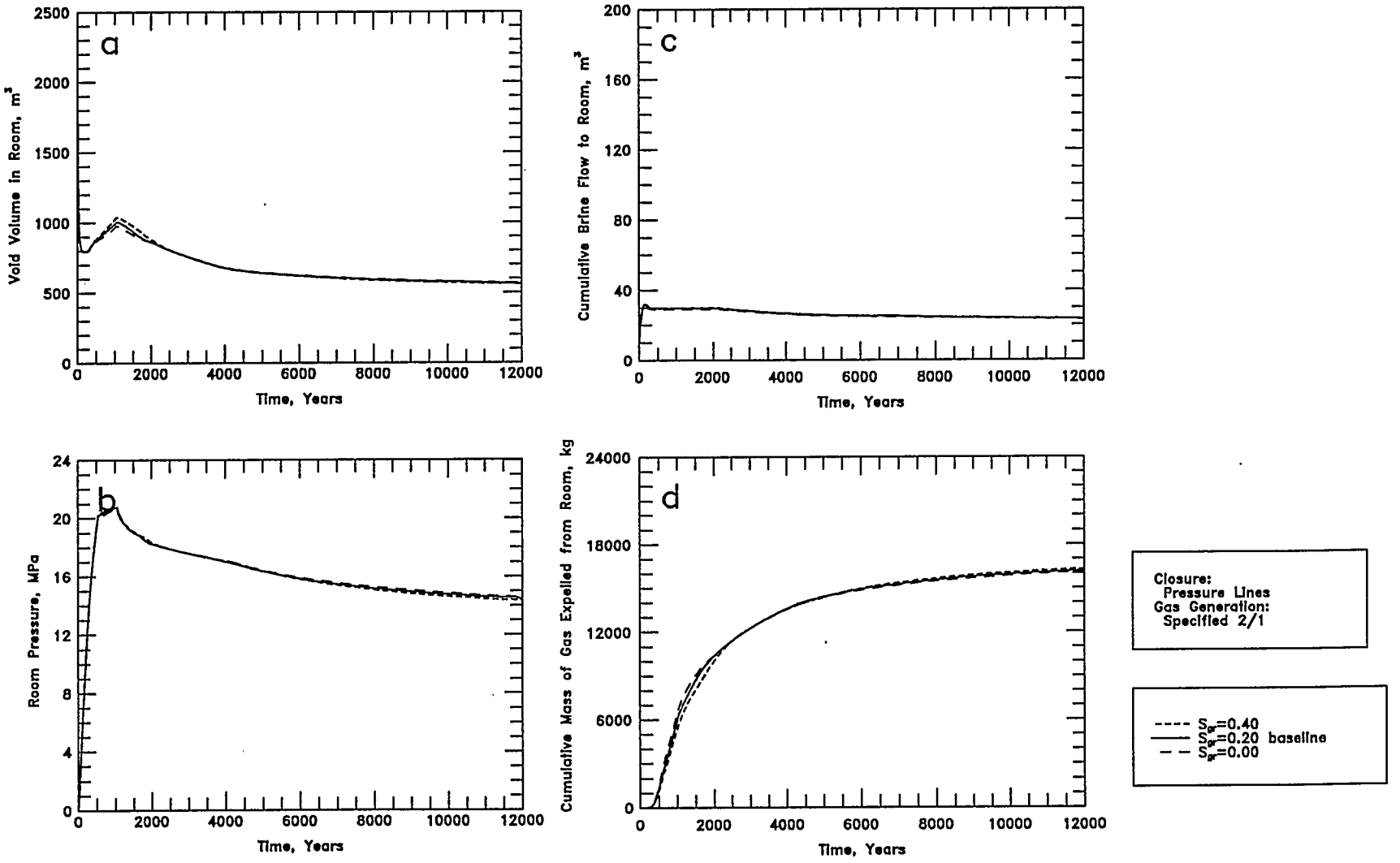

Figure B-24 (a-d). Sensitivity to Interbed Residual Gas Saturation:
a - Void Volume; b - Gas Pressure; c - Brine Flow; d - Gas Expulsion

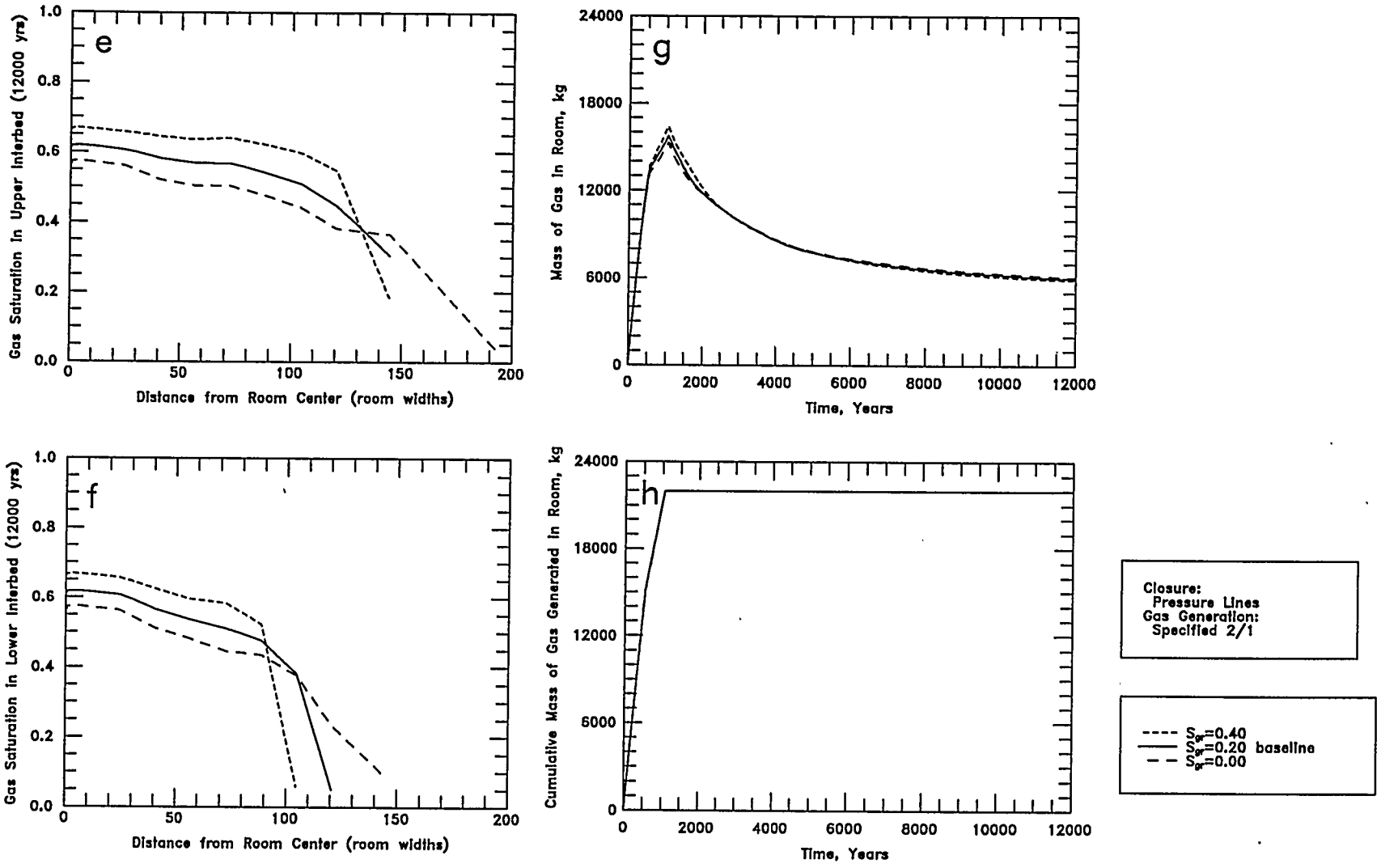

Figure B-24 (e-h). Sensitivity to Interbed Residual Gas Saturation:
e - Upper Interbed Gas Profile; f - Lower Interbed Gas Profile;
g - Room Gas Mass; h - Gas Generation

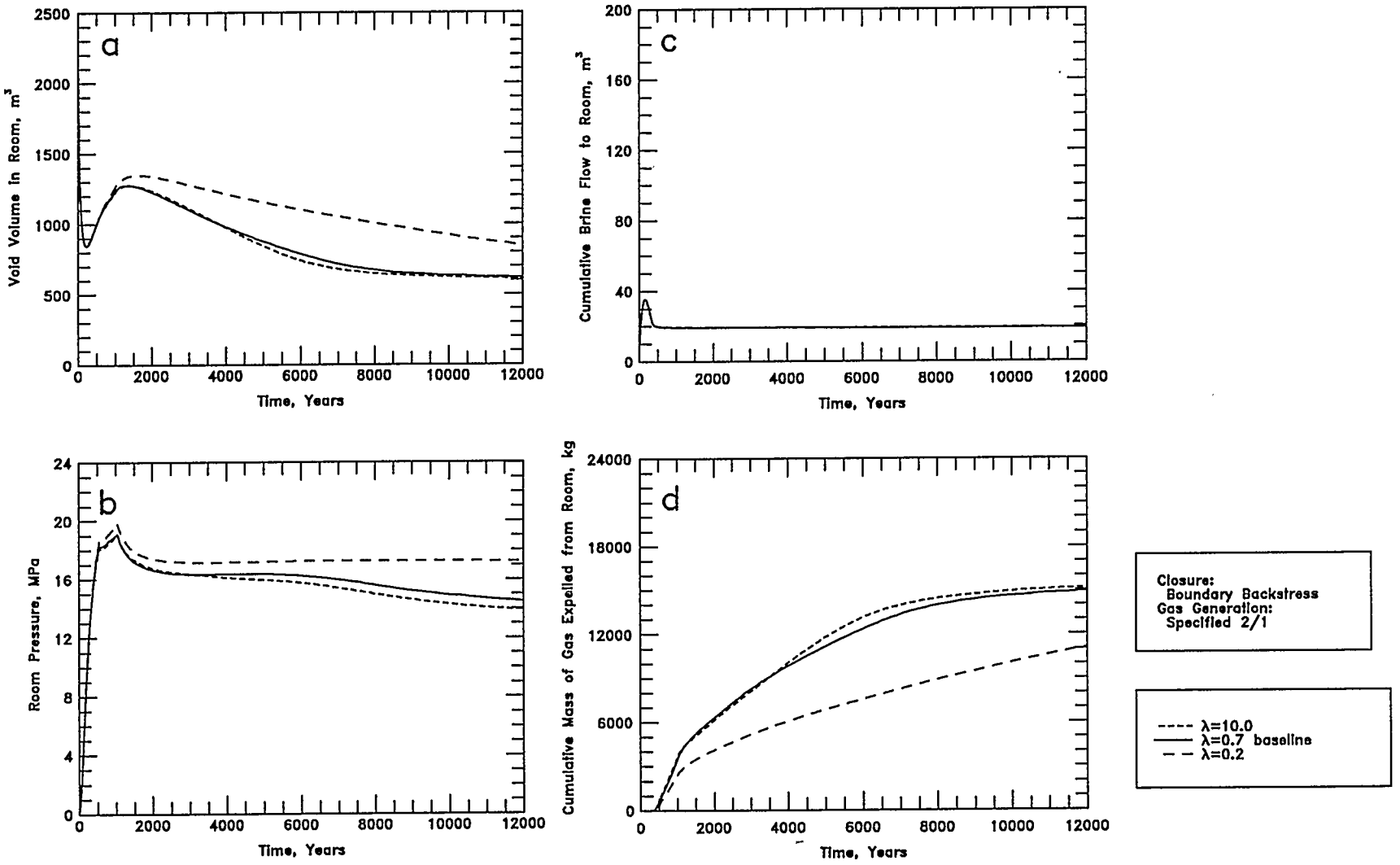

Figure B-25 (a-d). Sensitivity to Interbed Pore-Size Lambda:
a - Void Volume; b - Gas Pressure; c - Brine Flow; d - Gas Expulsion

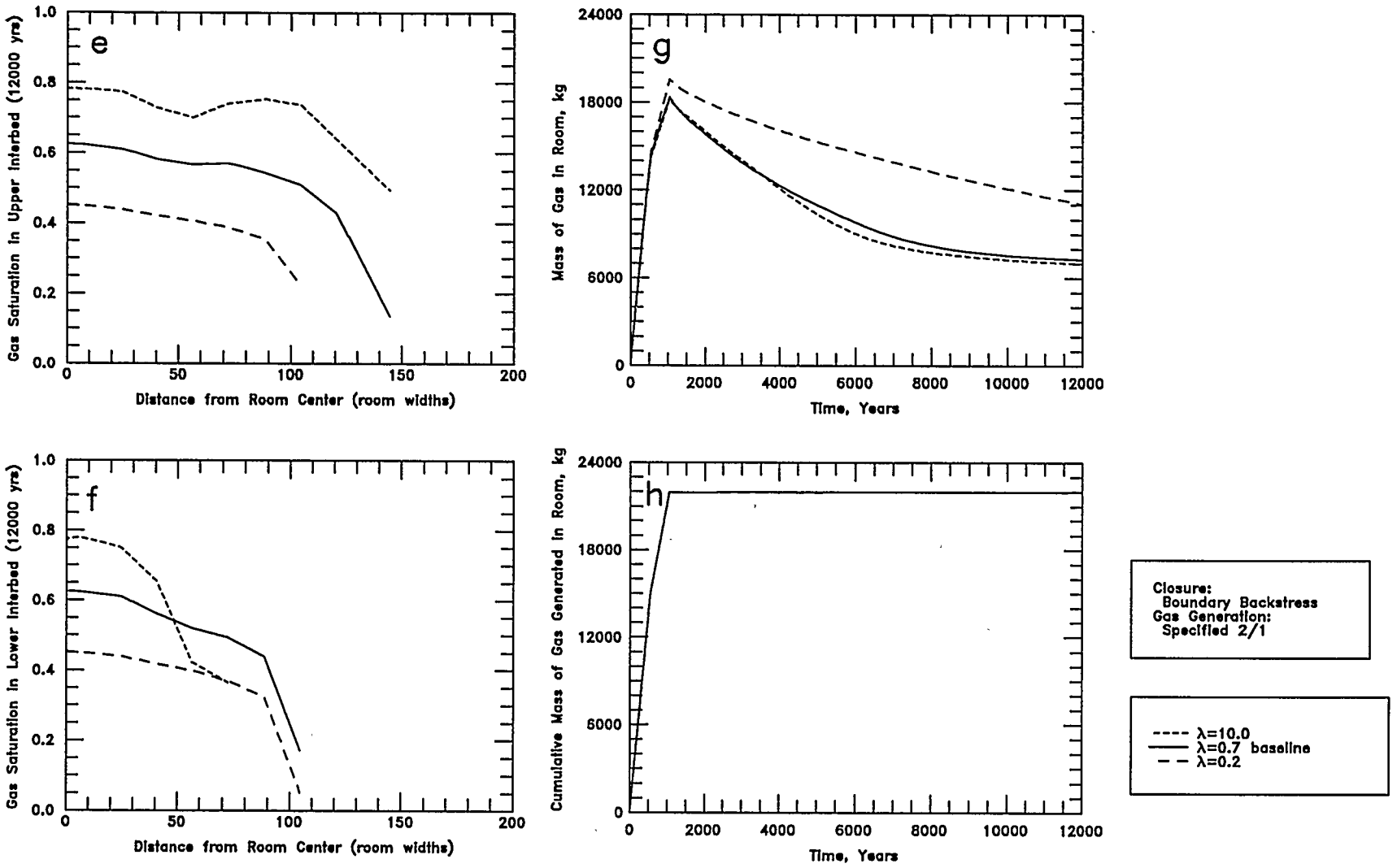

Figure B-25 (e-h). Sensitivity to Interbed Pore-Size Lambda:
e - Upper Interbed Gas Profile; f - Lower Interbed Gas Profile;
g - Room Gas Mass; h - Gas Generation

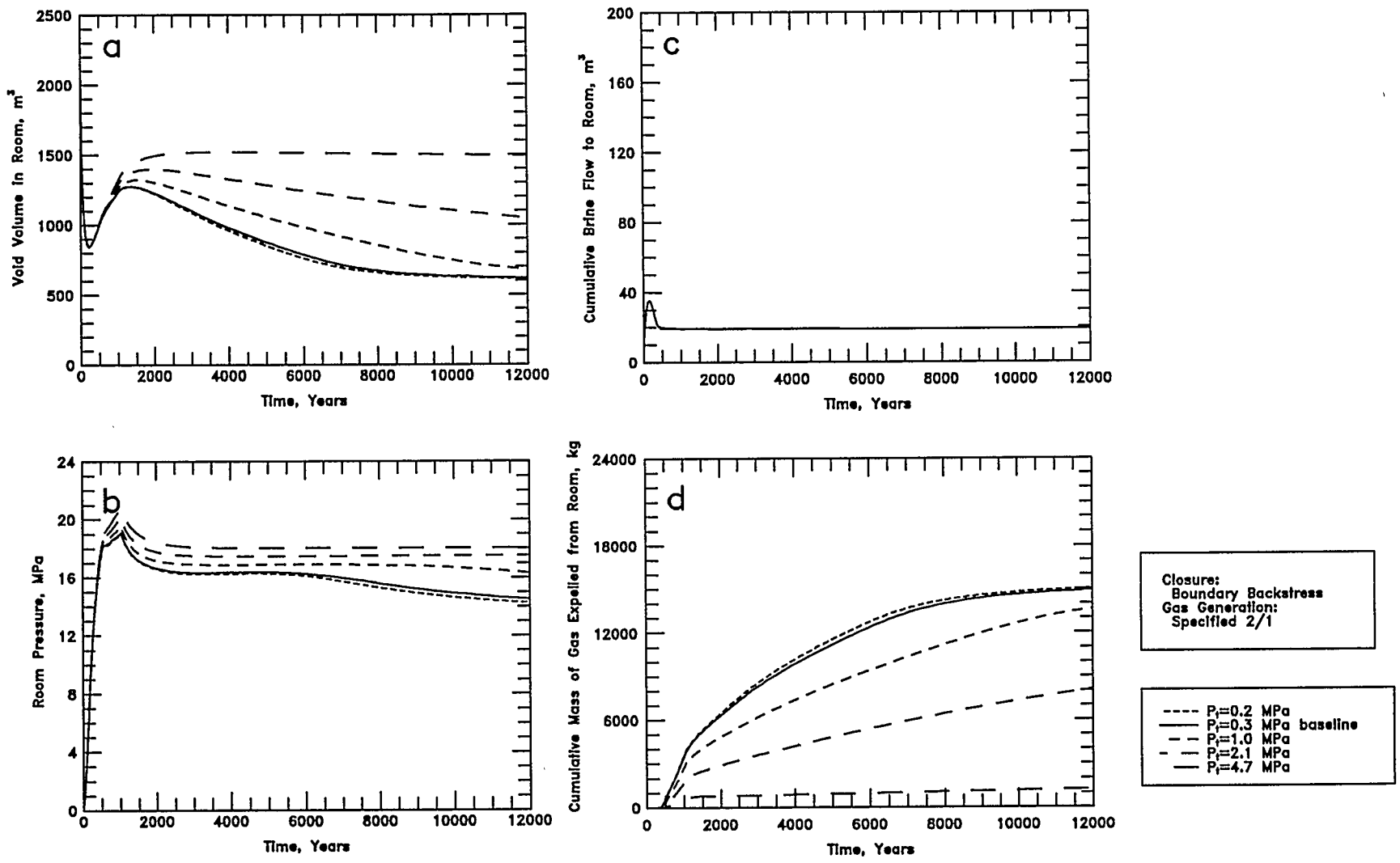

Figure B-26 (a-d). Sensitivity to Interbed Threshold Pressure:
a - Void Volume; b - Gas Pressure; c - Brine Flow; d - Gas Expulsion

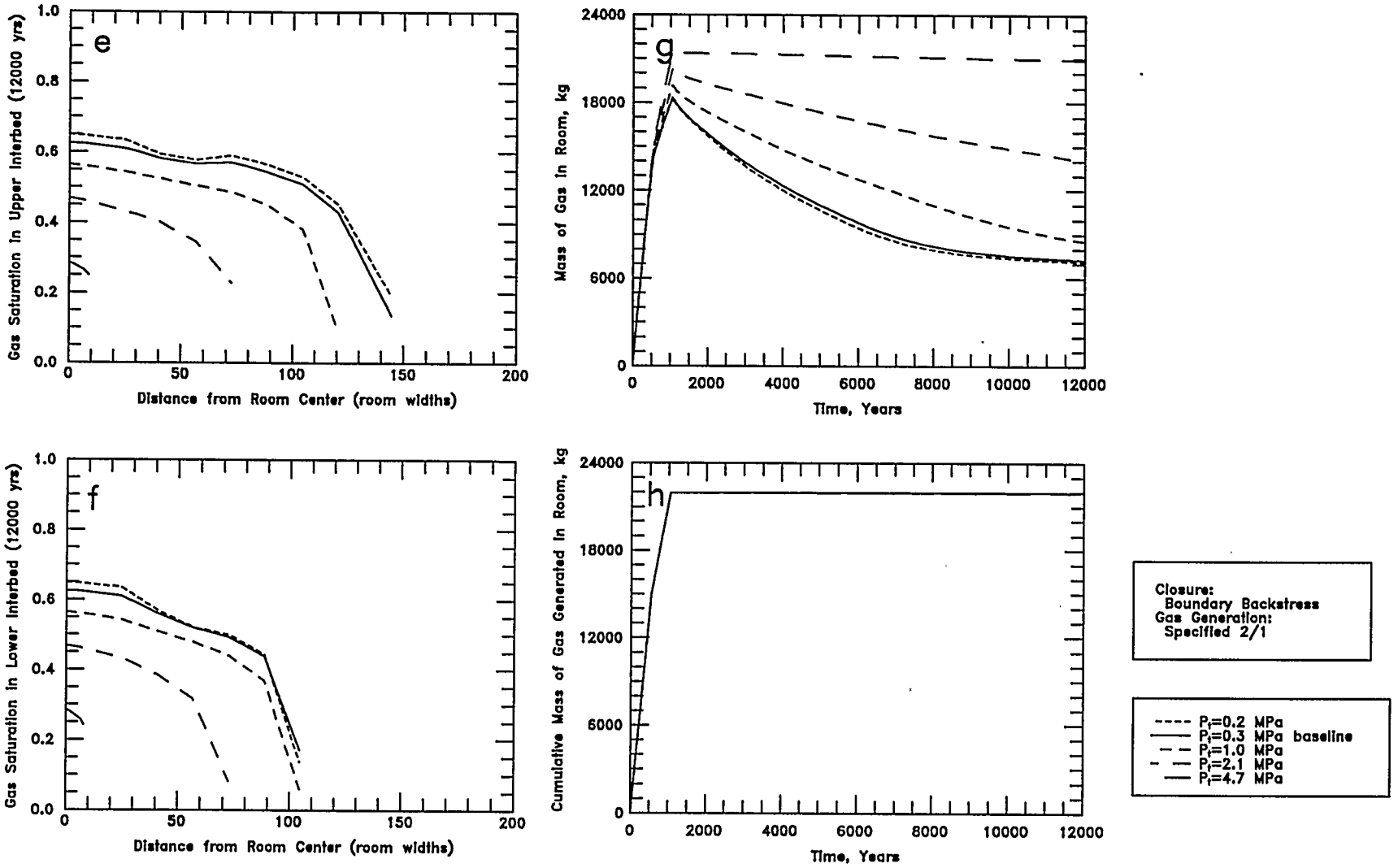

Figure B–26 (e–h). Sensitivity to Interbed Threshold Pressure:
e – Upper Interbed Gas Profile; f – Lower Interbed Gas Profile;
g – Room Gas Mass; h – Gas Generation

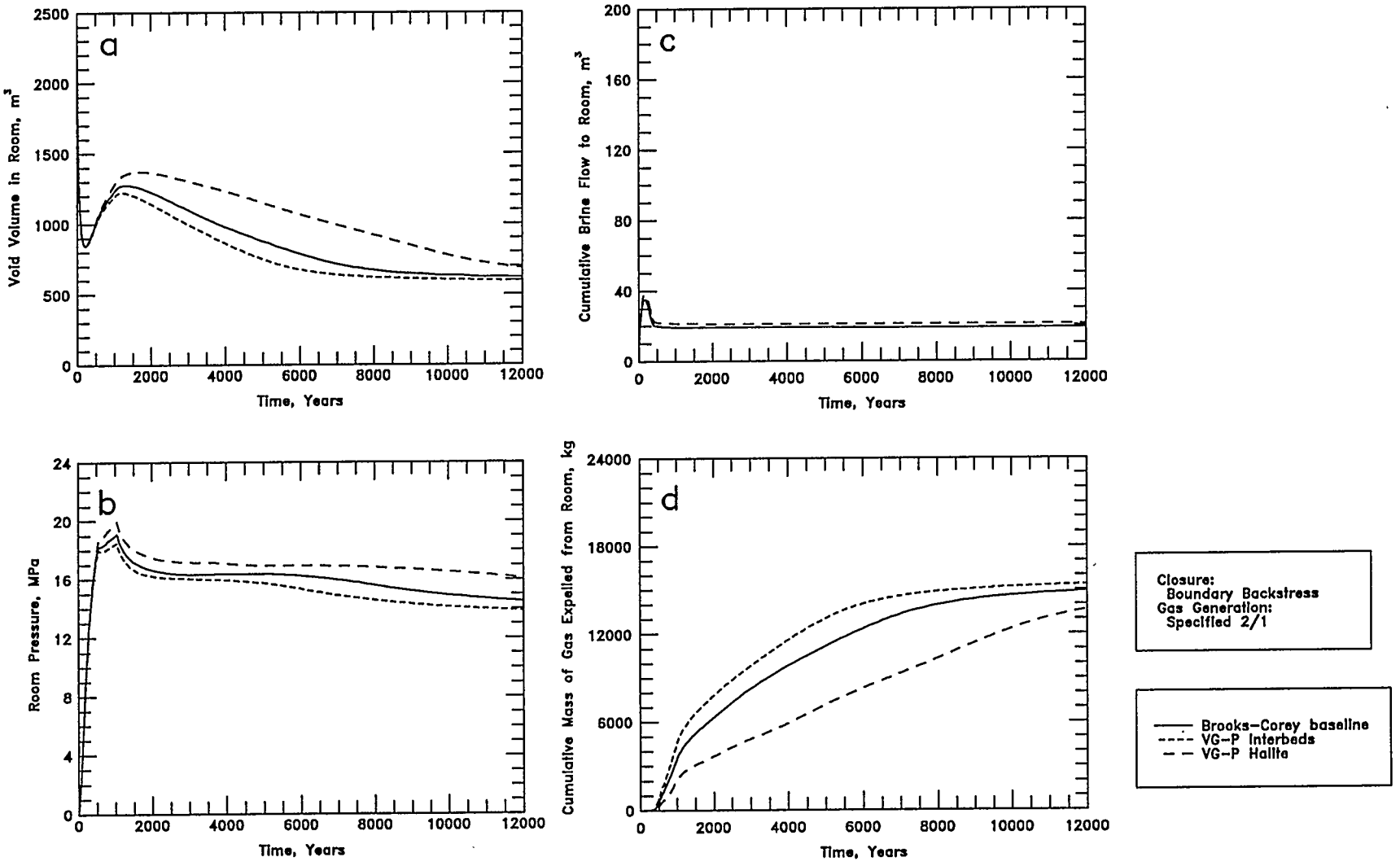

Figure B-27 (a-d). Sensitivity to Interbed Two-Phase Characteristic Relationship: a - Void Volume; b - Gas Pressure; c - Brine Flow; d - Gas Expulsion

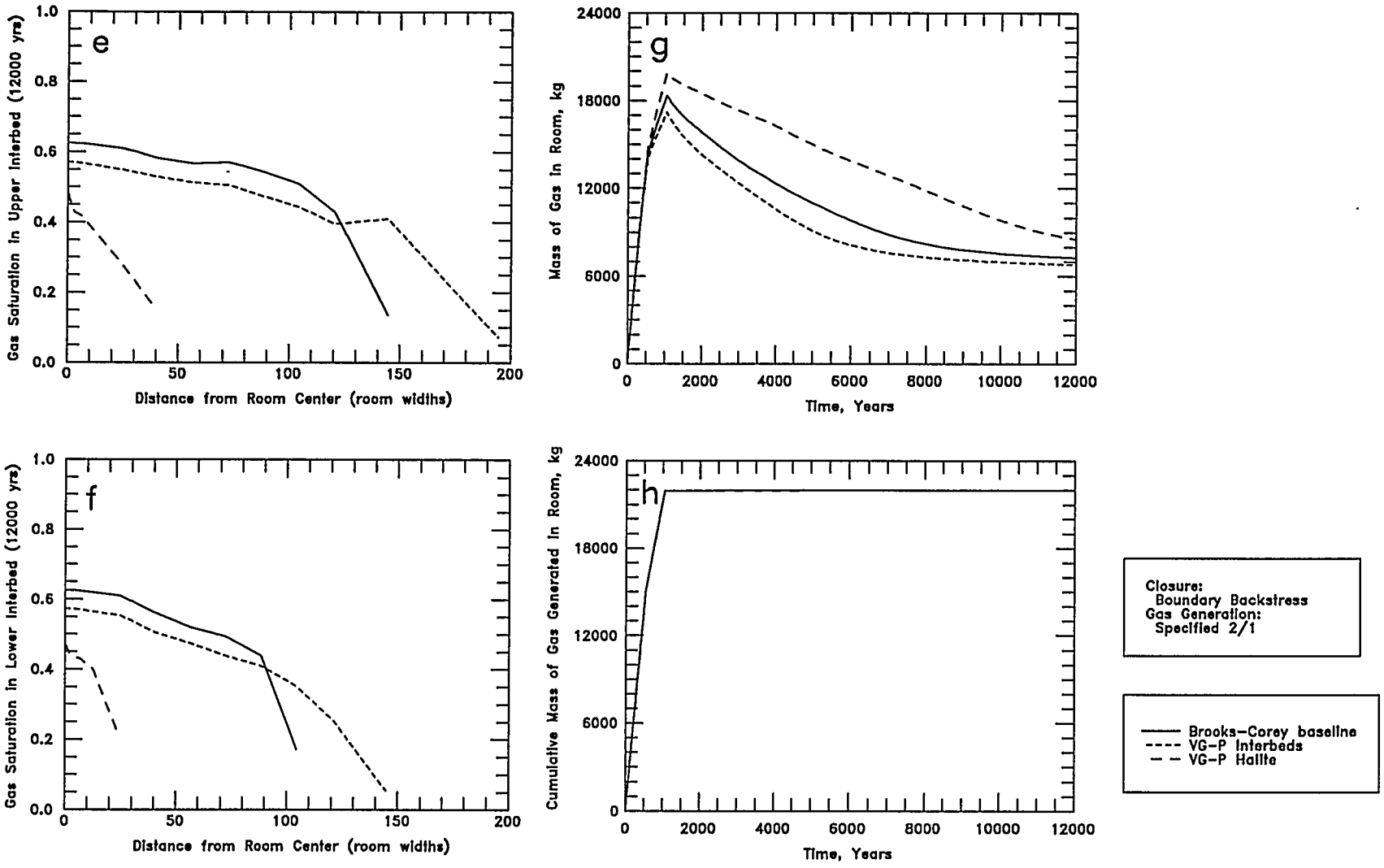

Figure B-27 (e-h). Sensitivity to Interbed Two-Phase Characteristic Relationship: e - Upper Interbed Gas Profile; f - Lower Interbed Gas Profile; g - Room Gas Mass; h - Gas Generation

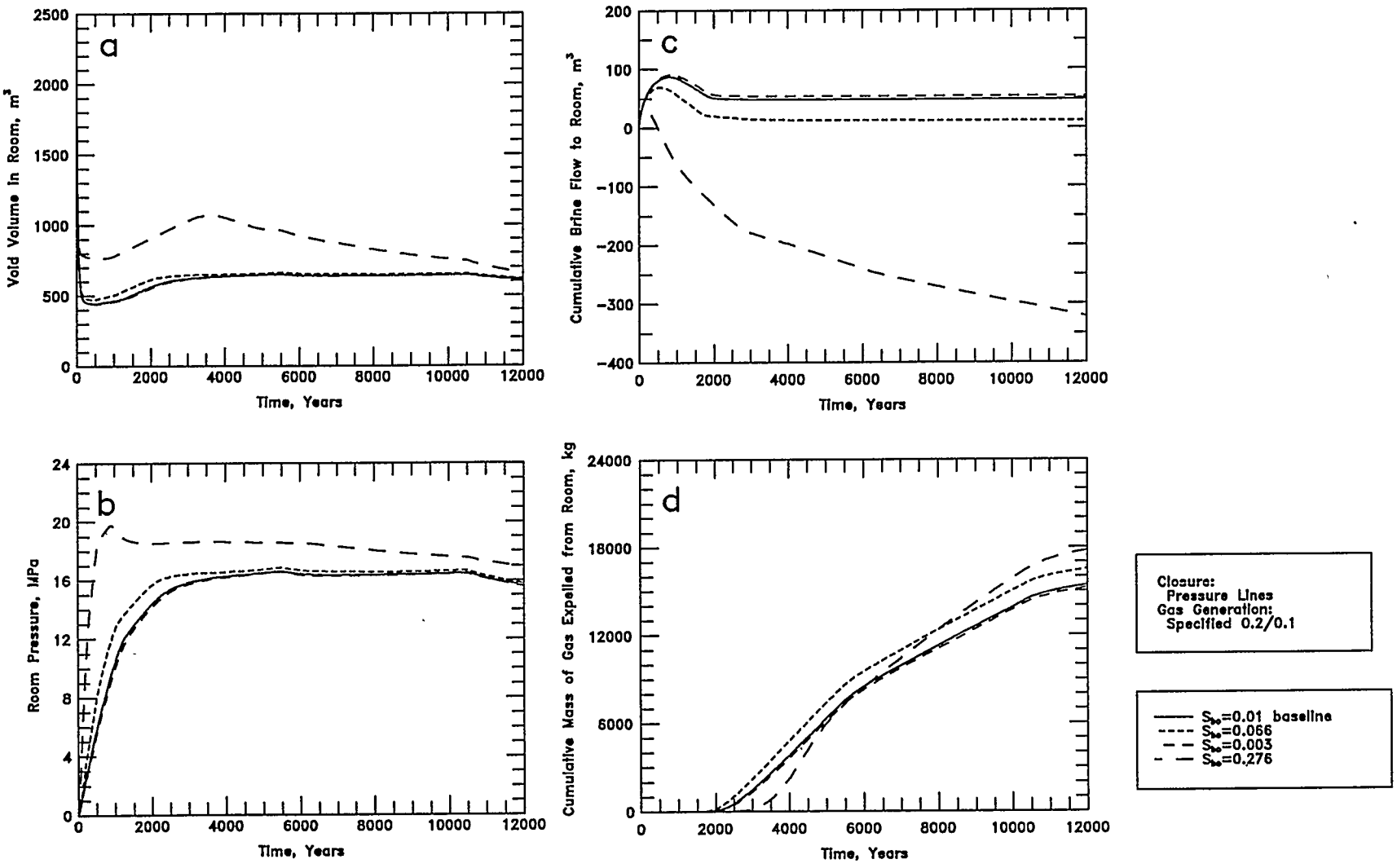

Figure B-28 (a-d). Sensitivity to Disposal Room Initial Brine Saturation: a - Void Volume; b - Gas Pressure; c - Brine Flow; d - Gas Expulsion

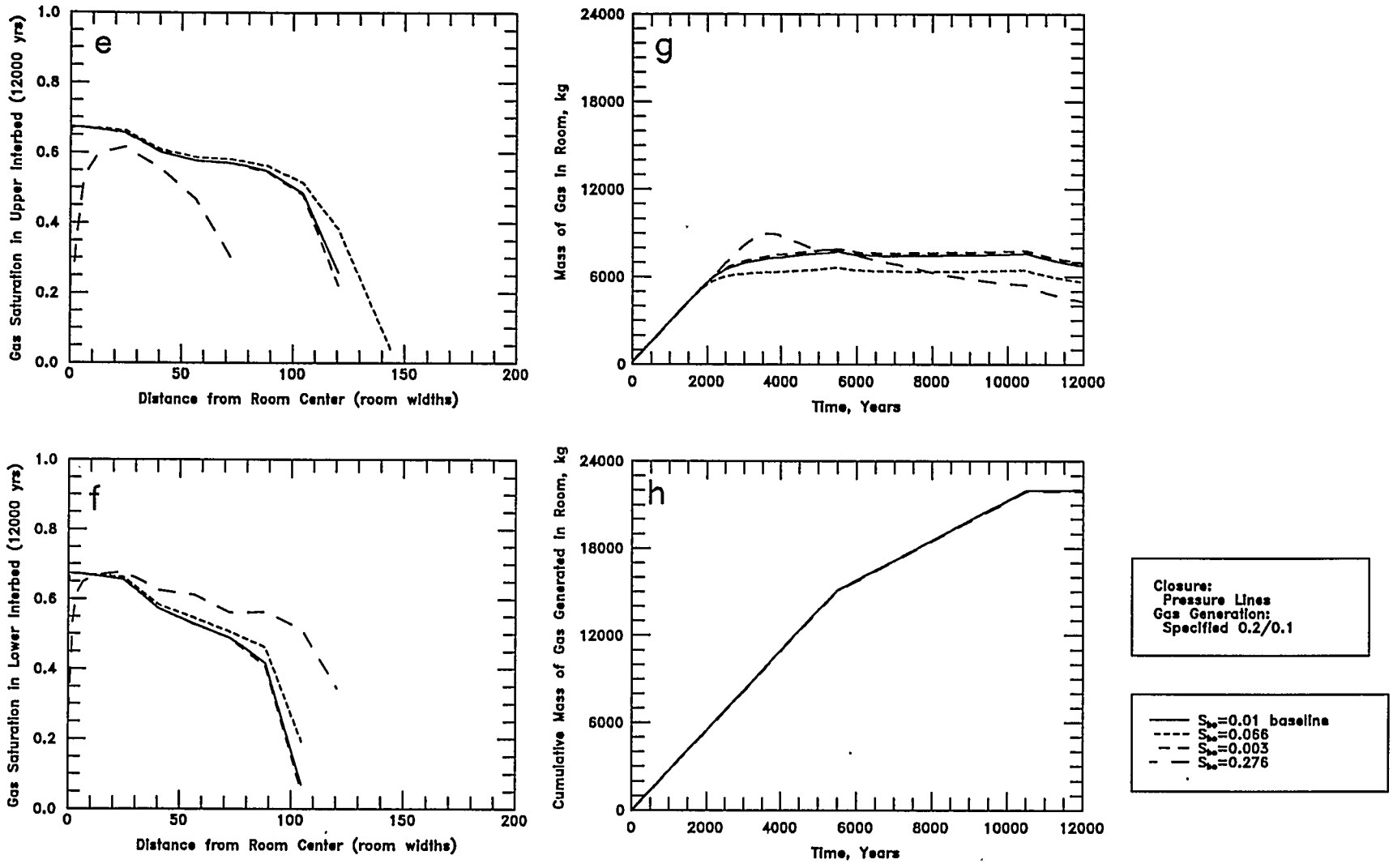

Figure B-28 (e-h). Sensitivity to Disposal Room Initial Brine Saturation:
e - Upper Interbed Gas Profile; f - Lower Interbed Gas Profile;
g - Room Gas Mass; h - Gas Generation

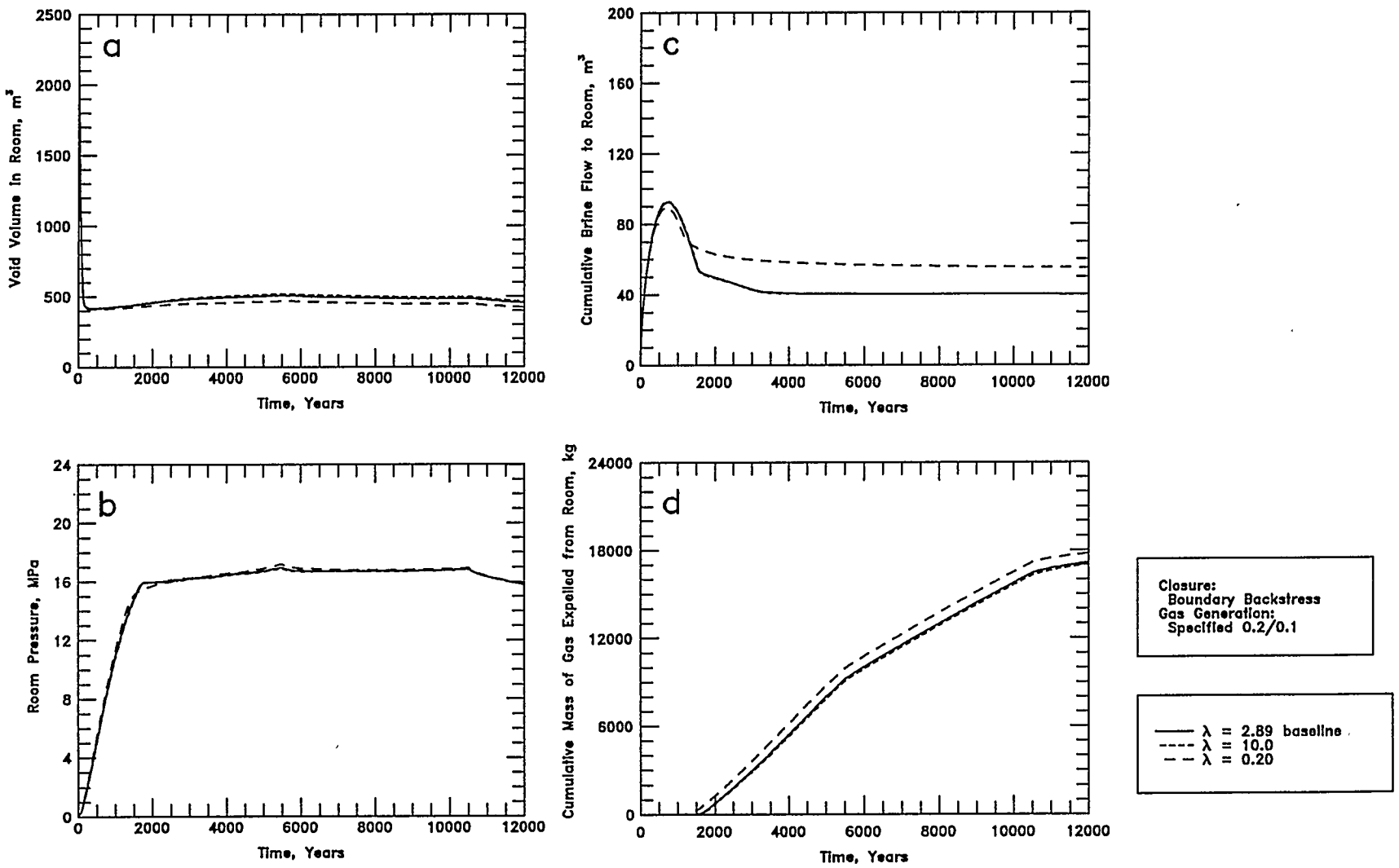

Figure B-29 (a-d). Sensitivity to Disposal Room Pore-Size Lambda:
a - Void Volume; b - Gas Pressure; c - Brine Flow; d - Gas Expulsion

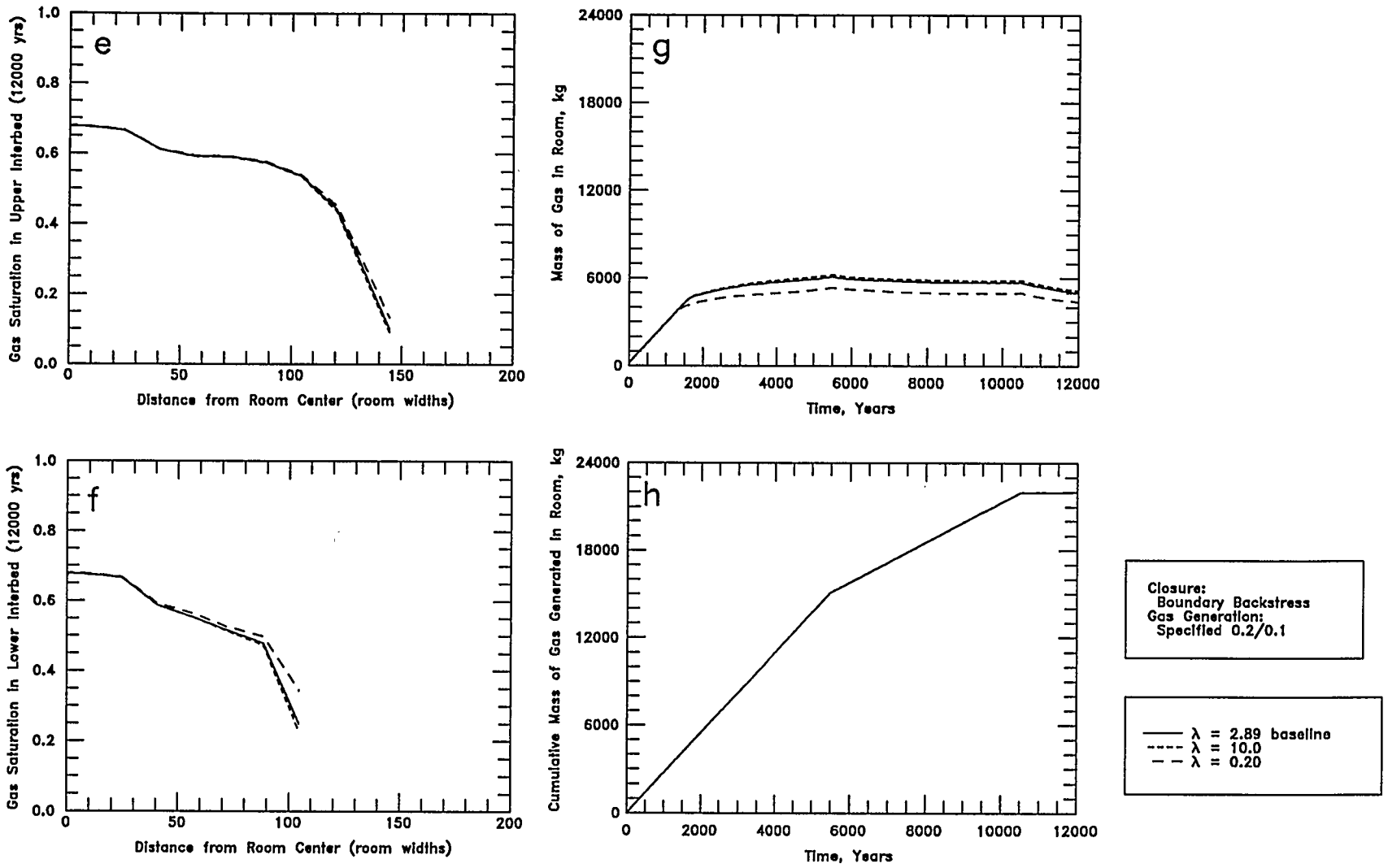

Figure B-29 (e-h). Sensitivity to Disposal Room Pore-Size Lambda:
e - Upper Interbed Gas Profile; f - Lower Interbed Gas Profile;
g - Room Gas Mass; h - Gas Generation

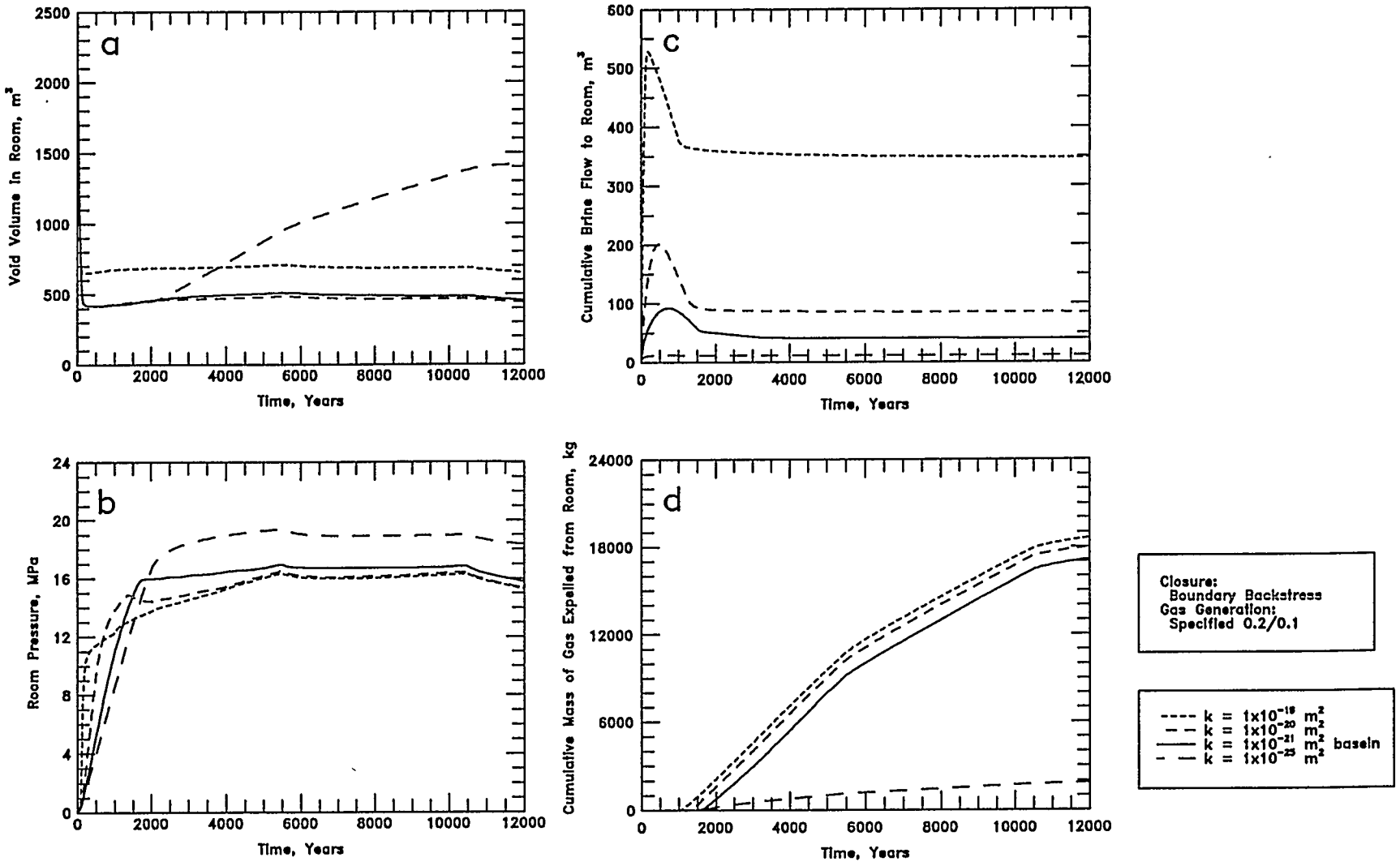

Figure B–30 (a–d). Sensitivity to Halite Intrinsic Permeability (constant threshold pressure): a – Void Volume; b – Gas Pressure; c – Brine Flow; d – Gas Expulsion

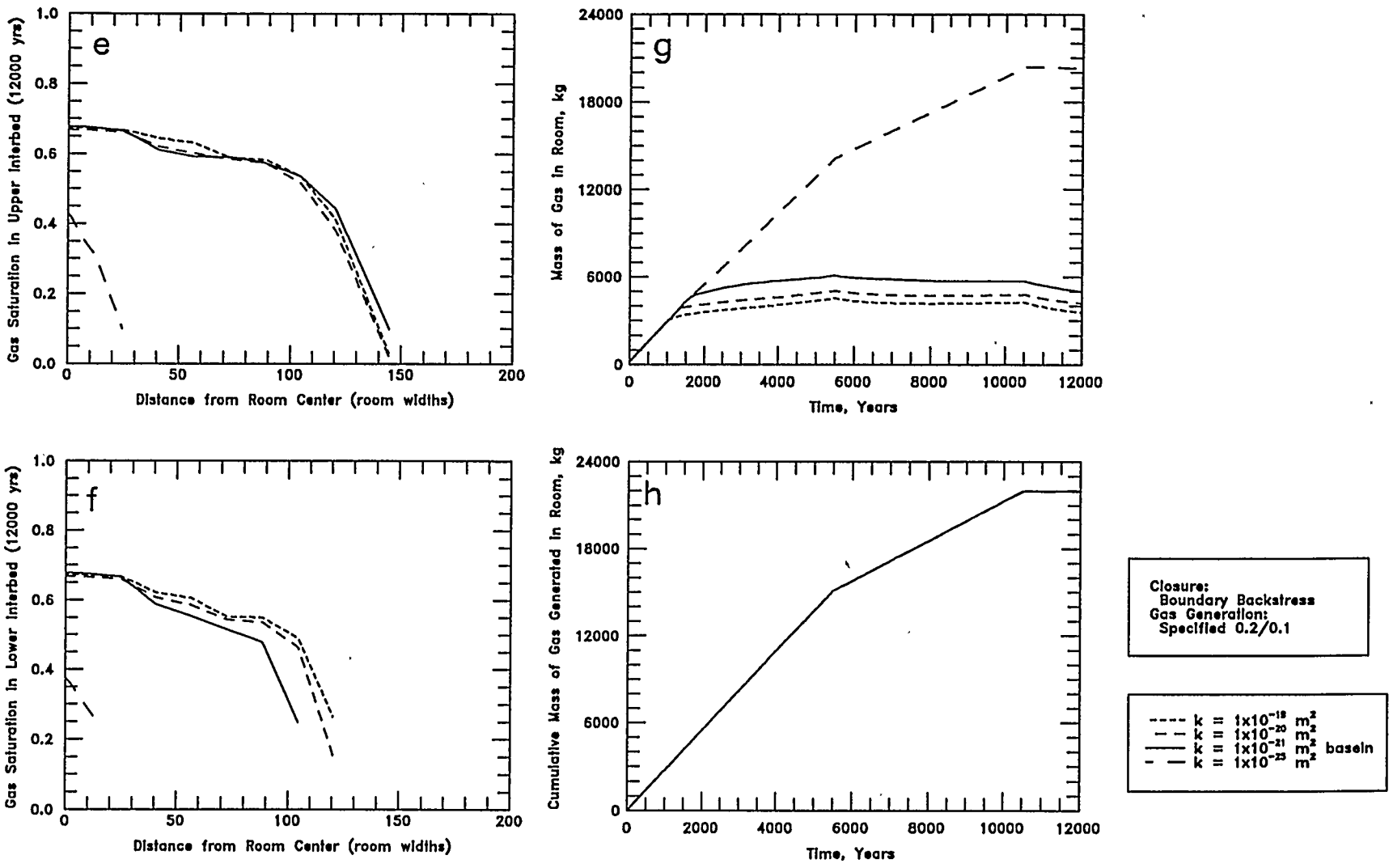

Figure B-30 (e-h). Sensitivity to Halite Intrinsic Permeability (constant threshold pressure): e - Upper Interbed Gas Profile; f - Lower Interbed Gas Profile; g - Room Gas Mass; h - Gas Generation

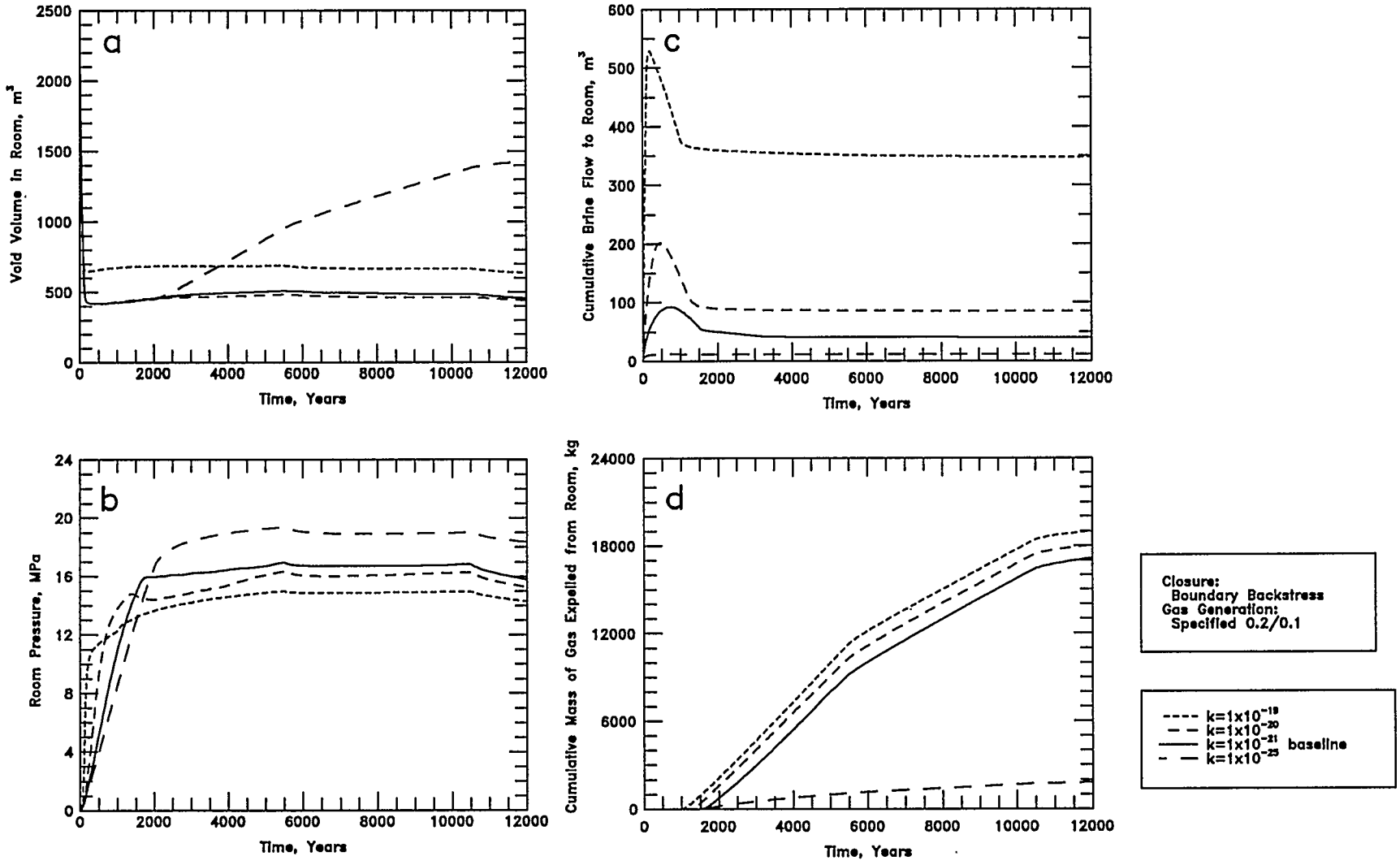

Figure B-31 (a-d). Sensitivity to Halite Intrinsic Permeability (variable threshold pressure): a - Void Volume; b - Gas Pressure; c - Brine Flow; d - Gas Expulsion

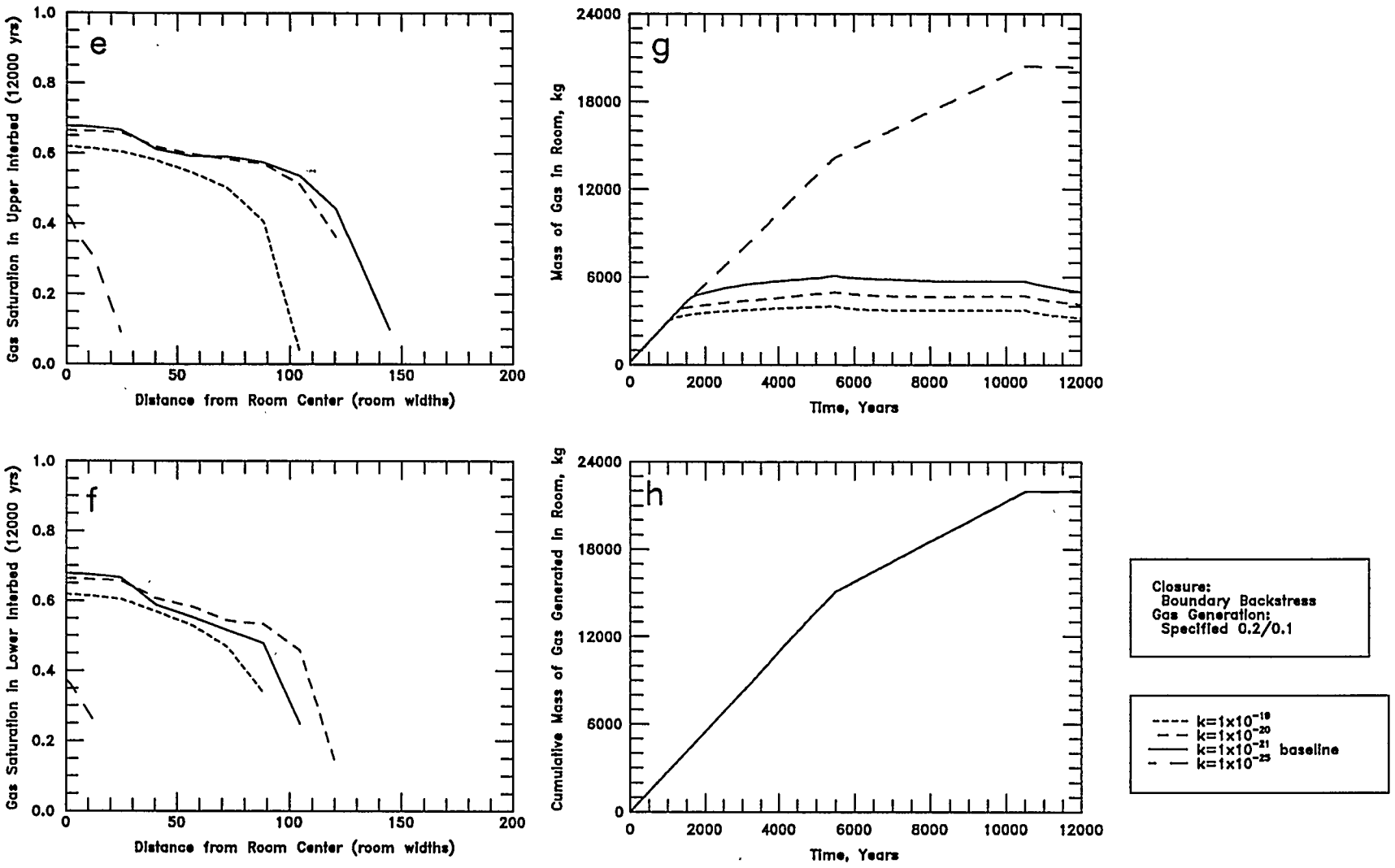

Figure B-31 (e-h). Sensitivity to Halite Intrinsic Permeability (variable threshold pressure): e - Upper Interbed Gas Profile; f - Lower Interbed Gas Profile; g - Room Gas Mass; h - Gas Generation

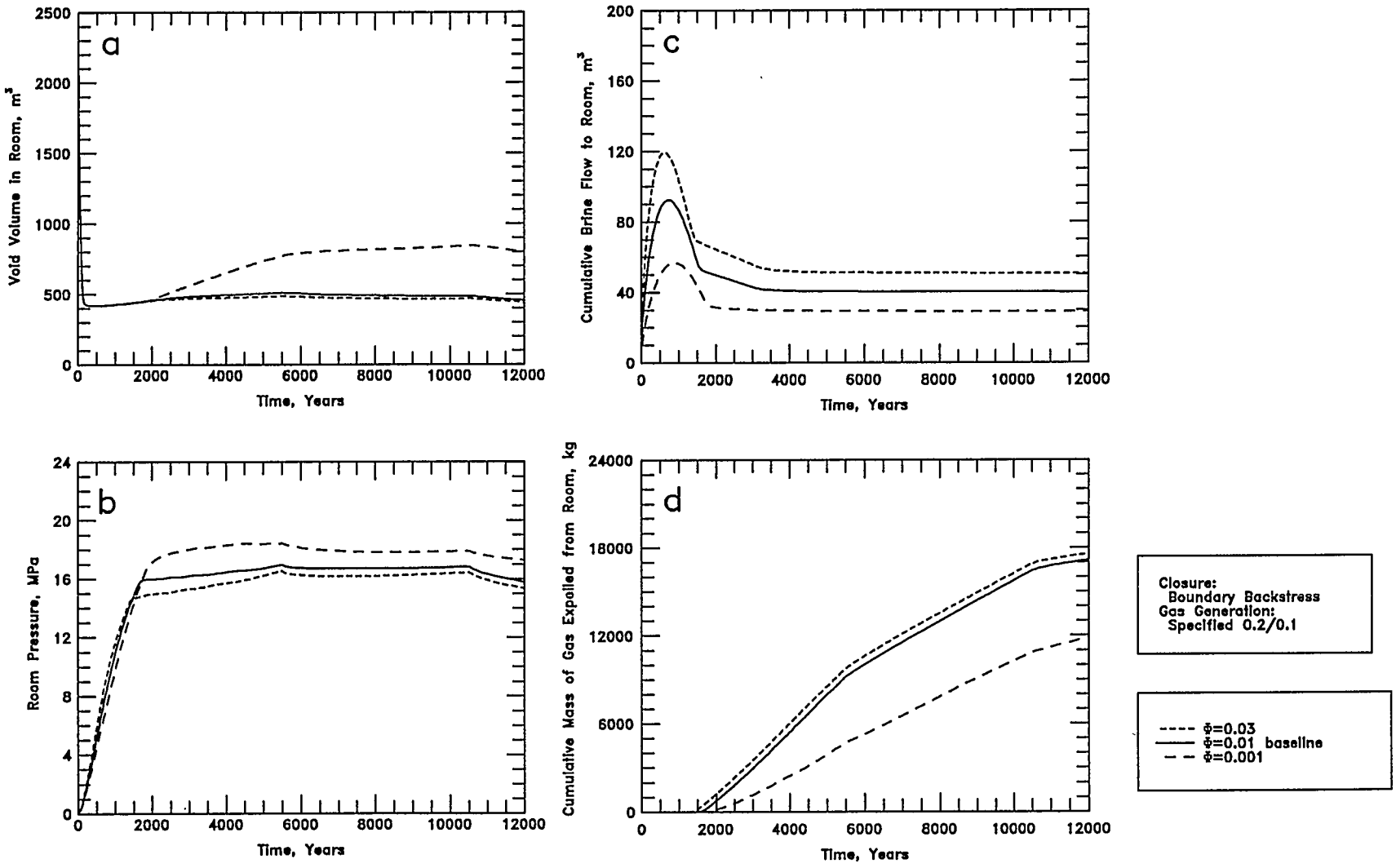

Figure B-32 (a-d). Sensitivity to Halite Porosity (constant pore volume compressibility): a - Void Volume; b - Gas Pressure; c - Brine Flow; d - Gas Expulsion

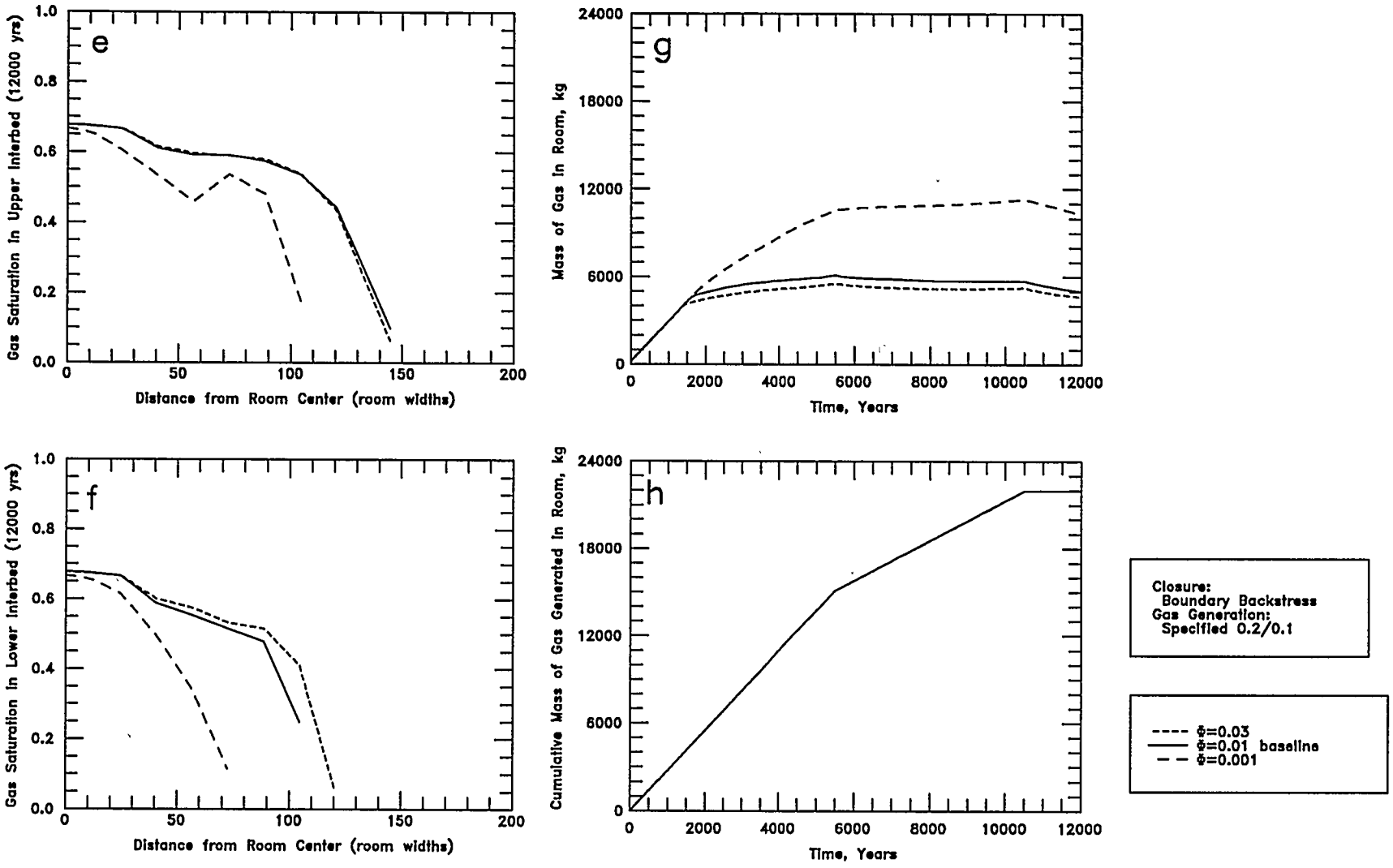

Figure B-32 (e-h). Sensitivity to Halite Porosity (constant pore volume compressibility): e - Upper Interbed Gas Profile; f - Lower Interbed Gas Profile; g - Room Gas Mass; h - Gas Generation

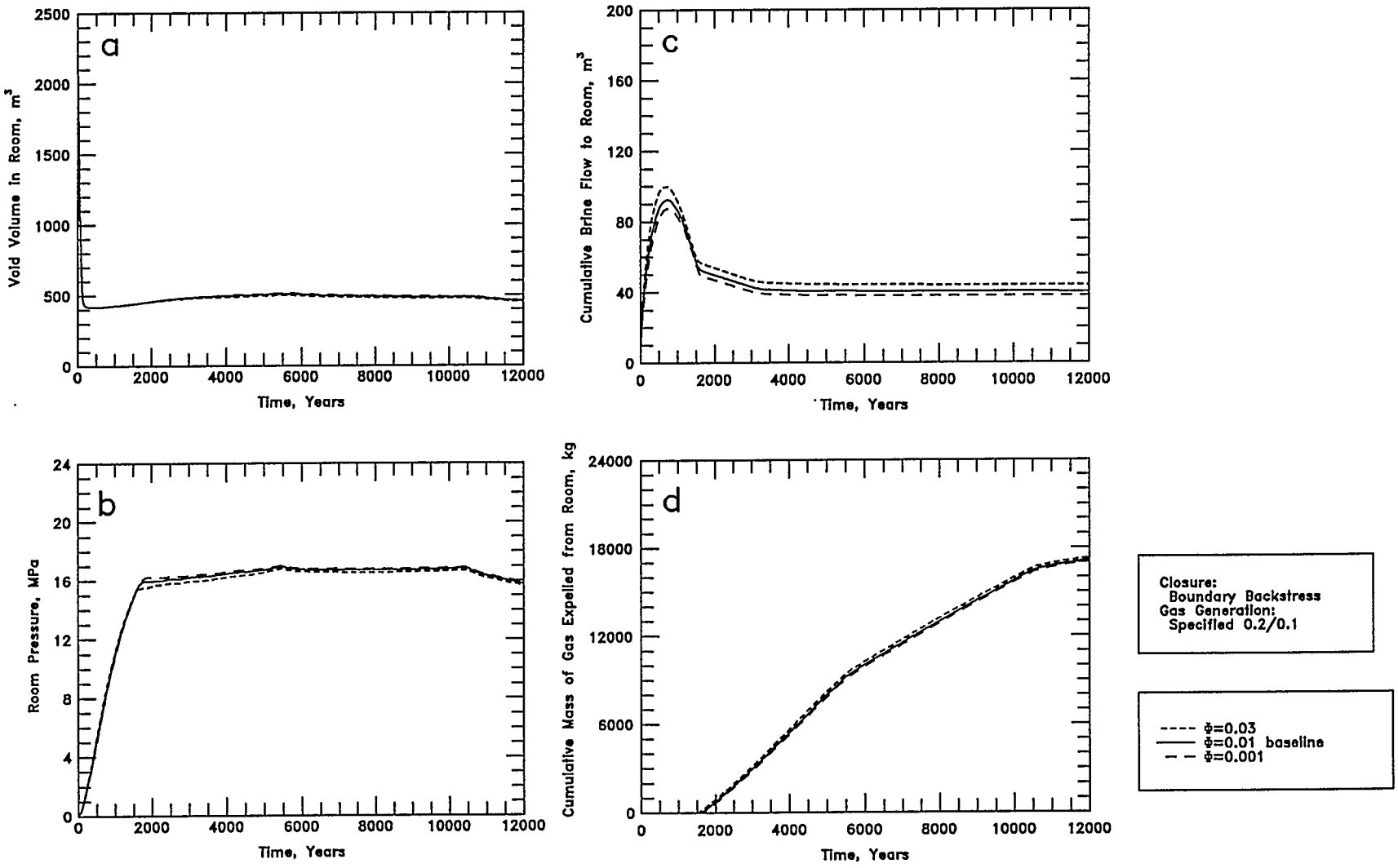

Figure B-33 (a-d). Sensitivity to Halite Porosity (constant rock compressibility): a - Void Volume; b - Gas Pressure; c - Brine Flow; d - Gas Expulsion

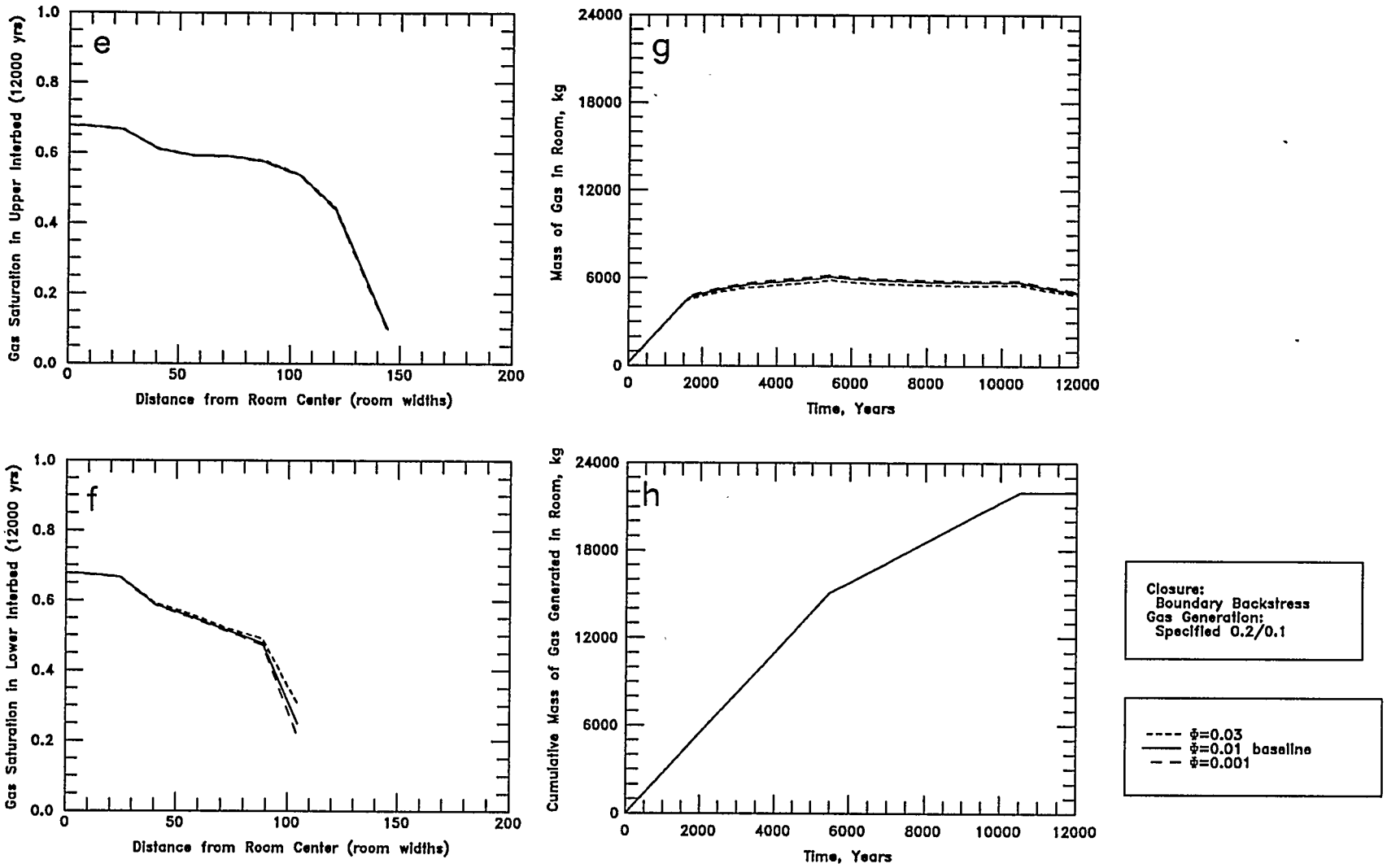

Figure B-33 (e-h). Sensitivity to Halite Porosity (constant rock compressibility): e - Upper Interbed Gas Profile; f - Lower Interbed Gas Profile; g - Room Gas Mass; h - Gas Generation

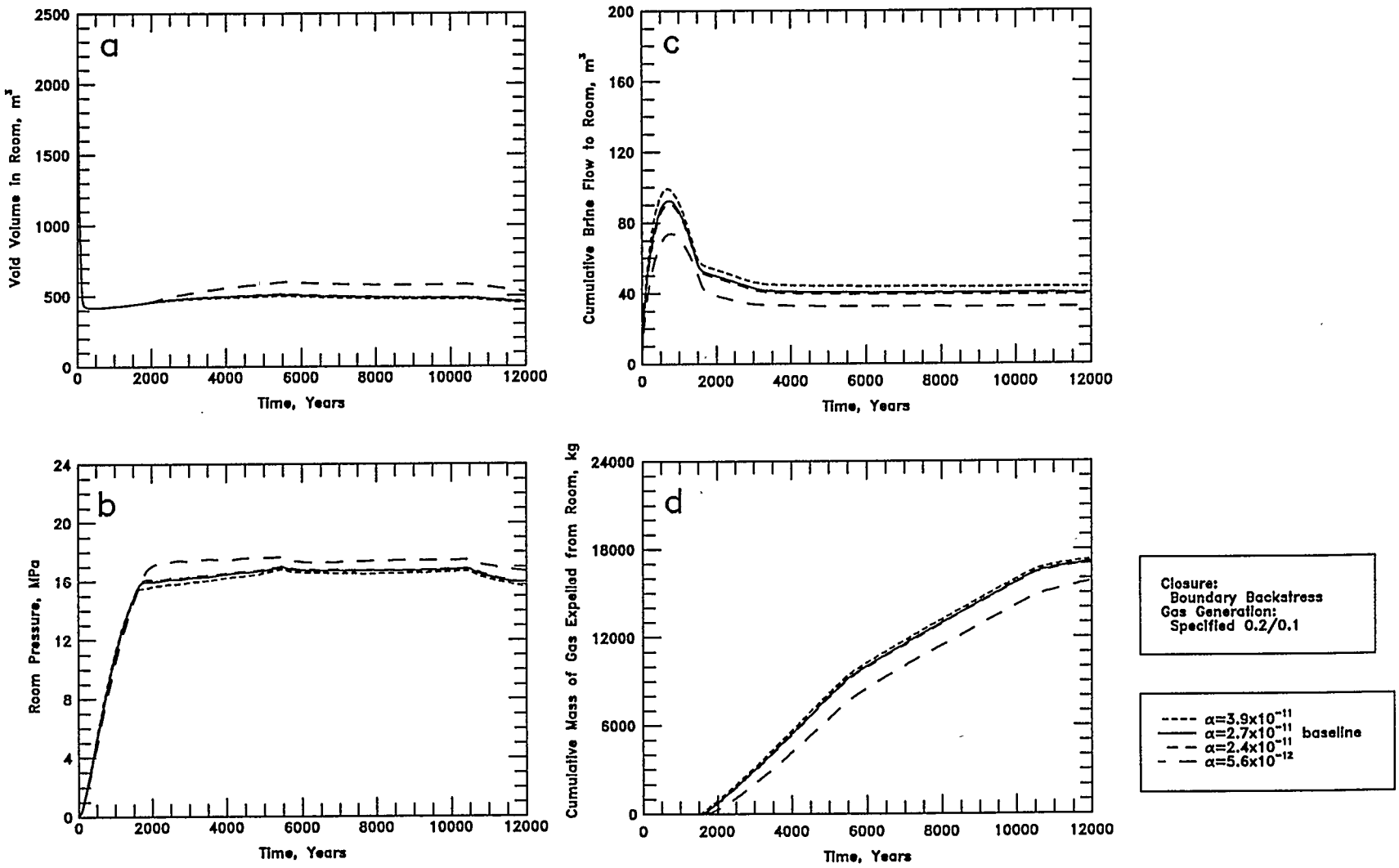

Figure B-34 (a-d). Sensitivity to Halite Rock Compressibility:
a - Void Volume; b - Gas Pressure; c - Brine Flow; d - Gas Expulsion

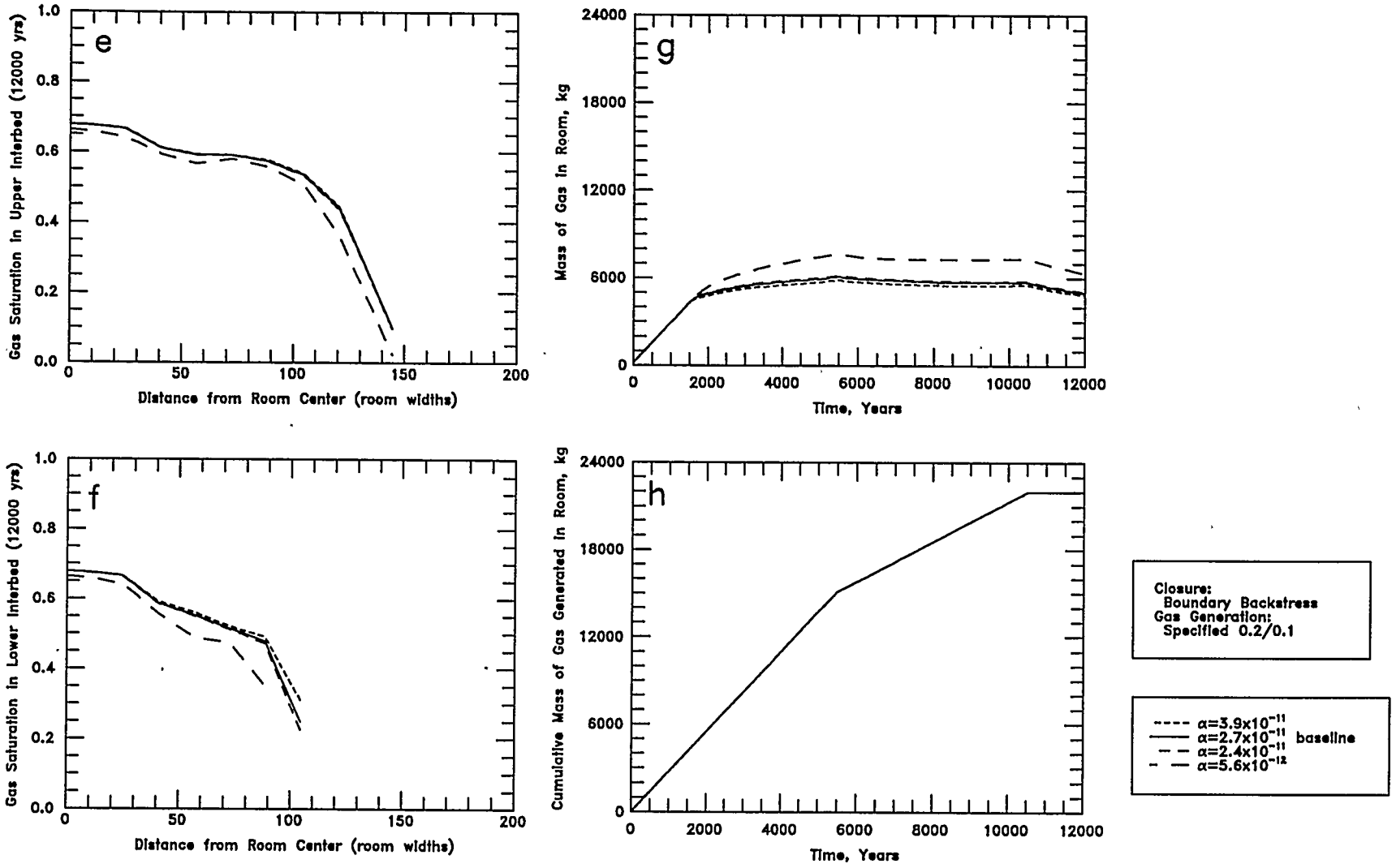

Figure B-34 (e-h). Sensitivity to Halite Rock Compressibility:
e - Upper Interbed Gas Profile; f - Lower Interbed Gas Profile;
g - Room Gas Mass; h - Gas Generation

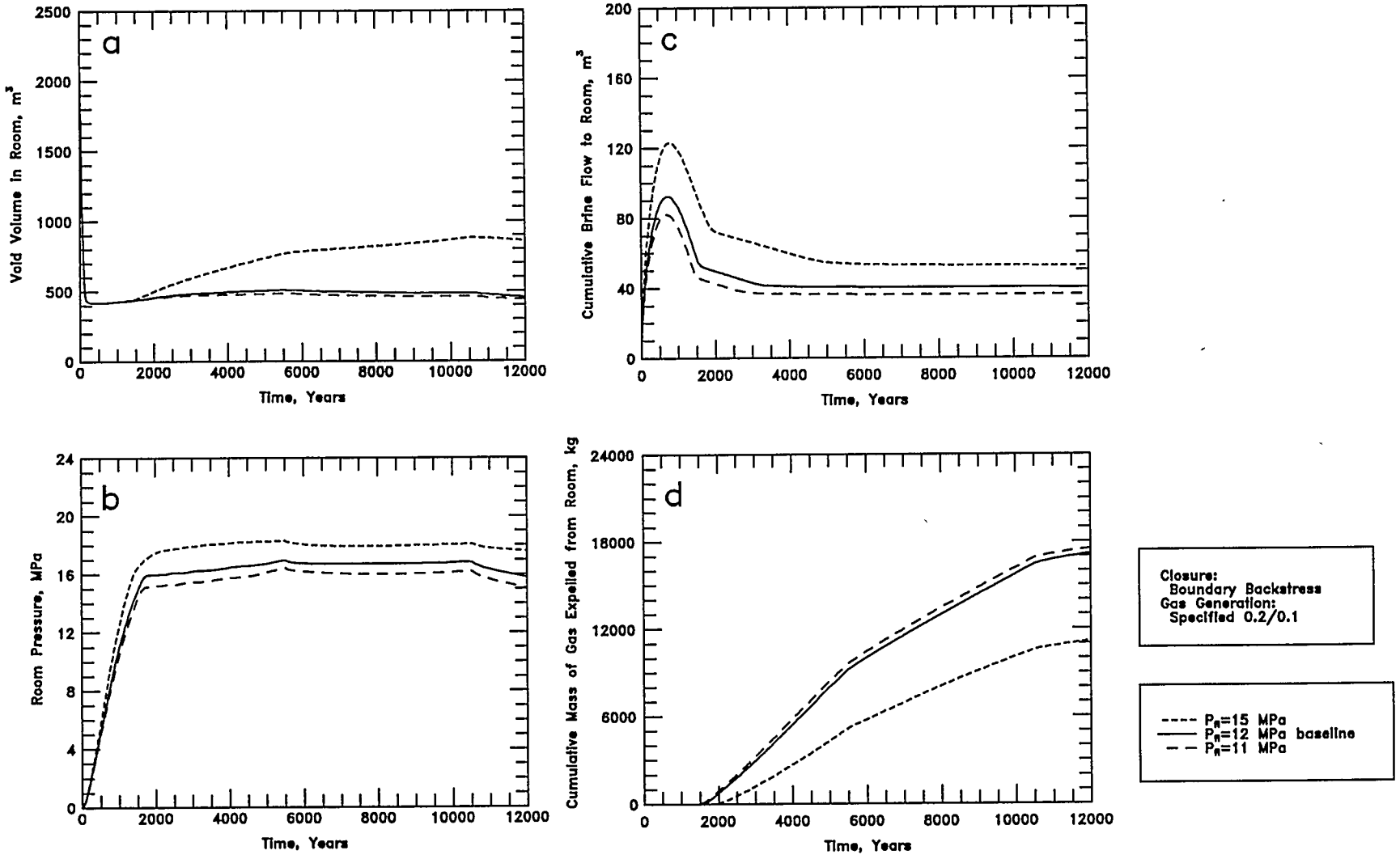

Figure B-35 (a-d). Sensitivity to Intitial Salado Formation Pressure:
a - Void Volume; b - Gas Pressure; c - Brine Flow; d - Gas Expulsion

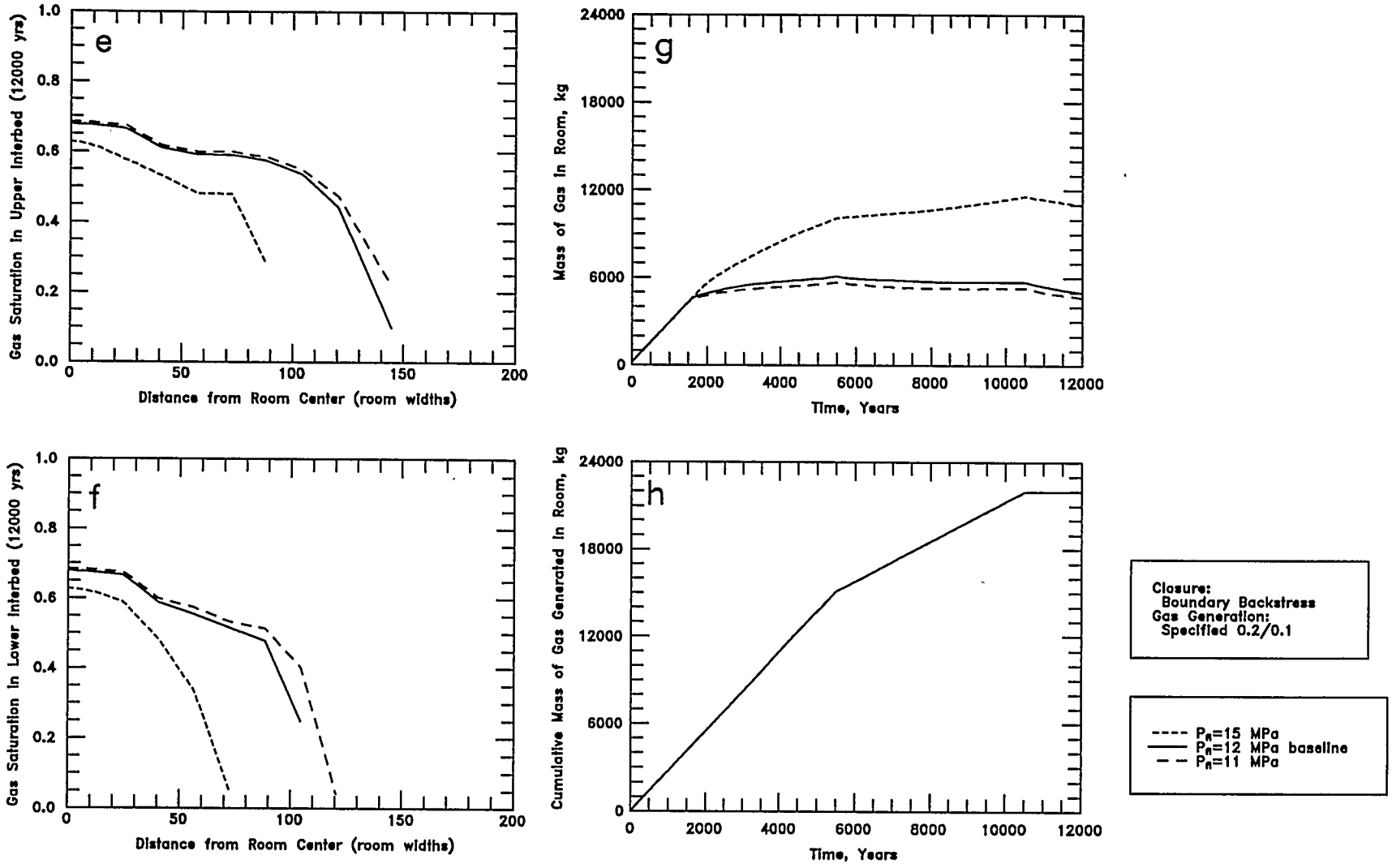

Figure B-35 (e-h). Sensitivity to Intitial Salado Formation Pressure:
e - Upper Interbed Gas Profile; f - Lower Interbed Gas Profile;
g - Room Gas Mass; h - Gas Generation

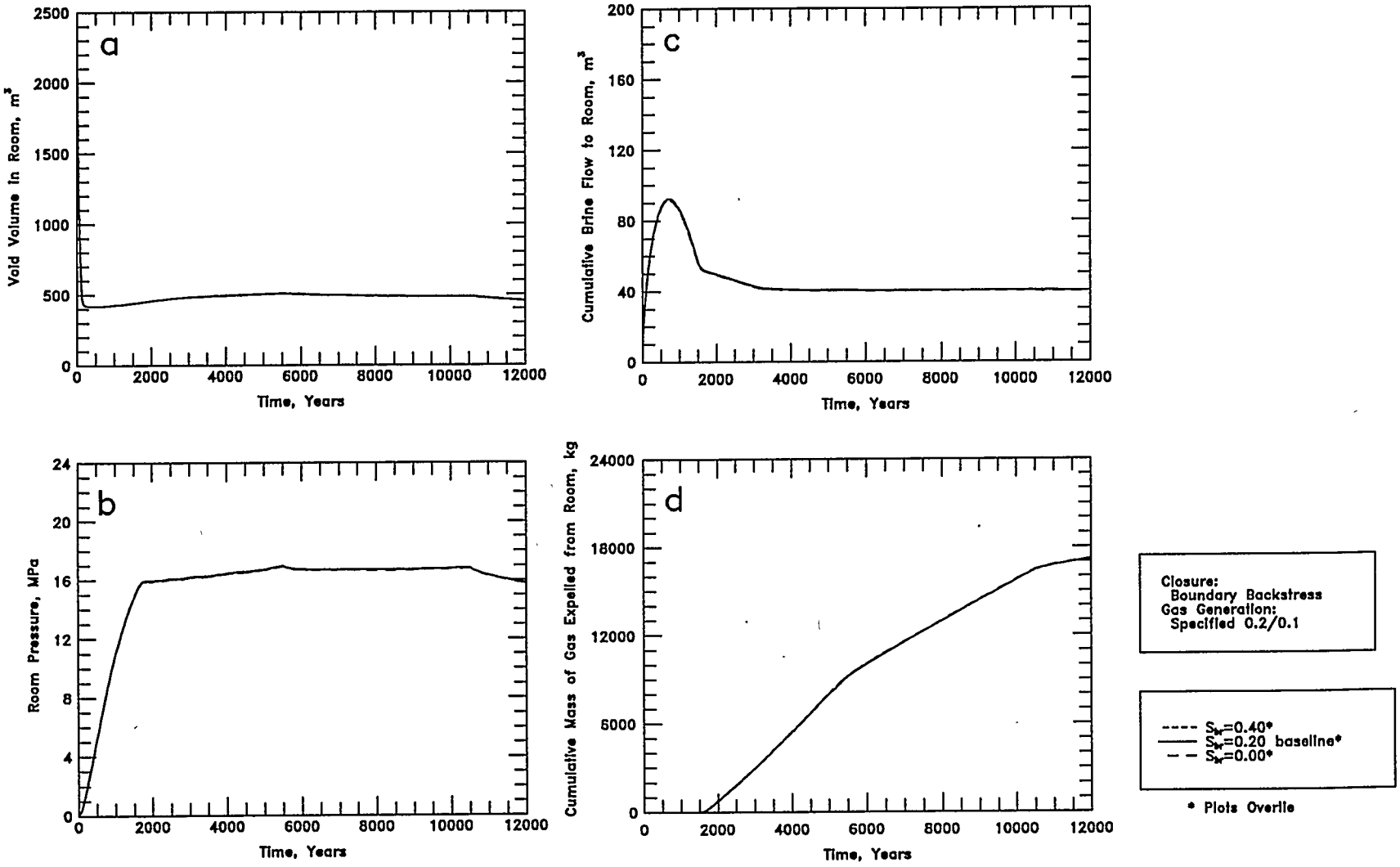

Figure B-36 (a-d). Sensitivity to Halite Residual Brine Saturation:
a - Void Volume; b - Gas Pressure; c - Brine Flow; d - Gas Expulsion

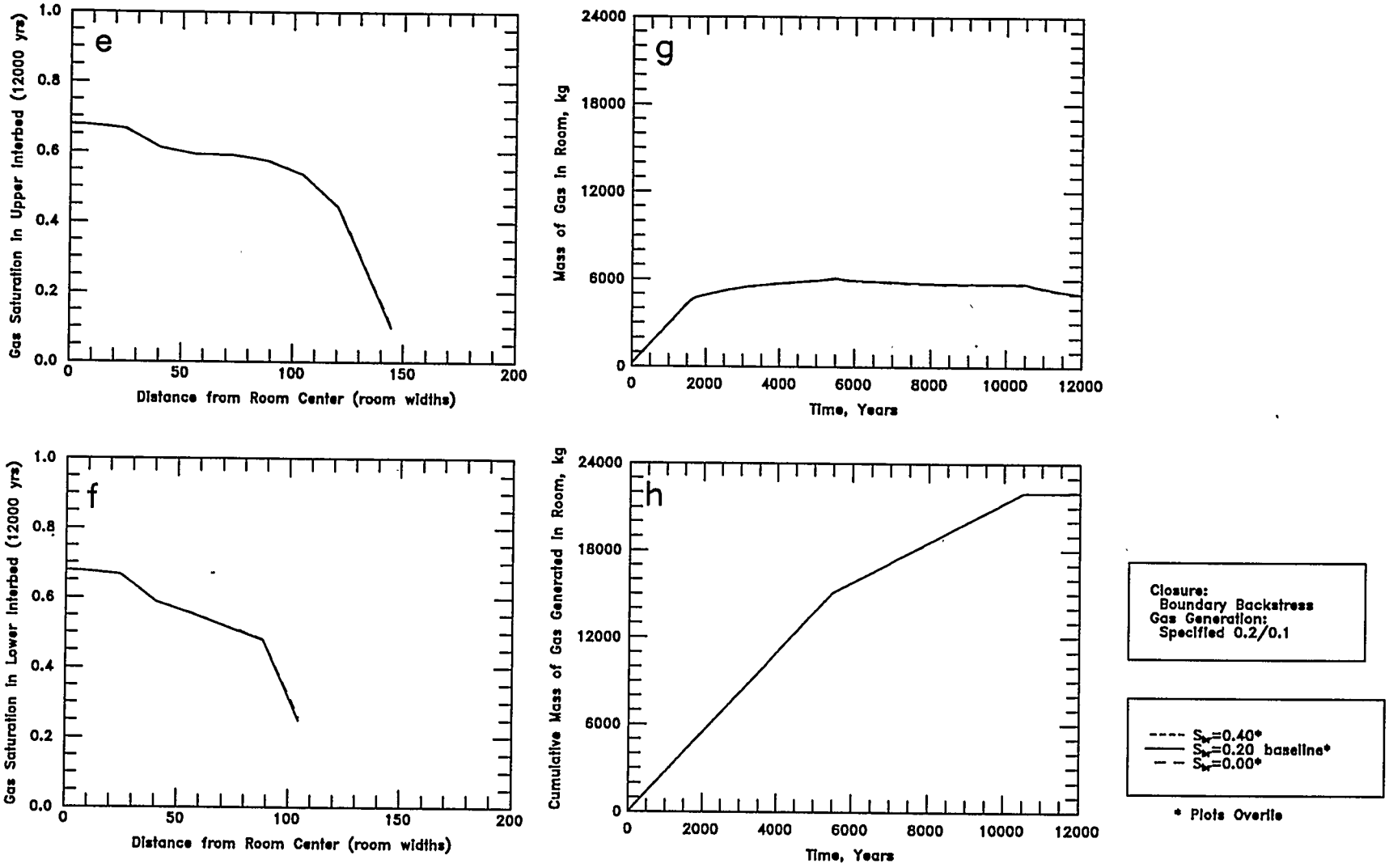

Figure B-36 (e-h). Sensitivity to Halite Residual Brine Saturation:
e - Upper Interbed Gas Profile; f - Lower Interbed Gas Profile;
g - Room Gas Mass; h - Gas Generation

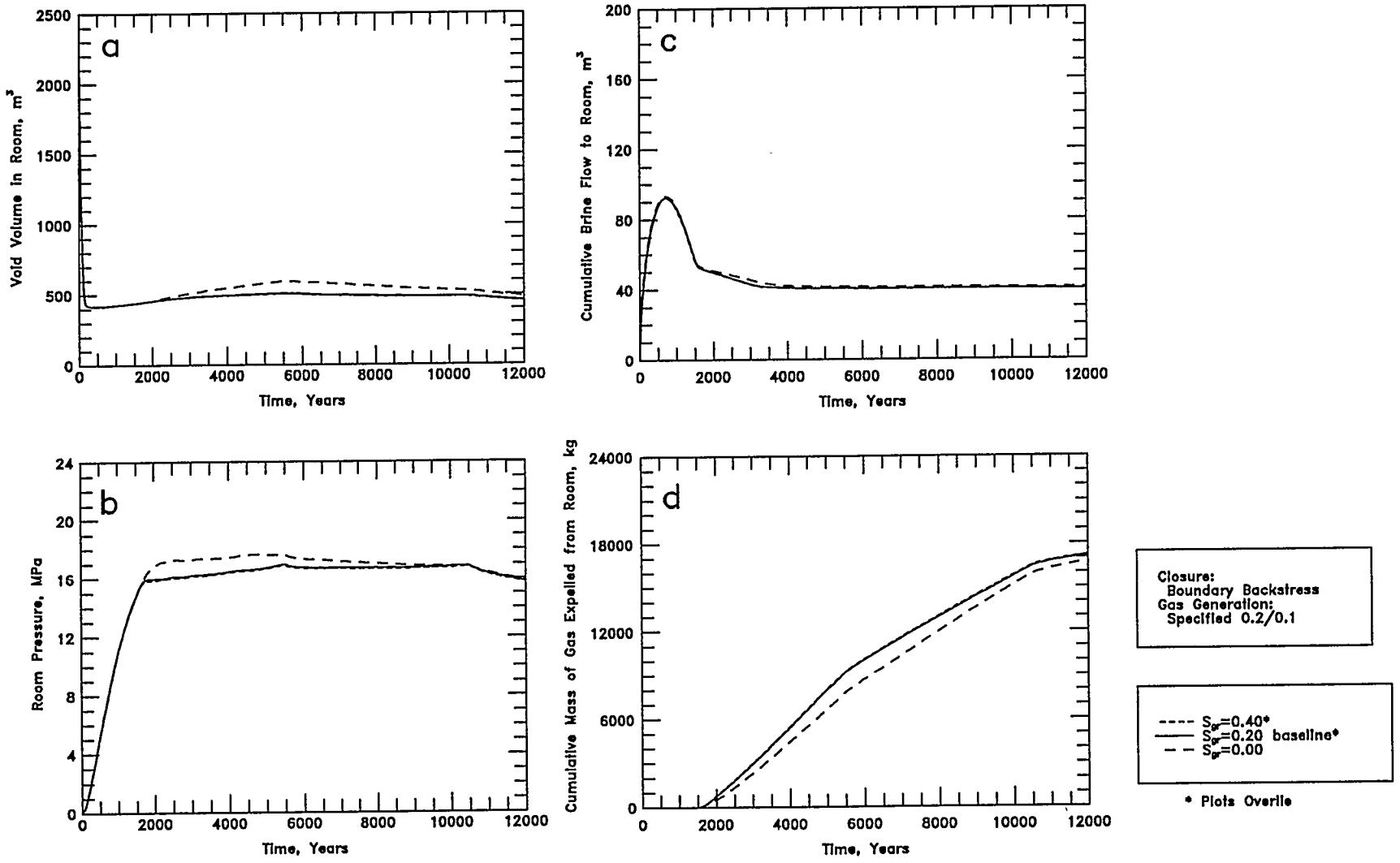

Figure B-37 (a-d). Sensitivity to Halite Residual Gas Saturation:
a - Void Volume; b - Gas Pressure; c - Brine Flow; d - Gas Expulsion

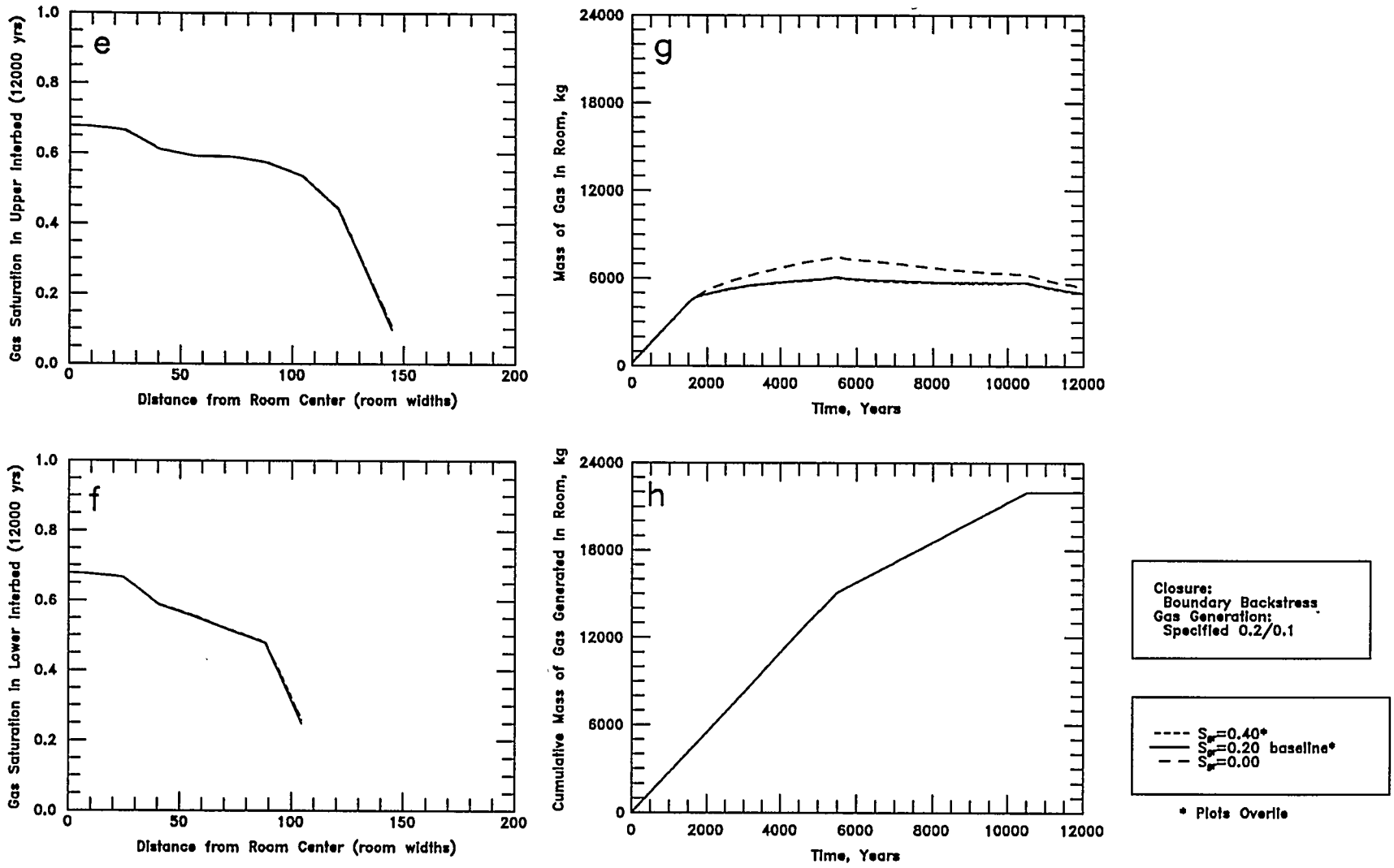

Figure B-37 (e-h). Sensitivity to Halite Residual Gas Saturation:
e - Upper Interbed Gas Profile; f - Lower Interbed Gas Profile;
g - Room Gas Mass; h - Gas Generation

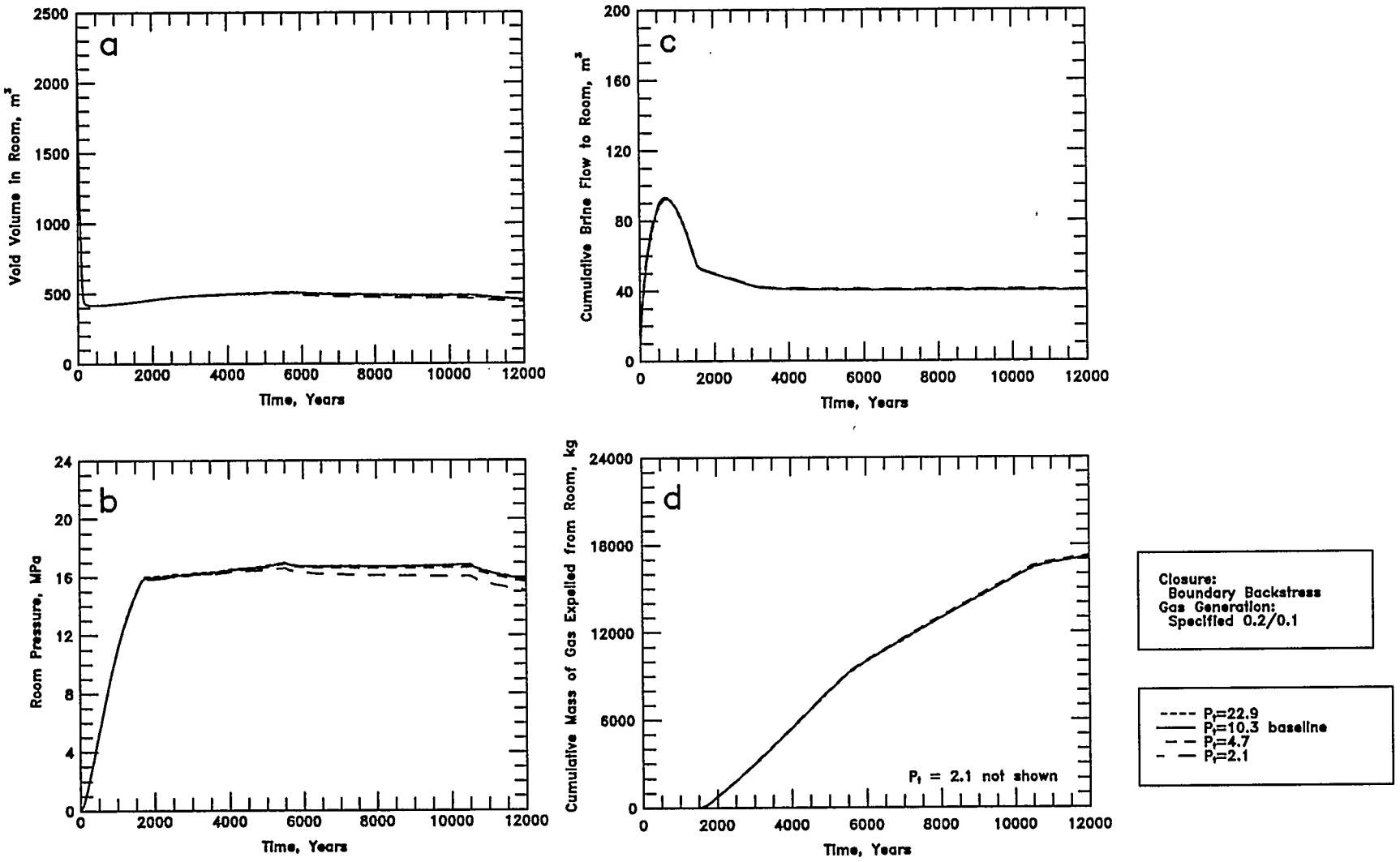

Figure B-38 (a-d). Sensitivity to Halite Threshold Pressure:
a - Void Volume; b - Gas Pressure; c - Brine Flow; d - Gas Expulsion

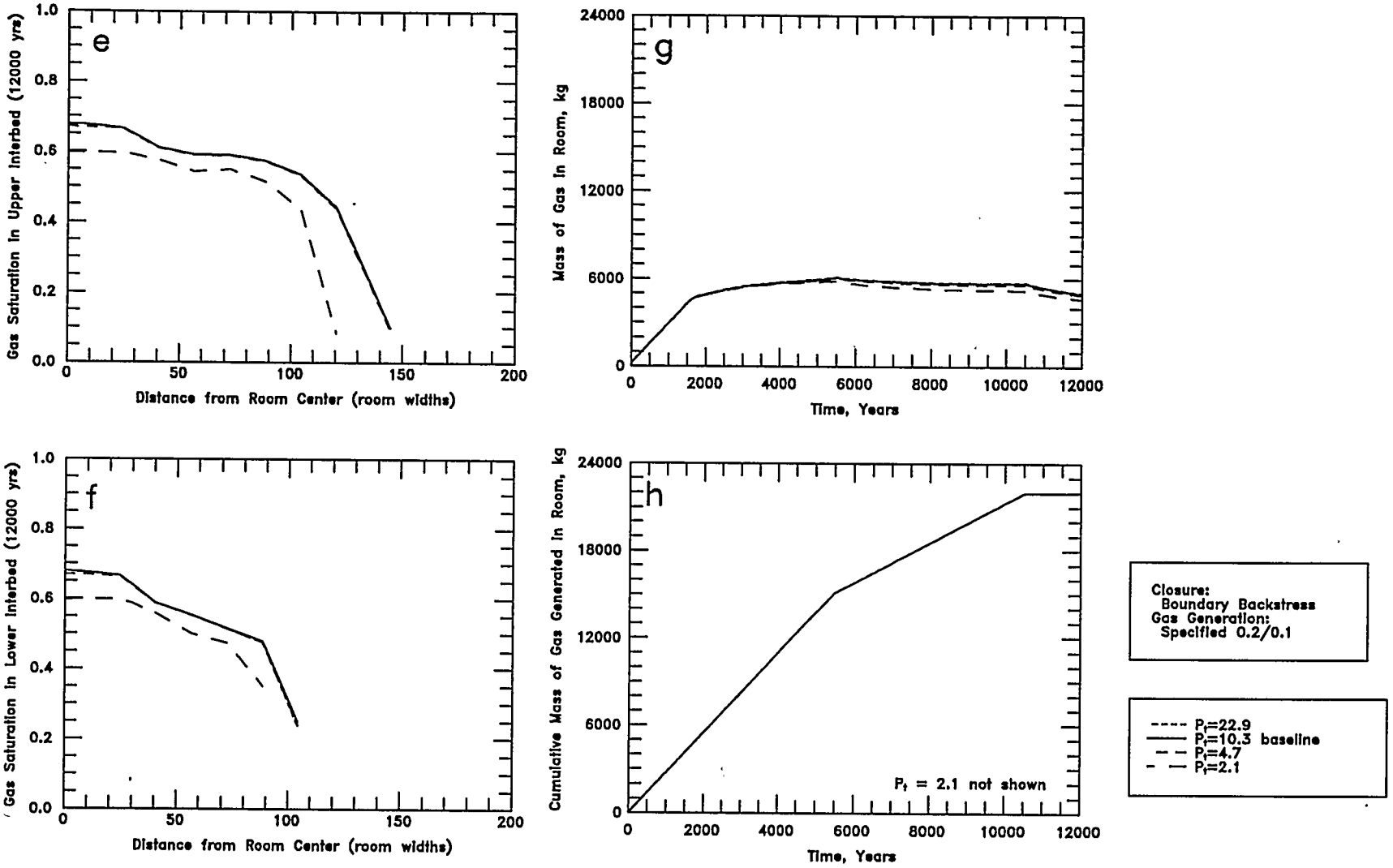

Figure B-38 (e-h). Sensitivity to Halite Threshold Pressure:
e - Upper Interbed Gas Profile; f - Lower Interbed Gas Profile;
g - Room Gas Mass; h - Gas Generation

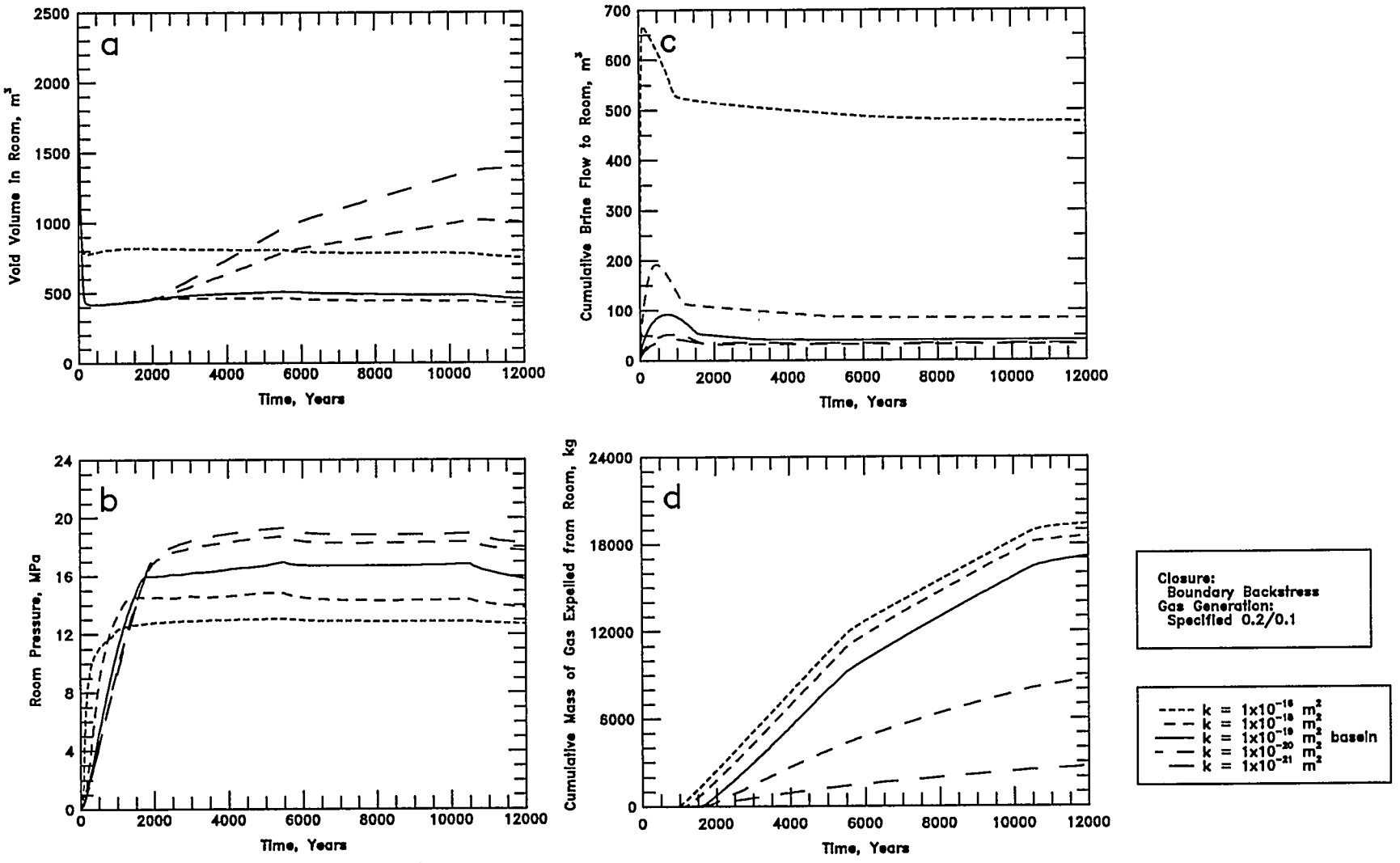

Figure B-39 (a-d). Sensitivity to Interbed Intrinsic Permeability (constant threshold pressure): a - Void Volume; b - Gas Pressure; c - Brine Flow; d - Gas Expulsion

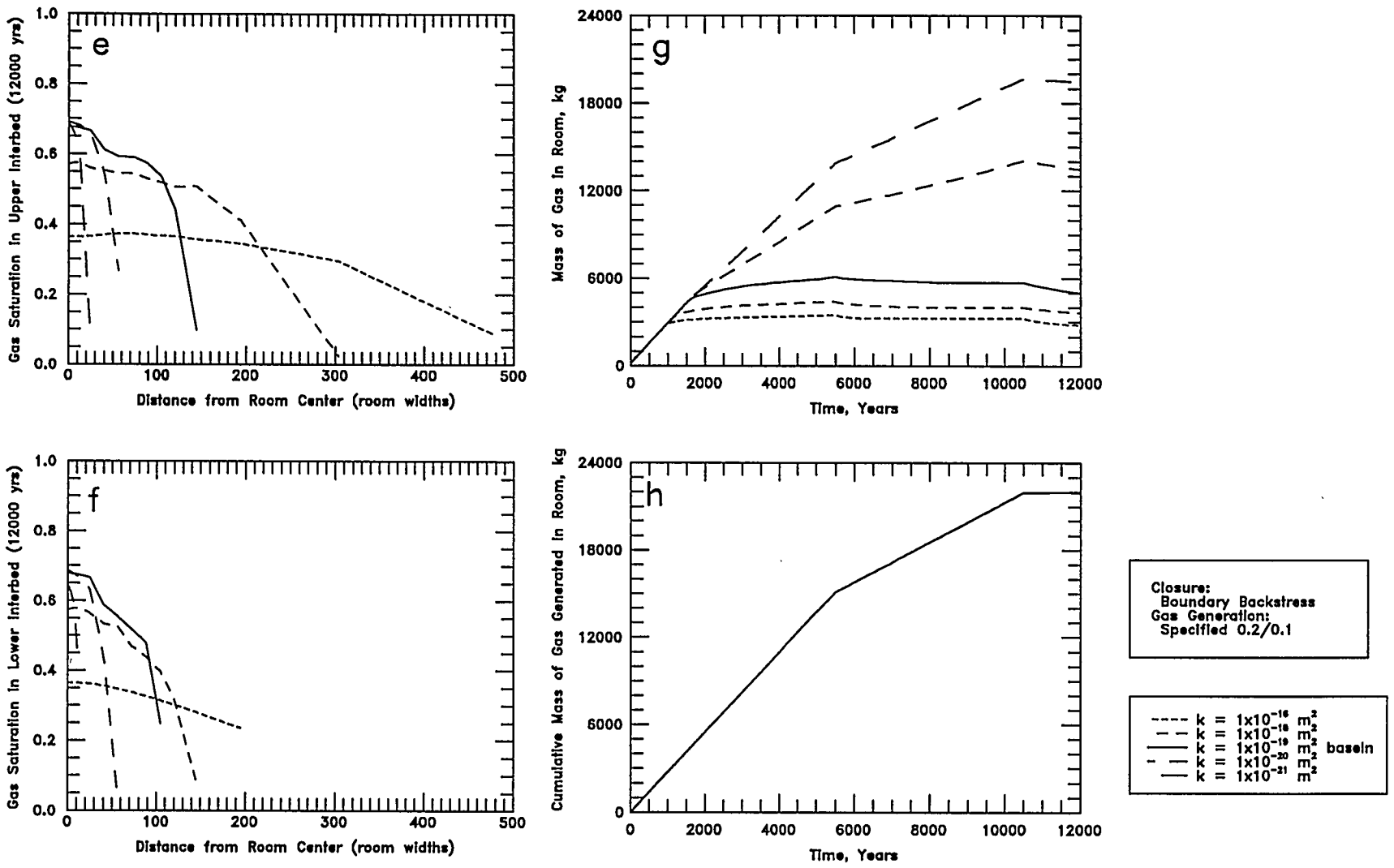

Figure B-39 (e-h). Sensitivity to Interbed Intrinsic Permeability (constant threshold pressure): e - Upper Interbed Gas Profile; f - Lower Interbed Gas Profile; g - Room Gas Mass; h - Gas Generation

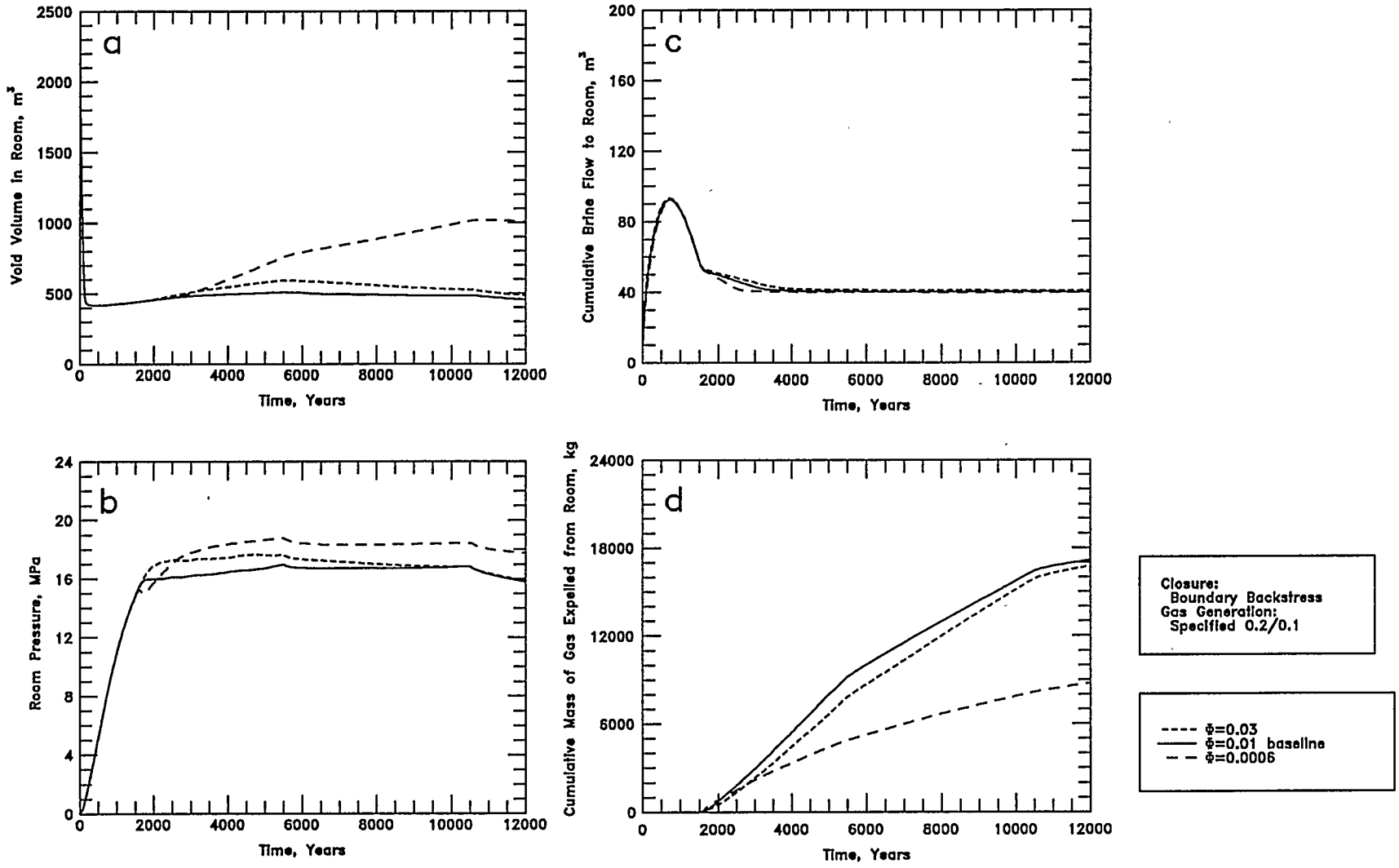

Figure B-40 (a-d). Sensitivity to Interbed Porosity (constant pore volume compressibility): a - Void Volume; b - Gas Pressure; c - Brine Flow; d - Gas Expulsion

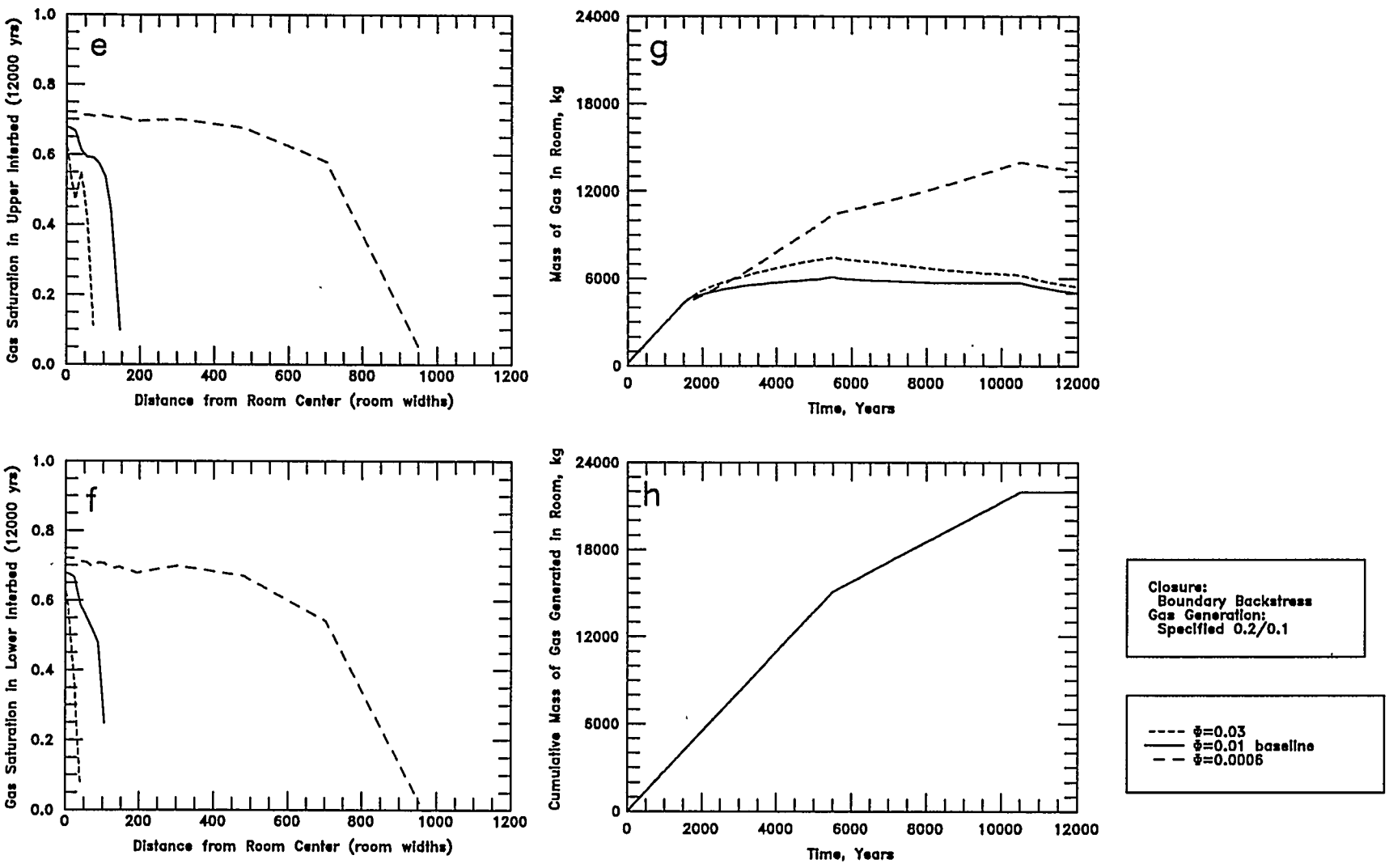

Figure B-40 (e-h). Sensitivity to Interbed Porosity (constant pore volume compressibility): e - Upper Interbed Gas Profile; f - Lower Interbed Gas Profile; g - Room Gas Mass; h - Gas Generation

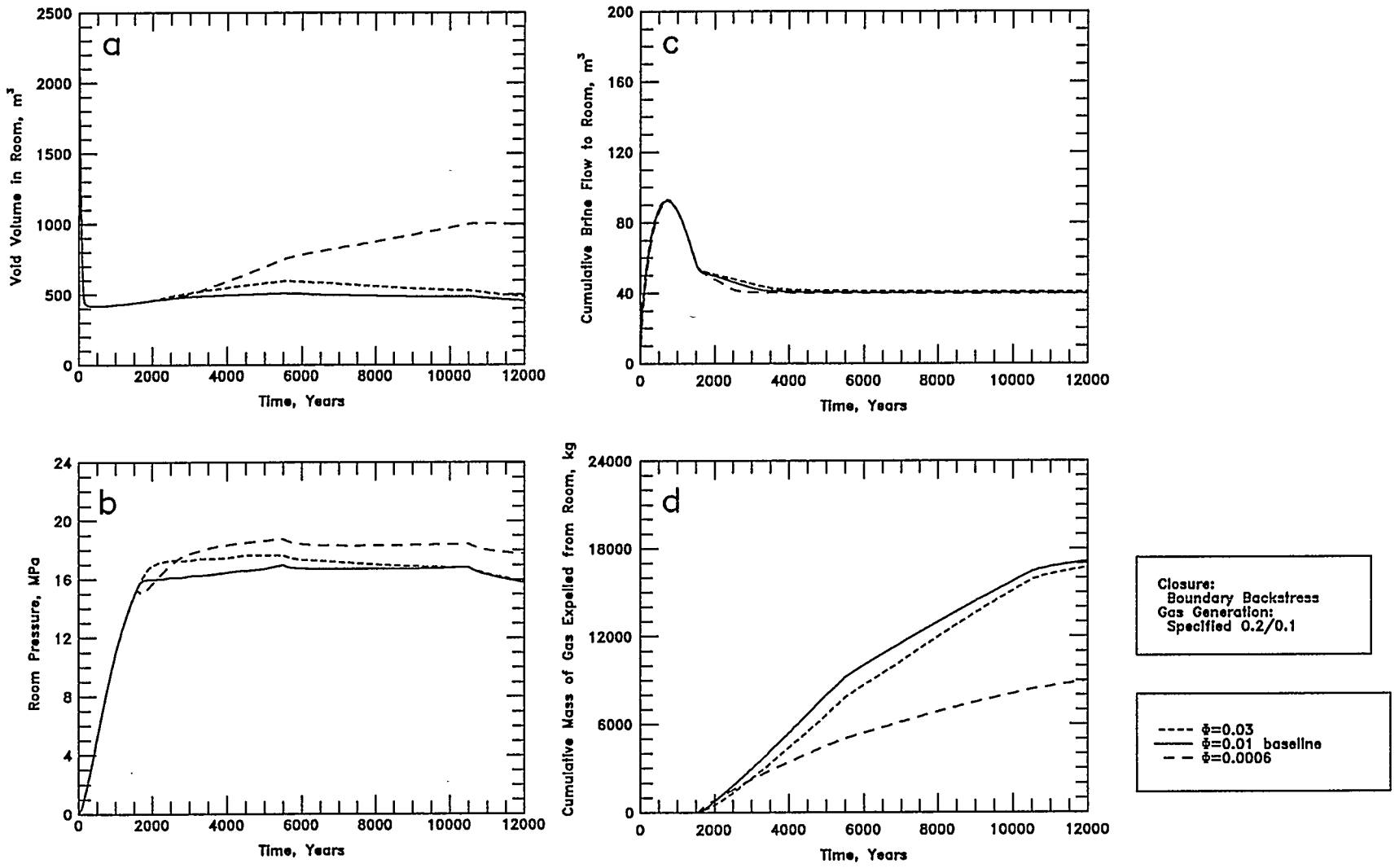

Figure B-41 (a-d). Sensitivity to Interbed Porosity (constant rock compressibility): a - Void Volume; b - Gas Pressure; c - Brine Flow; d - Gas Expulsion

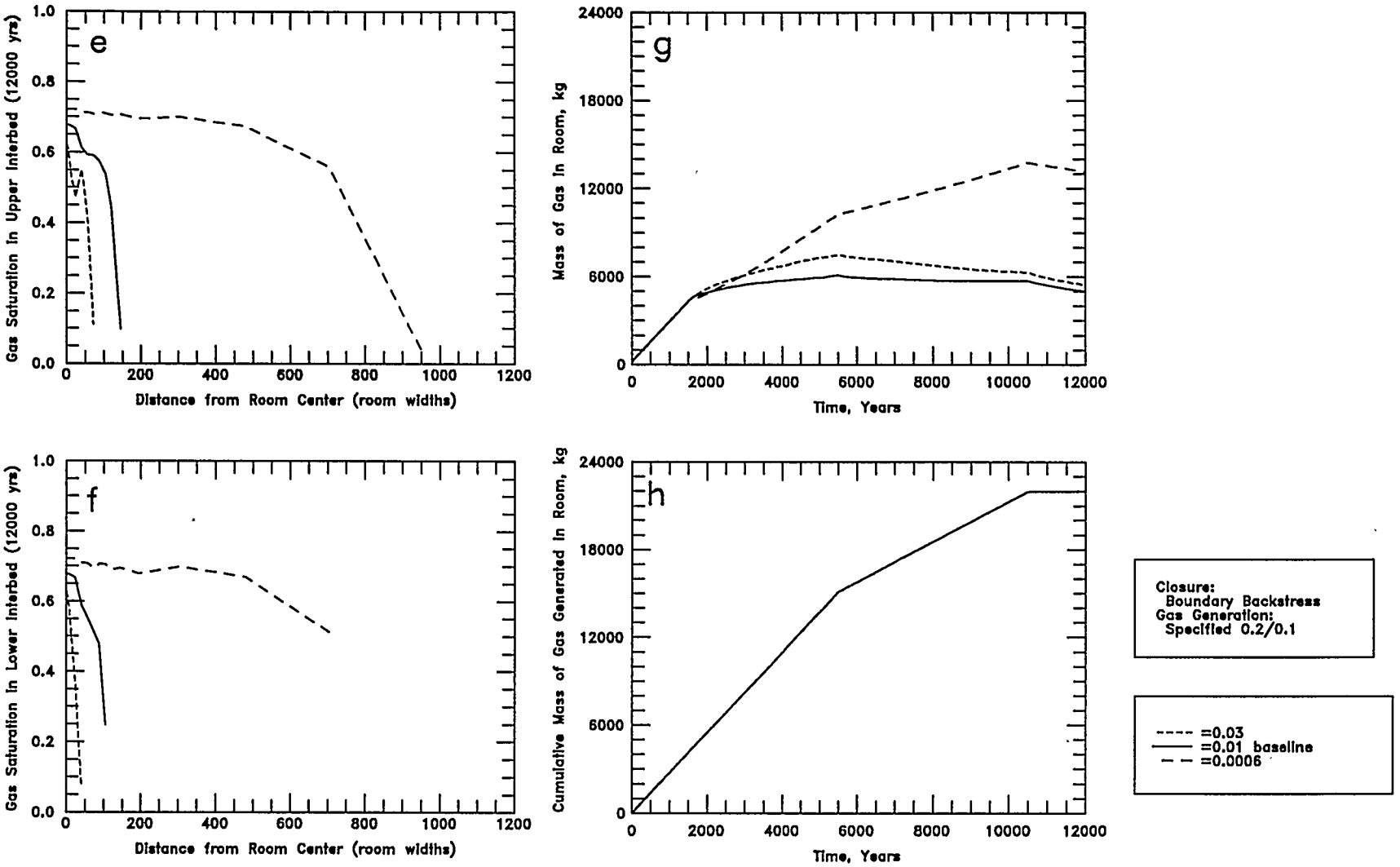

Figure B-41 (e-h). Sensitivity to Interbed Porosity (constant rock compressibility): e - Upper Interbed Gas Profile; f - Lower Interbed Gas Profile; g - Room Gas Mass; h - Gas Generation

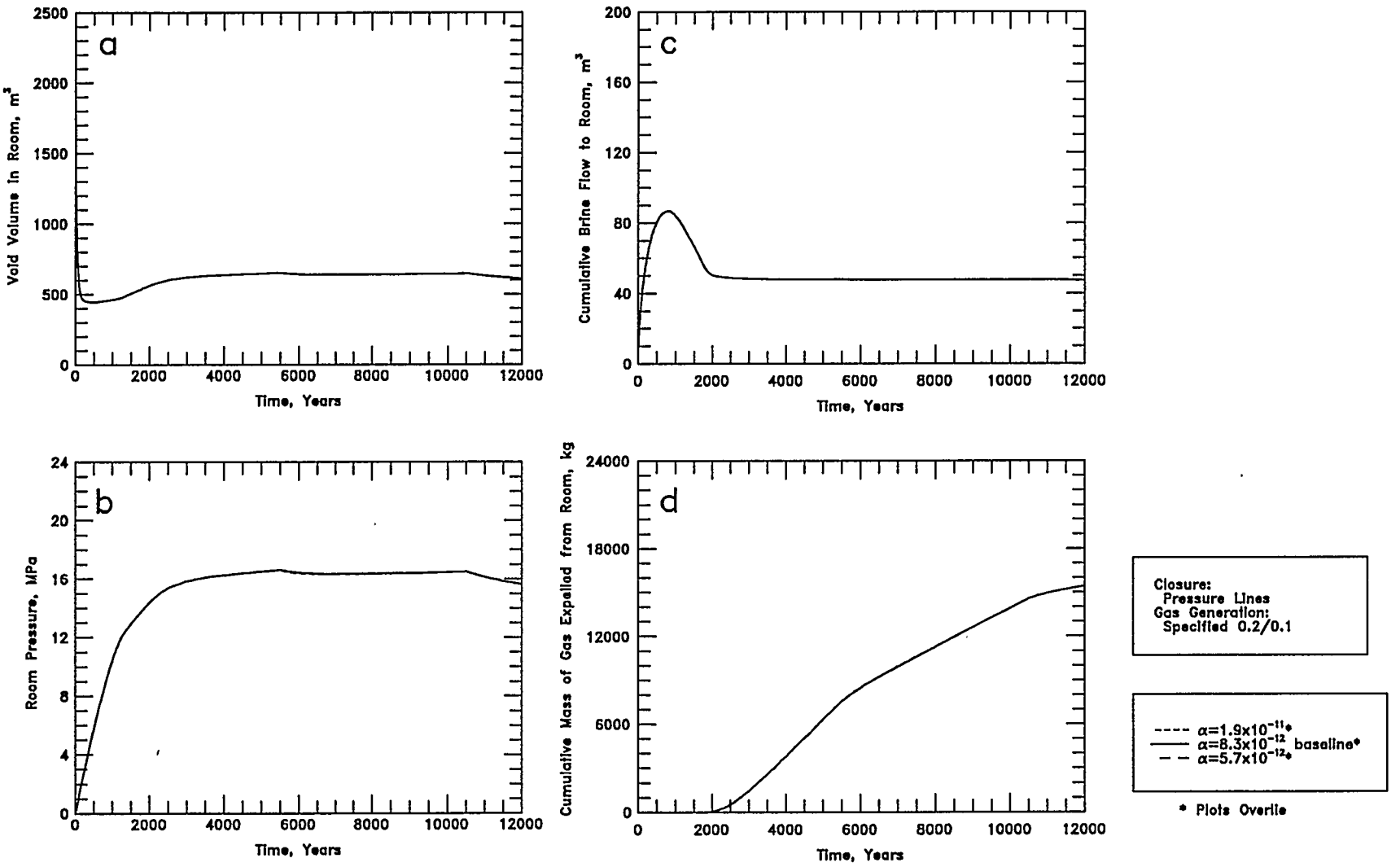

Figure B–42 (a–d). Sensitivity to Interbed Rock Compressibility:
a – Void Volume; b – Gas Pressure; c – Brine Flow; d – Gas Expulsion

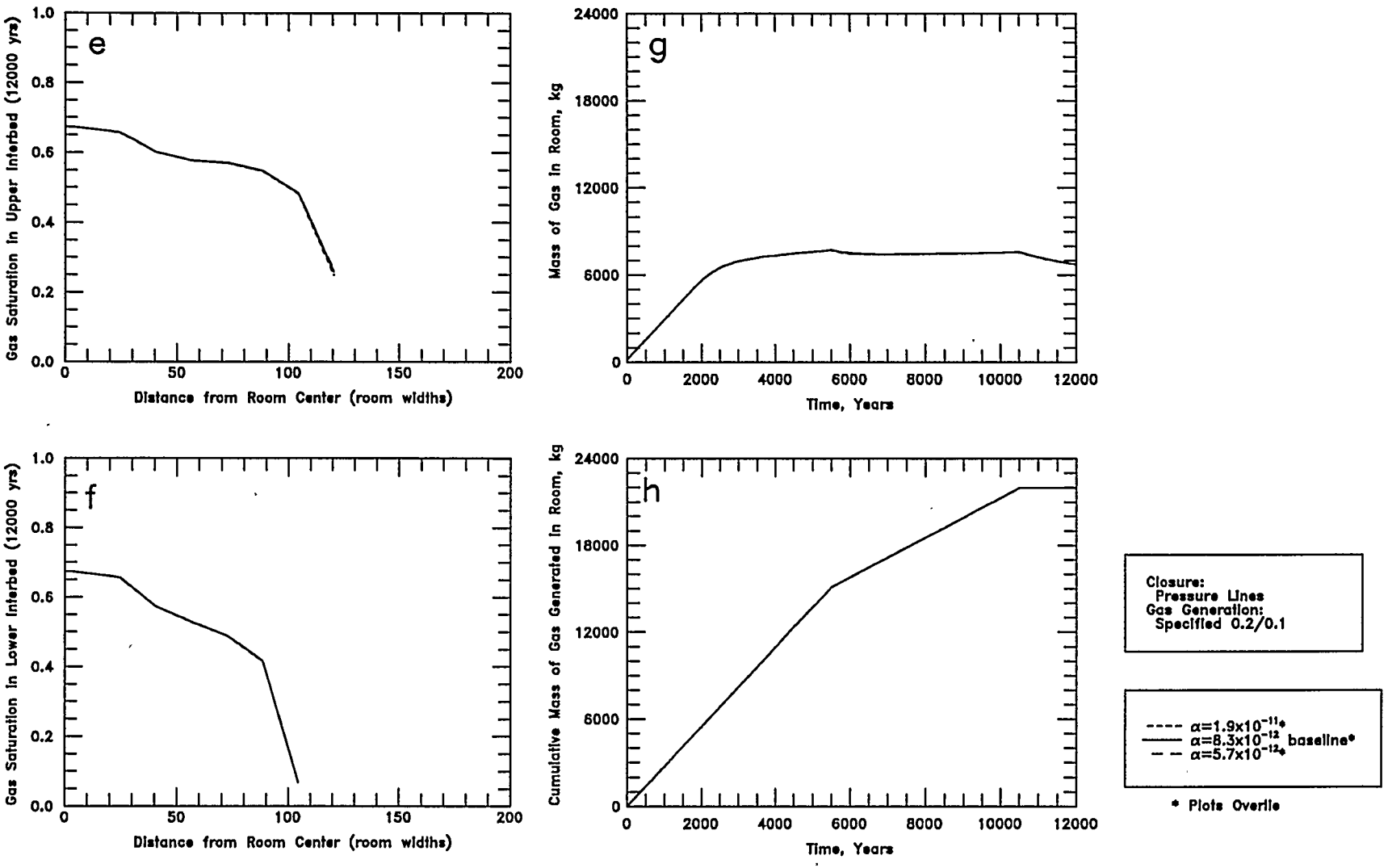

Figure B-42 (e-h). Sensitivity to Interbed Rock Compressibility:
e - Upper Interbed Gas Profile; f - Lower Interbed Gas Profile;
g - Room Gas Mass; h - Gas Generation

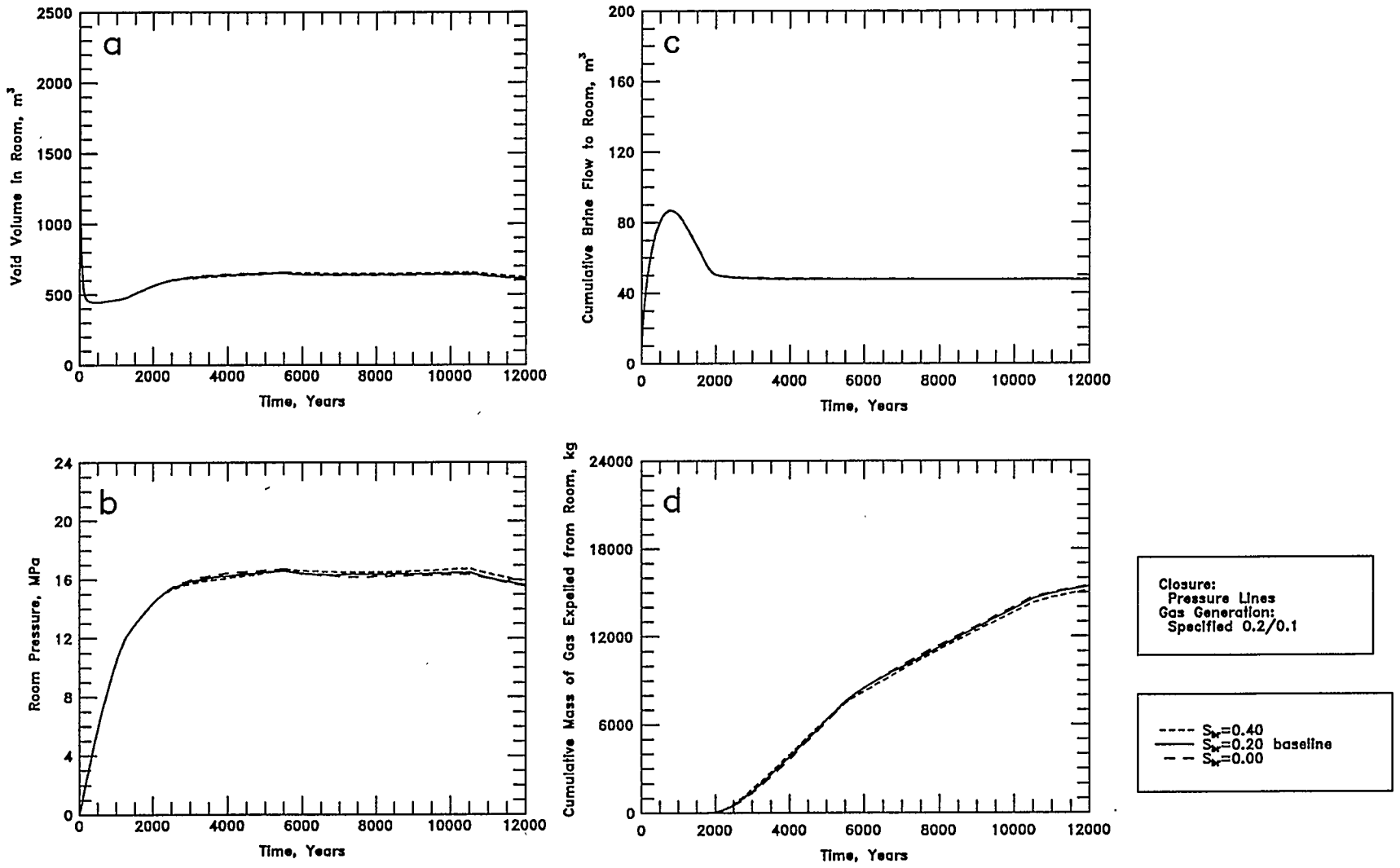

Figure B-43 (a-d). Sensitivity to Interbed Residual Brine Santuration:
a - Void Volume; b - Gas Pressure; c - Brine Flow; d - Gas Expulsion

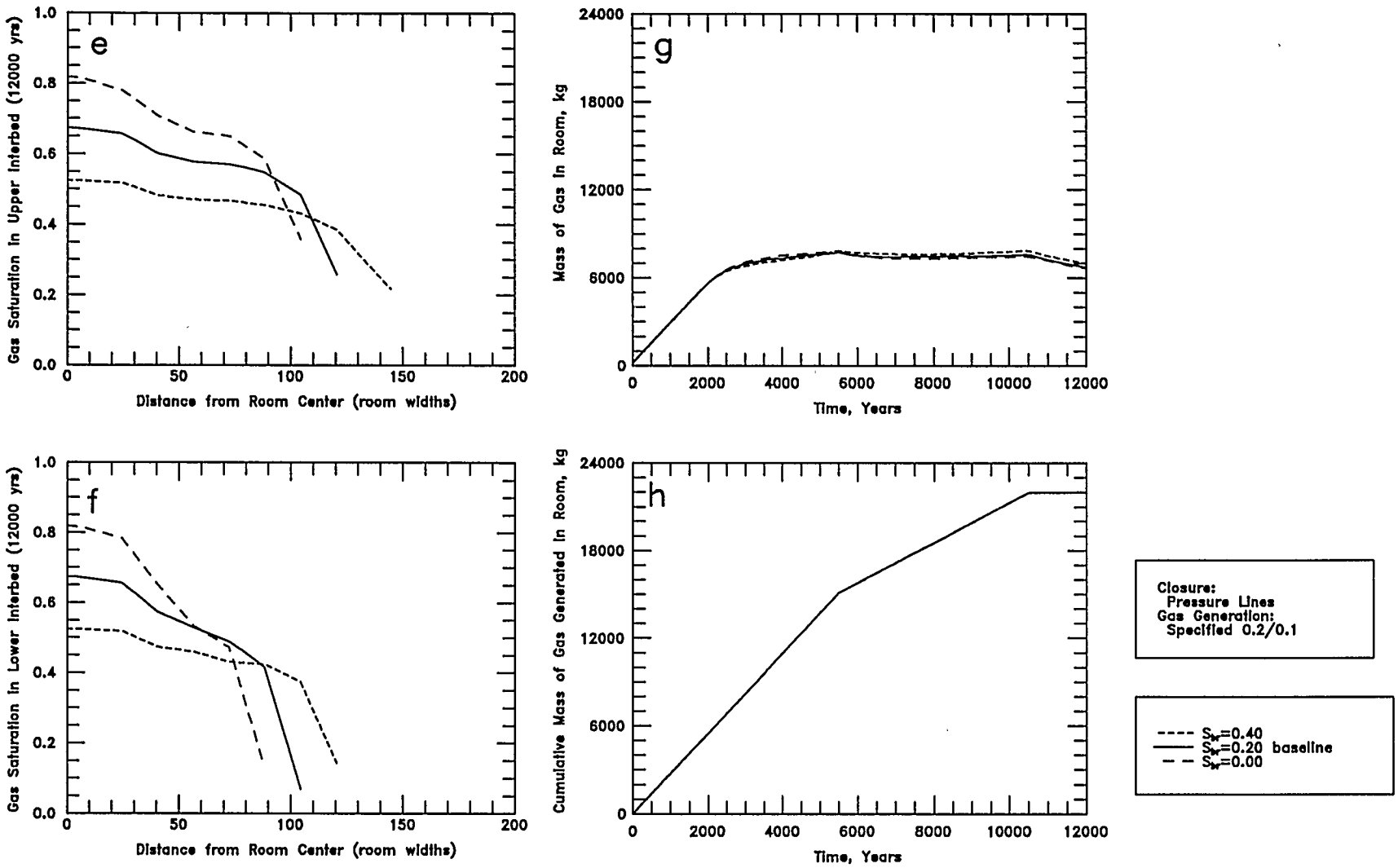

Figure B-43 (e-h). Sensitivity to Interbed Residual Brine Santuration:
e - Upper Interbed Gas Profile; f - Lower Interbed Gas Profile;
g - Room Gas Mass; h - Gas Generation

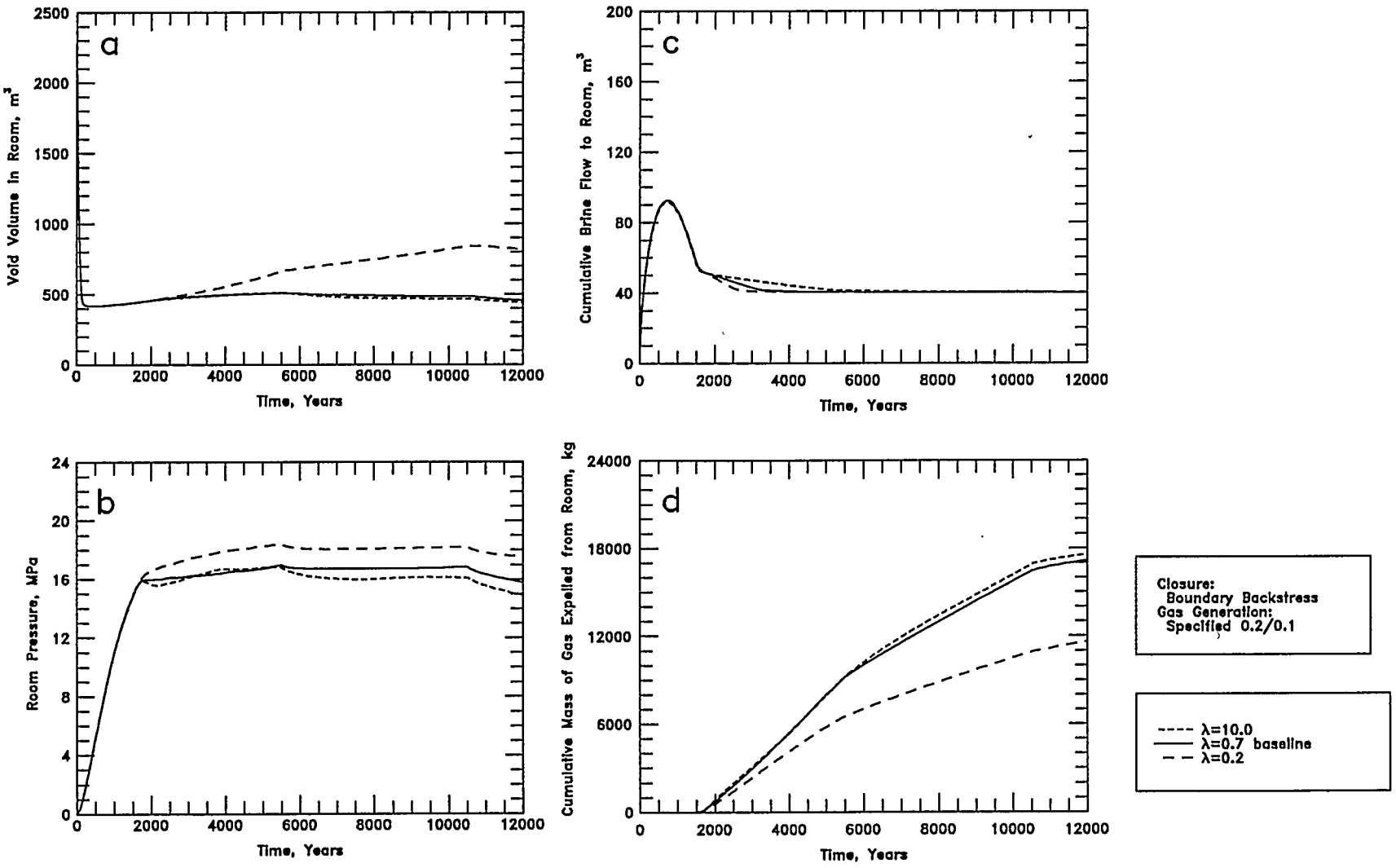

Figure B-44 (a-d). Sensitivity to Interbed Pore-Size Lambda:
a - Void Volume; b - Gas Pressure; c - Brine Flow; d - Gas Expulsion

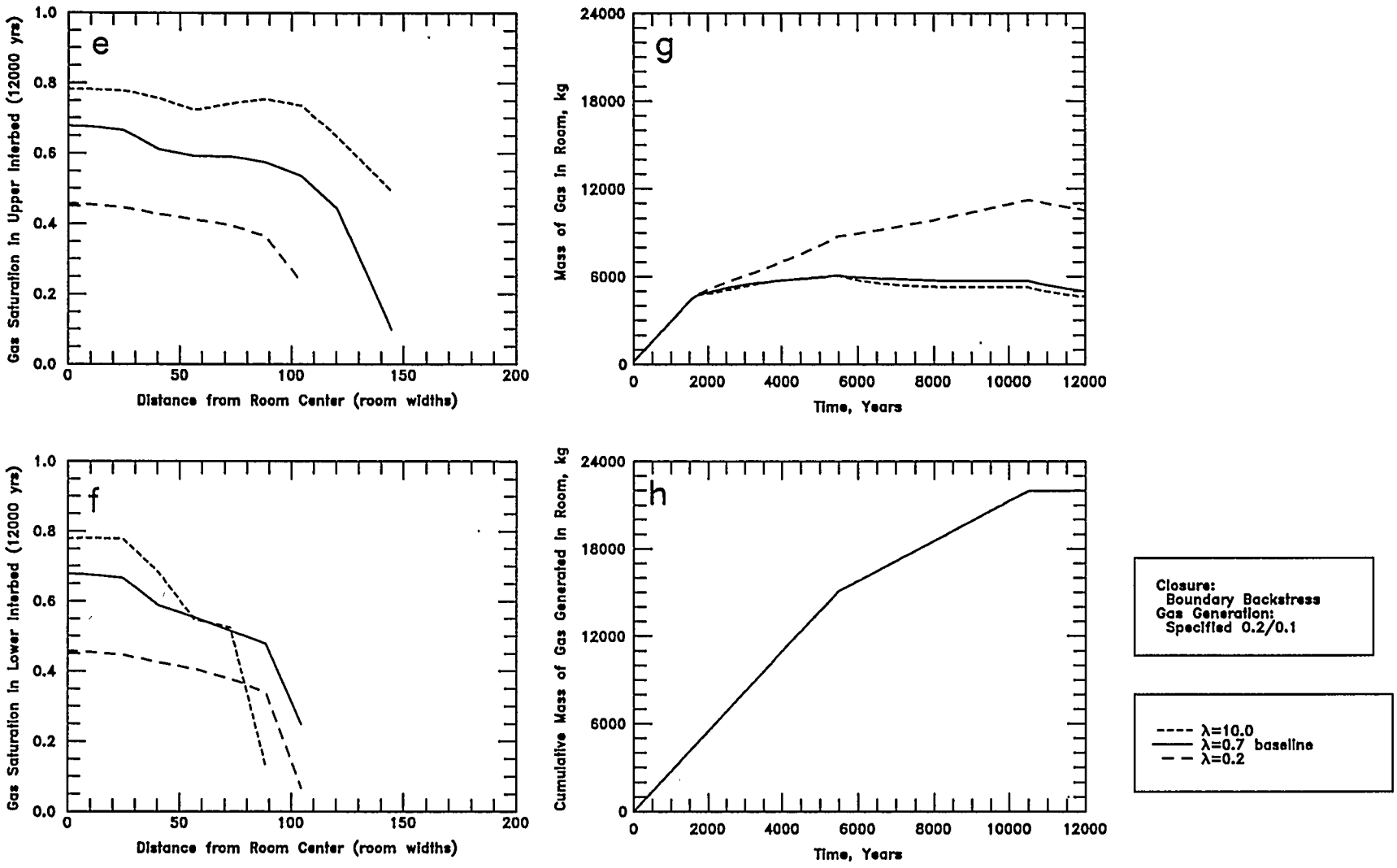

Figure B-44 (e-h). Sensitivity to Interbed Pore-Size Lambda:
e - Upper Interbed Gas Profile; f - Lower Interbed Gas Profile;
g - Room Gas Mass; h - Gas Generation

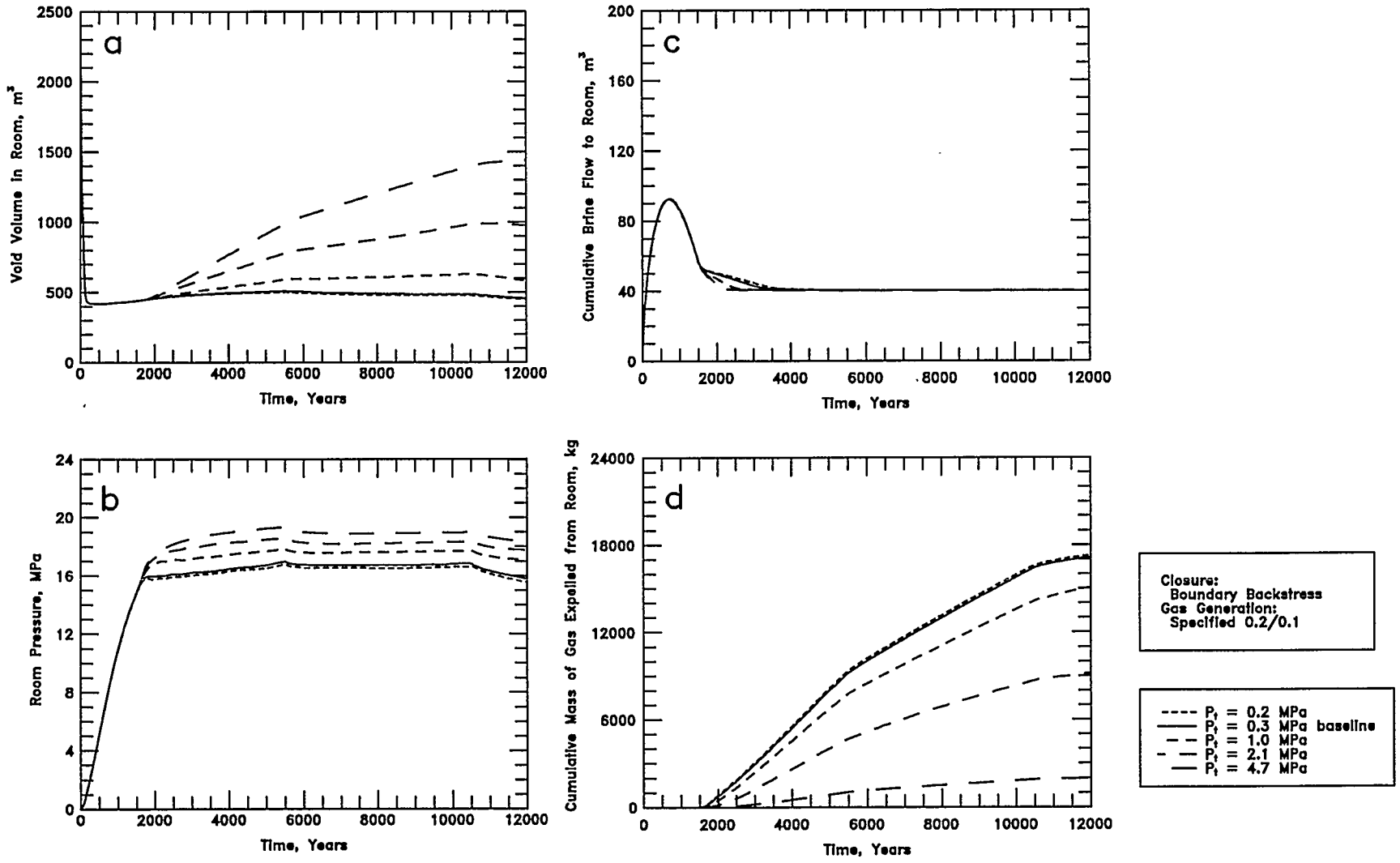

Figure B–45 (a–d). Sensitivity to Interbed Threshold Pressure:
a – Void Volume; b – Gas Pressure; c – Brine Flow; d – Gas Expulsion

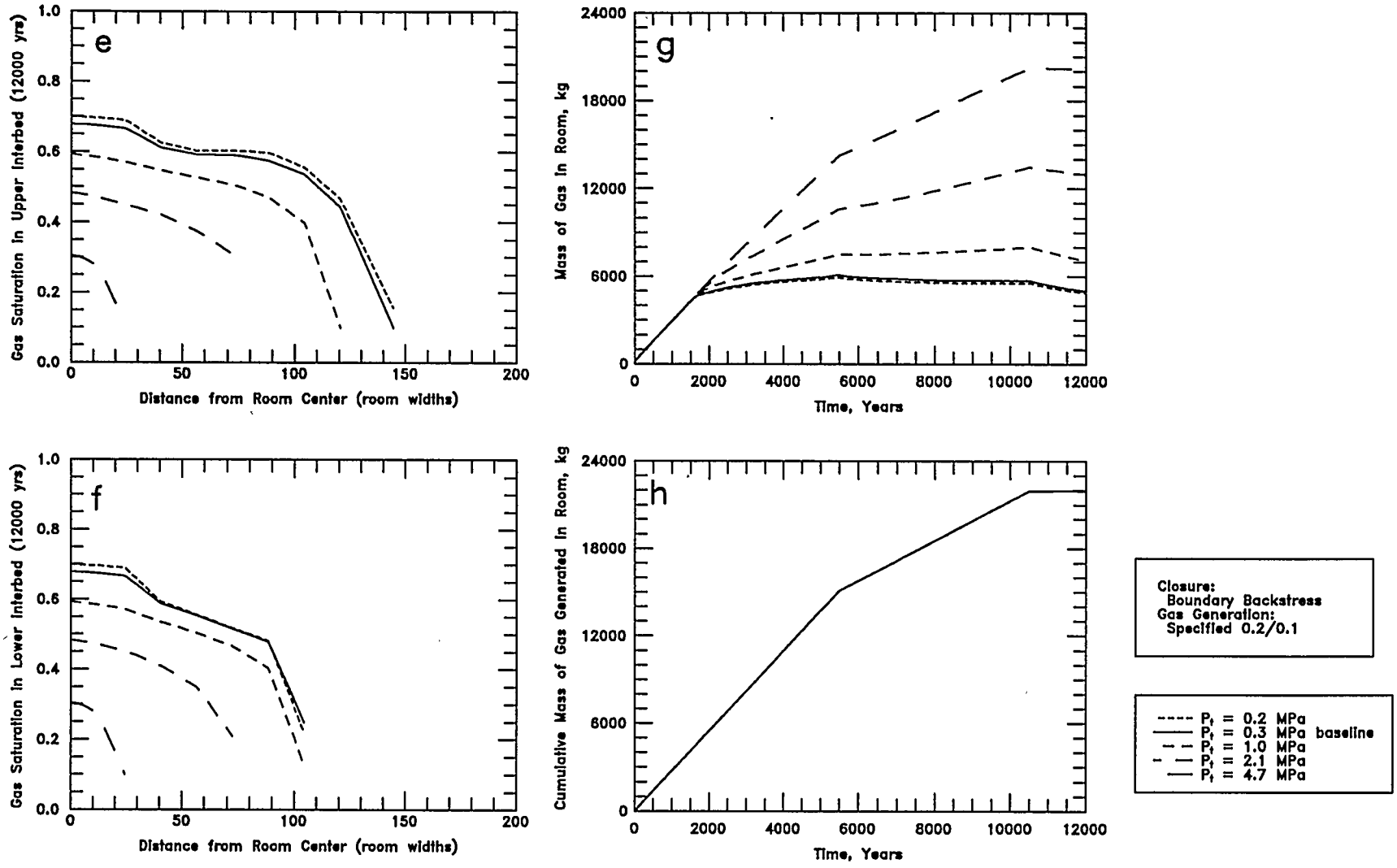

Figure B–45 (e–h). Sensitivity to Interbed Threshold Pressure:
e – Upper Interbed Gas Profile; f – Lower Interbed Gas Profile;
g – Room Gas Mass; h – Gas Generation

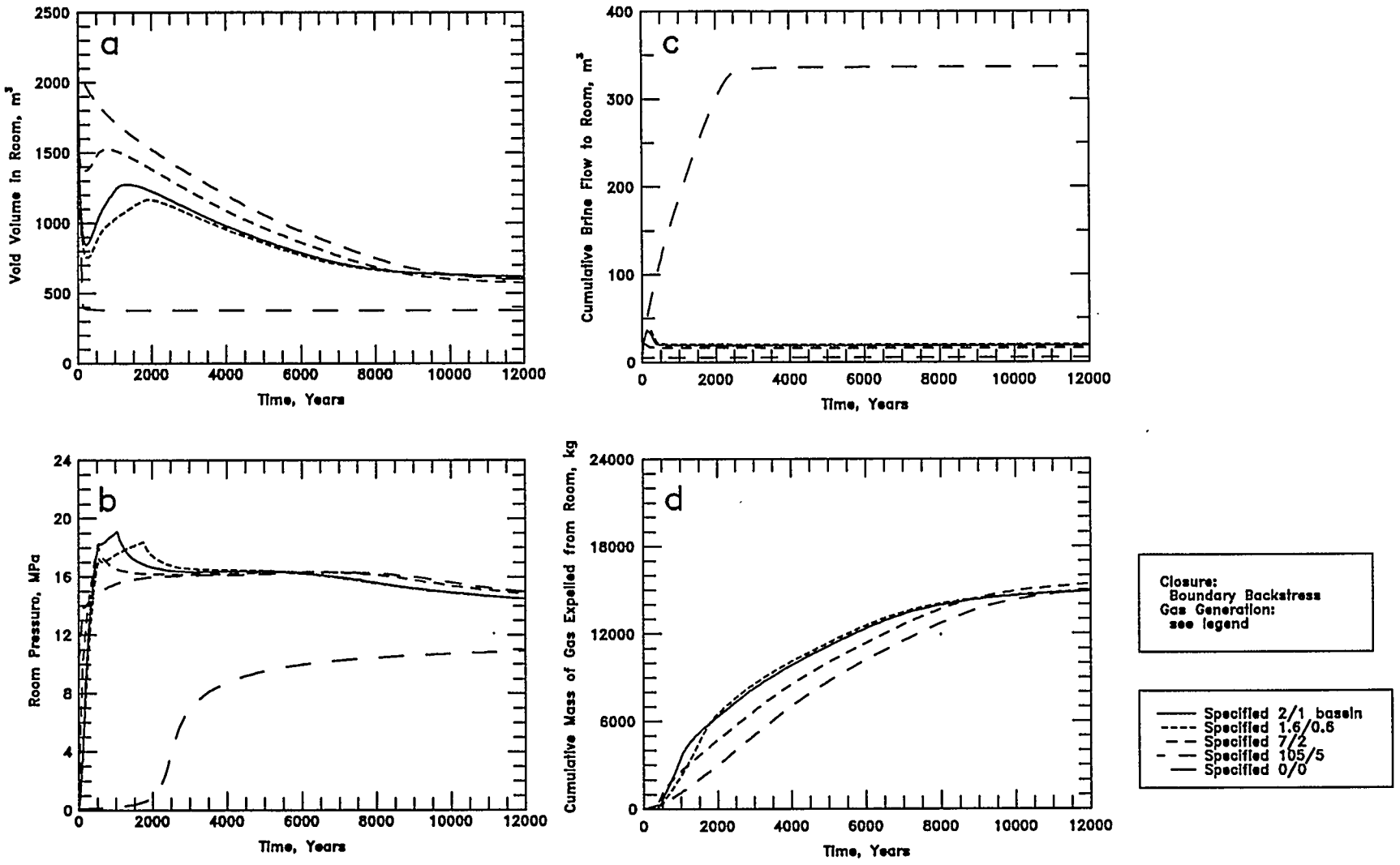

Figure B–46 (a–d). Sensitivity to Specified Gas–Generation Rate History: a – Void Volume; b – Gas Pressure; c – Brine Flow; d – Gas Expulsion

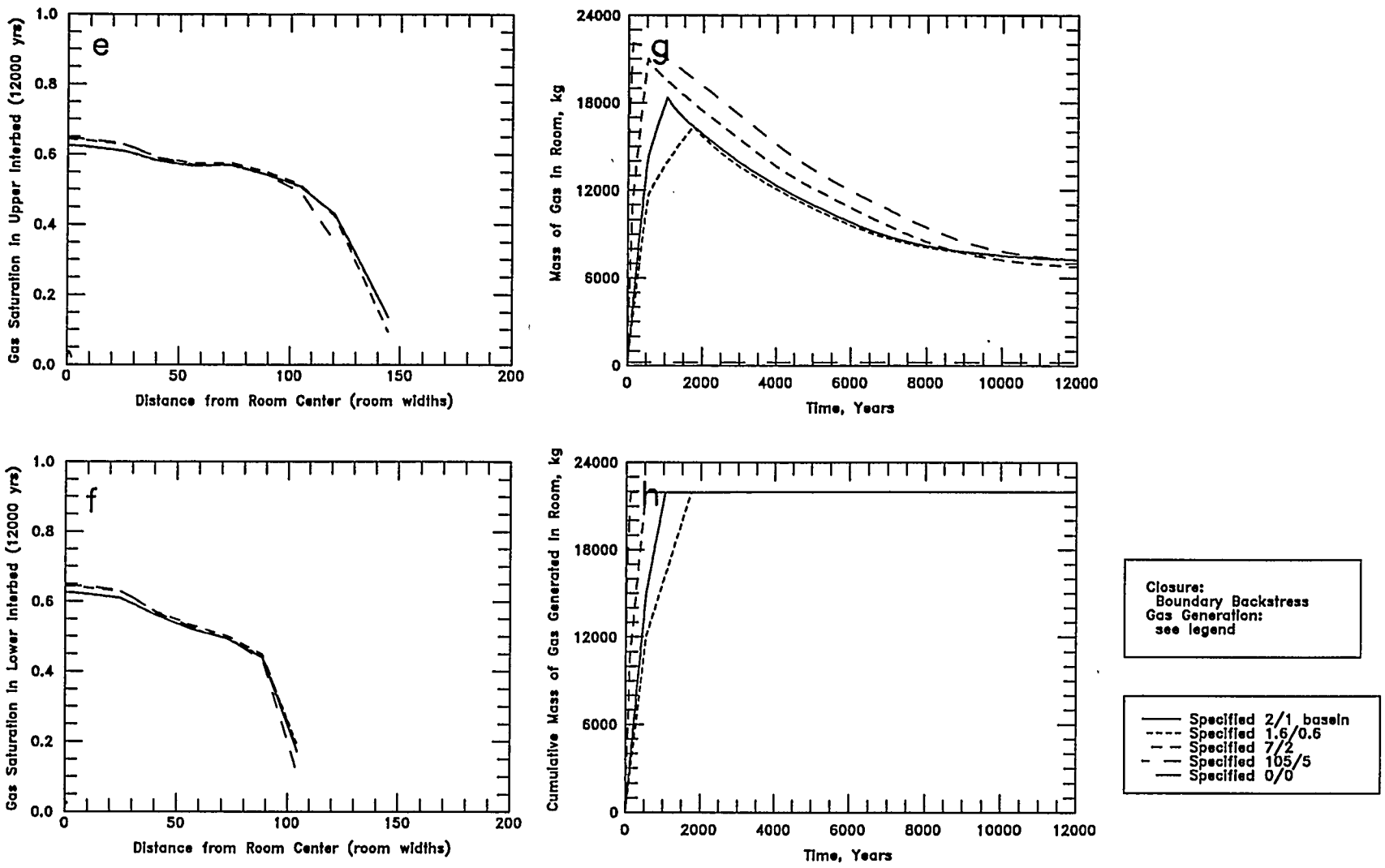

Figure B-46 (e-h). Sensitivity to Specified Gas-Generation Rate History: e - Upper Interbed Gas Profile; f - Lower Interbed Gas Profile; g - Room Gas Mass; h - Gas Generation

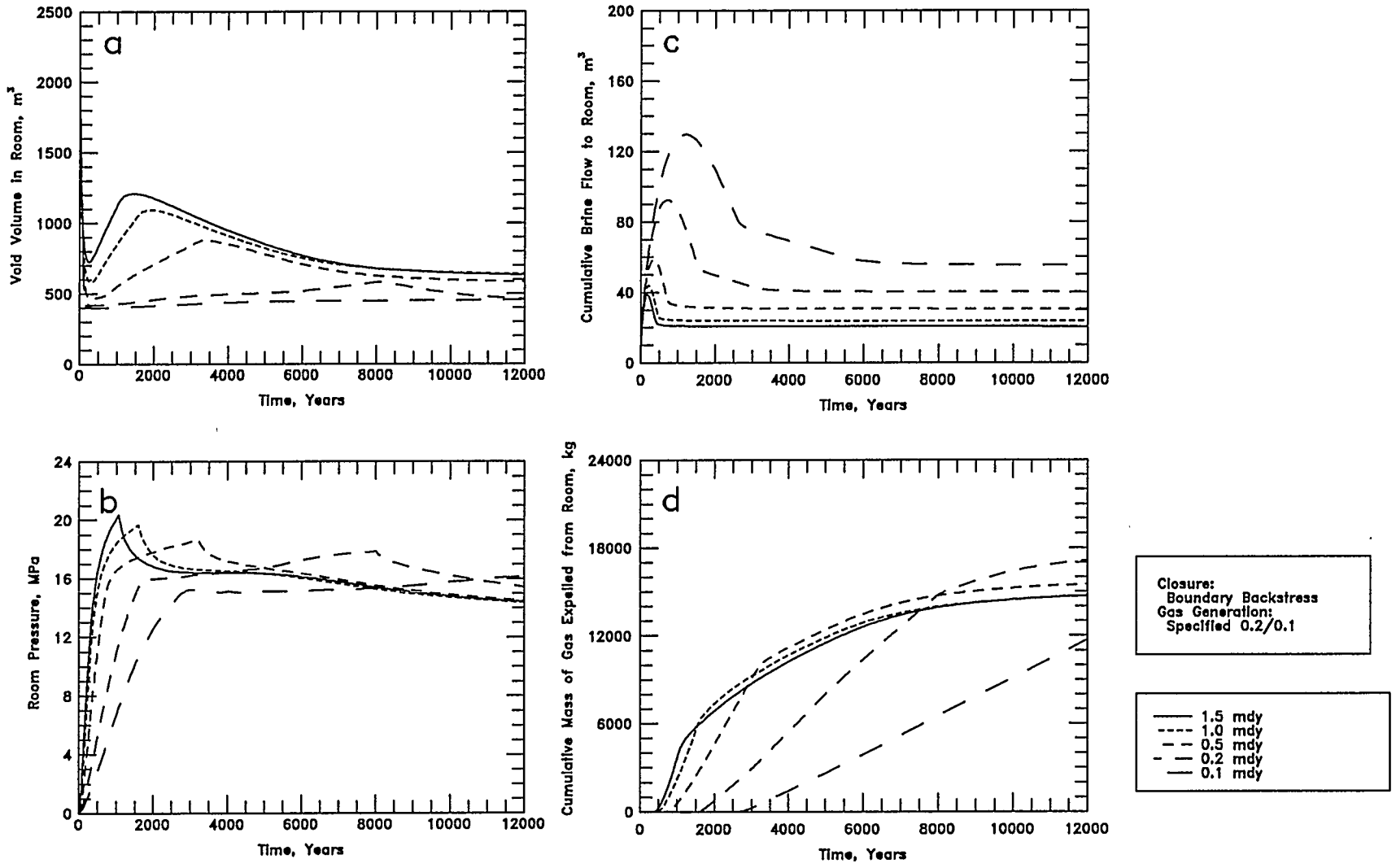

Figure B-47 (a-d). Sensitivity to Constant Gas-Generation Rate:
a - Void Volume; b - Gas Pressure; c - Brine Flow; d - Gas Expulsion

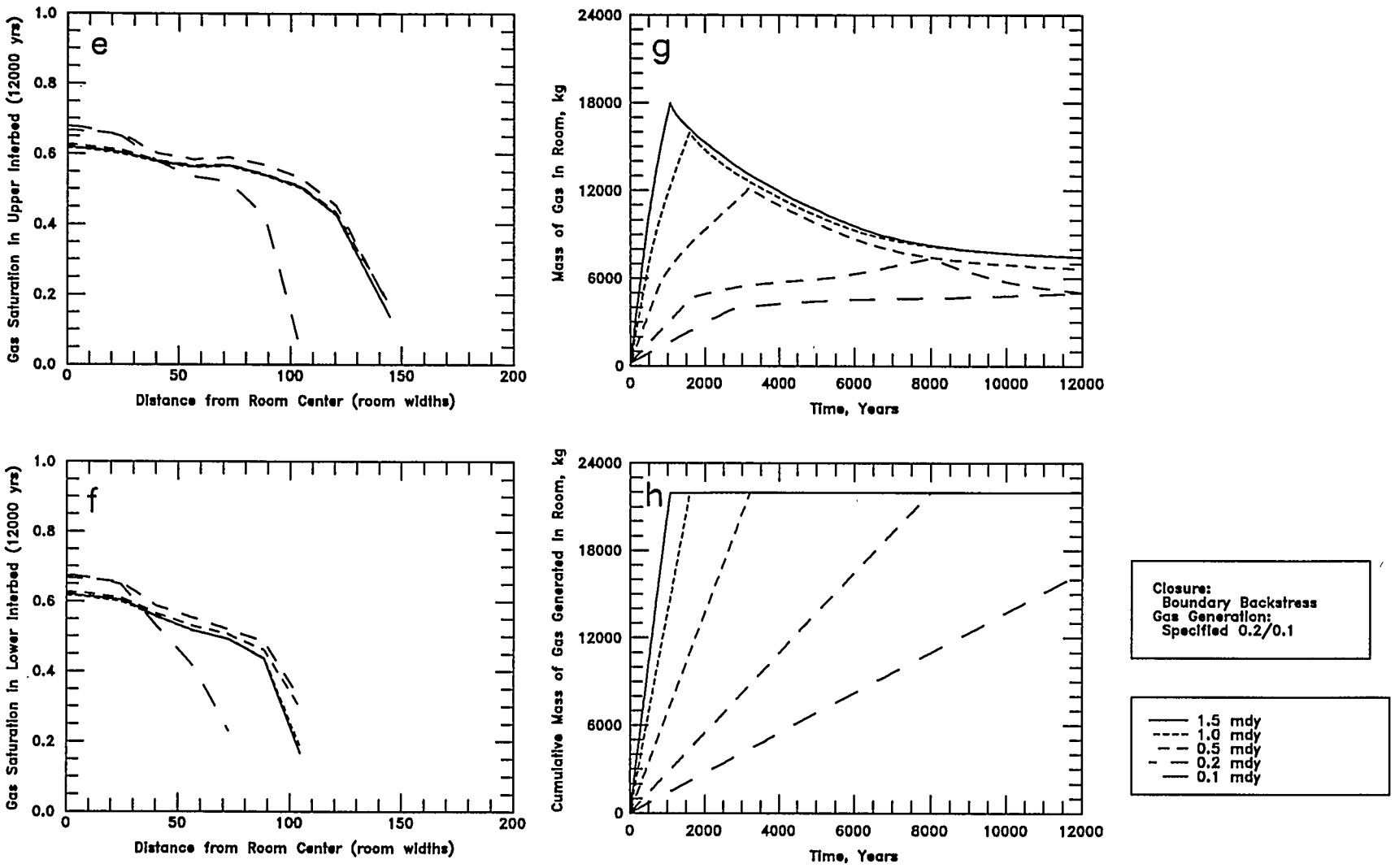

Figure B-47 (e-h). Sensitivity to Constant Gas-Generation Rate:
e - Upper Interbed Gas Profile; f - Lower Interbed Gas Profile;
g - Room Gas Mass; h - Gas Generation

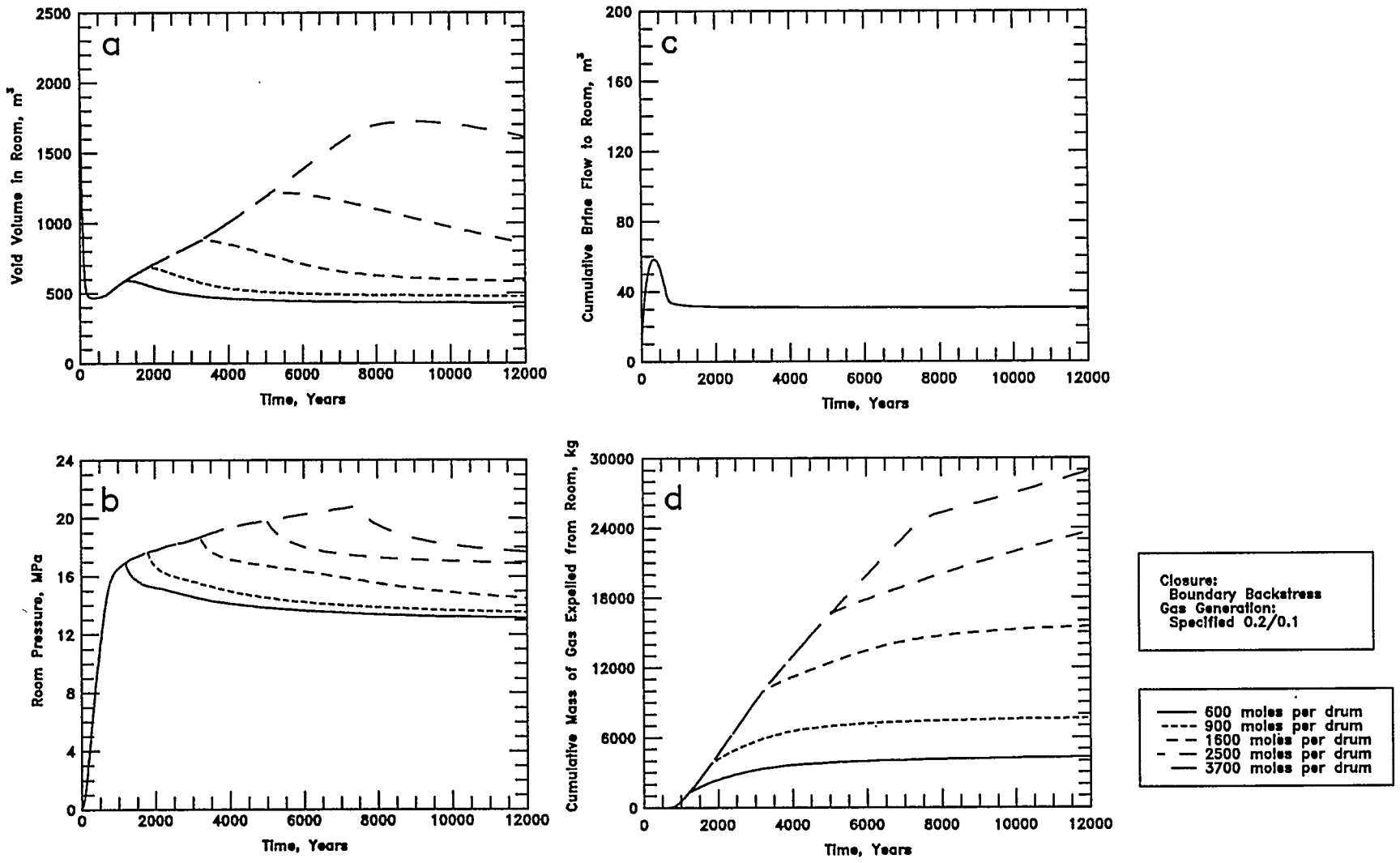

Figure B-48 (a-d). Sensitivity to Gas-Generation Potential:
a - Void Volume; b - Gas Pressure; c - Brine Flow; d - Gas Expulsion

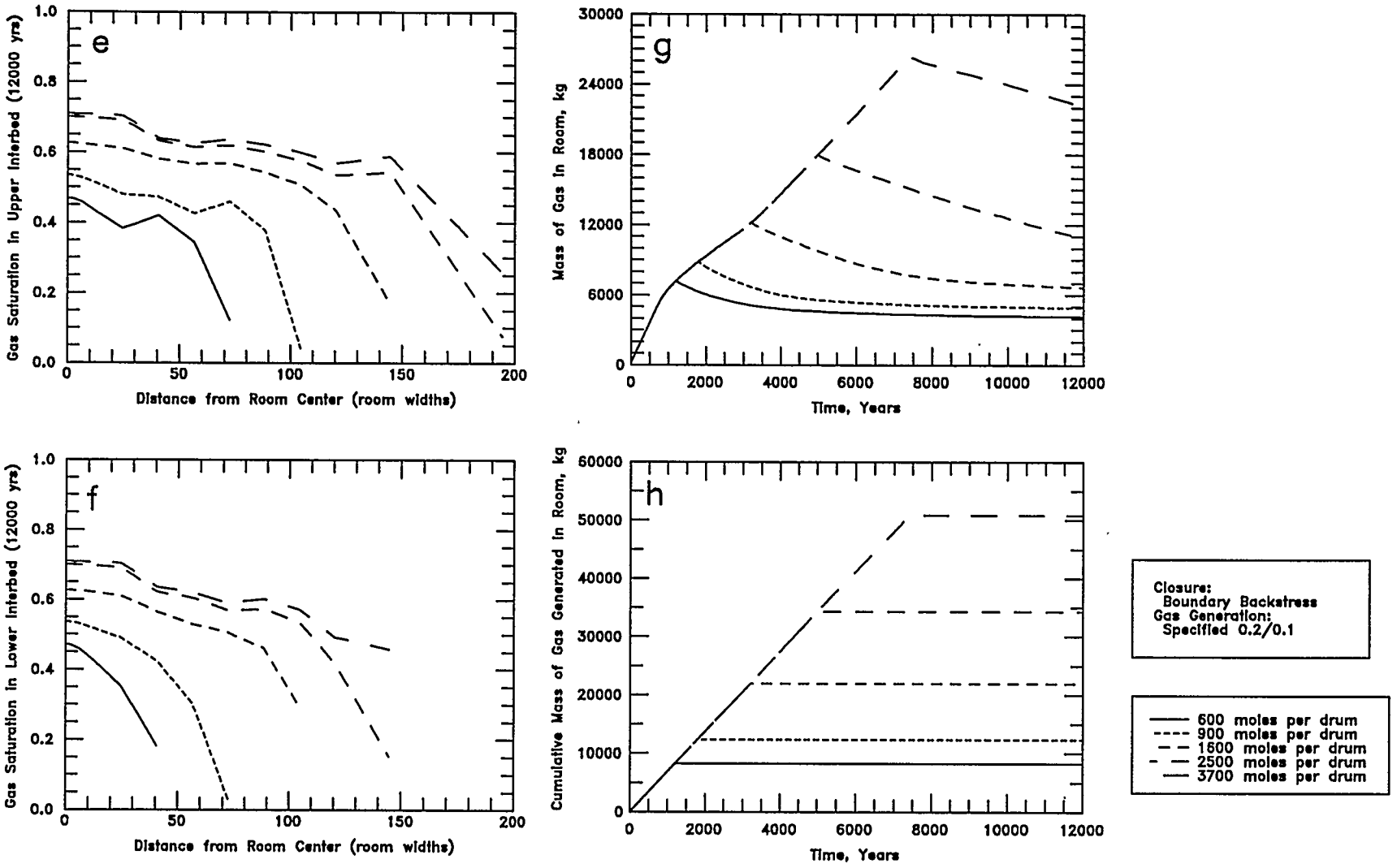

Figure B-48 (e-h). Sensitivity to Gas-Generation Potential:
e - Upper Interbed Gas Profile; f - Lower Interbed Gas Profile;
g - Room Gas Mass; h - Gas Generation

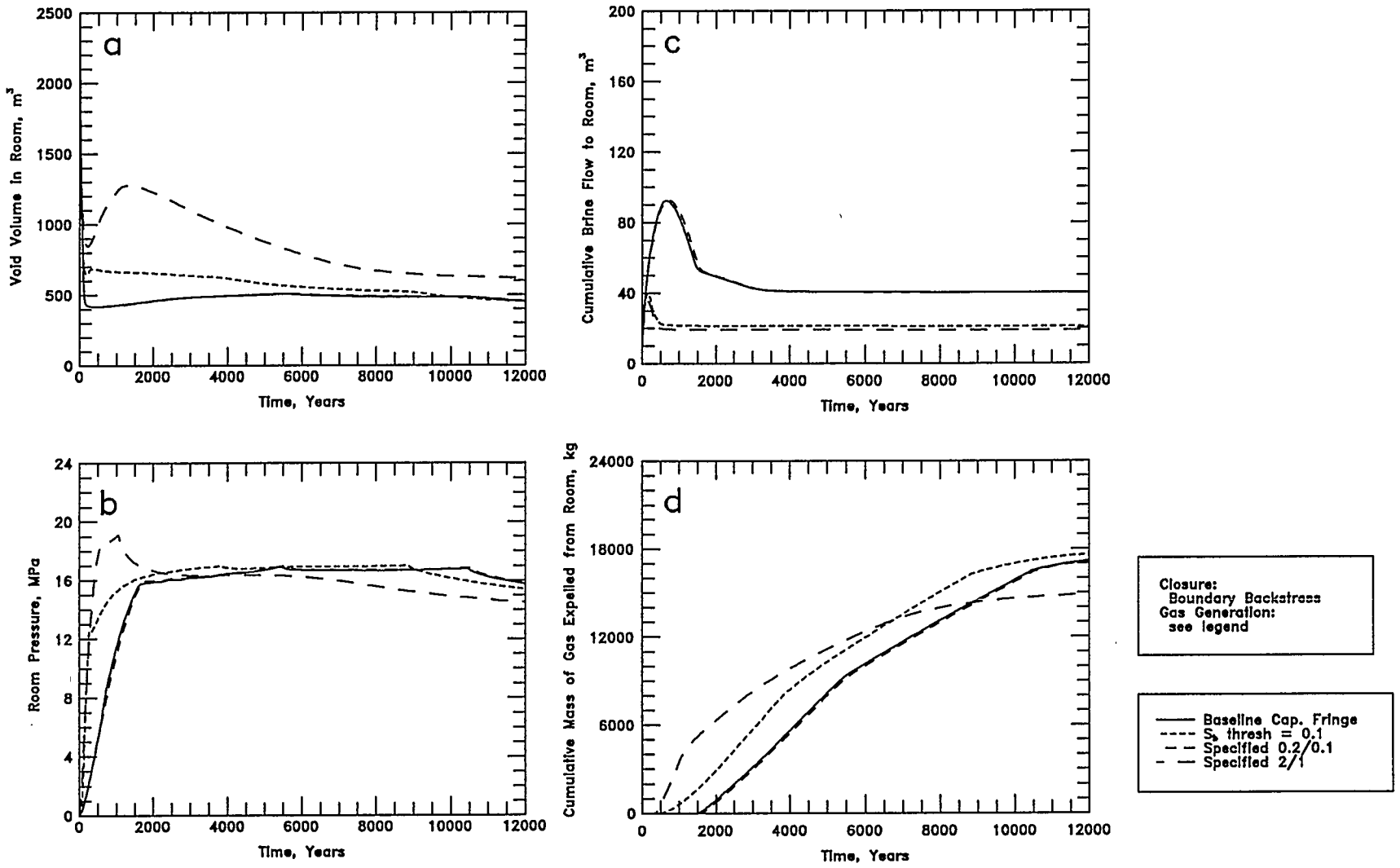

Figure B-49 (a-d). Sensitivity to Capillary Fringe Threshold Brine Saturation: a - Void Volume; b - Gas Pressure; c - Brine Flow; d - Gas Expulsion

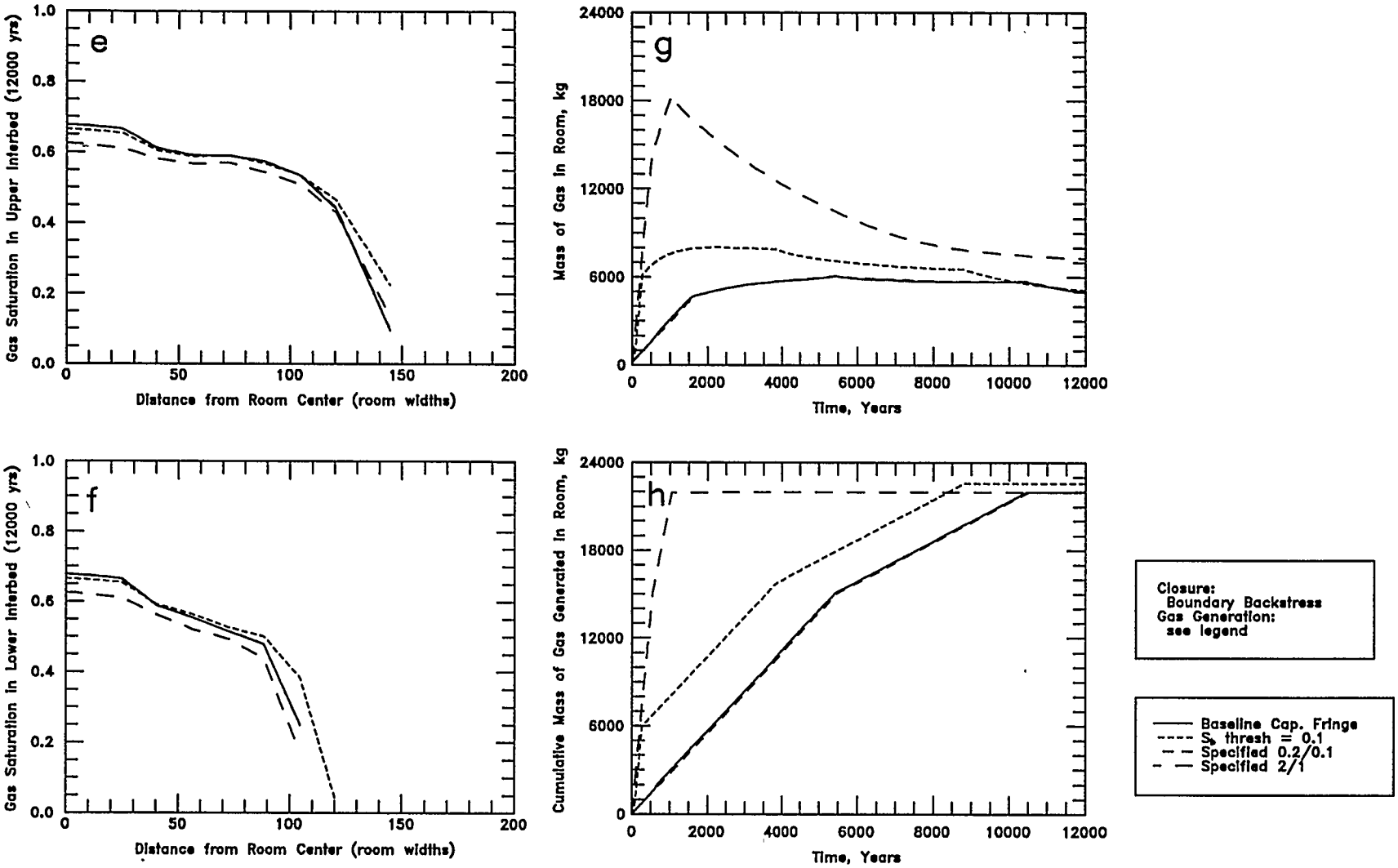

Figure B-49 (e-h). Sensitivity to Capillary Fringe Threshold Brine Saturation: e - Upper Interbed Gas Profile; f - Lower Interbed Gas Profile; g - Room Gas Mass; h - Gas Generation

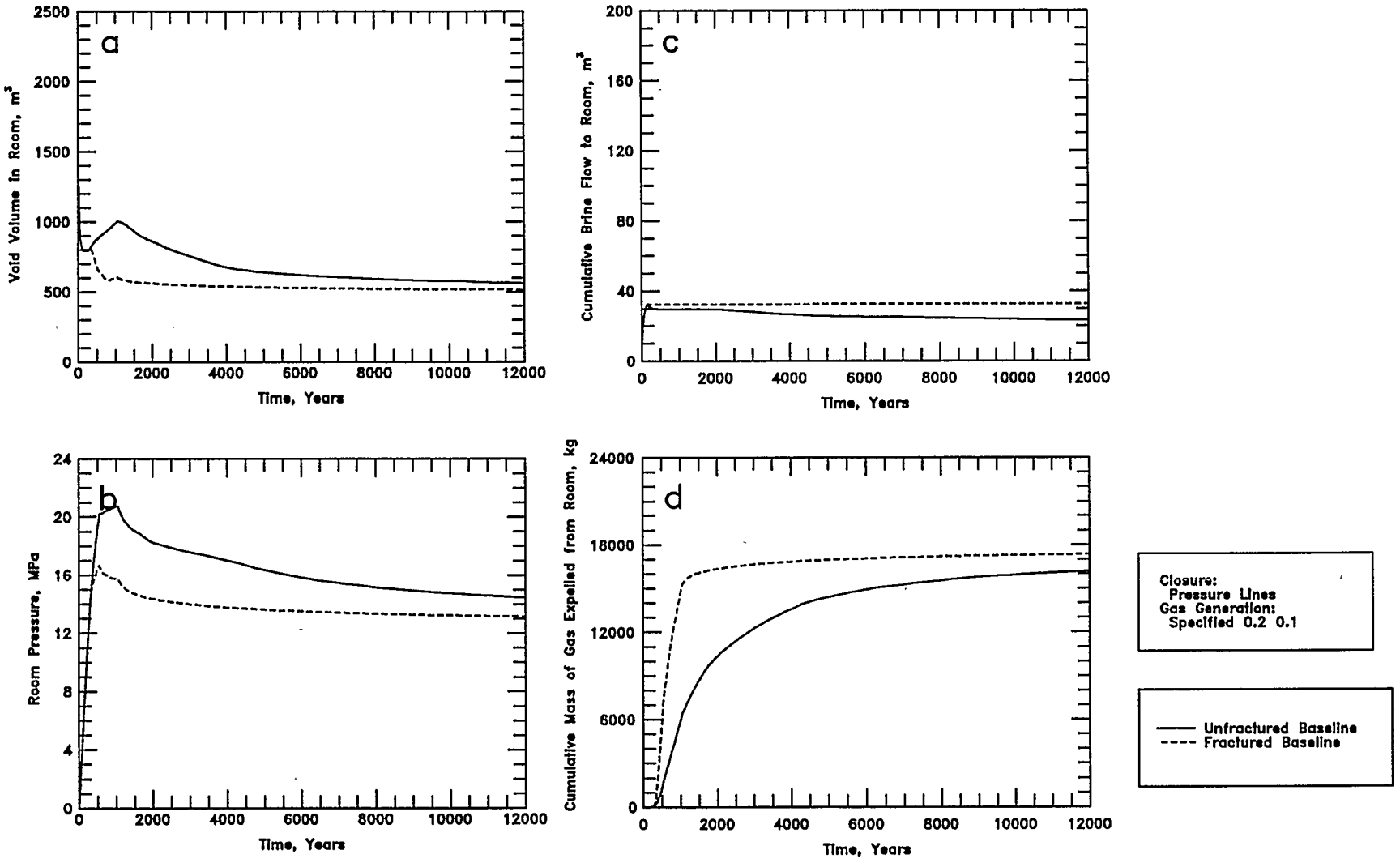

Figure B–50 (a–d). Results from Interbed Fracture Alternative Conceptual Model:
a – Void Volume; b – Gas Pressure; c – Brine Flow; d – Gas Expulsion

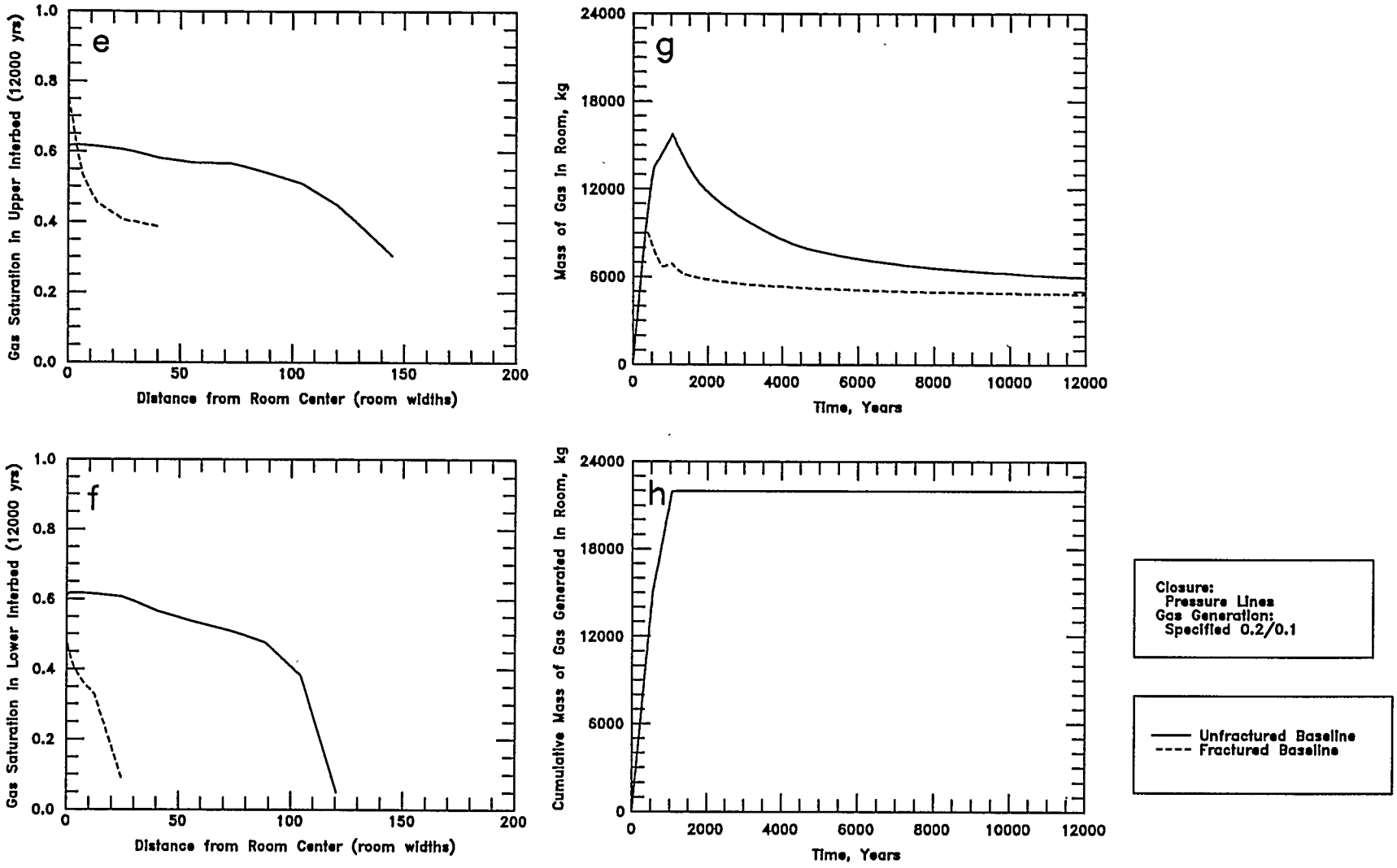

Figure B-50 (e-h). Results from Interbed Fracture Alternative Conceptual Model: e - Upper Interbed Gas Profile; f - Lower Interbed Gas Profile; g - Room Gas Mass; h - Gas Generation

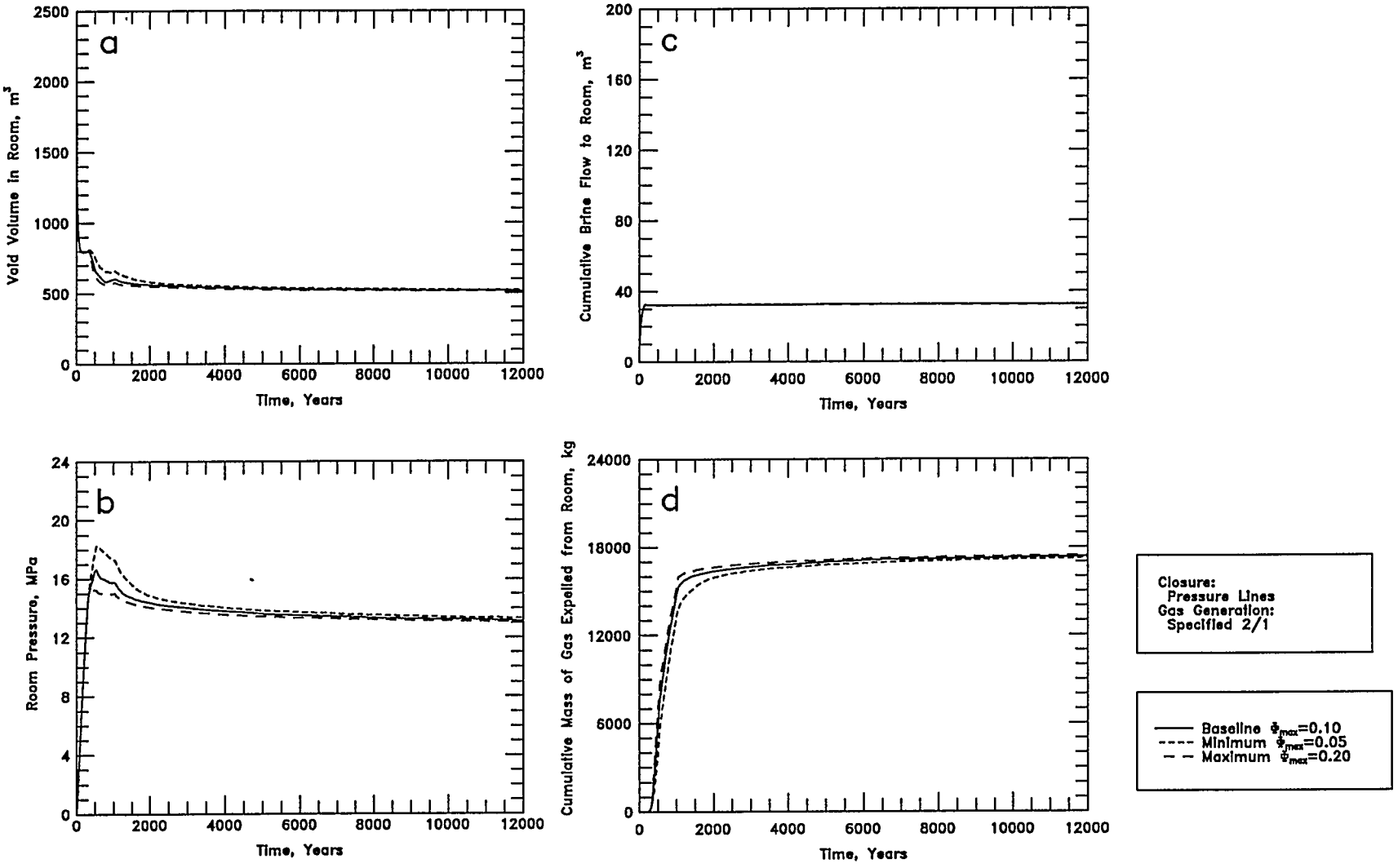

Figure B-51 (a-d). Sensitivity to Maximum Interbed Fracture Porosity, Φ_{max}: a - Void Volume; b - Gas Pressure; c - Brine Flow; d - Gas Expulsion

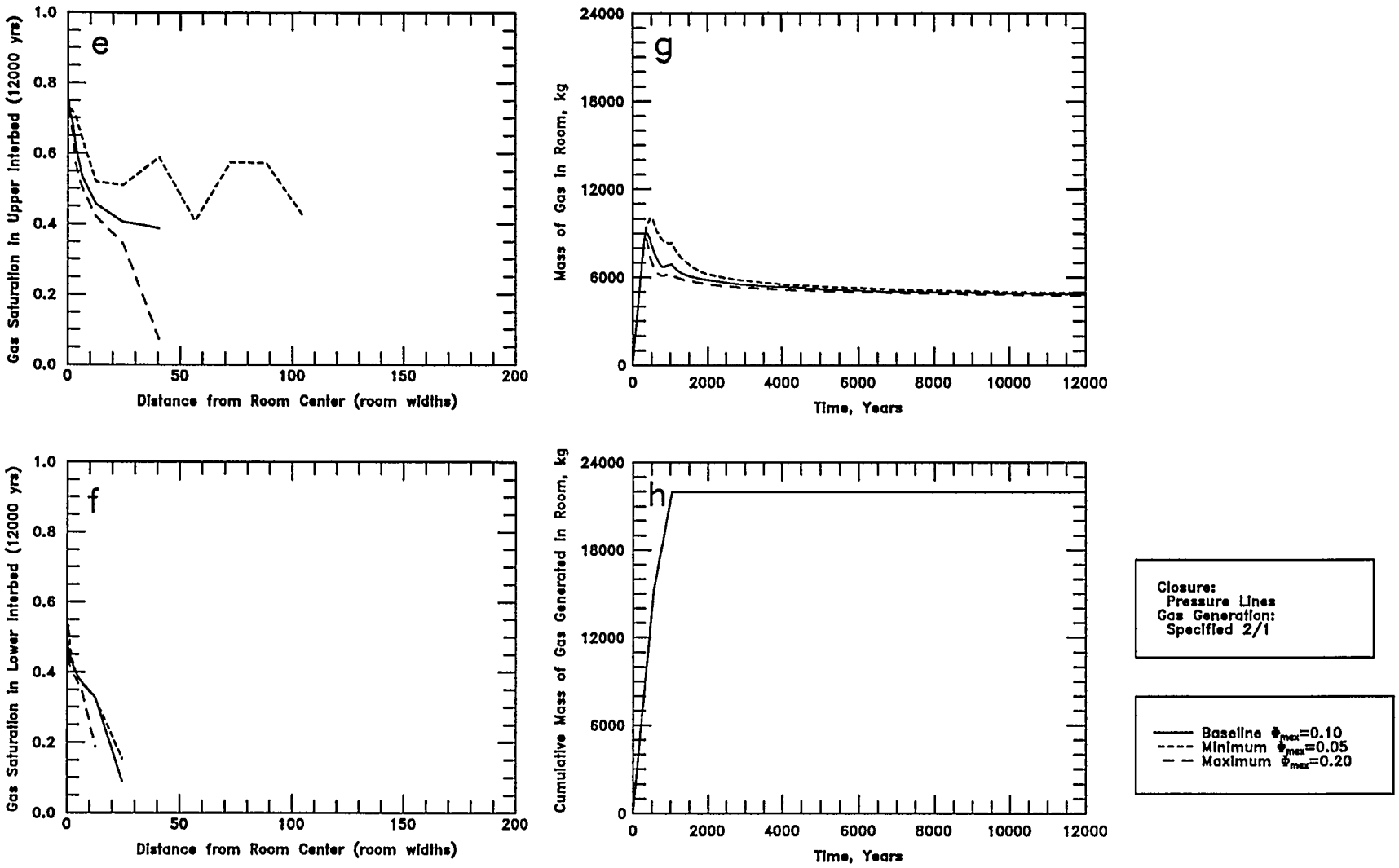

Figure B-51 (e-h). Sensitivity to Maximum Interbed Fracture Porosity, Φ_{max}: e - Upper Interbed Gas Profile; f - Lower Interbed Gas Profile; g - Room Gas Mass; h - Gas Generation

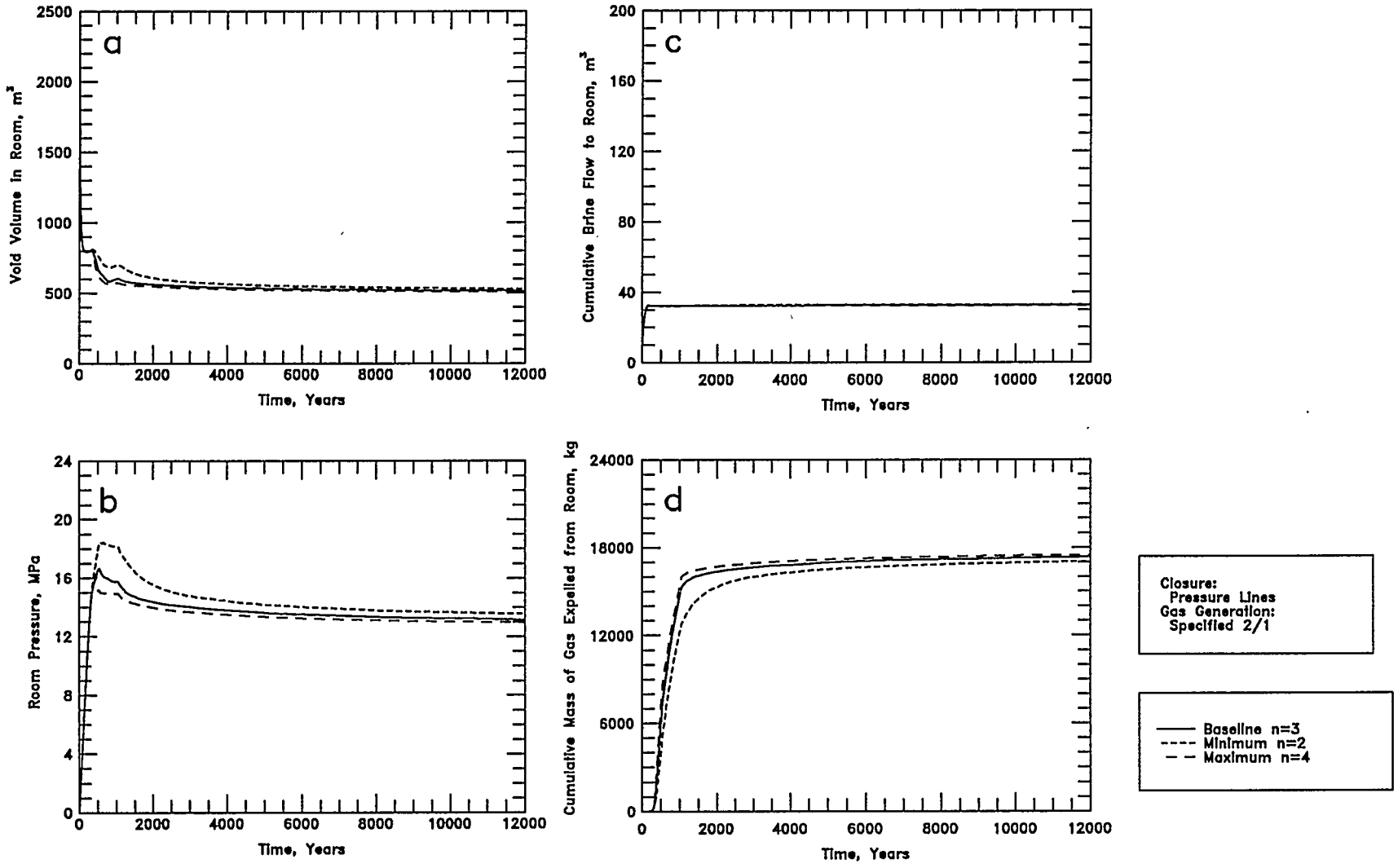

Figure B–52 (a–d). Sensitivity to Interbed Fracture Permeability Exponent, n:
a – Void Volume; b – Gas Pressure; c – Brine Flow; d – Gas Expulsion

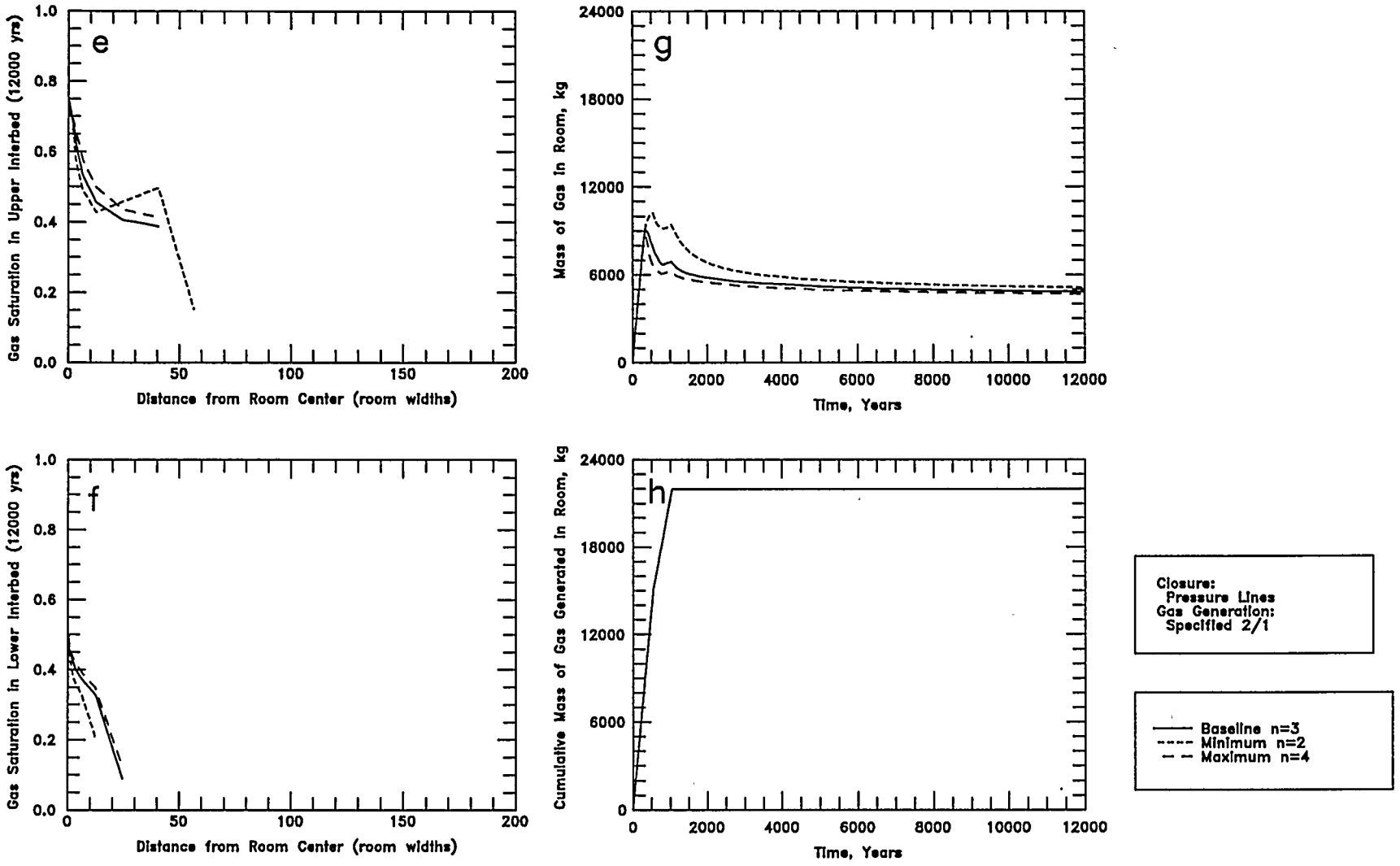

Figure B-52 (e-h). Sensitivity to Interbed Fracture Permeability Exponent, n:
e - Upper Interbed Gas Profile; f - Lower Interbed Gas Profile;
g - Room Gas Mass; h - Gas Generation

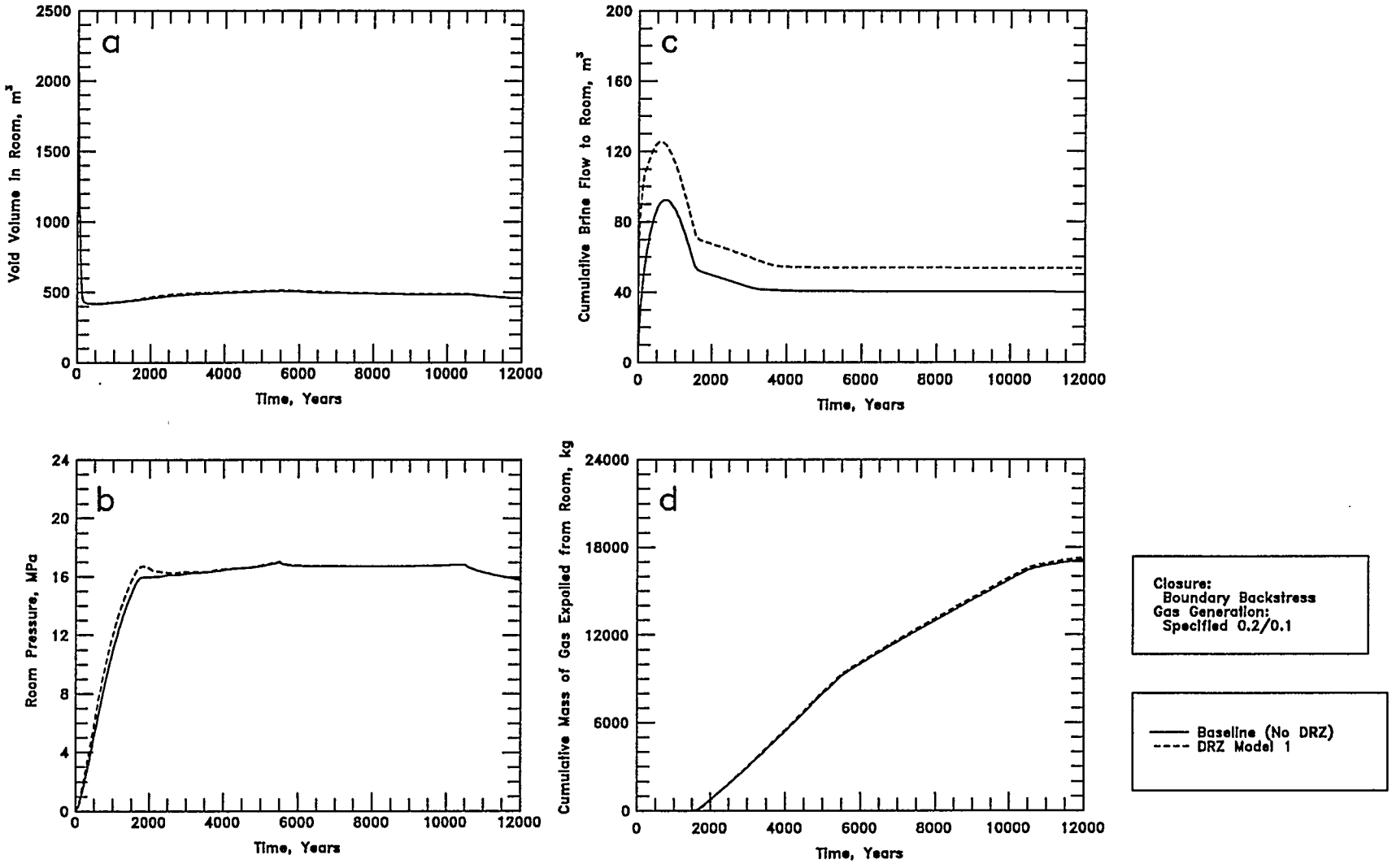

Figure B–53 (a–d). Results from Disturbed Rock Zone Alternative Conceptual Model: a – Void Volume; b – Gas Pressure; c – Brine Flow; d – Gas Expulsion

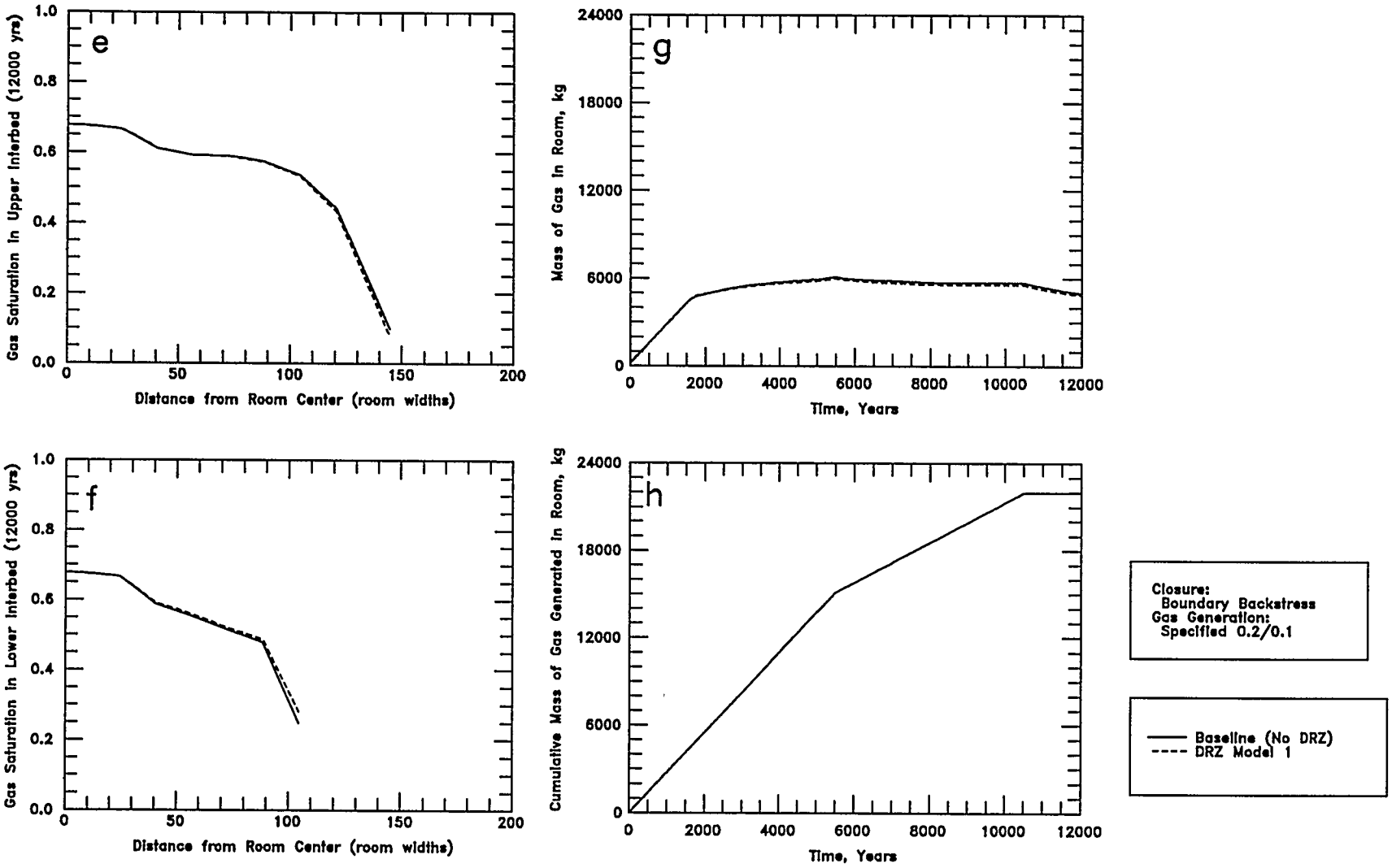

Figure B-53 (e-h). Results from Disturbed Rock Zone Alternative Conceptual Model: e - Upper Interbed Gas Profile; f - Lower Interbed Gas Profile; g - Room Gas Mass; h - Gas Generation

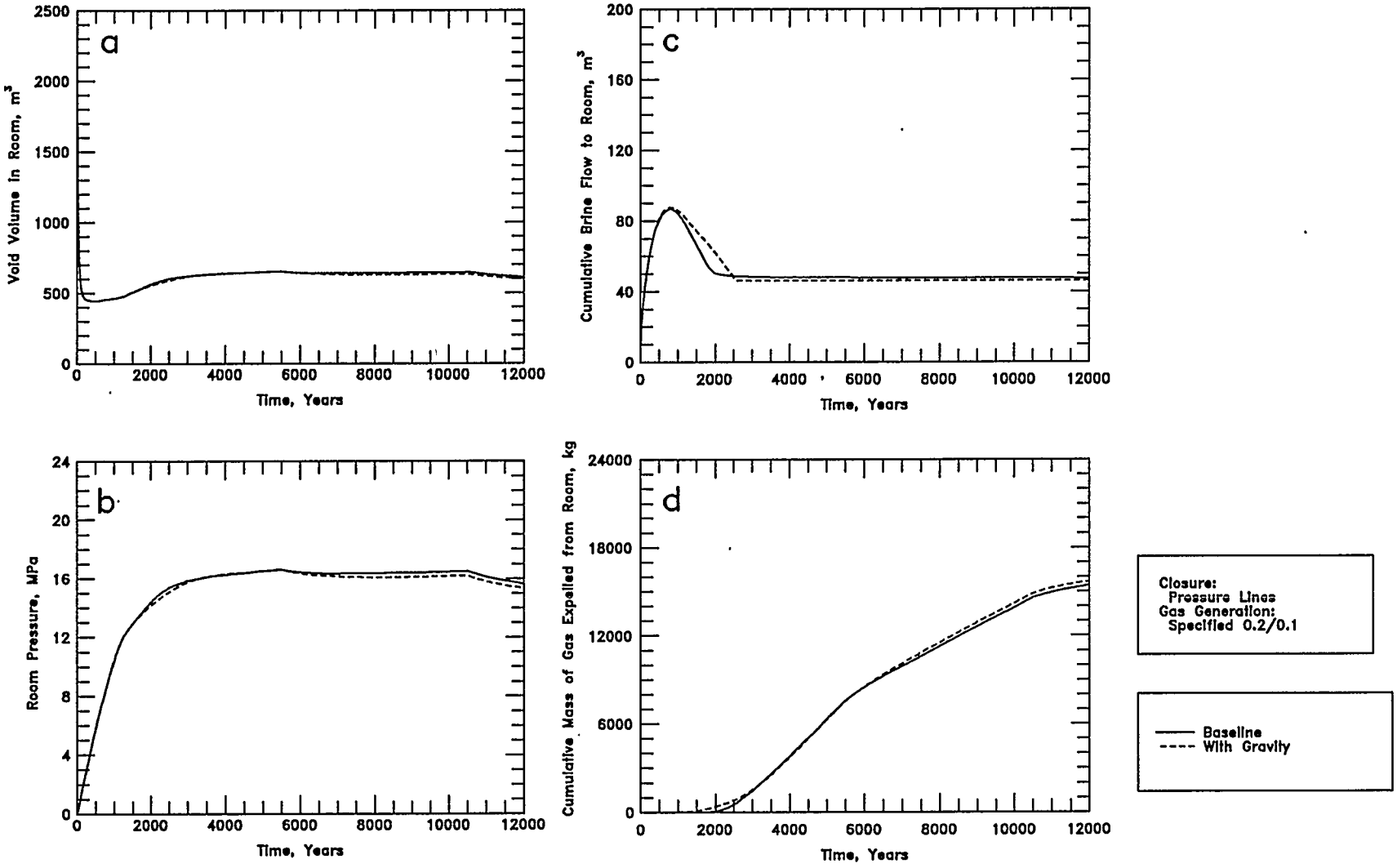

Figure B-54 (a-d). Results from Gravity Alternative Conceptual Model:
a - Void Volume; b - Gas Pressure; c - Brine Flow; d - Gas Expulsion

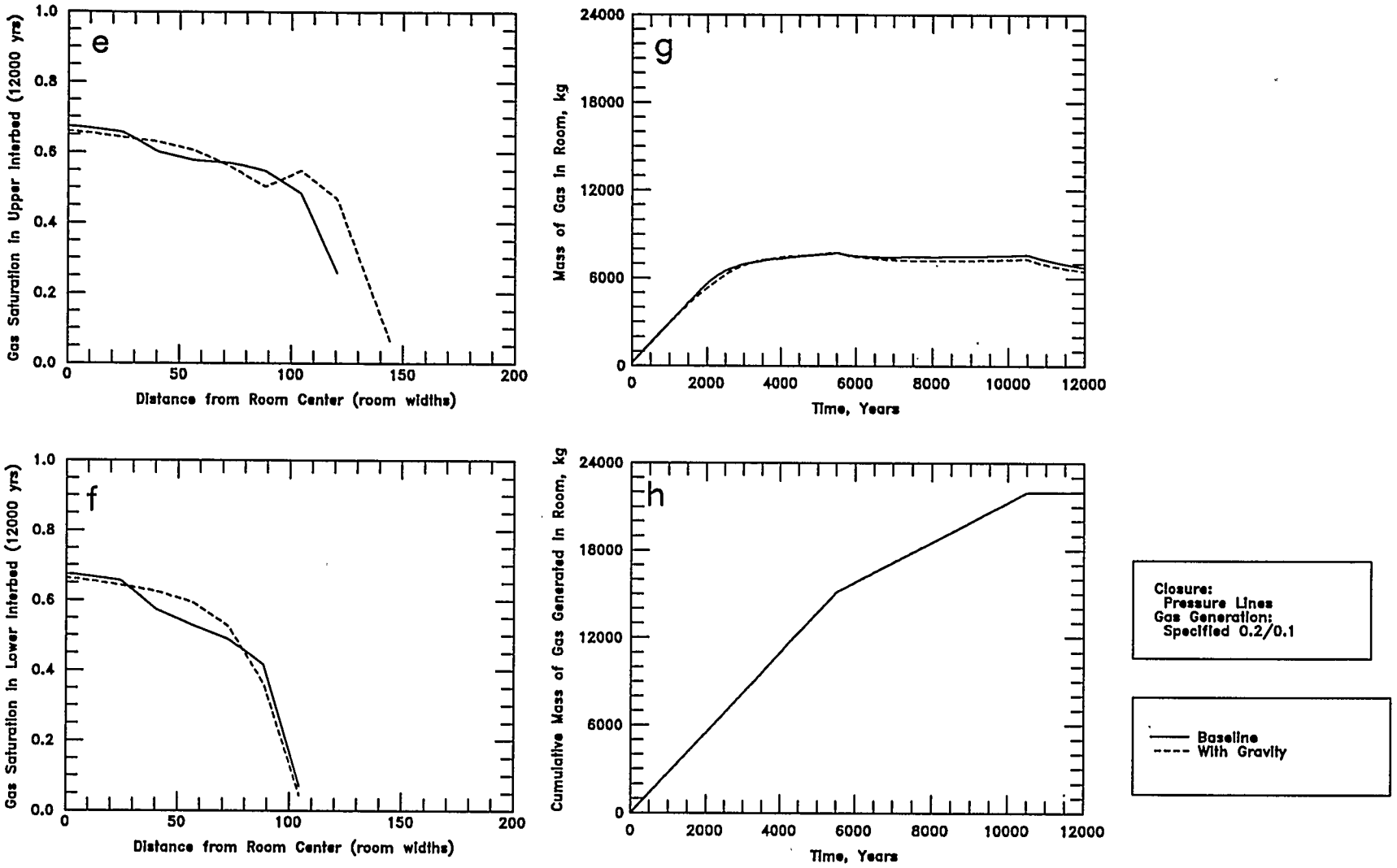

Figure B-54 (e-h). Results from Gravity Alternative Conceptual Model:
e - Upper Interbed Gas Profile; f - Lower Interbed Gas Profile;
g - Room Gas Mass; h - Gas Generation

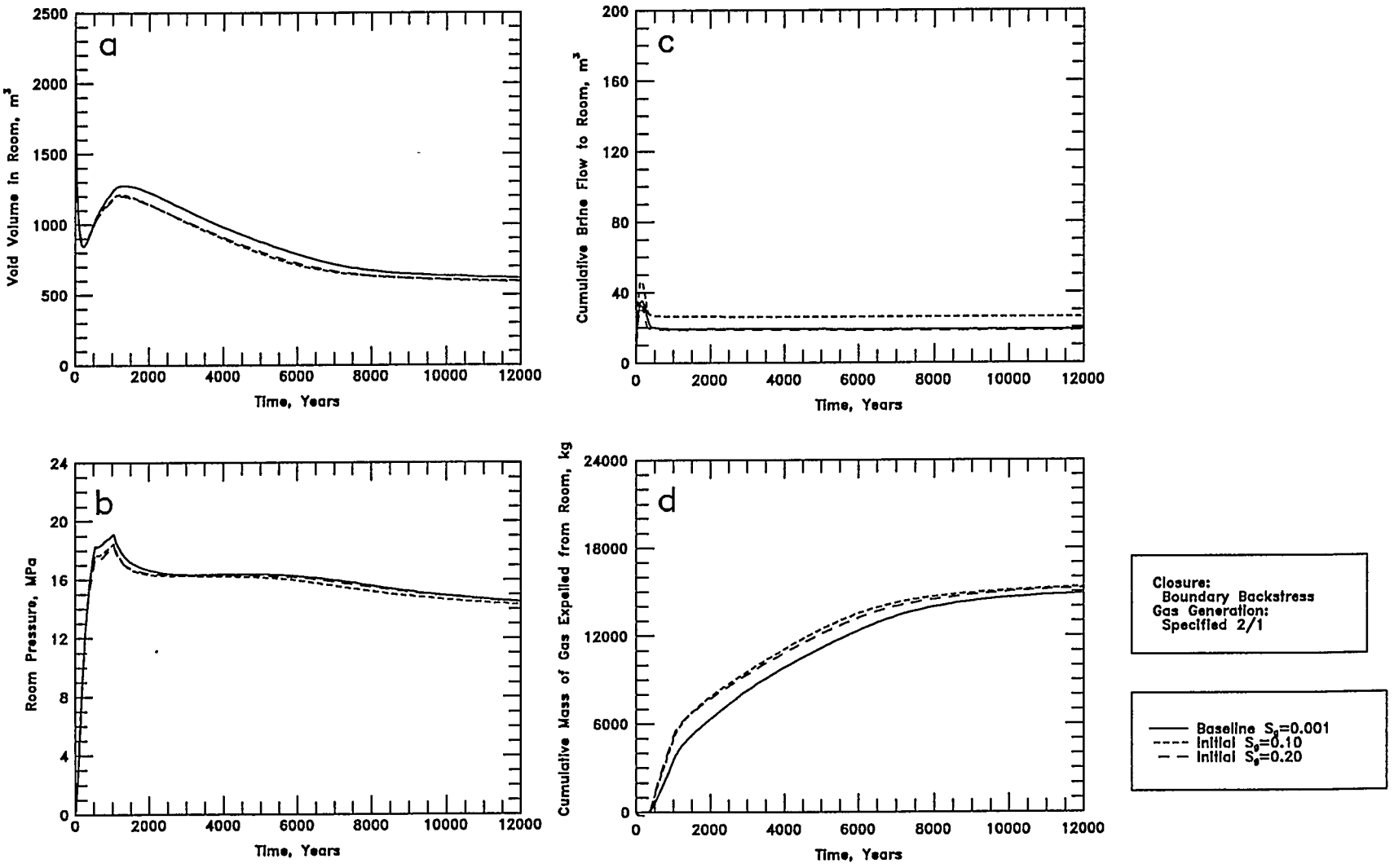

Figure B–55 (a–d). Results from Gas Exsolution Alternative Conceptual Model: a – Void Volume; b – Gas Pressure; c – Brine Flow; d – Gas Expulsion

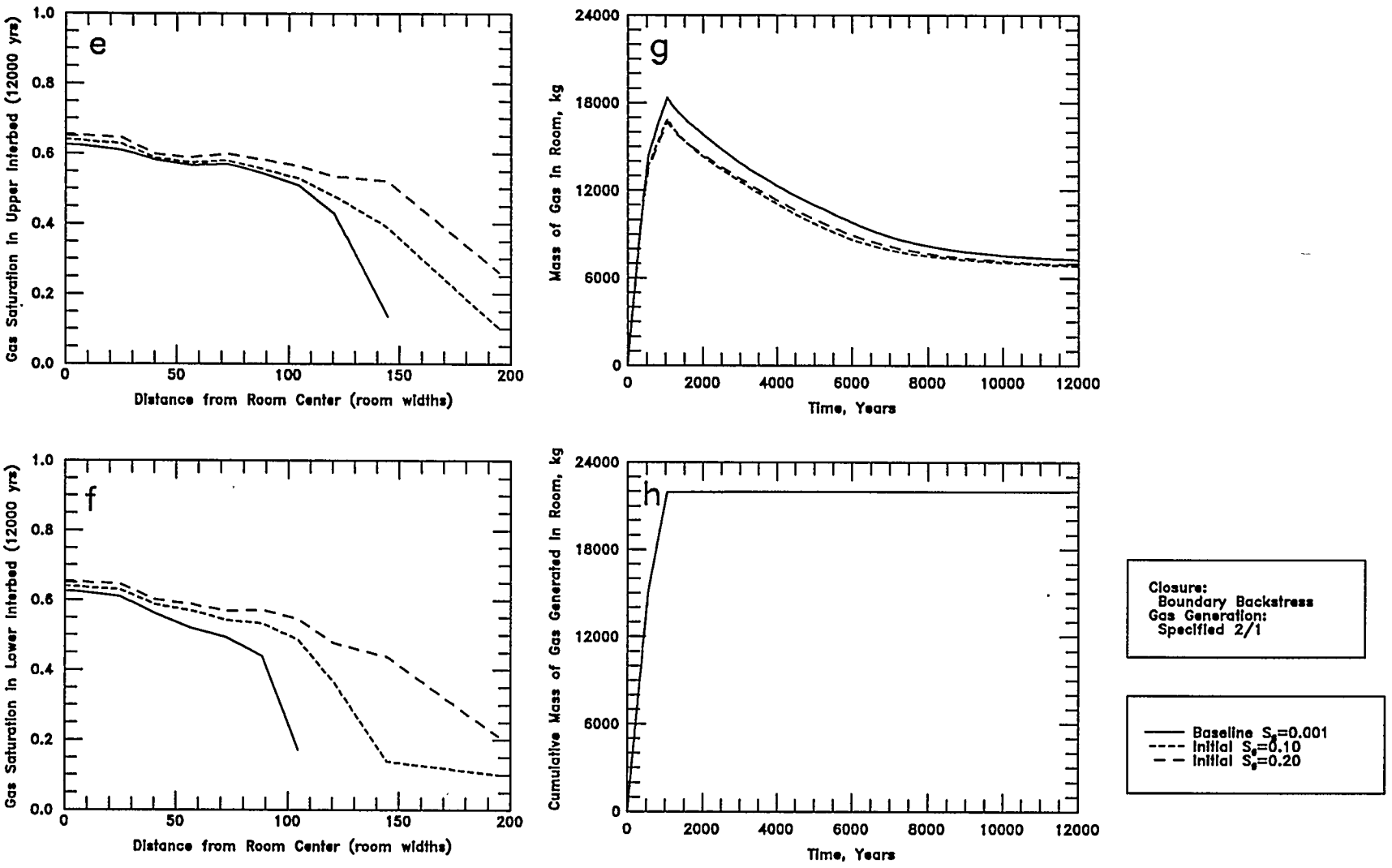

Figure B-55 (e-h). Results from Gas Exsolution Alternative Conceptual Model: e - Upper Interbed Gas Profile; f - Lower Interbed Gas Profile; g - Room Gas Mass; h - Gas Generation

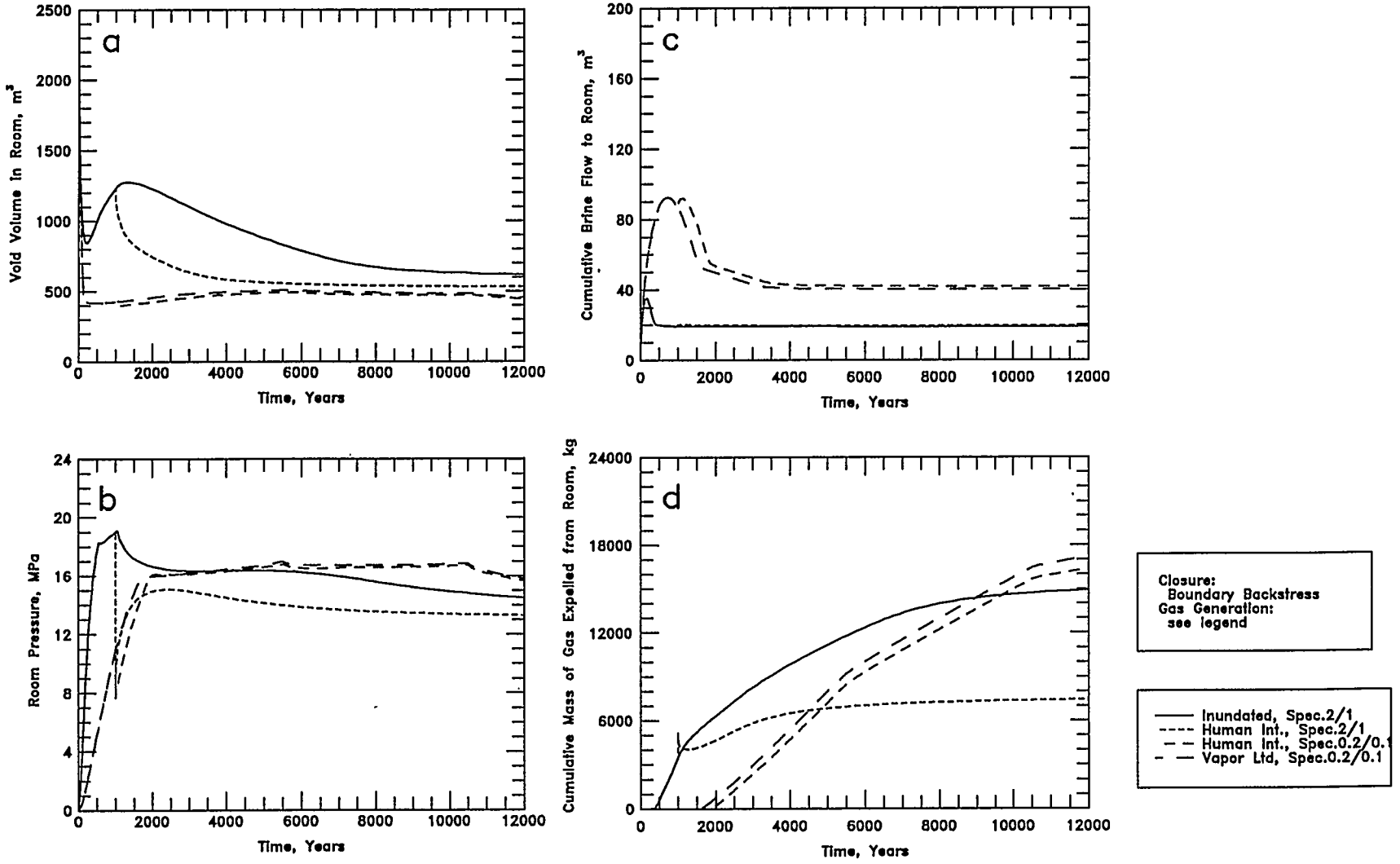

Figure B-56 (a-d). Results from Instantaneous Room Depressurization Alternative Conceptual Model: a - Void Volume; b - Gas Pressure; c - Brine Flow; d - Gas Expulsion

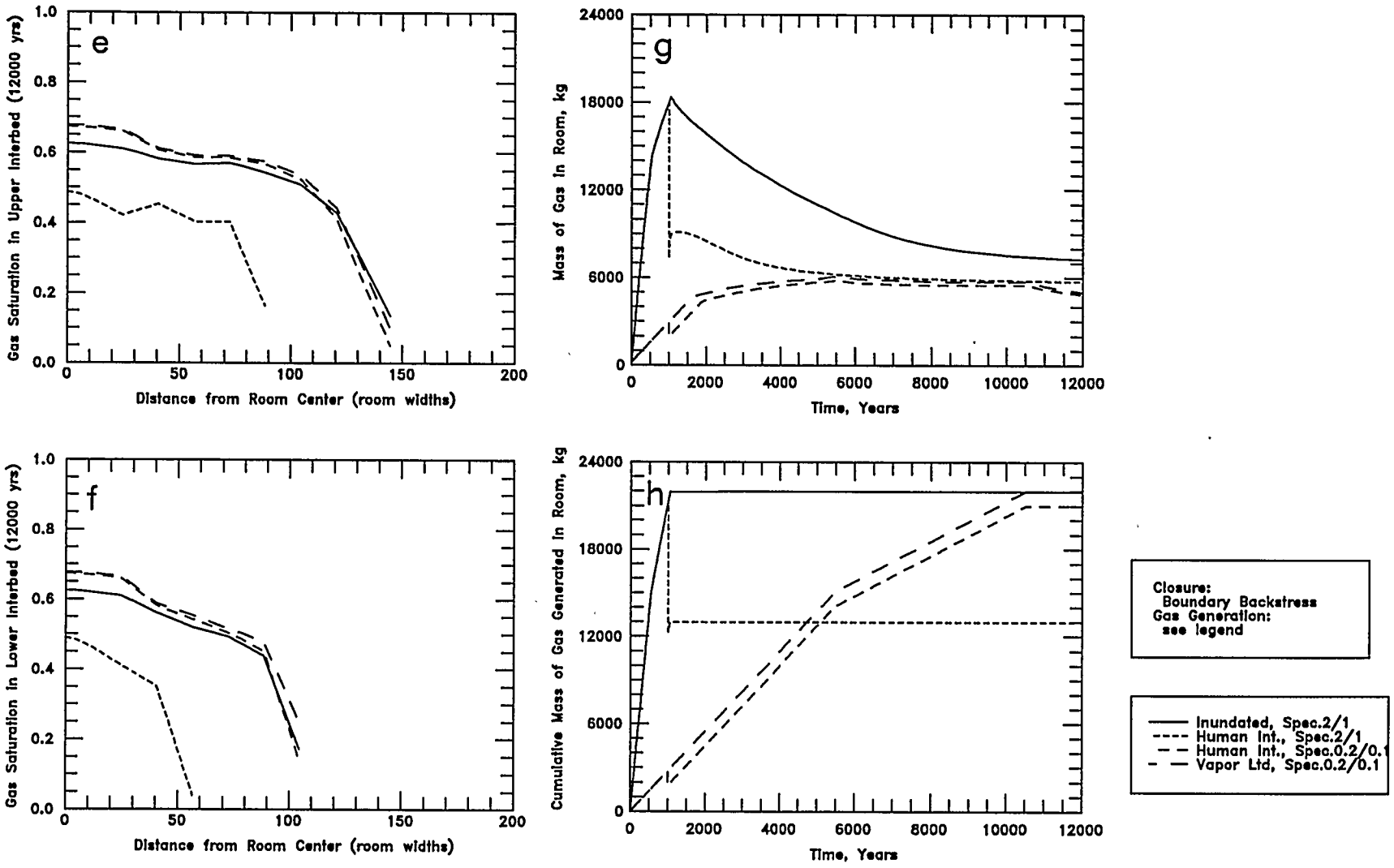

Figure B-56 (e-h). Results from Instantanteous Room Depressurization Alternative Conceptual Model: e - Upper Interbed Gas Profile; f - Lower Interbed Gas Profile; g - Room Gas Mass; h - Gas Generation

This page intentionally left blank

APPENDIX C: REFERENCED MEMORANDA

This page intentionally left blank

Appendix C: Referenced Memoranda

This page intentionally left blank

Sandia National Laboratories

Albuquerque, New Mexico 87185

date: April 21, 1993

to: M. S. Tierney, 6342

B. M. Butcher R. C. Lincoln

from: B. M. Butcher, R. C. Lincoln, 6345

subject: The Initial Brine Saturation of Waste and Backfill Within WIPP Disposal Rooms (WBS 1.1.1.2.3)

The draft information copy of the PA Volume 3 Comparison for 1992 describes the initial saturation of the unmodified CH waste form as ranging from 0 to 0.13, with a median of 0.07. This saturation appears to be much too high and should be replaced by a range from 0.0003 to 0.018, with a median of 0.011. The assumption in proposing this change is that the initial saturation represents the condition of the room contents before any brine from the surrounding formation enters the room. The new distribution is justified in the following discussion:

The median value for the initial saturation is based on the requirement that no more than 1 percent by volume free liquid can be present in waste that is shipped to WIPP (WAC Section 3.3.2.1). Regardless of whether or not one believes that this requirement can be met, the burden is on the waste generators to demonstrate that it is feasible, or tell us otherwise. For the saturations quoted here, we assume that the 1% volume in the waste is entirely water, whereas at least some of it is likely to be other liquids. The moisture content of the backfill is based on the assumption that no brine is lost from the backfill during its mining, processing, and emplacement. According to Volume 3, the porosity of solid halite varies from 0.001 to 0.03 with a median of 0.01. Complete brine saturation is assumed. Clearly these are worse case assumptions, even for the median value.

The lower bound simply reflects the possibility that there may be no free moisture in the waste because of the presence of desiccant materials. The sole source of water for the lower value of the brine saturation is therefore the brine in the backfill. It is considered useful to preserve the brine content of the backfill because the presence of water will facilitate backfill consolidation. However, even if the rate of consolidation of the backfill was not important, a totally dry state would be unacceptable because it would be difficult to dry our the backfill salt completely.

The upper bound for the initial saturation is based on the fact that RTR examination of waste for fluids may not detect a sealed container that is completely filled with liquid. We learned in a conversation with Paul Drez that NRC is reported to have agreed that a 5% probability that a container is filled with fluid is allowable for shipping (the TRUPACT II SAR was given as reference), although this criteria has not yet been approved by either the EPA or New Mexico state. Although this criterion is indefinite because it is a very loose interpretation of the wording in the suggested reference, it will be adopted for calculation of the maximum brine saturation value. Since a one gallon container is the largest size sealed container allowable within the waste (WAC Section 3.4.7.2), the upper initial saturation limit is determined by assuming that there is a 5% probability that a single gallon container filled with water can exist in each drum of combustible and metals waste. No sealed containers are assumed to exist in the sludges.

The values cited in the previous paragraphs are absolute upper bounds because:

- All liquids were assumed to be water.
- No credit was taken for desiccant materials purposely added to the waste to remove free water.
- Drying of the backfill because of mine ventilation was not considered.
- Any bentonite mixed with crushed salt for backfill would also remove water.

The last factor is considered most important because a salt-bentonite mixture for the backfill would have the potential of sorbing of the order of from 10 to 50 m3 of water per room (Butcher, 1991, Table 4-1). For comparison, the upper limit of the initial saturation of 0.018 quoted above corresponds to approximately 40 m^3 of brine in the room.

References:

Waste Acceptance Criteria for the Waste Isolation Pilot Plant, WIPP/DOE - 069, Revision 4, December 1991.

NuPac TRUPACT-II SAR, Rev. 1, May 1989.

"The Advantages of a Salt/Bentonite Backfill for Waste Isolation Pilot Plant Disposal Rooms," B. M. Butcher, SAND90-3074, April 1991.

Copy to:
6115 P. B. Davies
6115 K. Larson (INTERA)
6119 S. W. Webb
6303 W. D. Weart
6305 A. R. Lappin
6340 SWCF(DRM)
6342 D. R. Anderson
6342 M. E. Fewell
6342 M. G. Marietta
6342 P. Vaughn
6345 R. C. Lincoln
6345 B. M. Butcher (Day file)
6345 F. T. Mendenhall

date: June 4, 1993

to: D. R. Anderson, 6342

B. M. Butcher R. C. Lincoln

from: B. M. Butcher, R. C. Lincoln, 6345

subject: Upper limit of initial brine saturation in waste and backfill.

A suggestion was made during a recent PA parameter review meeting that a useful calculation for examining the upper limit of initial brine saturation would be to determine how much brine could exist in the pore space of cellulosics waste in the fully saturated condition. This contribution to the water content could then be added to the brine in the backfill and remainder of the waste, to provide guidance with regard to the upper limit. The amount of wood was not to be included in the analysis, because of the limiting effect of its tight cellular structure on water release.

Upon further consideration of this request, it became apparent that the concept of pore volume in the paper and wood would be misleading. Bulk paper and cloth pore volumes are not suitable parameters for several reasons: (1) a unique pore volume for these components is impossible to define because they are not segregated, but rather mixed with the rest of the waste; (2) the sorption process in fabrics is more complex than simple saturation of a granular material. Instead, we have defined wet as the maximum amount of water that paper and cloth can sorb and retain in a non-drying atmosphere. The term "wet" therefore is the amount of water retained after a sample of the material has been (1) fully immersed in water, (2) removed from water, and (3) any excess water allowed to drain out of it.

In searching the literature, we were unable to quickly identify any sources of information about sorption potential of various types of paper and cloth. This literature search is continuing. Because of the urgency of the need for this information, we have attempted to obtain an indication of the sorption potential of materials such as lab coats, rags, and Kimwipes from a test. In this test, a well-laundered handkerchief, after being weighted, was saturated by holding it under tap water so that it was dripping wet. The sample was then supported inside a large beaker, so that water was free to drip off it. The container was then covered tightly with Saran Wrap, so that it essentially became a closed system, allowed to stabilize for 24 hours, and the sample reweighed to determine the amount of water retained. This is the only test that we have had time to perform.

Descriptions of the results of the test and a MATHCAD copy of the calculation are included in the attachments to this memo. The MATHCAD calculation has not been independently checked. The results are as follows:

Summary:

maximum room average initial brine saturation without wet cellulosics	- 0.025
maximum room average initial brine saturation including wet paper and cloth	- 0.064

In addition to the above results, we were able to find a reference giving an average value for the amount of sorbed water in wood (Marks' Standard Handbook for Mechanical Engineers, 8th edition, page 6-122). Inclusion of this contribution gives:

maximum room average initial brine saturation including all cellulosics	- 0.066

All room averages include estimates of moisture in the backfill and nonporous waste constituents.

Copy to:

6115 P. B. Davies
6303 W. D. Weart
6305 A. R. Lappin
6340 SWCF(DRM: WBS 1.1.1.2.3)
6341 A. L Stevens
6342 M. G Marietta
6342 M. S. Tierney
6342 P. Vaughn
6345 F. T. Mendenhall
6345 B. M. Butcher (day file)

Sandia National Laboratories

Albuquerque, New Mexico 87185

date: September 10, 1993

to: P.B. Davies, 6115

from: S. W. Webb, 6115

subject: Countercurrent Flow in a Marker Bed and Implications for Gas Migration - Brine Inflow

The general conclusion that gas migration will shut off brine inflow has been questioned by Webb (1993). This conclusion may be due to parameter selections employed in current calculations such as the fracturing pressure and the assumption of a perfectly horizontal repository. The attachment to the present memo considers the horizontal repository situation and the effect of including the repository dip on fluid flow patterns. Calculations indicate that inclusion of the repository dip allows countercurrent flow in a marker bed and simultaneous gas migration and brine inflow, possibly increasing gas generation. Gas migration distances are also expected to increase due to the lower resistance to gas migration and an asymmetric migration pattern if the repository dip is included.

More detailed simulations are currently planned to address this issue. Note that if radial geometry is used, as is currently done by PA, a three-dimensional model must be used if the repository dip is included. Therefore, current plans are to use cartesian geometry for the scoping calculations to investigate the effects of repository dip.

Reference

Webb, S.W. (1993), Memo to P.B. Davies, "Additional TOUGH2 Simulations Addressing Gas Migration - Brine Inflow Questions," August 10, 1993.

Copy to:
6115 R.L. Beauheim
6115 G. Freeze (Intera)
6115 K. Larson (Intera)
6119 F. Gelbard
6303 W.D. Weart
6305 S.A. Goldstein
6305 A.R. Lappin
6342 D.R. Anderson
6342 E.A. Boucheron
6342 M.E. Fewell
6342 M.G. Marietta
6342 J.D. Schreiber
6342 P. Vaughn
WBS 1.1.4.2.2 - Salado Hydrology and Transport - Model Development

Gas-Liquid Flow Regimes in Porous Media
With Application to Gas Migration and Brine Inflow at the WIPP

Stephen W. Webb, 6115

September 10, 1993

I. Introduction

Analysis of gas migration from the WIPP repository involves gas displacing brine in the interbeds which are modelled as porous media or fractures. In analyses to date, the repository has been assumed to be perfectly horizontal, and migration of gas away from the repository has also resulted in flow of brine away from the repository. In this case, additional brine inflow into the room is shut off, and the gas generation is limited by the brine inventory in the room.

If the repository dip, or angle, is included in the modeling, it is possible for gas to migrate out of the room while brine flows into the repository. Therefore, gas migration may not limit brine inflow, possibly increasing gas generation in the room. This situation is investigated below.

II. Model Development

Consider the flow of two fluids, one wetting (liquid) and one nonwetting (gas), between two points A and B in a porous medium as shown in Figure 1. The gas and liquid pressure at each point are different due to capillary pressure, and each phase undergoes its own friction and gravitational pressure change between the two points as noted. Cocurrent and countercurrent cases are illustrated in Figure 1. Note that these flow patterns occur in a single flow path.

For an arbitrary direction α which is at an angle θ above horizontal as depicted in Figure 2, the Darcy velocity for each fluid is commonly assumed to be given by Darcy's Law or (de Marsily, 1986)

$$V_j = - k \frac{k_{rj}}{\mu_j} \left(\nabla P_j + \rho_j \bar{g} \nabla z \right). \tag{1}$$

When z is defined vertically upward, the above equation can be written as

$$V_j = - k \frac{k_{rj}}{\mu_j} \left(\frac{\partial P_j}{\partial \alpha} + \rho_j g_c \sin \theta \right). \tag{2}$$

Relationships for the two phases are

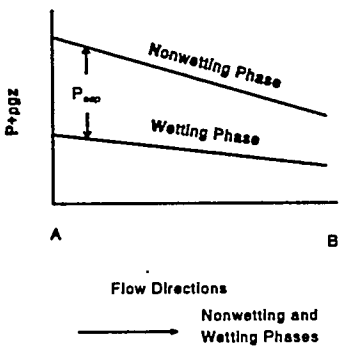

Cocurrent Flow

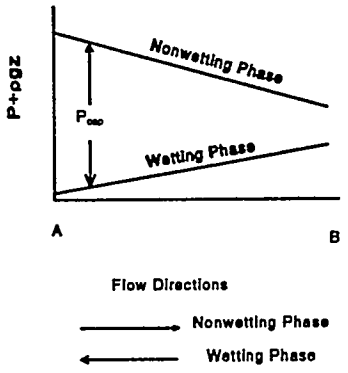

Countercurrent Flow

Figure 1
Flow Regimes

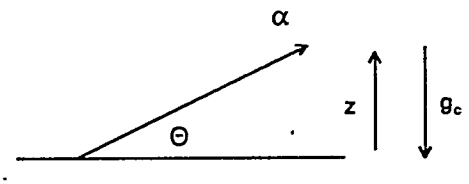

Figure 2
Coordinate System

$$V_w = - k \frac{k_{r,w}}{\mu_w} \left(\frac{\partial P_w}{\partial \alpha} + \rho_w g_c \sin \theta \right) \tag{3}$$

$$V_{nw} = - k \frac{k_{r,nw}}{\mu_{nw}} \left(\frac{\partial P_{nw}}{\partial \alpha} + \rho_{nw} g_c \sin \theta \right) . \tag{4}$$

The capillary pressure expresses the difference in the phasic pressures or

$$P_c = P_{nw} - P_w . \tag{5}$$

Assume that gas migration from the repository is occurring, so the nonwetting Darcy velocity is positive. Equation (3) for the wetting phase Darcy velocity can be written in terms of the nonwetting phase pressure gradient and capillary pressure as

$$V_w = - k \frac{k_{r,w}}{\mu_w} \left(\frac{\partial P_{nw}}{\partial \alpha} - \frac{\partial P_c}{\partial \alpha} + \rho_w g_c \sin \theta \right) . \tag{6}$$

Determination of the wetting phase flow direction, and whether the flow is cocurrent or countercurrent, depends on the value of the term in parentheses, or

$$\frac{\partial P_{nw}}{\partial \alpha} - \frac{\partial P_c}{\partial \alpha} + \rho_w g_c \sin \theta . \tag{7}$$

The nonwetting phase pressure gradient can be expressed as

$$\frac{\partial P_{nw}}{\partial \alpha} = - \frac{V_{nw}}{k} \frac{\mu_{nw}}{k_{r,nw}} - \rho_{nw} g_c \sin \theta \tag{8}$$

so the wetting phase Darcy velocity expression becomes

$$V_w = - k \frac{k_{r,w}}{\mu_w} \left[- \frac{V_{nw}}{k} \frac{\mu_{nw}}{k_{r,nw}} - \frac{\partial P_c}{\partial \alpha} + (\rho_w - \rho_{nw}) g_c \sin \theta \right] . \tag{9}$$

At the limit of zero wetting phase Darcy velocity, or the transition between cocurrent and countercurrent flow, the term in brackets equals zero. This transition nonwetting phase Darcy velocity is

$$V_{nw,tr} = k \frac{k_{r,nw}}{\mu_{nw}} \left[- \frac{\partial P_c}{\partial \alpha} + (\rho_w - \rho_{nw})\, g_c \sin \theta \right]. \quad (10)$$

If V_{nw} is higher than this value, the term in brackets in equation 9 becomes negative, and V_w becomes positive. Since V_{nw} is positive, the flow pattern is cocurrent as gas and liquid flow in the same direction. However, if V_{nw} is lower than this transition value, V_w becomes negative, and countercurrent flow occurs with gas and liquid flowing in opposite directions.

Figure 3 shows the variation of the transition value with saturation. Naturally, the shape of the curve depends on the shape of the nonwetting phase relative permeability. However, the end point values as $k_{r,nw}$ equals 0 and 1 remain the same. Note that the transition Darcy velocity can be zero or negative depending on the capillary pressure gradient, the density difference between the wetting and nonwetting phases, and the angle. In this case, only cocurrent flow is encountered.

In the case of gas migration from the repository, the liquid or wetting phase saturation increases with distance, or

$$\frac{\partial S_w}{\partial \alpha} > 0 . \quad (11)$$

Since capillary pressure generally decreases monotonically with increasing wetting phase saturation, for gas migration

$$\frac{\partial P_c}{\partial \alpha} < 0 \quad (12)$$

and inclusion of the capillary pressure increases the V_{nw} transition value.

The transition value varies with gas saturation due to the relative permeability term and, therefore, will vary with distance from the repository. As depicted in Figure 4, the possibility exists that the countercurrent limit may be reached at an intermediate saturation, so part of the displacement is cocurrent while part is countercurrent. In this case, cocurrent flow would occur in the nose or front of the displacement, while countercurrent flow may occur in the tail.

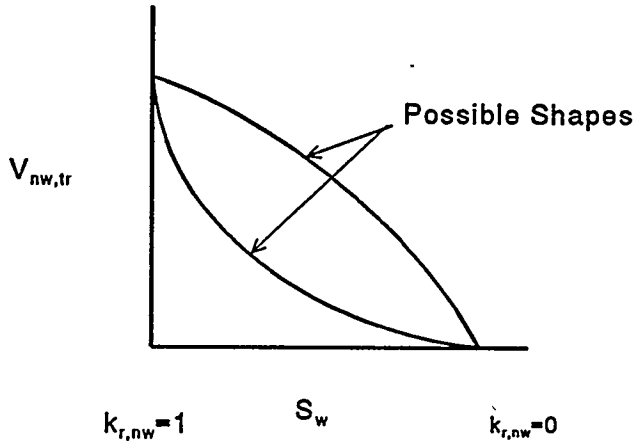

Figure 3
Transition Darcy Velocity Variation

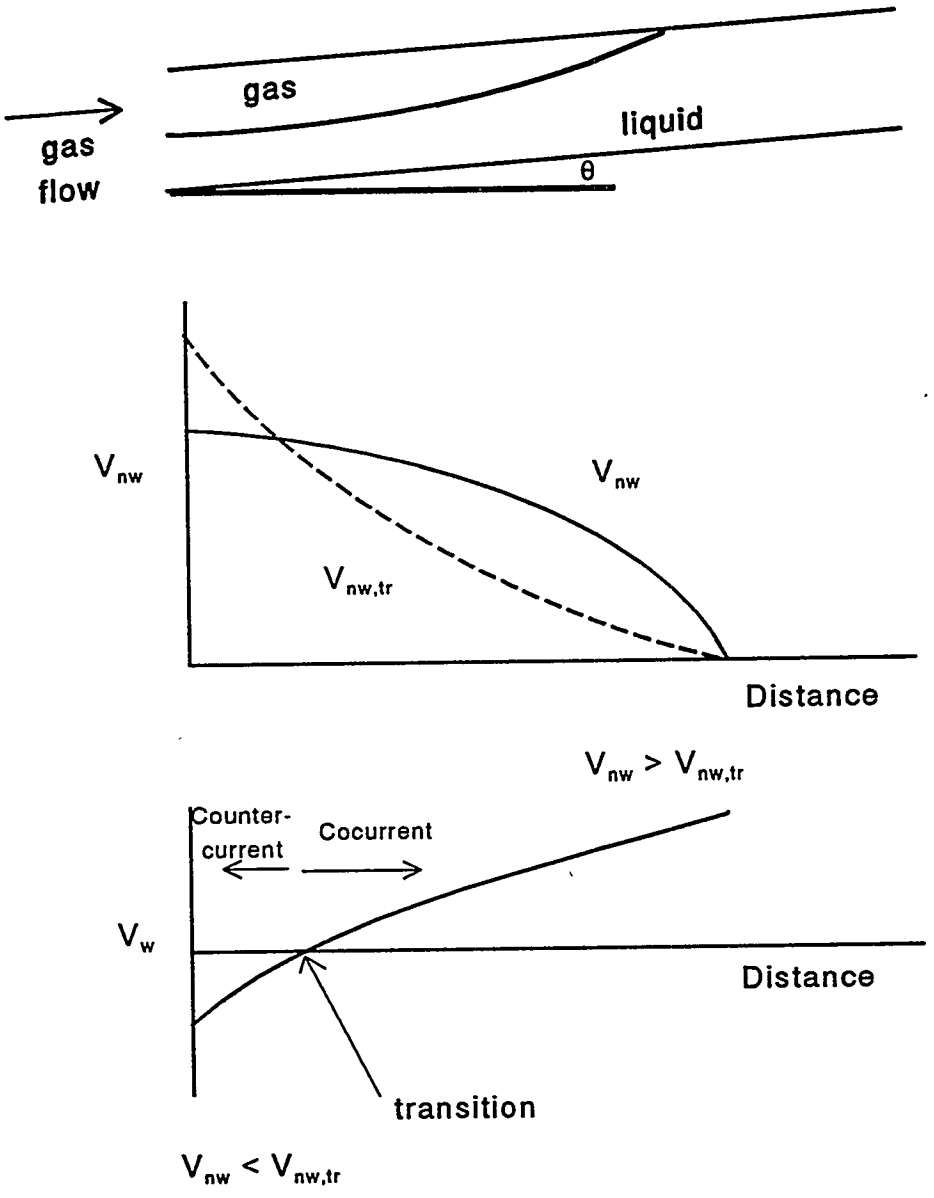

Figure 4
Gas Migration Variation

For completeness, the situation of migration of a wetting phase into a media saturated with a nonwetting phase results in a transition wetting phase Darcy velocity given by

$$V_{w,tr} = k \frac{k_{r,w}}{\mu_w} \left[\frac{\partial P_c}{\partial \alpha} - (\rho_w - \rho_{nw})\, g_c \sin \theta \right]. \quad (13)$$

Special Cases

For a zero capillary pressure gradient,

$$V_{nw,tr} = k \frac{k_{r,nw}}{\mu_{nw}} (\rho_w - \rho_{nw})\, g_c \sin \theta\ . \quad (14)$$

In the case of horizontal flow ($\sin \theta = 0°$), the expression is

$$V_{nw,tr} = k \frac{k_{r,nw}}{\mu_{nw}} \left[- \frac{\partial P_c}{\partial \alpha} \right]. \quad (15)$$

As mentioned above, the capillary pressure gradient for gas migration is negative, so countercurrent flow is possible even for the horizontal case. However, countercurrent flow would tend to reduce the saturation gradient (and capillary pressure gradient) reducing countercurrent flow. This mitigating effect is probably the reason that counterflow has not been observed to date.

Finally, the minimum nonwetting Darcy velocity to ensure cocurrent flow can be evaluated by setting the relative permeability equal to 1.0. In this case, the minimum nonwetting Darcy velocity is given by

$$V_{w,tr} = \frac{k}{\mu_w} \left[\frac{\partial P_c}{\partial \alpha} - (\rho_w - \rho_{nw})\, g_c \sin \theta \right]. \quad (16)$$

If the nonwetting Darcy velocity were always greater than or equal to this value, only cocurrent flow would occur.

III. Application to the WIPP

a. Transition Value

For application to the WIPP, typical parameter values for fractured interbeds will be used assuming a negligible capillary pressure gradient. In this case, the transition value is given by

$$V_{nw,tr} = k \frac{k_{r,nw}}{\mu_{nw}} g_c \sin\theta \, (\rho_w - \rho_{nw}) \qquad (17)$$

For the following parameter values

$k = 10^{-15}$ m^2 (fractured interbeds)
$\mu_{nw} = 10^{-5}$ Pa·s
$\theta = 1°$
$\rho_w = 1200$ kg/m^3
$\rho_{nw} = 200$ kg/m^3,

the value of the transition nonwetting Darcy velocity is

$$V_{nw,tr} = 1.7x10^{-8} \, k_{r,nw} \; m/s = 0.54 \, k_{r,nw} \; m/yr \; .$$

For a porosity of 1%, the appropriate pore velocity is

$$v_{nw,tr} = 1.7x10^{-6} \, k_{r,nw} \, / \, S_{nw} \;\; m/s \; .$$

The gas or nonwetting phase relative permeability in fractures is often assumed to be equal to the nonwetting saturation; this currently is the relationship used in PA calculations. In this case,

$$v_{nw,tr} = 1.7x10^{-6} \; m/s = 54 \; m/yr \; .$$

The actual value of the gas migration velocity is expected to be less than 54 m/yr, so countercurrent flow in which gas migrates from the repository and brine flows into the repository is anticipated if the repository dip is included in the analysis. If the pore velocity is greater than this value during some point of the simulation, brine inflow will stop and gas generation may be limited. However, due to the limited gas generation, the pore velocity may drop below the above value at a later time, and brine inflow will resume, resulting in additional gas generation and migration.

In view of the above numbers, some additional studies using the TOUGH2 code have been performed. In addition to providing gas saturation profiles, the simulations also provide a check on the analysis presented above.

b. One-Dimensional Simulations

One-dimensional simulations of flow in a fracture or in a porous media have been conducted using TOUGH2. The nodalization consists of 102 elements as depicted in Figure 5. Element 1 on the left is meant to simulate the repository and is specified as all gas at a pressure of 12.6 MPa. The rest of the volumes are initialized as being in hydrostatic equilibrium with the room at 12.5 MPa; these volumes have a minimal gas saturation of 0.0001 for numerical purposes. Therefore, the room has a pressure 0.1 MPa higher than hydrostatic, similar to the conditions anticipated at the WIPP. Angles with respect to the vertical of 0 and 1 degrees have been simulated. Naturally, for 0 degrees, there is no hydrostatic gradient, so the initial conditions are all 12.5 MPa. For the 1 degree case, the initial pressures decrease from 12.5 MPa in element 2 to 12.3 MPa at element 102 due to the elevation change. Element 102 is specified as a constant pressure element to avoid pressure buildup in the model. The simulations were run for 3×10^8 seconds. Consistent with current PA models, no capillary pressure was specified. Linear relative permeabilities as shown in Figure 5 are used with a minimal gas residual saturation of 0.001 to avoid gas flow during the hydrostatic calculation.

For 0 degrees, a thin gas layer develops, migrating about 180 m at the end of the simulation as depicted in Figure 6. Gas and liquid Darcy velocities are also shown indicating cocurrent flow as expected. For 1 degree, the same results are shown in Figure 7. For the same time period, the gas migrates 420 m, or over twice as far as in the 0 degree case. The nonwetting phase Darcy velocity and calculated transition velocity based on the saturations are given, indicating cocurrent-countercurrent flow transition at about 150 m. The liquid Darcy velocity shows the transition, as the flow pattern is counterflow from 0 to 150 m (brine inflow to the room), and cocurrent flow further out.

Gas migration is much further for the 1 degree case than for 0 degrees. The reason for the difference is that, for 0 degrees, the gas has to push the water down the entire porous media or fracture length. For 1 degree angle, some of the water flows into the room, out of the way of the migrating gas, making it easier for gas migration. Therefore, not only will the dip of the repository increase brine inflow into the room (which may increase the amount of gas generated), it will also increase gas migration distances for the same amount of gas. The gas migration pattern is also expected to be asymmetric since migration upward will be much easier than downward. Gas migration distances are expected to increase dramatically compared to the horizontal case.

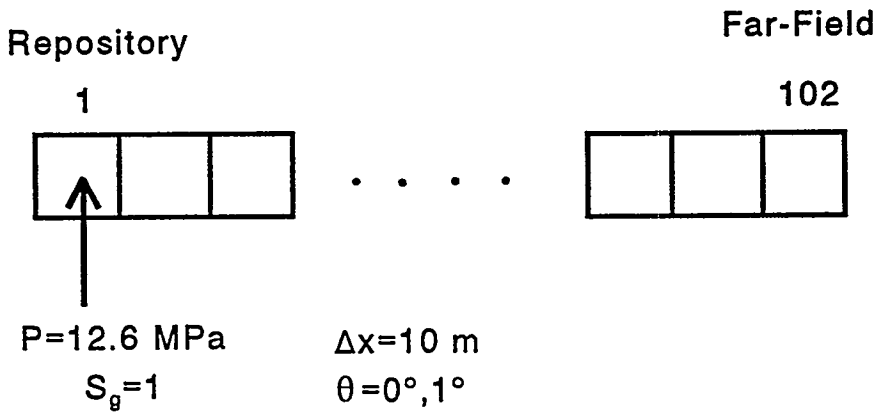

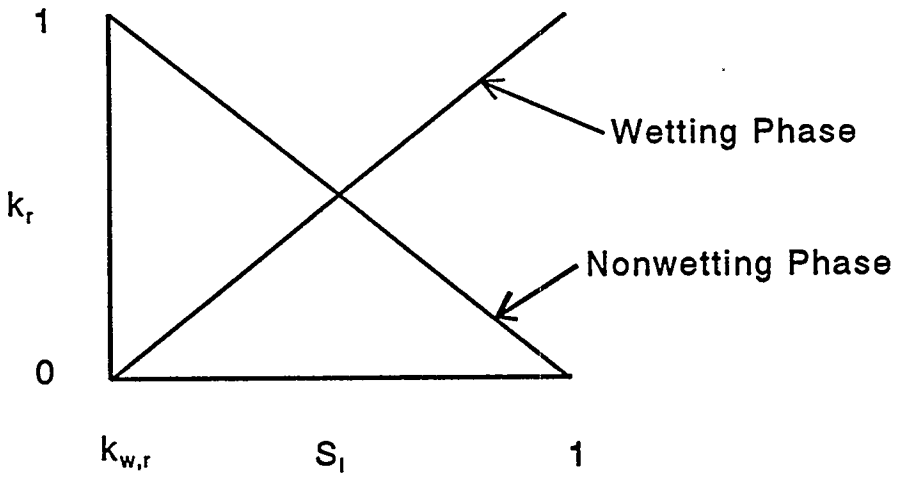

$k_{w,r}$ = 0.001

Figure 5
One-Dimensional Model

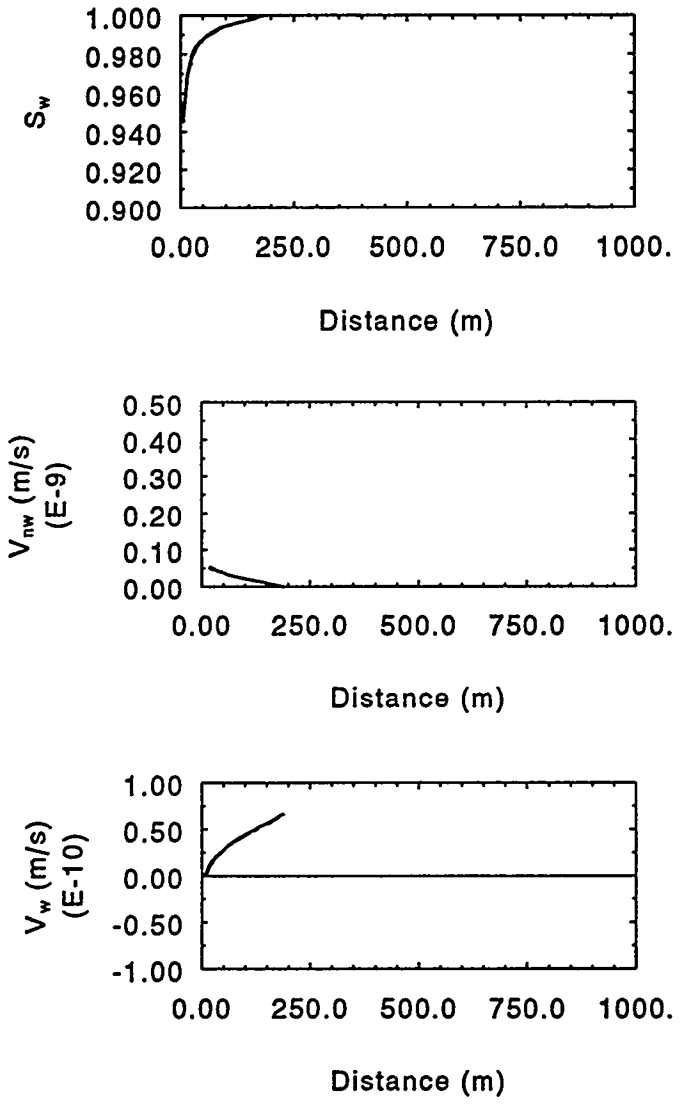

Figure 6
Zero Degree Results

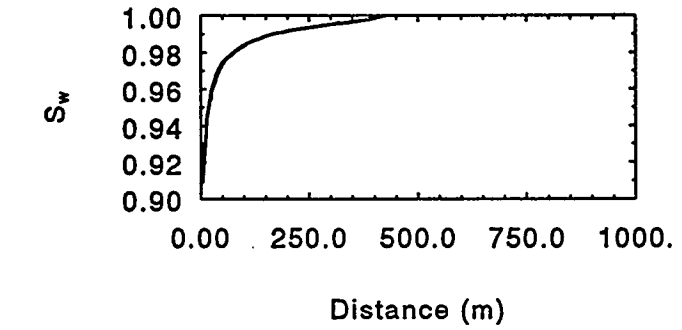

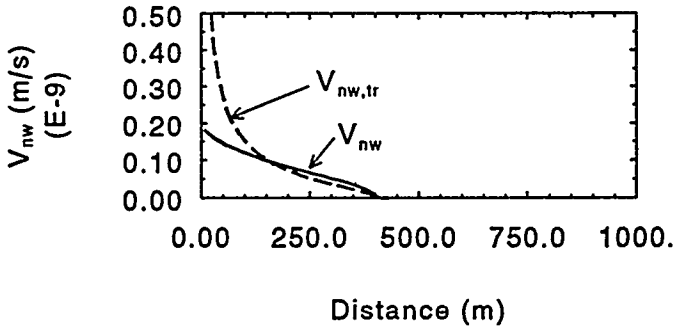

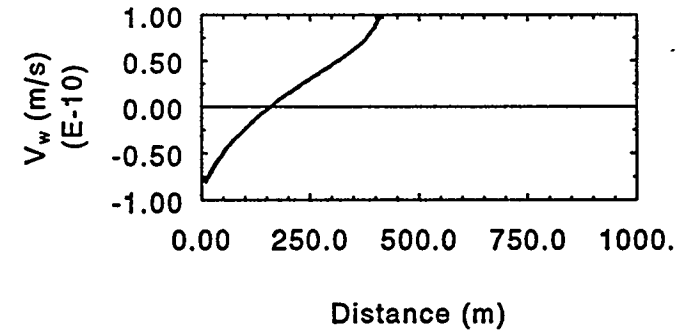

Figure 7
One Degree Results

IV. Discussion

The above analysis is based strictly on Darcy's law with the attendant physics. Note that Darcy's law is used in the current suite of codes commonly employed on the WIPP project such as TOUGH2 (Pruess, 1991) and BRAGFLO (WIPP PA Department, 1992). In addition to Darcy's law, the stability of the gas-liquid interface should be considered. In the present case, a less viscous fluid (gas) is displacing a more viscous fluid (brine), and the fluid interface is potentially unstable. This condition could result to viscous or capillary fingering as discussed by Lenormand, et al. (1988) among others. Fingering could alter the regions of cocurrent and countercurrent flow. Therefore, care should be used in applying the above criteria too strictly; it is only a guideline and only as good as the physics included in Darcy's law.

V. Conclusions

Inclusion of the repository dip in gas migration calculations could have a significant impact on gas migration distances. In the above simplified model, inclusion of the repository dip allowed simultaneous gas migration and brine inflow, possibly increasing the amount of gas generated. In addition, the gas migration distance increased by a factor of two or more due to the lower resistance to gas migration. The gas migration flow pattern will be asymmetric if the repository dip is included as migration upward is easier than downward. Such conditions need to be analyzed in more detail.

Simulations are currently planned to address this issue. Note that if radial geometry is used, as is currently done by PA, a three-dimensional model must be used if the repository dip is included. Therefore, current plans are to use cartesian geometry for the scoping calculations to investigate the effects of repository dip.

VI. Nomenclature

g	gravitational vector
g_c	gravitational constant
k	permeability
P	pressure
S	saturation
v	pore velocity
V	Darcy velocity

Greek

α	arbitrary direction
θ	angle with respect to the horizontal
μ	viscosity
ρ	density

subscripts

c	capillary
j	direction
nw	nonwetting
r	relative
tr	transition
w	wetting

VII. References

de Marsily, G. (1986), Quantitative Hydrology, Academic Press, Inc., Orlando, FL.

Lenormand, R., E. Touboul, and C. Zarcone (1988), "Numerical models and experiments on immiscible displacements in porous media," F. Fluid Mech., Vol. 189. pp. 165-187.

Pruess, K. (1991), "TOUGH2 - A General-Purpose Numerical Simulator for Multiphase Fluid and Heat Flow," LBL-29400, Lawrence Berkeley Laboratory, May 1991.

WIPP Performance Assessment Department (1992), Preliminary Performance Assessment for the Waste Isolation Pilot Plant, December 1992 - Volume 2: Technical Basis, SAND92-0700/2, Sandia National Laboratories, December 1992.

— WP09193

date: February 21, 1994 **INFORMATION ONLY**

to: Rip Anderson
Jde for Palmer Vaughn Jde for Jde for

from: Dan Stoelzel, Palmer Vaughn, Jim Bean, Jim Schreiber

subject: Summary of 1993-94 WIPP Preliminary Undisturbed Repository Calculations

1994 Performance of Untreated Wastes for the Undisturbed Repository: Comparison to 1992 PA, Preliminary Results & Sampled Consequences vs. Mean / Median Calculation

1. Model Conceptualization:
The model set-up for the 1994 calculations is summarized in Table 1. The grid layout is essentially unchanged from that used in the 1992 calculations (see Figures 1, 2, and 3), with the exception being an increase in stratigraphy from the Castile to the surface (same as for the intrusion scenarios). This did not affect gas migration to the surface, since the gas stopped at the lower shaft seal for all the calculations. In addition, the waste region is divided into two areas, labeled Repository and Panel. The fluid and material parameters for the two waste areas are exactly the same, the only difference being that the Panel volume represents one excavated panel (the North Equivalent Panel), and the Repository volume contains the waste for the remaining panels in the proposed site. The "Entire Repository" is the Panel and the Repository together. This conceptualization of the waste region was not done for previous PA's and should provide a better representation of fluid flow within the entire repository.

2. Description of the Input Parameters and Changes from the 1992 Model:
Tables 2 through 6 describe the input variables used for the 50 calculations performed for this study. Twenty three of the variables were sampled over a specified range. One additional calculation was made (the "Example Calculation"), in which the input variables were determined by a "best guess" within the distribution of values for each parameter: either the median (for rock properties) or the mean (for the remaining parameters such as corrosion rates and waste inventory). This calculation was made to show the non-linear relationship that exists between the input parameters and the model consequences after 10,000 years. As expected, the results from the "example" run did not match the mean or median of the consequences from the 50 runs with sampled input parameters. Major changes from the 1992 PA models are described below:

   A. Fracturing of the anhydrite layers is approximated based on pressure dependent alterations to the rock compressibility, permeability and porosity of the affected layers. The intact compressibility, permeability and porosity are increased when the brine pressure is above the fracture pressure of 12.6 MPa to a maximum value calculated at 15.0 MPa (the alteration zone). The full fracture permeability and porosity (upper limit at 15.0 MPa) are shown on Table 5. The fracture model was explained in a previous memo from Sam Key (RE/SPEC) dated 3-Sep-1993. Essentially, anhydrite compressibility is increased linearly to a maximum value, based on the increase in pore pressure due to gas generation. Porosity (ϕ) is related to compressibility, and absolute permeability (k_{abs}) is related to porosity, hence, ϕ and k_{abs} also increase within the anhydrite layers as pressure increases. This is shown in Figures 4 and 5. The methodology adopted for this model was reviewed by the Fracture Expert Group, and deemed reasonable for a "first effort". It was also recognized by the group that experimental data is needed to support the model or any alternative.

   B. Permeability and porosity data were provided by Rick Beauheim and Susan Howarth. The anhydrite intact (absolute) permeability was modified for the 1994 assessment. The median value was increased slightly from 5.0×10^{-20} m^2 to 6.3×10^{-20} m^2, with the sample range reduced from five orders of magnitude to three orders of magnitude, mainly at the high end. This is in contrast to the 1992 range of permeabilities, which were arbitrarily extended to 1×10^{-16} m^2 to "approximate" fracturing in the anhydrite. The anhydrite median porosity was increased from 1.0% in 1992 to 1.4% in the current calculations. These changes, along with the fracture model, resulted in an overall increase in gas migration distances in the anhydrite, and a decrease in repository pressures.

   C. The permeability of the lower shaft seal (<200 years) was changed from a sampled range of 1×10^{-19} m^2 - 5×10^{-16} m^2 to a fixed value of 8×10^{-18} m^2, as recommended by Ray Finley. This greatly

reduced gas migration up the shaft, and diverted gas to MB 138 instead. For the 1994 undisturbed calculations, gas flow did not go past the top of the Salado Formation.

D. The disturbed rock zone (DRZ) porosity was changed from a sampled value designed to be slightly greater than the halite porosity (although not to exceed the maximum allowable halite porosity of 0.1% to 6.0%); to a fixed value of 1.5%. This had the effect of reducing the available gas storage in the DRZ. These changes were made as a result of recommendations by Dept. 6115 and others.

E. The values for initial liquid (brine) saturation in the waste were reduced from a sampled range of 0% - 14% (7.0% median) to 0.04% - 5.2% with a 0.44% median. These values are based on a Westinghouse analysis of free liquid content in EG&G / INEL waste, and a study done by Barry Butcher to estimate the brine content in the backfill and residual liquid in the cellulosics. This new range lowered the volumes of gas generated, since there was less initial brine available for reaction.

F. The gas generation submodel parameters were also changed (see Table 5). New estimates were provided by Larry Brush. The range of values for inundated corrosion rate was increased significantly (from a maximum of 2 mol/drum/year to 150 mol/drum/year), and the range for humid corrosion rate was greatly reduced (with a median value of zero). This caused an increase in gas generation for wet environments, and lower gas generation in humid environments.

3. Preliminary Results:

A. Pressures in the Waste: Figure 6 shows a time plot of the volume averaged Panel pressures for all 50 calculations. The Repository pressures are nearly identical, and are therefore not shown. The affects of the fracture model and higher anhydrite permeability are seen as the gas is allowed to flow more easily into the anhydrite and most of the pressures peak below the fracture upper pressure limit of 15.0 MPa. The pressure behaved differently in the 1992 calculations, in which half of the realizations remained above the 14.8 MPa lithostatic pressure to 10,000 years, many in the 20 MPa range. For the current calculations, the average pressure peaks at 14.7 MPa and declines to 13.5 MPa after 10,000 years, which is much closer to the far-field pressure (12.5 MPa) than was reached by the 1992 calculations. For one third of the current realizations, pressures reach levels higher than lithostatic, usually within the first 1,500 years, and then decline rapidly. The reason for this is still under investigation, but is probably a result of the interaction between the fracturing model and the two phase flow behavior within the DRZ and anhydrite layers. It is possible that the effective permeability for gas (as defined by the relative permeability model used for each consequence) may be restricting the gas flow leaving the repository at low gas saturations. Figure 7 shows a histogram of the Panel pressures at 10,000 years. The majority of the pressures ended in the 12 to 14 MPa range, whereas the 1992 pressures ended in a fairly even distribution from 6 to 22 MPa. The pressure resulting from the Example Calculation peaked slightly lower than the average of the consequences, (14.0 MPa compared to 14.7 MPa), but was very close to the mean after 10,000 years.

B. Brine Saturation in the Waste: Brine saturation is important, as it is needed for the corrosion and biodegradation processes in gas generation. Figure 8 shows brine saturation behavior over time for the Panel (the Repository saturations were nearly identical). This pattern is similar to the one seen in the 1992 calculations, with a rapid, early increase in saturation as the reduction in porosity due to creep closure results in an increase in brine saturation, and a small amount of brine flows in from the DRZ and anhydrite layers. Brine saturation then drops rapidly as it is consumed in the corrosion process. The brine saturations in the waste remain higher through time for the 1992 calculations due to higher initial brine saturations, and increased brine inflow from the surrounding DRZ and anhydrite layers. Note that the Example Calculation brine saturation remains fairly close to the median of the 50 consequences.

C. Brine Flow in the Waste: As in the 1992 calculations, net brine flow was generally *into* the Repository; however, the volume of brine inflow was less for the 1994 runs. In the 1992 calculations, several realizations exceeded 10,000 m^3 brine inflow, whereas the 1994 runs had only a few exceeding 5,000 m^3 brine inflow to the Repository (see Figure 9). This discrepancy may be in part due to the lower DRZ porosity in the 1994 model, which reduced the available brine volume in the rock surrounding the waste region, as well as the lower permeability in the intact anhydrites, which are the major pathways

for brine inflow. The updated representation of the undisturbed model may also have an influence on fluid flow, especially that of the brine. In the 1992 mesh the waste is one continuous region, whereas in the 1994 conceptualization, the waste region is split into two distinct areas: the Panel and the Repository, separated by a panel seal. For the majority of the calculations, the net brine flow was *out of* the Panel (Figures 10, 11, and 12). As in the 1992 calculation, the main pathway for brine flow is in the anhydrite layers. The brine flowing into the waste region most likely originates from the South, since the brine from the Northern layers has a greater distance to travel to reach the waste and must pass through a lower permeability backfill and seal region. Brine flowing from the South is partially diverted to the Repository on its way to the Panel. This is illustrated in Figure 13, which shows the brine inflow to the Panel for all realizations. The brine volumes flowing into the Panel were extremely low, with the average of the 50 consequences being 152 m^3 and the median 15 m^3. Hence, fluid flow through the system is influenced by the conceptualization of the repository, especially on how the panels are represented within the waste region. For the Example Calculation, the net brine flow for the Repository was 1,890 m^3 inward, which fell between the mean and median values of the 50 consequences, whereas the Example net brine flow for the Panel, 224 m^3 outward, was somewhat less than the mean and median values. In addition figure 13 shows that the brine flowing into the Panel for the Example Calculation (7 m^3) is considerably lower than the mean and median of the consequences.

D. Gas Generation : Changes in the gas generation model, along with a reduction in available brine for reaction, resulted in less gas generation than in the 1992 calculations. Figure 14 shows total gas generated over time for the Entire Repository. At 10,000 years, cumulative gas produced ranged from 146 to 1,107 mol/drum, or 2.9×10^6 m^3 to 22.0×10^6 m^3, compared to 160 to 1600 mol/drum, (3.0×10^6 to 32.0×10^6 m^3) for the 1992 PA (all gas volumes are measured at reference conditions of 300.15 K and 101.325 kPa). For comparison, the range of gas that could theoretically be generated if all reactants were consumed, based on maximum and minimum inventory and stoichiometry, would be 860 to 1940 mol/drum (17.1×10^6 m^3 to 38.6×10^6 m^3). The gas generated as a result of the corrosion process is shown in Figure 15. Two distinct patterns are evident. At high corrosion rates, gas production rises rapidly until the available brine is consumed, at which point the gas generation either stops or slows down dramatically. The rapid gas generation causes a steep increase in repository pressure above the far-field pore pressure of 12.5 MPa, which restricts brine flow into the repository to limit reaction even more. The other major trend is a slow, steady increase in gas generation. Because the repository pressure does not rise as rapidly in these scenarios, it is possible to have a steady influx of brine. Figure 16 shows iron content in the Panel over time (similar curves were observed for iron content in the Repository). Figure 17 is a histogram of the iron remaining at 10,000 years. Note that none of the calculations resulted in 100% iron consumption, unlike the 1992 results, in which 26% of the scenarios resulted in complete iron consumption. Gas production resulting from biodegradation also follows two distinct trends (Figure 18). On average, the biodegradation rates are higher than the corrosion rates, hence, about 50% of the scenarios resulted in 100% consumption of the cellulosics (Figures 19 and 20). Because there was a smaller inventory of cellulosics than metals, the volume of gas produced by biodegradation was about half of that resulting from corrosion. The total gas generated in the Example Problem closely matched the median value of gas generation for the 50 consequences. However, the Example Problem was lower in gas resulting from corrosion, and higher in gas resulting from biodegradation than the mean and median of the 50 consequences.

E. Gas Migration: Table 7 summarizes gas migration distances in each of the anhydrite layers for all 50 realizations and the shaft. The maximum distance reached by the gas within each anhydrite layer was determined by adding together the x-dimensions of the grid blocks containing gas leading away from the edge of the repository. The distance reached in the farthest most grid block containing gas was determined by proportioning the x-dimension of that grid block by its S_{gmax} / S_{gr} ratio. Because of the rectangular flaring concept used to describe the geometry of the anhydrite layers, the pore volumes increase in the grid cells leading away from the repository (note the Δx and Δz dimensions in Figures 3, 4, and 5). Therefore the coarseness of the mesh around the Land Withdrawal Boundary (LWB) affects the calculation of the gas migration distances to some degree. It is planned to run a set of calculations in a model with a finer mesh leading away from the repository to improve the resolution of the migration distances. For the current calculations, eighteen of the fifty realizations (36%) had gas reach the LWB at 2,400 meters. Gas migration distance was also highly dependent on the relative-permeability sub-model used to determine two phase flow, as well as the permeability and porosity

changes resulting from the fracture model. Approximately one third (16 out of 50) of the scenarios used the Van Genuchten / Parker (VG/P) submodel, and the remaining two thirds used the Brooks-Corey (B-C) relationship to determine relative permeability. Each of the models requires two key parameters to determine the shape of the relative permeability curves: a residual brine saturation (S_{br}) and a pore size distribution parameter (λ). In addition, the Brooks-Corey model requires a residual gas saturation (S_{gr}). All three of these parameters were sampled to create fifty different relative permeability curves. Figures 21 and 22 show the relative permeability curves used for realization #6, which uses the VG/P model, and realization #16, which uses the B-C model. The importance of S_{gr} becomes obvious when comparing these two models. For the VG/P curves, gas is mobile as soon as it enters the grid block (the k_{rg} curve in Figure 21). For the B-C model, gas must first exceed S_{gr} before it can move through the grid block (compare the k_{rg} curve in Figure 22), creating gas storage proportional to (grid block pore volume) x S_{gr} for each grid block within the anhydrite layers. This is why 14 of the 16 realizations using the VG/P model had gas reach the LWB since the gas was able to move freely through the layers, even at low gas saturations. Only 4 of the 34 realizations using the B-C model reached the LWB, as the gas mobility was restricted by the residual gas storage inherent in the relative permeability model. Note that the four B-C calculations (realizations 17, 18, 27, and 37) that reached the LWB had relatively low residual gas saturations (< 10%), meaning lower gas storage. Similarly, the increase in anhydrite permeability due to the fracture flow model assisted flow out of the repository, offsetting the increase in gas storage resulting from higher fracture porosities. It would appear that the two-phase flow properties, specifically the permeability changes due to the fracture model and relative permeability models, have a greater impact on gas migration distance than do the other sampled properties such as gas generation (i.e. corrosion rates) and porosities. Many of the realizations in which large amounts of gas were generated have relatively short migration distances due to their high residual gas saturations. Because of the fracture model, at least half of the calculations had gas volumes of $1x10^6$ m^3 or more escape the repository into the anhydrite layers, but very few of those had gas make it to the LWB due to their mobility as defined by their fluid's relative permeabilities. This is illustrated by figures 23, 24, and 25 for Anhydrite A&B South. Of the top six realizations with gas escaping the repository, only one (realization #6) had significant amounts of gas escape to the LWB. A similar pattern was seen for the other anhydrite layers. These gas migration results differ significantly from the 1992 calculations. Only 6 out of 70 scenarios (9%) had gas reach the LWB, in spite of the larger amounts of gas generated. Gas migration up the shaft was insignificant (Figure 26) compared to the 1992 PA. The gas that may have otherwise escaped up the shaft appears to have been diverted laterally into MB 138, as gas migration occurred there (see Table 7), where it had not been apparent in the 1992 PA. The maximum migration distance reached for the Example Problem was 866 meters from the repository edge in Anhydrite A&B South. This was significantly less than the mean and median distances of the 50 consequences for that layer. Once again, this illustrates the extreme non-linearity of the system, and the value of the Monte-Carlo sampling method when experimental input data is unavailable. It should be noted that the effects of capillarity are not accounted for in this model due to lack of capillary pressure data. The gas (and brine) migration distances may change significantly if capillary pressure were added to the model.

4. Conclusions:
   A. For the 1994 undisturbed PA, gas migration to the Land Withdrawal Boundary is influenced by fluid flow parameters such as relative permeability, as well as altered rock properties caused by the fracturing model.

   B. The incorporation of a fracture approximation sub-model played a major role in reducing repository pressures and allowing more gas to escape.

   C. The reduced lower shaft seal permeability effectively stopped gas flow through the shaft to the Culebra, but in diverting the gas away from the shaft, an increase in lateral migration to MB 138 resulted.

   D. Using a mean or median value for input parameters in lieu of accurate experimental data may lead to significant inaccuracies in model results when compared to the statistical findings (maximum, minimum, mean, median, etc.) resulting from Monte Carlo uncertainty analysis, due to the non-linearities inherent in the system.

Table 1. Summary of Conceptual Models Associated with Repository and Salado Fluid Flow in Performance Assessment.

Geometry/ Stratigraphy (PA)	Fluid Flow and Storage in Host Rock	Repository Processes	Seal/Shaft Treatment	Multi-Phase, Porous Media Flow
• Repository with DRZ, Salado to surface, three anhydrite interbeds	• Intact halite and anhydrite - Darcy flow model • DRZ (P. Davies) - provide communication through enhanced permeability only • Altered anhydrite (Fracture Expert Group, R. Beauheim) - rock compressibility increases with pore pressure and is reflected in permeability and porosity changes	• Disposal room consolidation (B. Butcher) - pressure based porosity surface • Gas generation - linear correlation/ average stoichiometry model (P. Davies) - corrosion of Ferrous Metals; biodegradation of Cellulosics (L. Brush)	• Hydrologic properties specified in two time periods (panel and shaft) (J. Tillerson)	• Standard assumptions common in multi-phase flow literature (J. Bear) • Two-phase behavior based on literature values (P. Davies)

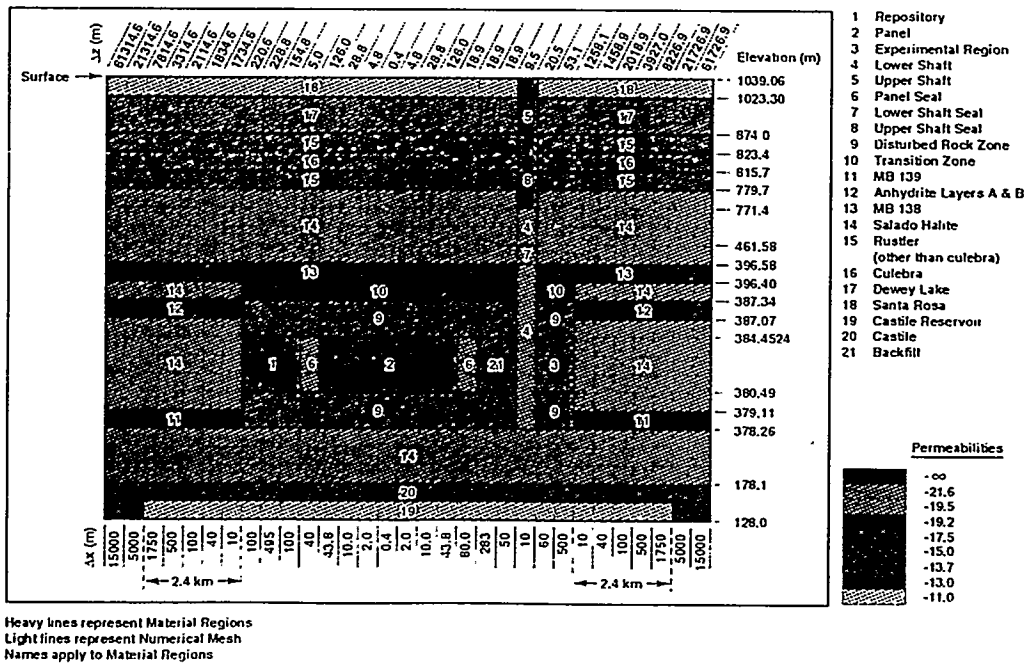

Heavy lines represent Material Regions
Light lines represent Numerical Mesh
Names apply to Material Regions

Figure 1. Material Permeabilities for 1994 Undisturbed Repository Simulations.

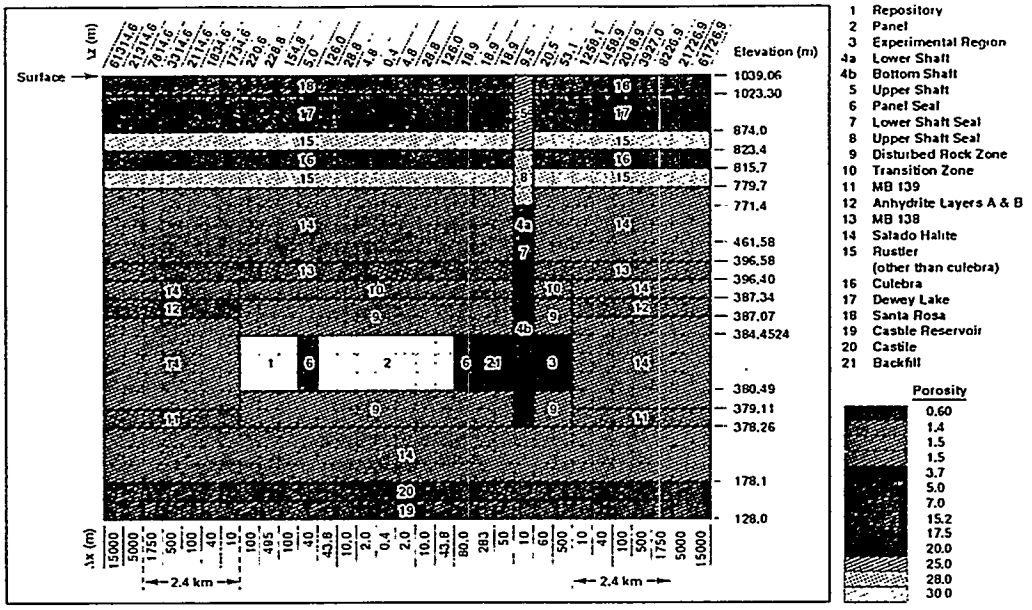

Heavy lines represent Material Regions
Light lines represent Numerical Mesh
Names apply to Material Regions

Figure 2. Material Porosity for 1994 Undisturbed Repository Simulations.

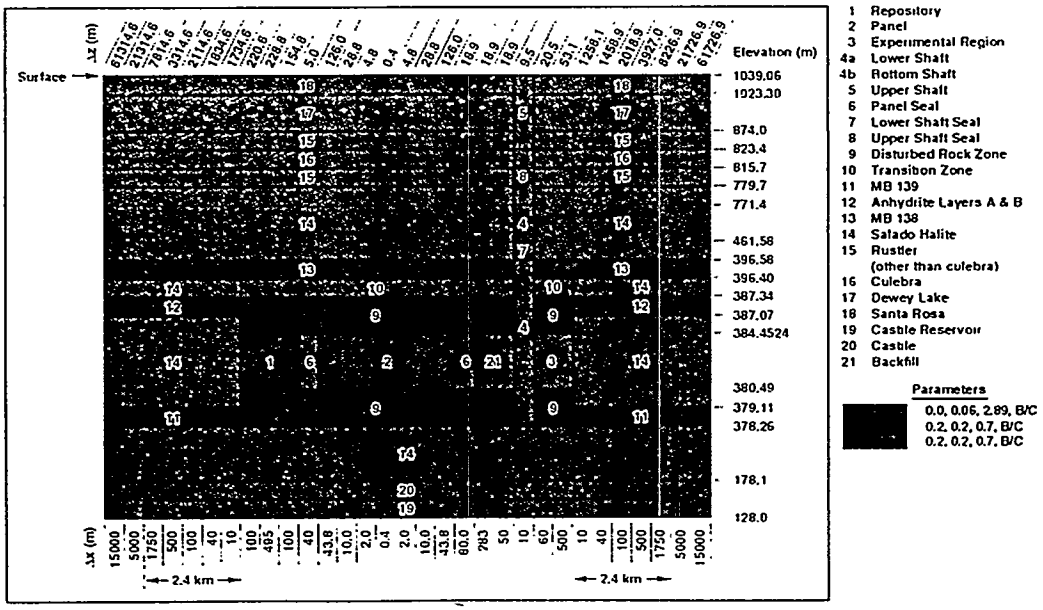

Heavy lines represent Material Regions
Light lines represent Numerical Mesh
Names apply to Material Regions

Figure 3. Two Phase Flow Parameters for 1994 Undisturbed Simulations.

Table 2. Material Permeabilities for 1994 Undisturbed Repository Simulations.

Material Name	Time Period Other Than >0 yr	Sampled	Log (Permeability) [Log (m^2)] Range Minimum	Range Maximum	Example Calculation
Impermeable		N	--	--	$-\infty$
Halite		Y	-22.4	-20.2	-21.6
Panel Seals Lower Shaft Lower Shaft Seal	(>200 yr) (>200 yr)	Y	-21.0	-18.0	-19.5
Anhydrite A & B MB138 MB139 Transition Zone		Y	-20.0	-18.0	-19.2
Rustler (other than Culebra)		N	--	--	-17.5
DRZ Experimental Backfill Bottom Shaft Dewey Lake Red Beds		N	--	--	-15.0
Culebra		N	--	--	-13.7
Waste Disposal Region Upper Shaft Upper Shaft Seal		N	--	--	-13.0
Castile Brine Pocket Santa Rosa		N	--	--	-11.0
Lower Shaft Lower Shaft Seal	(<200 yr) (<200 yr)	Y N	-19.0 --	-15.0 --	-17.0 -17.1

Table 3. Material Porosities for 1994 Undisturbed Repository Simulations.

Material Name	Sampled	Range		Porosity [% of Material Volume]		
		Minimum	Maximum	Mean	Median	Example
Castile	N	--	--	0.55	0.50	0.60
Anhydrite A & B MB138 MB139	Y	0.4	2.7	1.4	1.4	1.4
Halite Transition	N	--	--	1.5	1.0	1.5
DRZ	N	--	--	1.0	1.5	1.5
Experimental; Backfill Bottom Shaft	Y	1.0	7.5	3.7	3.7	3.7
Power Shaft Lower Shaft Seal	N	--	--	5.0	5.0	5.0
Panel Seal	N	--	--	7.0	7.0	7.0
Culebra	Y	9.5	25.2	15.2	15.2	15.2
Santa Rosa	N	--	--	17.5	13.0	17.5
Dewey Lake	N	--	--	20.0	20.0	20.0
Upper Shaft	N	--	--	25.0	25.0	25.0
Upper Shaft Seal	N	--	--	28.0	28.0	28.0
Rustler (not Culebra)	N	--	--	30.0	30.0	30.0

Table 4. Two Phase Flow Parameters for 1994 Undisturbed Simulations.

Material Region	Parameter Name	Sampled/ Fixed	Range		Mean	Median	Example
			Minimum	Maximum			
Halite	Residual Gas Saturation	F	--	--	0.2	0.2	0.2
Transition	Residual Brine Saturation	F	--	--	0.2	0.2	0.2
Culebra	Pore Distribution Parameter	F	--	--	5.1	0.7	0.7
Rest of Rustler	Sub-Model	F	--	--	B/C	B/C	B/C
Dewey Lake							
Santa Rosa							
Panel Seals							
Shaft Seals							
Shaft Fill							
Anhydrite A & B	Residual Gas Saturation	S	0	0.4	0.2	0.2	0.2
MB138	Residual Brine Saturation	S	0	0.4	0.2	0.2	0.2
MB139	Pore Distribution Parameter	S			5.1	0.7	0.7
DRZ	Sub-Model	S	B/C	VG/P	B/C	B/C	B/C
Waste Disposal	Residual Gas Saturation	F	--	--	0.0	0.0	0.0
Area	Residual Brine Saturation	F	--	--	0.06	0.06	0.06
	Pore Distribution Parameter	F	--	--	2.89	2.89	2.89
	Sub-Model	F	--	--	B/C	B/C	B/C

Notes
Threshold Displacement Pressure Correlated to Permeability Except in Anhydrite.
Threshold Displacement Pressure of Anhydrite is Assumed to be Zero.

Table 5. Altered Anhydrite Flow Parameters.

Name	Sampled/ Fixed	Range		Mean	Median	Example
		Minimum	Maximum			
Log (Full Fracture Permeability limit) [log (m^2)]	S	-9	-13	-11	-11	-11
Full Fracture Porosity limit [% volume]	F	--	--	.10	.10	.10

Table 6. Gas Generation Parameters.

Name	Sampled/ Fixed	Range		Mean	Median	Example
		Minimum	Maximum			
Initial Brine Saturation (% void) In Waste Disposal Area	S	0.03	5.16	2.6	0.36	0.36
Corrosion Rates (mol/drum/yr)						
Humid	S	0.0	0.096	3.8×10^{-3}	0.0	0.0 Median
Inundated	S	0.0	150.0	30.6	0.6	0.6 Median
Biodegradation Rates (mol/drum/yr)						
Humid	S	0.0	1.0	0.18	0.1	0.1 Median
Inundated	S	0.0	5.0	1.8	1.0	1.0 Median
Gas Stoichiometry (mol gas/mol reactant)						
Corrosion	S	1.0	1.33	1.17	1.17	1.17 Median
Biodegradation	S	0.0	1.67	.835	.835	.835 Median
Inventory (Volume Fraction)						
Metals	S	.321	.521	.421	.421	.421 Median
Cellulose	S	.272	.472	.372	.372	.372 Median

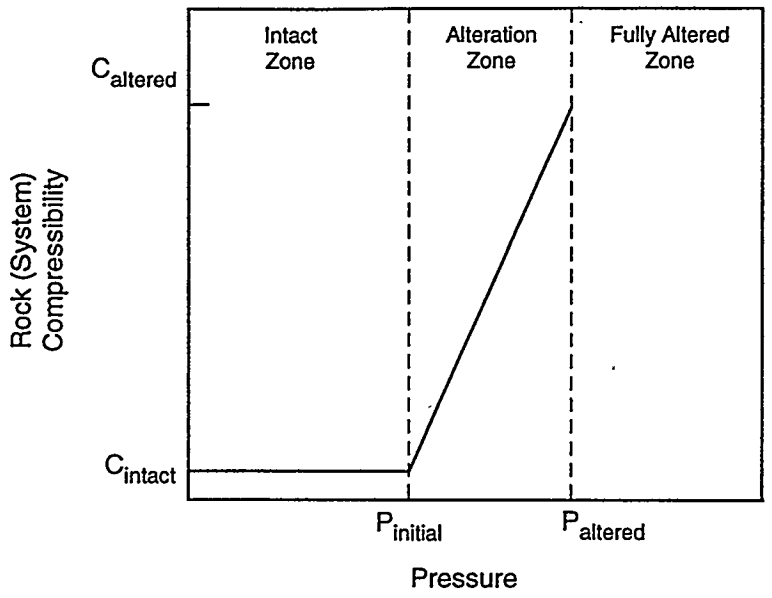

Figure 4. Compressibility Dependencies on Pore Pressure.

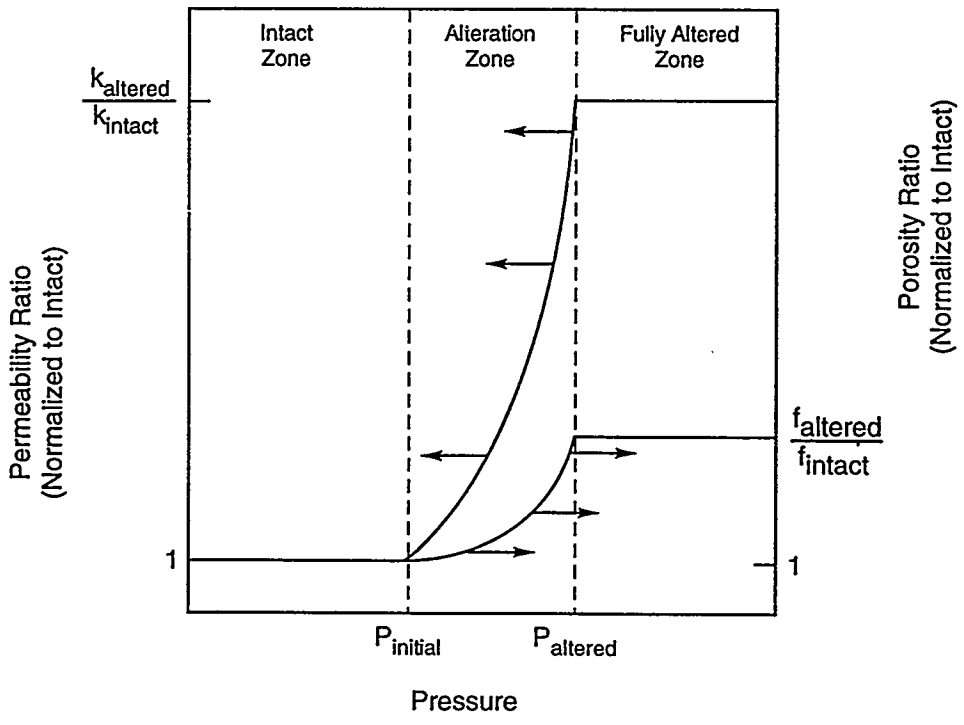

Figure 5. Permeability and Porosity Dependencies on Pore Pressure.

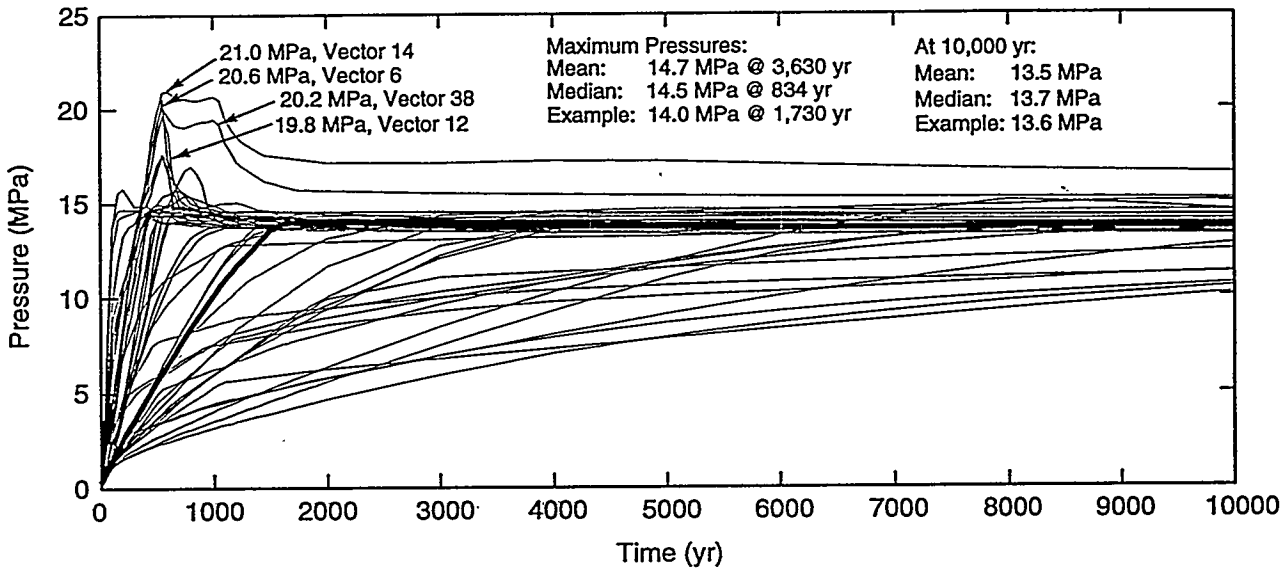

Figure 6. Volume Average Pressure in the Panel.

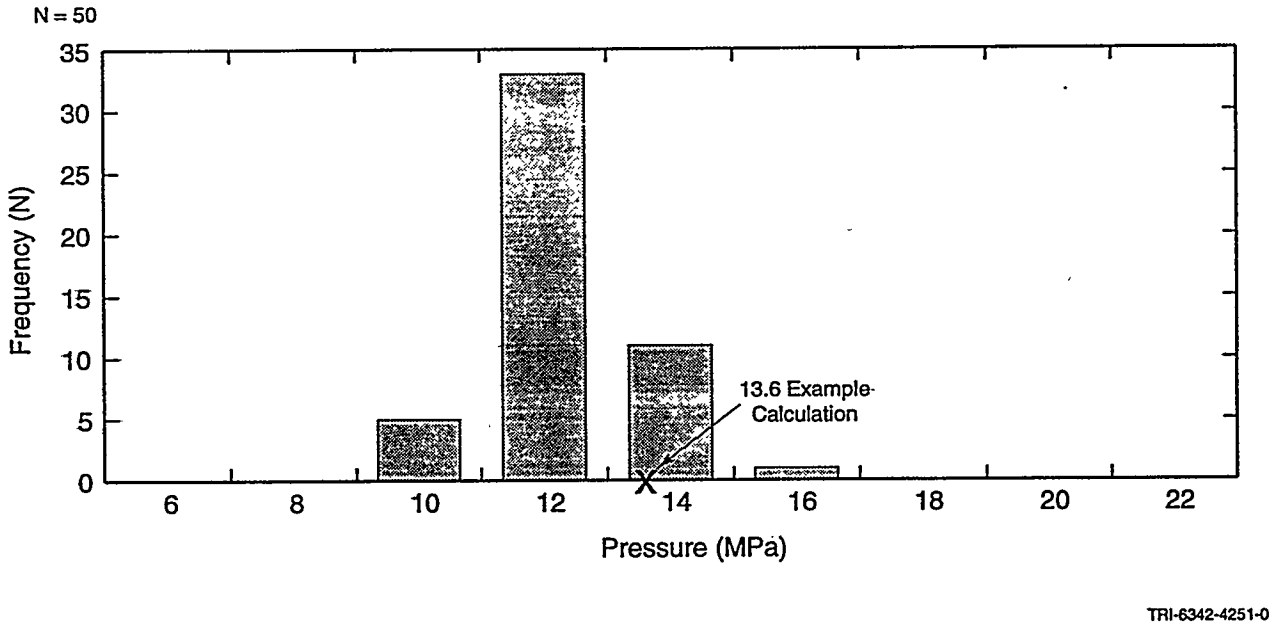

Figure 7. Volume Average Panel Pressure at 10,000 yr.

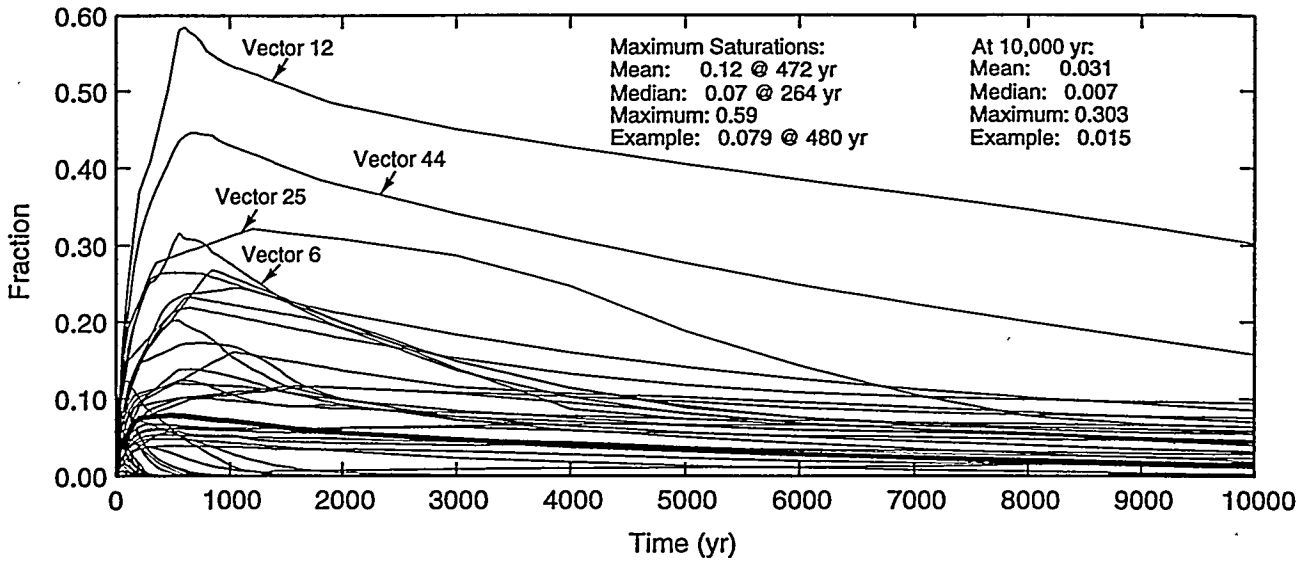

TRI-6342-4252-0

Figure 8. Volume Average Brine Saturation in the Panel.

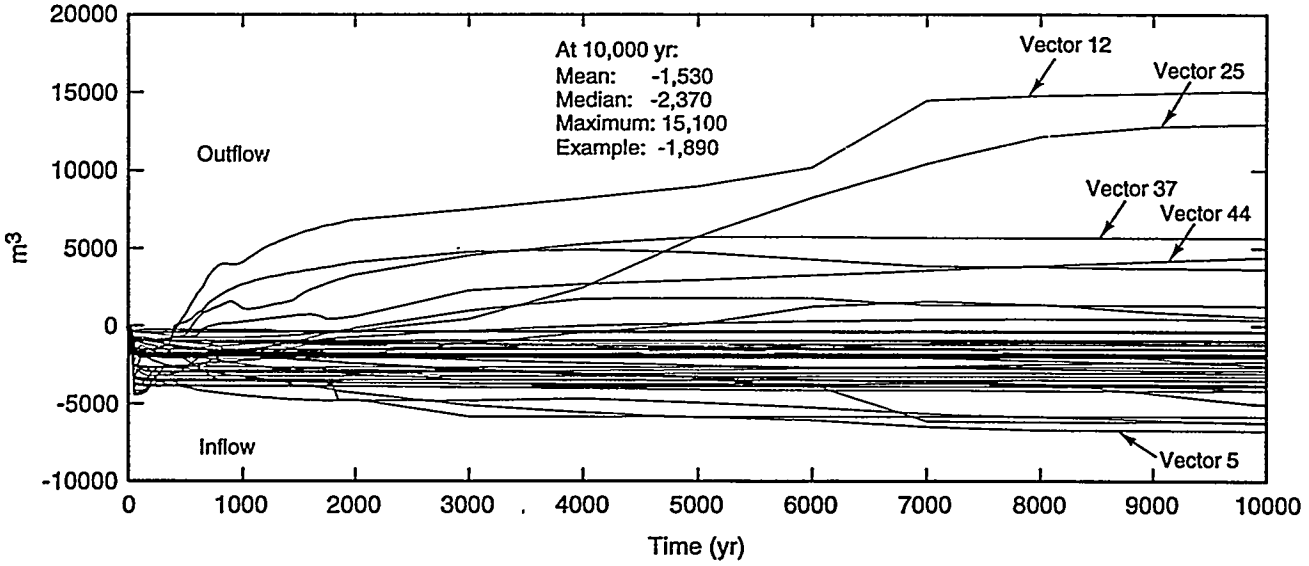

TRI-6342-4253-0

Figure 9. Net Brine Flow Out of (or Into) the Repository.

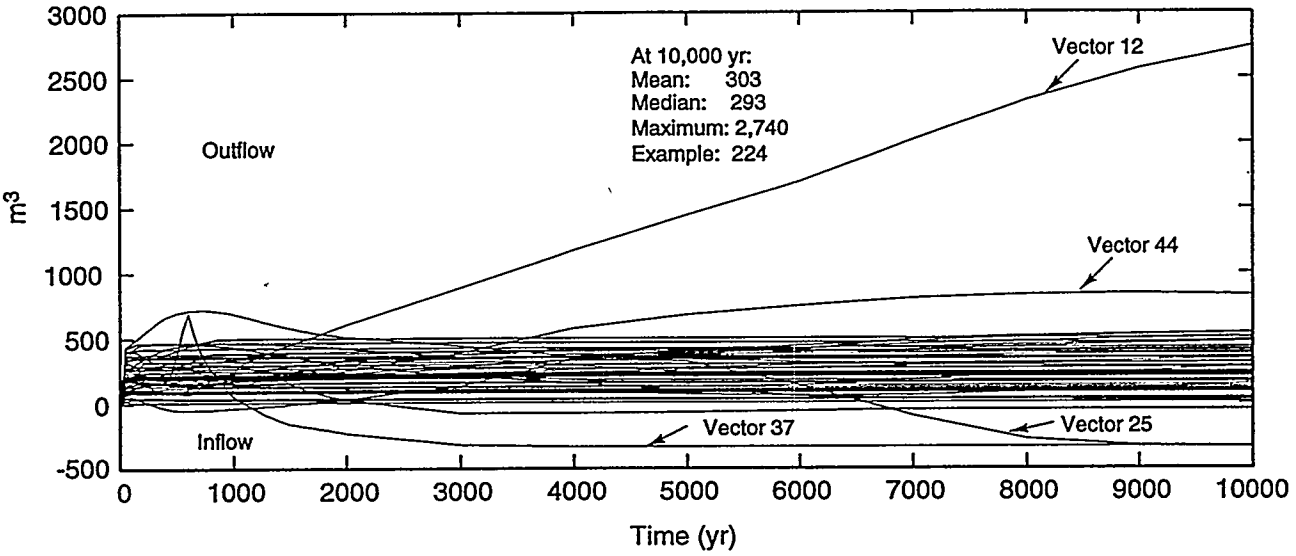

Figure 10. Net Brine Flow Out of (or Into) the Panel.

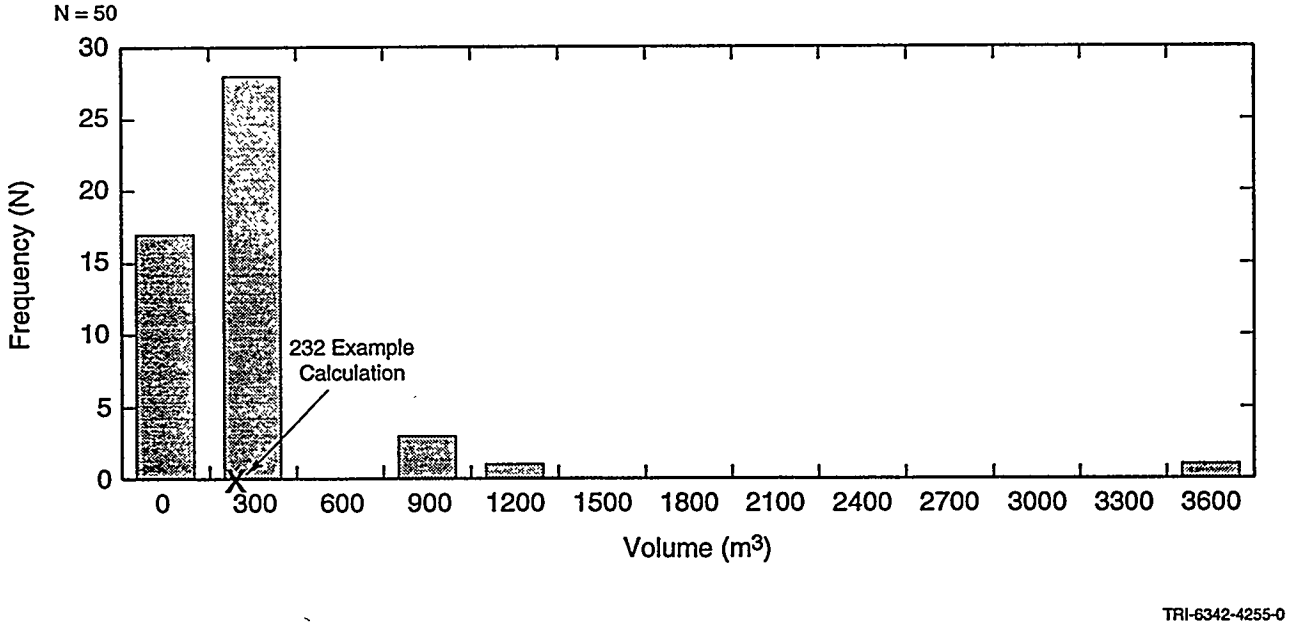

Figure 11. Brine Outflow from Panel After 10,000 yr.

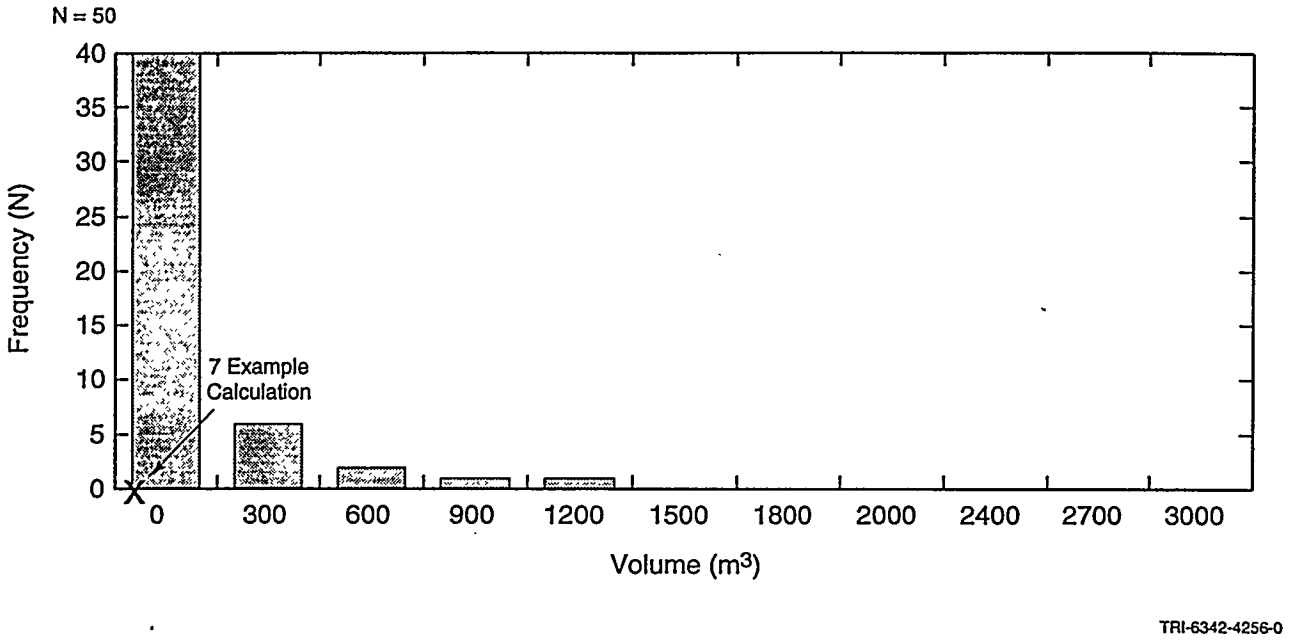

Figure 12. Brine Inflow to Panel After 10,000 yr.

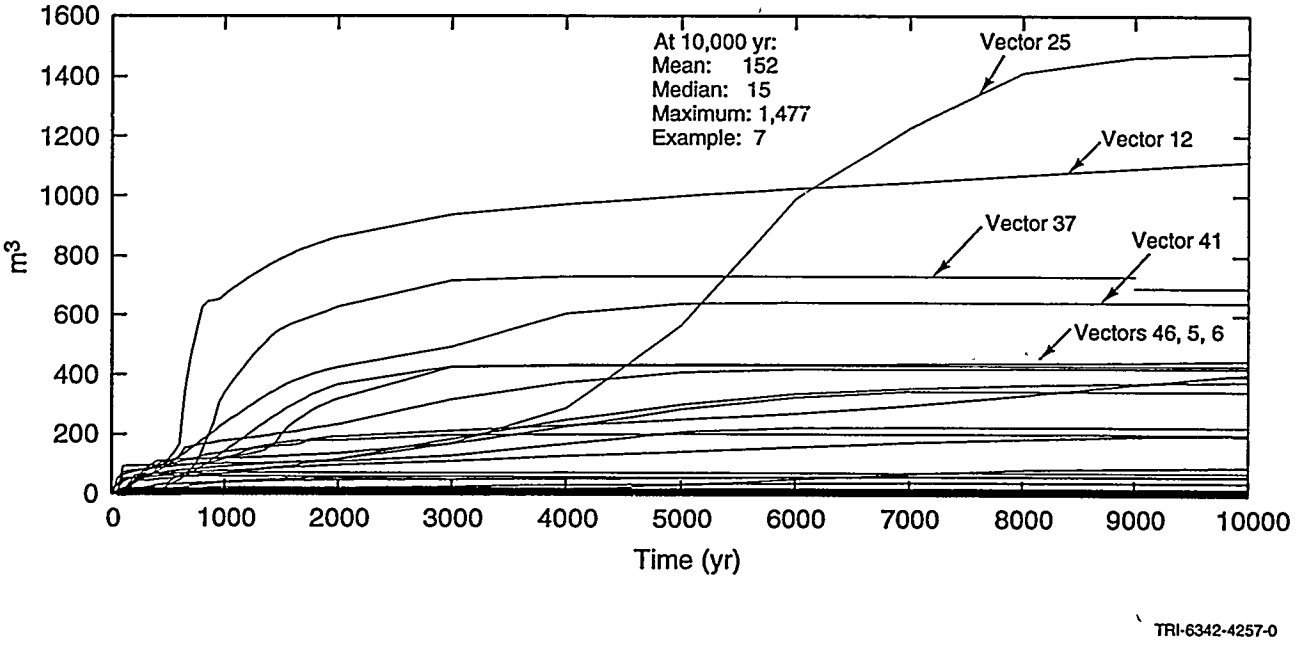

Figure 13. Total Brine Flowing Into the Panel.

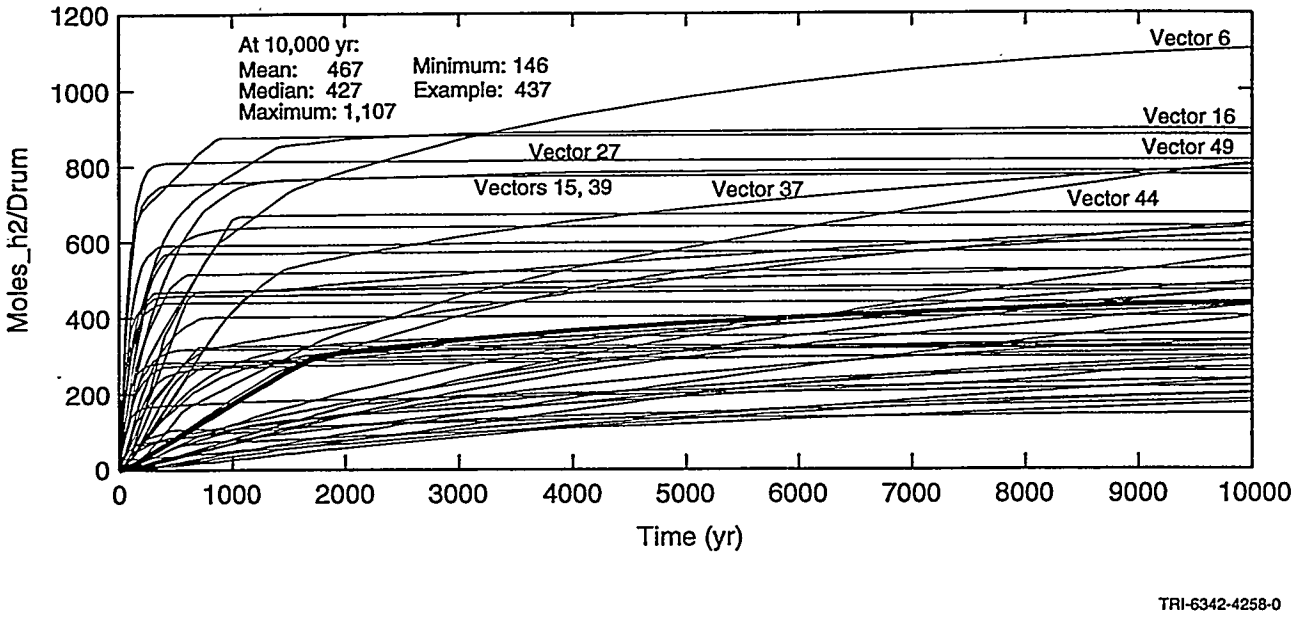

Figure 14. Total Gas Generated in the Entire Repository.

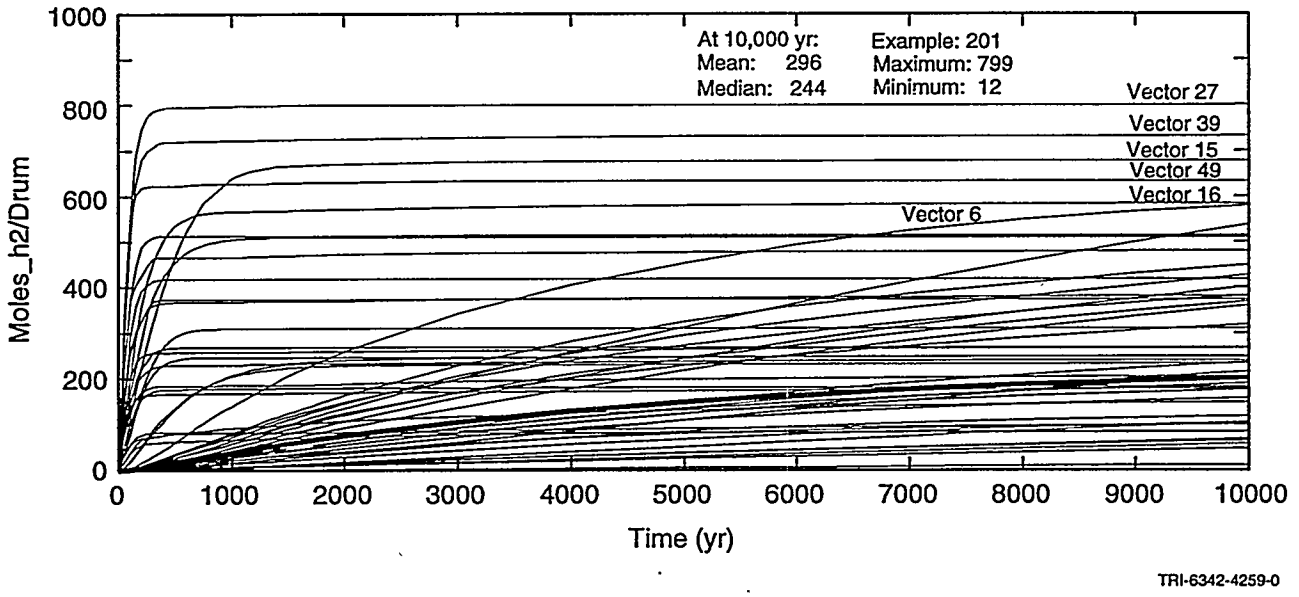

Figure 15. Total Gas Generated from Corrosion in the Entire Repository.

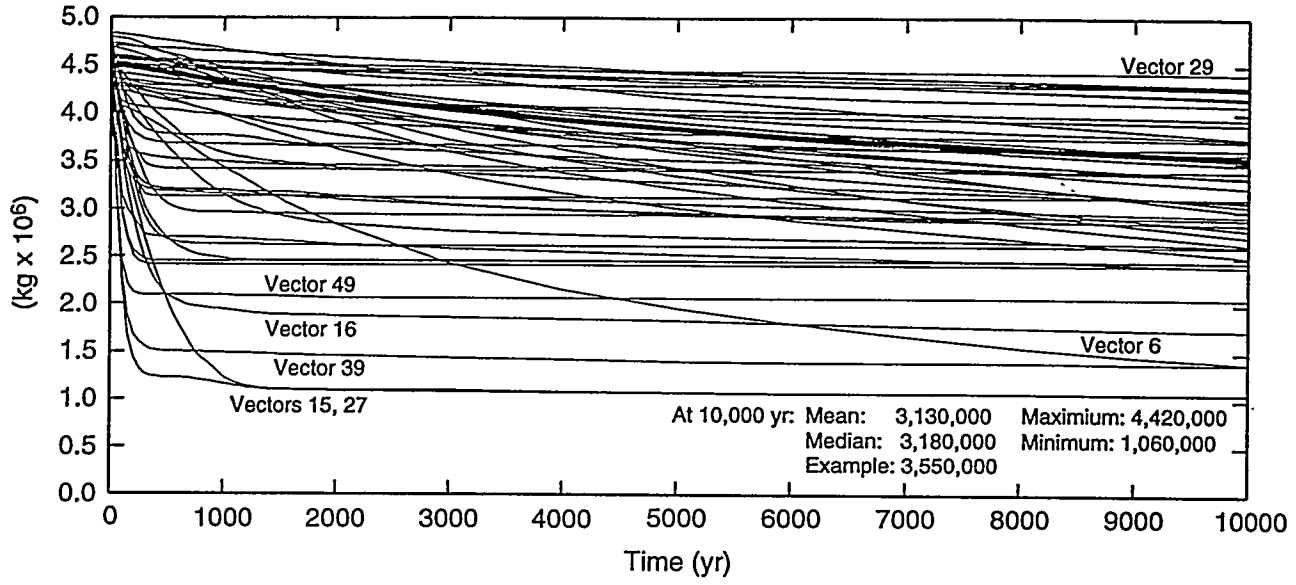

TRI-6342-4260-0

Figure 16. Ferrous Metals in the Panel.

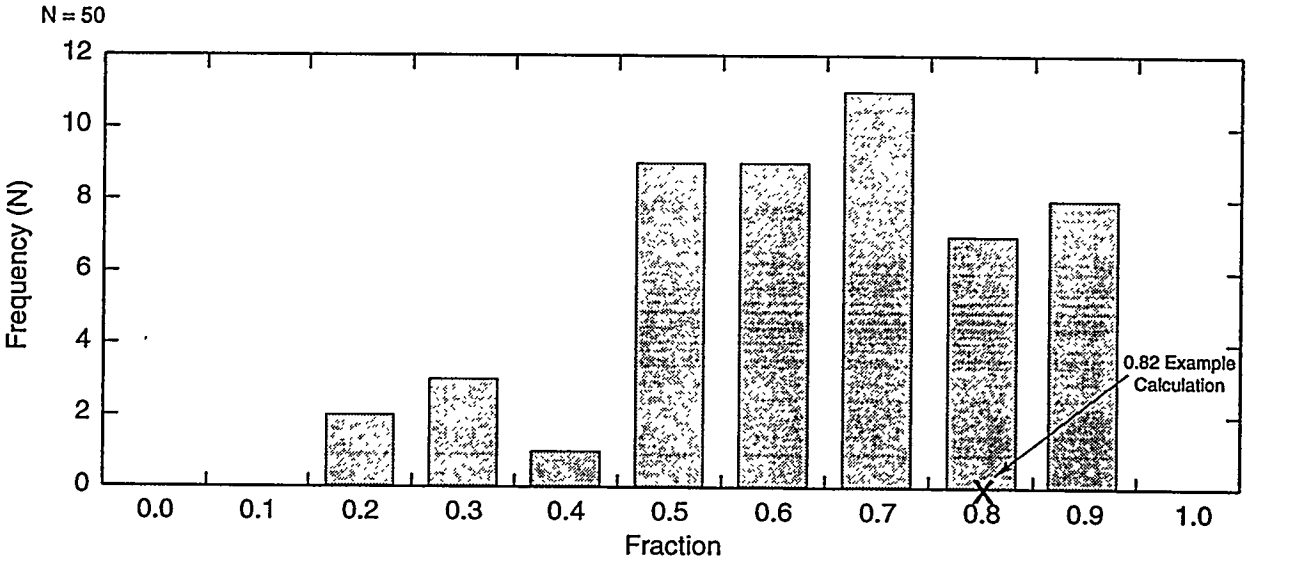

TRI-6342-4261-0

Figure 17. Ferrous Metal Remaining in Panel After 10,000 yr.

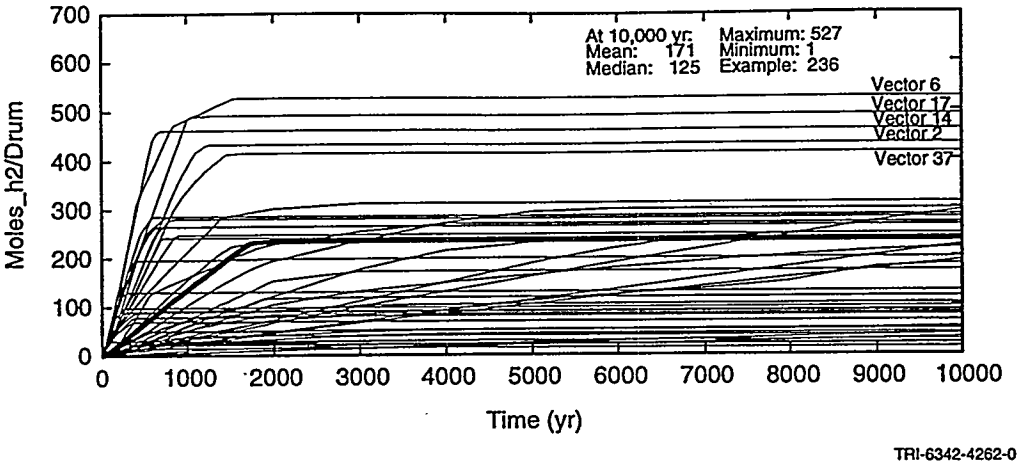

Figure 18. Total Gas Generated from Biodegradation in the Entire Repository.

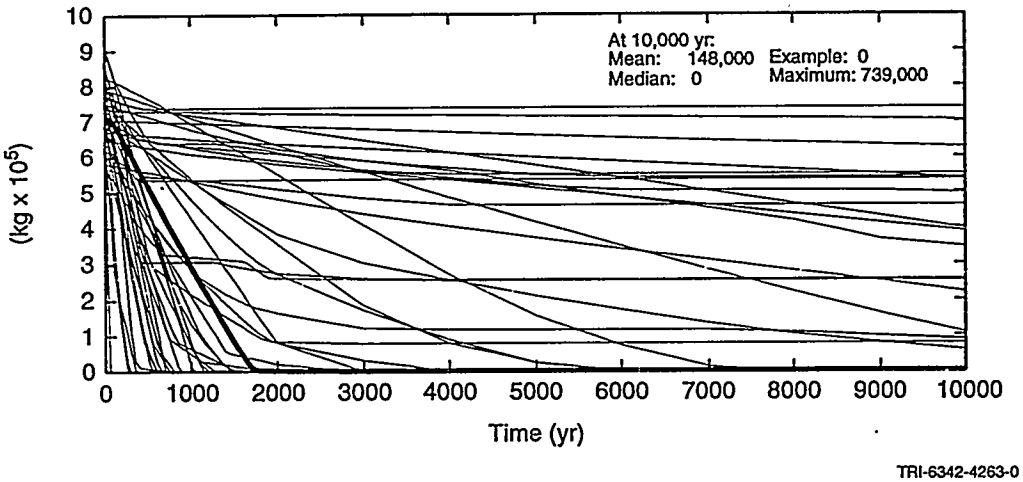

Figure 19. Cellulosics in the Panel.

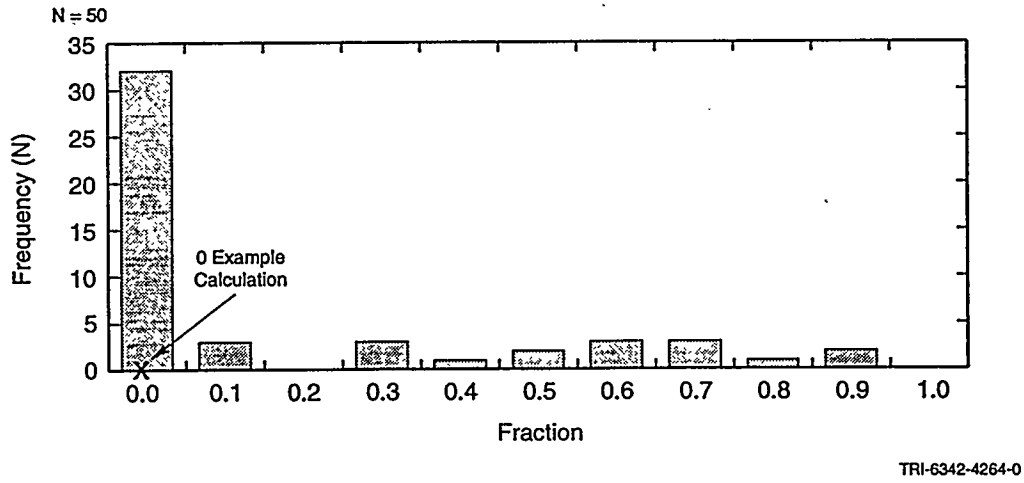

Figure 20. Cellulosics Remaining in Panel After 10,000 yr.

Table 7. Gas Migration Distances.

		Gas Migration							
	Sampled Value	Outward (m)							Upward (m)
Vector #	S_{gr}	K_r Model	MB139 S.	MB139 N.	Anh AB S.	Anh AB N.	MB138 S.	MB138 N.	Shaft
1	0.061	VG/P	2,400	151	2,400	2,400	1,046	2,400	116
2	0.181	B-C	90	0	1,158	1,032	1,004	1,196	15
3	0.134	B-C	664	0	905	723	10	778	31
4	0.112	B-C	0	0	0	0	0	0	0
5	0.122	B-C	0	0	50	0	0	0	0
6	0.278	VG/P	2,401	150	2,403	2,401	2,403	2,403	15
7	0.196	VG/P	2,404	2,400	2,405	2,403	2,405	2,403	75
8	0.078	B-C	0	0	0	0	0	0	0
9	0.142	B-C	32	0	650	485	650	650	0
10	0.391	B-C	301	0	660	660	41	596	65
11	0.327	B-C	0	0	32	0	0	0	2
12	0.380	B-C	0	0	1,183	769	857	999	4
13	0.222	B-C	317	0	651	407	728	803	7
14	0.291	B-C	0	0	739	0	0	71	0
15	0.344	VG/P	2,400	150	2,400	2,400	2,400	2,400	0
16	0.347	B-C	877	0	1,044	1,006	1,157	1,152	111
17	0.068	B-C	1,844	0	2,400	2,400	2,400	2,400	39
18	0.022	B-C	2,400	0	2,400	0	1,811	2,400	0
19	0.175	B-C	36	0	820	0	0	98	17
20	0.265	B-C	0	0	0	0	0	0	0
21	0.259	VG/P	2,404	650	2,405	2,403	2,400	2,403	0
22	0.283	B-C	43	0	177	158	0	7	0
23	0.366	VG/P	2,400	0	2,401	2,400	2,400	2,400	20
24	0.308	B-C	181	0	318	275	8	184	0
25	0.094	B-C	1	0	86	0	0	0	0
26	0.039	B-C	0	0	5	0	0	0	0
27	0.027	B-C	2,400	0	2,400	2,400	2,400	2,400	33
28	0.004	VG/P	0	0	2,517	2,409	1,678	2,401	0
29	0.086	B-C	0	0	157	84	0	6	0
30	0.100	VG/P	2,403	0	2,404	2,401	2,401	2,400	0
31	0.051	VG/P	650	0	1,255	779	738	940	4
32	0.146	B-C	835	0	1,286	1,224	652	900	5
33	0.165	B-C	912	0	1,567	831	790	1,332	8
34	0.246	B-C	0	0	699	0	0	50	3
35	0.188	VG/P	2,400	0	2,400	715	650	667	4
36	0.232	VG/P	650	0	652	652	0	50	0
37	0.011	B-C	682	0	2,402	2,400	2,401	2,400	63
38	0.297	B-C	0	0	1,897	0	1	960	0
39	0.376	VG/P	2,401	152	2,403	2,402	2,400	2,403	58
40	0.208	B-C	924	0	1,129	926	817	1,124	2
41	0.317	B-C	145	0	1,267	933	545	691	0
42	0.252	B-C	36	0	381	0	0	5	0
43	0.156	B-C	650	0	657	652	0	669	2
44	0.043	VG/P	0	0	2,403	2,401	2,403	2,403	26
45	0.333	B-C	0	0	4	1	0	0	0
46	0.238	B-C	49	0	1,638	59	1,046	1,213	109
47	0.392	VG/P	2,400	0	2,400	2,400	650	2,400	5
48	0.117	VG/P	2,401	650	2,401	2,400	652	2,400	0
49	0.358	B-C	882	0	1,317	29	40	798	6
50	0.204	VG/P	2,401	650	2,401	2,400	650	2,400	45
Mean	0.201	N/A	888	99	1,315	1,016	853	1,135	18
Median	0.200	N/A	483	0	1,219	719	650	920	3
Maximum	0.392	N/A	2,404	2,400	2,517	2,409	2,405	2,403	116
Example	0.200	B-C	667	0	866	717	571	713	4

Vector = 6
S_{gr} = 0.278
S_{br} = 0.0101
Lambda = 1.39
S_b @ S_{gr} = 0.722

Brine Sat	Eff Sat (SE)	K_{rg}	K_{rw}
0	-0.010203	1	0
0.0101	0	1	0
0.05	0.0403071	0.975083	1.09E-06
0.1	0.0908173	0.935603	2.68E-05
0.15	0.1413274	0.889475	0.000154
0.2	0.1918376	0.838117	0.00052
0.25	0.2423477	0.782574	0.001321
0.3	0.2928579	0.723727	0.002828
0.35	0.343368	0.662372	0.005388
0.4	0.3938782	0.599258	0.009443
0.45	0.4443883	0.535109	0.015547
0.5	0.4948985	0.470643	0.024399
0.55	0.5454086	0.406584	0.036874
0.6	0.5959188	0.34368	0.054091
0.62	0.6161228	0.319014	0.062617
0.65	0.6464289	0.282708	0.077502
0.7	0.6969391	0.224502	0.109038
0.75	0.7474492	0.169971	0.15137
0.8	0.7979594	0.120142	0.208397
0.85	0.8484695	0.07622	0.286295
0.9	0.8989797	0.039725	0.39625
0.95	0.9494898	0.012822	0.564516
1	1	0	1

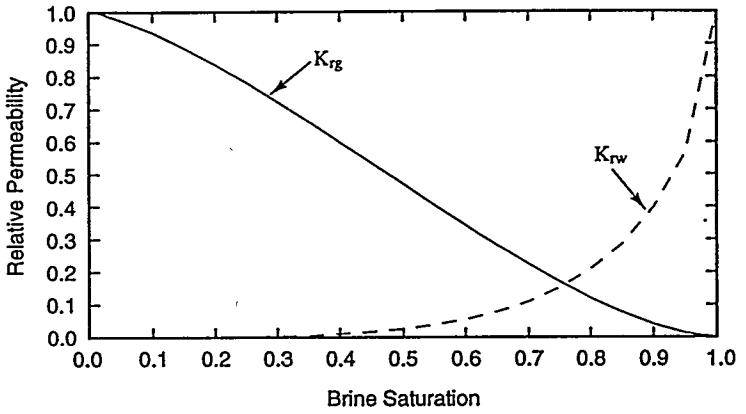

TRI-6342-4265-0

Figure 21. Van Genuchten/Parker Brine-Water Relative Permeability Curves for Vector Number 6.

Vector = 16
S_{gr} = 0.347
S_{br} = 0.085
Lambda = 2.3
S_b @ S_{gr} = 0.653

Brine Sat	Eff Sat (SE)	K_{rg}	K_{rw}
0	-0.092896	1	0
0.05	-0.038251	1	0
0.085	0	1	0
0.1	0.0163934	0.946819	1.23E-07
0.15	0.0710383	0.770597	3.6E-05
0.2	0.1256831	0.60395	0.000327
0.25	0.1803279	0.453488	0.001322
0.3	0.2349727	0.323421	0.003682
0.35	0.2896175	0.216152	0.00827
0.4	0.3442623	0.132504	0.016142
0.45	0.3989071	0.071853	0.028546
0.5	0.4535519	0.032206	0.046913
0.55	0.5081967	0.010262	0.072857
0.6	0.5628415	0.001457	0.108169
0.625	0.5901639	0.000219	0.129946
0.653	0.620765	0	0.158022
0.7	0.6721311	0	0.214942
0.75	0.726776	0	0.290858
0.8	0.7814208	0	0.385045
0.85	0.8360656	0	0.500154
0.9	0.8907104	0	0.639002
0.95	0.9453552	0	0.804569
1	1	0	1

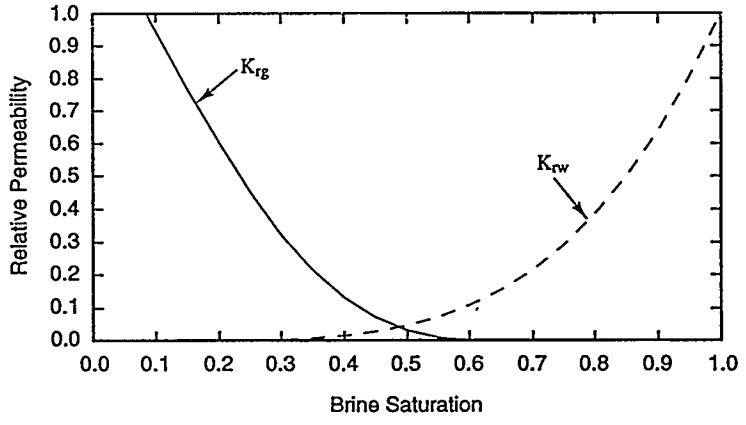

TRI-6342-4266-0

Figure 22. Brooks-Corey Brine-Water Relative Permeability Curves for Vector Number 16.

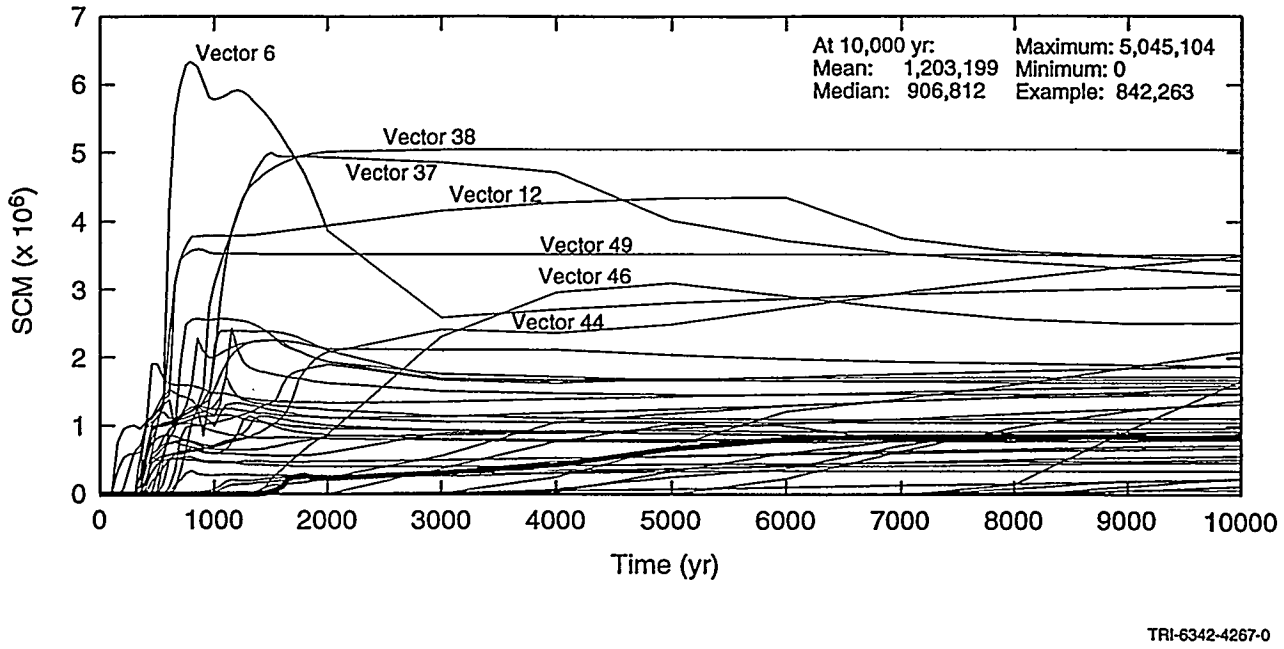

Figure 23. Cumulative Gas Flow Entering Anhydrite A & B South from the Repository Interface.

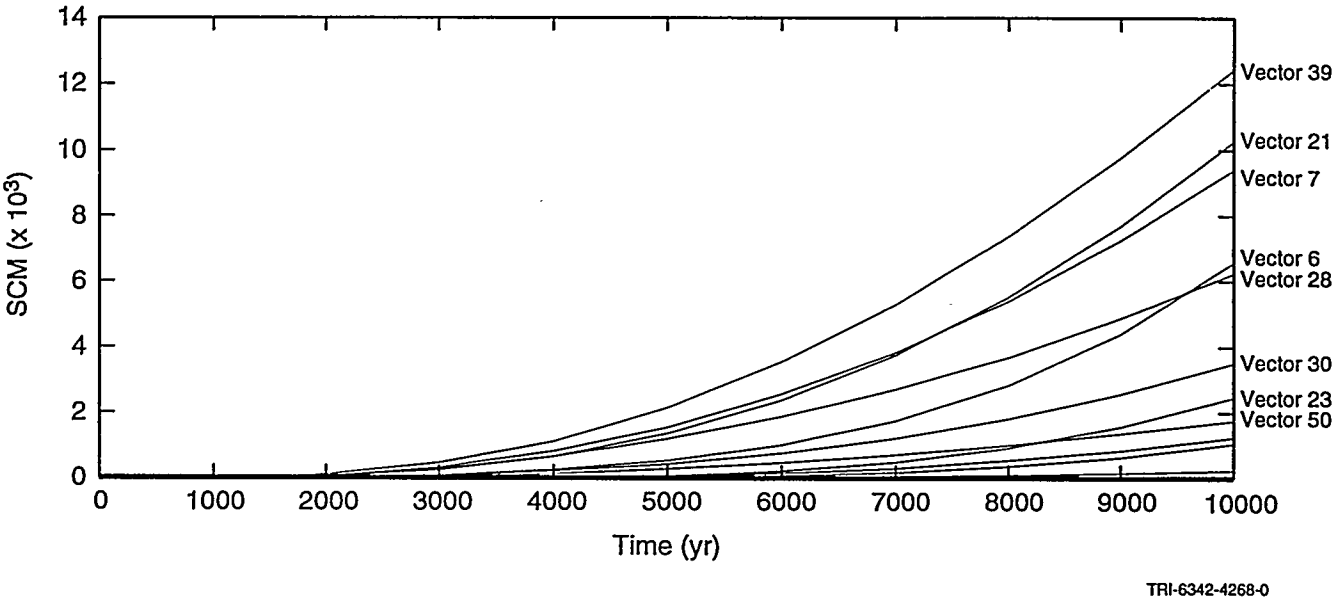

Figure 24. Cumulative Flow of Gas Out Anhydrite A & B South at 2.4 km Boundary.

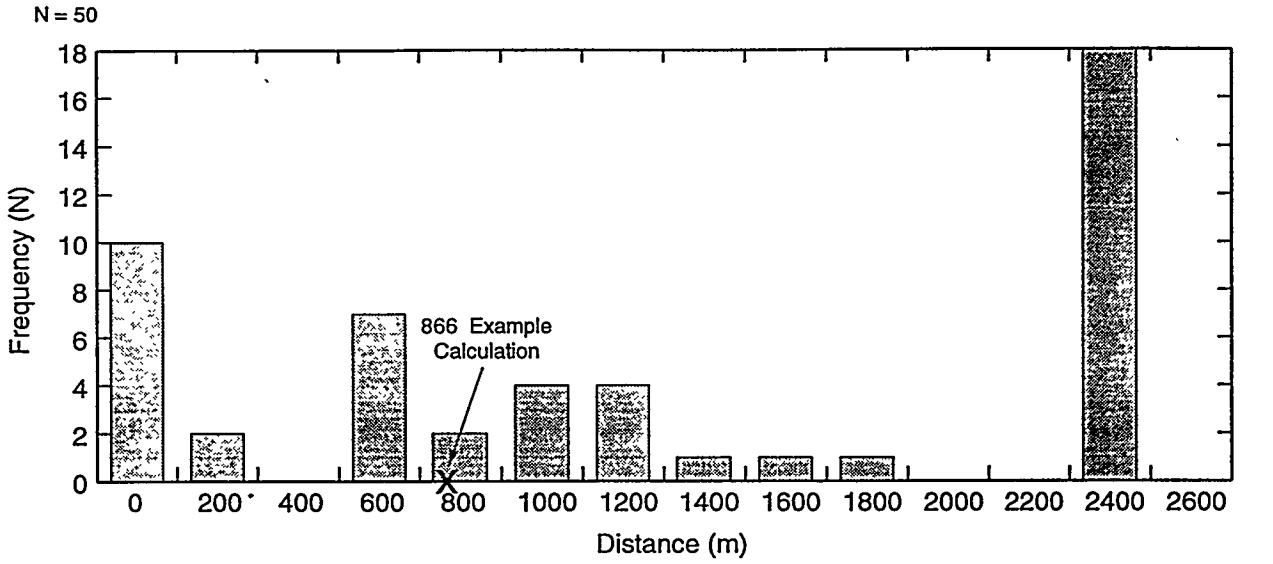

TRI-6342-4269-0

Figure 25. Gas Migration Distance: Anhydrite A & B South.

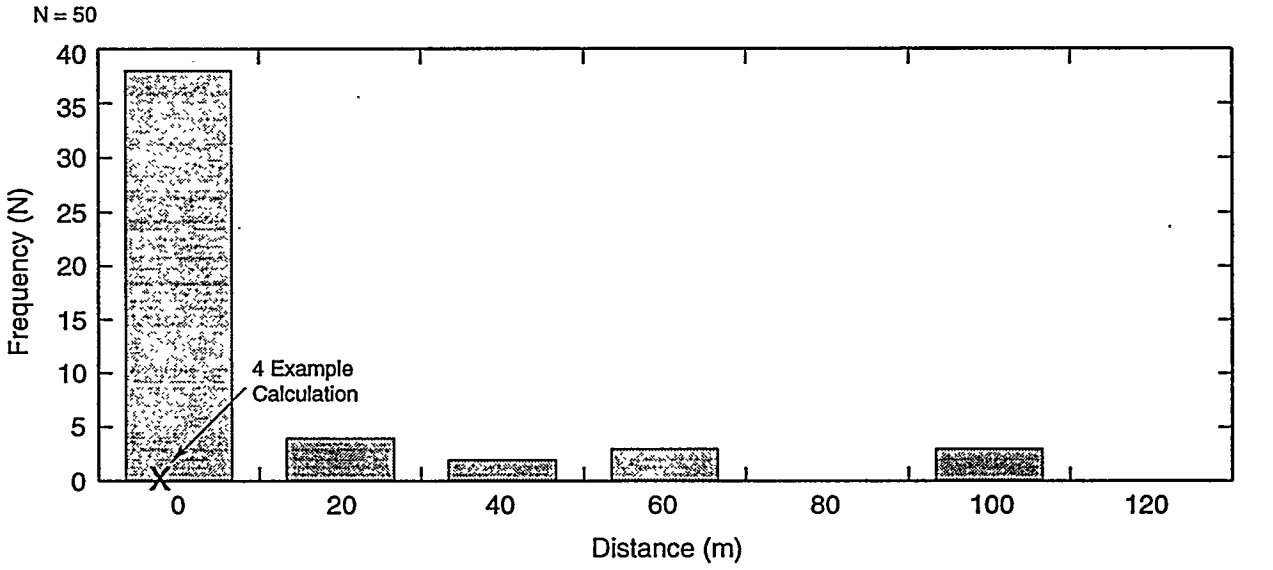

TRI-6342-4270-0

Figure 26. Gas Migration Distance: Up Through the Shaft.

Rip Anderson

Copy to:
6115/MS1324 P. B. Davies
6115/MS1324 R. L. Beuheim
6115/MS1324 S. M. Howarth
6115/MS1324 S. W. Webb
6115/MS1324 C. Larson (INTERA)
6117/MS0751 W. R. Wawersik
6119/MS1320 E. J. Nowak
6121/MS1322 J. R. Tillerson
6303/MS1335 W. E. Weart
6305/MS1335 S. A. Goldstein
6307/MS1345 P. A. Davis
6307/MS1345 A. R. Lappin
6319/MS1333 R. R. Richards
6342/MS1328 J. Bean
6342/MS1328 M. G. Marietta
6342/MS1328 L. C. Sanchez
6342/MS1328 J. Schreiber
6342/MS1328 D. Stoelzel
6342/MS1328 P. N. Swift
6345/MS1341 R. C. Lincoln
6347/MS1341 D. R. Schafer
6348/MS1341 J.T. Holmes
6348/MS1341 L. H. Brush
6743/MS1395 V. Harper-Slaboszewicz
6352/MS1330 SWCF WBS 1.1.6.2.5 PA
6342/MS1328 P. Vaughn

This page intentionally left blank

WIPP
UC721 - DISTRIBUTION LIST

Federal Agencies

US Department of Energy (6)
Office of Civilian Radioactive Waste Mgmt.
Attn: Deputy Director, RW-2
Associate Director, RW-10/50
Office of Prog. & Resources Mgmt.
Office of Contract Business Mgmt.
Director, RW-22
Analysis & Verification Division
Associate Director, RW-30
Office of Systems & Compliance
Associate Director, RW-40
Office of Storage & Transportation
Director, RW-4/5
Office of Strategic Planning and International Programs
Office of External Relations
Forrestal Building
Washington, DC 20585

US Department of Energy
Albuquerque Operations Office
Attn: National Atomic Museum Library
P.O. Box 5400
Albuquerque, NM 87185-5400

US Department of Energy
Research & Waste Management Division
Attn: Director
P.O. Box E
Oak Ridge, TN 37831

US Department of Energy (5)
Carlsbad Area Office
Attn: G. Dials
D. Galbraith
M. McFadden
R. Lark
J. A. Mewhinney
P.O. Box 3090
Carlsbad, NM 88221-3090

US Department of Energy
Attn: E. Young
Room E-178
GAO/RCED/GTN
Washington, DC 20545

US Department of Energy
Office of Environmental Restoration and Waste Management
Attn: J. Lytle, EM-30
Forrestal Building
Washington, DC 20585-0002

US Department of Energy (3)
Office of Environmental Restoration and Waste Management
Attn: M. Frei, EM-34, Trevion II
Washington, DC 20585-0002

US Department of Energy
Office of Environmental Restoration and Waste Management
Attn: S. Schneider, EM-342, Trevion II
Washington, DC 20585-0002

US Department of Energy (2)
Office of Environment, Safety & Health
Attn: C. Borgstrom, EH-25
R. Pelletier, EH-231
Washington, DC 20585

US Department of Energy (2)
Idaho Operations Office
Fuel Processing & Waste Mgmt. Division
785 DOE Place
Idaho Falls, ID 83402

US Environmental Protection Agency (2)
Radiation Protection Programs
Attn: M. Oge
ANR-460
Washington, DC 20460

Boards

Defense Nuclear Facilities Safety Board
Attn: D. Winters
625 Indiana Ave. NW, Suite 700
Washington, DC 20004

Nuclear Waste Technical Review Board (2)
Attn: Chairman
S. J. S. Parry
1100 Wilson Blvd., Suite 910
Arlington, VA 22209-2297

State Agencies

Attorney General of New Mexico
P.O. Drawer 1508
Santa Fe, NM 87504-1508

Environmental Evaluation Group (3)
Attn: Library
7007 Wyoming NE
Suite F-2
Albuquerque, NM 87109

NM Energy, Minerals, and Natural Resources Department
Attn: Library
2040 S. Pacheco
Santa Fe, NM 87505

NM Environment Department (3)
Secretary of the Environment
Attn: Mark Weidler
1190 St. Francis Drive
Santa Fe, NM 87503-0968

NM Bureau of Mines & Mineral Resources
Socorro, NM 87801

NM Environment Department
WIPP Project Site
Attn: P. McCasland
P.O. Box 3090
Carlsbad, NM 88221

Laboratories/Corporations

Battelle Pacific Northwest Laboratories
Attn: R. E. Westerman, MSIN P8-44
Battelle Blvd.
Richland, WA 99352

INTERA, Inc. (10)
Attn: G. A. Freeze
1650 University Blvd. NE, Suite 300
Albuquerque, NM 87102

INTERA, Inc. (5)
Attn: J. F. Pickens
6850 Austin Center Blvd., Suite 300
Austin, TX 78731

INTERA, Inc.
Attn: S. Mishra
101 Convention Center Drive
MS 423
Las Vegas, NV 89109

INTERA, Inc.
Attn: W. Stensrud
P.O. Box 2123
Carlsbad, NM 88221

Los Alamos National Laboratory
Attn: B. Erdal, INC-12
P.O. Box 1663
Los Alamos, NM 87544

RE/SPEC, Inc
Attn: Angus Robb
4775 Indian School NE, Suite 300
Albuquerque, NM 87110-3927

RE/SPEC, Inc
Attn: J. L. Ratigan
P.O. Box 725
Rapid City, SD 57709

Southwest Research Institute (2)
Center for Nuclear Waste Regulatory Analysis
Attn: P. K. Nair
6220 Culebra Road
San Antonio, TX 78228-0510

Tech Reps, Inc. (4)
Attn: J. Chapman (2)
T. Peterson (2)
5000 Marble NE, Suite 222
Albuquerque, NM 87110

Lawrence Berkeley Laboratory (2)
Attn: K. Pruess
G. Moridis
Earth Sciences Division
MS 50E
Berkeley, CA 94720

Westinghouse Electric Corporation (5)
Attn: J. Epstein
J. Lee
B. A. Howard
R. Kehrman
Library
P.O. Box 2078
Carlsbad, NM 88221

S. Cohen & Associates
Attn: Bill Thurber
1355 Beverly Road
McLean, VA 22101

National Academy of Sciences, WIPP Panel

Howard Adler
Oxyrase, Incorporated
7327 Oak Ridge Highway
Knoxville, TN 37931

Ina Alterman
Board of Radioactive Waste Management
GF456
2101 Constitution Ave.
Washington, DC 20418

Rodney C. Ewing
Department of Geology
University of New Mexico
Albuquerque, NM 87131

Charles Fairhurst
Department of Civil and Mineral Engineering
University of Minnesota
500 Pillsbury Dr. SE
Minneapolis, MN 55455-0220

B. John Garrick
PLG Incorporated
4590 MacArthur Blvd., Suite 400
Newport Beach, CA 92660-2027

Leonard F. Konikow
US Geological Survey
431 National Center
Reston, VA 22092

Carl A. Anderson, Director
Board of Radioactive Waste Management
National Research Council
HA 456
2101 Constitution Ave. NW
Washington, DC 20418

Christopher G. Whipple
ICF Kaiser Engineers
1800 Harrison St., 7th Floor
Oakland, CA 94612-3430

John O. Blomeke
720 Clubhouse Way
Knoxville, TN 37909

Sue B. Clark
University of Georgia
Savannah River Ecology Lab
P.O. Drawer E
Aiken, SC 29802

Konrad B. Krauskopf
Department of Geology
Stanford University
Stanford, CA 94305-2115

Della Roy
Pennsylvania State University
217 Materials Research Lab
Hastings Road
University Park, PA 16802

David A. Waite
CH_2 M Hill
P.O. Box 91500
Bellevue, WA 98009-2050

Thomas A. Zordon
Zordan Associates, Inc.
3807 Edinburg Drive
Murrysville, PA 15668

Universities

University of New Mexico
Geology Department
Attn: Library
141 Northrop Hall
Albuquerque, NM 87131

University of Washington
College of Ocean & Fishery Sciences
Attn: G. R. Heath
583 Henderson Hall, HN-15
Seattle, WA 98195

Libraries

Thomas Brannigan Library
Attn: D. Dresp
106 W. Hadley St.
Las Cruces, NM 88001

Government Publications Department
Zimmerman Library
University of New Mexico
Albuquerque, NM 87131

New Mexico Junior College
Pannell Library
Attn: R. Hill
Lovington Highway
Hobbs, NM 88240

New Mexico State Library
Attn: N. McCallan
325 Don Gaspar
Santa Fe, NM 87503

New Mexico Tech
Martin Speere Memorial Library
Campus Street
Socorro, NM 87810

WIPP Public Reading Room
Carlsbad Public Library
101 S. Halagueno St.
Carlsbad, NM 88220

Foreign Addresses

Studiecentrum Voor Kernenergie
Centre d'Energie Nucleaire
Attn: A. Bonne
SCK/CEN Boeretang 200
B-2400 Mol, BELGIUM

Atomic Energy of Canada, Ltd.
Whiteshell Laboratories
Attn: B. Goodwin
Pinawa, Manitoba, CANADA R0E 1L0

Francois Chenevier (2)
ANDRA
Route de Panorama Robert Schumann
B. P. 38
92266 Fontenay-aux-Roses, Cedex
FRANCE

Claude Sombret
Centre d'Etudes Nucleaires de la Vallee Rhone
CEN/VALRHO
S.D.H.A. B.P. 171
30205 Bagnols-Sur-Ceze, FRANCE

Commissariat a L'Energie Atomique
Attn: D. Alexandre
Centre d'Etudes de Cadarache
13108 Saint Paul Lez Durance Cedex
FRANCE

Bundesanstalt fur Geowissenschaften und
Rohstoffe
Attn: M. Langer
Postfach 510 153
D-30631 Hannover, GERMANY

Bundesministerium fur Forschung und
Technologie
Postfach 200 706
5300 Bonn 2, GERMANY

Institut fur Tieflagerung
Attn: K. Kuhn
Theodor-Heuss-Strasse 4
D-3300 Braunschweig, GERMANY

Gesellschaft fur Anlagen und Reaktorsicherheit
(GRS)
Attn: B. Baltes
Schwertnergasse 1
D-50667 Cologne, GERMANY

Physikalisch-Technische Bundesanstalt
Attn: P. Brenneke
Postfach 3345
D-3300 Braunschweig, GERMANY

Shingo Tashiro
Japan Atomic Energy Research Institute
Tokai-Mura, Ibaraki-Ken, 319-11
JAPAN

Netherlands Energy Research Foundation ECN
Attn: L. H. Vons
3 Westerduinweg
P.O. Box 1
1755 ZG Petten
THE NETHERLANDS

Svensk Karnbransleforsorjning AB
Attn: F. Karlsson
Project KBS (Karnbranslesakerhet)
Box 5864
S-102 48 Stockholm
SWEDEN

Nationale Genossenschaft fur die Lagerung
Radioaktiver Abfalle (2)
Attn: S. Vomvoris
P. Zuidema
Hardstrasse 73
CH-5430 Wettingen
SWITZERLAND

AEA Technology
Attn: J. H. Rees
D5W/29 Culham Laboratory
Abington, Oxfordshire OX14 3DB
UNITED KINGDOM

AEA Technology
Attn: W. R. Rodwell
044/A31 Winfrith Technical Centre
Dorchester, Dorset DT2 8DH
UNITED KINGDOM

AEA Technology
Attn: J. E. Tinson
B4244 Harwell Laboratory
Didcot, Oxfordshire OX11 ORA
UNITED KINGDOM

D. R. Knowles
British Nuclear Fuels, plc
Risley, Warrington, Cheshire WA3 6AS
1002607 UNITED KINGDOM

INTERA Switzerland (3)
Attn: R. Senger
Mellingerstrasse 207
CH-5405 Baden
SWITZERLAND

Internal

MS	Org.	
0827	1502	P. J. Hommert
1324	6115	P. B. Davies (6)
1324	6115	S. W. Webb
1324	6115	A. R. Lappin
1324	6115	T. Christian-Frear
1320	6119	E. J. Nowak
1332	6121	J. R. Tillerson
1395	6700	P. Brewer
1335	6705	M. Chu
1395	6707	M. Marietta
1335	6303	W. Weart
1395	6701	L. Shephard
1341	6706	A. L. Stevens
1395	6701	L. Shephard
1341	6747	K. W. Larson (6)
1341	6748	B. M. Butcher
1328	6749	D. R. Anderson
1328	6749	P. Vaughn
1395	6743	V. H. Slaboszewicz
1341	6747	D. R. Schafer
1341	6748	J. T. Holmes
1328	6741	H. N. Jow
1330	6352	C. B. Michaels (2)
1330	6352	NWM Library (20)
9018	8523-2	Central Technical Files
0899	4414	Technical Library (5)
0619	12613	Print Media
0100	7613-2	Document Processing (2) for DOE/OSTI